Unclassified **NEA/CSNI/R(2005)5/VOL3**

Organisation de Coopération et de Développement Economiques
Organisation for Economic Co-operation and Development **06-Sep-2005**

English text only

NUCLEAR ENERGY AGENCY
COMMITTEE ON THE SAFETY OF NUCLEAR INSTALLATIONS

NEA/CSNI/R(2005)5/VOL3
Unclassified

INTERNATIONAL STANDARD PROBLEM NO. 48
CONTAINMENT CAPACITY

Appendices H to L

The complete document is only available in pdf format.

JT00188857

English text only

ORGANISATION FOR ECONOMIC CO-OPERATION AND DEVELOPMENT

Pursuant to Article 1 of the Convention signed in Paris on 14th December 1960, and which came into force on 30th September 1961, the Organisation for Economic Co-operation and Development (OECD) shall promote policies designed:

- to achieve the highest sustainable economic growth and employment and a rising standard of living in member countries, while maintaining financial stability, and thus to contribute to the development of the world economy;
- to contribute to sound economic expansion in member as well as non-member countries in the process of economic development; and
- to contribute to the expansion of world trade on a multilateral, non-discriminatory basis in accordance with international obligations.

The original member countries of the OECD are Austria, Belgium, Canada, Denmark, France, Germany, Greece, Iceland, Ireland, Italy, Luxembourg, the Netherlands, Norway, Portugal, Spain, Sweden, Switzerland, Turkey, the United Kingdom and the United States. The following countries became members subsequently through accession at the dates indicated hereafter: Japan (28th April 1964), Finland (28th January 1969), Australia (7th June 1971), New Zealand (29th May 1973), Mexico (18th May 1994), the Czech Republic (21st December 1995), Hungary (7th May 1996), Poland (22nd November 1996), Korea (12th December 1996) and the Slovak Republic (14 December 2000). The Commission of the European Communities takes part in the work of the OECD (Article 13 of the OECD Convention).

NUCLEAR ENERGY AGENCY

The OECD Nuclear Energy Agency (NEA) was established on 1st February 1958 under the name of the OEEC European Nuclear Energy Agency. It received its present designation on 20th April 1972, when Japan became its first non-European full member. NEA membership today consists of 28 OECD member countries: Australia, Austria, Belgium, Canada, the Czech Republic, Denmark, Finland, France, Germany, Greece, Hungary, Iceland, Ireland, Italy, Japan, Luxembourg, Mexico, the Netherlands, Norway, Portugal, Republic of Korea, the Slovak Republic, Spain, Sweden, Switzerland, Turkey, the United Kingdom and the United States. The Commission of the European Communities also takes part in the work of the Agency.

The mission of the NEA is:

- to assist its member countries in maintaining and further developing, through international co-operation, the scientific, technological and legal bases required for a safe, environmentally friendly and economical use of nuclear energy for peaceful purposes, as well as
- to provide authoritative assessments and to forge common understandings on key issues, as input to government decisions on nuclear energy policy and to broader OECD policy analyses in areas such as energy and sustainable development.

Specific areas of competence of the NEA include safety and regulation of nuclear activities, radioactive waste management, radiological protection, nuclear science, economic and technical analyses of the nuclear fuel cycle, nuclear law and liability, and public information. The NEA Data Bank provides nuclear data and computer program services for participating countries.

In these and related tasks, the NEA works in close collaboration with the International Atomic Energy Agency in Vienna, with which it has a Co-operation Agreement, as well as with other international organisations in the nuclear field.

COMMITTEE ON THE SAFETY OF NUCLEAR INSTALLATIONS

The NEA Committee on the Safety of Nuclear Installations (CSNI) is an international committee made up of senior scientists and engineers, with broad responsibilities for safety technology and research programmes, and representatives from regulatory authorities. It was set up in 1973 to develop and co-ordinate the activities of the NEA concerning the technical aspects of the design, construction and operation of nuclear installations insofar as they affect the safety of such installations.

The committee's purpose is to foster international co-operation in nuclear safety amongst the OECD member countries. The CSNI's main tasks are to exchange technical information and to promote collaboration between research, development, engineering and regulatory organisations; to review operating experience and the state of knowledge on selected topics of nuclear safety technology and safety assessment; to initiate and conduct programmes to overcome discrepancies, develop improvements and research consensus on technical issues; to promote the coordination of work that serve maintaining competence in the nuclear safety matters, including the establishment of joint undertakings.

The committee shall focus primarily on existing power reactors and other nuclear installations; it shall also consider the safety implications of scientific and technical developments of new reactor designs.

In implementing its programme, the CSNI establishes co-operative mechanisms with NEA's Committee on Nuclear Regulatory Activities (CNRA) responsible for the program of the Agency concerning the regulation, licensing and inspection of nuclear installations with regard to safety. It also co-operates with NEA's Committee on Radiation Protection and Public Health (CRPPH), NEA's Radioactive Waste Management Committee (RWMC) and NEA's Nuclear Science Committee (NSC) on matters of common interest.

Foreword

The International Standard Problem No.48- Containment Capacity report NEA/CSNI/R(2005)5 is divided into three Volumes:

While Volume 1 is the Synthesis Report, Volumes 2 and 3 contain the contributions of participating organizations for both phases 2 and 3.

Table of Contents

Appendix H: Japan PCCV Research Group
Phase 2: no report available
Phase 3: H-1 to H-52

Page intentionally left blank

International Standard Problem No.48

Phase 3 Report

Analysis Results of a 1:4-Scale Prestressed Concrete Containment Vessel (PCCV) Model Subjected to Pressure and Thermal Loading

Prepared for ISP 48 final meeting in Lyon, France

April 4, 2005

Presented by

JAPC PCCV RESEARCH GROUP

The Japan Atomic Power Company
Obayashi Corporation
Mitsubishi Heavy Industries, Ltd.
Taisei Corporation

ANALYSIS RESULTS OF A 1:4-SCALE PRESTRESSED CONCRETE CONTAINMENT VESSEL SUBJECTED TO PRESSURE AND THERMAL LOADING

M. Ohba[1], T. Kawasato[1], A. Kato[1], A. Shimizu[2], T. Ogata[2], Y. Hino[2], T. Kitani[3] and Y. Murazumi[4]

1) The Japan Atomic Power Company
2) Obayashi Corporation
3) Mitsubishi Heavy Industries, Ltd.
4) Taisei Corporation

Abstract

This report describes the finite element analysis results of a 1:4-scale model of a prestressed concrete containment vessel (PCCV) subjected to pressure and thermal loading beyond the design basis and summarizes the modeling approach, the analysis results, the influence of thermal loading on the nonlinear behaviors of the model and the scaling issues for the thermal loading.

Two types of global analysis models used are as follows.

1) An axisymmetric model which idealizes a general portion at 135 degrees of azimuth
2) A 3D180-degree model which idealizes one half sector of a 1:4-scale model including openings

It was found that no steel materials have reached critical strains within this range of the conditions and the nonlinear behaviors of 1:4-scale model of PCCV are largely influenced by the substantial fluctuations of both the pressure and thermal loads.

1. Introduction

Static high-pressure tests (Limit State Test) on a 1:4-scale prestressed concrete containment vessel (PCCV) model were performed in September, 2000 by the Nuclear Power Engineering Corporation (NUPEC) of Japan and the U.S. Nuclear Regulatory Commission (NRC) [1]. The main objective of the present FE analysis is to evaluate the failure load of the PCCV as well as its failure mechanism when the PCCV model is subjected to pressure and thermal loading beyond the design basis.

Before and after the Test, Round Robin analysis meetings were held in order to improve the existing analysis methods for the nonlinear behaviors of PCCVs. The Japan PCCV research group participated in the meetings. For the meetings, many types of global and local analyses were carried out on the model to establish an analysis methodology that can predict the nonlinear behaviors of actual PCCVs subjected to increasing internal pressure. At the Posttest meeting, it had been confirmed that the analysis results demonstrated the nonlinear behaviors of the test results up to the ultimate state with good accuracy [2]-[3].

This report describes the finite element analysis results of a 1:4-scale model subjected to pressure and thermal loading beyond the design basis and summarizes the modeling approach, the influence of thermal loading on the nonlinear behaviors of the model and the scaling issues for the thermal loading.

Two types of global analysis models used are as follows.

1) An axisymmetric model which idealizes a general portion at 135 degrees of azimuth
2) A 3D180-degree model which idealizes one half sector of a 1:4-scale model including openings

The computer code used here is FINAL [4] using the finite element method, which has been developed by Obayashi Corporation for nonlinear analysis of reinforced concrete structures.

2. Numerical methods for analyses and analytical modeling

2.1 Numerical methods for analyses

In this research, all of the numerical analysis tasks were performed using the finite element method (FEM), taking material nonlinearity into account. All of the analyses were performed by two- and/or three-dimensional FEM, where a tangential incremental loading method and the Newton method for convergence criteria were adopted.

Global analyses to grasp global non-linear behaviors of a 1:4-scale PCCV model are as follows.

1) Axisymmetric model at 135 degree of azimuth.
2) Three-dimensional 180˚ shell model including E/H and A/L openings and buttresses.

The concrete was modeled using 8-node solid element in the axisymmetric model, or 4-node quadrilateral multi-layered shell element in the shell model. The rebars were represented with truss elements or orthogonal layers. The tendons were replaced with truss elements, and tendon friction elements which take into account the friction effects between concrete and tendons were adopted. The bond characteristics between the concrete and the rebars were assumed to be bonded perfectly. The liner was replaced with 4-node shell elements and a perfect bond between concrete and liner was assumed in the analyses. The prestressing forces of the tendons were considered in the analyses as an initial stress state.

The heat transfer FEM analyses for Case1 and Case2 were carried out on the assumption in the heat transfer analysis report [5]. The heat transfer FEM model for the axisymmetric analyses was the same model as the stress analysis, and one dimensional FEM models corresponding with each wall thickness were used for the three-dimensional shell analyses. It was confirmed that the results of the heat transfer analysis were consistent with the analysis results in the heat transfer analysis report [5].

Material constitutive models are as follows:

As for the concrete, the equivalent uniaxial stress-strain model proposed by Darwin et al. was adopted, and the smeared crack model was used. Kupfer's failure criteria for a biaxial stress state and a five parameter model by Willam et al. for a triaxial stress state were used [6]-[8]. The five parameters obtained from the experiments by Ohnuma et al. were also adopted [9].

As for the steel materials, such as liner, rebars and tendons, the elasto-platic theory based on the von Mises yield criterion was used. The uniaxial stress-strain relationships of steel materials were assumed to be multi linear.

2.2 Analytical modeling

2.2.1 Axisymmetric finite element model

In the analytical model shown in Figure 2-1, a 3D FEM for the narrow wedge of the vertical section(2˚) is used instead of the normal axisymmetric FEM . This model plane is chosen at 135 degree of azimuth, which is reasonably far from the penetrations.

The concrete is modeled as an 8-nodes solid element. The meridional tendons are represented by truss elements and attached to the concrete by sliding elements. The bond characteristics between concrete and the meridional tendons are assumed to be unbonded. Rebars are represented by truss elements in the meridional direction and shell layers which are given an area equivalent to the rebar area, and a Poisson's Ratio of zero to avoid any in-plane/out of plane stress - strain interactions in the hoop direction. The liner is constructed of quadratic shell elements. Perfect bonding is assumed between the rebars and the concrete, and between the liner and the concrete also.

Because the deformation of the basemat may be large when the thermal load is loaded with Case 1, the soil is modeled as the rigid spring element with the tension cutoff characteristics to consider uplift of the basemat.

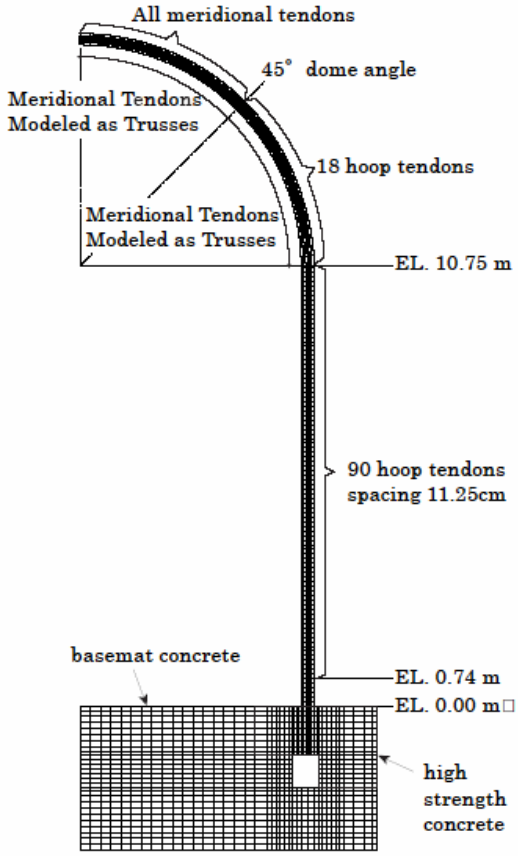

Figure 2-1 Computational grids of axisymmetric FEM model

2.2.2 Three-dimensional shell finite element model

The analyses are conducted for the sections between azimuths 0˚ to 90˚ and 270˚ to 360˚ which include the large openings (A/L, E/H) of the PCCV model. These analyses are used to determine the overall behavior of these sections taking into account the effects of the large openings and the buttress, as well as the distribution characteristics of tendon strain and the determination of the boundary conditions.

Figure 2-2 shows the analytical models. These models incorporate the buttress, as well as reinforcement around openings A/L and E/H, and use a multi-layered shell element for the entire reinforced concrete. Tendons are modeled as a truss element every two for the meridional tendon and every three for the hoop tendon. The tendon arrangements around the dome and openings areas are faithful reproductions of those found in the model. The bottom of the cylindrical wall is fixed. The friction coefficient between the tendon and concrete is defined to be 0.21.

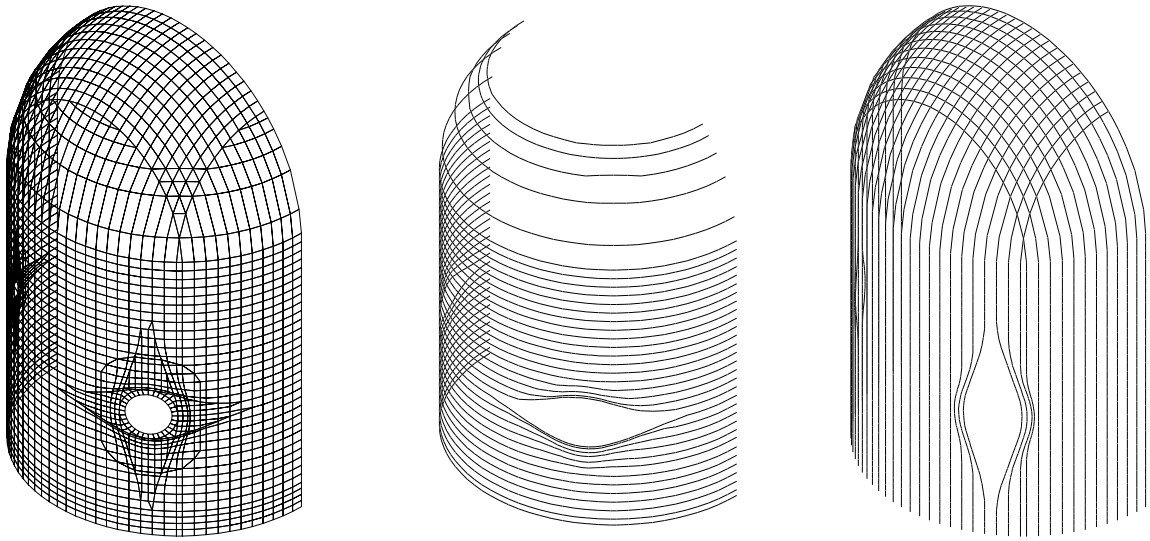

(a) Concrete (b) Hoop tendon (c) Meridional tendon

Figure 2-2 Computational grids of three-dimensional FEM model

Figure 2-3 is a schematic diagram of the sliding surface between the friction element, which transmits frictional force between the tendon and the reinforced concrete skeleton, and the tendon. The friction element, which connects the tendon to the reinforced concrete skeleton, consists of 3 axial springs which transmit frictional force as well as normal stress. The axial springs are oriented perpendicular to the tendon's slide direction. The tendon's sliding surface is defined as a plane given by the nodal points X2, X1 and X3. X2 slides along this plane in direction. The frictional force used in this element is based on Coulomb's Law of Friction. Figures 2-4 and 2-5 show the stress-displacement relationship of the element friction. The friction characteristics in the slide direction are indicated as the characteristics of a spring with perfect elasto-plasticity, whose initial stiffness is extremely high. Normal stress is transmitted by the two elastic springs with the same initial stiffness.

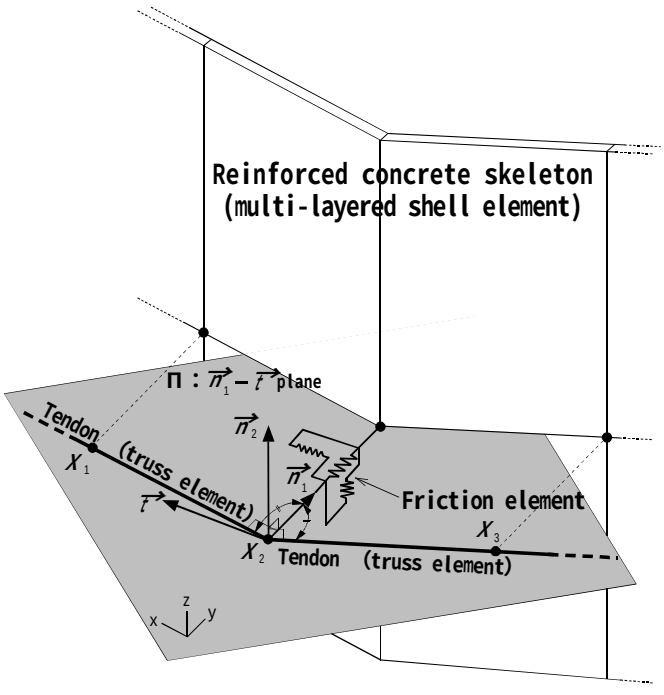

Figure 2-3 Tendon friction element

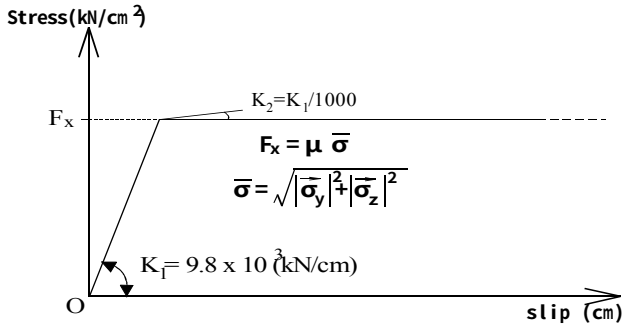

Figure 2-4 Relationship between slip and friction force (x direction)

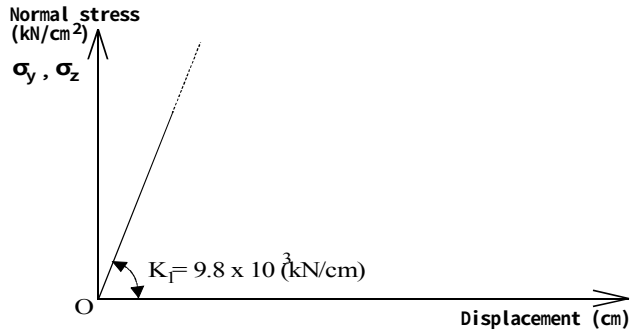

Figure 2-5 Relationship between displacement and normal stress (y,z direction)

3. Material characteristics

The material models and critical strain of each material such as concrete, rebar, tendon, and liner are set up based on the design package.

The thermal characteristics of the materials are set in accordance with the assumptions in the heat transfer analysis report [5]. However, the coefficients of linear thermal expansion are calculated by the following equations.

concrete; $\alpha c=9.0\times10^{-6}+6.9\times10^{-11}\times T^2$ (T in ˚C) Eq.(3-1)

steel; $\alpha s=1.2\times10^{-5}+0.8\times10^{-8}\times T$ (T in ˚C) Eq.(3-2)

3.1 Concrete

For the concrete model, the authors adopted the equivalent uniaxial strain model proposed by Darwin et al. and developed for three-dimensional analysis by Murray [10]. A smeared crack model is assumed for the modification of cracks.

- Basic Uniaxial Stress -Strain Relationship
  The modified Ahmad model [11] shown in Figure 3-1 is used in the compression zone. Elastic behavior is assumed until cracking occurs in the tensile zone. After cracking, tension cut-off or tension stiffening (c=0.8 at Izumo model) is assumed.
- Failure Surface
  The five-parameter model developed by Willam et al. in the 3D model, and Kupfer's model in a shell model is used to model a failure surface [7], [8]. The five parameters obtained from the experiments by Ohnuma et al. are adopted [9].
- Shear Retention Model in Cracked Plane.
  The Al-Mahaidi equation shown in Figure 3-2 is used to model shear retention in a cracked plane [12].

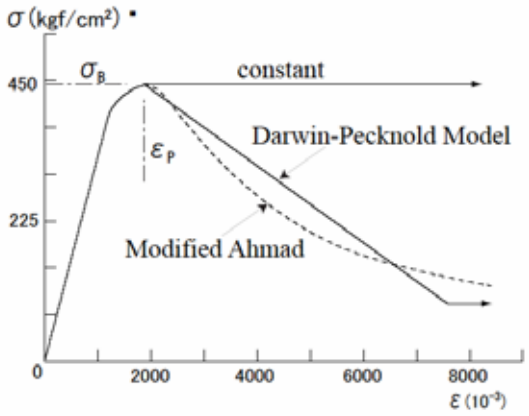

Figure 3-1 Uniaxial Stress -Strain Relationship(compression)

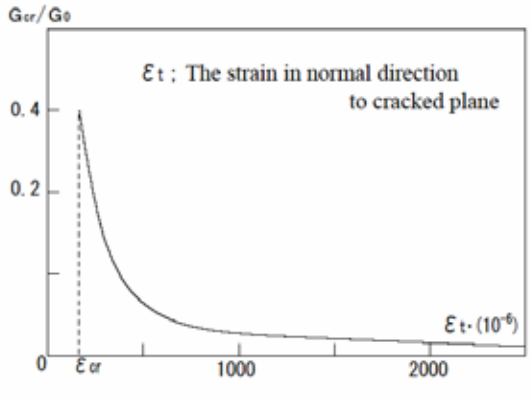

Figure 3-2 Shear Retention Model in Cracked Plane

The compressive strength of the concrete used in the analyses is the same as the design strength recommended by SNL. Young's modulus(E_0), tensile strength(ft), and strain (ε_p) at maximum strength, used in the analyses, are obtained from the following equations [13].

$$\varepsilon_p = (13.97\sigma_B + 1690)/10^6 \quad ; \quad \sigma_B = 44.13\text{MPa}, \quad \varepsilon_p = 0.0023 \qquad \text{Eq.(3-3)}$$

$$E_0 = (3.57\sqrt{\sigma_B} + 5.71)\ (\text{kN/mm}^2)\ ; E_0 = 2.94\times10^4\text{MPa} \qquad \text{Eq.(3-4)}$$

$$ft = 0.196\text{MPa} \qquad \text{Eq.(3-5)}$$

As for Case2, the difference between the temperature distributions of the sectional direction will have much effect on the analysis result. This is because the element meshing in the section direction of the stress analysis models is too large to evaluate the temperature distribution accurately. Figure 3-3 shows the accurate values and the calculated values calculated by axisymmetric model on the temperature distributions. Therefore, the coefficients of linear thermal expansion of concrete calculated by Eq.(3-1) for the stress analysis must be multiplied by 0.3 to evaluate the influence by a concrete thermal expansion appropriately. This coefficient is determined on the condition that the heat strain energy calculated with the average temperature value of a element becomes equivalent to that calculated with the accurate gradients.

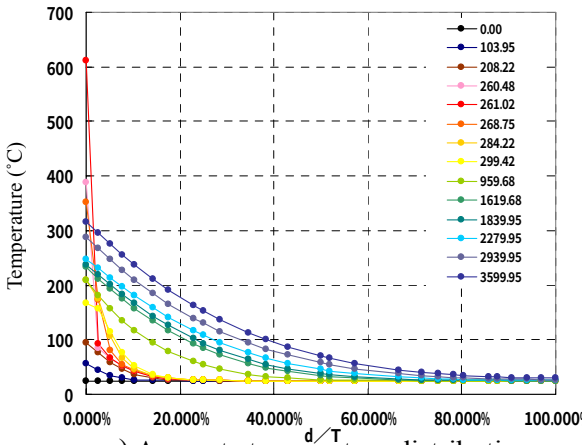

a) Accurate temperature distribution

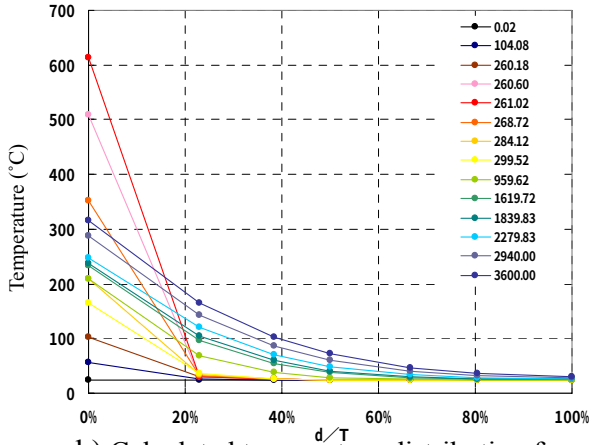

b) Calculated temperature distribution for axisymmetric model

Figure 3-3 Temperature distribution

3.2 Rebars

3.2.1 Modeling method

The rebar stress-strain relationship obtained from the material test results are approximated as polygonal lines where the following parameters are used:

- Yield point, strain hardening point, 4% strain point, 6% strain point and critical point. Next, using the stress-strain relationship from the polygonal line approximation, the stress-strain relationship of the rebars is determined according to the following:
- Determine 3 types of stress-strain relationships by averaging the test results for the 5 points stated above for each reinforcement material (SD345, SD390 and SD490).
- Test results for dumbbell-type specimens are not to be used.

3.2.2 Stress-strain relationship

Figure 3-4 shows the stress-strain relationships approximated as the polygonal lines. The stress-strain relationship for the SD390 rebar to be used in the analyses is shown in the thick line. SD390 is the main reinforcement used in the cylindrical portion of the 1/4 PCCV specimen. The critical strain is 21.3%, and is equal to the mean rupture strain of the SD390 rebars.

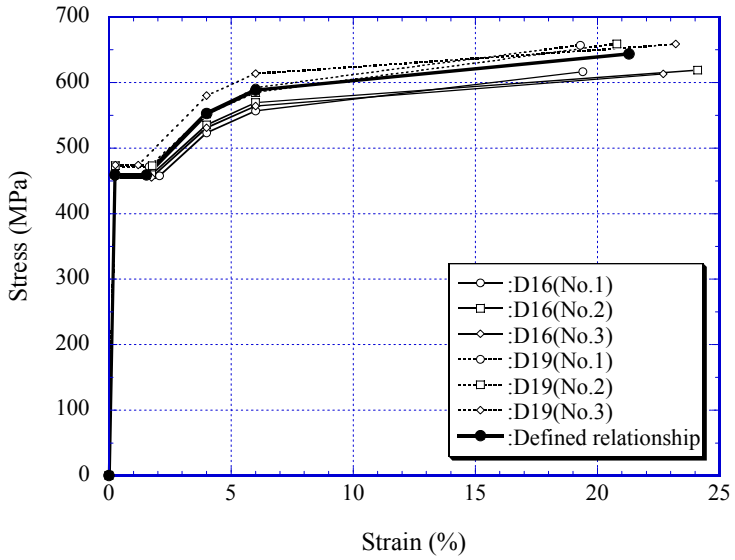

Figure 3-4 Stress -Strain Relationship for the SD390 Rebar

3.3 Tendon

The stress - strain relationship of the tendons used in the analyses is modeled referring to the results of the PCCV tendon system tensile test and the PCCV tendon strand static tensile test.

Detailed modeling procedure is as follows;

(1) The stress - strain relationship below the critical strain level in the tendon system tensile test is

modeled referring to the results of the test.

(2) The relation beyond the critical strain level in the tendon system tensile test is modeled referring to the results of the tendon strand static tensile test.

The modeled stress -strain relationship for the analyses is shown in Figure 3-5 with the stress - strain curves by the both tests. The stress - strain relationship is modeled as a tri-linear up to the critical strain of 3.7% in the system test. The stress increase was hardly observed beyond 3.7% in the strand static tensile test, therefore the stress is assumed to be constant beyond that strain level.

The critical strain in straight part near the anchorage is assumed to the critical strain of 3.7% in the system tensile test in which the influence of the wedge anchor was taken into account. The reason is that the tendons are supposed to be ruptured at a lower strain level by the influence of the wedge anchor.

The critical strain in curved part in the cylinder wall is assumed to be 8.0% referring to the tendon strand static tensile test. The critical strain is summarized in Table 3-1

Table 3-1 Critical strain of the tendons

	Straight part	Curved part
critical strain (%)	3.7	8.0

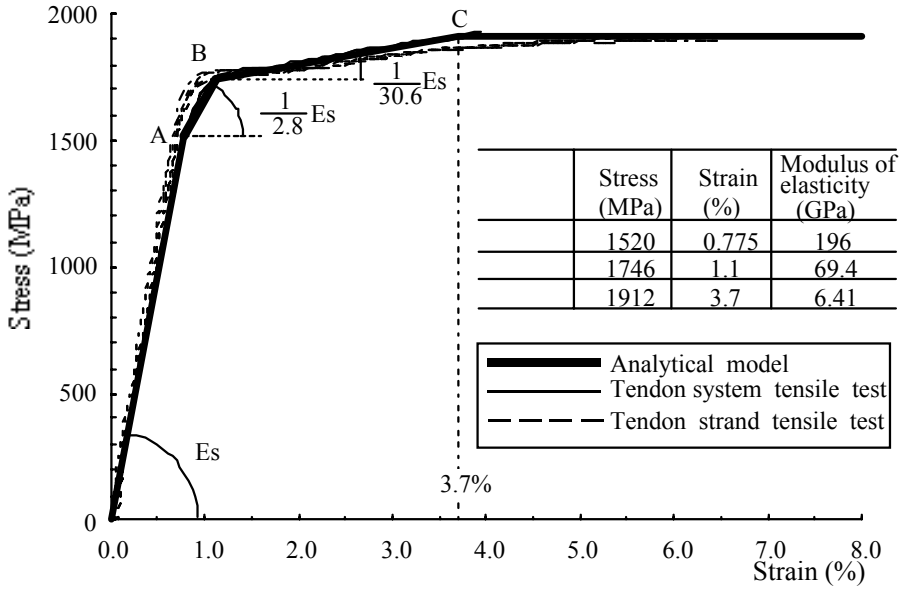

Figure 3-5 Stress -Strain Relationship for the Tendons

3.4 Liner

The analysis employs the material properties specified in the PCCV Design Package issued on Nov. 17, 1997. The material tests of the liner material, SGV410, were carried out with several test pieces

obtained along with the rolling direction of the plates. The test results demonstrate that the liner materials have 20MPa variations in the yielding points and the variations of other values such as young's modulus and Poisson ratio are within the allowable range. Accordingly the material properties are defined as an average behavior as follows;

The stress-strain relationship was constructed for the analysis as shown in Figure 3-6. From Figure3-6, the critical strain of liners is obtained as 33%.

However, because the critical strain of liners in the welded joint is about 17% which is half level of the mother material according to the past studies and it is confirmed that the strain concentration magnification at the scallop in the E/H neighborhood becomes 2.5 or less, the critical strain of the liners is assumed to be 6.8 %(=17%/2.5) in this research.

Stress σ [MPa]	Total strain ε [%]	σ /E	Plastic strain ε_p[%]
0	0.000	—	—
382	0.177	0.177	0.000
382	2.000	0.177	1.823
408	2.440	0.189	2.251
436	3.600	0.202	3.398
457	5.000	0.212	4.788
500	33.000	0.232	32.768

Material properties

- Young's modulus E = 2.16×10^5 MPa
- Poisson's ratio ν = 0.3
- Yield stress σ_y = 382 MPa
- Critical strain ε_{cr} = 33%

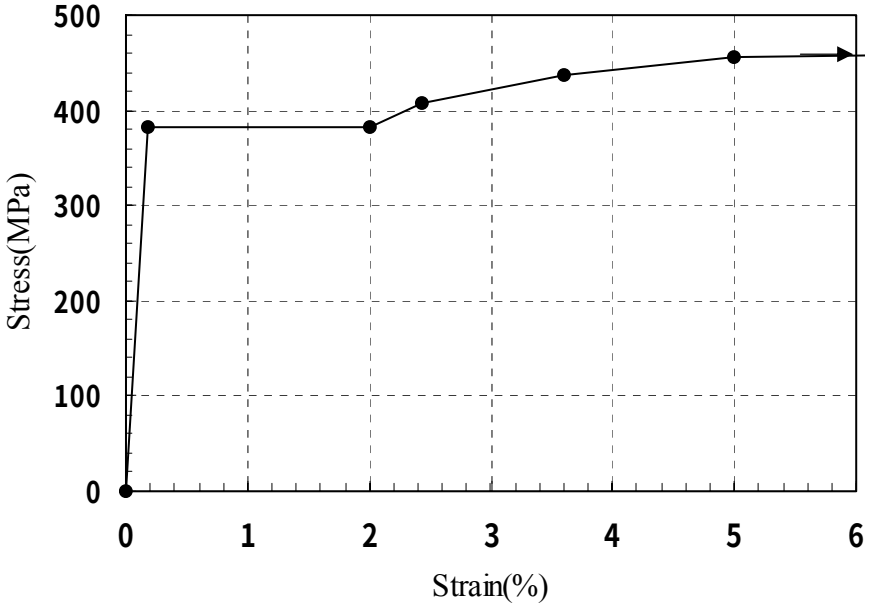

Figure 3-6 Analytical material property (liner : SGV410)

4. Analytical results

4.1 Results at the Standard Output Locations (SOLs)

(1) Case1

Displacement

As shown in Figure 4-1 through Figure 4-3, the analysis results in the case of pressure and thermal loading (Hereafter it is called C1(P+T)) indicate larger displacements compared with those of only pressure loading (Hereafter it is called C1(P)) at the same internal pressure. This may be caused by thermal expansion. Both C1(P+T) and C1(P) show larger displacement on the upper portions of the openings of A/L and E/H (See Figure 4-10 and Figure 4-13).

Strain of the liner

As shown in Figure 4-5 and Figure 4-6, the tensile strain of the liner for C1(P+T) is less than that for C1(P) at the same internal pressure. This may be caused by additional compressive stress applied by the thermal moment. However, over all strain distributions show little difference between C1(P+T) and C1(P), and generally large strain is observed around the mid height of the cylinder wall (See Figure 4-14 and Figure 4-15).

Strain of the inner rebar

As shown in Figure 4-3, the tensile strain of the inner rebar for C1(P+T) is less than that for C1(P) at the same internal pressure. This may be caused by additional compressive stress applied by a thermal moment (it is a constraint-moment of the deformation induced by thermal gradient in the member). However, over all strain distributions show little difference between C1(P+T) and C1(P), and generally large strain is observed around the center of the cylinder portion (not opening areas) (See Figure 4-16 and Figure 4-17).

Strain of the outer rebar

As shown in Figure 4-4 and Figure 4-5, the tensile strain of the outer rebar for C1(P+T) is more than that for C1(P) at the same internal pressure. This may be caused by additional tensile stress applied by the thermal moment. However, over all strain distributions show little difference between C1(P+T) and C1(P), and generally large strain is observed around the center of the general cylinder portion (See Figure 4-18 and Figure 4-19).

Strain of the tendon

As shown in Figure 4-7 and Figure 4-8, the strain of the tendons does not show considerable differences between C1(P+T) and C1(P). This is because of the location of the tendons; as the tendons are located near the center of the concrete wall depth, the thermal moment does not affect the tendons' strain. Overall strain distributions show little difference between C1(P+T) and C1(P), and generally large strain is observed around the center of the general cylinder portion (See Figure 4-20 and Figure 4-21).

(2) Case2

Displacement

As shown in Figure 4-22 through Figure 4-24, Figure 4-33, and Figure 4-34, the analysis results of pressure and thermal loading (Hereafter it is called C2(P+T)) indicate considerably larger displacements compared with those of only pressure loading (Hereafter it is called C2(P)) when the hydrogen burn occurred. This may be caused by reduced stiffness of the element due to cracks caused by the thermal moment. The large difference is maintained until the last stage of loading, however this may be caused by thermal expansion (See Figure 4-35 and Figure 4-36).

Strain of the liner

As shown in Figure 4-26 and Figure 4-27, the compressive strain of the liner for C2(P+T) is remarkably larger than that for C2(P) when the hydrogen burn occurred. This may be caused by constraining a rapid thermal expansion of the liner by concrete. At the last loading stage, however, C2(P+T) is slightly less than C2(P) because of the thermal moment (See Figure 4-39 and Figure 4-40).

Strain of the inner rebar

As shown in Figure 4-41 and Figure 4-42, the tensile strain of the inner rebar for C2(P+T) is considerably larger than that for C2(P) when the hydrogen burn occurred. This may be caused by reduced stiffness of the concrete. At the last loading stage, however, C2(P+T) is less than C2(P) because of the thermal moment similar to the Case 1 results (See Figure 4-43 and Figure 4-44).

Strain of the outer rebar

As shown in Figure 4-45 and Figure 4-46, the tensile strain of the outer rebar for C2(P+T) is considerably larger than that for C2(P) when the hydrogen burn occurred. Same as the inner rebar, this may be caused by reduced stiffness of the concrete. At the last loading stage, C2(P+T) is still more than C2(P) because of the thermal moment similar to the Case 1 results (See Figure 4-47 and Figure 4-48).

Strain of the tendon

As shown in Figure 4-28 and Figure 4-29, the strain of the tendons does not show considerable differences between C2(P+T) and C2(P). Same as the result for Case 1, this is because of the location of the tendons; as the tendons are near the center of the concrete wall depth, the thermal moment does not affect to the tendons' strain very much.

4.2 Thermal effects

(1) Case1

Pressure at yielding of steel materials

- The pressure at yielding of the liner is 0.96MPa for C1(P) and is 1.04MPa for C1(P+T). The liner yields at the higher pressure due to the thermal loading.
- The pressure at yielding of the rebar is 0.93MPa for C1(P) and is 0.82MPa for C1(P+T). The liner yields at the lower pressure due to the thermal loading.
- The pressure at yielding of hoop tendon is 1.21MPa for C1(P) and is 1.20MPa for C1(P+T). The

hoop tendon yields almost at the same pressure for C1(P) and C1(P+T).

Maximum strains of steel materials

- The maximum strain of the liner is 2.32% for C1(P) and is 2.48% for C1(P+T). Both the maximum strains don't reach the critical strain of 6.8%.
- The maximum strain of the outer rebar is 2.82% for C1(P) and is 3.41% for C1(P+T). Both the maximum strains don't reach the critical strain of 21.3%.
- The maximum strain of the hoop tendon is 2.17% for C1(P) and is 2.24% for C1(P+T). Both the maximum strains don't reach the critical strain of 8.0%.
- The ratio of the maximum strain to the critical strain of the liner is the largest among the liner, the rebar and the tendon regardless of the thermal loading. The ratio is 0.34 for C1(P) and is 0.36 for C1(P+T).

(2) Case2

Pressure at yielding of steel materials

- The pressure at yielding of the liner is 0.94MPa for C2(P) and is 0.23MPa for C2(P+T). The liner yields at the much lower pressure. This may be caused by additional compressive strain applied by the rapid thermal expansion of liner when the hydrogen burn occurred, and this time, compressive strain of liner reaches the yielding point. Then, the liner for C2(P+T) is yielding in tensile at the end of the hydrogen burn after a lapse of about 260 minutes.
- The pressure at yielding of the outer rebar is 0.91MPa for C2(P) and is 0.68MPa for C2(P+T). The outer rebar yields at the lower pressure. This may be caused by additional tensile strain applied by the thermal moment when the hydrogen burn occurred, and this time, tensile strain of rebar reaches the yielding point. On the other hand, the rebar strain of the C2(P) is tensile and doesn’t reach the yielding point.
- The pressure at yielding of the hoop tendon is 1.20MPa for C2(P) and is 1.18MPa for C2(P+T). The hoop tendon yields almost at the same pressure between the both C2(P) and C2(P+T).

Maximum strains of steel materials

- The maximum strain of the liner is 0.97% for C2(P) and is 0.65% for C2(P+T). Both the maximum strains don't reach the critical strain.
- The maximum strain of the rebar is 2.52% for C2(P) and is 4.08% for C2(P+T). Both the maximum strains don't reach the rupture strain.
- The maximum strain of the hoop tendon is 1.07% for C2(P) and is 1.18% for C2(P+T). Both the maximum strains don't reach the critical strain.
- The ratio of the maximum strain to the critical strain of the liner is largest among the liner, the rebar and the tendon for C2(P). The ratio is 0.14. On the other hand, the ratio of the rebar is largest for C2(P+T). The ratio is 0.19.

4.3 Liner tearing pressure and ultimate pressure

(1) Case 1

Liner tearing strain

The maximum strain of the liner for C1(P+T) is almost the same as that for C1(P) as shown Table 4-2. The temperature has little influence on the liner tearing pressure.

Ultimate pressure

Since the strains of the hoop tendon become critical from Table4-2 for both C1(P) and C1(P+T), it is predicted that the structural failure for both C1(P) and C1(P+T) occurs due to the rupture of the hoop tendon. Moreover, since the maximum strains of the hoop tendon are almost the same regardless of the temperature, the temperature has also little influence on the ultimate pressure.

In Case 1, it is found that the linear tearing precedes the occurrence of the structural failure due to the rupture of the rebar or tendon regardless of the thermal loading.

(2) Case 2

Liner tearing strain

The maximum strain of the liner for C2(P+T) is smaller than that for C2(P), as shown Table 4-2. From this point, the liner tearing for C2(P+T) occurs at the higher pressure than the liner tearing pressure for C2(P).

Ultimate pressure

It is predicted that the strains of the hoop tendon and the outer rebar become critical almost at the same pressure in C2(P) from Table4-2. On the other hand, the strain of the outer rebar becomes critical for C2(P+T). Therefore it is estimated that the structural failure is determined by the rupture of the hoop tendon or the outer rebar in C2(P), and is determined by the rupture of outer rebar for C2(P+T). Since the strains of tendon and outer rebar due to the thermal load are added to the strain due to the pressure, the structural failure is considered to occur at lower pressure.

It follows from these results that for C2(P) the liner tearing precedes the occurrence of the structural failure and for C2(P+T) the structural failure occurs initially.

4.4 The scale effect in thermal stress analyses

In this study, the temperature distributions in the section obtained from the heat transfer analyses by a full-scale model are applied to the 1:4-scale model. Therefore, although the average temperature and the gradient of the 1:4-scale model are equal to those of the full-scale model, the thermal slope of the equivalent linear temperature of the 1:4-scale model is four times as that of the full-scale model because the wall thickness is one fourth.

The thermal effect to the rupture of the PCCV is caused by addition of the thermal strain in case the change in the critical strain of the steel materials by heat is sufficiently small. The thermal strain in the 1:4-scale model may be as same as that in the full-scale model if their gradients are the same.

Consequently the thermal strains to be added in the both models are the same in the balanced conditions only by the steel materials near the ultimate state. It follows from this, that the scale effect on the thermal load may be small.

Table 4-1 Pressure at yielding of steel materials

	Liner		Outer Rebar				Tendon(Hoop)	
			Hoop		Meridional			
	Pressure (MPa)	(P+T) /P	Pressure (MPa)	(P+T) /P	Pressure (MPa)	(P+T) /P	Pressure (MPa)	(P+T) /P
C1(P+T)	1.04	1.08	0.82	0.88	0.89	0.91	1.20	0.99
C1(P)	0.96		0.93		0.98		1.21	
C2(P+T)	0.23	0.24	0.68	0.75	0.91	0.94	1.18	0.98
C2(P)	0.94		0.91		0.97		1.20	

Table 4-2 Maximum strains of steel materials

	Liner(Hoop) <Critical-Strain :6.8%>		Outer Rebar < Critical -Strain:21.3%>				Tendon(Hoop) < Critical -Strain:8.0%>	
			Hoop		Meridional			
	Max Strain	Max/ Rupture	Max Strain	Max/ Rupture	Max Strain	Max/ Rupture	Max Strain	Max/ Rupture
C1(P+T)	2.48%	0.36	3.41%	0.16	1.65%	0.08	2.24%	0.28
C1(P)	2.32%	0.34	2.82%	0.13	1.19%	0.06	2.17%	0.27
C2(P+T)	0.65%	0.10	4.08%	0.19	1.55%	0.07	1.18%	0.15
C2(P)	0.97%	0.14	2.52%	0.12	0.99%	0.05	1.07%	0.13

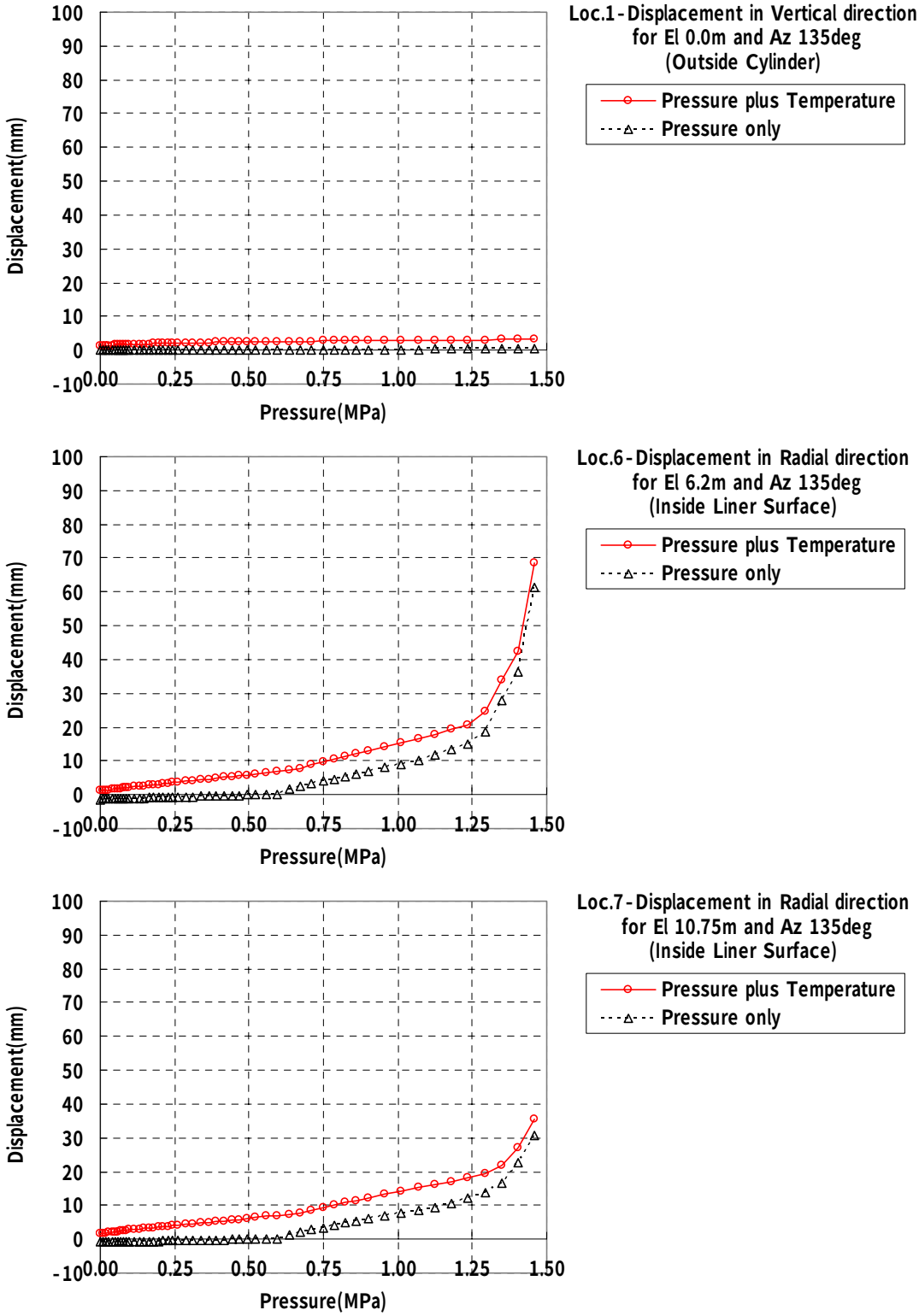

Figure 4-1 Comparison at standard Output Locations 1, 6 and 7(Case1)

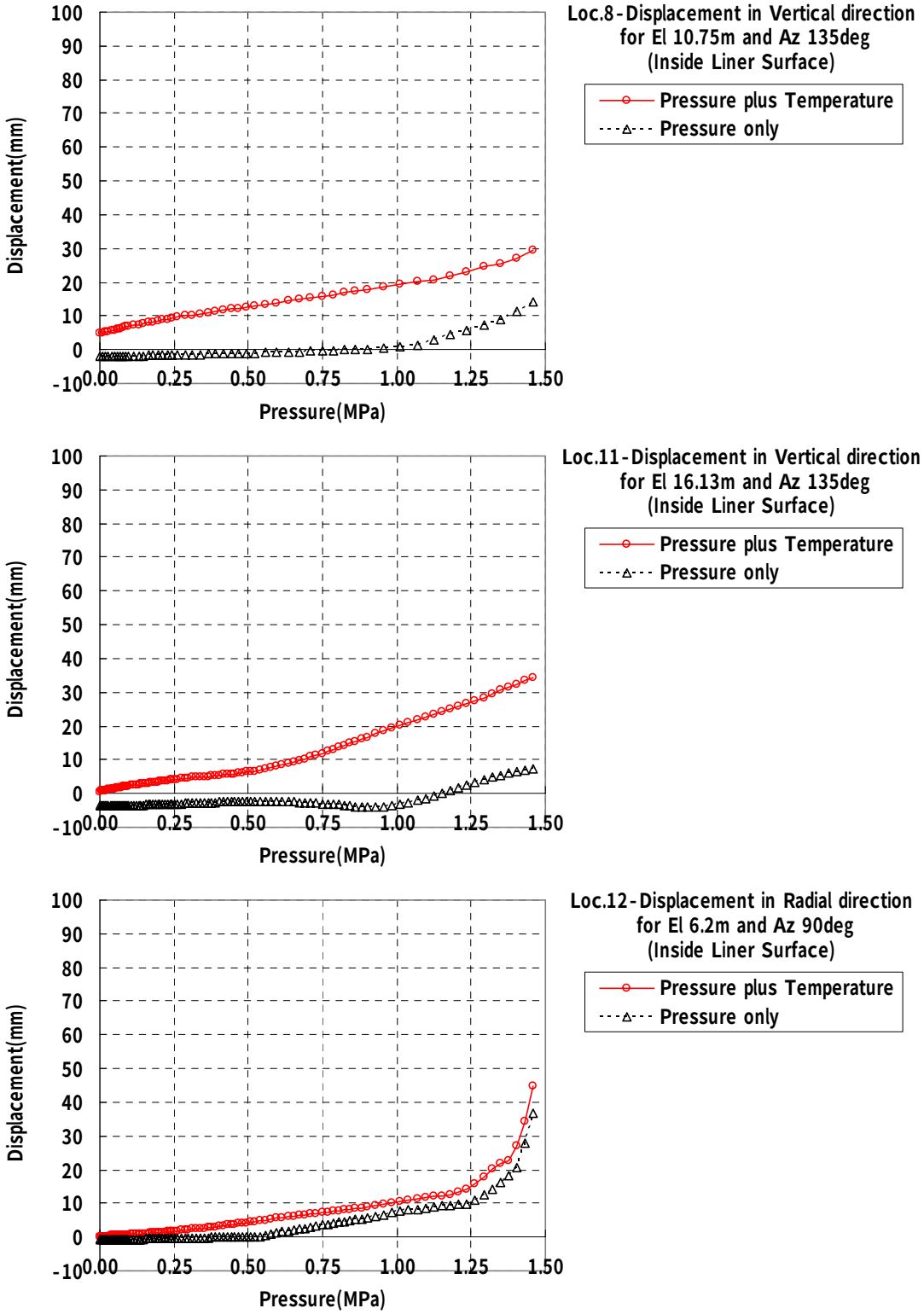

Figure 4-2 Comparison at standard Output Locations 8, 11 and 12(Case1)

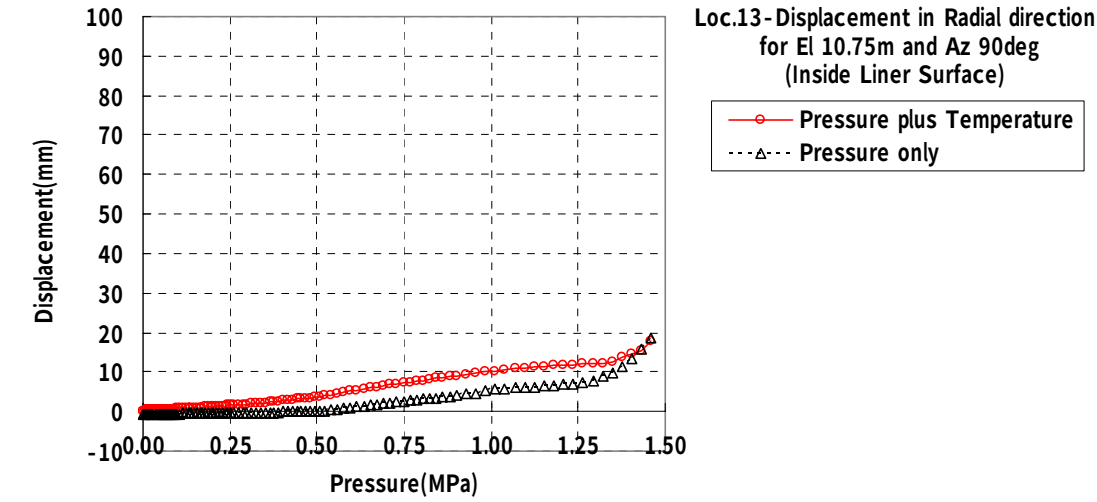

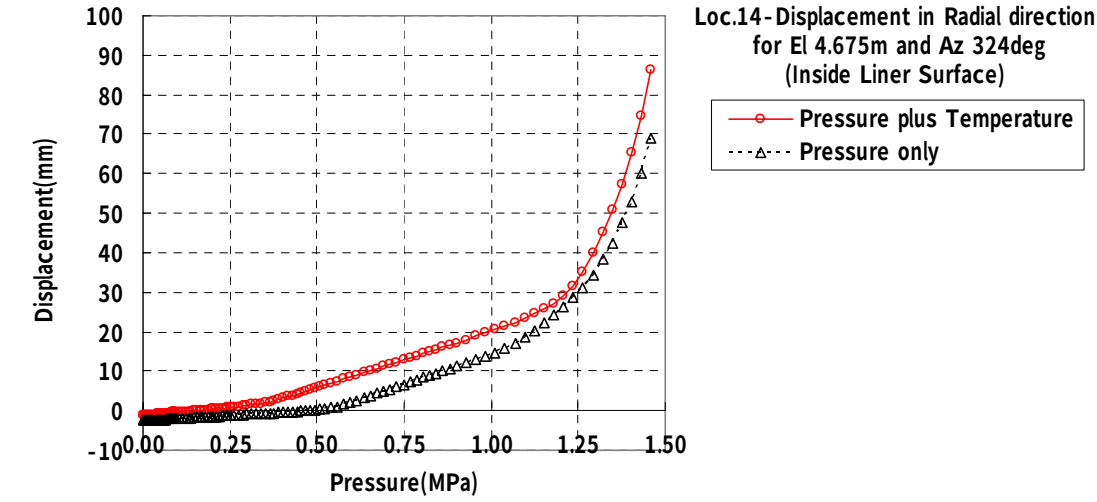

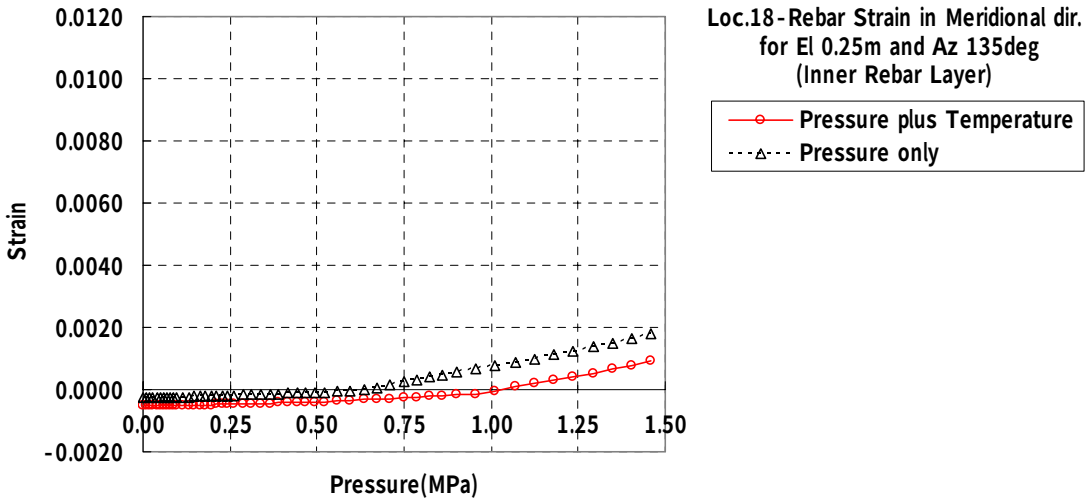

Figure 4-3 Comparison at standard Output Locations 13, 14 and 18(Case1)

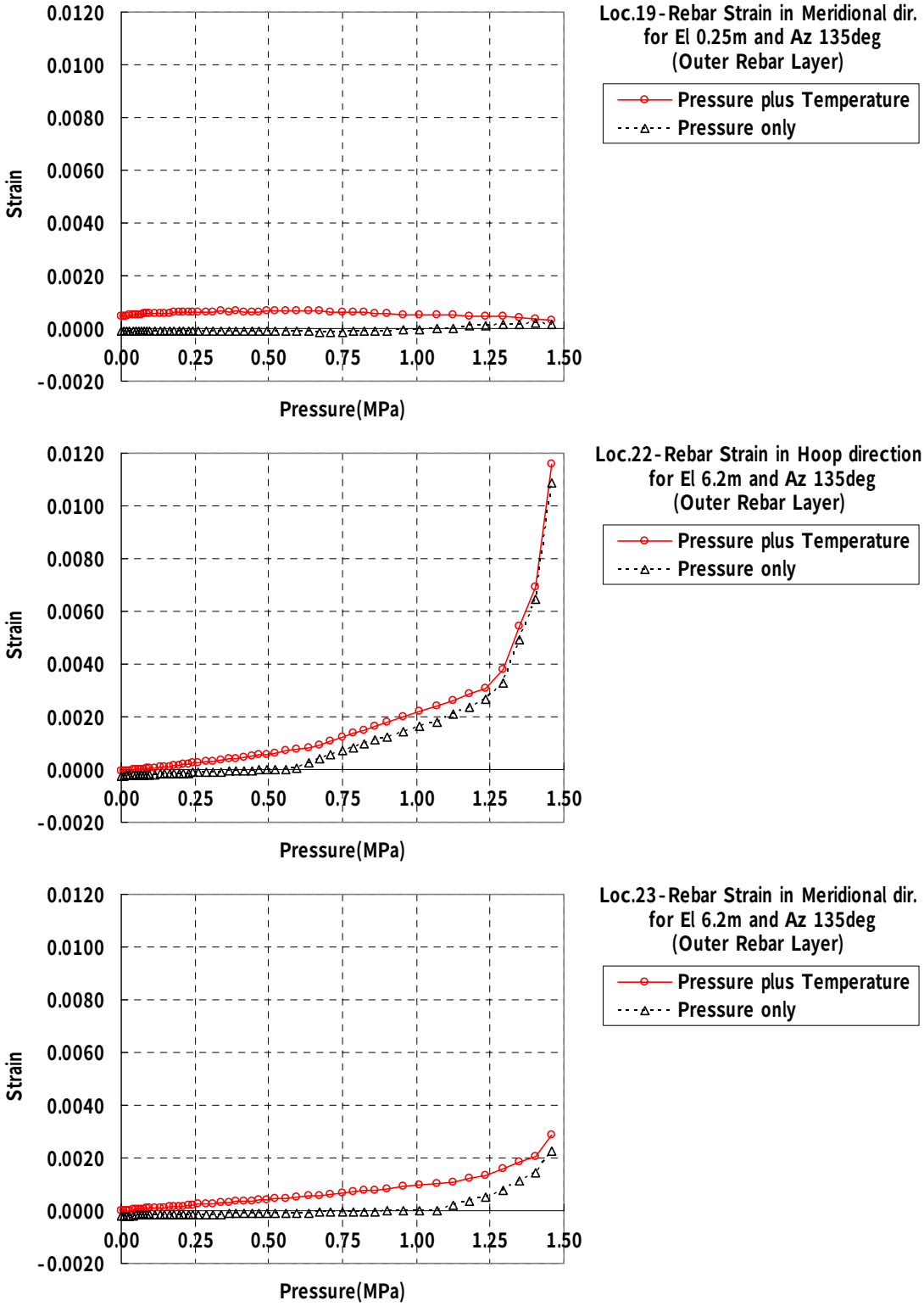

Figure 4-4 Comparison at standard Output Locations 19, 22 and 23(Case1)

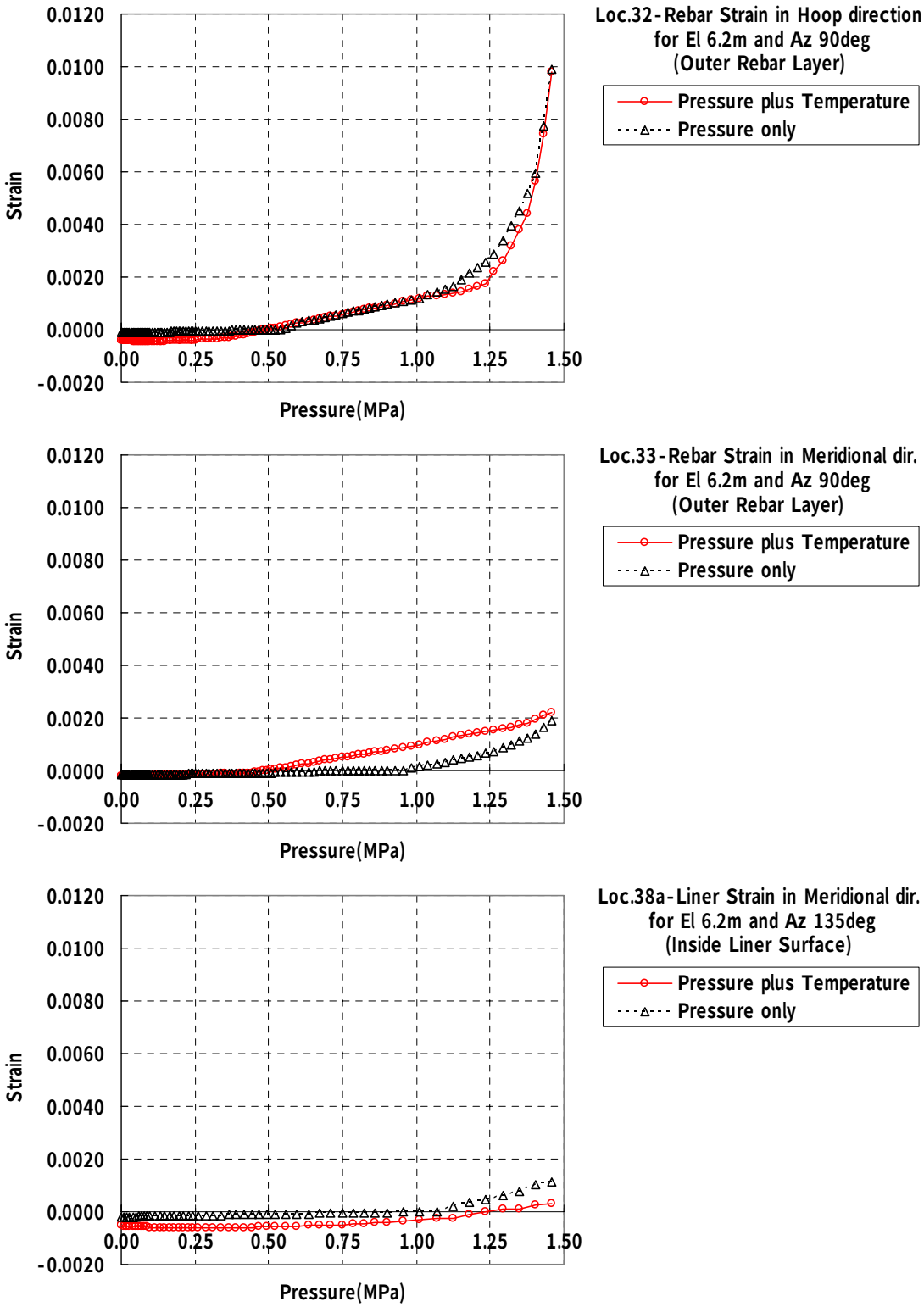

Figure 4-5 Comparison at standard Output Locations 32, 33 and 38(Case1)

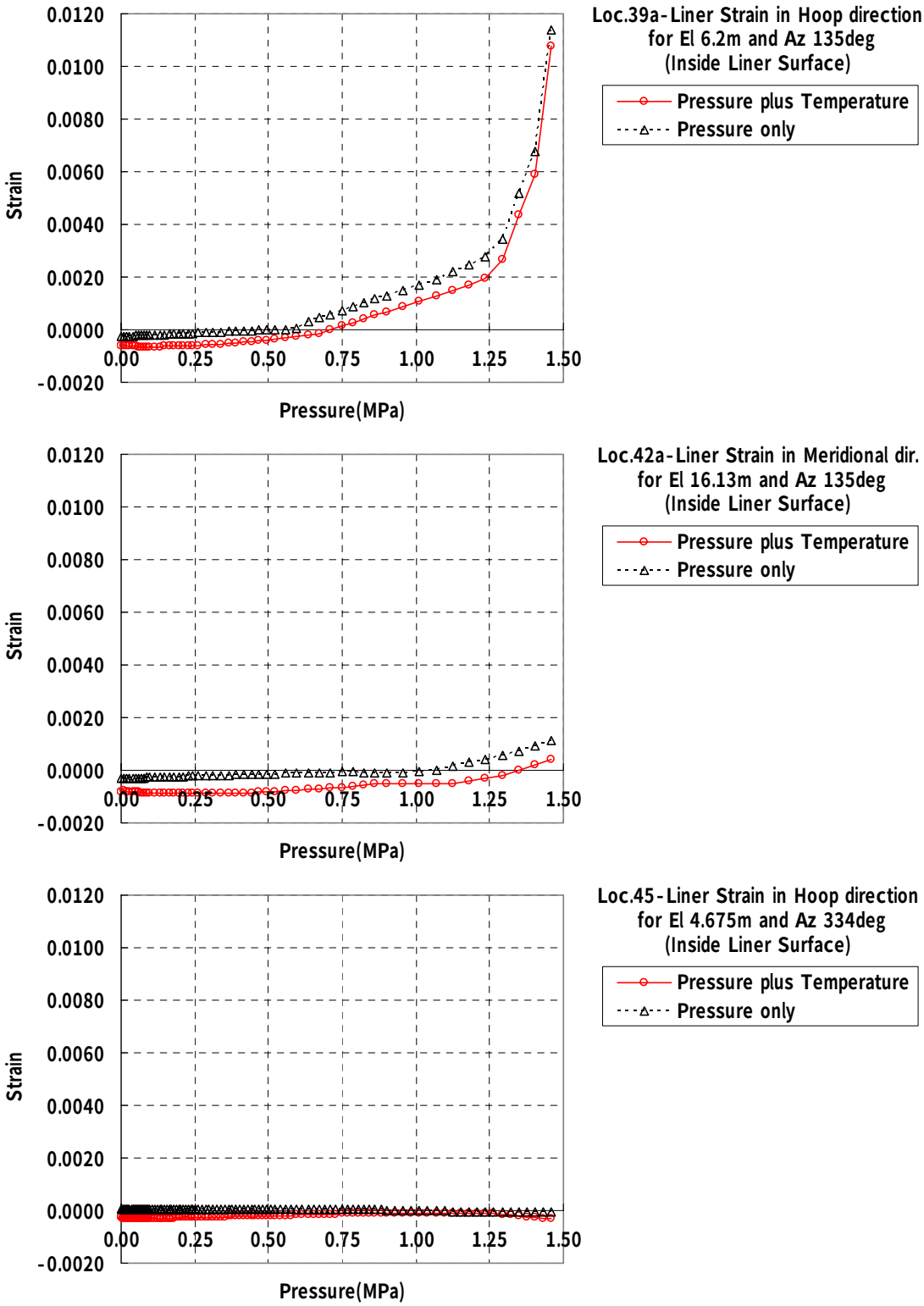

Figure 4-6 Comparison at standard Output Locations 39, 42 and 45 (Case1)

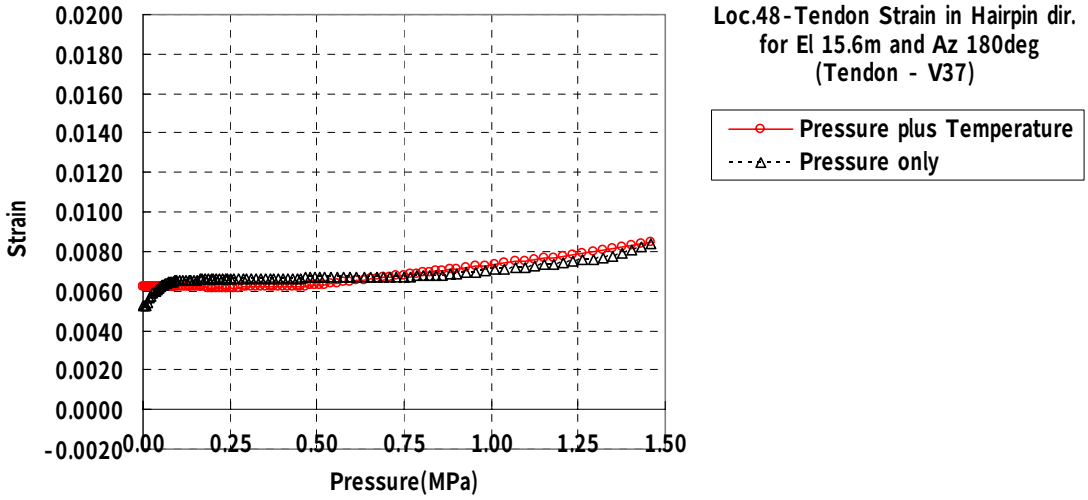

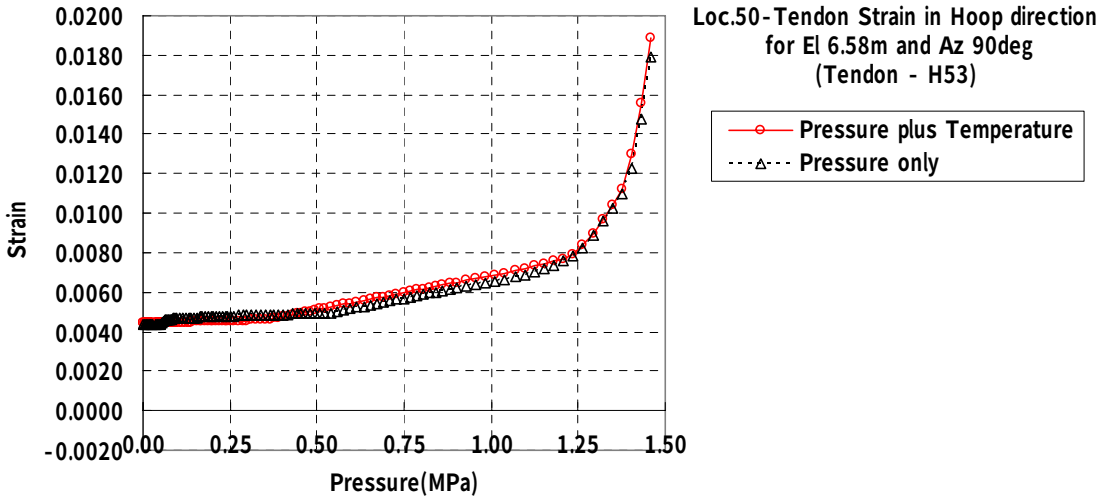

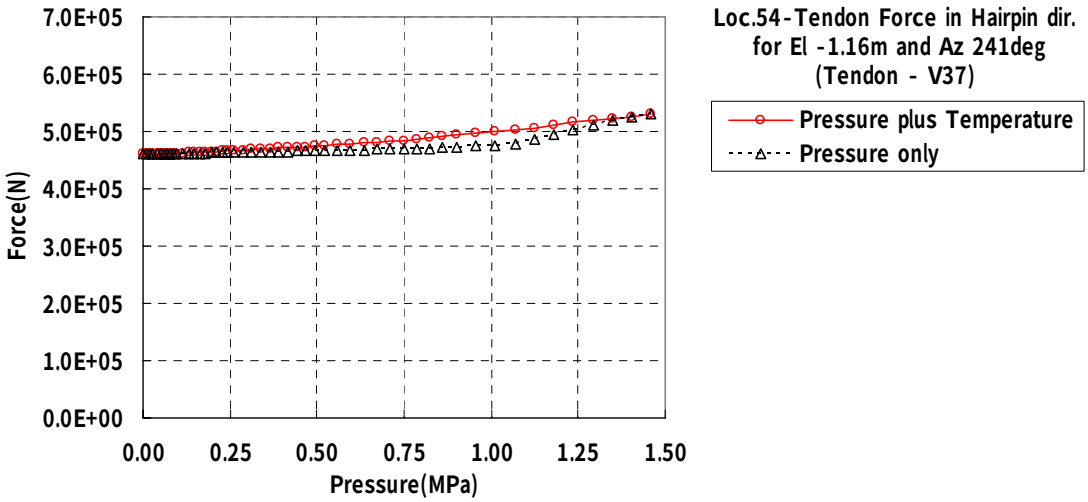

Figure 4-7 Comparison at standard Output Locations 48, 50 and 54(Case1)

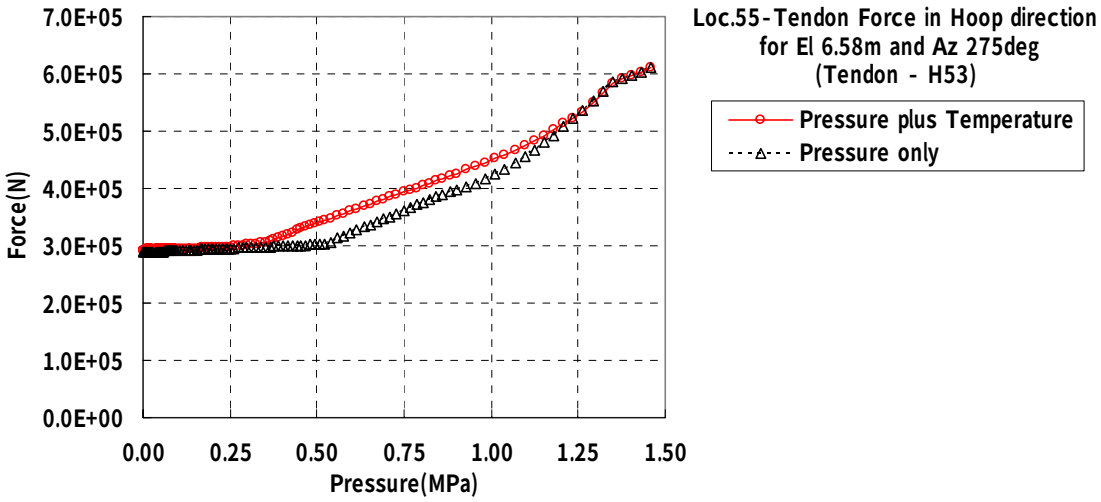

Figure 4-8 Comparison at standard Output Locations 55(Case1)

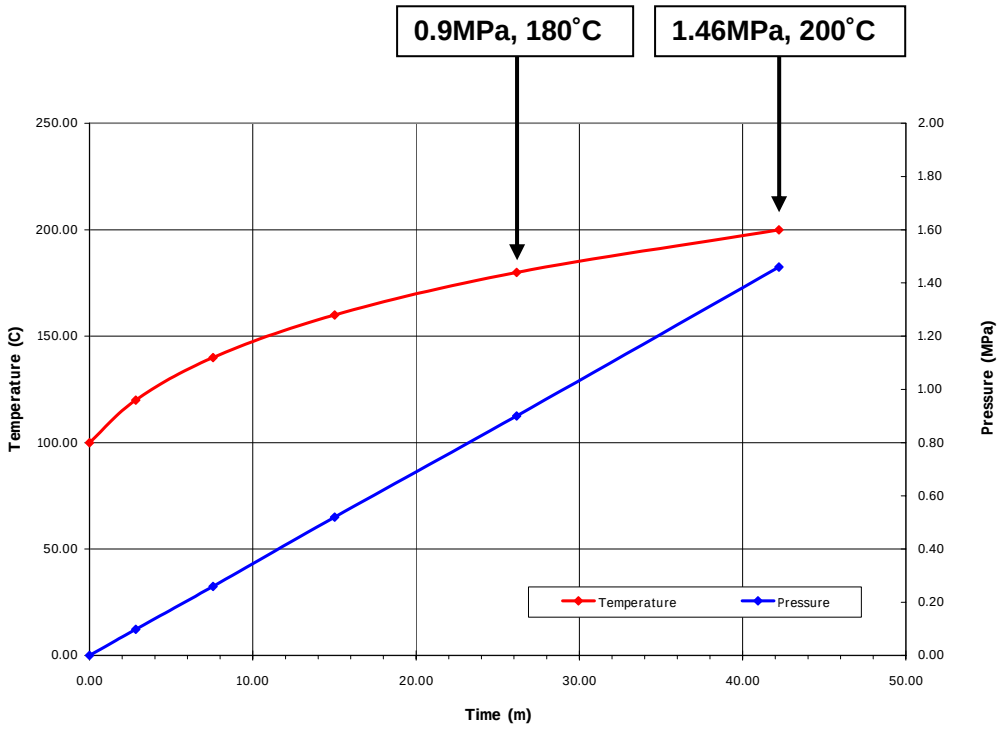

Figure 4-9 Showing point of contour (Case1)

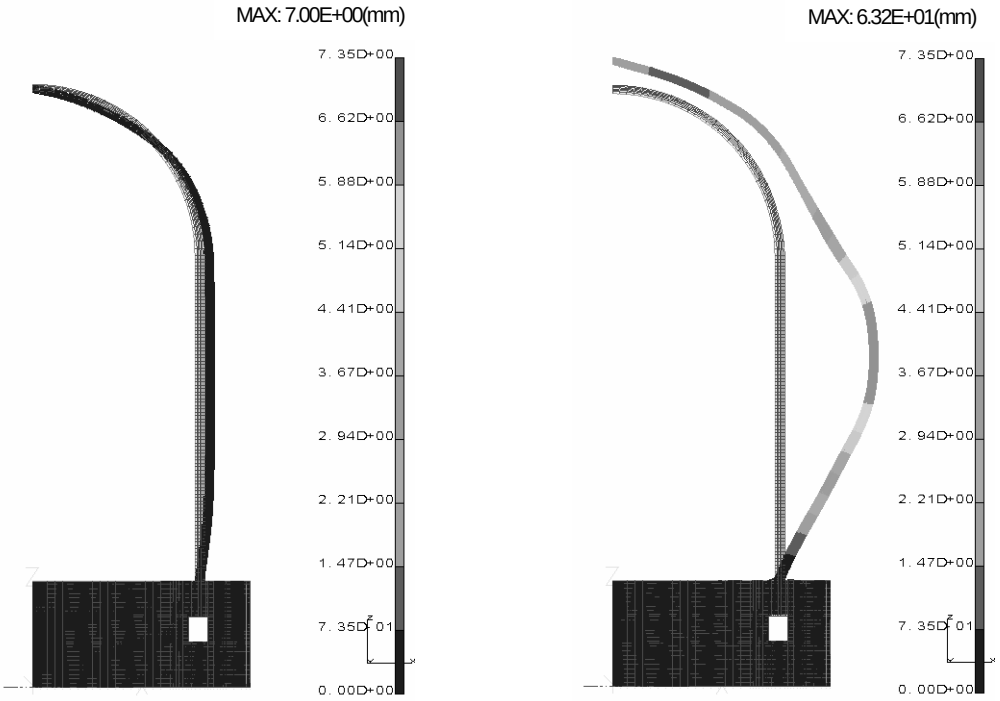

0.90MPa(26.16min) 1.46MPa(42.23min)

Figure 4-10 Deformation contour - Pressure only(Case1) (Scale factor:50)

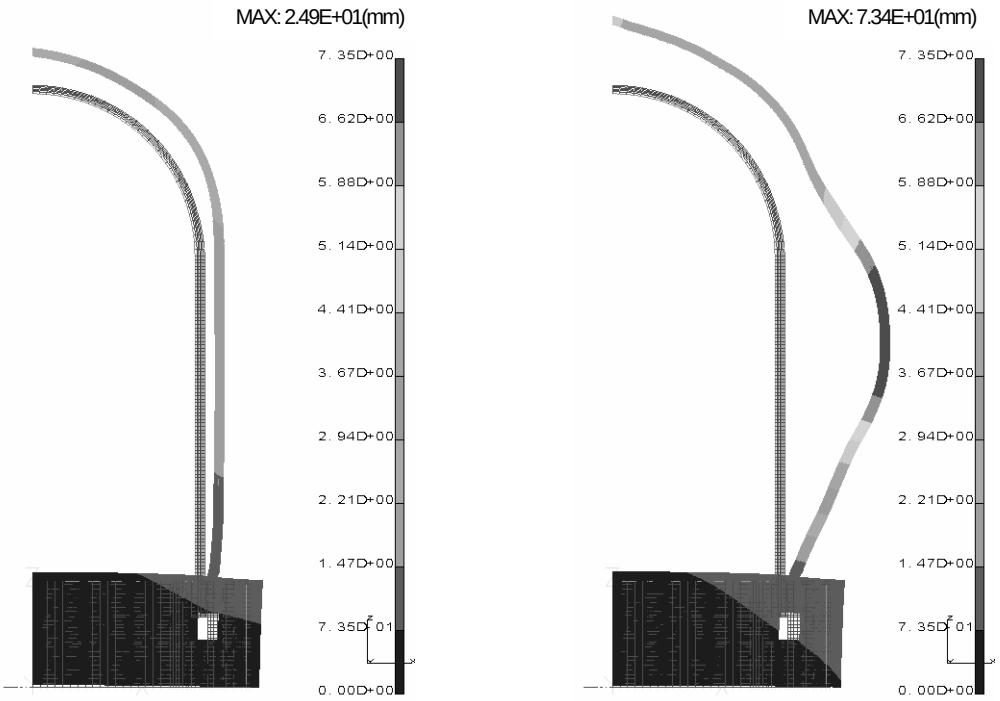

0.90MPa,180C(26.16min) 1.46MPa, 200C(42.23min)

Figure 4-11 Deformation contour - Pressure plus Temperature(Case1) (Scale factor:50)

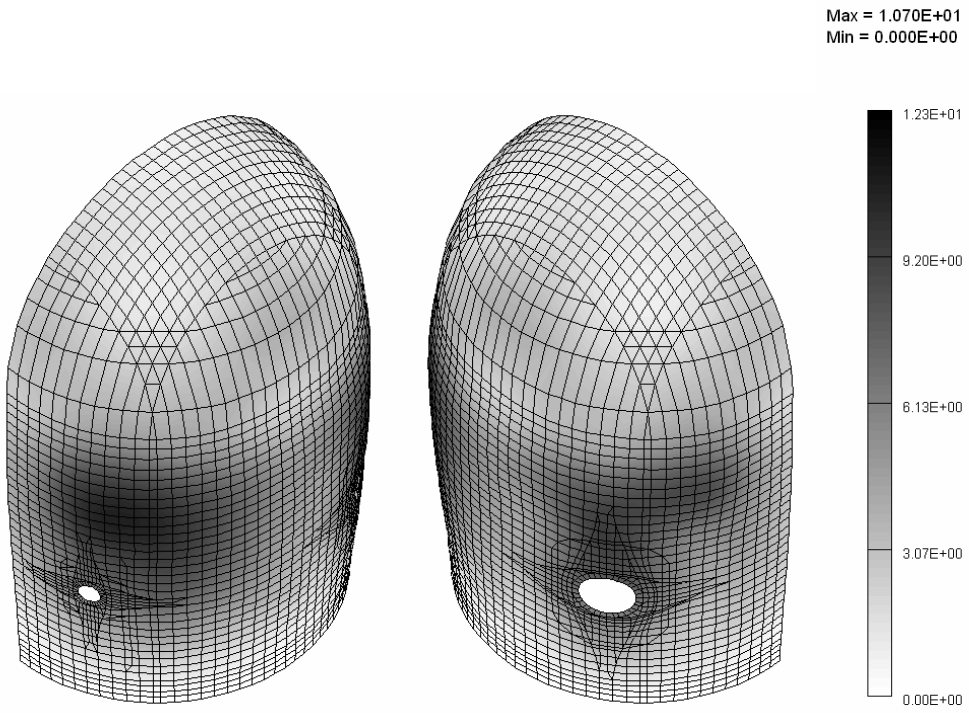

Figure 4-12 Deformation contour at 1.46MPa-Pressure only(Case1)

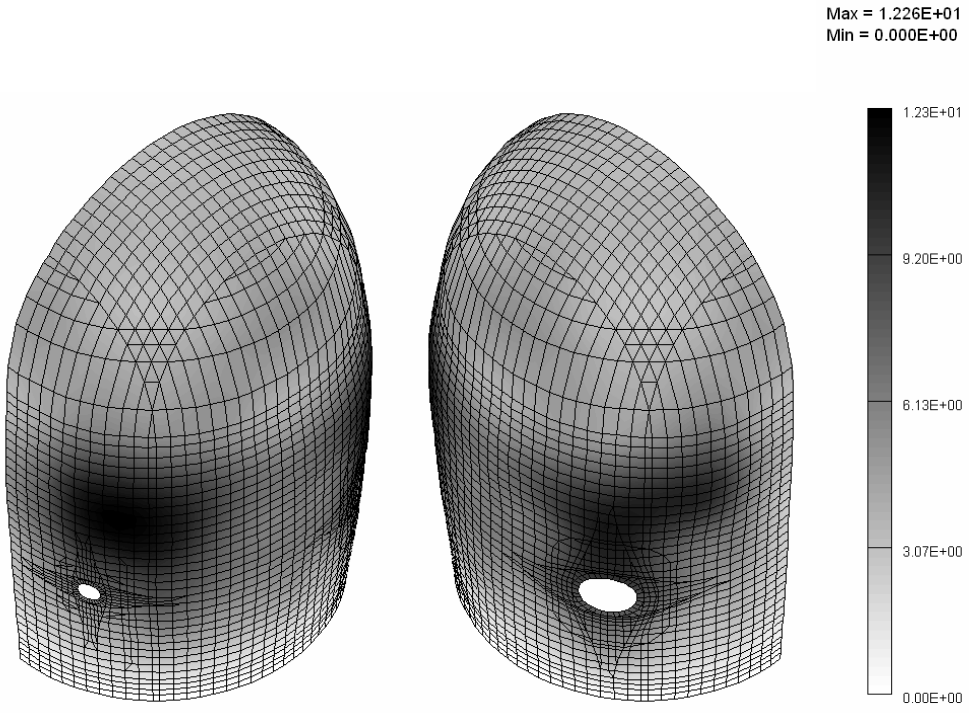

Figure 4-13 Deformation contour at 1.46MPa, 200˚C -Pressure plus Temperature(Case1)

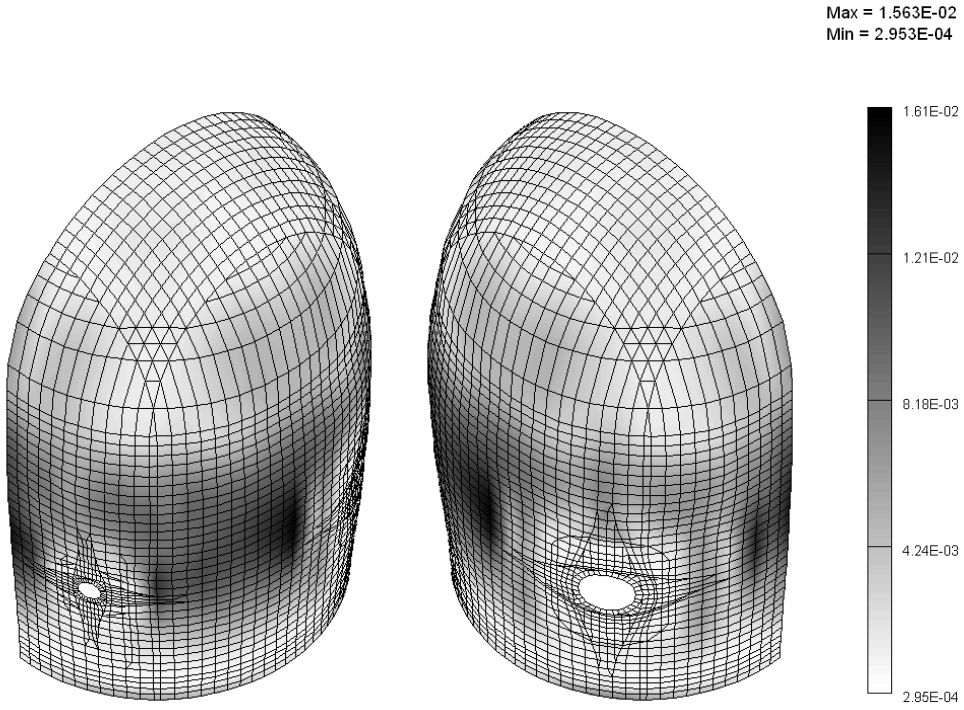

Figure 4-14 Von Mises strain contour of liner at 1.46MPa-Pressure only(Case1)

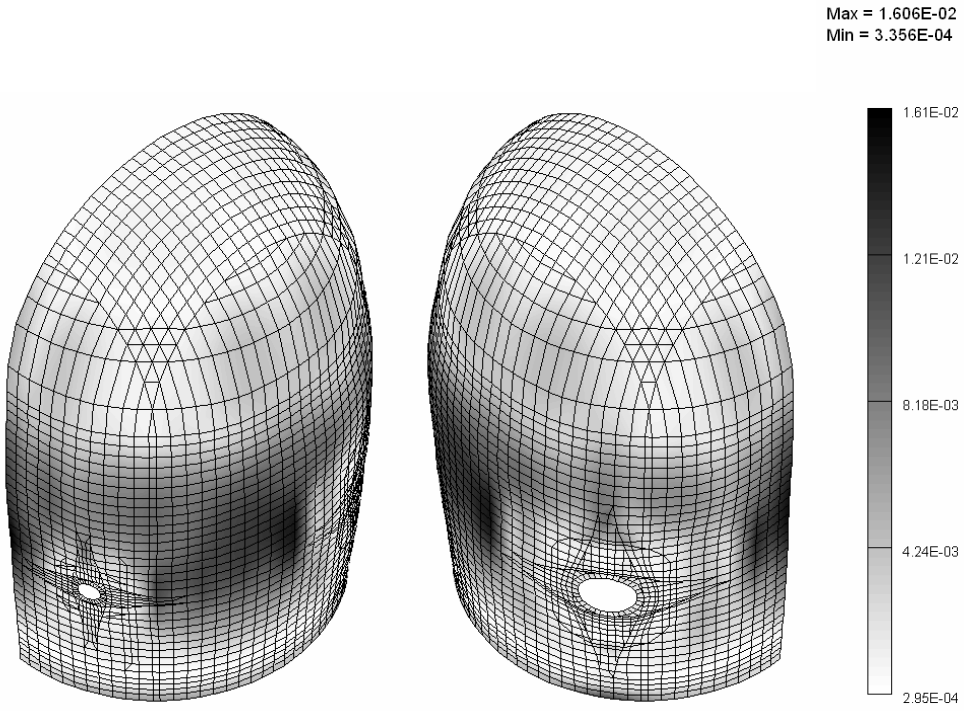

Figure 4-15 Von Mises strain contour of liner at 1.46MPa, 200˚C -Pressure plus Temperature(Case1)

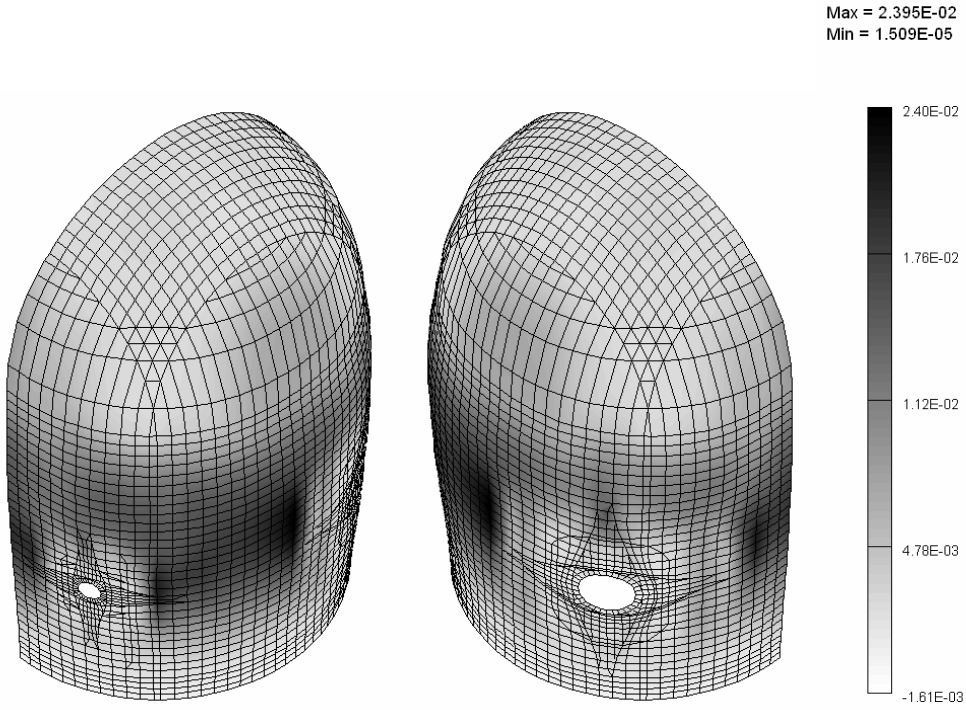

Figure 4-16 Strain contour of inner horizontal reinforcement at 1.46MPa -Pressure only(Case1)

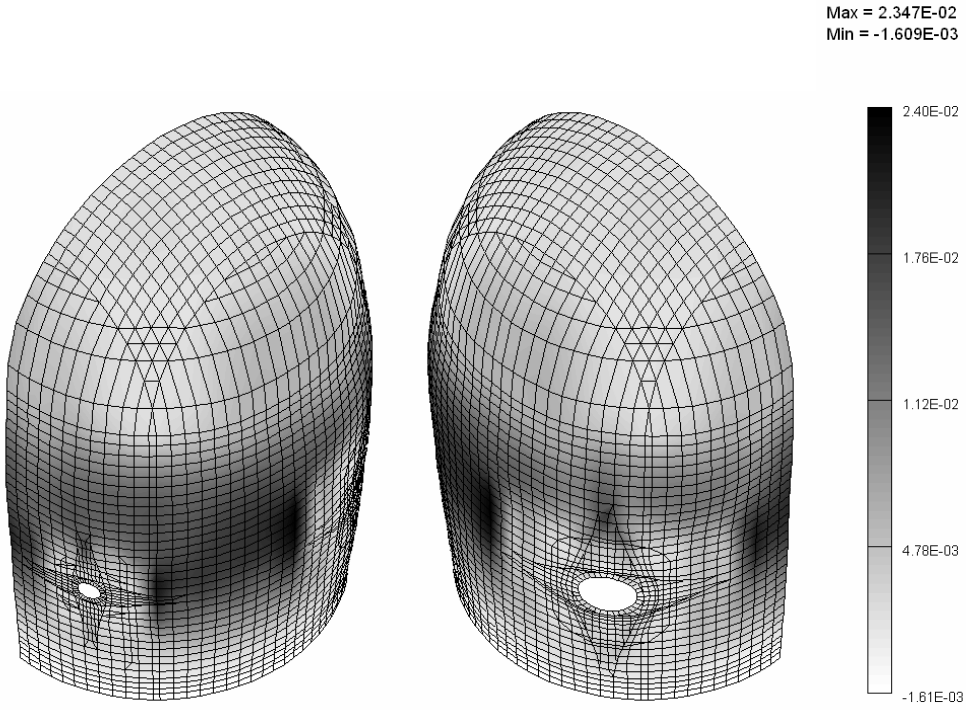

Figure 4-17 Strain contour of inner horizontal reinforcement at 1.46MPa, 200˚C -Pressure plus Temperature(Case1)

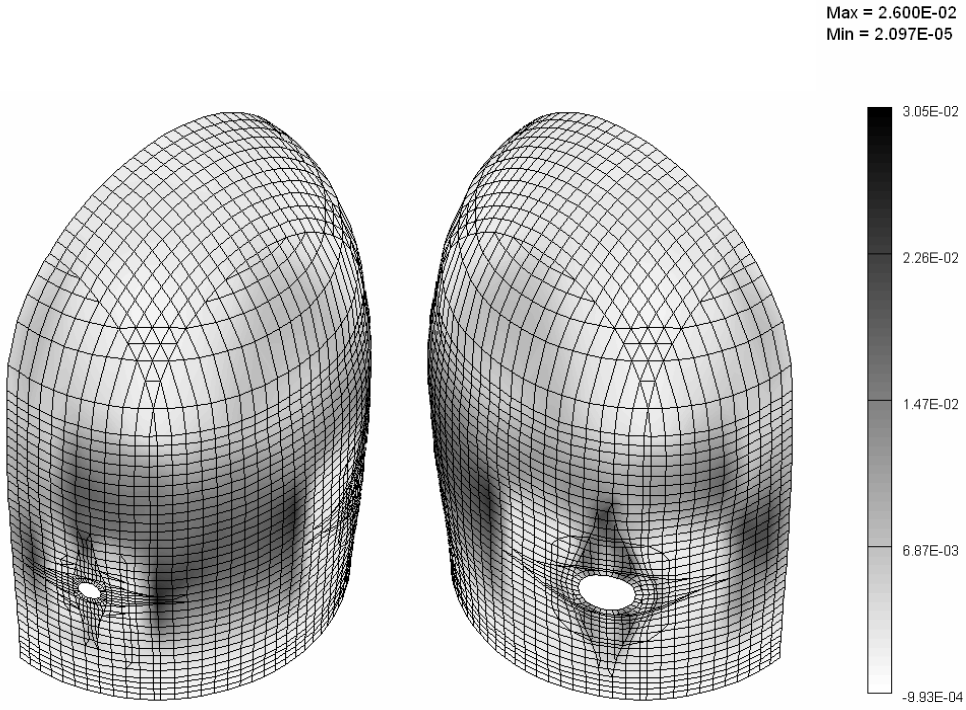

Figure 4-18 Strain contour of outer horizontal reinforcement at 1.46MPa -Pressure only(Case1)

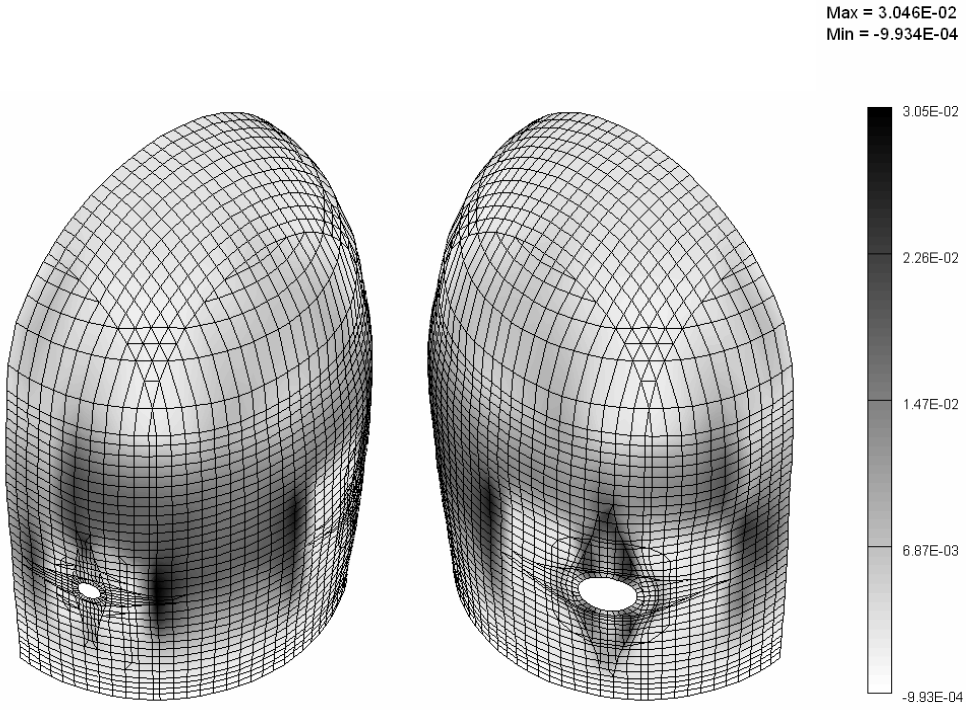

Figure 4-19 Strain contour of outer horizontal reinforcement at 1.46MPa, 200˚C -Pressure plus Temperature(Case1)

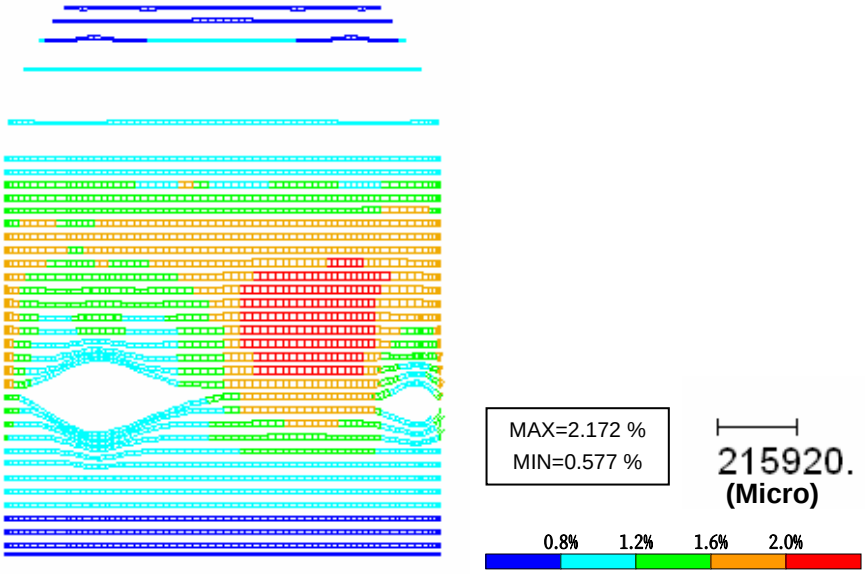

Figure 4-20 Strain contour of hoop tendon at 1.46MPa
-Pressure only(Case1)

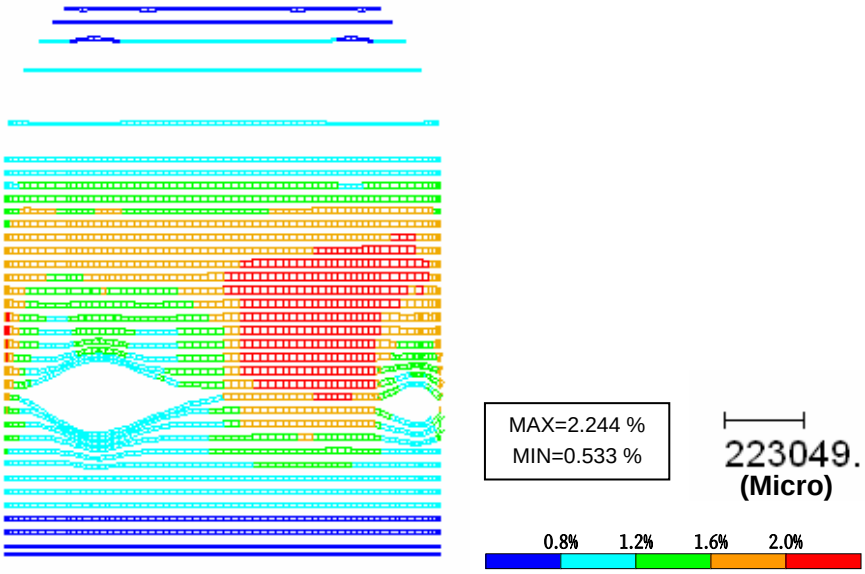

Figure 4-21 Strain contour of hoop tendon at 1.46MPa, 200˚C
-Pressure plus Temperature(Case1)

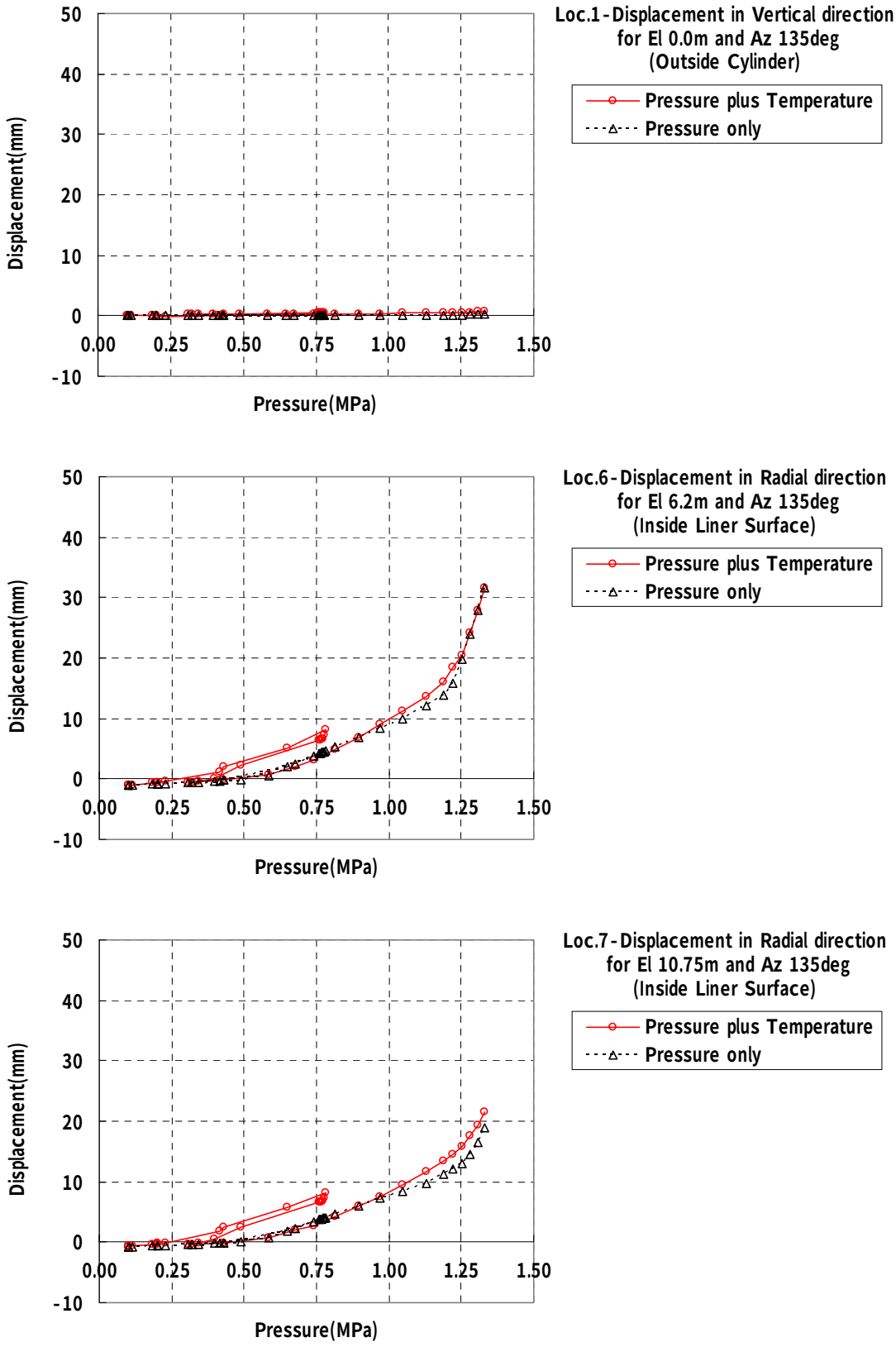

Figure 4-22 Comparison at standard Output Locations 1,6 and 7(Case2)

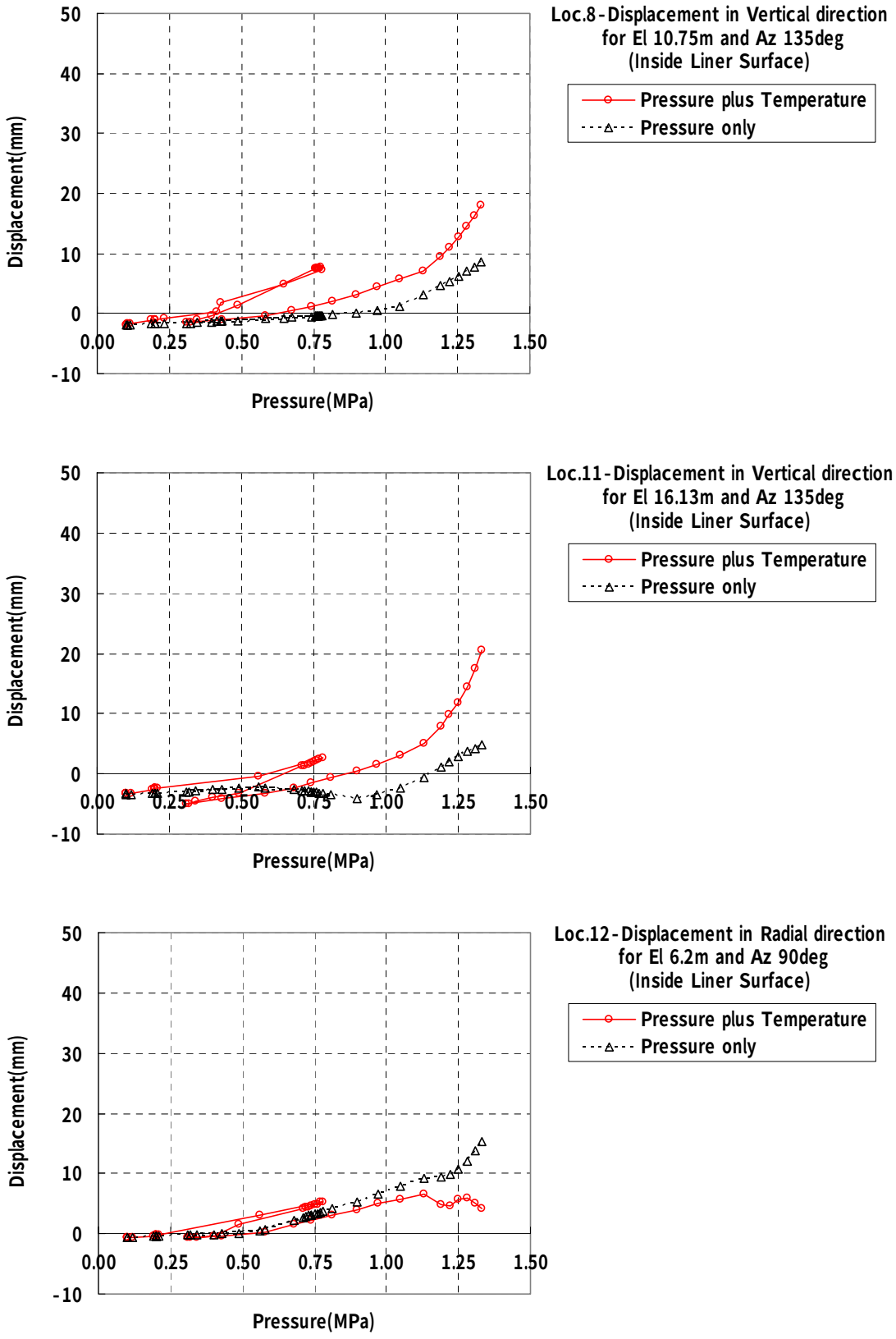

Figure 4-23 Comparison at standard Output Locations 8,11 and 12(Case2)

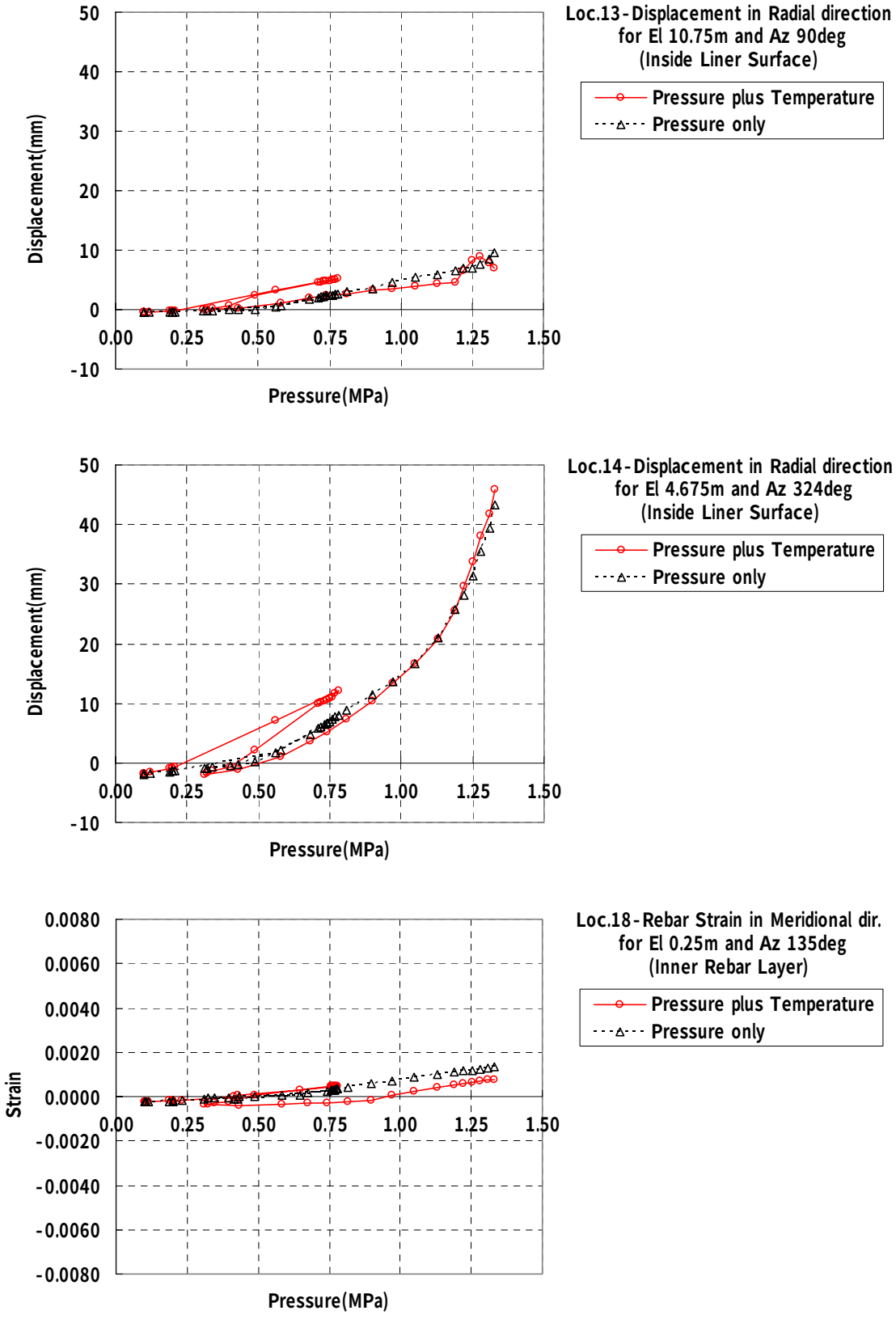

Figure 4-24 Comparison at standard Output Locations 13,14 and 18(Case2)

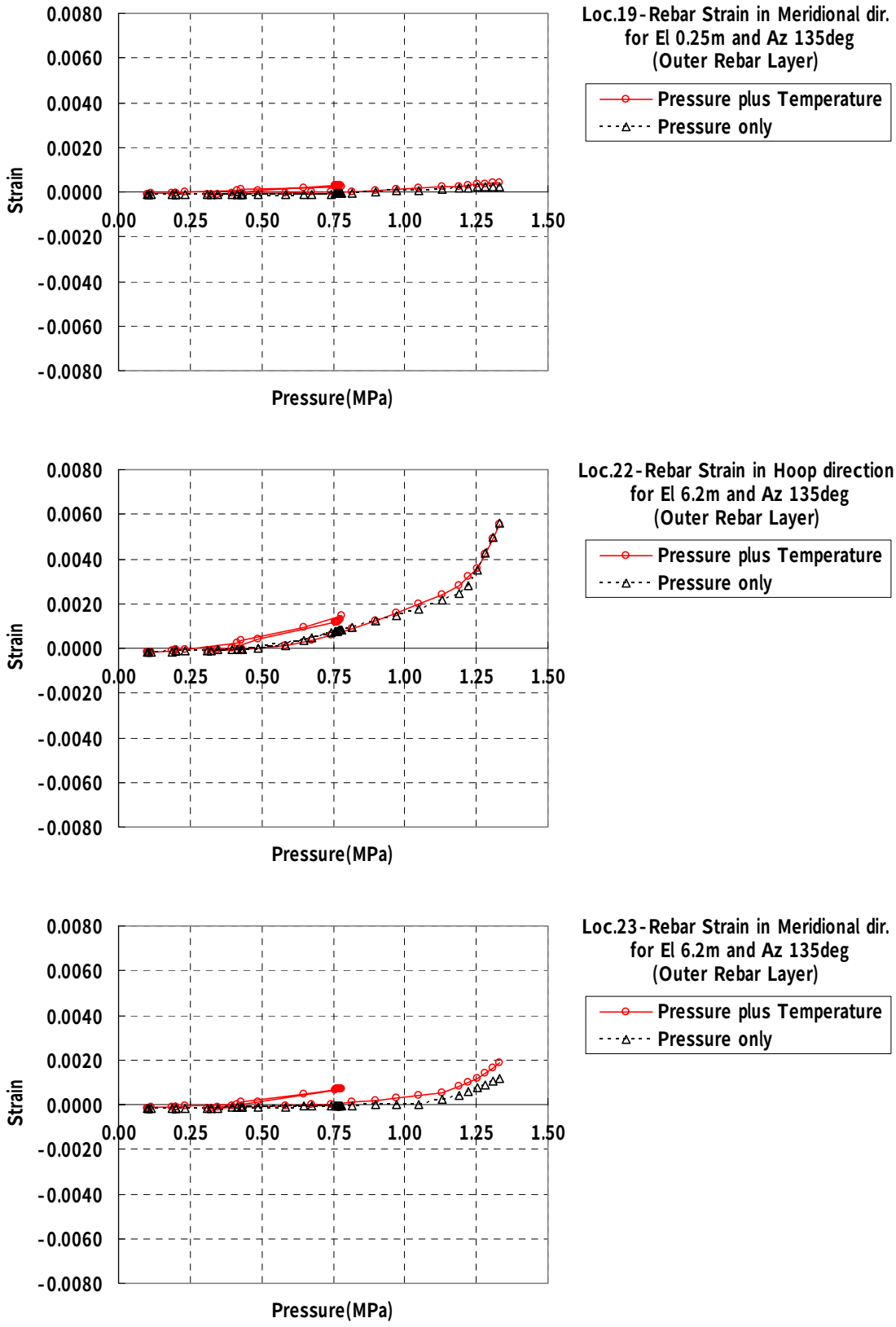

Figure 4-25 Comparison at standard Output Locations 19,22 and 23(Case2)

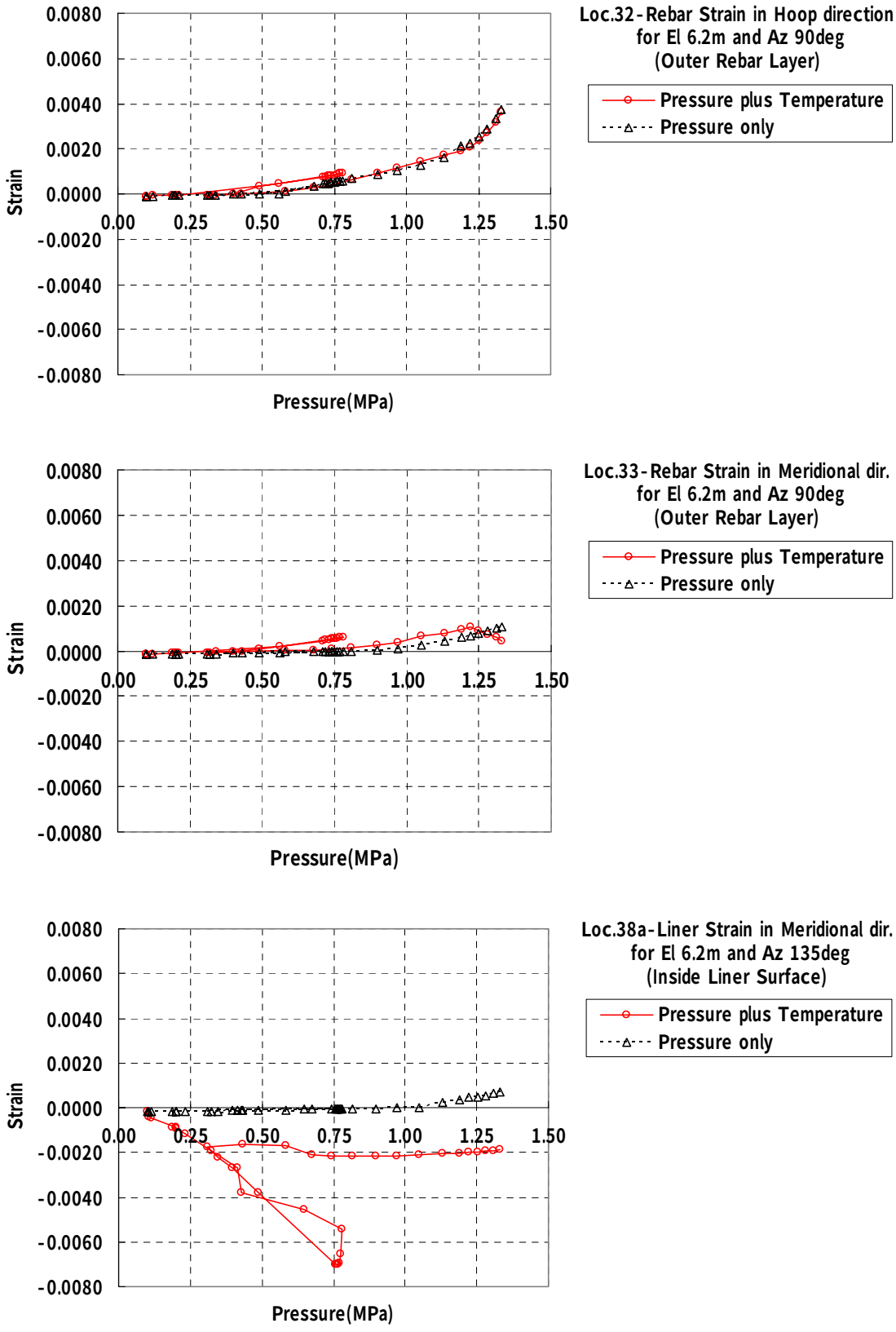

Figure 4-26 Comparison at standard Output Locations 32,33 and 38(Case2)

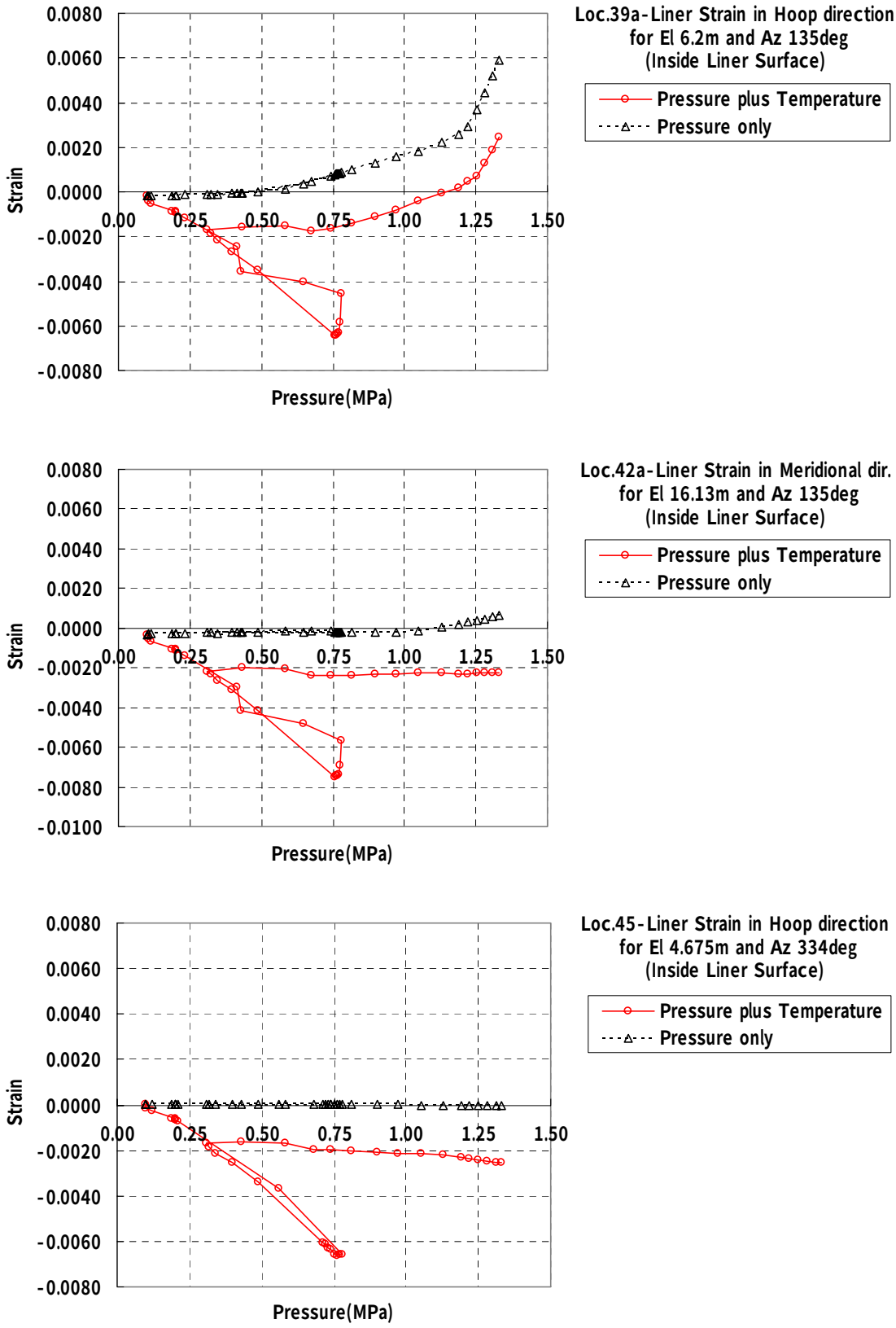

Figure 4-27 Comparison at standard Output Locations 39, 42 and 45(Case2)

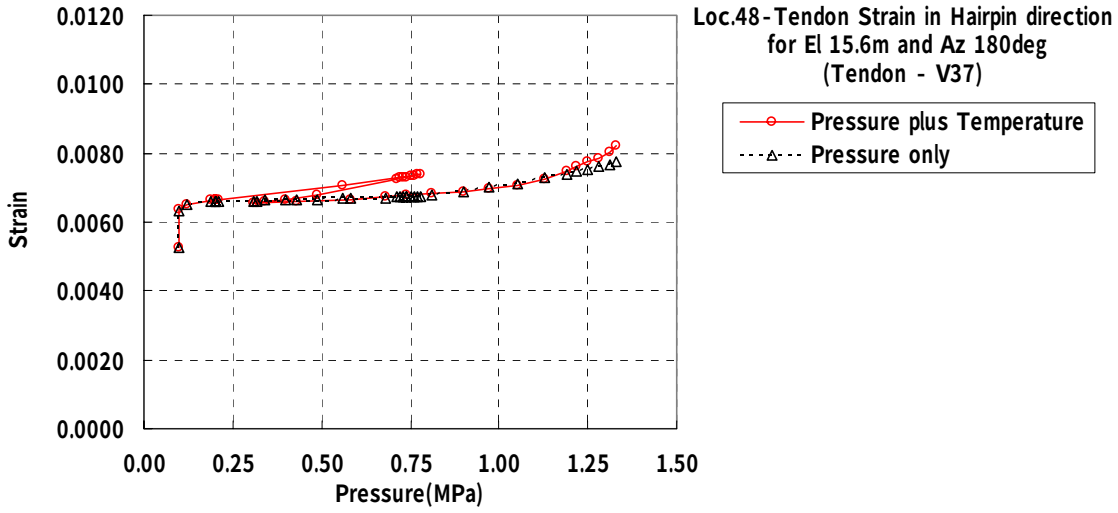

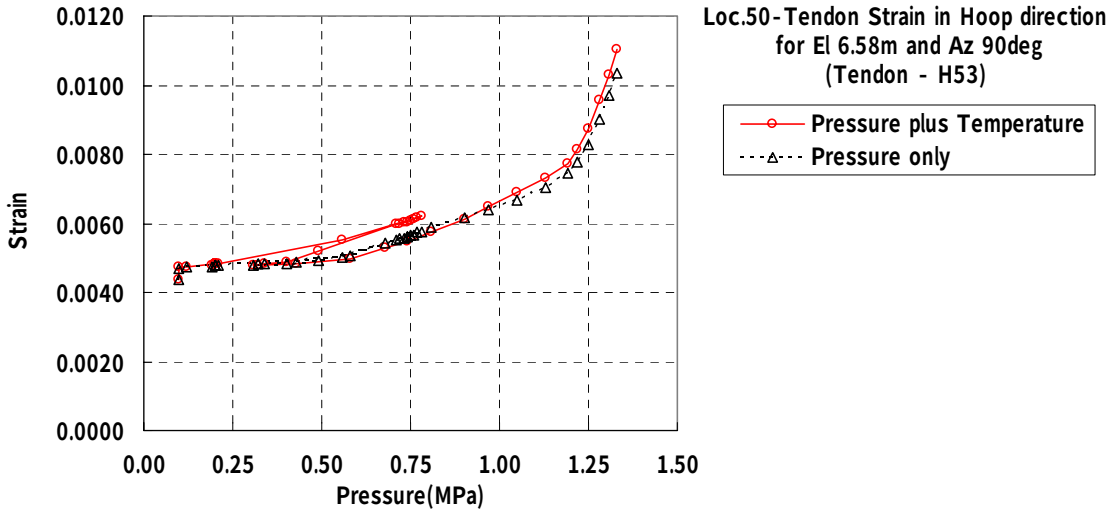

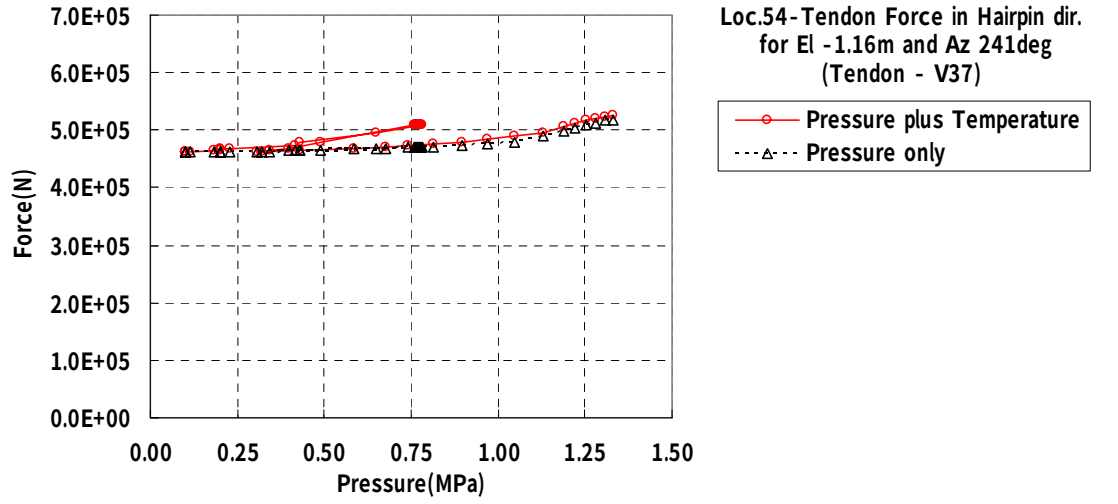

Figure 4-28 Comparison at standard Output Locations 48,50 and 54(Case2)

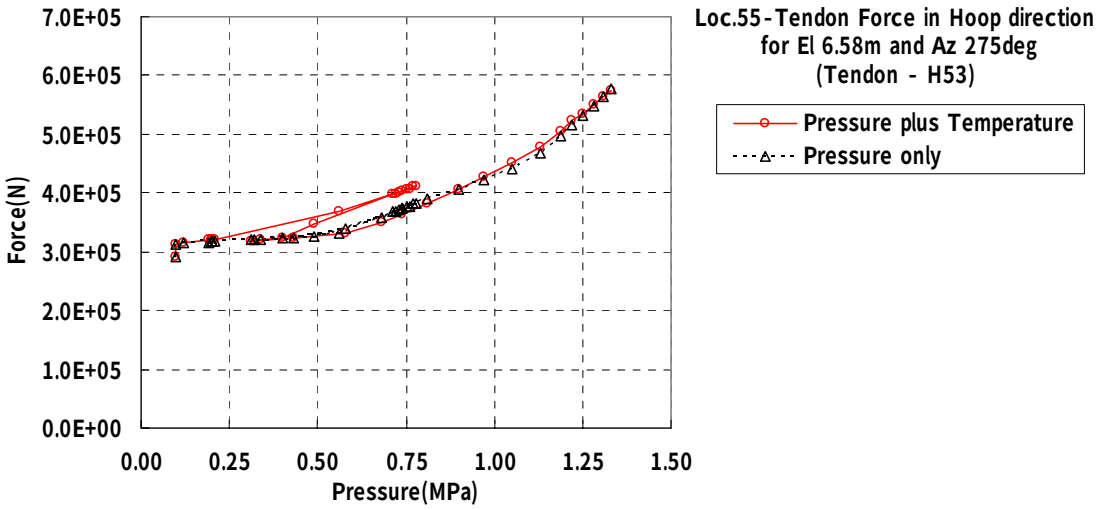

Figure 4-29 Comparison at standard Output Locations 55(Case2)

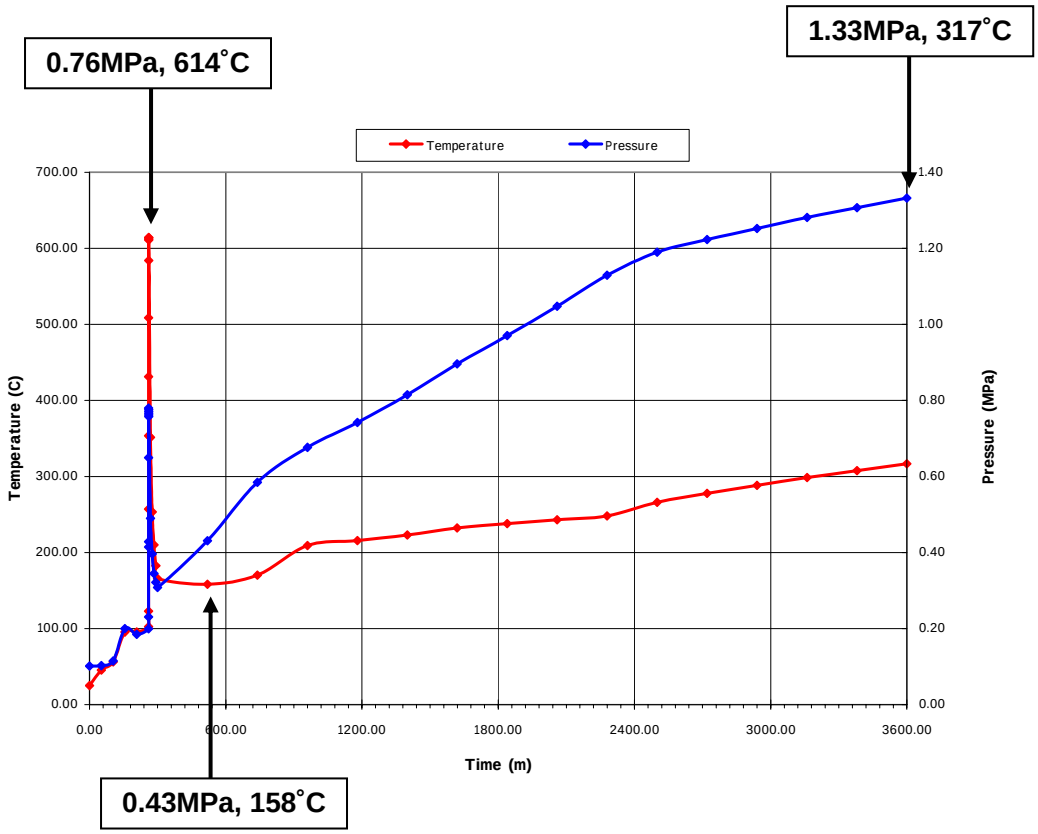

Figure 4-30 Figure 4.1.9 Showing point of contour (Case2)

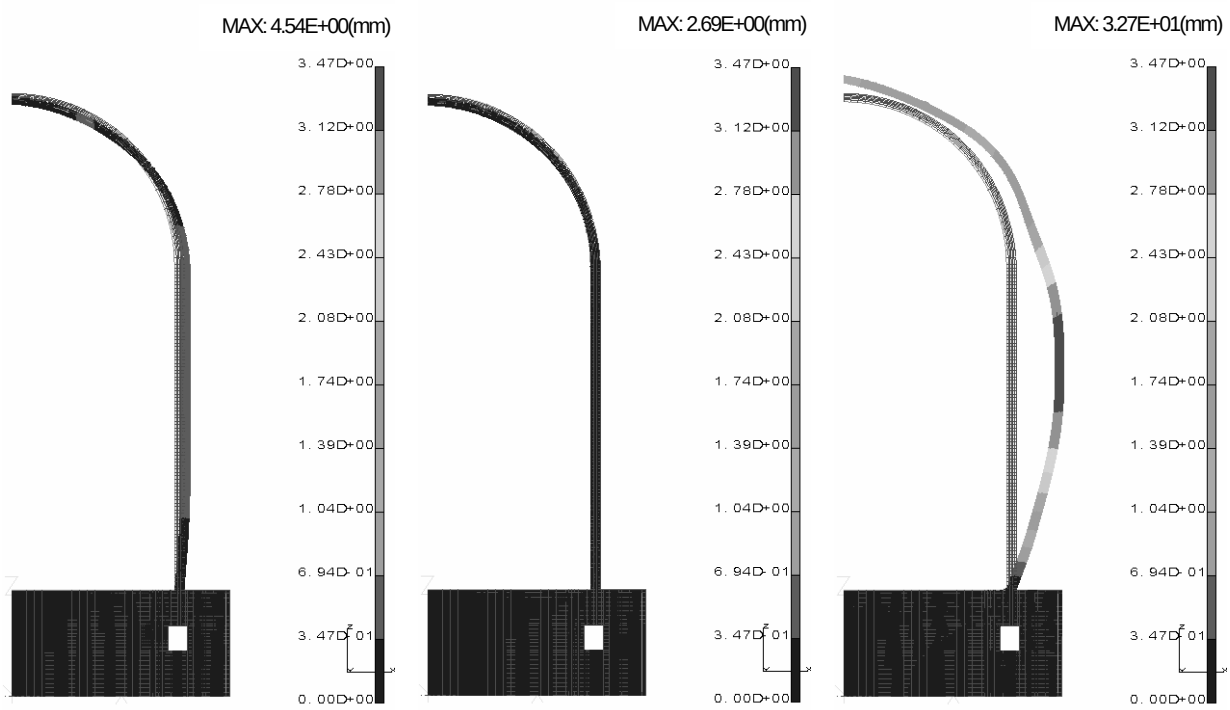

0.76MPa(261.02min) 0.43MPa(519.55min) 1.33MPa(3600.00min)

Figure 4-31 Deformation contour - Pressure only(Case2)(Scale factor:50)

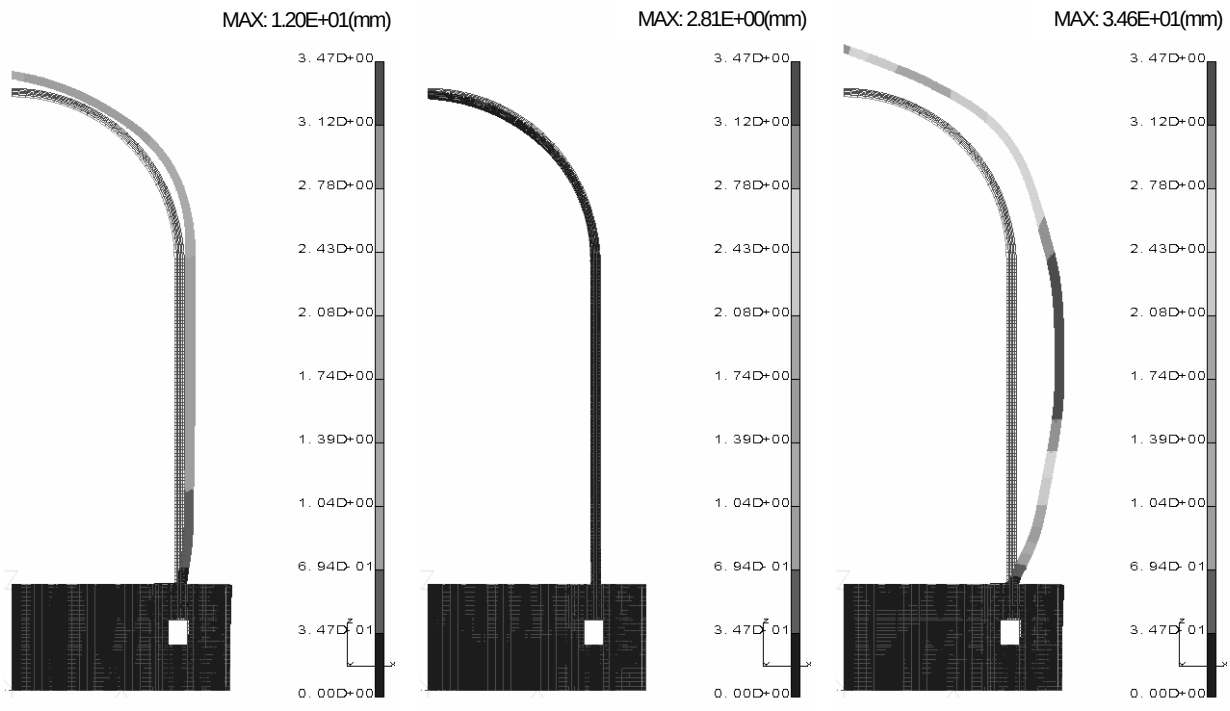

0.76MPa,614C (261.02min) 0.43MPa,158C (519.55min) 1.33MPa,317C (3600.00min)

Figure 4-32 Deformation contour - Pressure plus Temperature(Case2) (Scale factor:50)

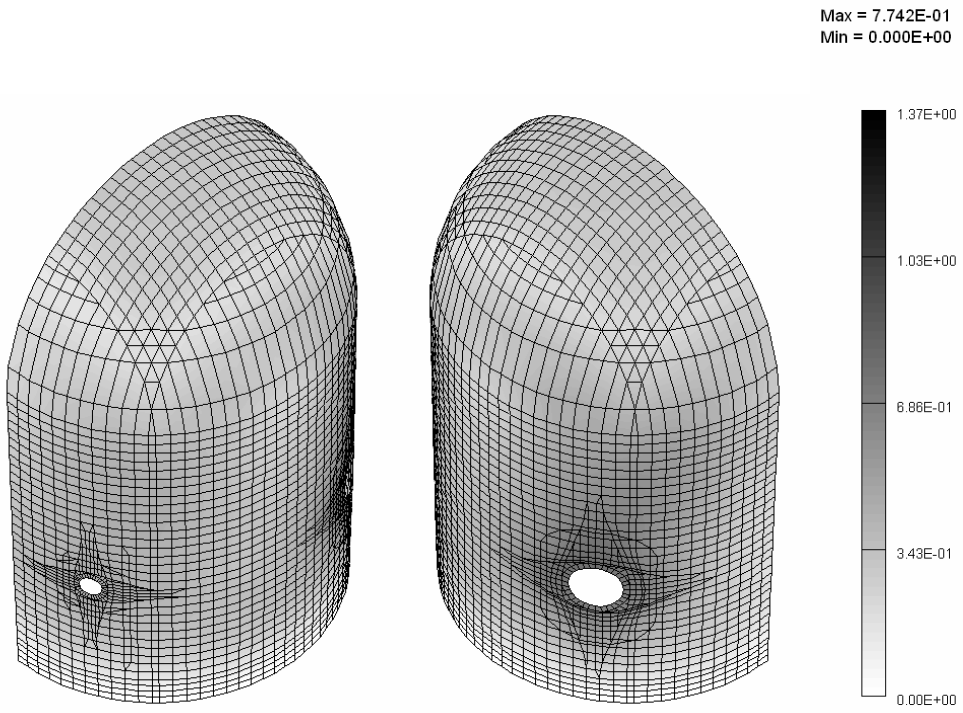

Figure 4-33 Deformation contour at 0.76MPa-Pressure only(Case2)

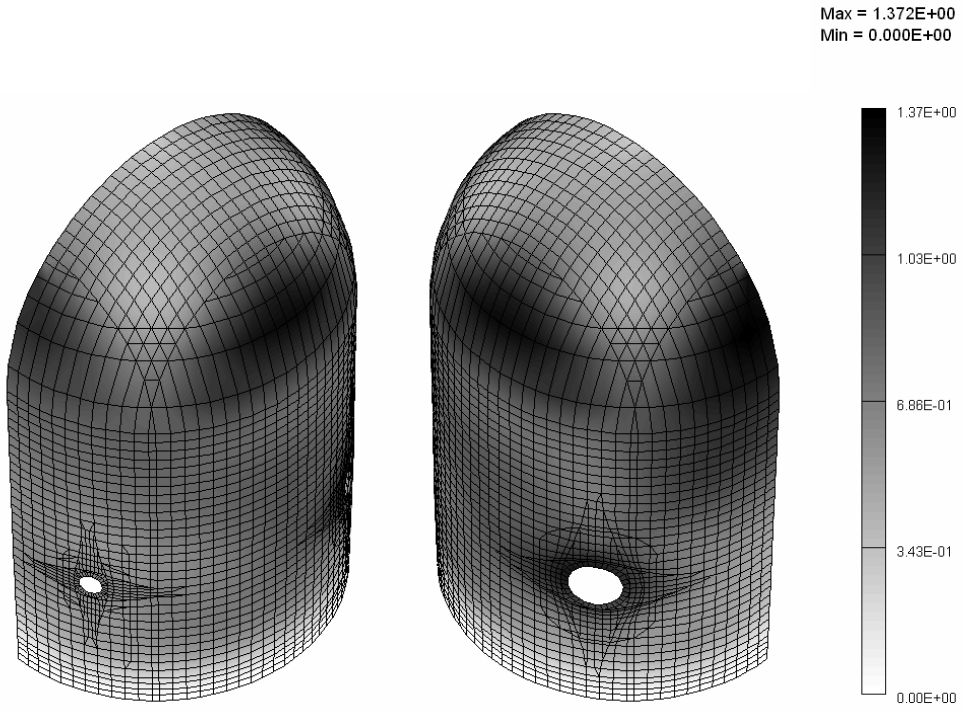

Figure 4-34 Deformation contour at 0.76MPa, 612˚C -Pressure plus Temperature(Case2)

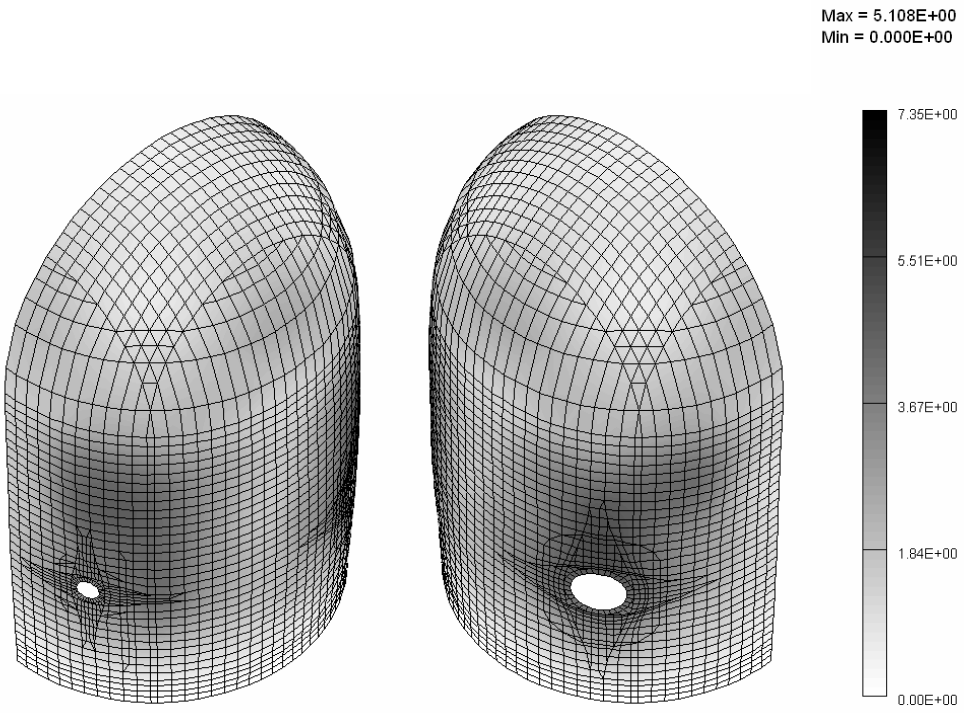

Figure 4-35 Deformation contour at 1.33MPa-Pressure only(Case2)

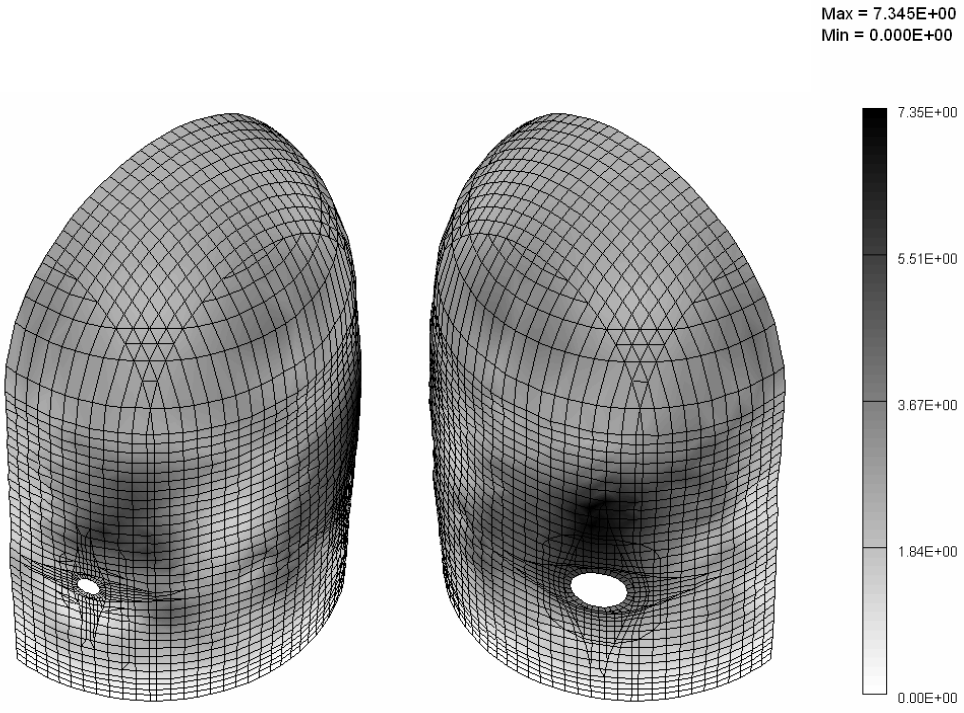

Figure 4-36 Deformation contour at 1.33MPa, 317˚C -Pressure plus Temperature(Case2)

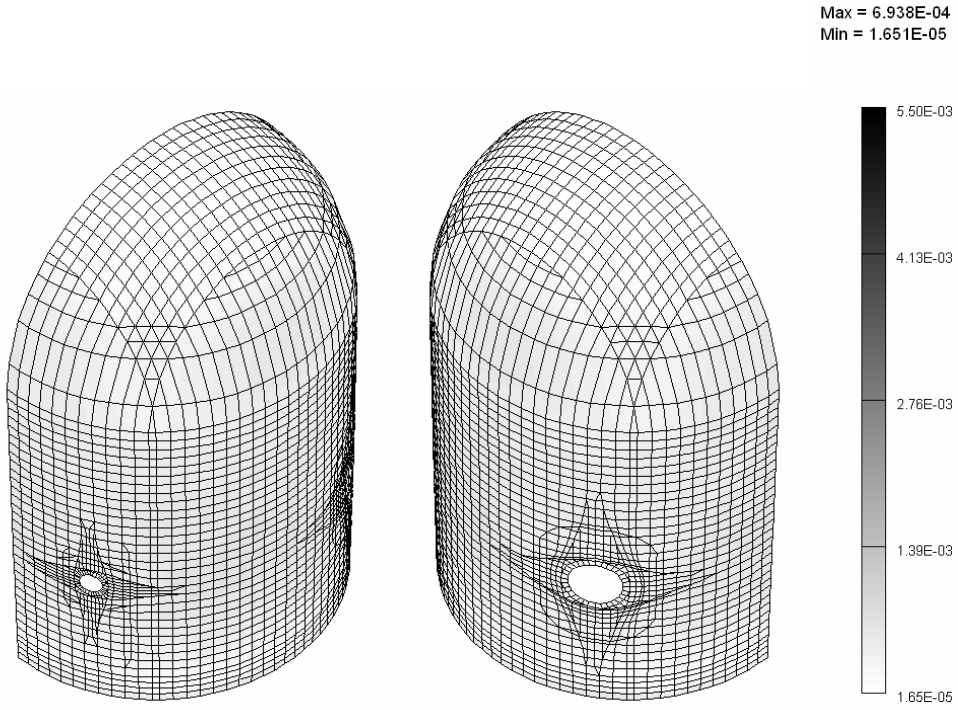

Figure 4-37 Von Mises strain contour of liner at 0.76MPa-Pressure only(Case2)

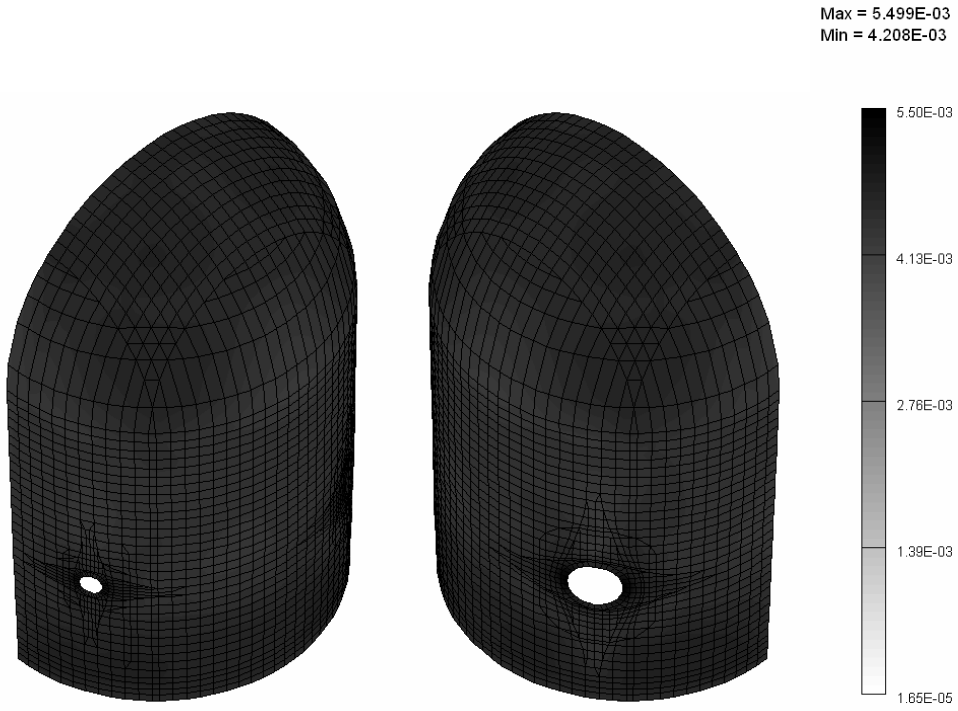

Figure 4-38 Von Mises strain contour of liner at 0.76MPa, 612˚C -Pressure plus Temperature(Case2)

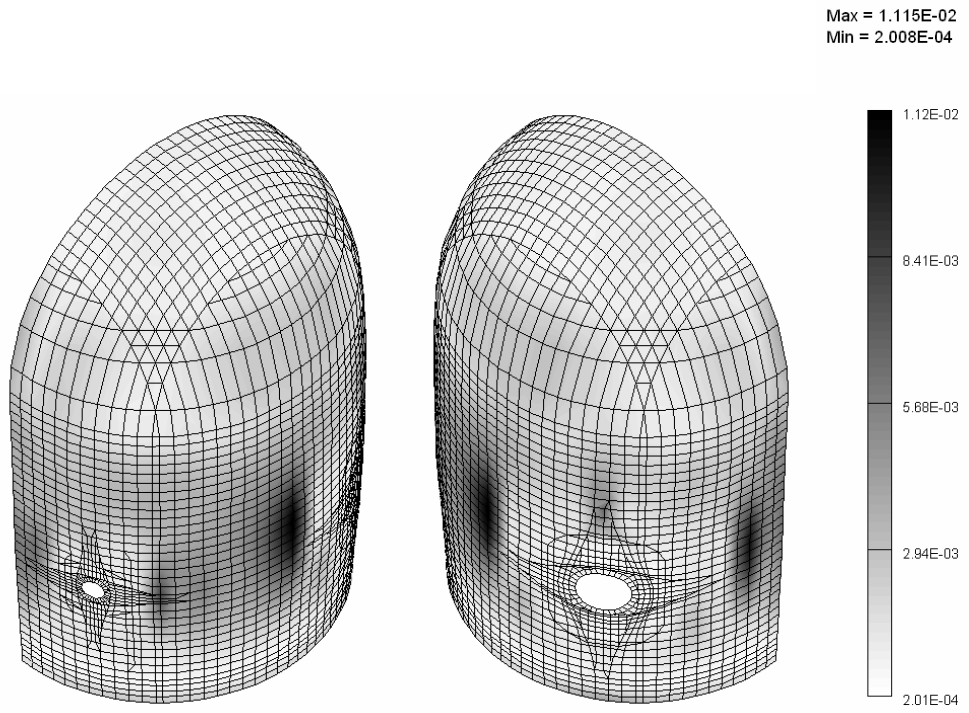

Figure 4-39 Von Mises strain contour of liner at 1.33MPa-Pressure only(Case2)

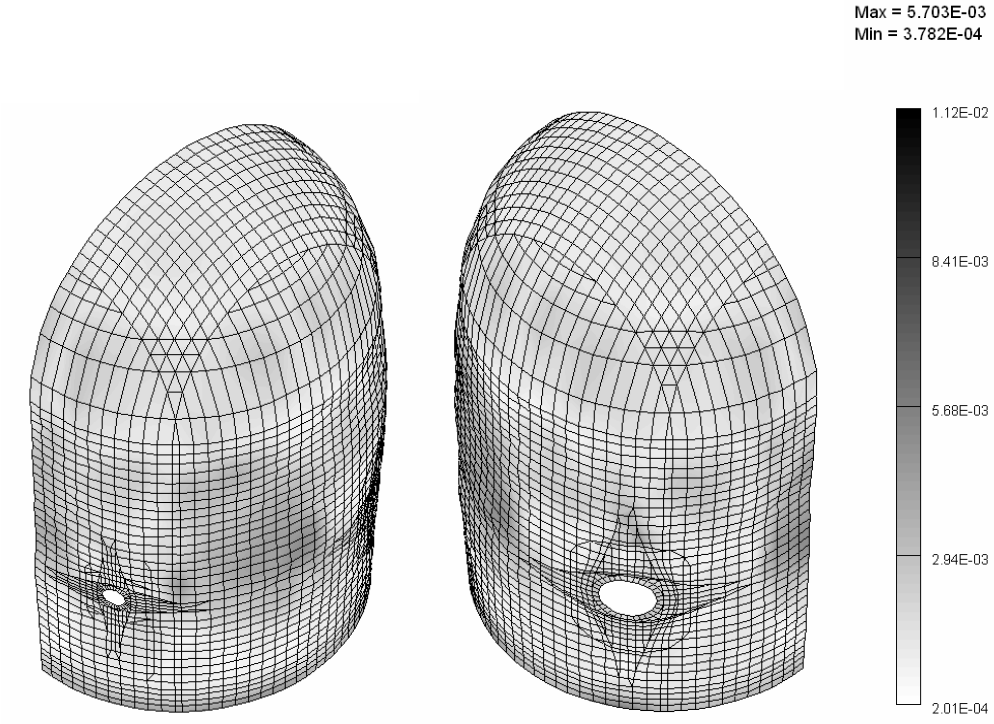

Figure 4-40 Von Mises strain contour of liner at 1.33MPa, 317˚C -Pressure plus Temperature(Case2)

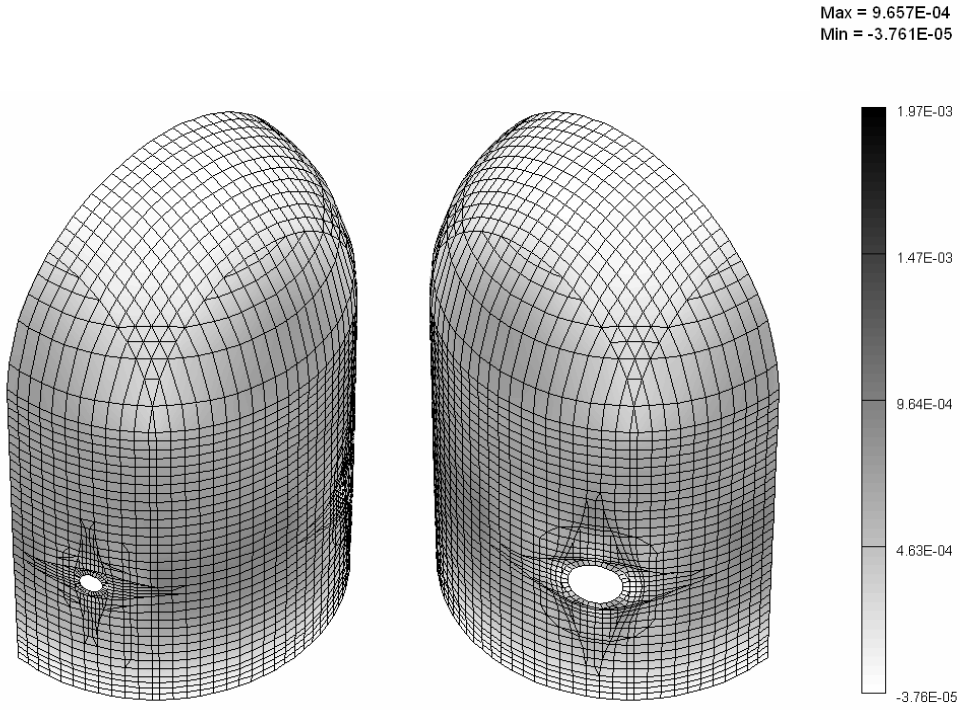

Figure 4-41 Strain contour of inner horizontal reinforcement at 0.76MPa -Pressure only(Case2)

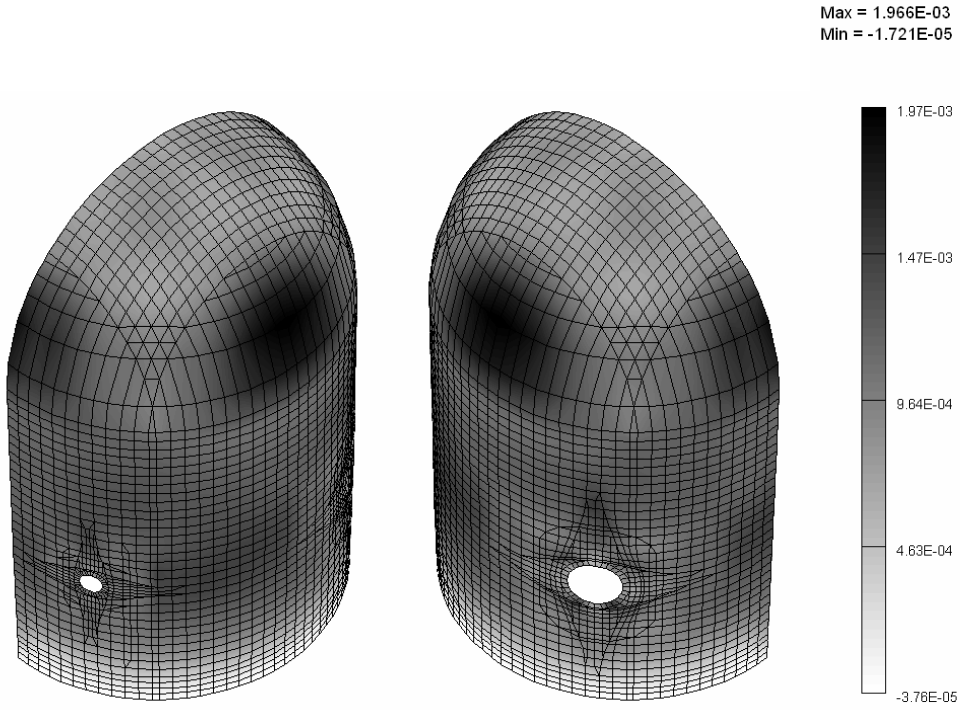

Figure 4-42 Strain contour of inner horizontal reinforcement at 0.76MPa, 612˚C -Pressure plus Temperature(Case2)

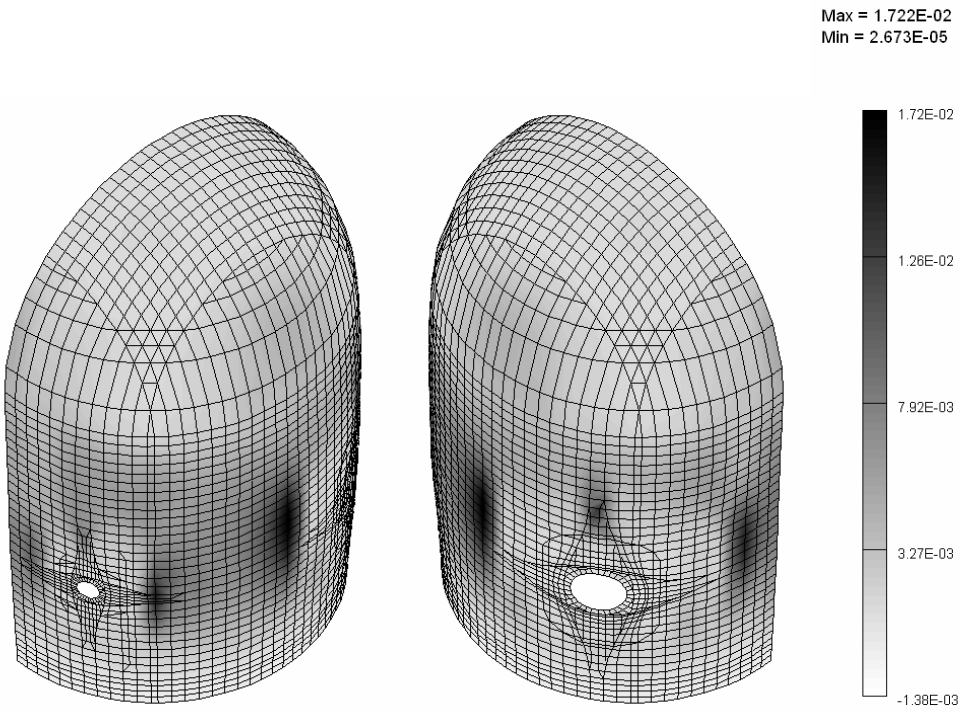

Figure 4-43 Strain contour of inner horizontal reinforcement at 1.33MPa -Pressure only(Case2)

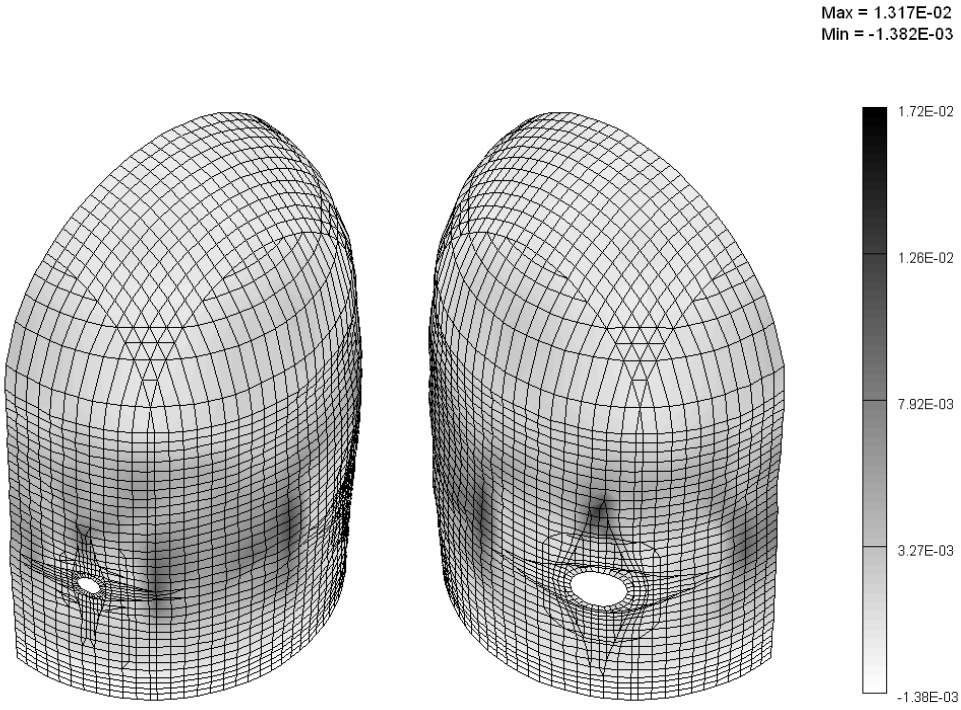

Figure 4-44 Strain contour of inner horizontal reinforcement at 1.33MPa, 317˚C -Pressure plus Temperature(Case2)

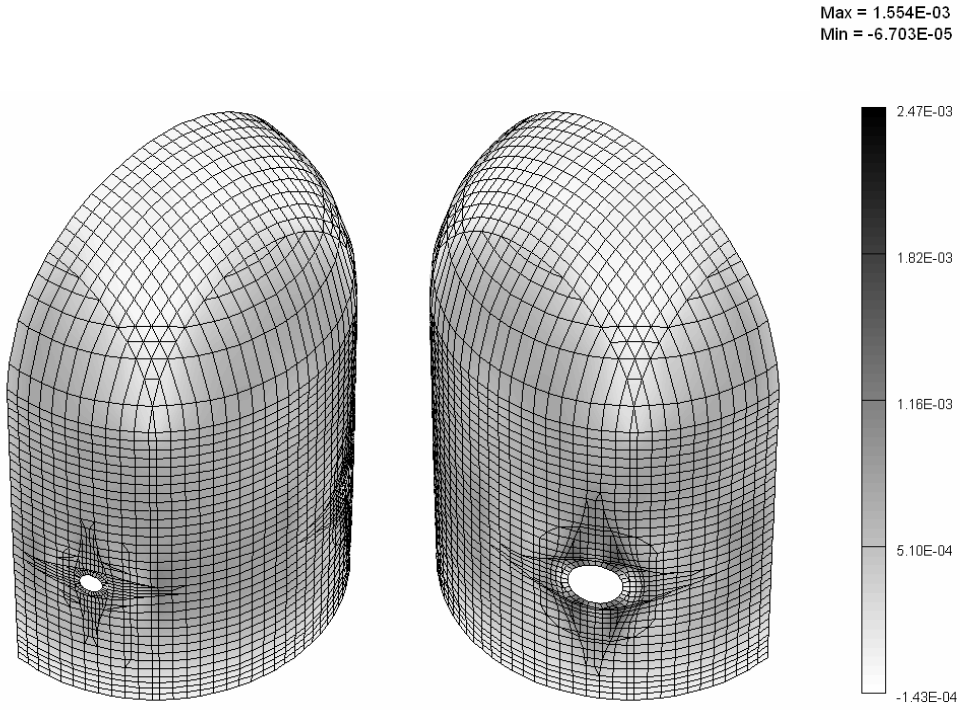

Figure 4-45 Strain contour of outer horizontal reinforcement at 0.76MPa -Pressure only(Case2)

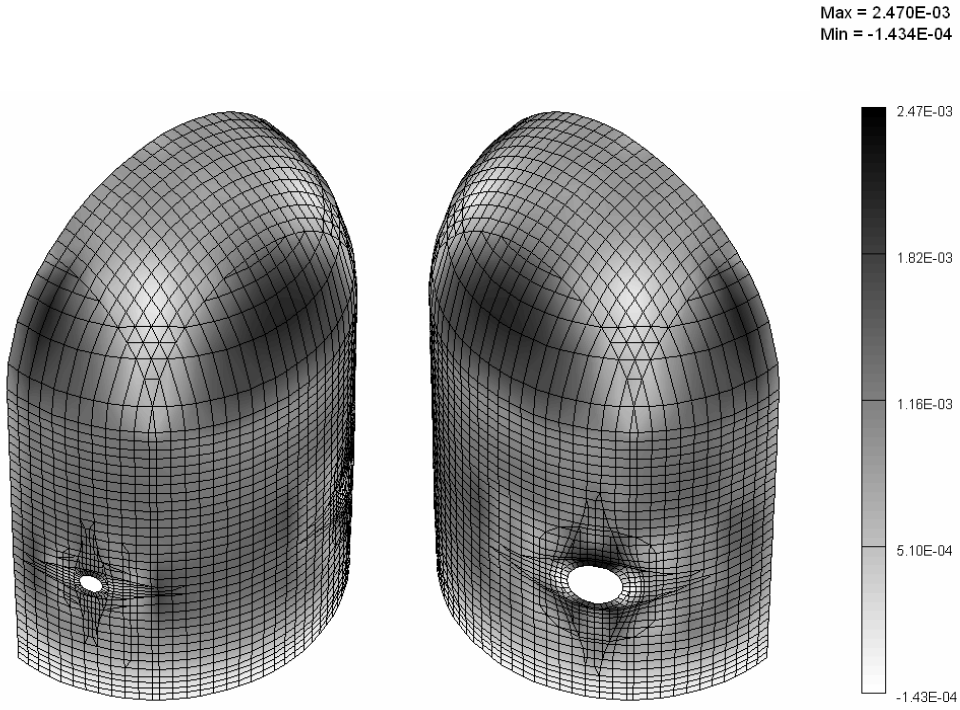

Figure 4-46 Strain contour of outer horizontal reinforcement at 0.76MPa, 612˚C -Pressure plus Temperature(Case2)

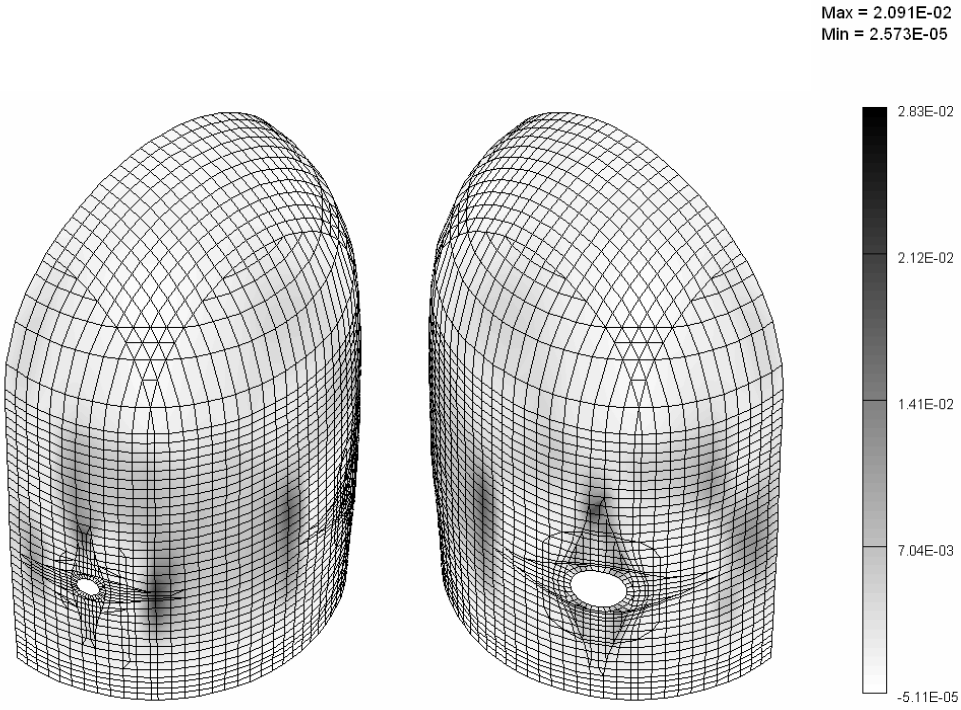

Figure 4-47 Strain contour of outer horizontal reinforcement at 1.33MPa -Pressure only(Case2)

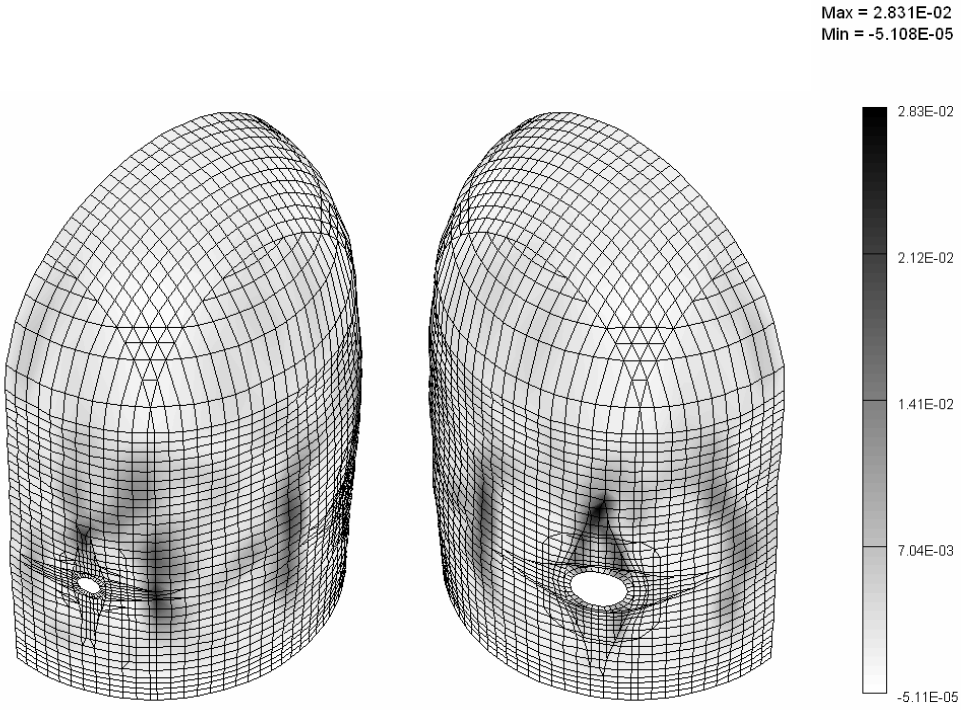

Figure 4-48 Strain contour of outer horizontal reinforcement at 1.33MPa, 317˚C -Pressure plus Temperature(Case2)

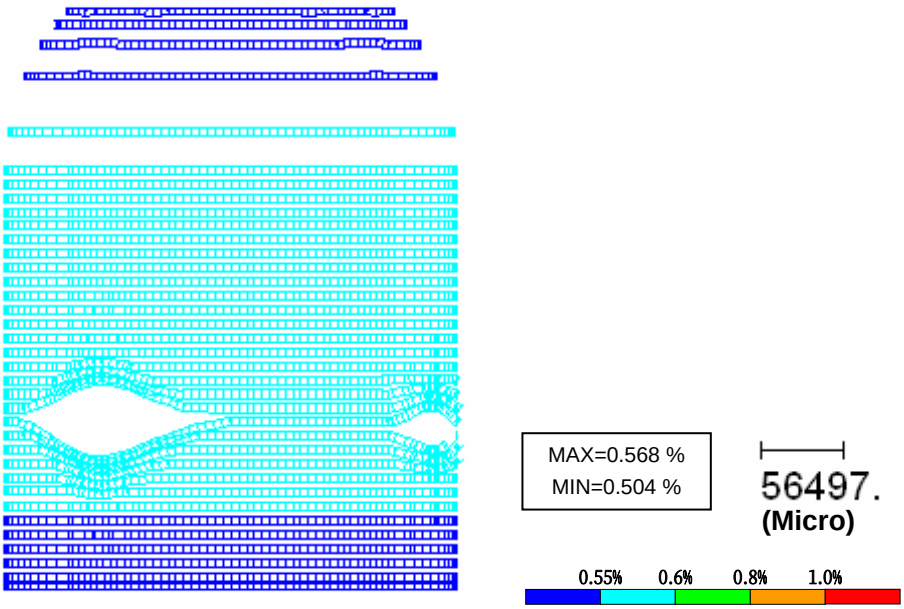

Figure 4-49 Strain contour of hoop tendon at 0.76MPa
-Pressure only(Case2)

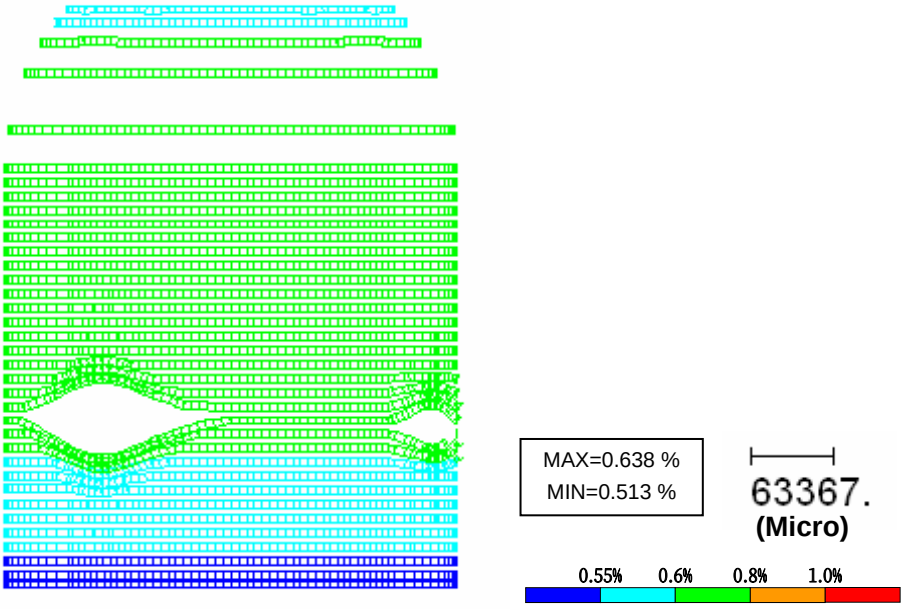

Figure 4-50 Strain contour of hoop tendon at 0.76MPa, 612°C
-Pressure plus Temperature(Case2)

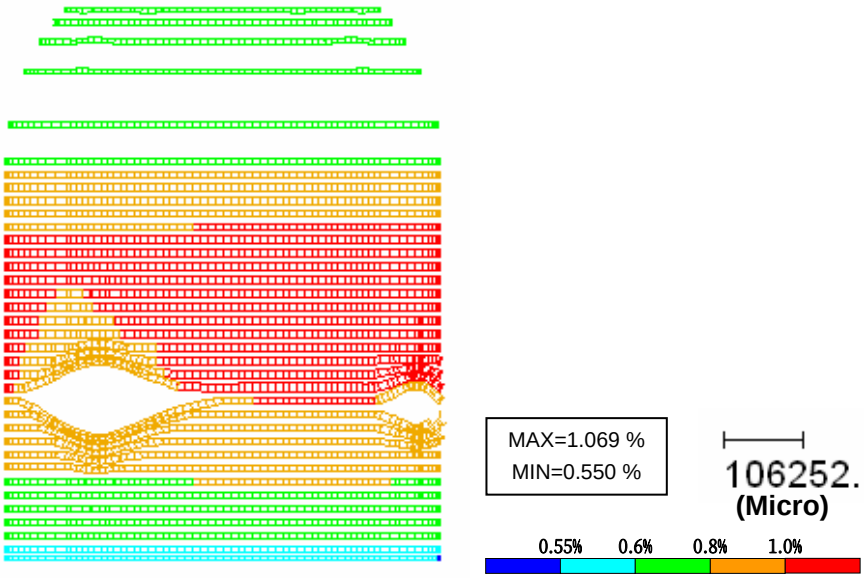

Figure 4-51 Strain contour of hoop tendon at 1.33MPa
-Pressure only(Case2)

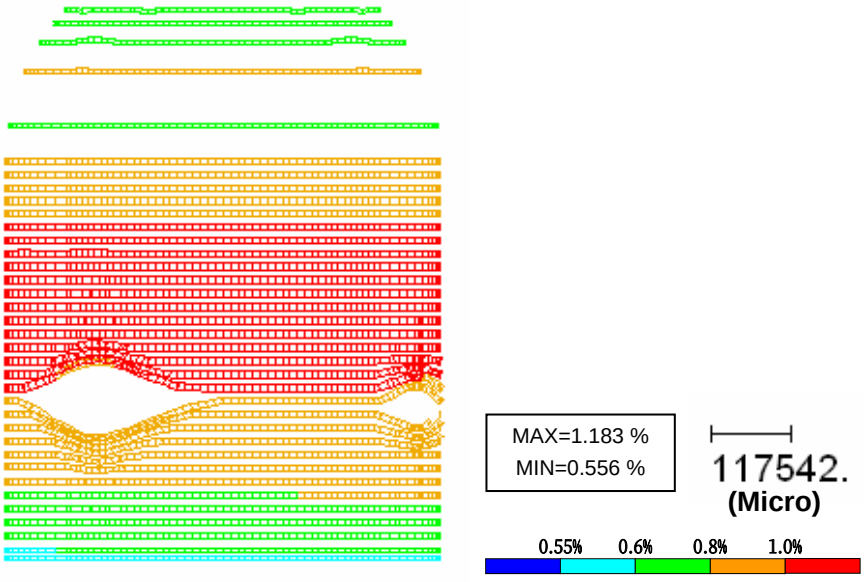

Figure 4-52 Strain contour of hoop tendon at 1.33MPa, 317°C
-Pressure plus Temperature(Case2)

5. Conclusions

The conclusions obtained from this analytical study are as follows.

(1) From analysis results of Case 1 in SOLs it was found that the influence of the temperature on the strains of the steel materials are small on condition that the thermal conditions are steady-state and the thermal gradient in a section is constant. Within this range of the pressure and thermal conditions, no steel materials have reached critical strains.

(2) From the analysis results of Case 2 in SOLs it was found that the influence of the temperature on the strains of the steel materials are large on condition that the thermal and pressure conditions are unsteady and the thermal gradient in a section changes drastically. Within this range of the pressure and thermal conditions, no steel materials have reached critical strains.

(3)In case the pressure and thermal loading is applied simultaneously, the strain due to the thermal moment will be added to the strain by the pressure. Consequently, compressive strain is added in the liner and the inner rebars, and tensile strain is added in the outer rebars. However, the strain added the thermal loading in the hoop tendon located near the neutral axis is small.

(4) The ultimate pressure would be estimated based on analysis results. In Case1, the rupture of the liner precedes. In Case2, the liner, the rebar and the tendon reach the critical strains almost at the same time. In the case of the thermal loading is added to the pressure loading, the strain of the liner decelerates and the strain of the outer rebar accelerates as compared with the results under only pressure loading. As a result, the strain ratio to critical strain of the outer rebar will become largest and it will reach the critical strain firstly.

(5) The thermal effect to the rupture of the PCCV is caused by addition of the thermal strain in case the change in the critical strain of the steel materials by heat is sufficiently small. The thermal strain in the 1:4-scale model may be as same as that in the full-scale model if their gradients are the same. Consequently the thermal strains to be added in the both models are the same in the balanced conditions only by the steel materials near the ultimate state. It follows from this, that the scale effect on the thermal load may be small.

6. References

[1] Overpressurization Test of a 1:4-Scale Prestressed Concrete Containment Vessel Model, NUREG/CR-6810 Report, USA, SAND2003-0840P.

[2] Pretest Round Robin Analysis of a Prestressed Concrete Containment Vessel Model, NUREG/CR-6678 Report, USA, SAND 00-1535.

[3] Yonezawa K., Imoto K., Kato A., Ozaki M., Kiyohara K., Murazumi Y., Sato K.: Pretest and Posttest Analyses for Nonlinear behavior of 1/4PCCV Model Subjected to Internal Pressure, E-298, The First FIB Congress in Osaka, 2002.

[4] Takeda T., Yamaguchi T. and Naganuma K.: Report on Tests of Nuclear Prestressed Concrete Containment Vessels, Concrete Shear in Earthquake, Edited by T. C. C. Hsu, S. T. Mau, Elsevier Applied Science, pp.163-172, 1992.

[5] Analysis of Axisymmetric Prestressed Concrete Containment Vessel (PCCV) Including Thermal Effects, May 27, 2004, Revised August 19, 2004

[6] Darwin, D. and Pecknold, D.A.: Nonliner Biaxial Stress-Strain Law for Concrete, J. of EM Div., ASCE, Vol.103, No. EM2, pp.229-241, April, 1977.

[7] Kupfer, H. B.: Behavior of Concrete under Biaxial Stress, J. of E. M. Div., ASCE, Vol.99, No.EM4, pp.853-866, Aug., 1973.

[8] Willam, K. J. et al.: Constitutive Model for the Triaxial Behavior of Concrete, Proc. of int. Assoc. for Bridge & Stru. Eng., Vol.19, pp.1-30, 1975.

[9] Ohnuma, H. et al.: Ultimate Strength Property of Concrete under Triaxial Compressive Stresses, Report of CRIEIPI, No.381021, Dec., 1981, in Japanese.

[10] Elwi, A. A. et al.: A 3D Hypoelastic Concrete Constitutive Relationship, J. of EM Div., ASCE, Vol. 105, No.EM4, pp.623-641, Aug., 1979.

[11] Naganuma, K.: Stress-Strain Relationship for Concrete under Triaxial Compression, Journal of structural and construction engineering (Transactions of AIJ), No.474, pp.163-170, Aug., 1995, in Japanese.

[12] Al-Mahaidi, R. S. H.: Nonlinear Finite Element Analysis of Reinforced Concrete Deep Members, Report 79-1, Dep. of Structural Engineering, Cornell Univ., Jan., 1979.

[13] Amemiya A. and Noguchi H.: Development of Finite Element Analytical Program for High Strength Reinforced Concrete Member Part1: Development of Concrete Model, Annual Convention of AIJ, Proceeding of Structures II, pp.639-640, Oct., 1990, in Japanese.

Appendix I: Korea Atomic Energy Research Institute
Phase 2: I-1 to I-26
Phase 3: no report available

FINITE ELEMENT ANALYSIS OF A 1:4 SCALE PCCV MODEL

Hong-pyo Lee, Young-sun Choun
Korea Atomic Energy Research Institute, Korea

Abstract

This report describes the finite element (FE) analysis results of a 1:4 scale model of a pre-stressed concrete containment vessel (PCCV) model. The objective of the present FE analysis is to evaluate the ultimate internal pressure capacity of the PCCV as well as its failure mechanism when the PCCV model is subjected to a monotonous internal pressure beyond its design pressure. The FE analysis used two concrete failure criteria with the commercial code ABAQUS. One is axi-symmetric model with modified Drucker-Prager failure criteria and the other is 3-dimensional model with damaged plasticity model. Finally, the FE analysis results on the ultimate pressure and failure modes have a good agreement with experimental data.

Introduction

This report describes the finite element (FE) analysis results of a 1:4 scale model of a pre-stressed concrete containment vessel (PCCV) tested by the Nuclear Power Engineering Corporation (NUPEC) of Japan and the U.S. Nuclear Regulatory Commission (NRC) [1]. The main objective of the present FE analysis is to evaluate the failure load of the PCCV as well as its failure mechanism when the PCCV model is subjected to a monotonous internal pressure beyond its design pressure 0.4MPa. In addition we try to evaluate the performance of the existing numerical simulation tool and intend to use its results as future numerical reference solutions.

Two FE models such as 2-dimensional axi-symmetric model and 3-dimensional model with opening and two buttresses are considered in the present nonlinear FE analysis. In the axi-symmetric model, all the portions of PCCV such as the cylinder wall, dome and basemat are considered in the FE analysis. Concrete part was modeled with 4-node axi-symmetric solid element and the steel liner was modeled with 2-node axi-symmetric membrane element. In addition, reinforcement and tendon were modeled with rebar element. Modified Drucker-Prager model [2] is used for concrete failure criterion. In the 3-dimensional model, concrete part was modeled with 8-node solid element and the steel liner was modeled with 4-node membrane element. Reinforcement and tendon are modeled with the embedded element. A damaged plasticity model [3] is adopted to be used as concrete failure criterion.

This report summarizes the FE analysis results produced by Korea Atomic Energy Research Institute (KAERI) with the above two FE models using the commercial code ABAQUS [4]. The material properties and detailed structural geometry used in the present FE analysis are provided in the following sections with numerical results.

Material Properties used in FE analysis

The material properties for concrete, steel rebars, post-tensioned tendons and steel liner are prepared by using the experiment data provided by Sandia National Laboratories (SNL)[1]. In this section, the material properties used in FE analysis are briefly described.

Concrete

Two types of concrete such as a normal strength concrete and a high strength concrete were used to construct the SNL PCCV test model [1]. In the present FE analysis, the material property data for the trial mix concrete based on a field curing are used. The material properties adopted in the FE analysis are described in Table 1.

Reinforcing Steel

The material properties for each type of rebar are selected from the test data. The material properties are summarized in Table 2 and the test data for reinforcing bar is illustrated in Figure 1 [1]. In FE analysis, we adopt the mean value for the material properties of rebar: (a) SD490 is used for the

basemat part; (b) SD390 is used for the cylinder wall and dome parts.

- Elastic modulus : 1.86E5 MPa (basemat), 1.848E5 MPa (wall and dome)
- Yield stress : 512.2 MPa (basemat), 479.9 MPa (wall and dome)
- Ultimate stress : 709.7 MPa (basemat), 628.7 MPa (wall and dome)
- Poisson's ratio : 0.3
- Elongation(%) : 17.8 MPa (basemat), 21.32 MPa (wall and dome)

Prestressing Tendon

TAISEI performed the calibration tests of six samples of a three-strand tendon assembly. The stress-stain data are calculated by the division of the measured forces by the initial cross section area ($339mm^2$) as shown in Figure 2 [5]. The ultimate stress and strain test data are summarized in Table 3[2].

Steel Liner Plate

Two sets of material samples for the steel liner plate, LPY in vertical direction and LPX in circumferential direction, were tested to evaluate their material properties. Each test set consists of three samples. The stress-strain data is illustrated in Figure 3 and the test results are summarized in Table 4.

Table 1. Material data for trial mix concrete (unit: MPa)

Material / Item	f_c'=29.42 (basemat)		f_c'=44.13 (dome & wall)	
	Standard curing	Field curing	Standard curing	Field curing
Compressive strength	51.39	41.68	60.21	48.84
Tensile strength	3.93	3.37	4.21	3.45
Flexural strength	5.37	4.00	5.58	5.51
Young's modulus	29,030	27,950	31,970	26,970
Poisson's ratio	0.20	0.18	0.20	0.18
Density (ton/m^3)	2.25	2.21	2.26	2.19

Figure 1. Stress-strain relationship for steel

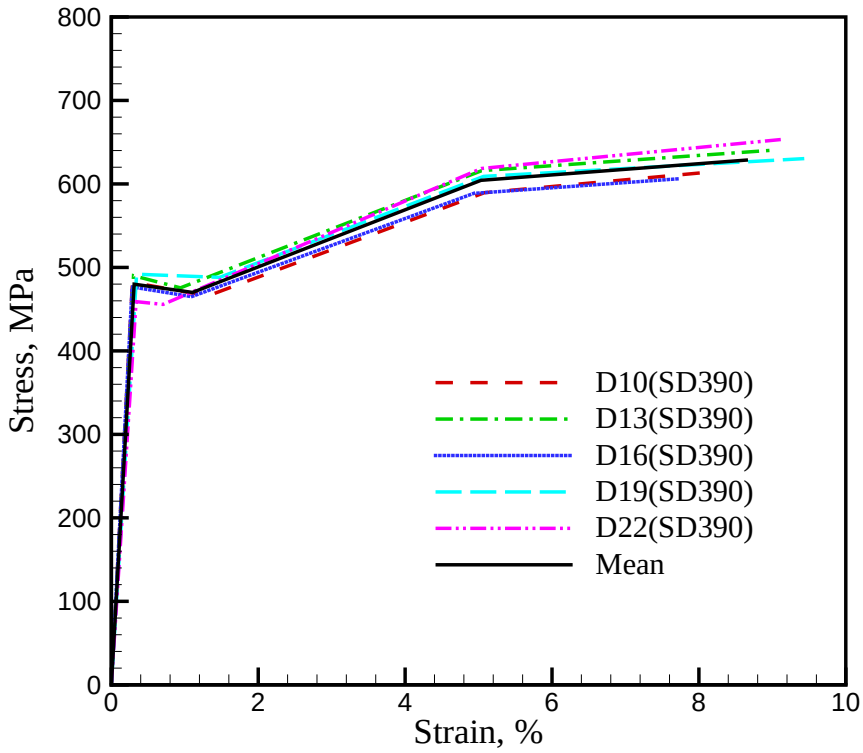

Table 2. rebar material properties (unit:MPa)

Material / Item	D10 (SD390)	D13 (SD390)	D16 (SD390)	D19 (SD390)	D22 (SD390)	D19 (SD490)
Elastic modulus	1.83E5	1.83E5	1.83E5	1.84E5	1.91E5	1.86E5
Poisson's ratio	0.3	0.3	0.3	0.3	0.3	0.3
Yield stress	482.0	490.1	476.6	491.9	459.0	512.2
Ultimate stress	613.6	640.4	606.2	630.4	653.2	709.7
Elongation (%)	20.5	24.2	22.1	21.1	18.7	17.8

Figure 2. Stress-Strain relationship for tendons

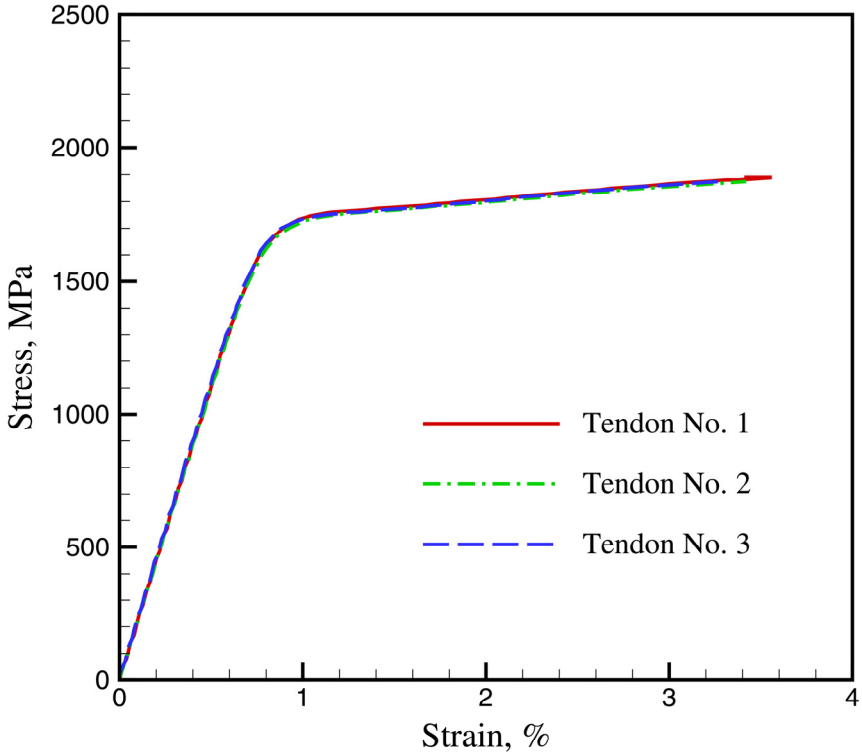

Table 3. Tendon material data

Test specimen	Ultimate stress (MPa)	Failure strain (%)
Specimen 1	1,924	3.32
Specimen 2	1,912	3.51
Specimen 3	1,932	3.36
Specimen 4	1,921	No strain gages
Specimen 5	1,934	No strain gages
Specimen 6	1,924	3.3
Mean	1,924.5	3.3

* Estimate based on surviving strain gages

Figure 3. Stress-strain relationship for steel liner

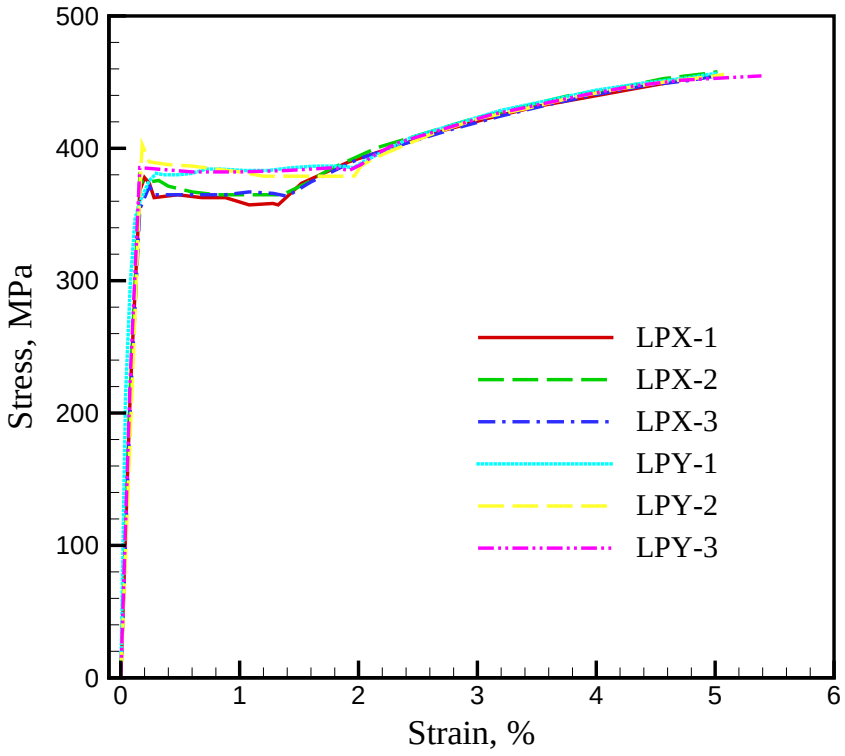

Table 4. Material data for steel liner

Material	Temperature	Test sample	Yield stress (MPa)	Ultimate stress (MPa)	Elongation (%)
SGV410	R.T.(23 °C)	LPY-1	381.5	495.2	33.8
"	"	LPY-2	403.1	498.2	33.0
"	"	LPY-3	385.4	497.2	33.6
"	"	LPX-1	377.6	499.2	33.0
"	"	LPX-2	377.6	500.1	33.0
"	"	LPX-3	370.7	497.2	33.0
Average			382.7	497.85	33.2

Constitutive Models

As briefly mentioned before, two FE models are prepared for the nonlinear analysis of 1:4-scale PCCV model. One is axi-symmetric FE model and the other is three-dimensional FE model considering the penetrations such as equipment hatch and personal airlock. This section describes the constitutive models used for two FE models.

Concrete model

2-dimensional axi-symmetric model

The modified Drucker-Prager's model [2] is used for 2-dimensional axi-symmetric FE analysis. In this model, three different yield criteria based on the shape of the yield surface in the meridional plane are provided in ABAQUS. These yield surfaces are a linear form, a hyperbolic form and a general exponent form. In the present analysis, the yield surface with linear form is adopted. The linear model used in FE analysis is written in terms of all three stress invariants.

$$F = t - p\tan\beta - d = 0 \tag{1}$$

where $t = \frac{1}{2}q\left[1 + \frac{1}{K} - \left(1 - \frac{1}{K}\right)\left(\frac{r}{q}\right)^3\right]$

p , q , r are stress invariants defined in stress and strain measurements.

β is the slope of the linear yield and is commonly referred to as the friction angle of the material,

d is the cohesion of the material and

K is the ratio of the yield stress in triaxial tension to the yield stress in triaxial compression and, thus controls the dependency of the yield surface on the value of the intermediate principal stress.

The values of K=1, t=q imply that the yield surface is the von Mises circle in the deviatoric principal stress plane (the π-plane), in which case the yield stresses in triaxial tension and compression are the same. It requires $0.778 \le K \le 1.0$ to ensure that the yield surface remains convex. In the present FE analysis, the friction angle and the dilation angle such as 71.56 degrees and

56.97 degrees are adopted respectively.

Figure 4. Typical yield and flow surfaces of the linear model in the deviatoric plane.

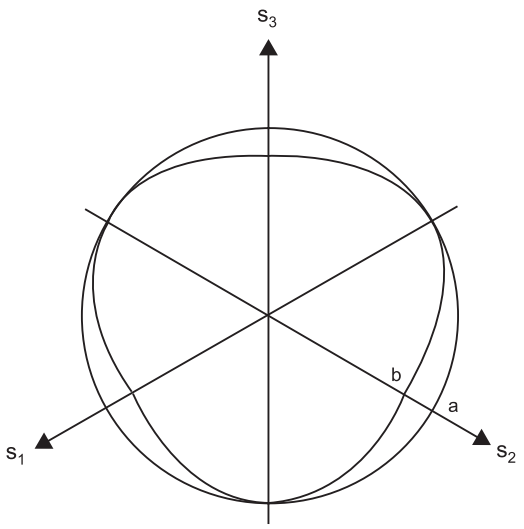

$$t = \frac{1}{2}q\left[1+\frac{1}{k}-\left(1-\frac{1}{k}\right)\left(\frac{r}{q}\right)^3\right]$$

Curve	K
a	1.0
b	0.8

3-dimensional model

The damaged plasticity model [3] is used for concrete material in the 3-dimentional FE analysis. Specifically, two main failure mechanisms such as tensile cracking and compressive crushing of the concrete material are considered in this model. The evolution of the yield (or failure) surface is controlled by two hardening variables, $\overline{\varepsilon}_t^{pl}$ and $\overline{\varepsilon}_c^{pl}$ which are related to failure mechanisms under tension and compression loading respectively. We refer to $\overline{\varepsilon}_t^{pl}$ and $\overline{\varepsilon}_c^{pl}$ as tensile and compressive equivalent plastic strains respectively.

In this model, the uniaxial tensile and compressive response of concrete is characterized by the damaged plasticity model as shown in Figure 5. Under uniaxial tension, the stress-strain relationship follows a linear elastic relationship until the value of the failure stress (σ_{t0}). The failure stress corresponds to the onset of micro-cracking in the concrete material. Beyond the failure stress, the formation of micro-cracks is represented macroscopically with a softening stress-strain response, which induces strain localization in the concrete structure. Under uniaxial compression the response is linear until the value of initial yield (σ_{c0}). In the plastic regime the response is typically characterized by a stress hardening followed by strain softening beyond the ultimate stress σ_{cu}.

It is assumed that the uniaxial stress-strain curves can be converted into stress versus plastic-strain curves. Thus,

$$\begin{aligned}\sigma_t &= \sigma_t\left(\bar{\varepsilon}_t^{pl}, \dot{\bar{\varepsilon}}_t^{pl}, \theta, f_i\right)\\ \sigma_c &= \sigma_c\left(\bar{\varepsilon}_c^{pl}, \dot{\bar{\varepsilon}}_c^{pl}, \theta, f_i\right)\end{aligned} \tag{2}$$

where the subscripts t and c refer to tension and compression respectively. $\bar{\varepsilon}_t^{pl}$ and $\bar{\varepsilon}_c^{pl}$ are the equivalent plastic strains and $\dot{\bar{\varepsilon}}_t^{pl}$ and $\dot{\bar{\varepsilon}}_c^{pl}$ are the corresponding plastic strain rates. θ is the temperature and $f_i\left(i=1,2,...\right)$ are other predefined field variables.

As shown in Figure 5, when the concrete specimen is unloaded from any point on to the strain softening branch of the stress-strain curves, the unloading response is weakened and the elastic stiffness of the material appears to be damaged (or degraded). The degradation of the elastic stiffness is characterized by two damage variables, d_t and d_c, which are assumed to be functions of the plastic strains, temperature, and field variables:

$$\begin{aligned}d_t &= d_t\left(\bar{\varepsilon}_t^{pl}, \theta, f_i\right); \quad 0 \le d_t \le 1\\ d_c &= d_c\left(\bar{\varepsilon}_c^{pl}, \theta, f_i\right); \quad 0 \le d_c \le 1\end{aligned} \tag{3}$$

Figure 5. Response of concrete to uniaxial loading in tension (left) and compression (right)

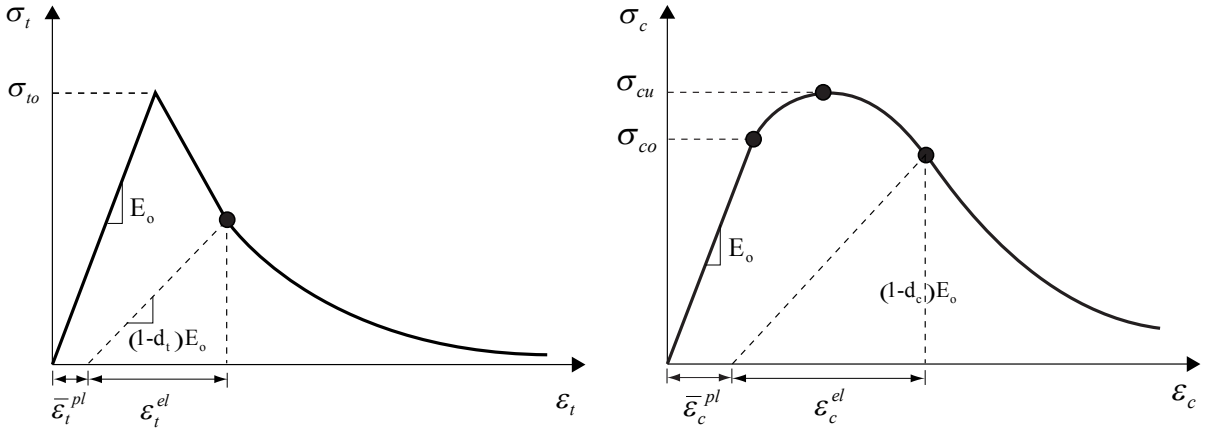

The damage variables can take values from zero, representing the undamaged material, to one, which represents total loss of strength. If E_0 is the initial (undamaged) elastic stiffness of the material, the stress-strain relations under uniaxial tension and compression loading are

$$\begin{aligned} \sigma_t &= \left(1-d_t\right) E_0 \left(\varepsilon_t - \overline{\varepsilon}_t^{pl}\right) \\ \sigma_c &= \left(1-d_c\right) E_0 \left(\varepsilon_c - \overline{\varepsilon}_c^{pl}\right) \end{aligned} \tag{4}$$

Tension stiffening model

Owing to the bond effect between concrete and reinforcing bars, the concrete can take a part of the tensile force even after crack formation. It makes that the stiffness of reinforced concrete remains higher than that of the reinforcing bars alone. This phenomenon is so called '*tension stiffening effect*'. In numerical simulation, this effect can be represented in two ways: one is to modify the stiffness of reinforcing bars and the other is to modify the stiffness of the concrete so that the concrete can carry the tensile force after cracks. In the present FE analysis, the latter tension-stiffening model proposed by Okamura [6] is adopted (see Figure 6).

From Okamura's study [6],

Ascending branch ($\varepsilon_t \le \varepsilon_{cr}$):

$$\sigma_t = E_c \cdot \varepsilon_t \tag{5}$$

Descending branch ($\varepsilon_t > \varepsilon_{cr}$):

$$\sigma_t = f_t \left(\frac{\varepsilon_{cr}}{\varepsilon_t} \right)^{0.2} \tag{6}$$

where ε_t is total strain in concrete, ε_{cr} is the cracking strain and f_t is the stress corresponding to the cracking strain.

Figure 6. Tension stiffening model for concrete

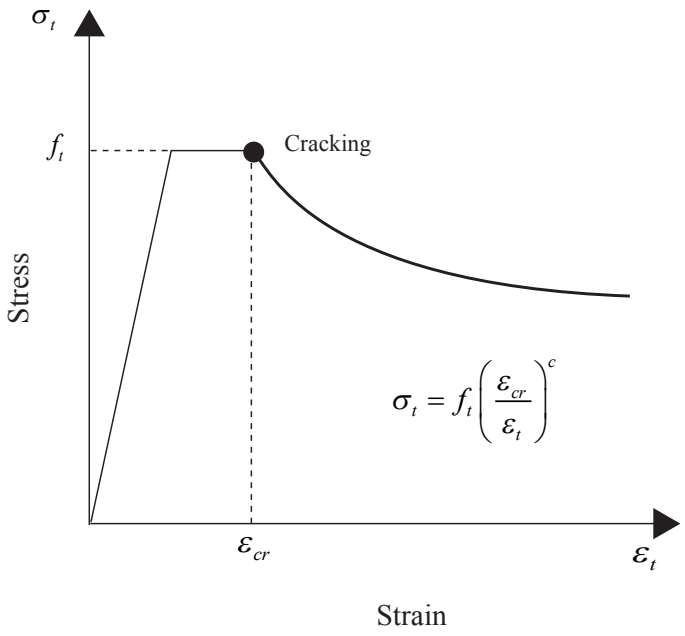

Steel model

The stress-strain relationship of the mild steel is usually assumed to be elasto-perfectly plastic with a distinct yield stress of f_y. However, when the reinforcing bars are surrounded by concrete, the average stress-strain relationship exhibits a quite different behaviour to the bare bar as shown in Figure 7. To consider this behaviour, we generally underestimate the yield stress f_y. In the present FE analysis, the stress-strain relationship for the steel bar is represented by Hsu's model [7] as follows:

$$\frac{\overline{f}_y}{f_y} = 1 - \frac{4}{\rho}\left(\frac{f_{cr}}{f_y}\right)^{1.5} \tag{7}$$

where f_y and $\overline{f}_y$ are the yield stresses of bare bar and embedded bar in concrete respectively. ρ is the reinforcement ratio and f_{cr} is the cracking stress value.

Figure 7. Average yield stress-strain curve

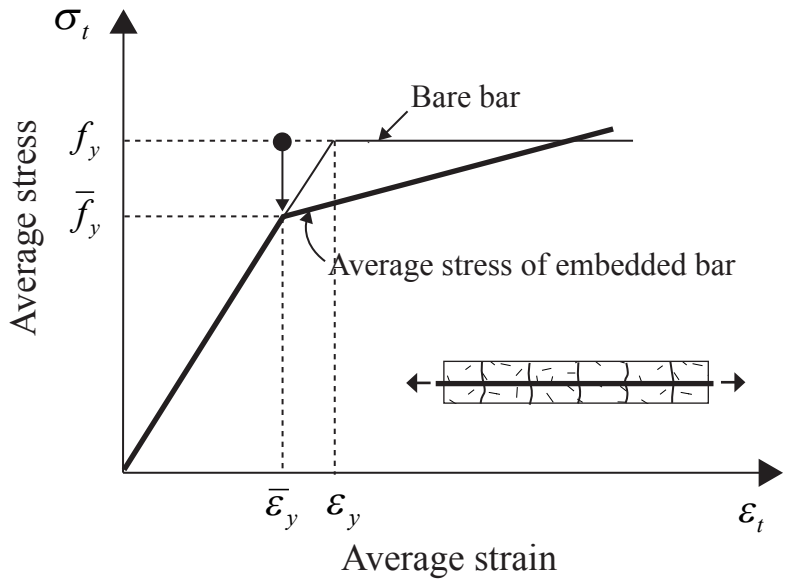

Tendon model

The stress-strain relationship for the tendons is evaluated from the tensile test results of the PCCV tendon system and the static tensile test of PCCV tendon strand. The tendon is theoretically modeled as an elasto-plastic material model with *PLASTIC option in ABAQUS. In the FE analysis, the stress-strain curve having three main data points is used as shown in Figure 8. The first point A represents the elastic limit value which is straight line up to $0.7 f_{pu}$ from zero point, where f_{pu} is the ultimate strength of the tendon. The third point C is the representative ultimate strength of the tendon. The prestressing data such as the average measured values of forces, friction and seating losses are summarized in Table 5.

The following material properties of tendon are used to prepare the input data for the FE analysis:

- Elastic modulus : 2.197E5 MPa
- Poission's ratio : 0.3
- Yield stress : 1,621 MPa
- Ultimate stress : 1,875.8 MPa
- Elongation : 3.42%

Figure 8. Stress-strain curve for tendon

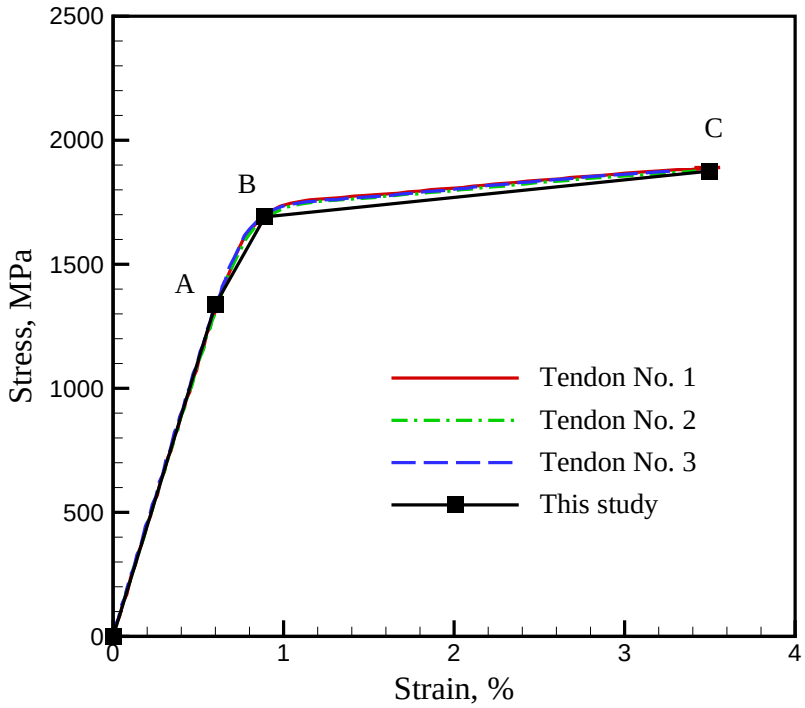

Table 5. Prestressing data summary

Item	Hoop tendons		Vertical tendons	
Average Tensile Force:				
Design:	44.41 T	97.9 kips	49.57 T	109.00 kips
Jack:	43.53 T	95.97 kips	49.02 T	108.07 kips
Jack(w/ Load Cells only):	43.61 T	96.14 kips	49.09 T	108.23 kips
Load Cell:	43.21 T	95.27 kips	48.20 T	106.27 kips
Average Lift-off Force:				
Design:	34.11 T	75.2 kips	46.31 T	102.10 kips
Jack:	34.02 T	75.01 kips	44.22 T	97.49 kips
Average Friction Coefficient:	0.18		0.22	
Average Seating Loss:	3.95mm	0.16 inch	4.95mm	0.19 inch
Jack:	9.51 T	20.96 kips	4.80 T	10.58 kips
Load Cell:	9.86 T	21.75 kips	4.64 T	10.23 kips
Average Final Load Cell Force:	33.34 T	73.52 kips	43.56 T	96.04 kips
Average Elastic Loss:	0.27 T	0.59 kips	0.58 T	1.29 kips

Liner plate model

The steel liner plate is modeled by using an elasto-plastic material model with *PLASTIC option in ABAQUS. In Figure 9, the stress-strain curve for the FE analysis is compared with experimental data provided by SNL.

The following material properties of liner plate are used to prepare the input data for the present FE analysis:

- Elastic moduls : 2.187E5 MPa
- Poission's ratio : 0.3
- Yield stress(MPa) : 382.7 MPa
- Ultimate tensile stress : 497.85 MPa
- Elongation(%) : 33.2

Figure 9. Stress-strain curve for liner plate

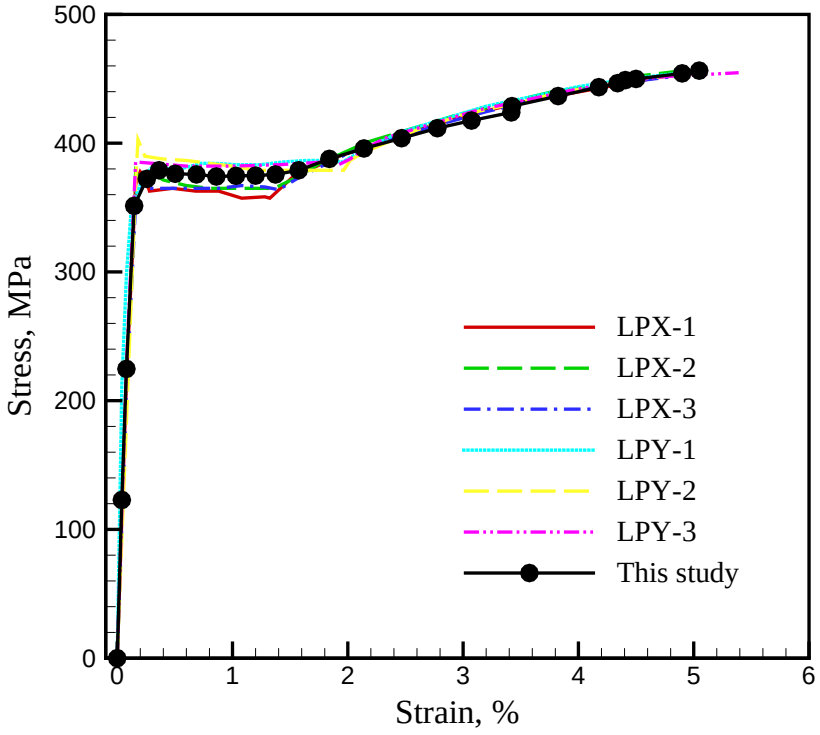

FE Analysis Procedure for ABAQUS Code

The numerical analysis steps used in the present FE analysis are:

(1) Gravity + Pre-stress force
(2) Gravity + Pre-stress force + Internal pressure

An initial load step in which the PCCV is brought into static equilibrium with the initial post-tensioning tendon loads and the self-weight is established. The weight of the embedded steel reinforcements and tendons has not been included as part of the total vessel weight.

After initial load step, a uniform pressure is applied to the faces of the liner plate elements that comprise of the internal surface of the vessel. The internal pressure is also applied to the penetrations cover plates such as personal airlock and equipment hatch.

Finite Element Model

2-dimensional axi-symmetric model

The axi-symmetric FE model used in the prediction of the overall response of the PCCV is illustrated in Figure 10. The FE model consists of 768 axi-symmetric 4-node solid elements (CAX4) to represent concrete layer and 2-node 203 axi-symmetric membrane elements (MAX1) to represent liner layer as shown in Figure 10. All rebars and tendons are modeled by using the rebar sub-element provided in the code ABAQUS. Therefore, they are assumed to be rigidly bonded to the concrete. The pre-stressing force for tendon is represented by the *INITIAL CONDITION option in ABAQUS. The boundary condition for the bottom of the base slab is assumed to be fixed so that the present FE model can not simulate the possible vertical uplift during internal pressurization.

3-dimensional model

The 3-dimensional FE model with large penetrations such as equipment hatch and air lock is also adopted as shown in Figure 11 and 12. The 3-dimensional model consists of 6,992 8-node solid elements (C3D8), 3,100 4-node liner elements (M3D4) and 9,522 truss elements (T3D3). The rebar

and tendon are modeled with embedded element. The layout of tendon used in the present FE analysis is illustrated in Figure 13. The pre-stressing force for tendon is represented by the *INITIAL CONDITION option in ABAQUS. The tendons are assumed to remain rigidly bonded to the concrete. Therefore, the slippage of a tendon within the tendon sheath can not be considered in the present FE analysis model. The boundary condition for the bottom of the base slab is assumed to be fixed similar to that used in the axi-symmetric model and this model also can not simulate the possible vertical uplift during internal pressurization.

Figure 10. Axi-symmetric finite element model

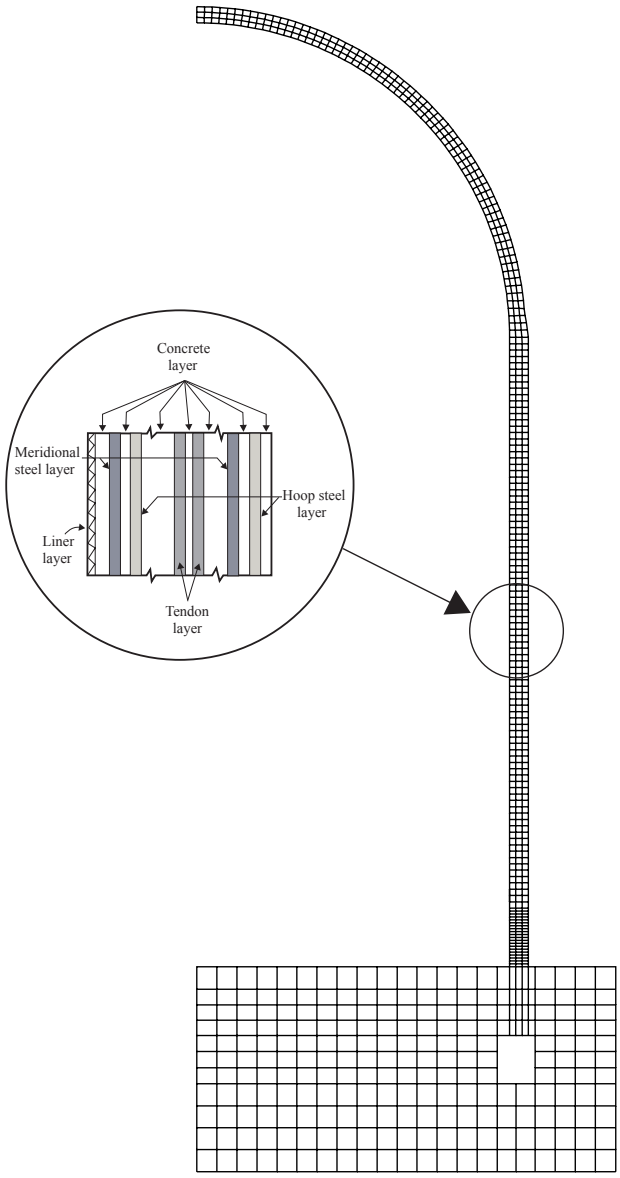

Figure 11. 3D FE mesh

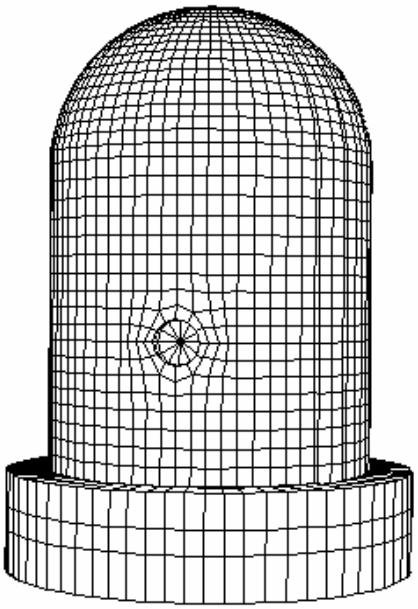

Figure 12. Buttress and Basemat FE mesh

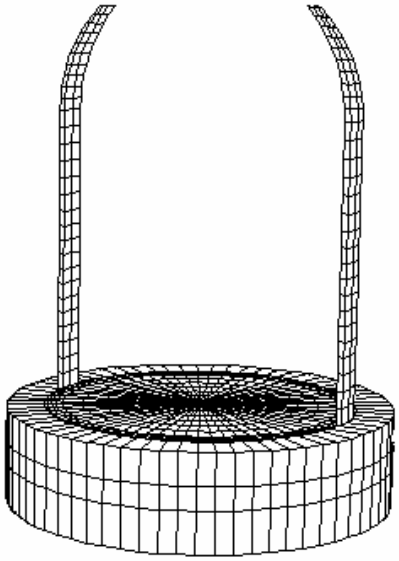

Figure 13. Hoop tendon (left) and meridional tendon (right)

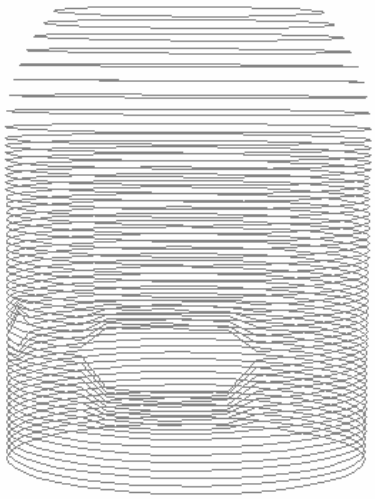

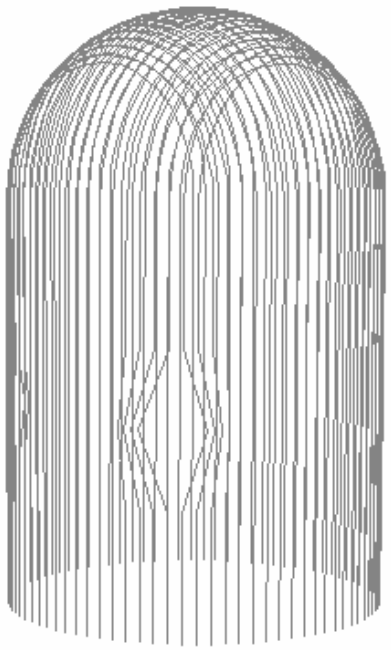

FE Analysis Results

The present FE analysis produces results at 37 standard output locations (SOLs) which are obtained from the axi-symmetric model and 52 standard output locations except SOL #35, #54, #55 from 3-dimensional model.

Axi-symmetric analysis results

The first cracking of concrete in cylinder wall due to hoop stress occurred at the value of 0.59MPa in the cylinder. The cracking of the cylinder due to meridional stress is initiated at the same pressure level at mid-height of the cylinder wall. Then, cracks spread all over the cylinder of the PCCV from the value of 0.67MPa.

The first crack occurs in the lower part of the dome and the cracks are observed at the values of 0.67MPa and 0.77MPa in the upper part of the dome.

The first yielding of hoop rebar is initiated at 1.036MPa at mid-height of the cylinder wall and the yielding of meridional rebar in wall-basemat juncture begun at 1.29MPa. The maximum strain of the rebar in the hoop direction is observed as 14.37% in the mid-height of the cylinder wall at the final stage.

The strain values of hoop tendons in cylinder wall reach 1%, 2% and 3% associated with the stress values of 1.43MPa, 1.47MPa and 1.50MPa respectively. The maximum strain of hoop tendon in cylinder wall is observed as a value of 15.26% at the final stage.

The deformed shape of axi-symmetric model at ultimate pressure state is shown in Figure 14.

Three-dimensional analysis results

The first hoop and meridional cracking of the cylinder wall are occurred at 0.62MPa as shown in Figure 15. This is a larger pressure value than the corresponding cracking pressure obtained from the axi-symmeric model. The first crack occurs at the lower part of dome and the cracks are also observed at the upper part of the dome at the values of 0.675MPa and 1.06MPa.

The first yielding of hoop rebar is initiated at 0.94MPa at mid-height of the cylinder wall as shown in Figure 16 and the yielding of meridional rebar in wall-basemat juncture begun at 1.19MPa. The maximum strain of hoop rebar is observed at midheight of the cylinder wall with the value of 0.55% at the final stage. The maximum value of the strain in the hoop tendon is observed as 0.51% at the final stage. Because numerical instability has occurred, there is no indication of tendon or rebar failure at the final load step. The deformed shape of 3-dimensional model at ultimate pressure state is illustrated in Figure 17.

Displacement verses internal pressure relationship comparisons at several Standard Output Locations (SOLs) such as mid-height of the cylinder, springline and dome apex are made in Figure 18 through Figure 21. There is a very good agreement for vertical displacement in the springline (Figure 20) as well as radial displacement in the mid-height of the cylinder (Figure 18) and springline (Figure 19) between analysis and test. As mentioned above, the first crack is occurred at 0.62MPa. The analysis and the test consistently exhibit a sharp jump in displacement at cracking pressure. There is poor correlation between analysis and test data for vertical displacement in dome apex. Unfortunately, test data between LST DOR and SFMT DYN has a quite different aspect.

Finally, The pressure levels due to the event milestones requested by SNL are summarized in Table 6.

Table 6. Pressure level due to the event milestones (unit: MPa)

Event milestones	Axi-symmetric model	3D model
First cracking of concrete in cylinder due to hoop stress	0.59	0.62
First cracking of concrete in cylinder due to meridional stress	0.59	0.62
First yield of hoop rebar in cylinder	1.036	0.94
First yield of meridional rebar in wall-basemat juncture	1.29	1.19
First cracking of dome concrete above 45^o dome angel	0.77	1.06
First cracking of dome concrete below 45^o dome angle	0.67	0.675
Hoop tendons in cylinder reaching 1% strain	1.43	-
Hoop tendons in cylinder reaching 2% strain	1.47	-
Hoop tendons in cylinder reaching 3% strain	1.50	-

Figure 14. Deformed shape of axi-symmetric model at ultimate pressure (x100)

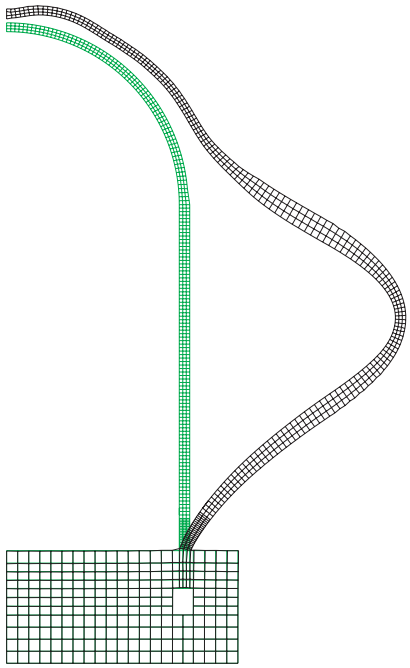

Figure 15. The first crack location of the concrete

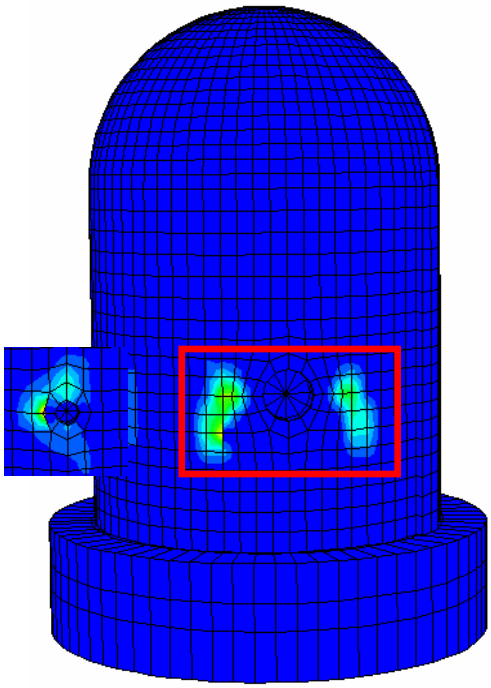

Figure 16. The first yielding location of the rebar

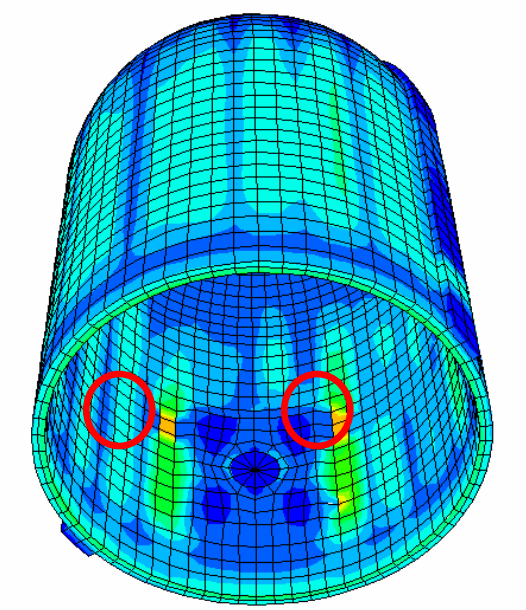

Figure 17. Deformed shape of 3D model at ultimate pressure (x100)

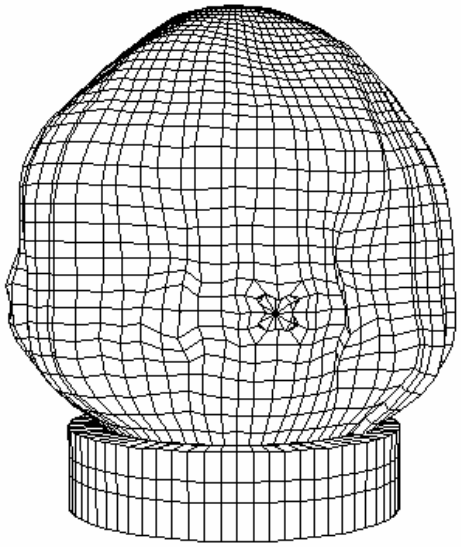

Figure 18. Radial displacement at the mid-height of cylinder (SOL #6)

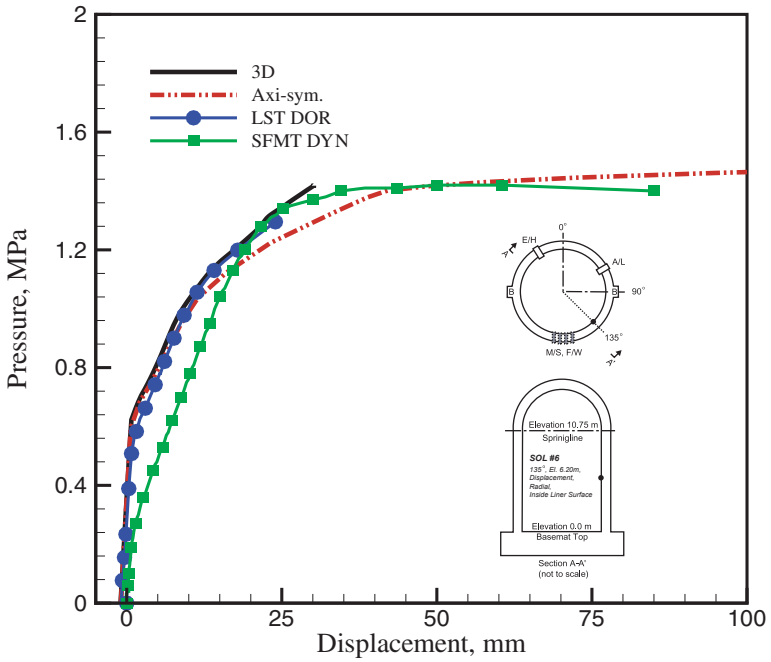

Figure 19. Radial displacement at springline (SOL #7)

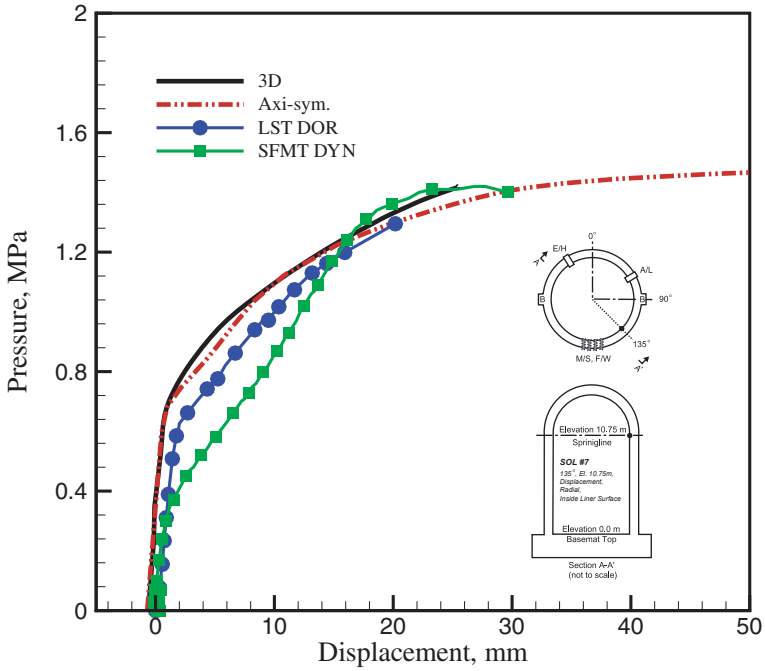

Figure 20. Vertical displacement at springline (SOL #8)

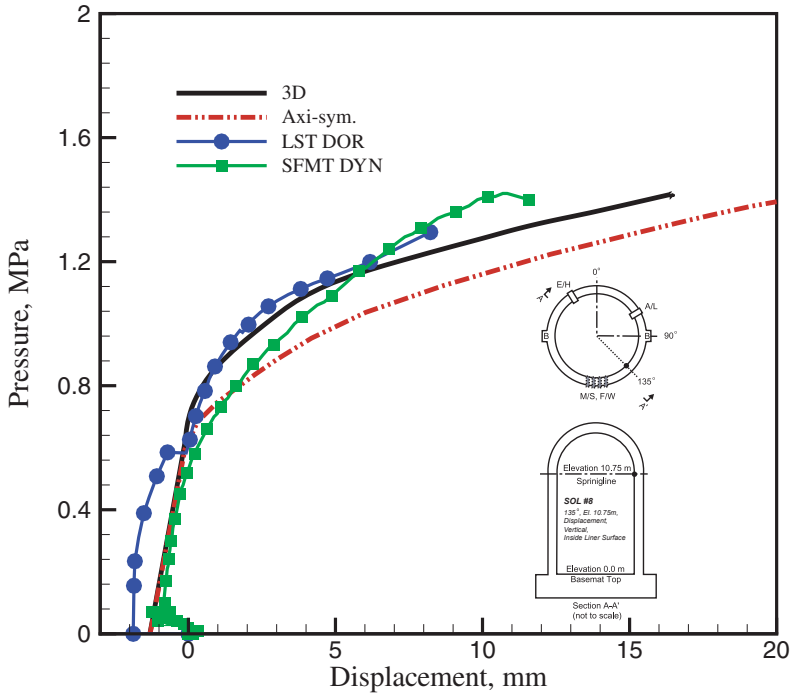

Figure 21. Vertical displacement at dome apex (SOL #11)

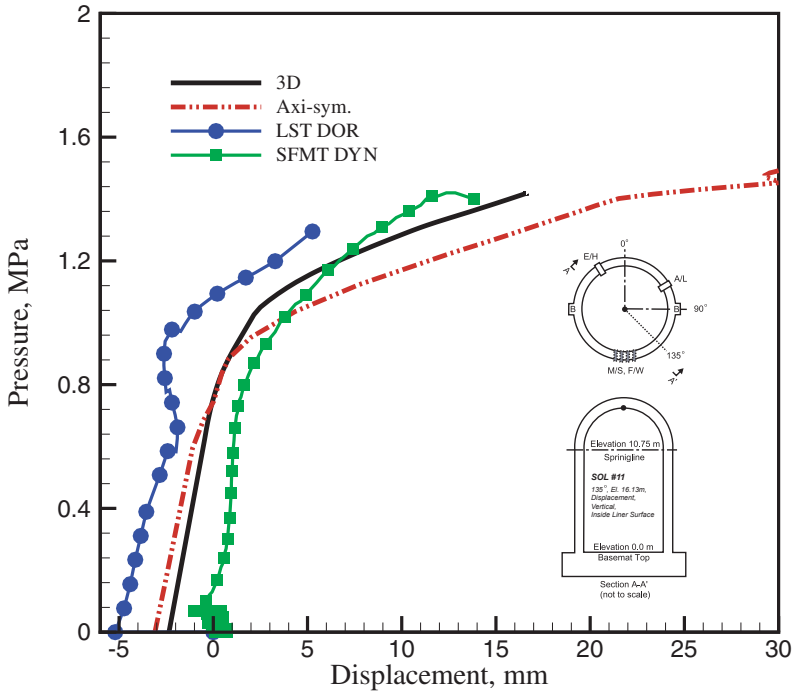

References

[1] Letter from V.K. Luk to M.N. Gray (1998), "PCCV Round Robin Analysis".

[2] Drucker, D.C. and W. Prager (1951), "A more fundamental approach to plastic stress-strain relation," *Proc. Natl, lnst. Appl. Mech.*, pp. 487-491.

[3] Lee, J. and G.L. Fenves (1998), "Plastic-damaged model for cyclic loading of concrete structures," *Journal of engineering mechanics*, Vol. 124, No. 8, pp. 892-900.

[4] Hibbit, H.D. (2002), ABAQUS User's Manual, Version 6.3, HKS Inc.

[5] Tendon Diskette (1999), Sandia National laboratories.

[6] Okamura, H., K. Maekawa and S. Sivasubramaniyam (1985), "Verification of modeling for reinforced concrete finite element, finite element analysis of reinforced concrete structures, " *ASCE*, pp. 528-543.

[7] Hsu, T.T.C. and A. Belarbi (1994), "Constitutive laws of concrete in tension and reinforcing bars stiffened by concrete," *ACI Structural Journal*, Vol. 91, No. 4, pp. 465-474.

Appendix J: Korea Power Engineering Company
Phase 2: J-1 to J-24
Phase 3: J-25 to J-62

Posttest Analysis of a Prestressed Concrete Containment Vessel Model

(Ultimate Pressure Capacity of 1:4 scale PCCV)

(PHASE 2)

KOREA POWER ENGINEERING COMPANY

Contents

-

1. Introduction

The purpose of the work contained herein is to summarize the posttest analysis results performed by Korea Power Engineering Company to simulate the structural responses accurately comparing the measured responses from SFMT (Structural Failure Mode Test) tested at Sandia National Laboratories [1].

To simulate the failure loading as well as the failure mode of the PCCV model, a three-dimensional full model involves at least two critical features for the structural idealization: one is by geometry model considering the effects due to presence of the openings and the buttresses in the PCCV. The other is by material property models for concrete, reinforcement, tendon and liner plate.

The computer program ABAQUS [2] was used to analyze a three dimensional model of containment with nonlinear material properties of concrete, liner plate, reinforcing steel, and prestressing tendon by increasing the internal pressure to failure. Thereby, the final results including the failure mode and the corresponding internal pressure level are determined.

The modeling approaches of geometry and materials and the analysis results with comparing the test results are summarized in the following sections.

2. Material Property and Modeling

2.1 General

To simulate the SFMT test results of the 1:4-scale prestressed concrete containment structure, the actual properties are used for the concrete, reinforcing steel, post-tensioning tendon, liner plate and soil. The actual material properties for these materials are established from test data provided by Sandia National Laboratories used in the construction of the 1:4-scale PCCV [3].

2.2 Concrete

Material Model

The concrete is characterized by a materially nonlinear deformation behavior. The material non-linearity is assumed to occur due to cracking of concrete in tension and plasticity of concrete in compression. However, the material non-linearity due to the latter is relatively less influence than that due to the former on the failure mode of the containment structure under internal pressure. Therefore, the Modified Drucker-Prager's failure model that is known to be suitable to represent the tensile concrete cracking of the three-dimensional finite element model is introduced in the numerical analysis.

The yield surface and flow potential parameters for elastic-plastic material yield surface in the modified Drucker-Prager's failure model with a non-associated flow potential and the strain hardening are defined by the model parameters *K*-factor, the friction angle β, and the dilation angle ψ. The material parameter $K(\theta, f_\alpha)$ controls the shape of the yield surface in the deviatoric plane and angle β is the angle between the yield surface and the pressure stress axis in the meridian plane [4].

The concrete structure was appeared to be damaged during the Limit State Test. Thus, to evaluate the effect of tensile and compression damage on the analysis results, the damage index $d_t = 0.1$ considering the micro damage level corresponding to the surface crack status showing some tensile cracking is introduced in the analysis [5]:

Material Property

The following concrete properties from the uniaxial strength test data for trial mix concrete are used in the analysis of the 1:4 scale PCCV model.

Table 1 Concrete Material Property

Property	Value for Basemat	Value for Shell & Dome
Elastic Modulus	27950 Mpa	26970 MPa
Uniaxial Compressive Strength	39.16 Mpa	47.30 MPa
Uniaxial Tensile Strength	3.37Mpa	3.45 MPa
Poisson's Ratio	0.18	0.18

2.3 Reinforcement Steels (Rebars)

Material Model

Rebar materials are generally incompressible when they deform plastically and yielding is independent of the pressure stress. The Von Mises failure criterion is therefore used for this steel material.

Hsu's study result [6] noted that the stress-strain curves for bare steel bar and for steel bar embedded in concrete are quite different as shown in Figure 1. Therefore, the stress-strain relationship of rebar embedded in concrete has been recommended in reinforced concrete structure to simulate the realistic behavior of the rebar in concrete.

The stress-strain curve of the rebar for the numerical analysis is idealized by bilinear curve having a slope of E_s before yielding and a slope of E_p after yielding as illustrated in Figure 1. The equations of two lines are expressed with the stress level designated as f_y' at which the two straight lines intersect

as equation (1) and (2). The plastic modulus E_p' after yielding can be taken a small fraction of the elastic modulus E_s.

$$f_s = E_s \varepsilon_s \qquad \text{for} \quad f_s \le f_y' \tag{1}$$

$$f_s = f_o' + E_p' \varepsilon_s \qquad \text{for} \quad f_s \succ f_y' \tag{2}$$

where f_o' is the vertical intercept of the post-yield straight line. The intersection stress level f_y' and the plastic modulus E_p' depend mainly on the level of the apparent yield stress f_y* illustrated in Figure 1. The values of f_y' and E_p' in the stress-strain relatinship introduced to the numerical analysis are calculated as equations (3) and (4) using the apparent yield stress f_y* and the strain-hardening modulus of the bare bar E_p from the actual material properties.

$$\frac{f_y'}{f_y} = 0.43 + 0.5\frac{f_y^*}{f_y} \tag{3}$$

$$\frac{E_p'}{E_p} = 3.3 - 2.5\frac{f_y^*}{f_y} \tag{4}$$

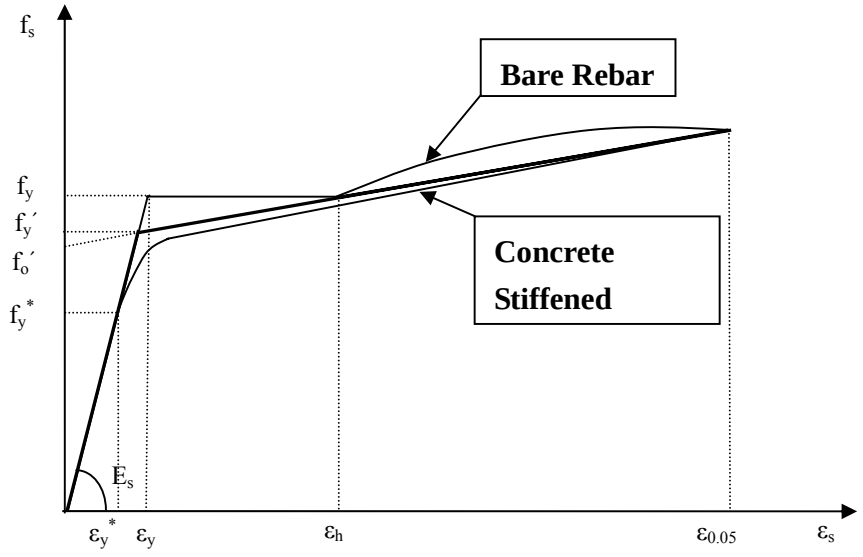

Figure 1 Stress-strain relationship of rebar using bilinear model

Material Property

The test results provided in the appendix of References [3] are used the rebar material properties. Table 2 presents the modulus of elasticity for each type and each size of the reinforcement steel.

Table 2 Reinforcing Material Properties

	D6 (SD345)	D10 (SD390)	D13 (SD390)	D16 (SD390)	D19 (SD390)	D22 (SD390)	D19 (SD490)
Elastic Modulus(Mpa)	1.69E5	1.83E5	1.83E5	1.83E5	1.84E5	1.91E5	1.86E5
Poisson's ratio	0.3	0.3	0.3	0.3	0.3	0.3	0.3
Yield Stress(Mpa)	369.4	472.9	432.3	457.5	473.1	459.0	512.2
Tensile Stress (Mpa)	489.4	665.9	610.6	616.5	658.3	680.8	709.7
Extension(%)	30.4	20.5	24.2	22.1	21.1	18.7	17.8

2.4 Prestressing Tendon

Material Model

The stress-strain curve of a bare prestressing tendon consisted of two straight lines jointed by curve knee shown in Figure 2 is used for the numerical analysis. The first part of the curve is a straight-line up to $0.7f_{pu}$ and the second part is expressed by Ramberg-Osgood equation(5) that meets the first part at the stress level of $0.7f_{pu}$.

$$f_p = \frac{E_{ps}'\varepsilon_p}{\left[1+\left(\frac{E_{ps}'\varepsilon_p}{f_{pu}}\right)^4\right]^{1/4}} \tag{5}$$

where f_{pu}, f_p, E_p' and ε_p is the ultimate strength of the tendon, the strength in the tendon, the tangential modulus Ramberg-Osgood curve at zero load and the sum of strain in the tendon, respectively [5].

The finite element code ABAQUS has no function to express the unbonded tendon and thus the prestressing tendons are modeled by the embedded approach available in ABAQUS using the rebar subelement in concrete. That is, the numerical modeling of tendons as rebar sub-elements implies that the tendons are assumed bonded to the concrete and the slippage of the tendon in the tendon sheath is not considered in the numerical analysis.

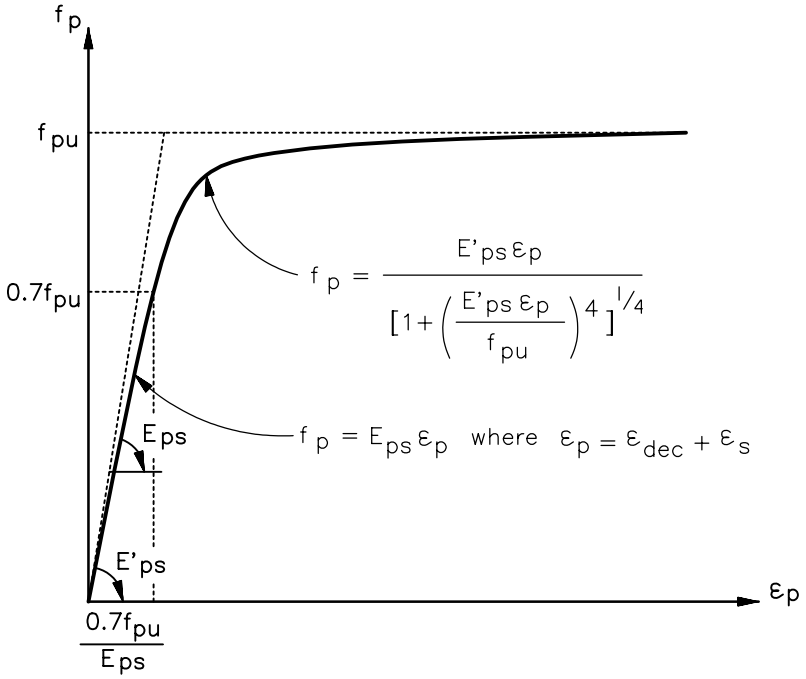

Figure 2 Stress-strain relationship of prestressing tendon

Material Property

The following material properties from Sandia Laboratories are used for the tendon modeling.

Table 3 Tendon Material Properties

Property	Values
Elastic Modulus	191000 MPa
Elatic Limit Stress	1339 Mpa
Yield Strength	1691 Mpa
Poisson's Ratio	0.3
Ultimate Strength	1912 MPa
Extension	4.5%

2.5 Steel Liner Plate

Material Model

The liner plate was partially teared during Limit State Test, but it is considered to contribute to the

structural strength during SFMT. Thus, the stress-strain behavior of the liner plate steel is modeled by using elasto-plastic model that is available in ABAQUS. The von Mises failure surface with kinematic hardening is used to represent the nonlinear behavior of the material.

Material Property

The material properties for liner plate introduced to the numerical analysis are as shown in Table 4.

Table 4 Steel Liner Material Properties

Property	Values
Elastic Modulus	218700 MPa
Elatic Limit Stress	1339 Mpa
Yield Strength	375.595 Mpa
Poisson's Ratio	0.3
Ultimate Tensile Strength	499.158 MPa

3. Finite Element Model

3.1 General

The three-dimensional finite element model includes two buttresses and large penetrations such as equipment hatch and airlock. These non-axisymmetric factors may cause deviation from an axisymmetric response and decrease the ultimate pressure capability of the PCCV. An interconnection between shell element in the base slab(or basemat) and shell elements in the wall is modeled by the composite shell element with orientation to properly simulate the shell/slab junction. All rebars embeded in the prestressed containment structure were modeled by using the rebar subelement provided by ABAQUS and the liner was modeled as a thin inner layer of the shell elements.

The model consists of 1822 four-node shell elements, 278 nonlinear soil spring elements and 1509 nodal points and the overall finite meshes are shown as Figure 4.

3.2 Shell and Dome Model

The dome and cylindrical wall are modeled with multi-layer shell elements consisting of a thin inner layer of steel representing the liner and a much thicker outer concrete layer including rebar and tendon. In order to simulate accurate displacements versus internal pressure extracted from the test data near these regions, a more refined mesh was considered around openings and the opening sleeve and hatch cover are also modeled using shell element as shown in Figure 5. All reinforcing bars in the

dome and cylindrical wall are modeled by using the rebar sub-element provided by ABAQUS computer program.

Due to limitation of the computer program ABAQUS, the tendons are assumed to remain rigidly bonded to the concrete and thus modeled by using the rebar sub-element with introducing prestressing stress provided by ABAQUS. Therefore, the actual condition including the slippage of tendon in the tendon sheath can not be considered in the analysis model. Prestressing stresses being induced in the tendons are expressed by using the *INITIAL STRESS command with the *PRESTRESS HOLD option in ABAQUS computer code to remain the tendon stresses at predetermined levels.

3.3 Base Slab Model

The reinforced concrete base slab is also modeled by four-node multi-layer shell elements consisting of an inner thin layer of steel representing the liner and a much thicker outer concrete layer. Since the base slab is modeled by shell elements, the tendon gallery is not included in the three-dimensional model.

The bottom of the base slab rests on soil foundation that is modeled by the nonlinear soil spring with tension cut-off. The soil properties were also not provided and thus an appropriate elastic modulus was introduced only to simulate the uplift by using the nonlinear spring with tension cut-off. That is, the compression stiffness was considered as the empirically large value not to develop the compressive behavior while the tension stiffness was neglected. All rebars in the basemat are modeled one-for-one by using the rebar sub-element of ABAQUS similarly to the wall and dome parts.

3.4 Prestressing Forces in Tendon

The meridional stress and hoop stress along the length of the tendon in the concrete are estimated as shown in Figure 6 with the prestressing losses at the time of testing and the prestressing force was introduced prior to applying the internal pressure to the numerical model. The four types of losses given specific modeling consideration are (1) the friction between the tendon and the concrete, (2) the elastic shortening of the concrete, (3) the creep and shrinkage of the concrete, and (4) the stress relaxation in the prestressed tendons.

The vertical prestressing forces of 106.27kips before anchoring and 96.04kips after anchoring are introduced from the PCCV Model-General Arrangement. Based on the prestressing forces at anchorage, the magnitudes of the vertical tendon stress are calculated along the length of the vertical tendon and considered in the finite element analysis model with considering the losses shown in Table 5. Similarly, the hoop tendon forces of 95.27kips before anchoring and 73.52kips after anchoring are used in the calculation of hoop tendon stress.

Table 5. Prestressing Losses

	Vertical Tendon Loss MPa (ksi)	Hoop Tendon Loss MPa (ksi)
Elastic shortening of concrete	31.855 (4.620)	31.855 (4.620)
Creep of concrete	66.999 (9.717)	83.829 (12.158)
Shrinkage of concrete	129.309 (18.754)	129.309 (18.754)
Steel relaxation	19.747 (2.864)	14.473 (2.099)
Total losses	247.910 (35.955)	259.473 (37.632)

3.5 Self-weight, Water Pressure and Internal Pressure

Because of the elastic support below the bottom slab, the effect of the weight of the structure had to be initially considered prior to internal pressurization. This is accomplished by specifying as mass proportional load for each material included in the 1:4 scale PCCV model prior to initiating the internal pressure. The weights of each material are considered in the numerical model by using the GRAVITY parameter of *DEAD LOAD option of ABAQUS.

The hydrostatic pressures from the water filled to 1.5m from the dome apex are calculated with Pascal's principle and loaded on the surface of the wall and base slab prior to internal pressurization. Internal pressure loads are specified to act as a uniformly-distributed force, remaining normal to the interior element surface of the containment shell, dome and base slab as it deformed.

4. Analysis Results and Discussion

All analysis results at 55 standard locations are selected and prepared as excel file to compare with SFMT test results. The three-dimensional finite element model (3DFEM) provided a good simulation of the SFMT test results. Most of the behavior comparisons show generally good correlation excepting some results of the 3DFEM showing differences between the 3DFEM and the SFMT (see Figures 7 through 10).

4.1 Displacements

The displacement transducer were 'zeroed' prior to the start of the SFMT before filling the vessel with water and thus the measured displacements reflect only the response to pressure (including the hydrostatic pressure) and not the effects of prestressing, nor any other previous loading [3]. Therefore, the numerical analysis displacements excluding the responses due to prestressing and dead load were

plotted and compared with the corresponding measured displacements. Most of the displacements comparisons show generally good correlation excepting some results of the 3DFEM showing differences between the 3DFEM and the SFMT (see Figure 7).

The displacements at EL. 1.43m and 2.63m show good agreement between the analysis and the test as shown in Figure 7(a) and (b). At the base of the wall (below EL. 0.25m), however, the numerical model deforms radially outward while the test measurement shows very small inward deformation (as shown in Figure 7(c)). This reverse trends near wall-mat junction is judged to come from the characteristics of the numerical model introducing shell element to basemat and putting soil spring under basemat to simulate uplift. That is, in the numerical analysis some flexural behaviors seem to be occurred in the basemat due to the overestimated uplift and plate bending larger than the test measurements reflected the actual behavior of the massive rigid basemat.

4.2 Rebar Strains

The residual rebar strain remained at each gage after LST was the initial strain at the start of the SFMT. Thus, both the analysis initial stains prior to pressure and the measured initial residual strains should be compared. Also, the strains due to only pressure need to compare for both the analysis and the test as the pressure increased.

The hoop outer rebar at the mid-height of cylinder (135°, EL. 6.20m) is the reinforcing steel D16 having a yield strain 0.25% calculated from a yield stress 457.5Mpa and elastic modulus 1.83E+05 in Table 2 [3]. The 3DFEM shows that the hoop outer rebar at the mid-height of cylinder is judged to yield at the pressure level of 1.10Mpa and the maximum strain in the hoop rebar indicates 3.8% at pressure level of 1.52Mpa(see Figure 8).

The strains in the meridional outer rebar at the elevation 0.05m and 0.25m show different trends. That is, the numerical model show the outer rebar strain changing from tension to compression while the test measurement indicates the outer rebar strain is very small but changing from compression to tension (as shown in Figure 9). These reverse trends near wall-mat junction are judged to come from the same reason as for the reverse trends for radial displacements at the same locations aforementioned in section 4.1. Also, to investigate the effects of the basemat uplift on the behaviors near the wall-mat junction, the outer rebar strains are compared depending on the boundary condition at the base of the cylidrical wall.

4.3 Tendon Strains

Tendon strains gages were ‘re-zeroed’ before the SFMT [3] and thus the analysis tendon strains prior to the start of pressurization were deducted from the tendon strains during pressure to directly

compare with the measured tendon strain.

Most of the tendon strains simulated by the 3DFEM model exhibit a good agreement with the test measured tendon strains as shown Figures 10(a) through (c). However, the strains measured at the hoop tendon passing near buttress (Az.90°, EL. 6.58m) show much larger values than those of 3DFEM as shown in Figure 10(d). The hoop tendon at the mid-height of the wall is started to yield at pressure level of 1.43Mpa and the maximum strain corresponding to the pressure of 1.54Mpa is appeared to reach 3.74%.

4.4 Liner Strains

The response of liner was not a critical objective during the SFMT and thus the measurements are not provided for comparison. The analysis results show that the liner at the mid-height of cylindrical wall, especially the regions near equipment hatch, is started to yield at the pressure level of 0.84 Mpa and the yield in liner is appeared extend to the bottom of wall at 1.45Mpa as shown in Figure 11.

4.5 Concrete Cracking

The finite element analysis results show that the first concrete cracking in the numerical model occurs at a pressure level of 0.58Mpa and is located at the surface of cylindrical wall at the wall and basemat joint. At the pressure level of 0.60Mpa, the elements near large openings of wall cylinder are cracked in both the hoop and meridional directions as shown in Figure 12.

Figure 13 illustrates the strain at the pressure level of 1.52 MPa judged to be the structural failure mode in the analysis and the distribution of concrete cracking at the failure can be indirectly compared with the test results. According to the strain distributions in the model, the final failure appeared to occur between the edge of equipment hatch and the buttress for the x-direction and there were large strains from the spring line upto 45 degrees of dome.

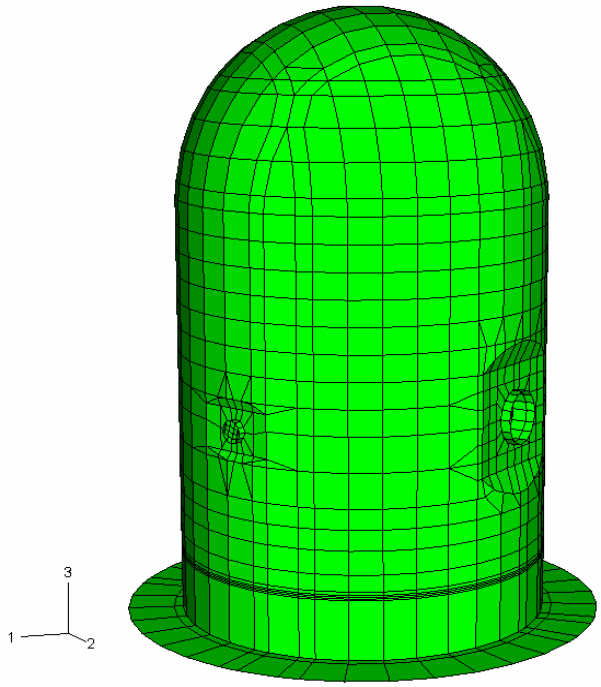

Figure 4 Overall View of Three-dimensional Finite Element Model

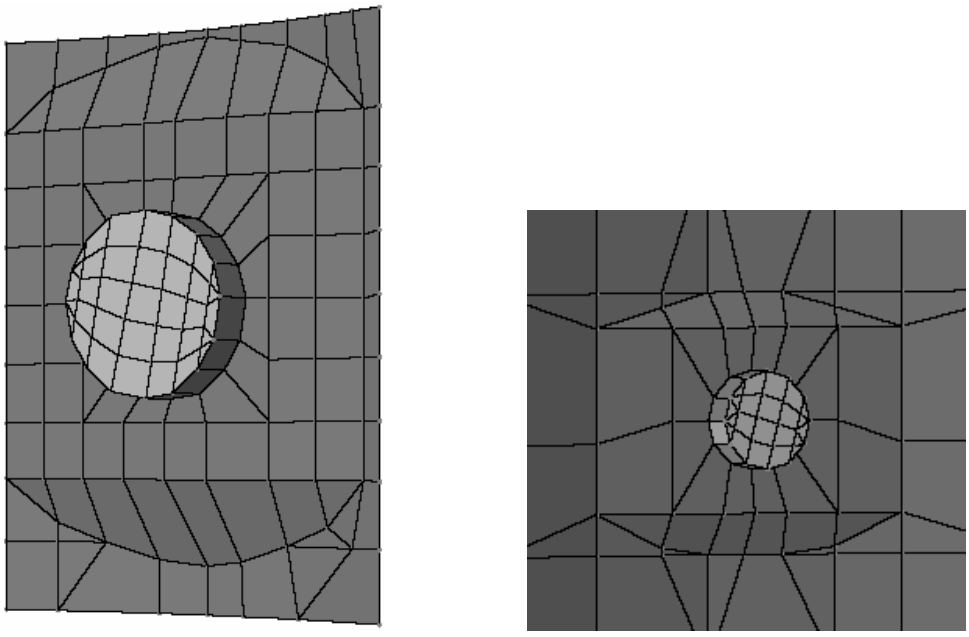

(a) Equipment Hatch (b) Personal Airlock

Figure 5 Refined Mesh around Large Penetrations in Model (Inside Surface)

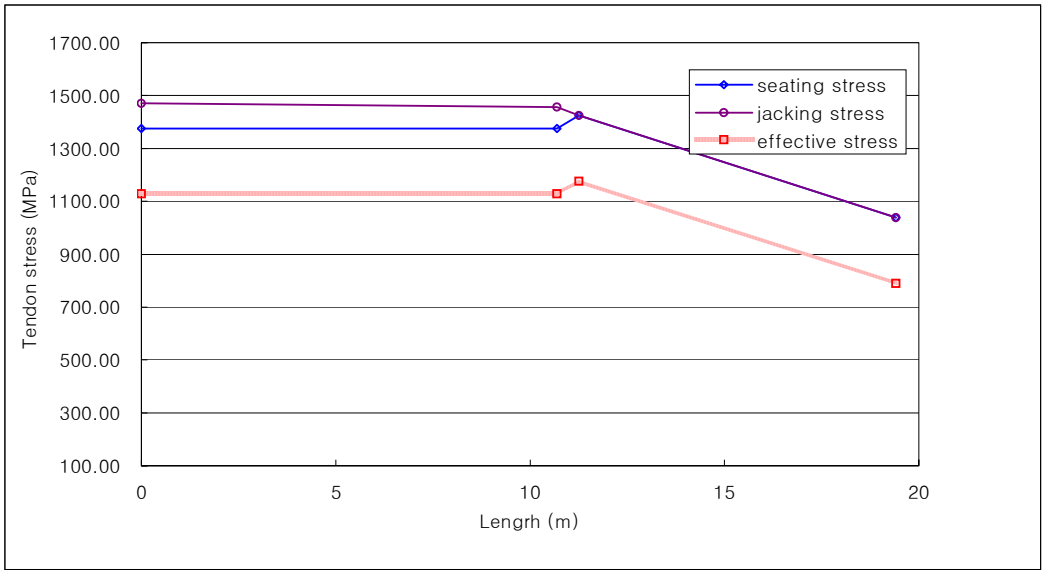

(a) Vertical Tendon Stress

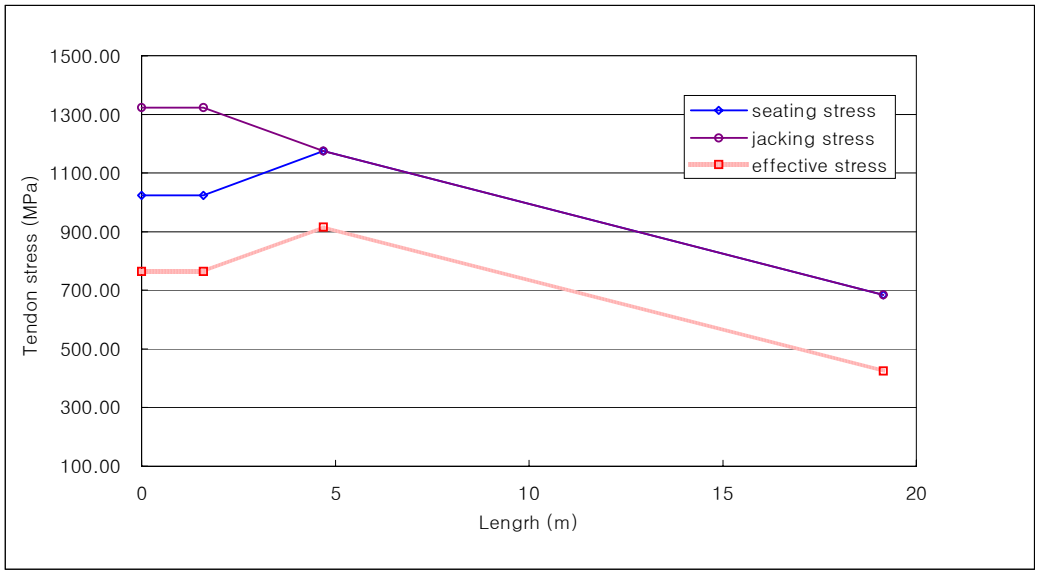

(b) Hoop Tendon Stress

Figure 6 Prestressing Stress Profile

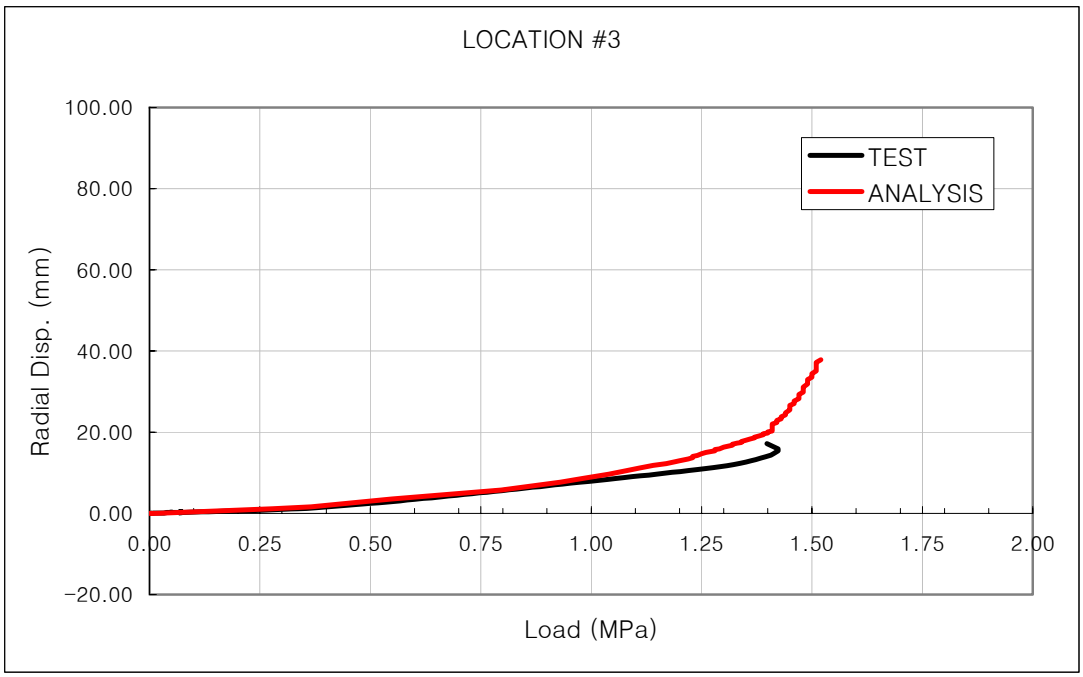

(a) Radial Displacement at AZ. 135°, EL. 1.43m

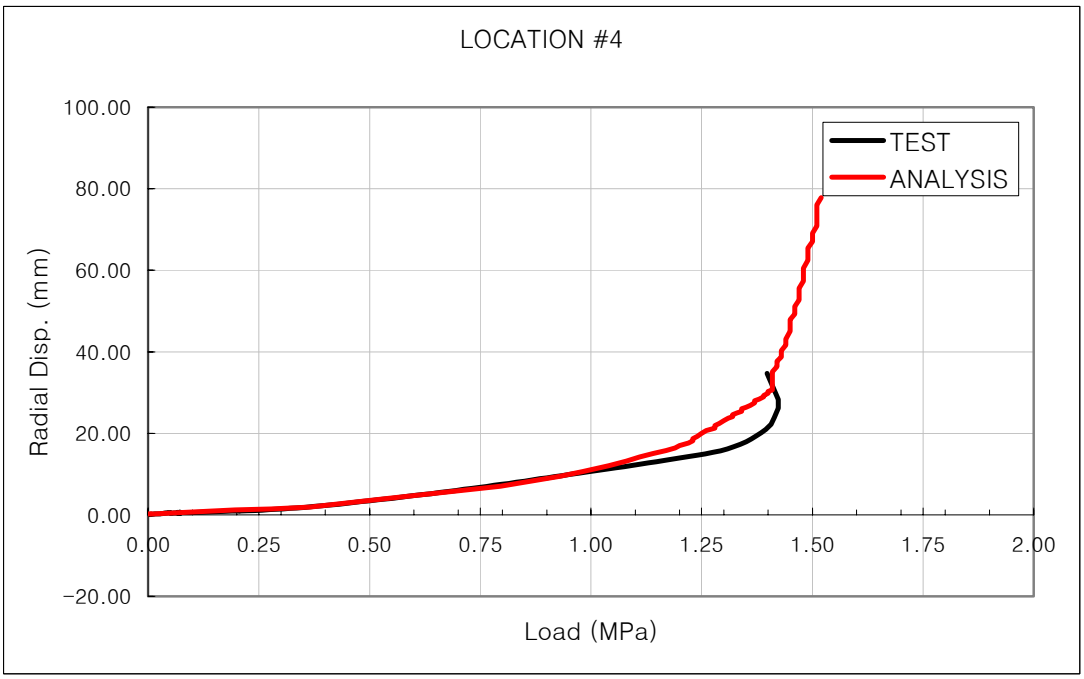

(b) Radial Displacement at AZ. 135°, EL. 2.63m

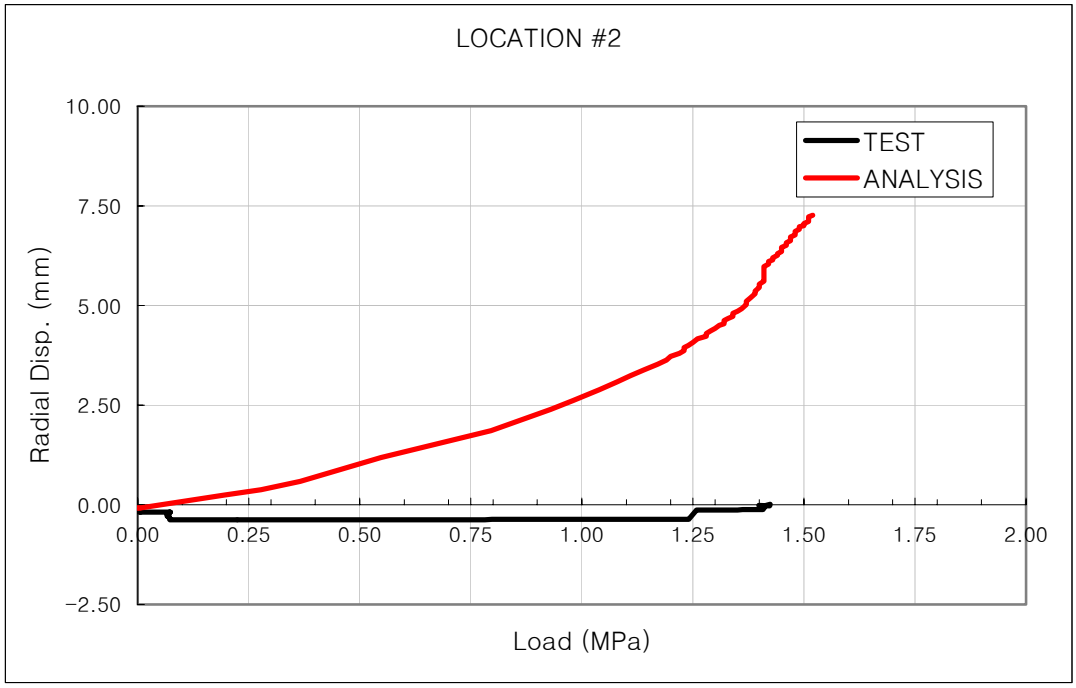

(c) Radial Displacements at AZ. 135°, EL. 0.25m

Figure 7 Radial Displacements at EL. 1.43m, EL. 2.63m, EL.0.25m

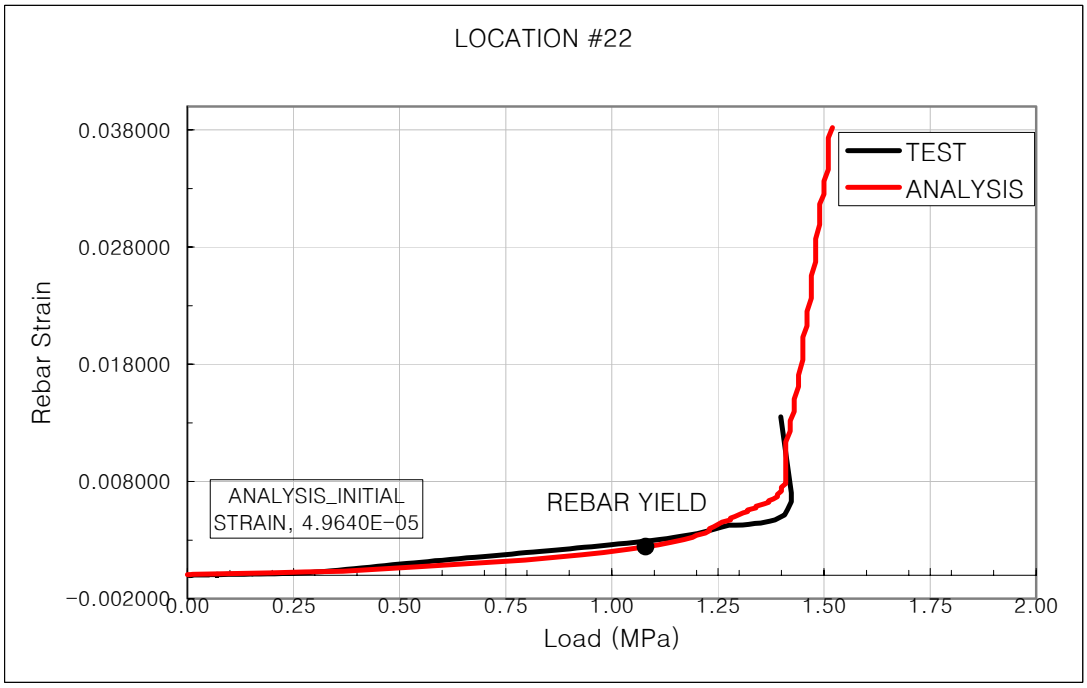

Figure 8 Hoop Rebar Strain at Mid-height

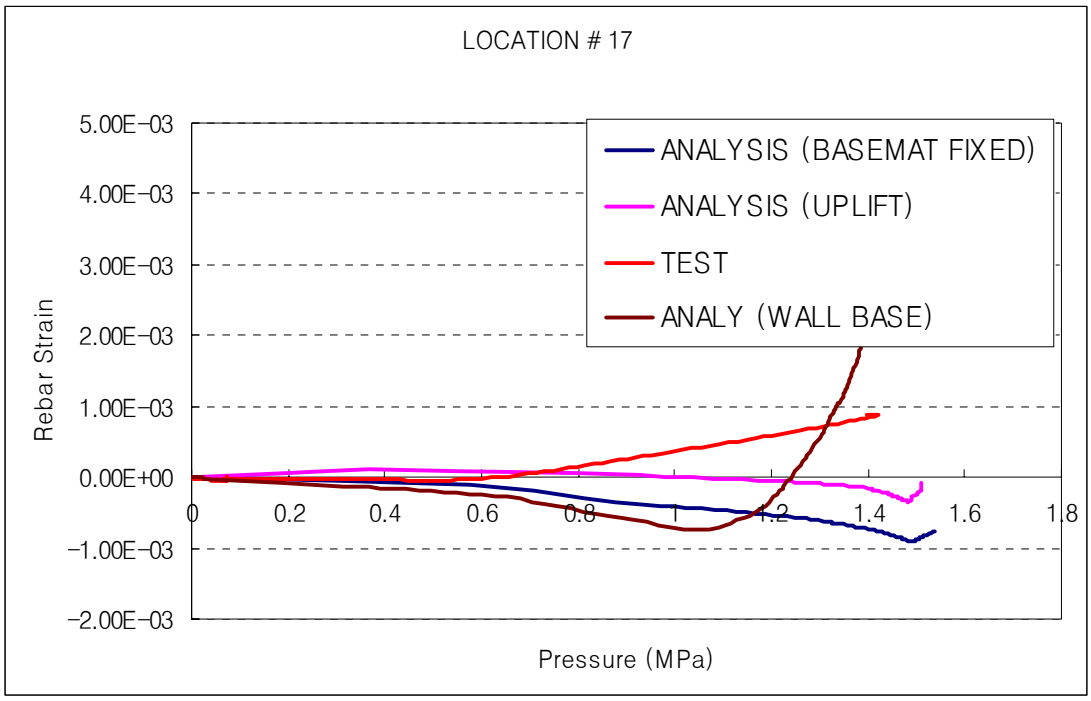

(a) At EL. 0.05m

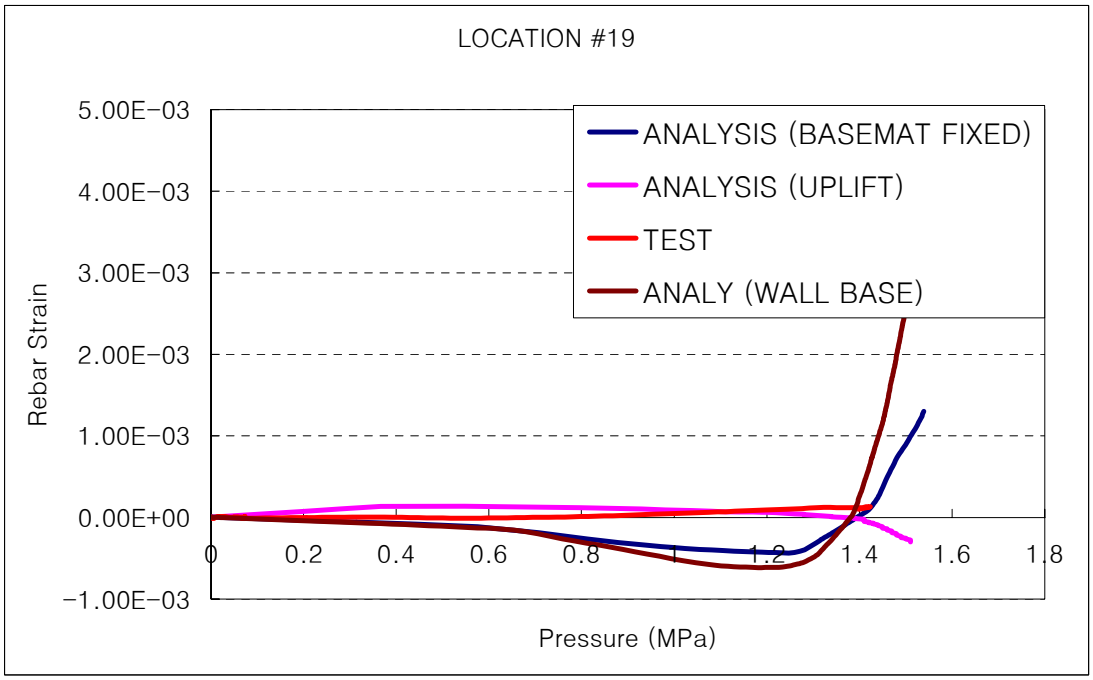

(b) At EL.0.25m

Figure 9 Comparisons of the outer Meridional Rebar Behavior at Wall Base

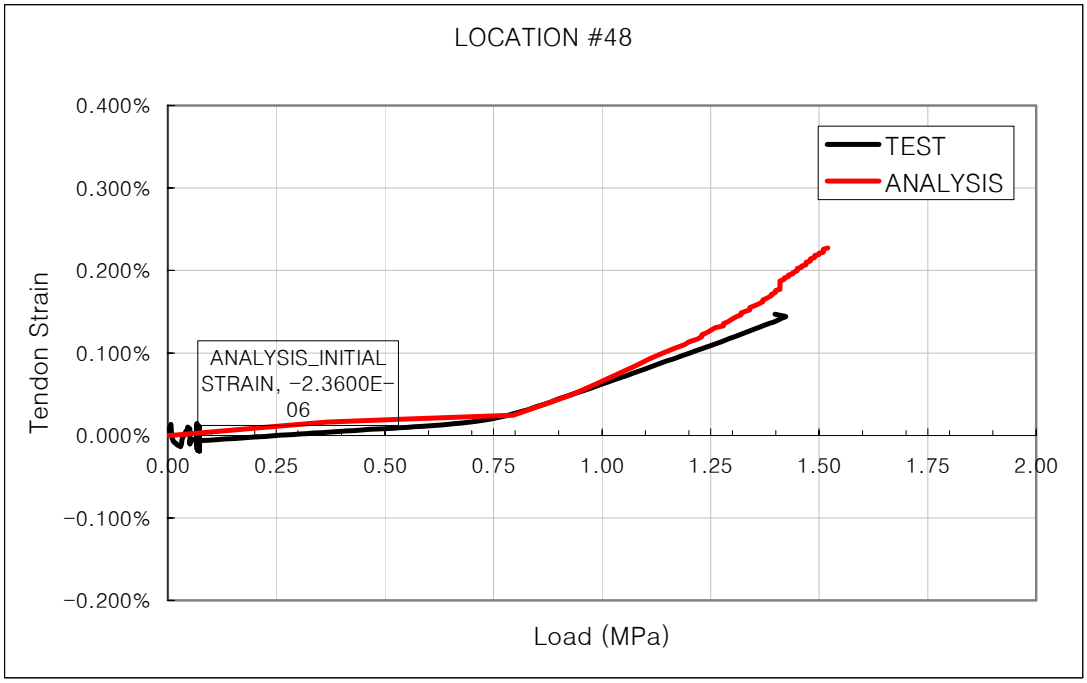

(a) Tendon Strain Hairpin around Dome Apex (180°, EL. 15.60m)

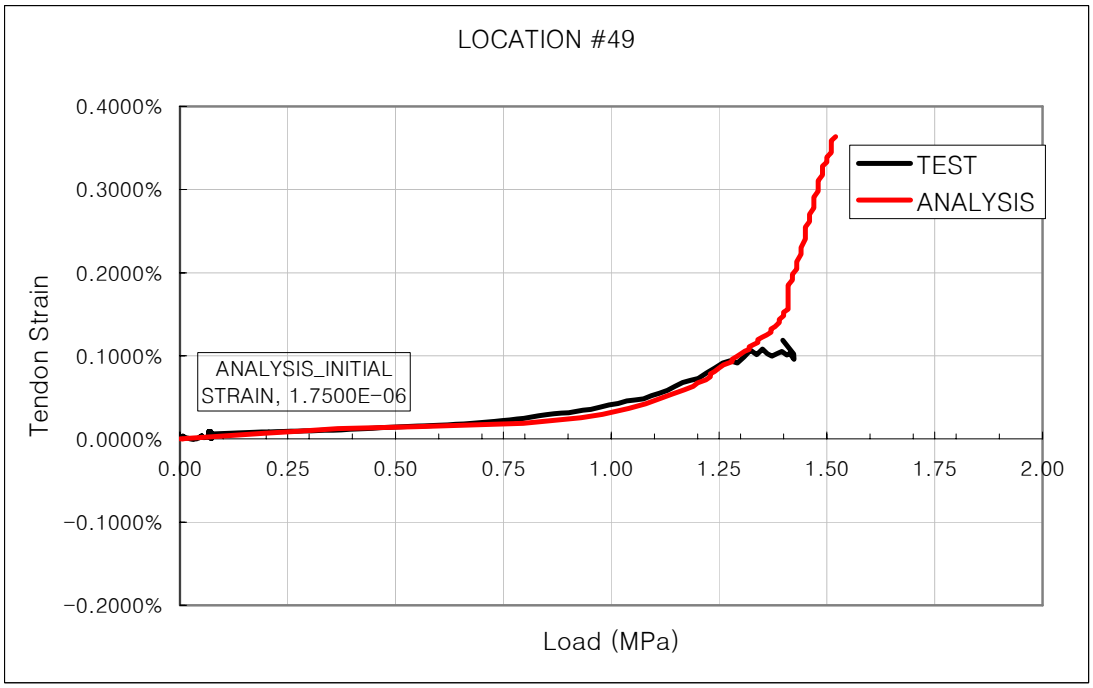

(b) Tendon Strain Hairpin at Spring Line (135°, EL. 10.75m)

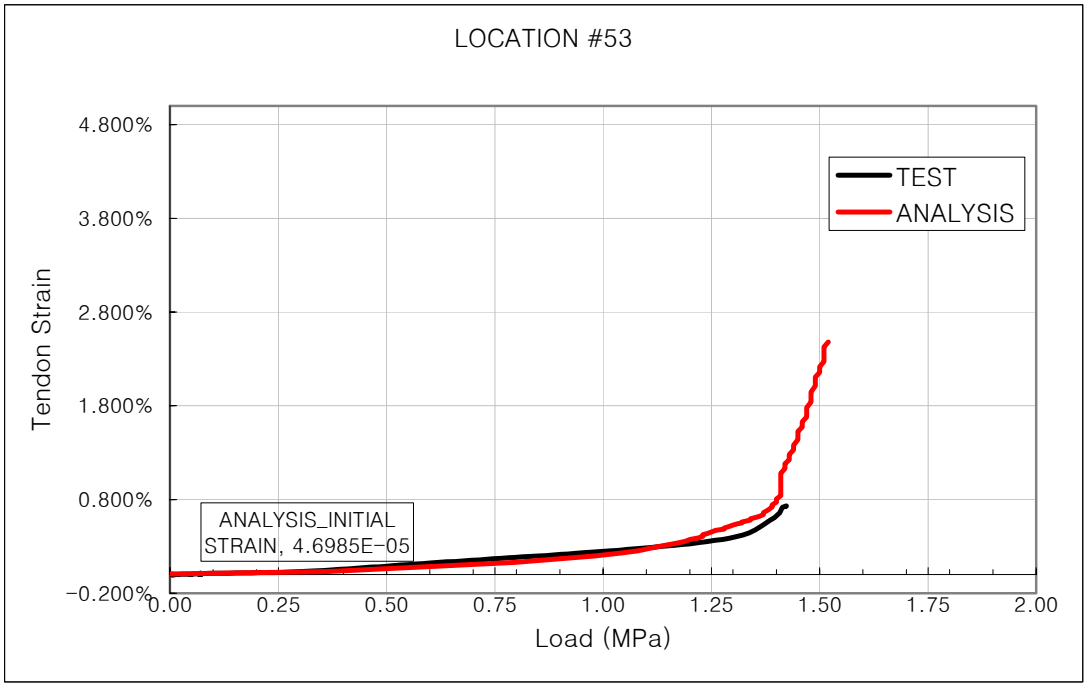

(c) Tendon Strain Hoop Tendon below Mid-height (0°, EL. 4.57m)

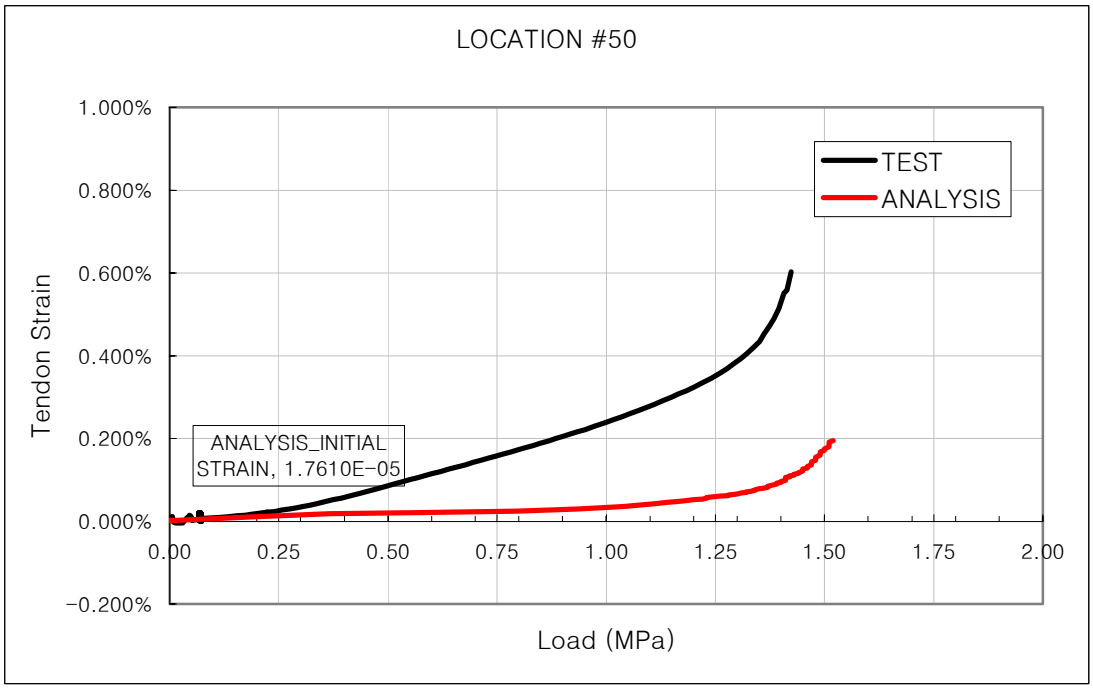

(d) Tendon Strain Hoop Tendon above Mid-height (at buttress, Az. 90°, EL. 6.58)

Figure 10 Comparisons of Tendon Strains

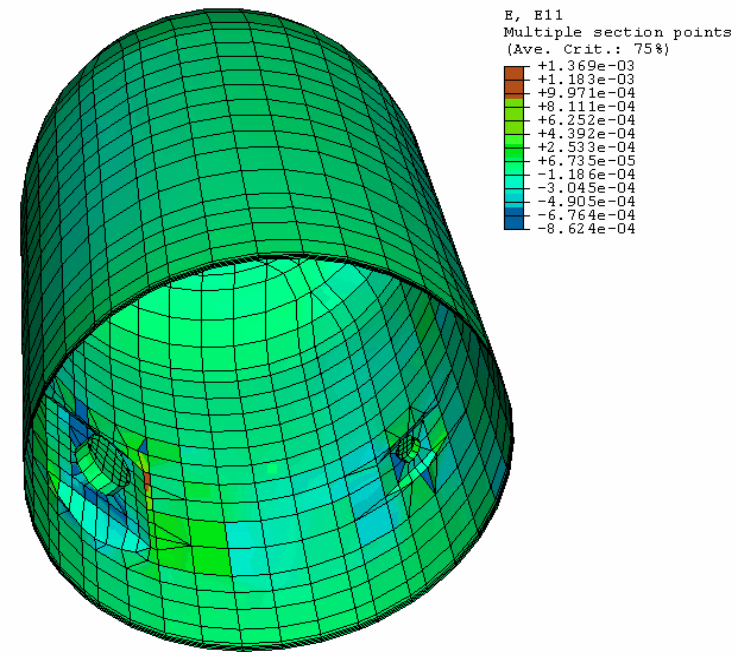

(a) The Regions of Liner Yield (at the pressure level of 0.84MPa)

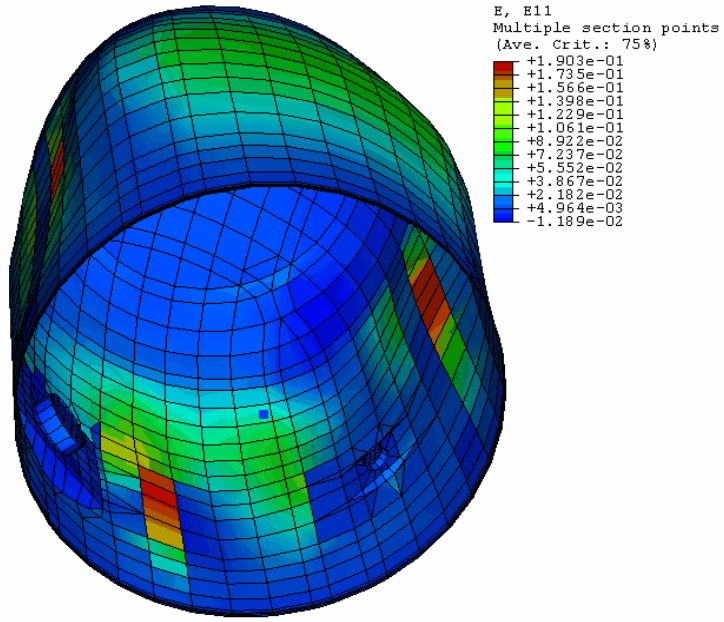

(b) Liner Tearing (1.45MPa, Liner Fracture Strain 19% considering Triaxial Factor)

Figure 11 Stress Contours for Liner Yield and Tearing

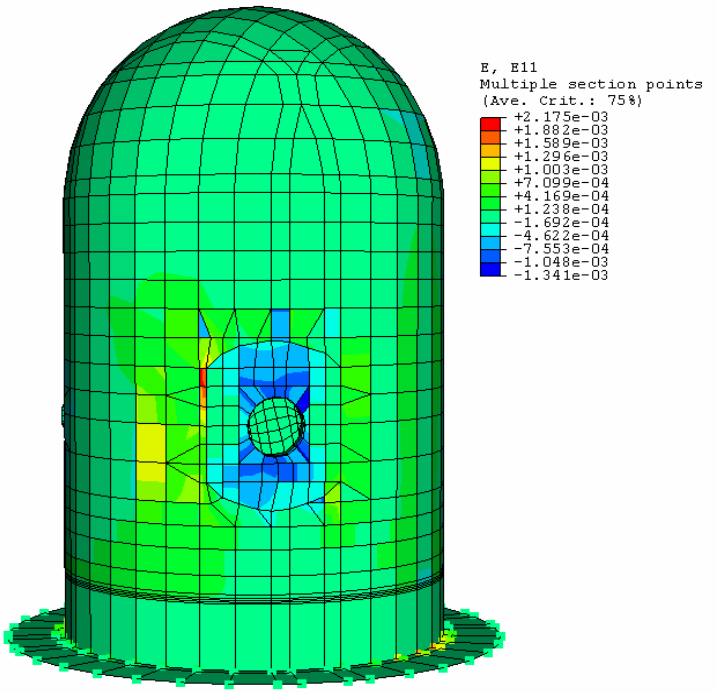

Figure 12 View of Initial Concrete Cracking Zone (at the pressure level of 0.60Mpa)

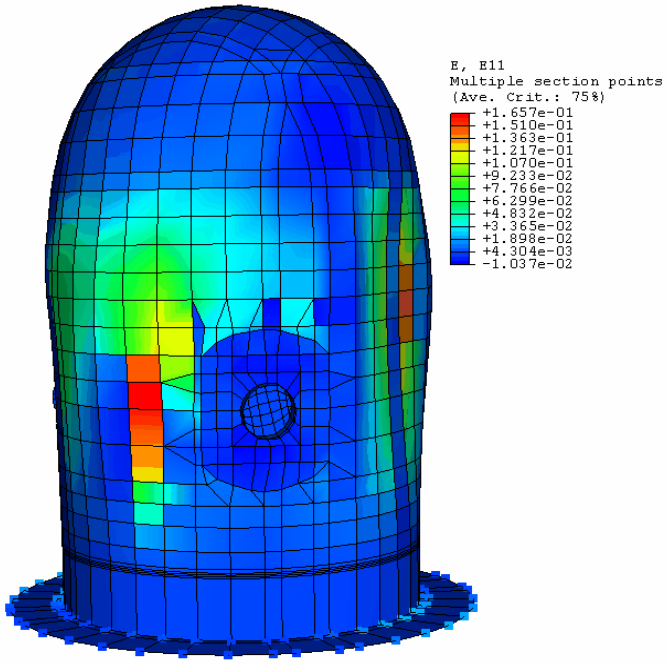

(a) X-Direction Strain (E11)

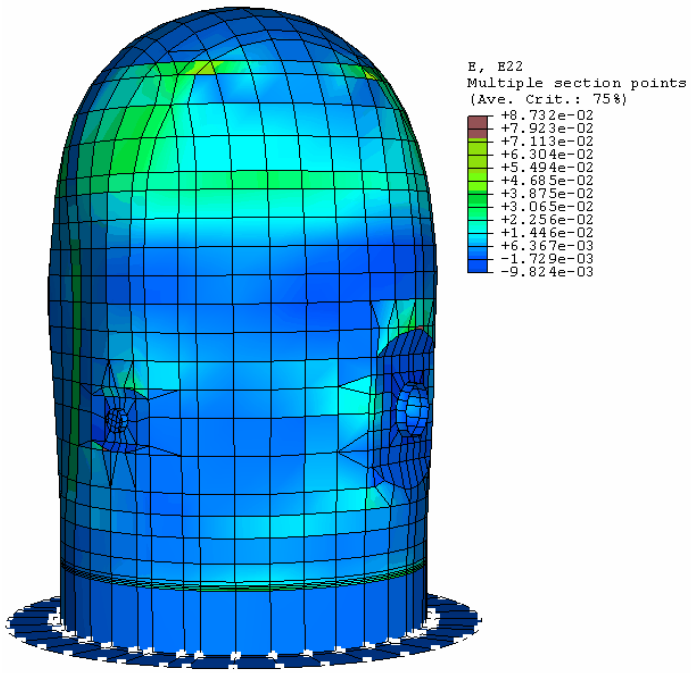

(b) Y-Direction Strain (E22)

Figure 11 Concrete Strains at Structural Failure (Pressure Level :1.52MPa)

5. References

1. R.A. Dameron, B.E. Hansen, D.R. Parker and Y.R. Rashid, *Posttest Analysis of NUPEC/NRC 1:4 Scale Prestresssed Concrete Containment Vessel Model*, NUREG/CR-6809 SAND2003-0839P ANA-01-0330, Sandia National Laboratories, Albuquerque, NM, March 2003.
2. ABAQUS User's Manual, Version 6.4, 2003. ABAQUS Inc.
3. M.F. Hessheimer, E.W. Klamerus, L.D. Lambert and G.S. Rightley, *Overpressurization Test of a 1:4-Scale Prestressed Concrete Containment Vessel Model*, NUREG/CR-6810, SAND2003-0840P, Sandia National Laboratories, Albuquerque, March 2003.
4. ABAQUS Theory Manual, Version 6.4, 2003. ABAQUS Inc.
5. Mazars J., Dube J.F., Flejou J.L. and Ghavamian Sh., *A Damage Multi-layered F.E. Model for the Seismic Response of R.C. Structures – A Tool for Understanding the Real Behaviour*, Proceeding 10th EAEE, 1994.
6. Thomas T.C. Hsu, *Unified Theory of Reinforced Concrete*, CRC Press 1993, 205-218 pp.

ANALYSIS OF 1:4 SCALE PRESTRESSED CONCRETE CONTAINMENT VESSEL (PCCV) MODEL SUBJECT TO PRESSURE AND THERMAL LOADING PHASE 3

Nam Ho Lee and Il Hwan Moon
Korea Power Engineering Company, Korea

Abstract

This paper describes the nonlinear analyses of a 1:4 scale model of a prestressed concrete containment vessel (PCCV) which incorporates both pressure and temperature effects. The analyses are performed using the results of the heat transfer analyses provided as time and/or pressure dependent thermal gradients at representative cross-sections in the model. This paper is focused on the behavior of the NUPEC/NRC 1:4-scale prestressed concrete containment vessel under pressure and temperature loading beyond the design basis

In the nonlinear finite element analyses, the 1/4-scale PCCV including the axi-symmetric cylindrical vessel, the spherical dome and the concrete base slab are idealized as an axi-symmetric global model with axi-symmetric solid elements and shell elements.

The temperature-dependent degradation properties of concrete and steel are considered. Both geometric and material nonlinearities including thermal effects are also addressed in the analyses. Menetrey-Willam concrete constitutive model with non-associated flow potential is adopted for this study. This study includes the results of the predicted thermal and mechanical behaviors of the PCCV subject to high temperature loading and internal pressure simultaneously.

In order to find the effect of accident high temperature on the ultimate capacity of each component, two kinds of analyses are performed; one for pressure only and the other for pressure with temperature. The results are compared with each other for the liner plate, reinforcement, prestressing tendon and concrete. The analysis results show that the temperature directly affects the behavior of the liner plate, but has a little impact on the ultimate pressure capacity of the PCCV.

Introduction

The purpose of the work contained herein is to describe the nonlinear analyses of a 1:4 scale model of prestressed concrete containment vessel (PCCV) that incorporates both internal pressure and thermal effects. The analyses are performed using the results of the heat transfer analyses provided as time and/or pressure-dependent thermal gradients at representative cross-section in the model.

This paper is focused on the behavior of the NUPEC/NRC 1:4-scale prestressed concrete containment vessel under pressure and temperature loading beyond design basis. In the nonlinear finite element analyses, the 1:4-scale PCCV including the axi-symmetric cylindrical vessel, the spherical dome and the concrete base slab are idealized as an axi-symmetric global model with axi-symmetric solid elements for concrete structure and shell elements for liner plate.

The temperature-dependent degradation properties of concrete and steel are incorporated in this

`

analysis. Both geometric and material nonlinearities including thermal effects are also addressed in this analysis. Menetrey-Willam concrete constitutive model with non-associated flow potential is adopted for the analyses. This study includes the results of the thermal and mechanical behavior of the PCCV under high temperature loading and pressure simultaneously. Concrete material properties are modified in accordance with Dameron et al. Research [1], and rebar and tendon materials are adjusted in accordance with the formulas proposed by Dameron et al. [1] and Holmes [2], respectively. Variation in Liner Plate material property due to temperature was incorporated in accordance with Dameron et al. Research [1] and the ASME Section III, Division 1 – Appendix I.

In order to find the effect of accident high temperature on the ultimate capacity of each component, two kinds of analyses were performed; a combined thermal-mechanical analysis of the 1:4-scale PCCV model for saturated steam conditions (Case 1) and for a severe accident scenario (Case 2). The numerical results for each case were documented for a reduced set of Standard Output Locations and compared with the numerical results for mechanical (pressure) for liner plate, reinforcement, prestressing tendon and concrete. The computer program ABAQUS [3] was used to analyze the axi-symmetric finite element model of PCCV with nonlinear and temperature-dependent material properties of concrete, liner plate, reinforcing steel, and prestressing tendon.

Material Property and Modeling

General

To simulate the PCCV, the actual (tested) properties of concrete, reinforcing steel, post-tensioning tendon, liner plate and soil are used in the analysis. The properties for these materials are from test data provided by Sandia National Laboratories and used in the construction of the 1:4-scale PCCV [4] at Sandia. The strength reductions from increase of temperature are appropriately introduced to account for material degradation since high accident temperatures are introduced with accident pressure to the PCCV model.

Concrete

Constitutive Model

The concrete is characterized by a materially nonlinear deformation behavior. The material non-linearity is assumed to occur due to cracking of concrete in tension and plasticity of concrete in compression. However, the material non-linearity due to the latter has relatively less influence than that due to the former on the failure mode of the containment structure under internal pressure.

The Menetrey-Willam's failure model with a non-associated plastic flow that is known to be suitable to represent the tensile concrete cracking of the axi-symmtric finite element model is introduced in the numerical analysis. The yield surface and flow potential parameters for elasto-plastic material yield surface in the Menetrey-Willam's failure model with non-associated plastic flow and the strain hardening are defined by the model parameters *r*-factor, the friction angle β, and the dilation angle ψ. The elliptic function $r(\theta, e)$ controls the shape of the yield surface in the deviatoric plane and angle β is the angle between the yield surface and the pressure stress axis in the meridian plane [3].

`

Material Properties

The following mechanical concrete properties from the uniaxial strength test data of the trial mix concrete are used in the analysis of the 1:4 scale PCCV model for mechanical (internal pressure load only) and thermal-mechanical (pressure + temperature) loading.

Table 1 Concrete Material Property

Property	Value for Basemat	Value for Shell & Dome
Elastic Modulus	27,950 MPa	26,970 MPa
Uniaxial Compressive Strength	39.16 MPa	47.30 MPa
Uniaxial Tensile Strength	3.37 MPa	3.45 MPa
Poisson's Ratio	0.18	0.18

Variation due to Temperature

A smooth curve for strength degradation versus temperature as estimated below (provided as a reference with temperature variation) is introduced into the finite element analysis model.

$$S_{Rc} = \exp -(T/632)^{1.8} \text{ , where T is in degree C} \quad (1)$$

Further, based on the literature, elastic modulus reduction is calculated by equation (2).

$$M_{Rc} = (S_{Rc})^{1/2} \quad (2)$$

The thermal expansion coefficient is assumed to be constant at 1.18E-5 cm/cm/^{o}C upto 260^{o}C of temperature rise and then gradually increases to 2.18E-5 cm/cm/^{o}C at 430 ^{o}C [6].

Reinforcement Steels (Rebars)

Constitutive Model

Rebar materials are generally incompressible when they deform plastically and their yielding is independent of the pressure stress. The von Mises failure criterion is used for this steel material. Hsu [5] noted that the stress-strain curves for bare steel bar and for steel bar embedded in concrete are quite different as shown in Figure 1. Therefore, the stress-strain relationship of rebar embedded in concrete has been used in reinforced concrete structure to simulate the realistic behavior of the rebar in concrete.

The stress-strain curve of the rebar for the numerical analysis is idealized by bilinear curve with a slope of E_s before yielding and a slope of E_p after yielding as illustrated in Figure 1. The equations of two lines are expressed at the stress level designated by f_y' at which the two straight lines intersect as shown in equations (3) and (4). The plastic modulus E_p' after yielding can be taken as a small fraction of the elastic modulus E_s.

`

$$f_s = E_s \varepsilon_s \qquad \text{for } f_s \le f_y' \tag{3}$$

$$f_s = f_o' + E_p' \varepsilon_s \qquad \text{for } f_s \succ f_y' \tag{4}$$

where f_o' is the vertical intercept of the post-yield straight line. The intersection stress level f_y' and the plastic modulus E_p' depend mainly on the level of the apparent yield stress f_y* illustrated in Figure 1. The values of f_y' and E_p' in the stress-strain relatinship used in the numerical analysis are calculated as equations (5) and (6) using the apparent yield stress f_y* and the strain-hardening modulus of the bare bar E_p from the actual material properties.

$$\frac{f_y'}{f_y} = 0.43 + 0.5\frac{f_y^*}{f_y} \tag{5}$$

$$\frac{E_p'}{E_p} = 3.3 - 2.5\frac{f_y^*}{f_y} \tag{6}$$

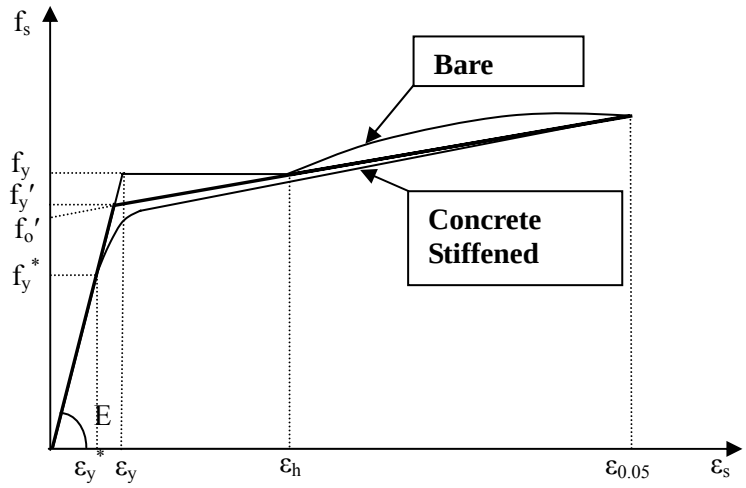

Figure 1 Stress-strain relationship of rebar using bilinear model

Material Property

The test results provided in the Appendix of References [4] are used in the numerical modeling of the rebar material properties. Table 2 presents the modulus of elasticity for each type and each size of the reinforcement steel

`

Table 2 Reinforcing Material Properties

	D6 (SD345)	D10 (SD390)	D13 (SD390)	D16 (SD390)	D19 (SD390)	D22 (SD390)	D19 (SD490)
Elastic Modulus (MPa)	1.69E5	1.83E5	1.83E5	1.83E5	1.84E5	1.91E5	1.86E5
Poisson's ratio	0.3	0.3	0.3	0.3	0.3	0.3	0.3
Yield Stress (MPa)	369.4	472.9	432.3	457.5	473.1	459.0	512.2
Tensile Stress (MPa)	489.4	665.9	610.6	616.5	658.3	680.8	709.7
Extension (%)	30.4	20.5	24.2	22.1	21.1	18.7	17.8

Variation due to Temperature

Temperature variation of steel is considered in the analysis model as idealized below.

$$S_{Rs} = \exp -[(T-340)/300]^{1.9} \quad \text{where T is in degree C} \qquad (7)$$
$$S_{Rs} = 1.0 \quad for \quad T \le \mathrm{C}340^{\circ}C$$

The thermal expansion coefficient of steel is assumed to be constant at 1.18E-5 cm/cm/^{o}C upto 614^{o}C of temperature rise.

Prestressing Tendon

Material Model

The stress-strain curve of a bare prestressing tendon comprised of two straight lines joined by a knee curve as shown in Figure 2 is used in the numerical analysis. The first part of the curve is a straight-line up to $0.7f_{pu}$ and the second part is expressed by Ramberg-Osgood equation(8) that meets the first part at the stress level of $0.7f_{pu}$.

$$f_p = \frac{E_{ps}'\varepsilon_p}{\left[1+\left(\frac{E_{ps}'\varepsilon_p}{f_{pu}}\right)^4\right]^{1/4}} \qquad (8)$$

where f_{pu}, f_p, E_p' and ε_p are the ultimate strength of the tendon, the strength in the tendon, the tangential modulus Ramberg-Osgood curve at zero load and the sum of strain in the tendon, respectively [5].

`

ABAQUS, the finite element program, has no function to incorporate the unbonded tendon. The prestressing tendons are modeled as rebar subelements in concrete using the embedded approach available in ABAQUS. The numerical modeling of tendons as rebar sub-elements implies that the tendons are assumed bonded to the concrete and slippage of the tendon in the tendon sheath is not considered in the numerical analysis.

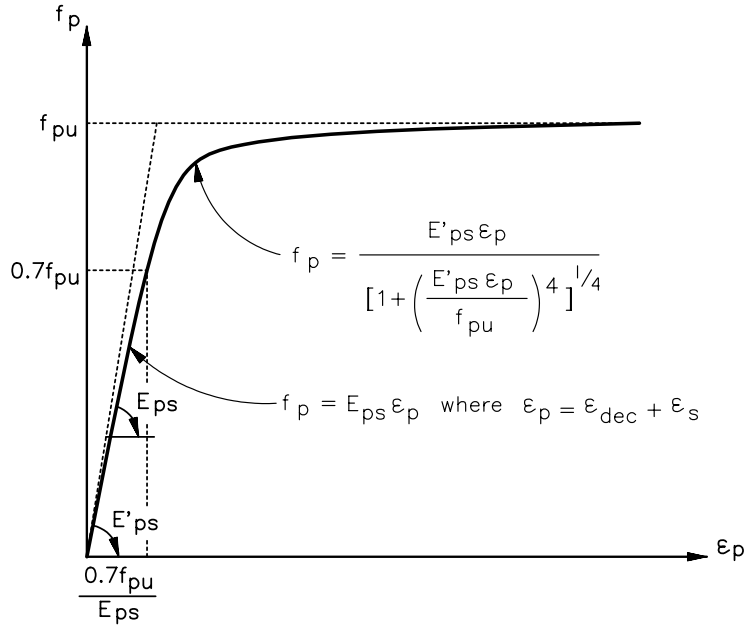

Figure 2 Stress-strain relationship of prestressing tendon

Material Property

The following material properties from Sandia Laboratories are used for the tendon modeling.

Table 3 Tendon Material Properties

Property	Values
Elastic Modulus	191000 MPa
Elastic Limit Stress	1339 MPa
Yield Strength	1691 MPa
Poisson's Ratio	0.3
Ultimate Strength	1912 MPa
Extension	4.5%

`

Variation due to Temperature

Temperature variation of steel is considered in the analysis model as idealized below.

$$S_{Rs} = \exp-[(T-340)/300]^{1.9} \quad \text{where T is in degree C} \qquad (7)$$
$$S_{Rs} = 1.0 \ \text{ for } \ T \le 340^{\circ}C$$

The thermal expansion coefficient of steel is assumed constant as 1.18E-5 cm/cm/^{o}C to 614^{o}C of temperature rise.

Steel Liner Plate

Constitutive Model

The stress-strain behavior of the liner plate steel is modeled by using elasto-plastic model available in ABAQUS. The von Mises failure surface with kinematic hardening is used to represent the nonlinear behavior of the material.

Material Property

The material properties of the liner plate used in the numerical analysis are shown in Table 4.

Table 4 Steel Liner Material Properties

Property	Values
Elastic Modulus	218,700 MPa
Elastic Limit Stress	1339 MPa
Yield Strength	375.595 MPa
Poisson's Ratio	0.3
Ultimate Tensile Strength	499.158 MPa

Variation due to Temperature

Temperature variation of steel is considered in the analysis model as idealized below:

$$S_{Rs} = \exp-[(T-340)/300]^{1.9} \quad \text{where T is in degree C} \qquad (7)$$
$$S_{Rs} = 1.0 \ \ for \ \ T \le 340^{\circ}C$$

`

The thermal expansion coefficient of steel is assumed constant at 1.18E-5 cm/cm/^{o}C up to 614^{o}C of temperature rise. The thermal expansion coefficient of liner steel exposed to high temperature is calculated by ASME Section III, Division 1, Appendix-I [ASME, 1986].

Finite Element Model

General

The axi-symmetric finite element model which is utilized to predict the overall response of the 1:4 scale PCCV under internal pressurization and/or thermal loading is shown in Figure 3. This model consists of the axi-symmetric cylindrical vessel, a spherical dome and the concrete base slab. This model is intended to provide the overall behavior of the PCCV model taking into account of uplift. This model consists of axi-symmetric solid elements for concrete portions, nonlinear soil spring elements between basemat and foundation, and three-node shell elements connected to the axi-symmetric solid elements for concrete portions using rigid link elements as shown in Figure 3.

Model for Shell and Dome

The concrete portions of dome and cylindrical wall are modeled with the eight-node axi-symmtric solid elements. The liner steel on the inside surface of the PCCV is made up of three-node shell elements. The liner elements, which are offset from the prestressed concrete elements, are connected to the concrete solid elements by rigid link elements. All rebars and tendons are assumed to remain rigidly bonded to the concrete and thus modeled by using the rebar sub-element provided by ABAQUS computer program. Vertical liner anchors are modeled as a beam of rectangular cross-section dimension. The cross-sections of liner anchors are computed based on the area and the bending stiffness of the embedment. Prestressing is induced in the tendons with a function through the *INITIAL CONDITIONS option in ABAQUS.

Model for Base Slab

The base slab is included in the finite element model to simulate the possible vertical uplift of the base during internal pressurization and to estimate the effect of the base slab on the failure mode. The previously described shell and dome model is connected to the base slab model consisting of eight-node solid elements with considering tendon gallery.

The liner plate simulated by three-node shell elements is assumed rigidly connected to the eight-node concrete solid elements unlike those for cylindrical shell since the interaction effect of liner steel and concrete during the flexural deformation of the slab is not significant in the thick base slab of PCCV. Reinforcements in the base slab are estimated from the provided structural drawings and are included in the analysis model. All rebars in the base slab are modeled as those of shell portion by using the rebar subelement of ABAQUS.

The bottom of the slab rests on a soil foundation modeled by nonlinear soil springs with tension cut-off. Since the soil properties were not provided by Sandia National Laboratories, an appropriate elastic modulus was used only to simulate the uplift by using the nonlinear spring with tension cut-off.

`

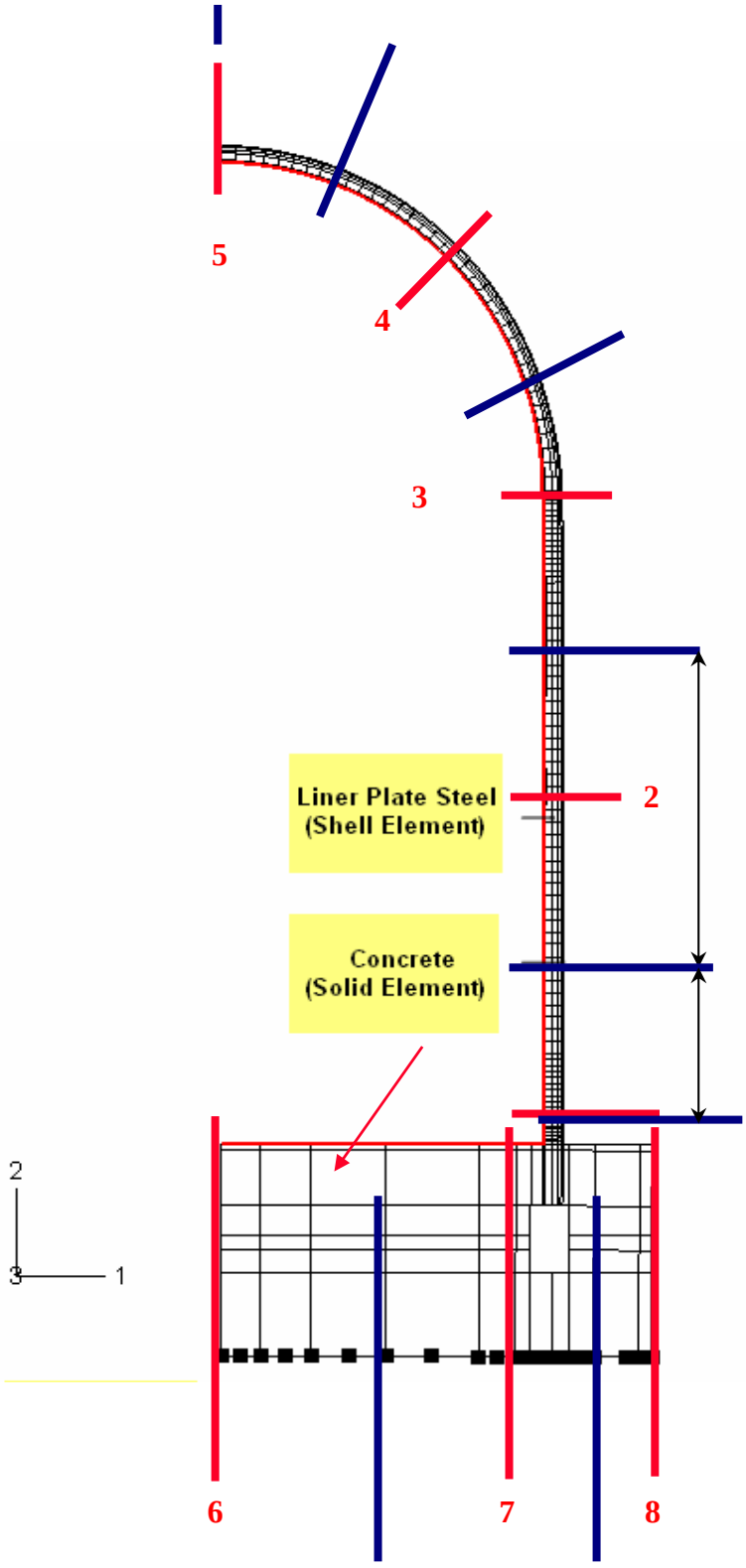

Figure 3 Axi-symmetric Finite Element Model of PCCV

Prestressing Forces in Tendon

The meridional stress and hoop stress along the length of the tendon in the concrete are estimated as shown in Figure 6 with the prestressing losses at the time of testing. The prestressing force was introduced prior to applying the internal pressure and/or thermal loadings to the numerical model. The four types of losses given in specific modeling consideration are (1) the friction between the tendon and the concrete, (2) the elastic shortening of the concrete, (3) the creep and shrinkage of the concrete, and (4) the stress relaxation in the prestressed tendons.

The vertical prestressing forces of 106.27kips before anchoring and 96.04kips after anchoring are introduced from the PCCV Model-General Arrangement. Based on the prestressing forces at anchorage, the magnitudes of the vertical tendon stress are calculated along the length of the vertical tendon and considered in the finite element analysis model using the losses shown in Table 5. Similarly, the hoop tendon forces of 95.27kips before anchoring and 73.52kips after anchoring are used in the calculation of hoop tendon stress.

Table 5 Prestressing Losses

	Vertical Tendon Loss MPa (ksi)	Hoop Tendon Loss MPa (ksi)
Elastic shortening of concrete	31.855 (4.620)	31.855 (4.620)
Creep of concrete	66.999 (9.717)	83.829 (12.158)
Shrinkage of concrete	129.309 (18.754)	129.309 (18.754)
Steel relaxation	19.747 (2.864)	14.473 (2.099)
Total losses	247.910 (35.955)	259.473 (37.632)

Self-weight, Internal Pressure and Thermal Loading

Because of the elastic support below the bottom slab, the effect of the weight of the structure had to be initially considered prior to internal pressurization and/or thermal loading. This is accomplished by specifying a mass proportional load for each material included in the 1:4 scale PCCV model prior to initiating the internal pressure and/or thermal loading. The weights of each material are considered in the numerical model by using the GRAVITY parameter of *DEAD LOAD option of ABAQUS. The loading histories of internal pressure and thermal loading are shown in Figure 4. The heat distribution result through thickness of wall and base slab provided by the Sandia National Laboratories are considered for thermal loading analyses.

Thermal gradients at eight sections including dome apex, 45° dome angle, spring line, mid-height, wall-mat junction, center of base slab, near wall-mat junction of base slab and edge of base slab are provided by Sandia National Lab. Thermal gradient specified at each thermal gradient section is identically applied to both halves of each thermal gradient section (mid-points of neighboring sections centering the section) as the thermal gradients of each neighboring thermal gradient section are not much different from those for each section. The temperature time history and pressure time history (shown in Figures 4-1 and 4-2) are applied at nodes of finite element model.

`

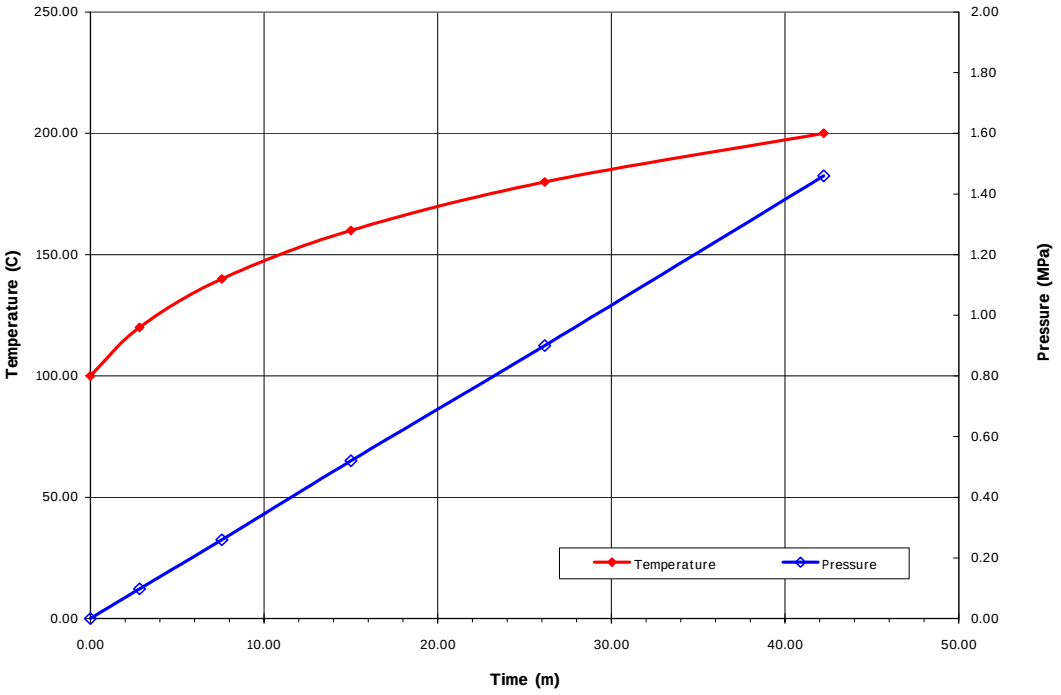

(a) Temperature and Pressure (Case 1)

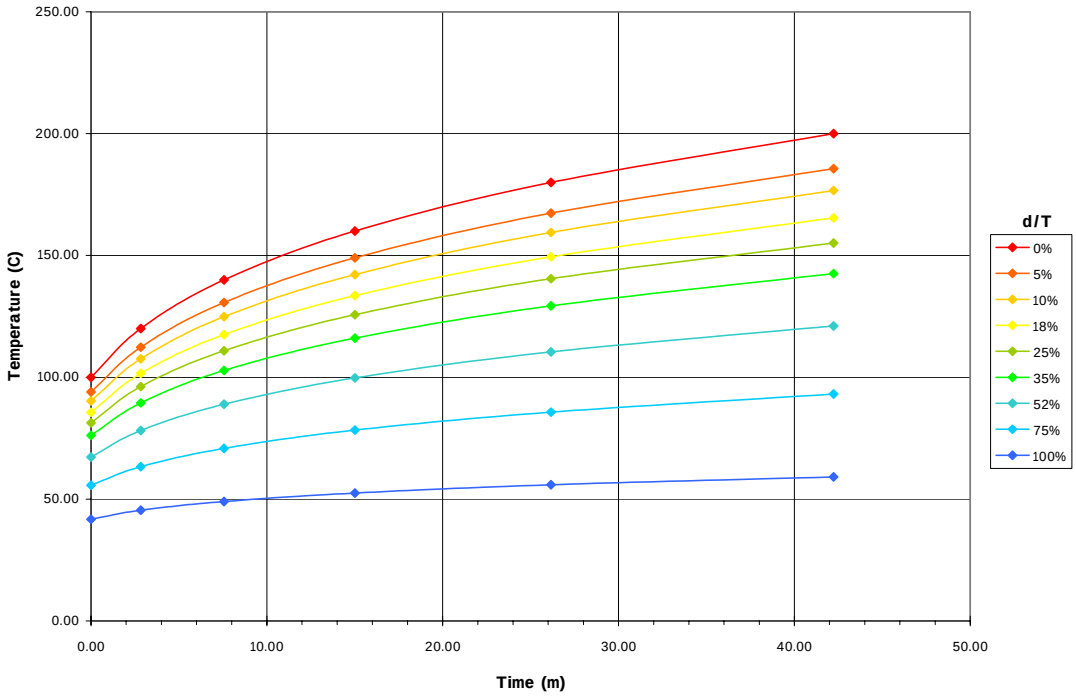

(b) Typical Temperature Distribution at Section 1 (Case 1)

Figure 4-1 Loading History for Steamed Saturated Condition

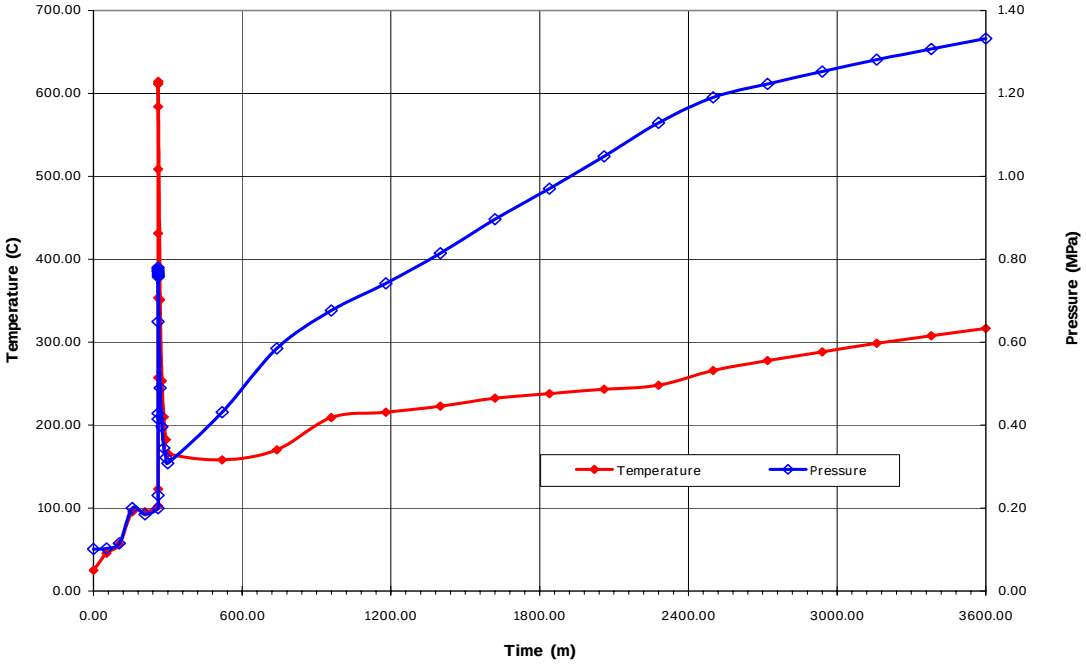

(c) Temperature and Pressure (Case 2)

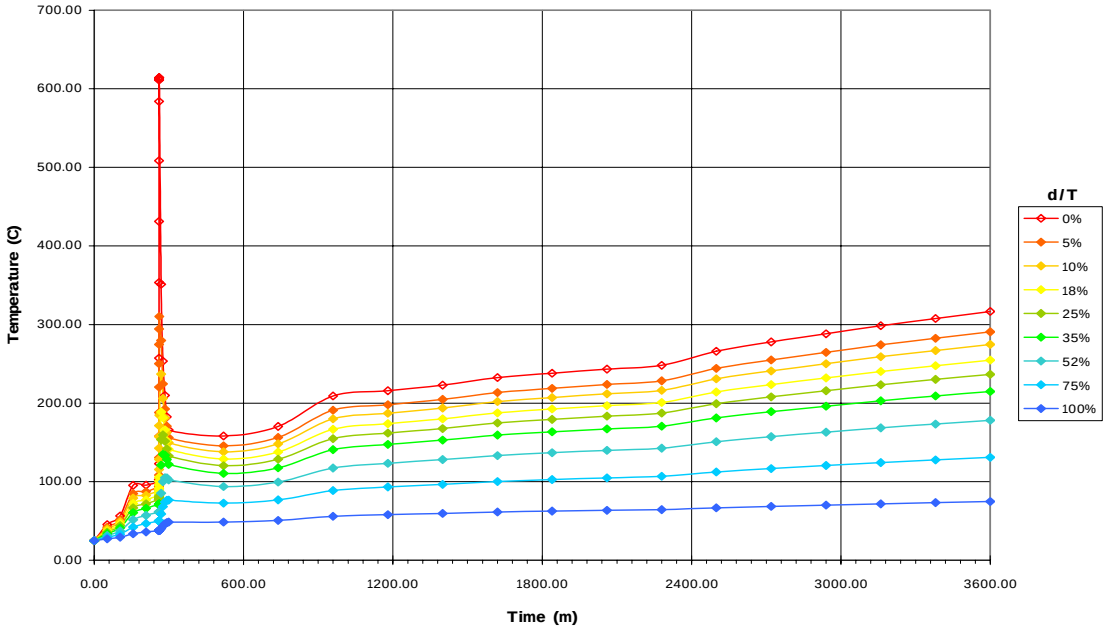

(b) Typical Temperature Distribution at Section 1 (Case 2)

Figure 4-2 Loading History for Severe Accident Scenario

Analysis Results and Discussion

Results at Standard Output Locations

The ISP-48 phase 2 analysis results at standard outputs locations (limited to azimuth 135 degrees) from three-dimensional analysis were officially submitted to the OECD/NEA and compared with the SFMT (Structural Failure Mechanism Test) results. However, axi-symmetric analysis results were also performed at the ISP-48 phase 2 and the analysis results from the finite element analysis for temperature and pressure loading histories provided by Sandia National Laboratories (see Appendix-A) and are basically submitted for ISP-48 phase 3.

The rebars are assumed yielded when the stresses in the rebars exceed the nominal yield stresses defined for each rebar type. The computer program ABAQUS tracks the yielding of each rebar included in the finite element model automatically and allows the corresponding pressure level to be computed. The behavior of concrete up to the tensile strength is characterized by the theory of linear elasticity and a crack is initiated at tensile strength. In ABAQUS, cracking is assumed to occur when stress reaches a failure surface, which is called the "crack detection surface", and the program indicates the cracking automatically.

Based on the above, the pressure levels corresponding to the event milestones requested by Sandia National Laboratories are shown in Table 6. Also, the behavior under high temperature and pressure loading histories are compared with SFMT test results and the pressure-dependent behavior as shown in Figures 7 through 40.

The liners are yielded and/or ruptured at higher pressure when both temperature and pressure were simultaneously applied than when subjected to pressure only.

Displacements

The displacement transducers were 'zeroed' prior to the start of the SFMT (Structural Failure Mechanism Test) before filling the vessel with water and the measured displacements reflect only the response to pressure (including the hydrostatic pressure). That is, the measured displacements in the SFMT did not include the effects of prestressing, nor any other previous loading [3]. Therefore, the displacements due to prestressing and dead load were subtracted from those of numerical analyses for comparison with the corresponding measured displacements.

Figures 5 through 14 show direct comparisons of analysis results and measured radial displacements versus pressure at various locations under pressure only and/or with thermal loading. To confirm whether the numerical model established at Phase 2 is appropriate for Phase 3, the results under pressure history alone are directly compared with those from SFMT. The additional hydraulic effects on the radial displacements are negligible relative to those from the ultimate internal pressure and therefore the hydraulic effects are not considered in the numerical analysis in Phase 3.

As shown in Figures 5 through 14, the radial displacements under pressure only correspond well with the numerical results and the measured displacements from SFMT, except for the displacement at Standard Location #7 (Az 135°, El. 10.75m Spring Line). A combined mechanical-thermal analysis simulating a saturated steam condition (Case 1) shows that the temperature history starting with 100°C created a sudden increase in displacements at initial stage, but the slopes expressing the pressure-displacement relationship with increasing temperature and pressure appeared very similar to the trend for the pressure only case.

`

In Case 2 for a severe accident scenario, the pressures were changed suddenly from 0.2 MPa to 0.78 MPa and back to 0.31 MPa for short periods between 260 through 300 minutes, and then increased to 1.33Mpa. The temperatures were also changed from 100°C to 615°C and then 165°C at the same short intervals as those for the pressure history and then increased gradually to 316°C at 3600 minute (see Figure 4).

The analysis results for Case 2 show that the displacements due to the sudden increase in temperature and pressure for a very short time period did not fully recover when returned to the starting temperature and pressure. This can be interpreted as a sort of residual deformation from damage to the liner plate and/or concrete portion due to instantaneous high temperature and pressure loading. Unfortunately, the analysis for Case 2 was stopped at 1.1974 MPa due to divergence and the behaviors could not be investigated beyond 1.1974 MPa. The ultimate capacity may drop rapidly with a sudden increase in deformation which in turn will induce divergence (see Figure 5 through Figure 14).

To evaluate the effects of the liner expansion caused by high temperature during very short periods on the structural behavior, a case (Case 3) of analysis was additionally performed with high temperature (Case 2 temperature history) applied only to the liner under pressure loading assuming no transfer of temperature to the concrete portion. The analysis results show that the displacements due to liner expansion do not increase significantly in comparison with those due to the pressure loading only, except for the vertical displacements in the dome portion.

`

(a) Pressure Only (at P= 1.46 MPa)

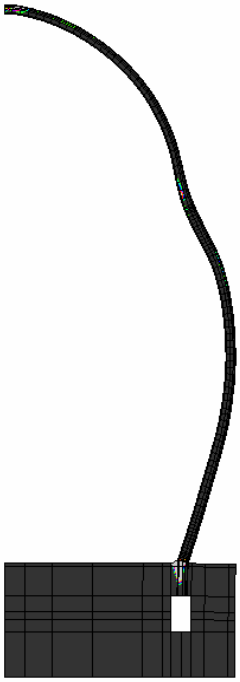

(b) Case 1(at P=1.46 MPa)

(c) Case 2(at P=1.197 MPa)

Figure 5-1 Deformed Configuration of Axi-symmetric Finite Element Model

`

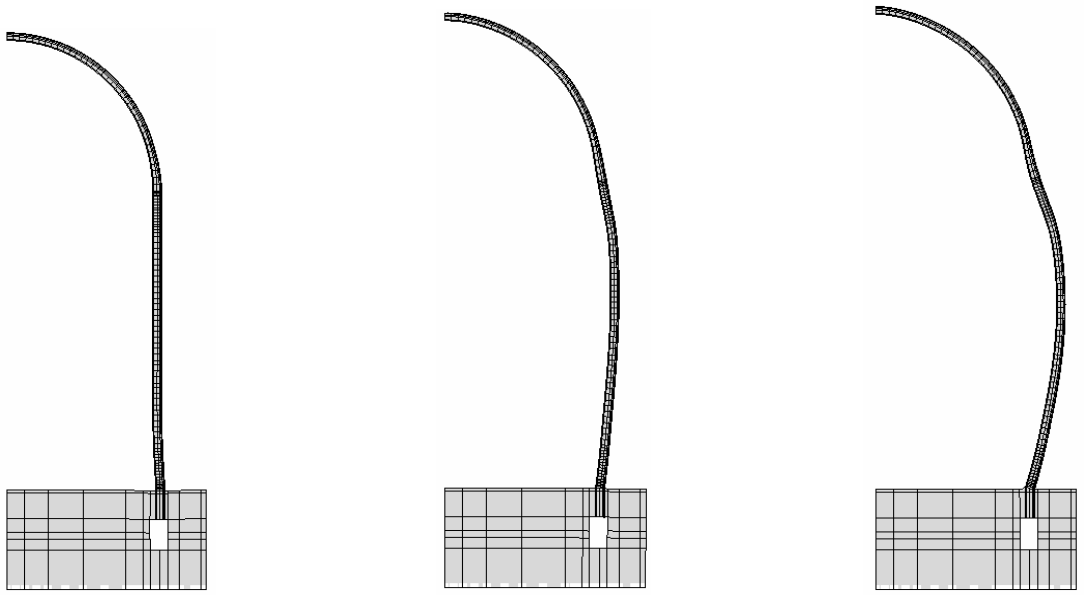

Figure 5-2 Comparison of Deformed Configuration (Pressure only and Case 1)

`

Table 6 Comparisons of Pressure Levels (MPa) Corresponding to Events Milestone

	Pressure Only	Case 1	Case 2
Cracking of concrete (hoop at mid-height)	0.64	0.64	0.64
Initial cracking of concrete (hoop and merid. at wall-mat junction)	0.49	0.10	0.10
Through cracking (hoop at mid-height for pressure only, many locations for Case 1 and 2)	0.57	0.66	0.86
Through cracking (meridional at mid-height for pressure only, many locations for Case 1 and 2)	0.84	0.26	0.42
Cracking of concrete (meridional at mid-height)	0.60	0.60	0.60
First yield of hoop rebar (mid-height)	1.16	0.88	0.78
First yield of meridional rebar (above dome 45^o)	1.42	1.03	0.59
Liner yield due to hoop stresses (mid-height)	0.98	0.81	0.49
Liner rupture(1% strain) due to hoop stresses (mid-height)	1.46	1.20	0.19
Liner yield due to meridional stresses (wall base, El. 0.25m)	1.42	1.46	0.49
Liner rupture(1% strain) due to meridional stresses (wall base, El. 0.25m)	-	-	0.46
Liner yield due to hoop stresses (splingline, El. 10.75m)	1.03	1.20	0.48
Liner plate rupture due to hoop stresses (springline, El.10.75m)	1.46	1.47	0.46
Liner yield due to meridional stresses (dome, El.16.13m)	1.10	1.35	0.48
Liner plate rupture due to meridional stresses (dome, El.16.13m)	-	1.47	-
Hoop tendons reaching 1% strain (mid-height)	1.43	1.41	-
Hoop tendons reaching 2% strain (mid-height)	1.48	1.46	-
Hoop tendons reaching 3% strain (mid-height)	1.51	1.47	-

Strains in Reinforcements

The strain gages were not reset after the LST (Limit State Tests). The residual strain was the base strain for the SFMT. To confirm the numerical model for rebars, the recorded residual strain at the beginning of SFMT was subtracted from the measured strains and compared with those from numerical analysis under pressure only (see Figures 17 through 30).

Figures 17 through 30 show that the strains in the reinforcements under pressure only compare well with the numerical results and the measured displacements from SFMT except for the strain at Standard Location #24 (Az 135°, El. 10.75m Hoop Outer Rebar Layer at Spring Line).

A combined mechanical-thermal analysis simulating a saturated steam condition (Case 1) shows that the thermal loading history starting with 100°C created abrupt increase in strains at initial stage similar to the displacements, but the slopes expressing the pressure-displacement relationships with increasing temperature and pressure appeared closer to the trend for pressure only.

`

The strains in the outer hoop rebar (D18) at mid-height of the cylinder (135°, EL. 6.20m) are typically 0.5%, 0.45%, 1.5% at 1.4 MPa for Case 1, Case 2 and pressure only respectively. Considering a yield strain 0.25% calculated from a yield stress 457.5 MPa and elastic modulus 1.83E+05 provided by Sandia Lab in Table 2 [4], the pressures corresponding to 0.25% of yield strain for bare bar are 0.81MPa, 0.77MPa and 1.42 Mpa, respectively.

The analysis results for Case 2 shows that the rebar strains due to the sudden increase of temperature and pressure for short durations, do not fully recover back to the strains at initial pressure and temperature. This can be interpreted as sort of residual deformations from damage to liner plate and/or concrete portion due to instantaneous high temperature and pressure loading. Unfortunately, the analysis for Case 2 was stopped at 1.1974Mpa due to divergence and the behaviors could not be investigated. The ultimate capacity may drop rapidly with a sudden increase in deformation which in turn will induce divergence (see Figures 7 through 16). Figure 17 and Figure 18 show that the strains in the merdional outer rebar near wall mat junction were not high and the residual strains are almost negligible. The residual strains remained in the inner layer of rebar around wall-mat junction during abrupt change of temperature.

Liner Strains and Stress

The recorded results of the liner from the SFMT were not meaningful to compare with the analysis results at Phase 2 since the line was already torn partially during LST and the recorded data for the liner plate including strains could not be compared with those from the numerical analysis under pressure only. The strains in the liner from the numerical analyses for pressure only, saturated steam condition (Case 1) and severe accident scenario (Case 2) were compared with each other.

Maximum compressive stresses in the liner versus the corresponding pressure loadings are illustrated in Table 7 at some typical locations. Case 2 shows that the stresses in liner were under compressive behavior at pressures between 0.2 MPa and 0.78 MPa and temperature between 100°C and 615°C) for short periods of around 260 through 300 minutes.

The buckling stress considering the horizontal spacing of liner anchor (150.15mm) is calculated to 122.2Mpa and thus most of stresses of Case 1 and Case 2 shown in Table 7 are beyond the calculated buckling stress.

Table 7 Max. Compressive Stress in Liner Surface with Pressure and Temperature

Location	Case 1			Case 2			Remark
	Pressure (MPa)	Tempera-ture (°C)	Stress (MPa)	Pressure (MPa)	Tempera-ture (°C)	Stress (MPa)	
#36	0.138	106.6	-86	0.42	353	-314	Merid. El. 0.25m
#37	0.14	106.6	-214	0.42	353	-417	Hoop El. 0.25m
#38	0.14	106.6	-181	0.42	353	-365	Merid. El. 6.20m
#39	0.14	106.6	-164	0.42	353	-375	Hoop El. 6.20m

`

#40	0	100.0	-58	0.42	353	-252	Merid. El. 10.75m
#41	0.14	106.6	-132	0.46	365	-424	Hoop El. 10.75m
#42	0.10	104.5	-146	0.46	365	-368	Merid. El. 16.13m

Tendon Stress

Tendon strains gages were 're-zeroed' before the SFMT [3] and thus the analysis tendon strains prior to the start of pressurization were deducted from the tendon strains during pressure to directly compare with the measured tendon strain.

Tendon strains under both temperature and pressure are increased in comparison with those under pressure only (see Figure 39 and Figure 40). Temperature has definitely an effect on the ultimate pressure capacity of PCCV.

Concrete Cracking

The finite element analysis under internal pressure only results show that the initial concrete cracking in the numerical model occurs at a pressure level of 0.49 MPa and is located at the surface of cylindrical wall at the wall and basemat junction. The through concrete cracking in hoop direction and meridional direction occurs at a pressure level of 0.57 MPa and 0.84MPa at midheight, respectively. Case 1 and Case 2 show that many through wall cracking at hoop direction are appeared at 0.66MPa (Case 1)and 0.86MPa (Case 2). The through wall cracks at meridional direction are appeared at 0.26MPa and 0.42MPa for Case 1 and Case 2, respectively. At the pressure level of 0.64 MPa, the elements at mid-height of wall cylinder are cracked in both the hoop and meridional directions.

`

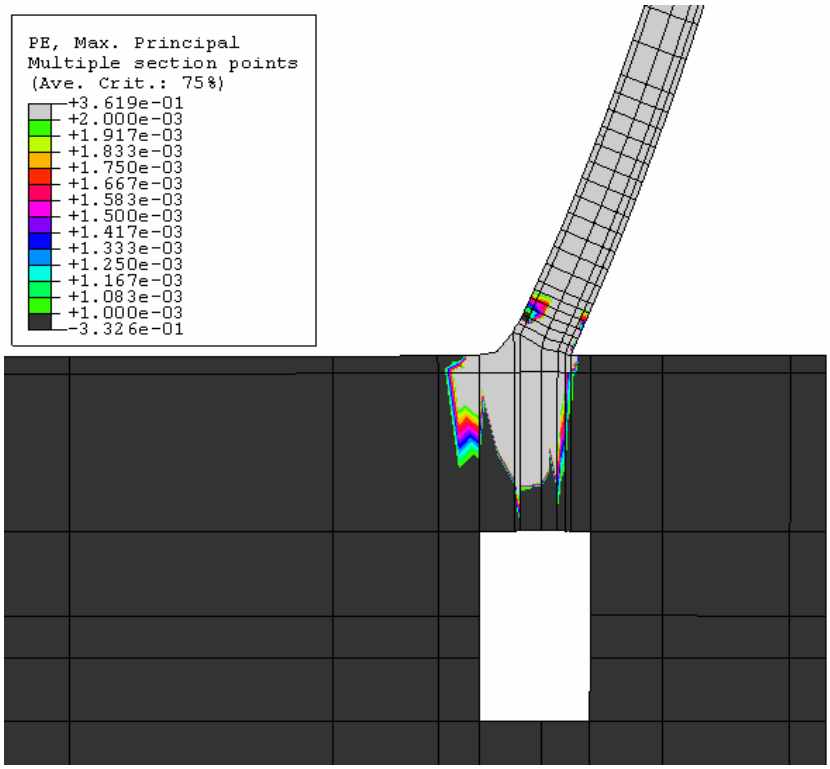

(a) Under Pressure Only (at P=1.46 MPa)

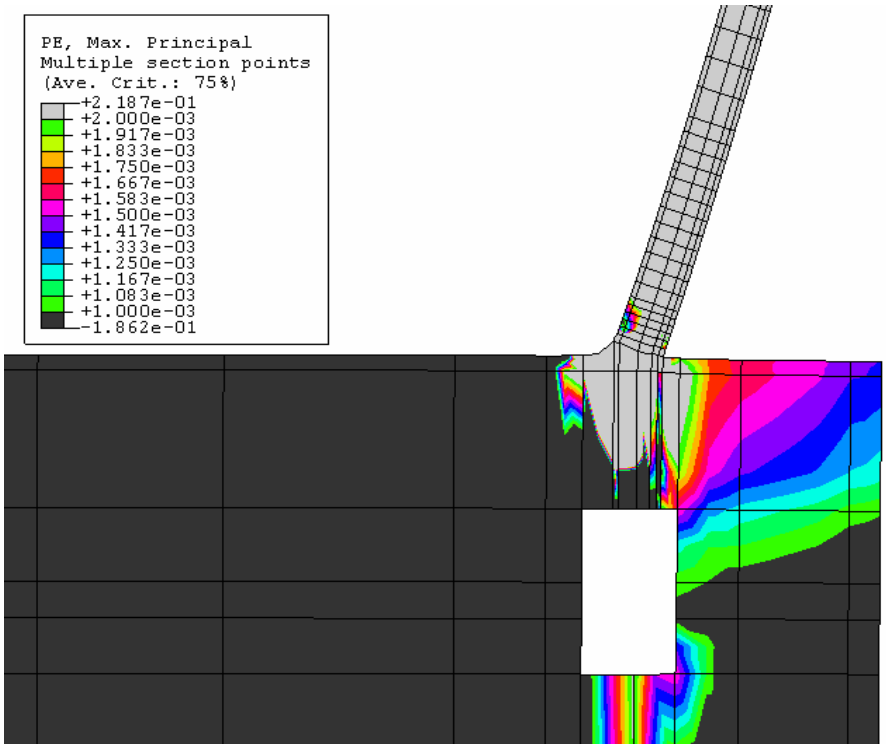

(b) Case 1(at P=1.46 MPa, T=200°C)

`

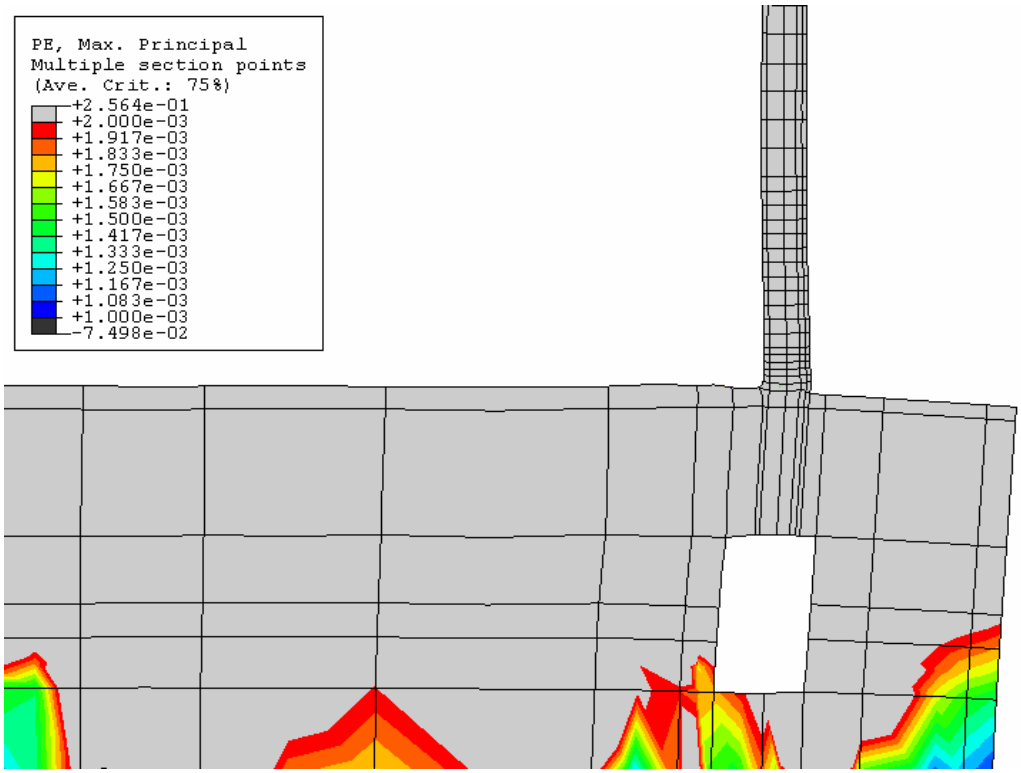

(c) Case 2(at P=1.197 MPa, T= 265°C)

Figure 6 Principal Stress (Crack Patterns) around Wall-Mat Junction (cont'd)

References

[1] Dameron, R.A., Hansen, B.E., Parker, D.R. and Rashid, Y.R., *Posttest Analysis of NUPEC/NRC 1:4 Scale Prestresssed Concrete Containment Vessel Model*, NUREG/CR-6809 SAND2003-0839P ANA-01-0330, Sandia National Laboratories, Albuquerque, NM, March 2003.
[2] Holmes, M., Anchor, R.D., Cook, M.D. and Crook, R.N., *The Effects of Elevated Temperatures on the Strength Properties of Reinforcing and Prestressing Steels*, The Structural Engineer, Vol. 60B, No. 1, March 1982
[3] ABAQUS User's Manual, Version 6.4, 2003. ABAQUS Inc.
[4] Hessheimer, M.F., Klamerus, E.W., Lambert, L.D. and Rightley, G.S., *Overpressurization Test of a 1:4-Scale Prestressed Concrete Containment Vessel Model*, NUREG/CR-6810, SAND2003-0840P, Sandia National Laboratories, Albuquerque, March 2003.
[5] Hsu, T. T.C., *Unified Theory of Reinforced Concrete*, CRC Press 1993, 205-218 pp.
[6] Mazars J., Dube J.F., Flejou J.L. and Ghavamian Sh., *A Damage Multi-layered F.E. Model for the Seismic Response of R.C. Structures – A Tool for Understanding the Real Behaviour*, Proceeding 10th EAEE, 1994.
[7] Neville, A.M., Properties of Concrete, The Pitman Press, 1981, pp. 433-528

`

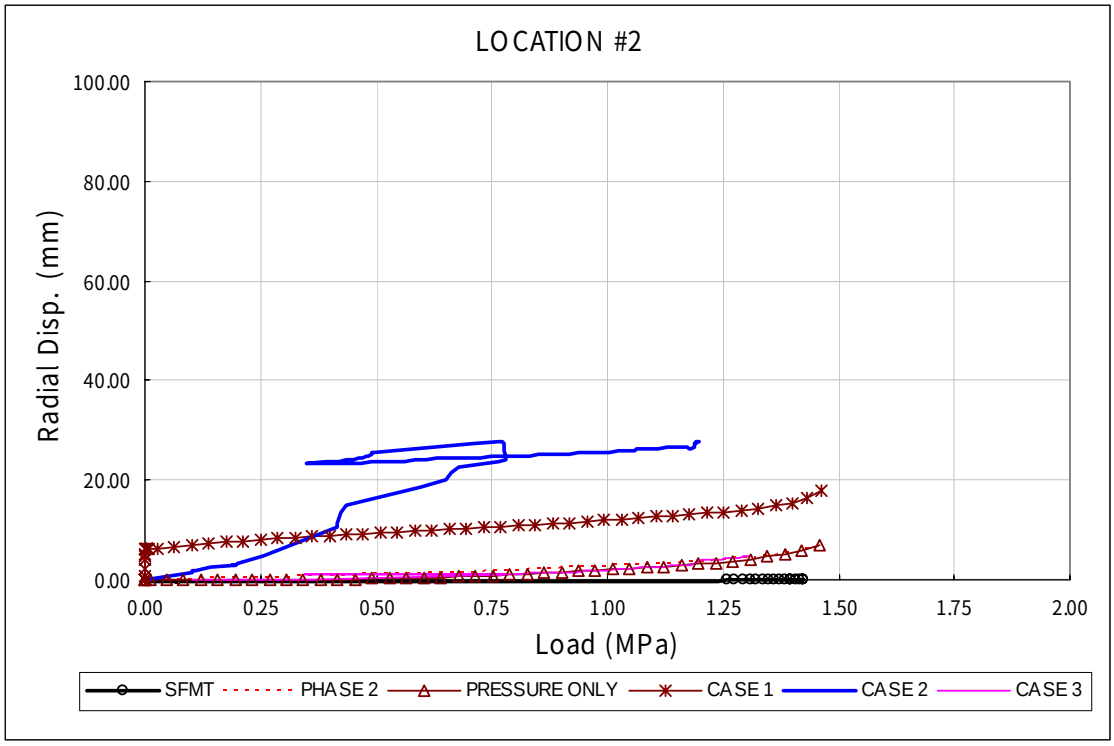

Figure 7 Load-Displacement (# 2, 135°, El. 0.25m, Radial, Inside Liner Surface)

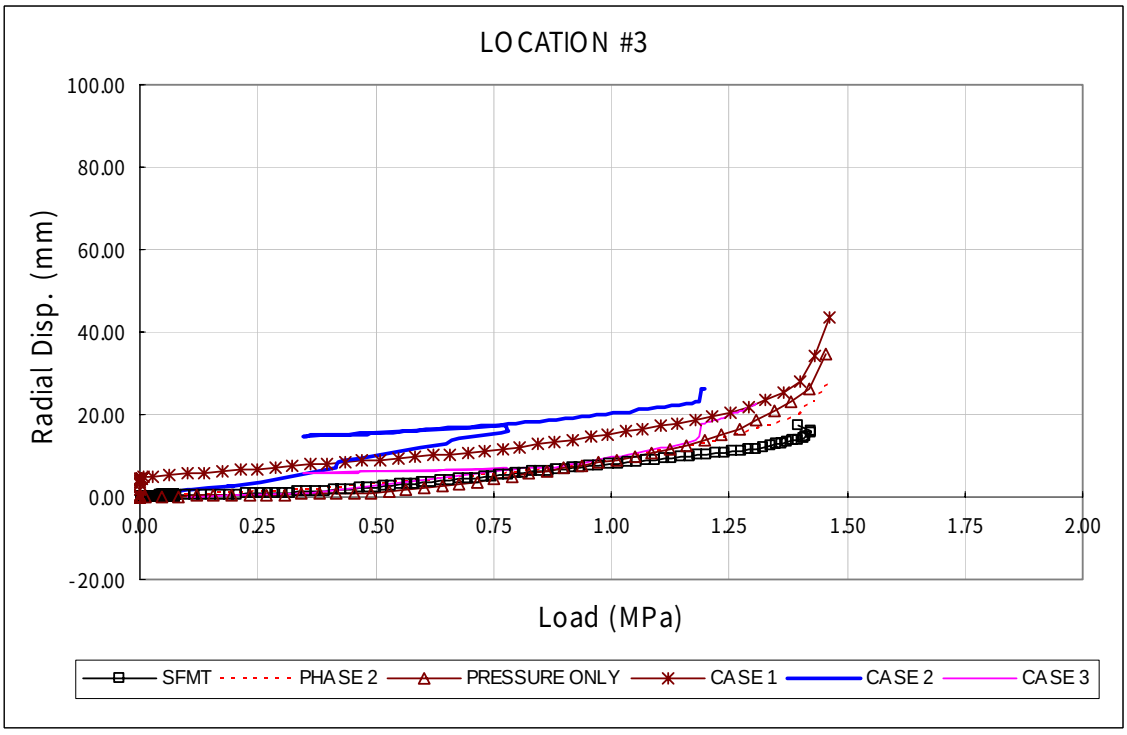

Figure 8 Load-Displacement (# 3, 135°, El. 1.43m, Radial, Inside Liner Surface)

`

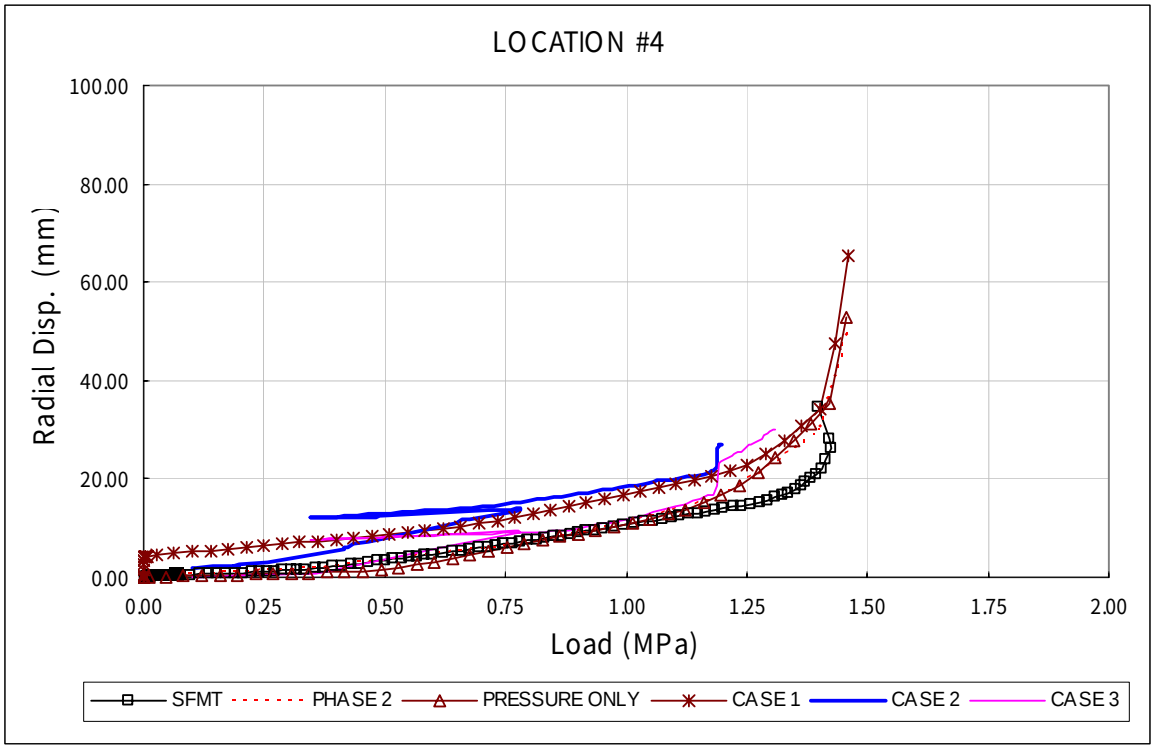

Figure 9 Load-Displacement (# 4, 135°, El. 2.63m, Radial, Inside Liner Surface)

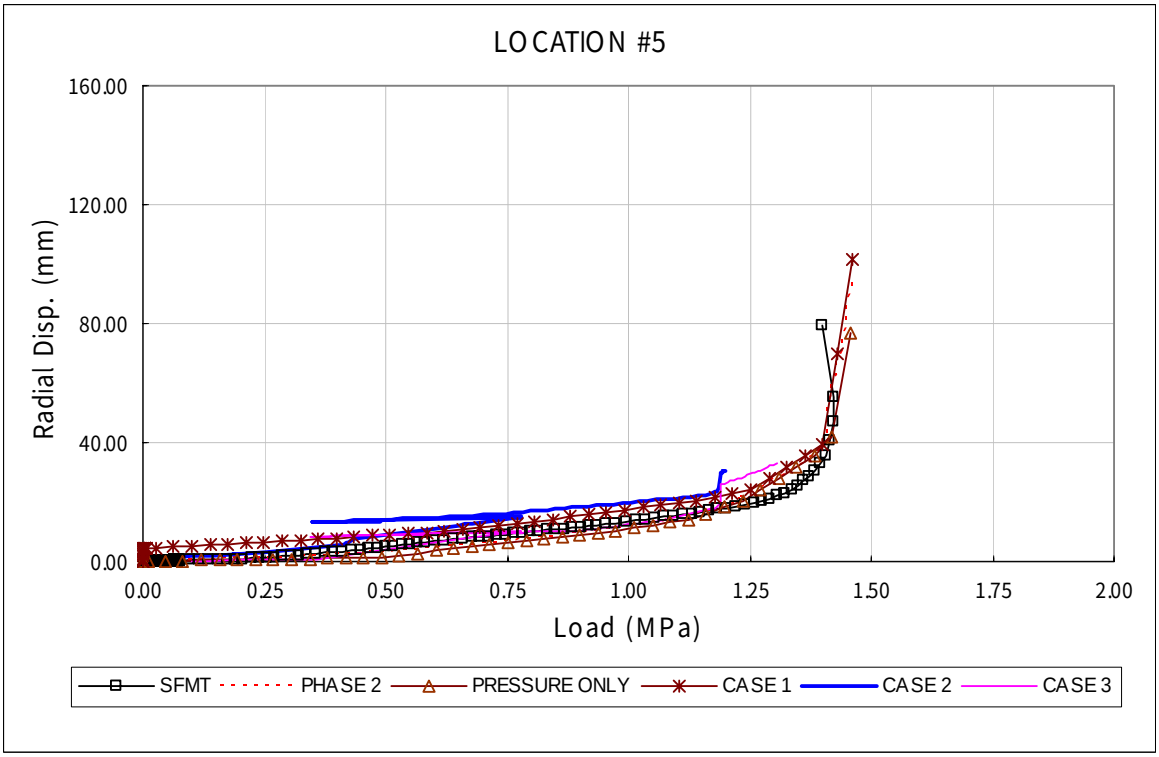

Figure 10 Load-Displacement (# 5, 135°, El. 4.68m, Radial, Inside Liner Surface)

`

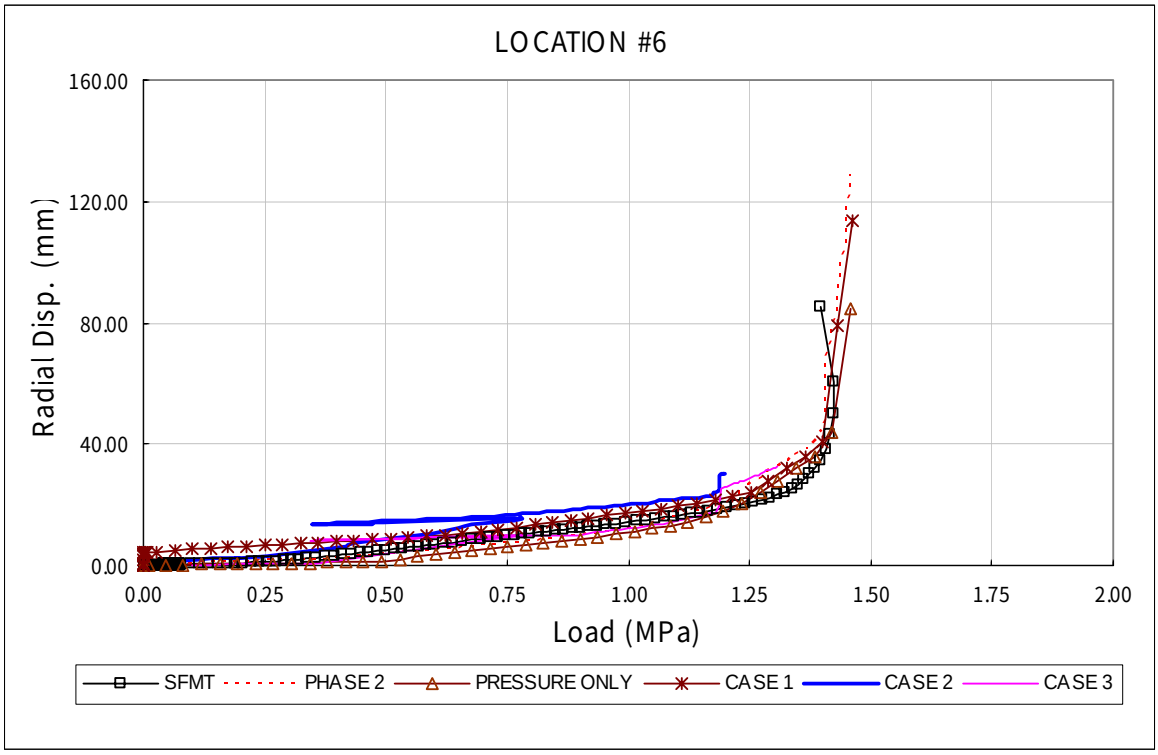

Figure 11 Load-Displacement (# 6, 135°, El. 6.20m, Radial, Inside Liner Surface)

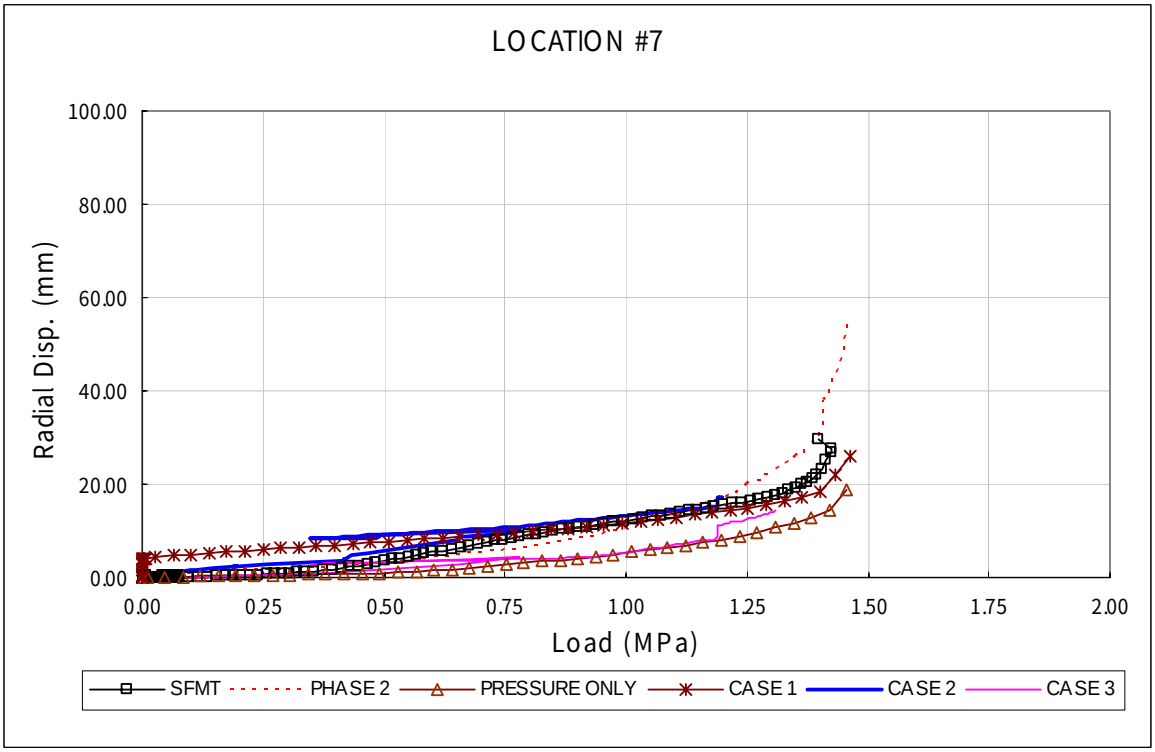

Figure 12 Load-Displacement (# 7, 135°, El. 10.75m, Radial, Inside Liner Surface)

`

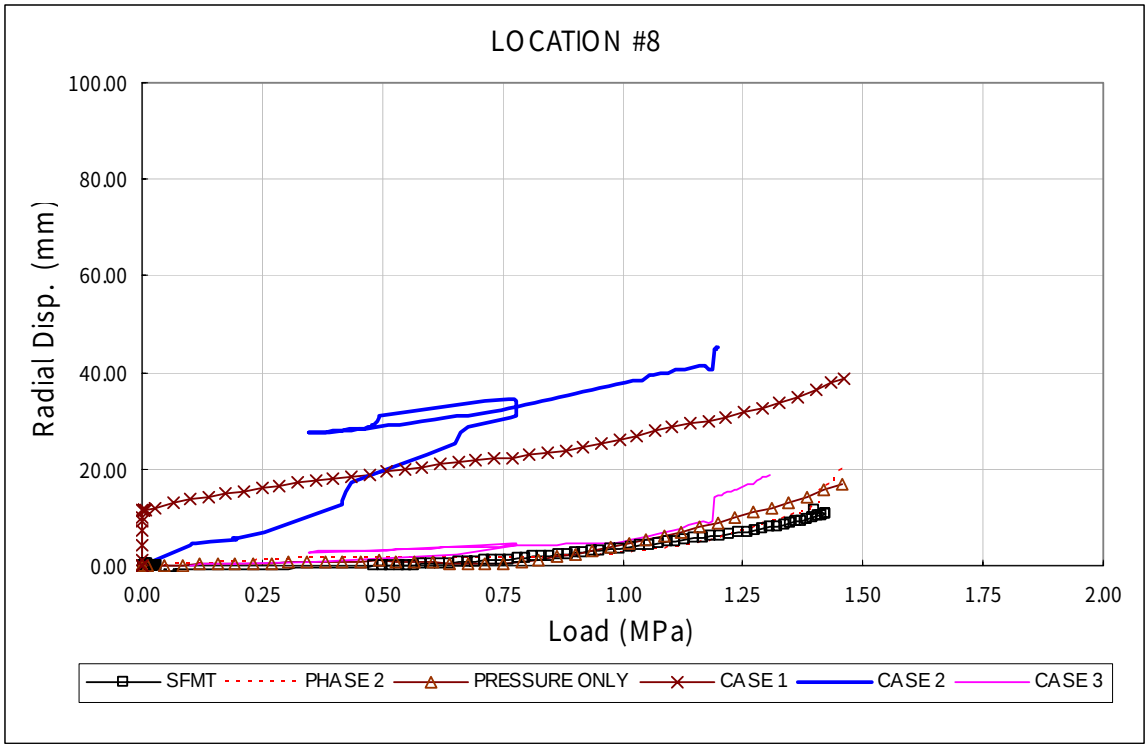

Figure 13 Load-Displacement (# 8, 135°, El.10.75m, Vertical, Inside Liner Surface)

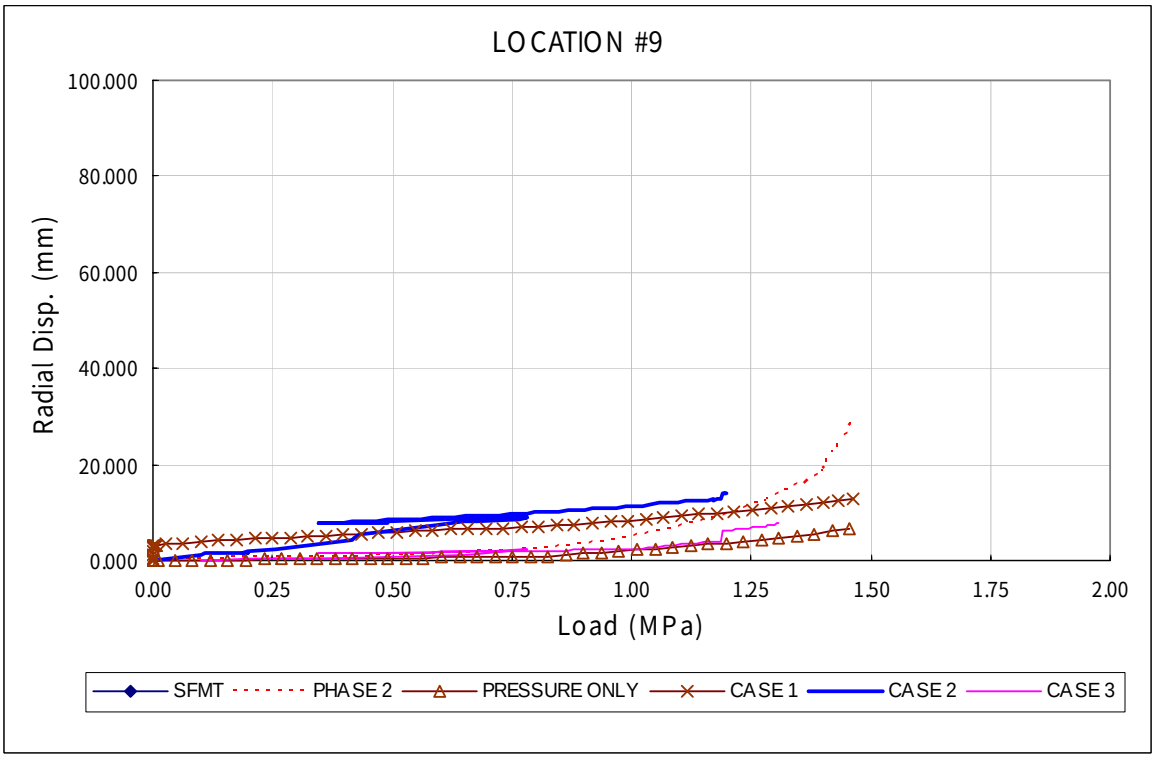

Figure 14 Load-Displacement (# 9, 135°, El. 14.55m, Horizontal, Inside Liner Surface)

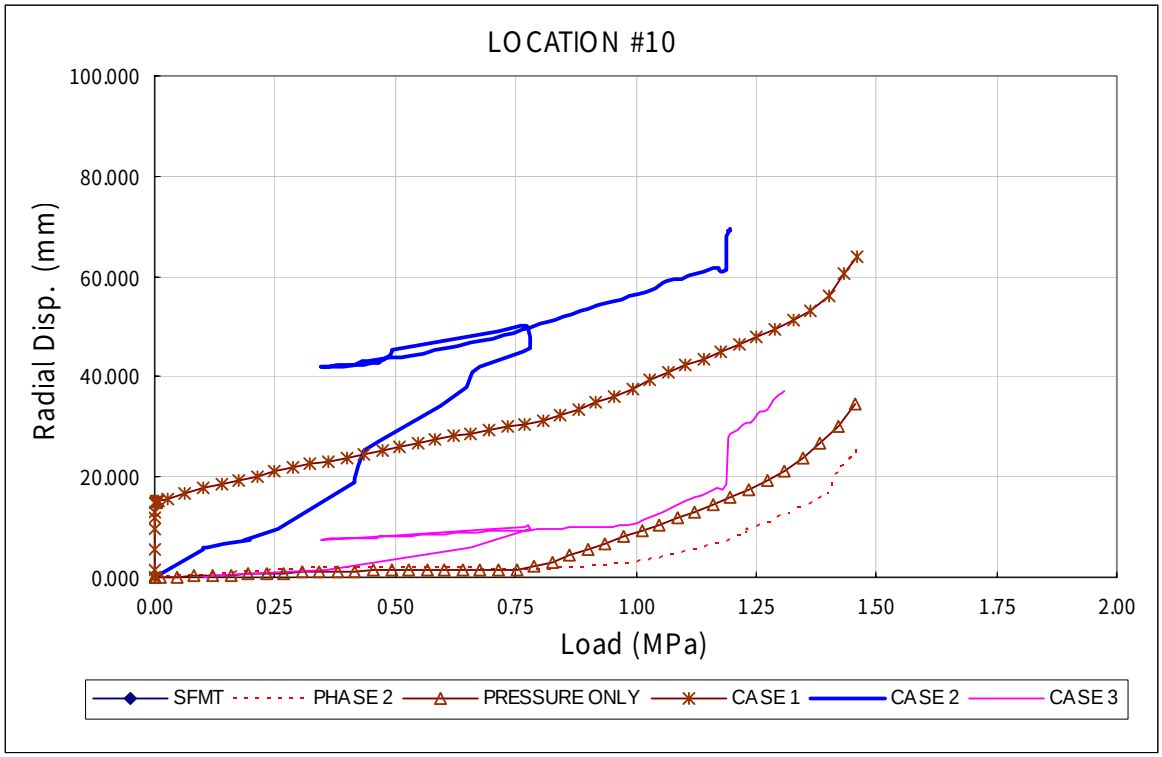

Figure 15 Load-Displacement (# 10, 135°, El. 14.55m, vertical, Inside Liner Surface)

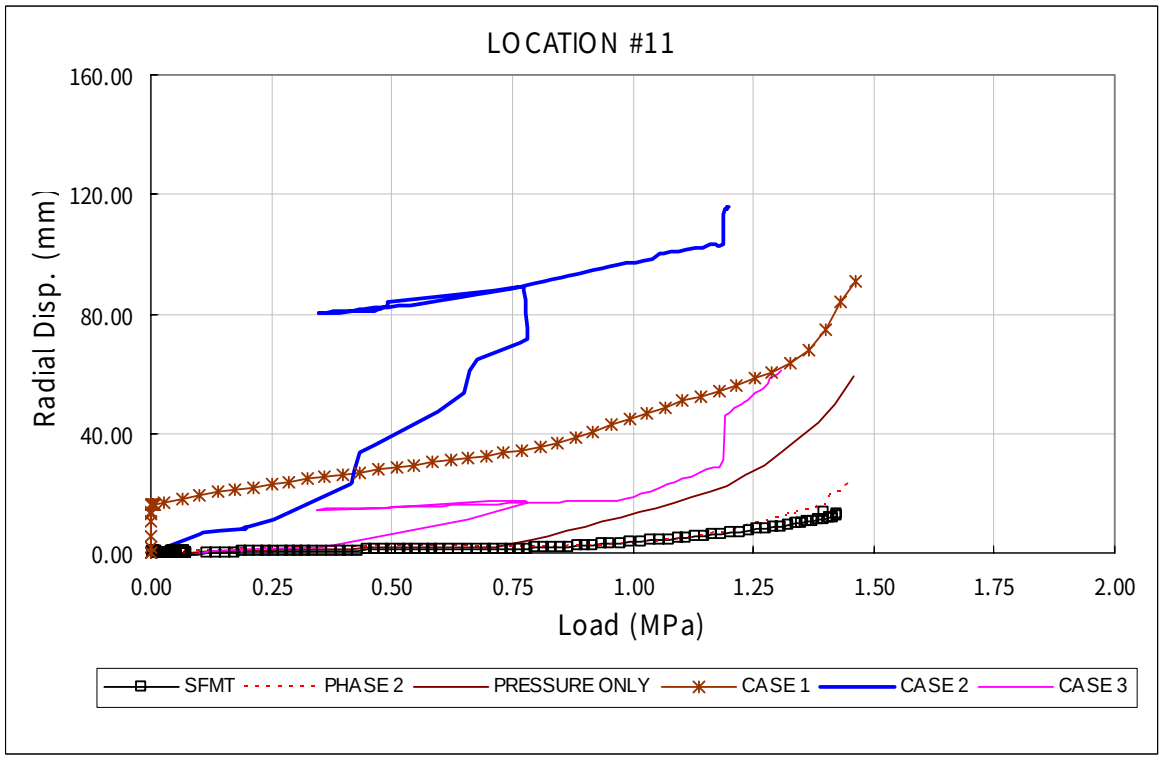

Figure 16 Load-Displacement (# 11, 135°, El.16.13m, Vertical, Inside Liner Surface)

`

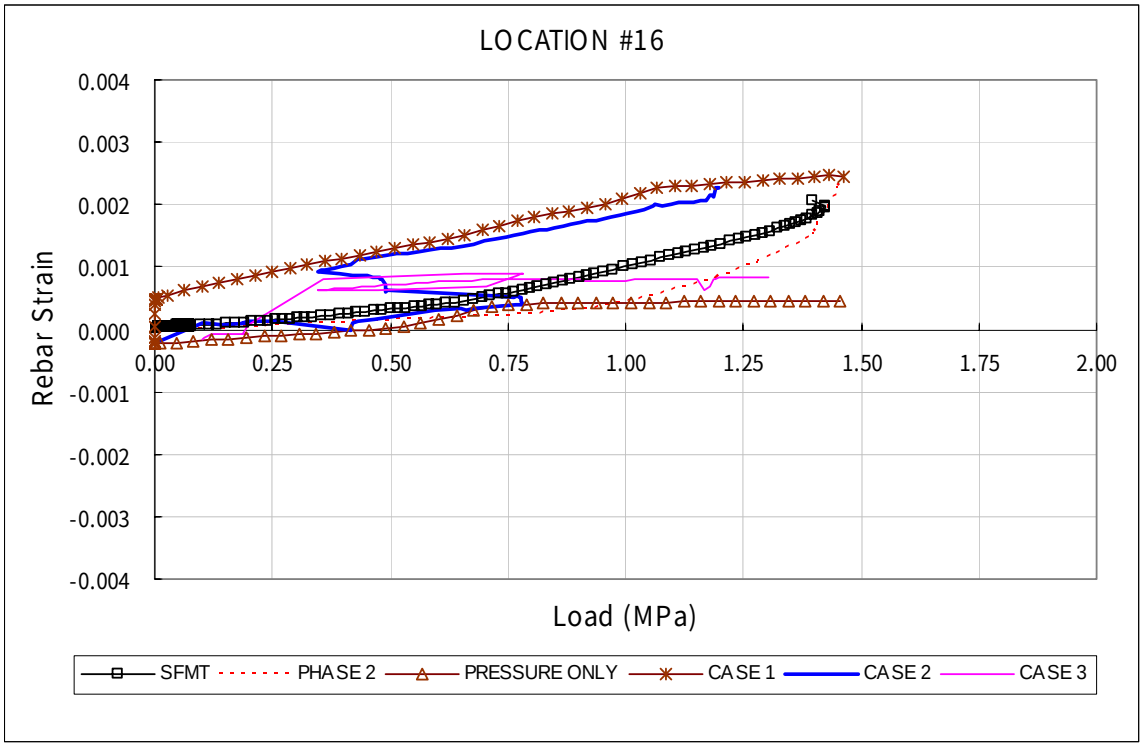

Figure 17 Load-Rebar Strain (# 16, 135°, El. 0.05m, Meridional Inner Rebar Layer)

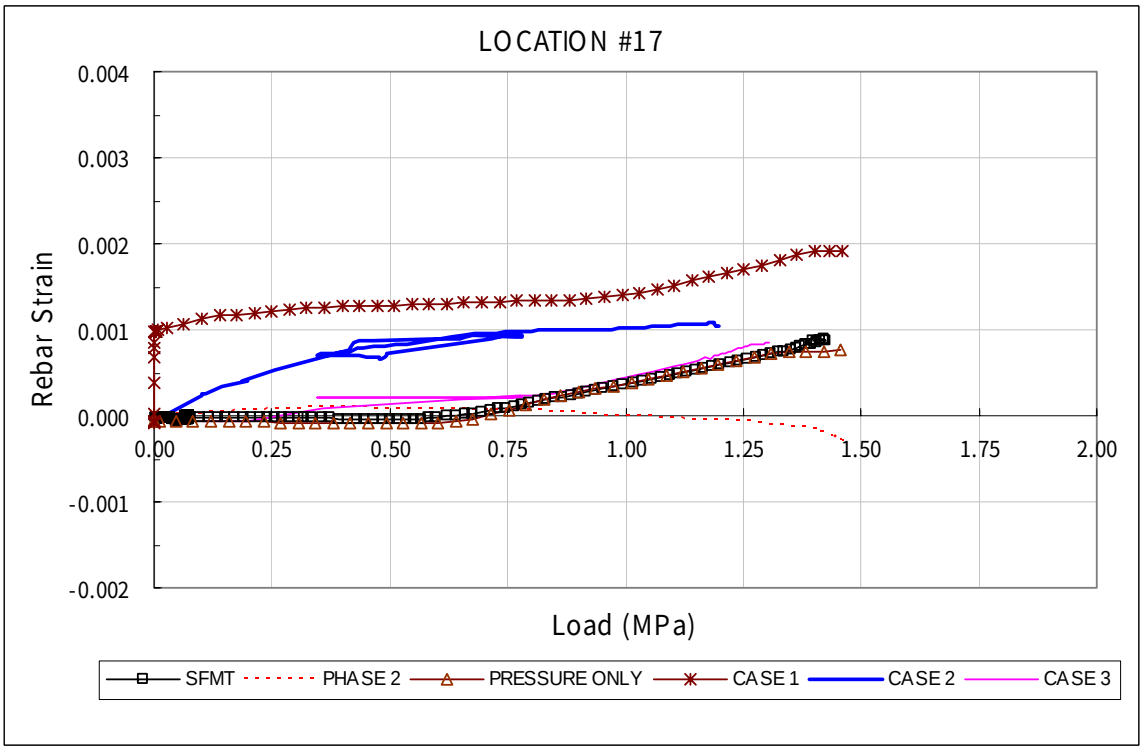

Figure 18 Load-Rebar Strain (# 17, 135°, El. 0.05m, Meridional Outer Rebar Layer)

`

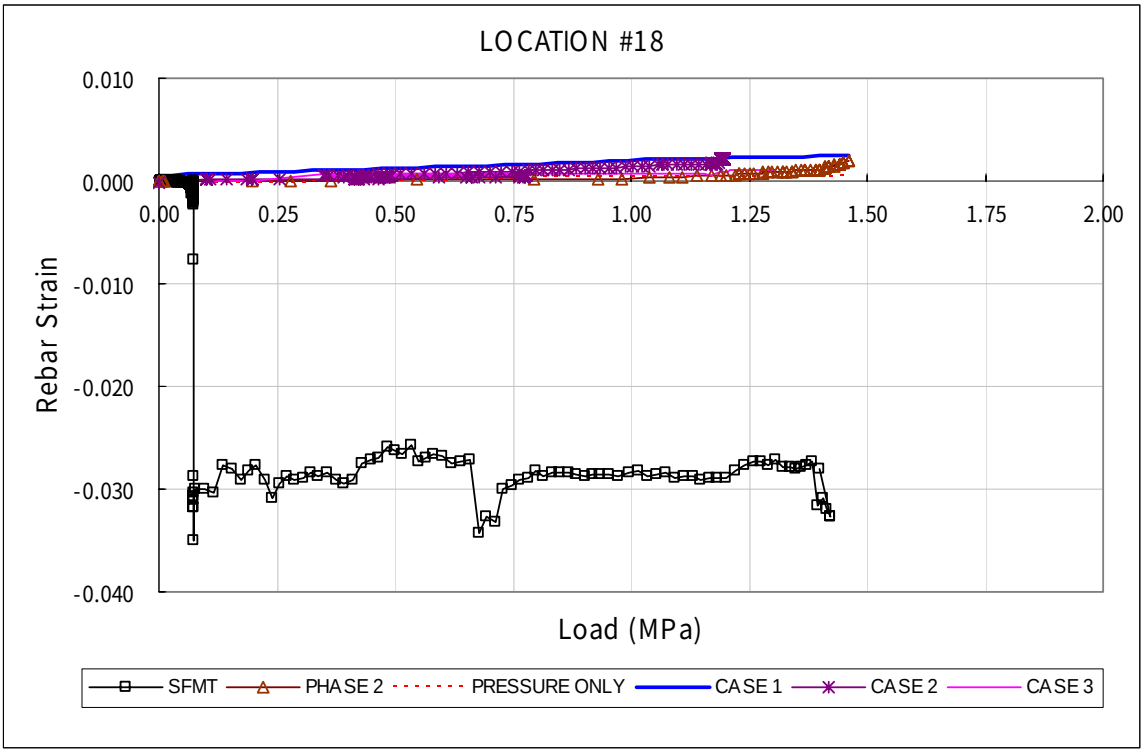

Figure 19 Load-Rebar Strain (# 18, 135°, El. 0.25m, Meridional Inner Rebar Layer)

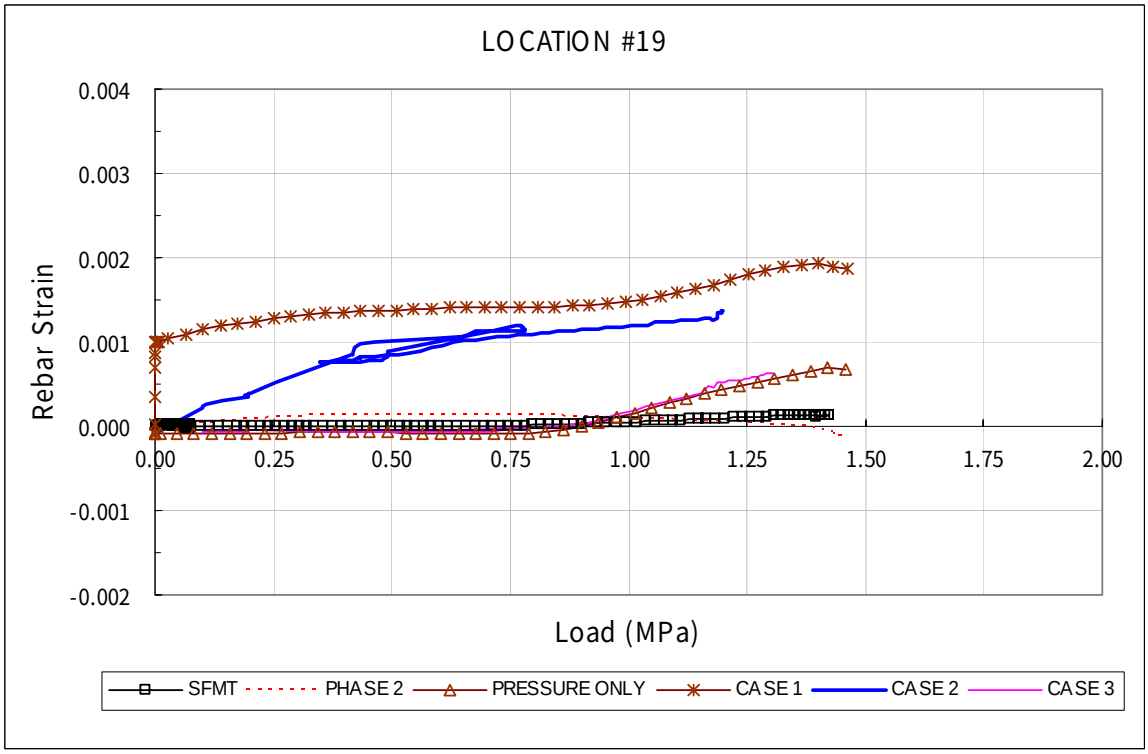

Figure 20 Load-Rebar Strain (# 19, 135°, El. 0.25m, Meridional Outer Rebar Layer)

`

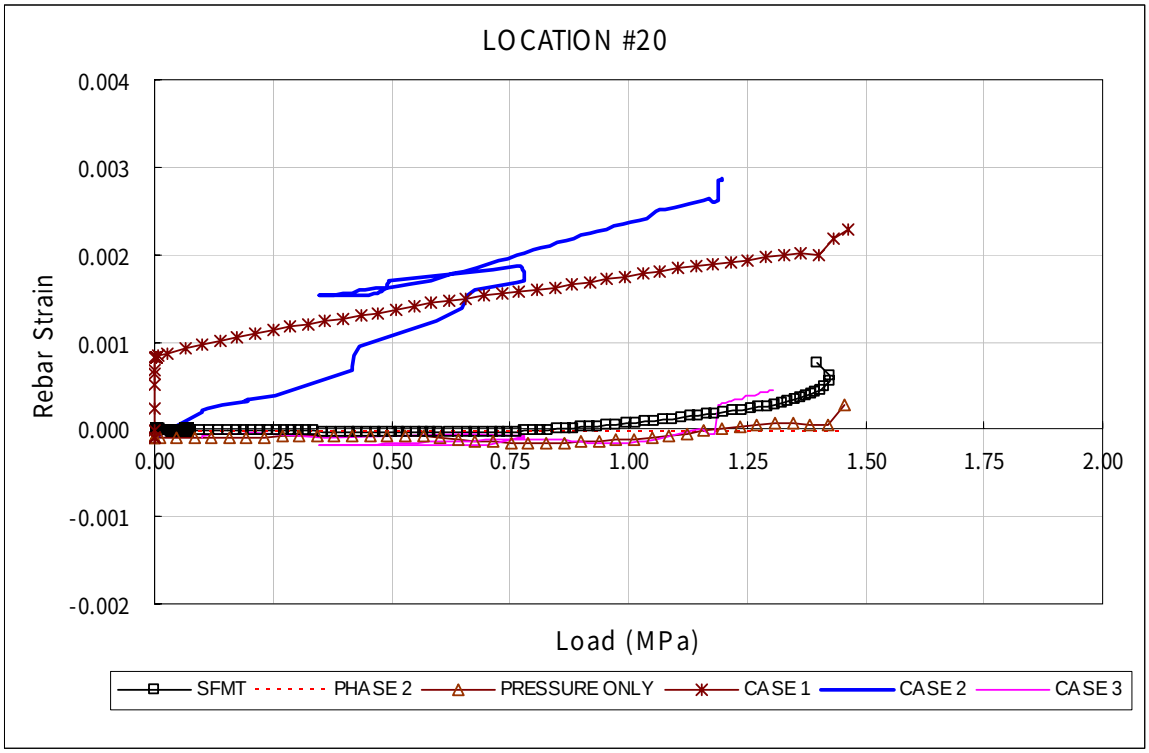

Figure 21 Load-Rebar Strain (# 20, 135°, El. 1.43m, Meridional Inner Rebar Layer)

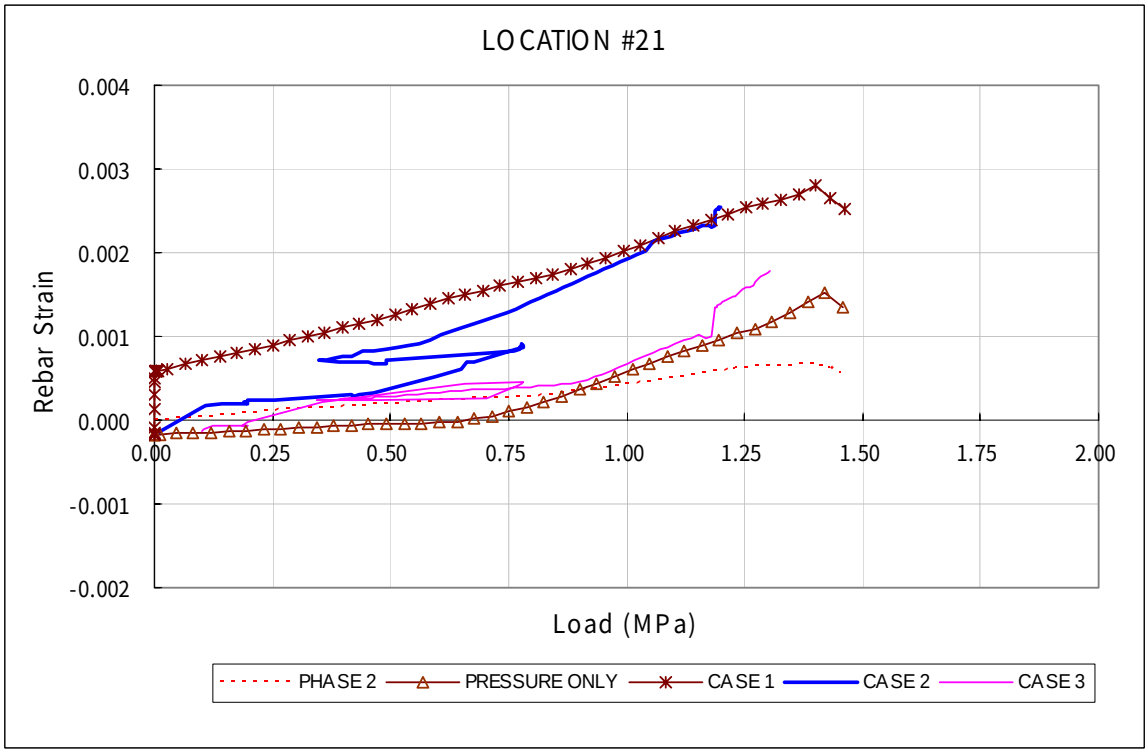

Figure 22 Load-Rebar Strain (# 21, 135°, El. 1.43m, Meridional Outer Rebar Layer)

`

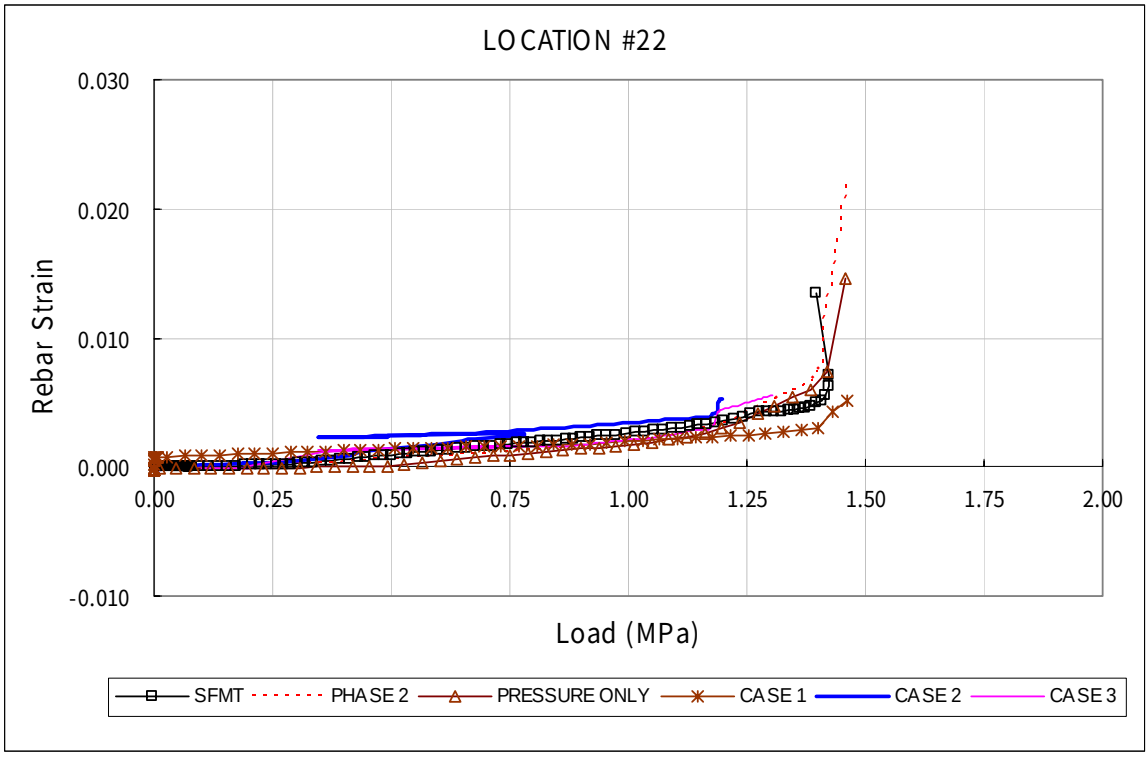

Figure 23 Load-Rebar Strain (# 22, 135°, El. 6.20m, Hoop Outer Rebar Layer)

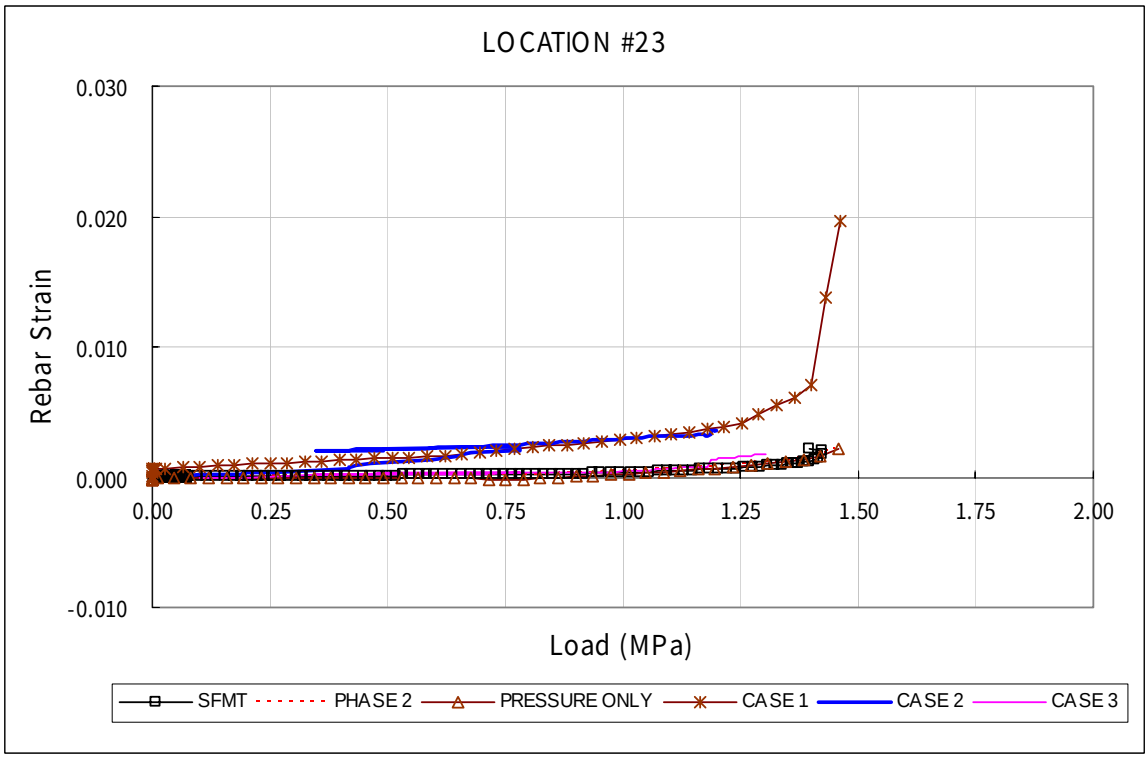

Figure 24 Load-Rebar Strain (# 23, 135°, El. 6.20m, Meridional Outer Rebar Layer)

`

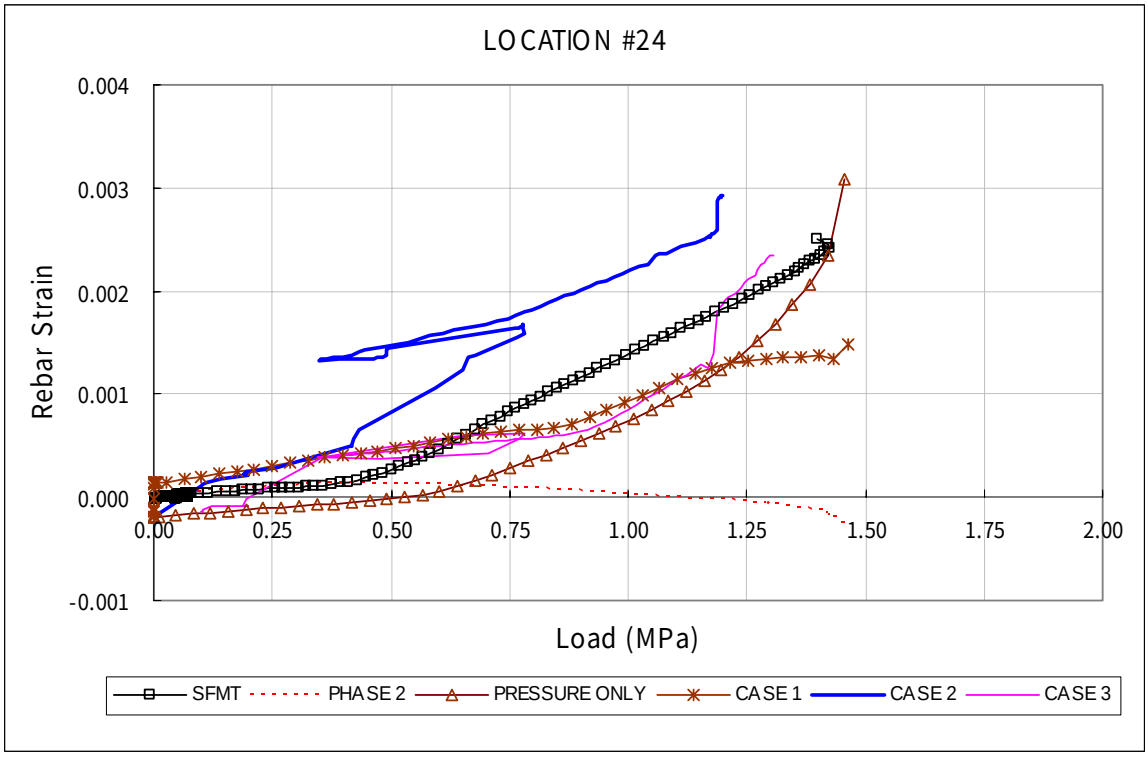

Figure 25 Load-Rebar Strain (# 24, 135°, El. 10.75m, Hoop Outer Rebar Layer)

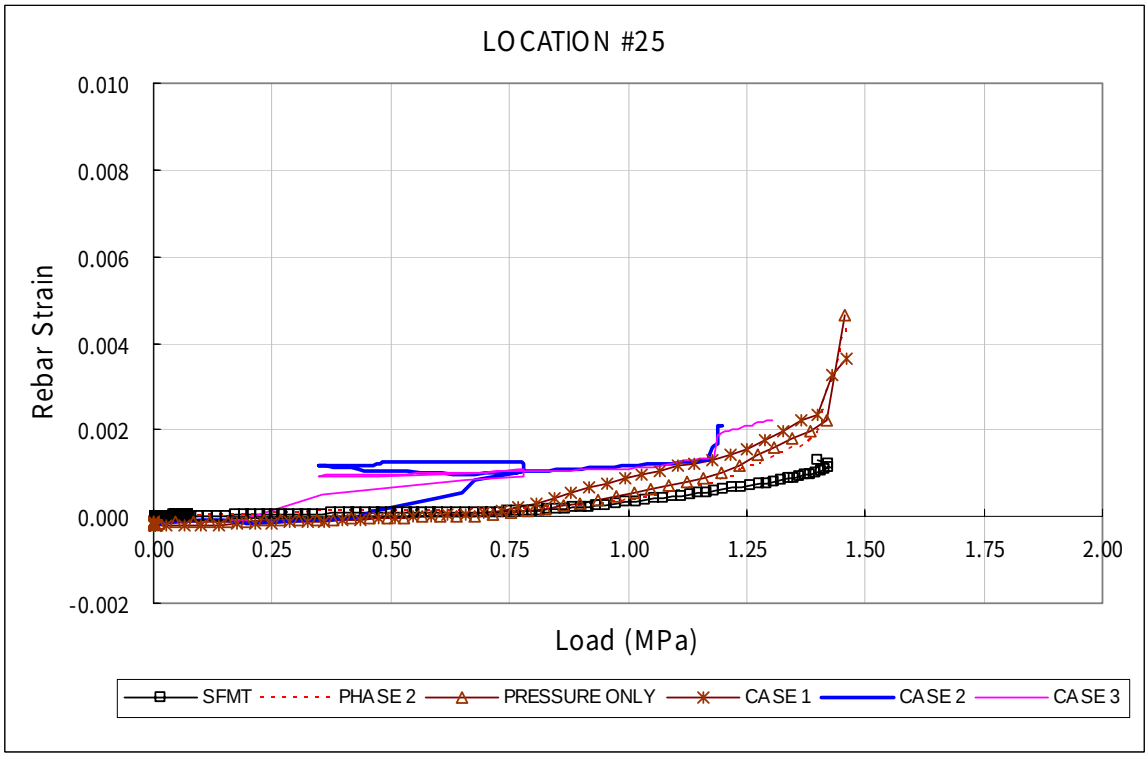

Figure 26 Load-Rebar Strain (# 25, 135°, El. 10.75m, Meridional Inner Rebar Layer)

`

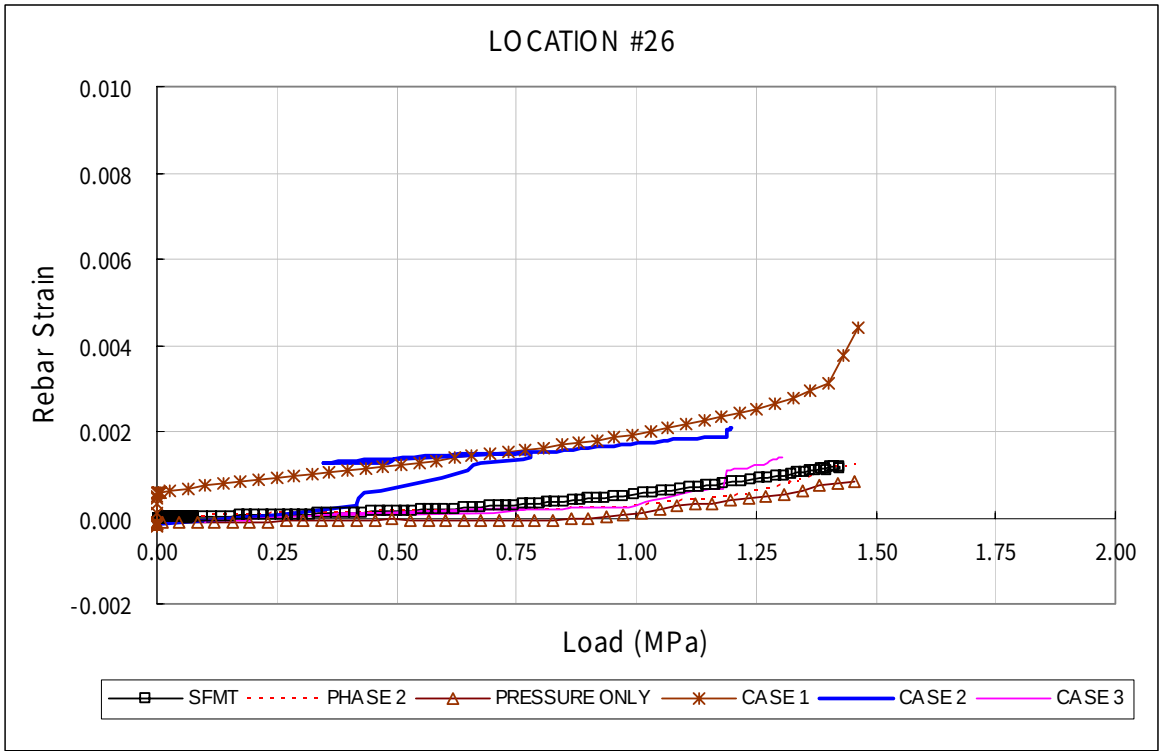

Figure 27 Load-Rebar Strain (# 26, 135°, El. 10.75m, Meridional Outer Rebar Layer)

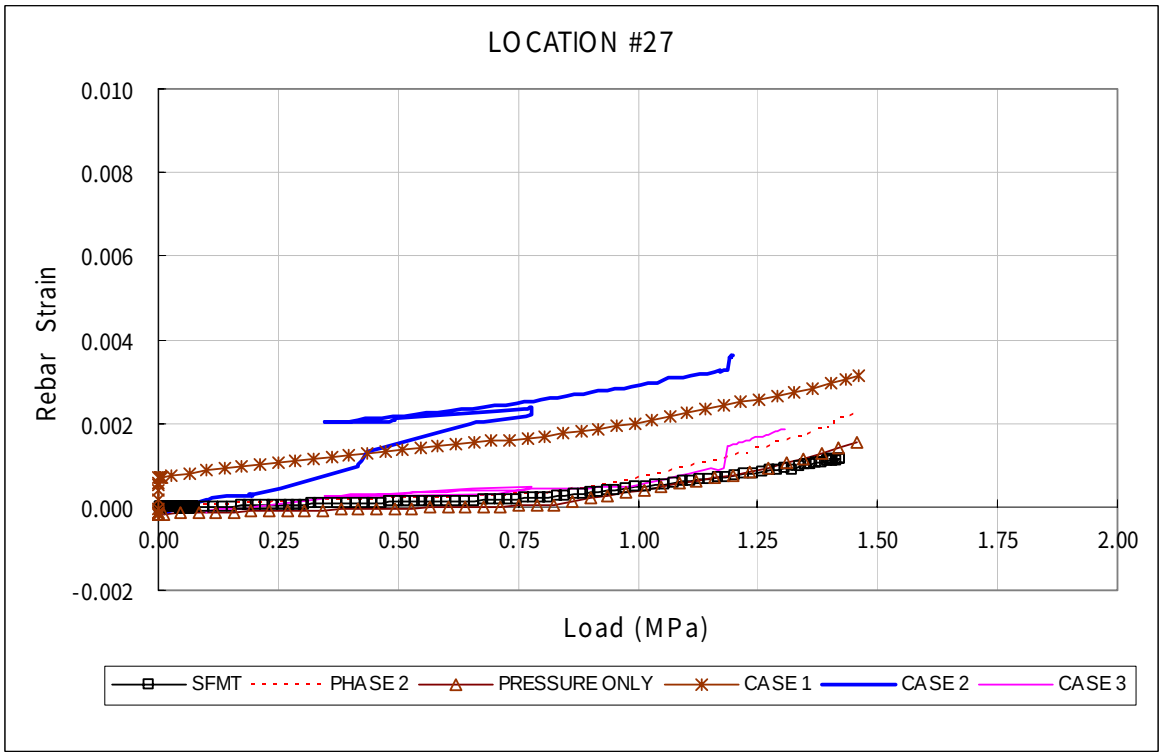

Figure 28 Load-Rebar Strain (# 27, 135°, El. 14.55m, Hoop Outer Rebar Layer)

`

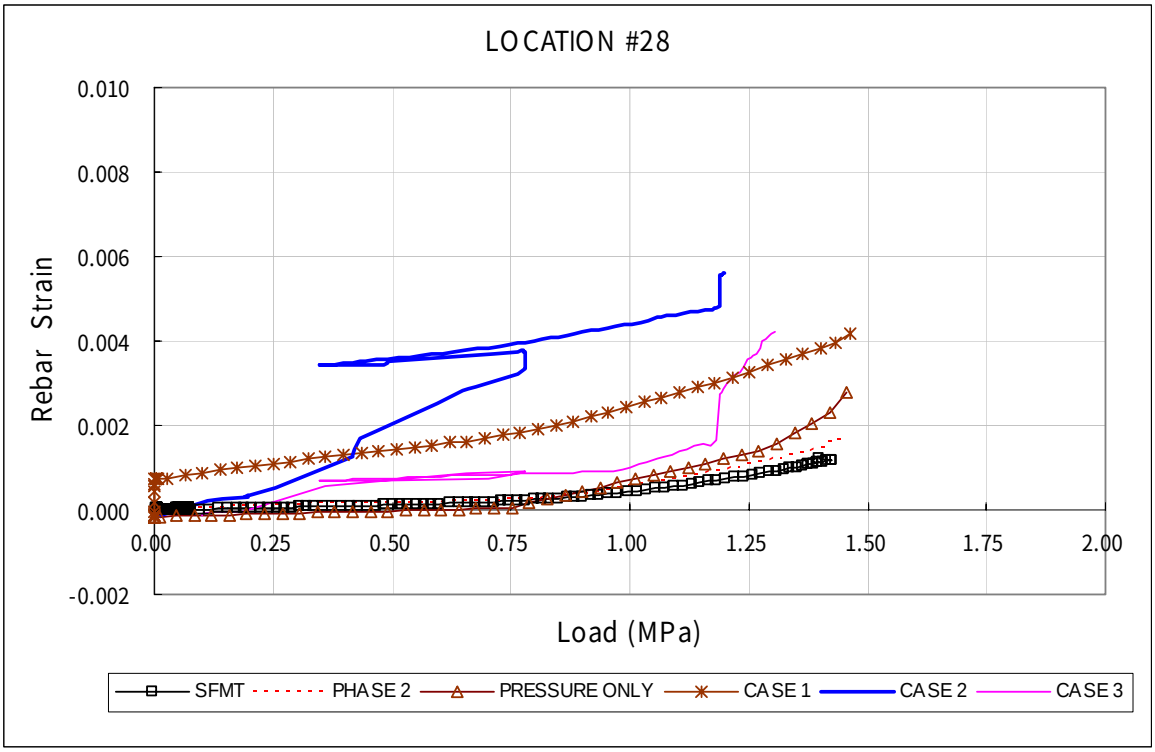

Figure 29 Load-Rebar Strain (# 28, 135°, El. 14.55m, Meridional Inner Rebar Layer)

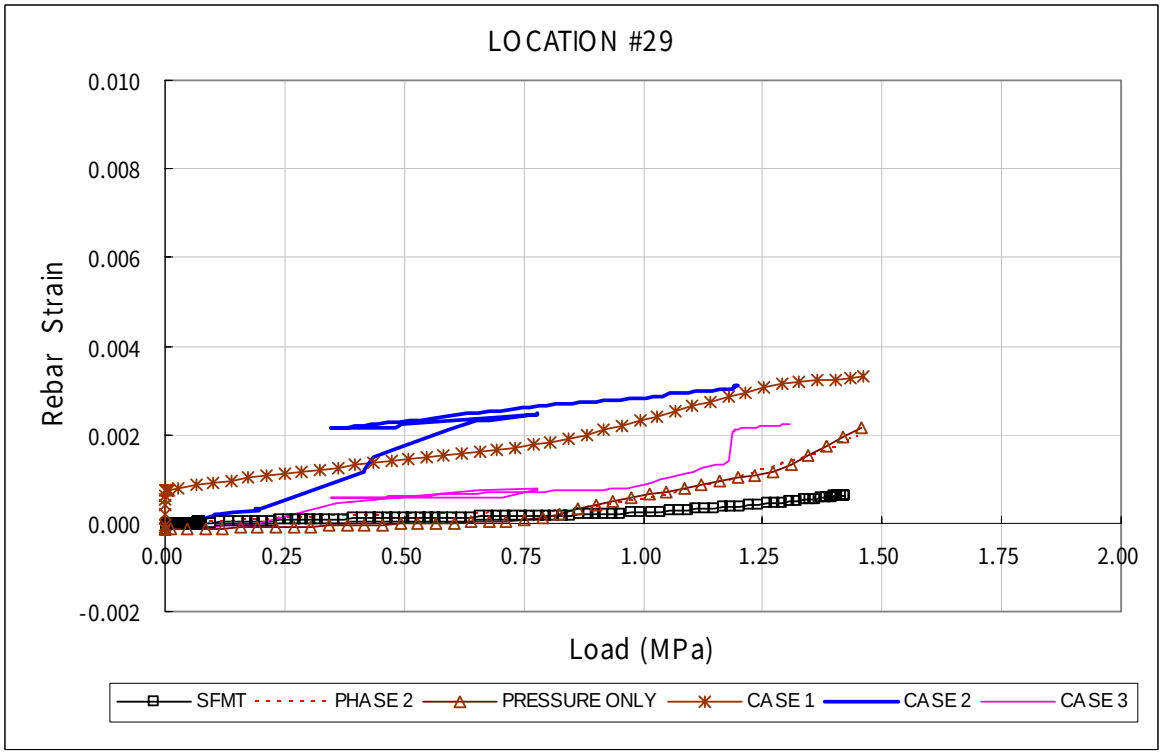

Figure 30 Load-Rebar Strain (# 29, 135°, El. 14.55m, Meridional outer Rebar Layer)

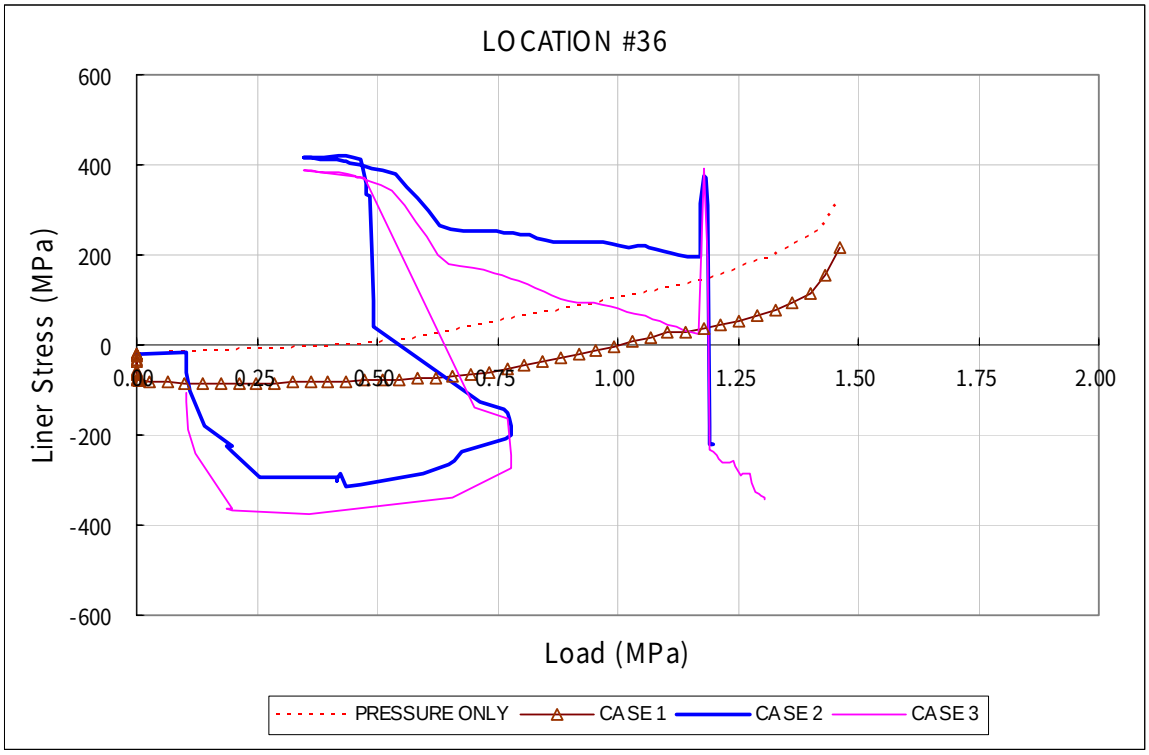

Figure 31 Load-Liner Stress (# 36, 135°, El. 0.25m, Meridional Inside Liner Surface)

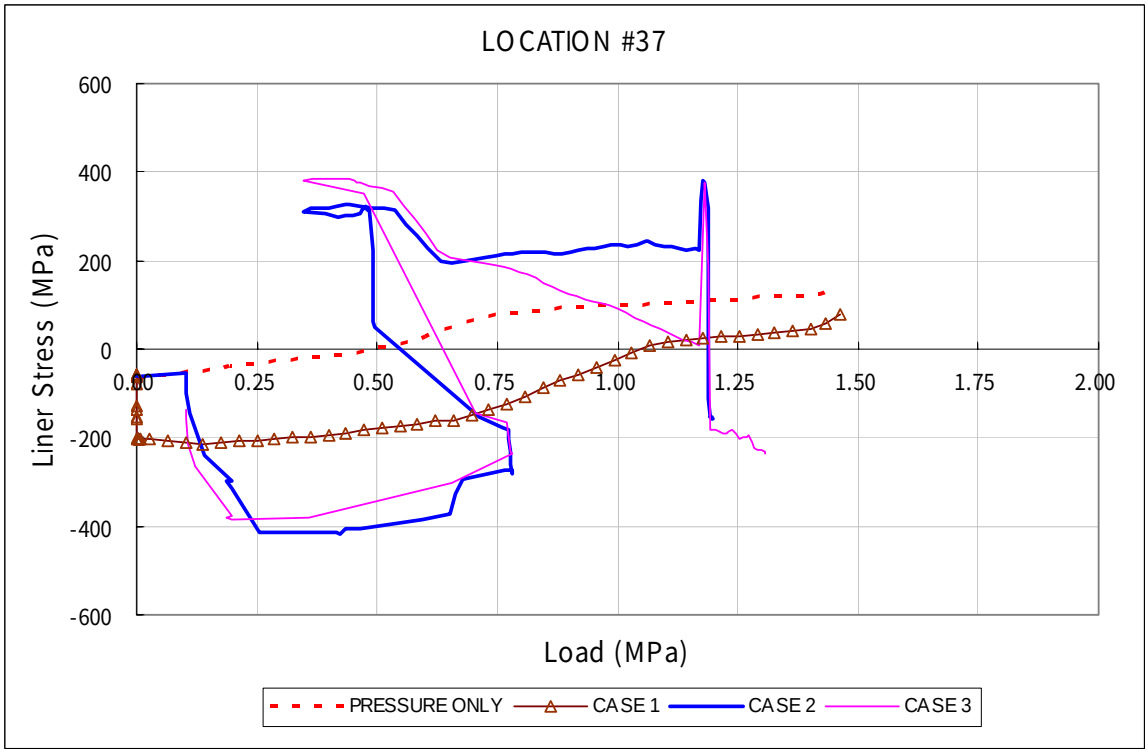

Figure 32 Load-Liner Stress (# 37, 135°, El. 0.25m, Hoop Inside Liner Surface)

`

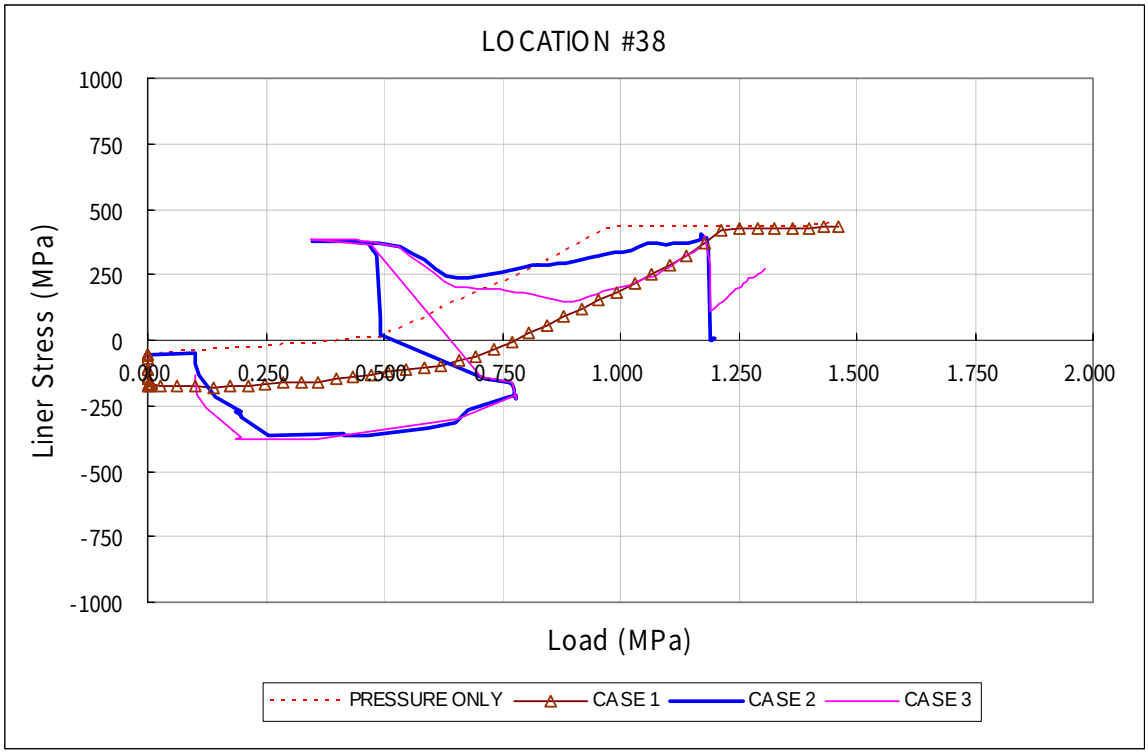

Figure 33 Load-Liner Stress (# 38, 135°, El. 6.2m, Meridional Inside Liner Surface)

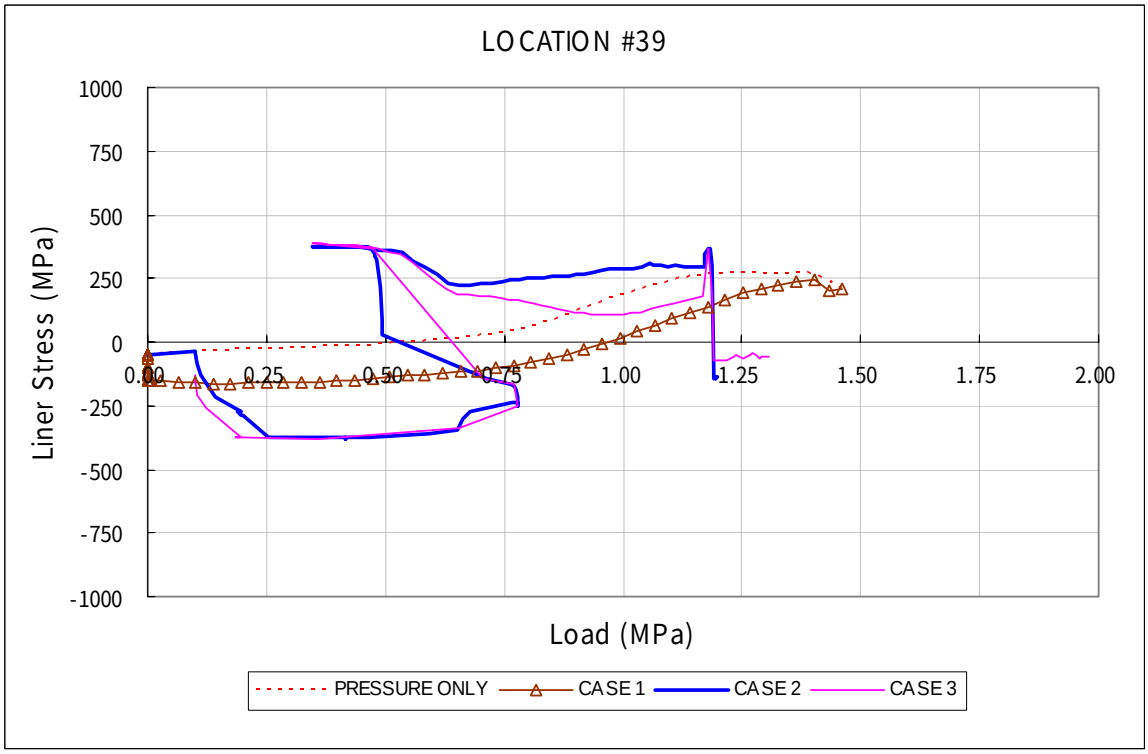

Figure 34 Load-Liner Stress (# 39, 135°, El. 6.2m, Hoop Inside Liner Surface)

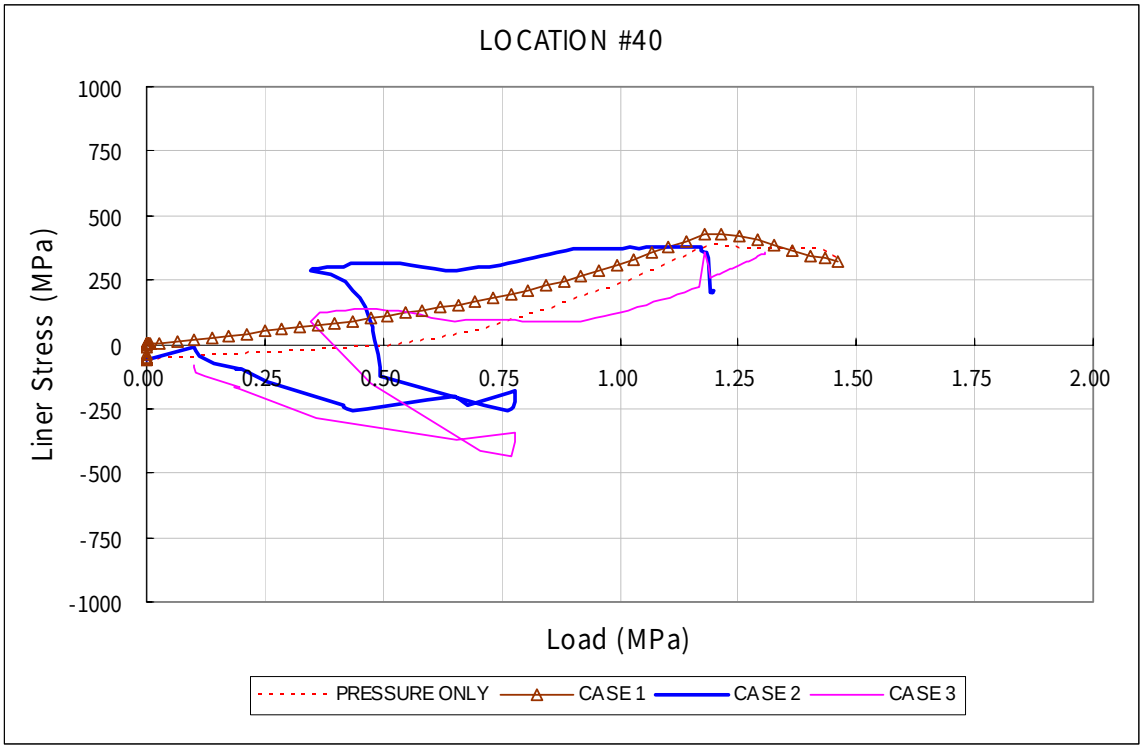

Figure 35 Load-Liner Stress (# 40, 135°, El. 10.75m, Meridional Inside Liner Surface)

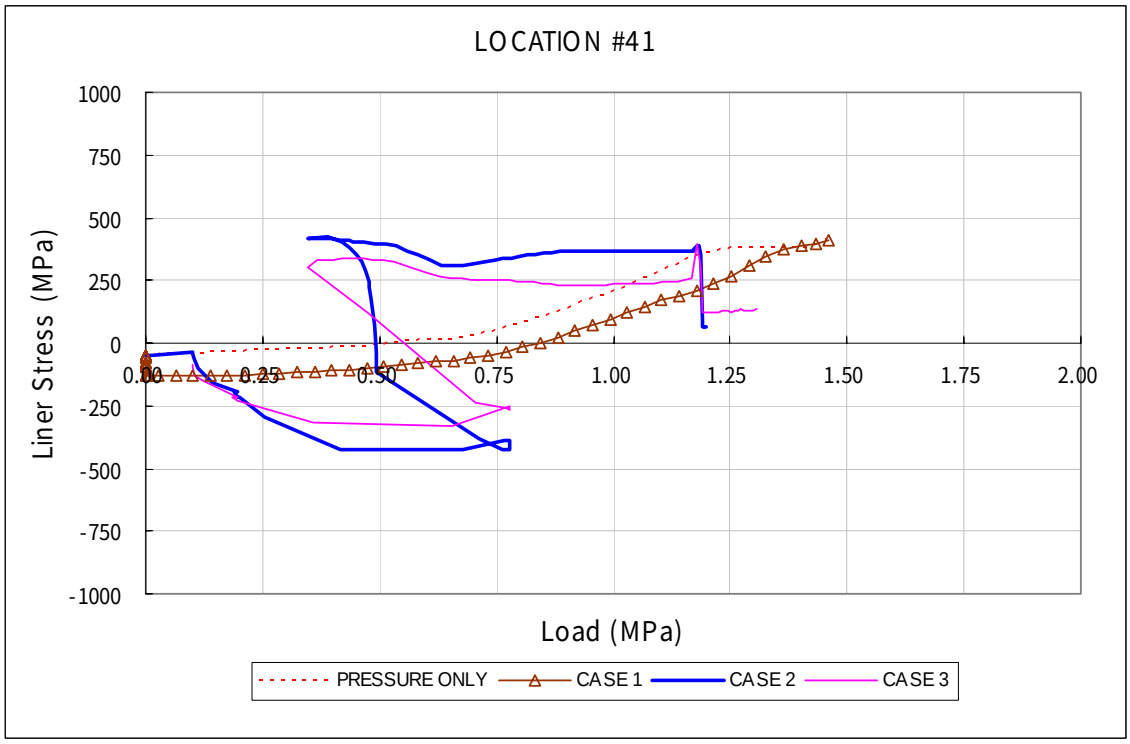

Figure 36 Load-Liner Stress (# 41, 135°, El. 10.75m, Hoop Inside Liner Surface)

`

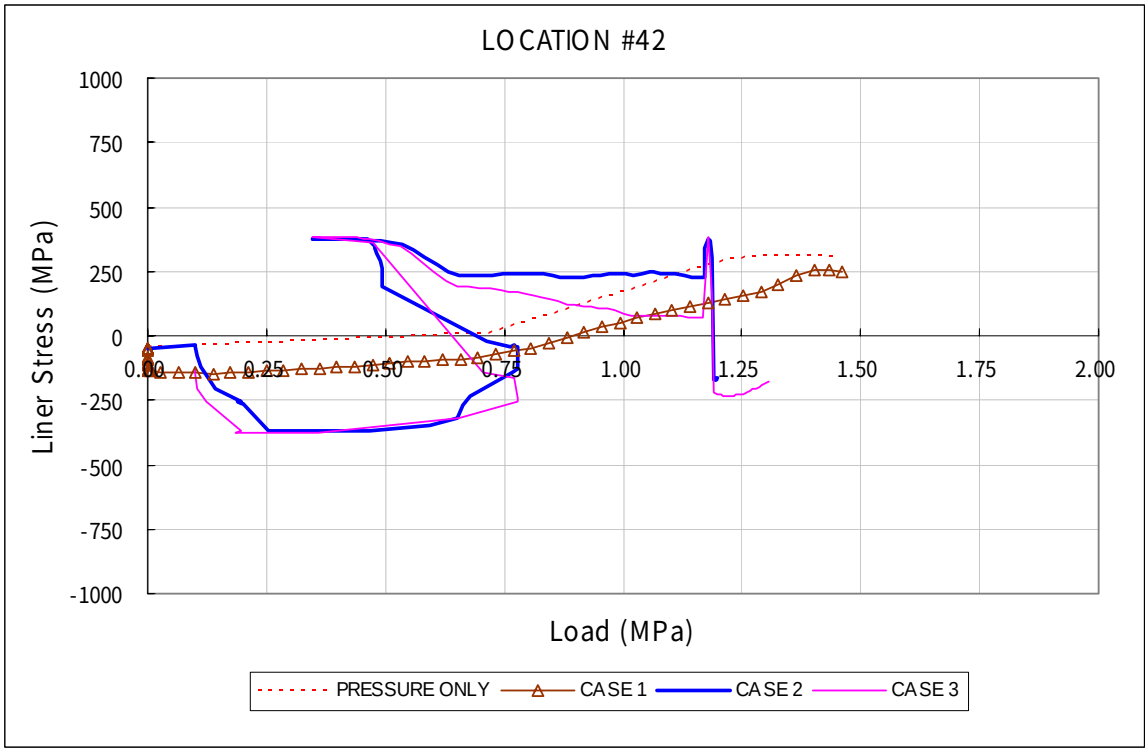

Figure 37 Load-Liner Stress (# 42, 135°, El. 16.13m, Meridional Inside Liner Surface)

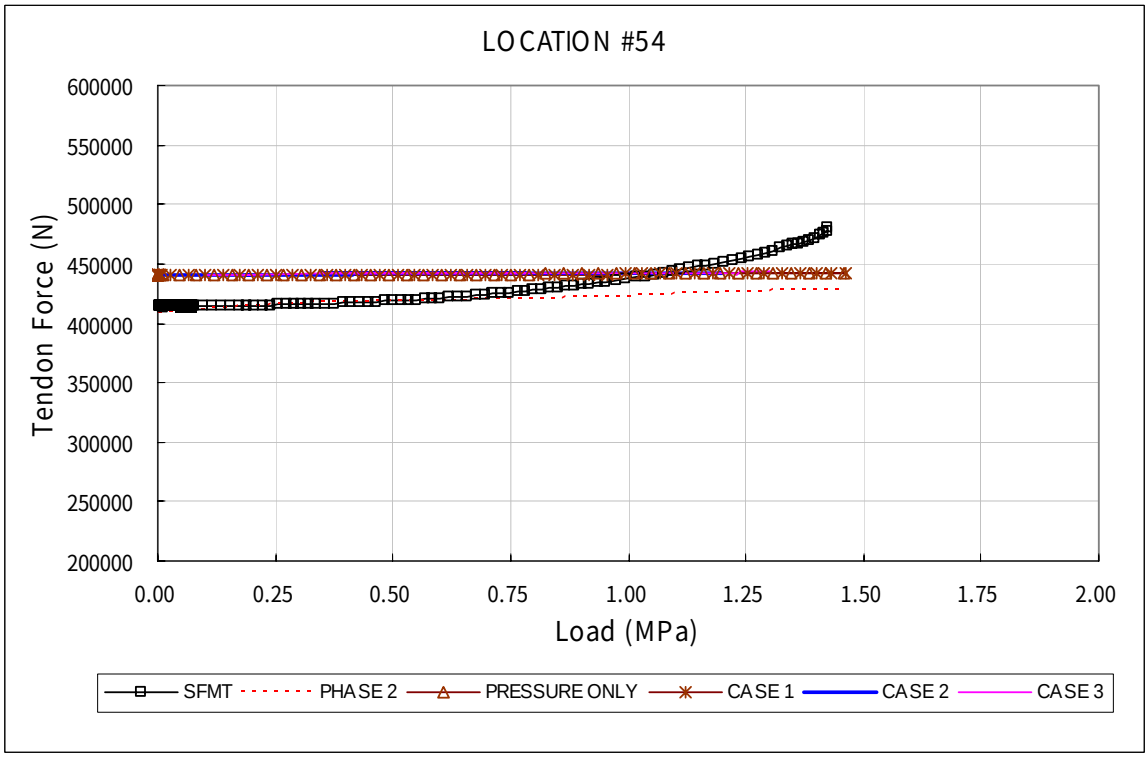

Figure 38 Load-Tendon Forces (# 54, 241°, El. –1.16m, tendon V37)

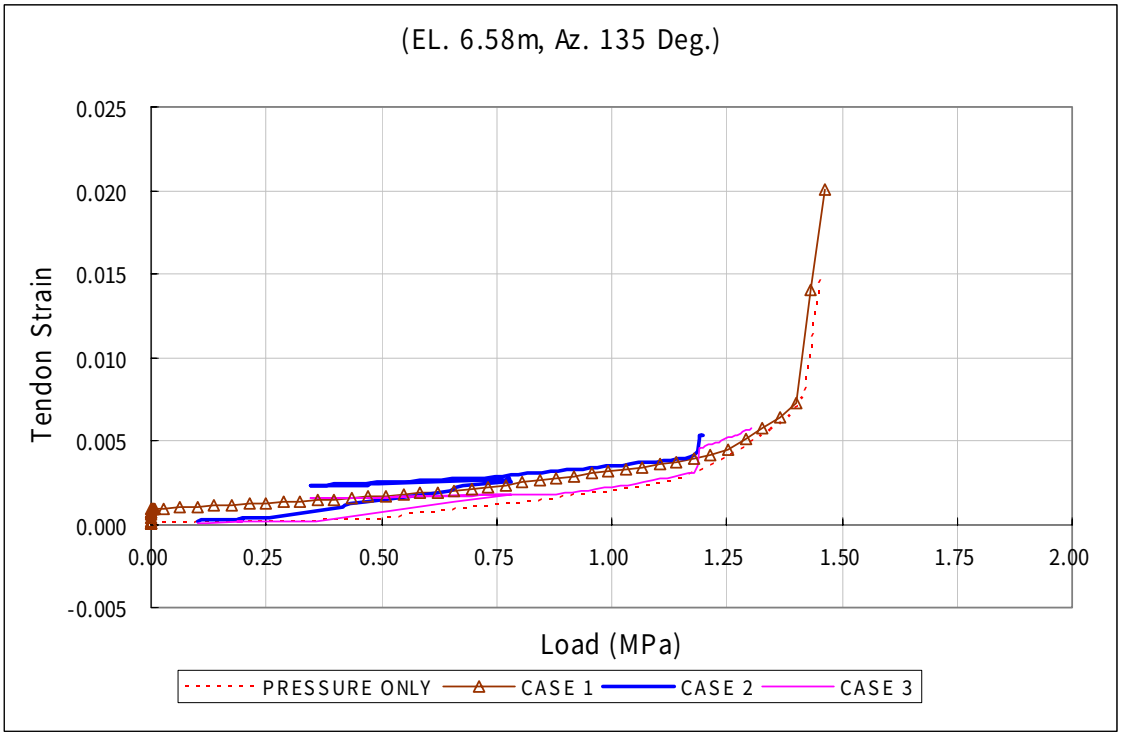

Figure 39 Load-Hoop Tendon Strain (135°, El. 6.58m)

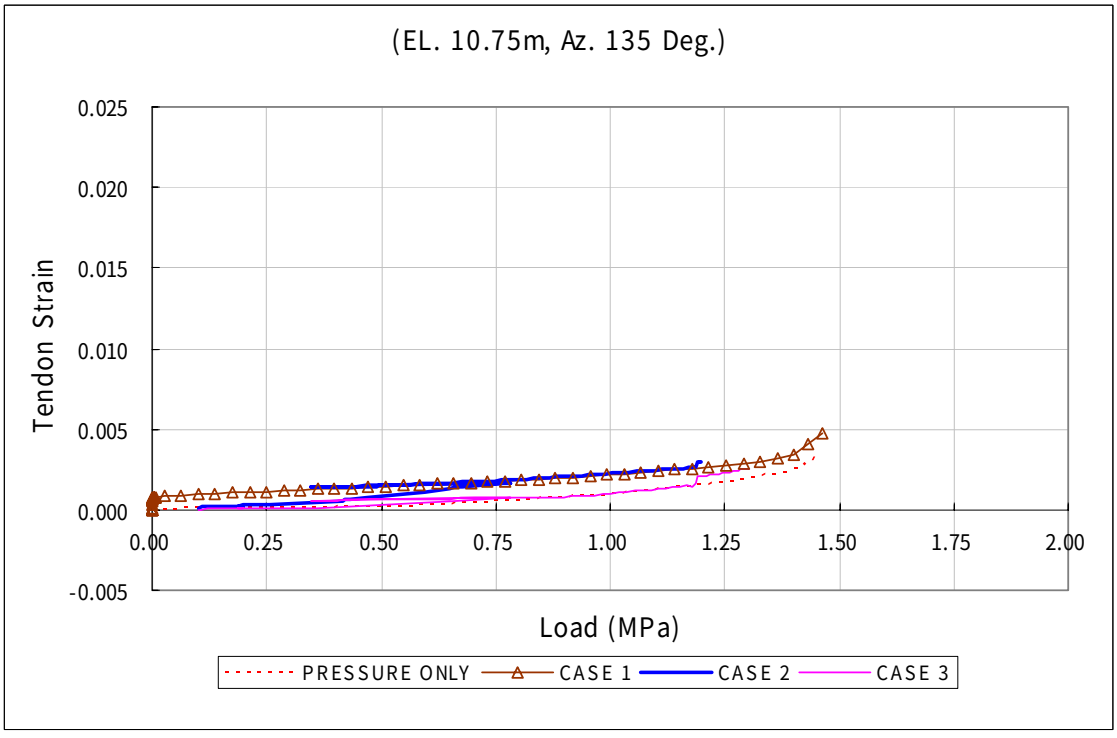

Figure 40 Load-Hoop Tendon Strain (135°, El. 10.75m)

`

Appendix K: US Nuclear Regulatory Commission
Sandia National Laboratories
David Evans and Associates

Phase 2: K-1 to K-66
Phase 3: K-67 to K-95

Analysis of a 1:4-Scale Prestressed Concrete Containment Vessel Model and Post-test Analytical Studies of Tendon Friction

Sandia / DEA report to NEA/CSNI's Int'l Standard Problem 48 (Phase 2 – Mechanical Loading)

R. A. Dameron[1)], B. E. Hansen[1)], E. R. Kelley[1)], and M. F. Hessheimer[2)]

1) David Evans and Associates, Inc., San Diego, CA, USA
3) Sandia National Laboratories, Albuquerque, NM, USA[1]

BACKGROUND and INTRODUCTION

The Nuclear Power Engineering Corporation (NUPEC) of Japan and the U.S. Nuclear Regulatory Commission (NRC), Office of Nuclear Regulatory Research, co-sponsored a Cooperative Containment Research Program at Sandia National Laboratories (SNL) in Albuquerque, New Mexico. As part of the program, a prestressed concrete containment vessel (PCCV) model (shown in Figure 1) was subjected to a series of overpressurization tests at SNL beginning in July 2000 and culminating in a functional failure mode or Limit State Test (LST) in September 2000 and a Structural Failure Mode Test (SFMT) in November 2001. The PCCV model, uniformly scaled at 1:4, is representative of the containment structure of an actual Pressurized Water Reactor (PWR) plant (OHI-3) in Japan. The objectives of the pressurization tests were to obtain measurement of the structural response to pressure loading beyond design basis accident in order to validate analytical modeling, to find pressure capacity of the model, and to observe its failure mechanisms. The model's limit state reached during the LST was liner tearing and leakage at various locations in the cylinder, as shown in Figure 2. The structural failure mode during the SFMT was gross rupture of the cylinder wall as shown in the post-SFMT photograph of Figure 3.

Sandia National Labs is also participating in the International Standard Problem (ISP 48) on containment integrity and providing assistance to NEA/CNSI in distributing data and interpretations from the PCCV model test to participants in the analysis exercise. David Evans & Associates, under a contract with SNL which began in 2003 is supporting SNL's involvement in the ISP 48 and conducting additional post-test analytical studies. This work is especially focusing on aspects of the PCCV behavior where analytical predictions were significantly different than the test measurements, and on possible scaling issues and "test model artifacts" that may influence interpretations and judgment which can be obtained from the test.

This report represents SNL's submittal to the ISP 48 Analysis Exercise, Phase 2 – Mechanical Loading. It compares results of pretest analytical studies of the PCCV model to the PCCV high pressure test measurements and describes results of post-test analytical studies. All of the pretest analyses and most of the post-test analyses have been performed by ANATECH Corp. under contract with SNL. These analyses conducted through 2002 are documented in detail in References [1], [2], and [3]. This ISP-48 submittal summarizes the modeling approach and analysis tools, comparisons between measured behavior and predicted behavior of the liner, concrete, rebar, and tendons, and the various failure modes and locations that were investigated. Comparison of pretest and post-LST analysis results to the SFMT data and additional analyses, to provide insight into the mechanisms leading to the structural failure, are also included in this report. Observations on the accuracy and adequacy of the prediction analyses, lessons learned from the 1:4 Scale PCCV, such as the modeling and behavior of prestressing and some unique liner seam details, are also discussed.

---

[1] *Sandia is a multi program laboratrory operated by Sandia Corporation, a Lockheed Martin Company, for the U.S. Department of Energy under Contract Number DE-AC04-94AL85000..*

SUMMARY OF PRETEST ANALYSIS

The models that constituted the final pretest predictions were the global axisymmetric, the semi-global three-dimensional cylinder midheight (3DCM) model, and local models of the E/H, Personnel Airlock (A/L), and Mainsteam (M/S) penetrations. These models are shown in Figures 4-7. (Figure 7 also shows strain contour result information plotted onto the finite element model.)

The ABAQUS general purpose finite element program [4] and the ANACAP-U concrete and steel constitutive modeling modules [5] were used for the analysis. Tendons and their prestressing were modeled to replicate expected tendon stress-strain behavior and friction effects. Concrete cracking was simulated with the "smeared crack" approach, where cracking is introduced at the finite element integration points. Cracks can form at orthogonal directions, up to three cracks per integration point, and once a crack forms, it can never heal. Rebar was always modeled with ABAQUS rebar subelements, which reside within the “parent” concrete element, and therefore, are required to have strain compatibility with the concrete. However, the rebar stress-strain law is completely different than the concrete and is represented by a J-2 plasticity model available within ANACAP-U. The tendons were modeled in various ways for the different models, depending on the level of detail. In some cases, the tendons were modeled with rebar subelements, and in other cases, modeled individually with beam elements in which the tendon elements were allowed to slide relative to the concrete. In these cases, friction was represented in various ways. Tendon friction modeling was studied in detail in this work, and this is described later in this report.

The local failure predictions were all driven by response versus pressure histories calculated by the 3DCM model. The only changes made between the 1999 pretest predictions reported in [2] and the final (2000) pretest predictions were to material properties and prestressing levels. Because visual inspection of the model revealed the existence of micro-cracking (probably due to curing and shrinkage) throughout the cylinder, the concrete tensile strength was reduced to a cracking strain of $\varepsilon_{cr} = 40 \times 10\text{-}6$, based on prior experience with similar test structures. A new suite of concrete compressive tests became available in February, 2000, so these were also incorporated into the final pretest analyses.

The failure predictions consisted of liner tearing locations, all occurring near the midheight of the cylinder near penetrations and weld seams with “rat-hole” details. The most likely location for the liner tearing failure was predicted to be near the Equipment Hatch (E/H) at the ending point of a vertical T-anchor, near where the liner is attached to the thickened liner insert plate (also a weld seam). The failure pressure was predicted to be 3.2 times the design pressure (P_d) of 0.39 MPa or 1.27 MPa.

COMPARISON OF PRETEST ANALYSIS TO THE TEST MEASUREMENTS

During the LST, liner tearing and leakage failure was first detected at a pressure of 2.5 P_d, and a subsequent increase in pressure to 3.3 P_d resulted in very extensive tearing at many strain concentration locations. Ultimately, the leak rate through the tears exceeded the flow capacity of the pressurization system so the test was concluded. In reviewing the PCCV test data, the 55 Standard Output Locations (SOLs) used for the Round Robin prediction exercise held in 1999 [6] were very useful comparison points. Pretest analysis test data comparisons (e.g., Figures 8-18) show comparisons of typical displacements, liner strains, and rebar strains. (Post-test analysis curves, described in the next section are also included on these plots.) Analysis data curves were “rezeroed” to the first point of the test data, i.e. the data reading occurring at the start of the test. This slightly shifted the analysis data, but it simplified the comparison of the response to internal pressure and eliminated differences in response to dead load, prestressing and creep or other time-dependent effects. This is justified because most of the PCCV instrumentation was initialized in March, 2000; after dead loads were applied, the model was prestressed, and underwent six months of outdoor temperature fluctuations and low- pressure testing prior to the start of the LST (September, 2000).

The conclusions from the comparisons of the pretest analysis with the LST were as follows:

- Radial displacements in the cylinder wall (Figure 8 and Figure 9) were well predicted by global axisymmetric analysis, but dome and overall vertical displacements (Figure 9 and Figure 10) were overpredicted.
- Wall-base juncture behavior, including many rebar and liner strain measurements, (e.g., Figure 1) were well predicted by the detailed wall-base juncture (axisymmetric) modeling.
- Functional failure (i.e. leakage in excess of 1% mass/day) at a pressure of 2.5 P_d occurred at a liner tear in an area of high strain that was not examined in detail by analysis, but was probably amplified due to defects associated with weld seam repair.
- Maximum pressure, 187.9 psig (3.30 P_d), was closely predicted by analysis, but the predicted failure location did not manifest. (Maximum pressure was also limited by the capacity of the pressurization system.) Ultimately, liner tears at many locations occurred, and many of these were identified by analysis.
- The average radial displacement at the midheight of the cylinder of 20mm at maximum pressure, equivalent to an average hoop strain of 0.37%, is within 10% of that predicted by global analysis (21.9 mm or 0.41%).
- Maximum radial displacement at E/H = 29mm, equivalent hoop strain of 0.0054, was reasonably predicted by 3DCM model, but prediction of displacements at other azimuths–like the buttresses–were poorly predicted by 3DCM model.
- Hoop tendon stress distribution simulated by analysis at start of LST showed fair agreement with measurements, implying that the angular friction and anchor set modeling assumptions at the start of the test were reasonable. Vertical tendon stress distribution at the start of the LST were less consistent with the initial modeling assumptions.
- For the hoop tendon stress distribution, gages interior from the ends were underpredicted by analysis *and* the anchor forces (gages near the ends) were overpredicted. The cylinder hoop tendon data, in total, shows evidence of the tendons slipping during pressurization, and measurements indicate that the shape of the tendon stress profile changes from its initial friction dominated "V-shape" to a nearly uniform stress profile during pressurization.

POST TEST ANALYSES

Global Axisymmetric posttest analyses were performed after the LST. Vertical and dome displacement comparisons were significantly improved by redistributing soil basemat springs according to tributary area, and by improving the dome meridional tendon representation to account for the added stiffness of the overlapping tendons due to the rectilinear "hairpin" layout. Comparisons were also improved by using no vertical tendon friction in the cylinder.

Extensive additional studies were also performed for the posttest 3DCM analysis. In the pretest analyses, the 3DCM model was developed to investigate the non-axisymmetric behavior of the cylinder wall and provide more realistic boundary conditions for the penetration's submodels. Buttresses above and below the 3DCM model boundaries have vertical beam stiffnesses that are not accounted for in a cylinder slice model. Equivalent spring properties were derived and then applied as radial spring elements. The other modeling assumption found to be at significant variance with observed test behavior was the tendon modeling, especially the representation of friction. As shown in Figure 19, the pretest models used tendon friction truss ties oriented at an angle of arctan(0.21) to simulate angular friction. Two important observations were made from the test about the hoop tendon behavior:

1. When pressure overcomes prestress, P = 0.59 MPa, tendon stress distributions change from the classical angular friction design assumption to an approximately uniform distribution; then they

stay fairly uniform at most higher pressures. Toward the end of the test, some tendon interior forces even slightly exceed the force at the anchor.

2. The apparent strain increases in tendons corresponding to force/strain gage readings are significantly larger (e.g. 0.48% versus 0.35%, for H53 as shown in Figure 20) than the strain that corresponds purely to radial expansion. This can only be explained by force redistribution associated with sliding. Thus the position of the tendon relative to the concrete must be allowed to change after initial prestress in order to adequately simulate tendon behavior during overpressurization. (The analytically predicted tendon force distributions are also shown in Figure 20.)

These observations led to changes in tendon friction modeling of the 3DCM model. Because observed tendon friction behavior turned out to be quite complex, new analysis strategies were chosen to bracket tendon behavior:

Model 6. Apply prestress. Then, by using the ABAQUS *MODEL CHANGE capability, fix the tendon nodes at their initially deformed position relative to the concrete. In other words, start from classical design prestress with friction and then effectively bond the tendons.

Model 7. Perform original analysis up to P = 1.5 P_d (0.59 MPa), then "MODEL CHANGE" friction elements to non-friction elements (truss ties aligned perpendicular to the tendons). In other words, perfectly unbond tendons.

Model 9. After prestress, keep the initial friction elements, but add friction elements in the reverse orientation so that if points on the tendon move relative to concrete in the reverse direction from that of initial prestress, they will experience reverse direction friction.

In general, the tendon friction simulation runs 6, 7, and 9 showed progressively better agreement with test measurements, with run 9 (tendon force profile shown in Figure 21) showing the best agreement at the anchors and at most points interior to the tendon ends. Based on these and the other observations, the results of run 9 were used to drive the submodels for E/H and M/S (and estimated feedwater (F/W)) penetrations posttest analysis. On tendon friction behavior, the test measurements and analytical evidence support the conclusion that tendon friction is important to the tendon behavior, but traditional friction design formulas that predict tendon stress distribution begin to break down once pressurization exceeds the pressure that overcomes prestress (in this case, roughly 1.5 P_d). The coefficient of angular friction appears to lessen, allowing sliding and force redistribution as the vessel expands, but more importantly, some parts of the tendon are forced to reverse direction of travel relative to the duct, reverse it from the direction of travel experienced during prestressing. Under this action, angular friction properties probably still hold, but the direction of friction must change sign from that assumed in a design calculation.

Posttest analyses were also performed for the penetration submodels. Liner strains measured in the vicinity of the E/H penetration collar were much lower than predicted by pretest analysis (Figure 22). Since the predicted high strain locations were fundamental to the failure predictions, significant effort was spent reanalyzing the E/H model after the test. As a result of this work, two hypotheses were developed.

Hypothesis 1: The liner in the E/H area had a high degree of bond-friction with concrete, preventing slippage of the liner relative to the concrete; relative slippage is required for elevated strains to develop near local discontinuities like T-anchors and stiffeners. This highly localized effect was not captured in the pretest analysis.

Hypothesis 2: A major crack near edge of E/H embossment further concentrated liner strains at edge of embossment.

Posttest analysis showed that by preventing relative slip between liner and concrete, the overall behavior of the system (concrete strains, tendon strains, liner strains away from the hatch) remained the same, but the elevated strains close to the collar were eliminated. In the final case, directed cracks were introduced to one row of elements, and a discrete crack was formed by adding double rows of nodes along an assumed crack line. This was found to create elevated liner strain. The additional strain concentration coincides with rat-hole weld seam details, and in the LST, elevated strains were measured and numerous tears occurred at these details. Based on results of detailed liner rat-hole analysis, the additional strains associated with such details is enough to exceed the liner tearing strain criteria. This shows that with discrete crack modeling and local rat-hole modeling, a liner tear could have been predicted to occur as early as 2.8 P_d. Based on the evidence provided by liner strain gages and by acoustic monitoring, one of the tears along this embossment edge may have even occurred as early as 2.5 P_d. (Note that this posttest analysis did not attempt to include as-built liner defects, such as local thinning or residual stresses resulting from initial fabrication or subsequent repairs.) The posttest E/H study thus presents a modeling strategy with results that correlate well with the LST measurements and observations. A somewhat higher strain prediction might be possible if a discrete crack (separate rows of nodes) were propagated all the way through the concrete wall, but this would require a change in rebar modeling strategy–one that is probably not practical even for very detailed analysis of containments.

The M/S and F/W penetration hot spots (both analysis and LST observations) occurred near the vertical T-anchor terminations and near the ‘equator’ of the thickened insert plate surrounding the penetration group, i.e. at the 3:00 and 9:00 positions as was previously shown in the strain contour of Figure 7. For the posttest analysis effort, no changes to the M/S model were necessary, other than updating the applied displacement versus pressure histories that were obtained from 3DCM posttest Model 9. After studying the F/W geometry in the posttest phase of the project, it was determined that the F/W penetration model was similar enough to the M/S penetration model that it would be assumed the posttest M/S model was reasonably representative of the F/W penetration. Several observations could be made from the well-instrumented M/S and F/W locations that are relevant to response predictions around containment penetrations.

- Many of the highest strains recorded during the LST are near the M/S and the F/W.
- There is wide variation in peak strain measurements, even at locations that are theoretically identical in geometry; factors contributing to these differences are: slight variations in liner thickness (due to manufacturing and weld repair grinding), gage position relative to the collar/weld, material properties (including welding heat effects), etc.
- The highest strain measurements can, but do not always, correspond to tear locations. Sometimes a gage can show evidence of rising prior to tear occurrence, then declining due to the stress relief caused by the tear; a gage located near a tear crack tip, on the other hand can show quite low strain up to 3.1 P_d and then suddenly jump.

Comparisons of analysis to the M/S and F/W liner strain gages showed that the posttest analysis of the M/S penetrations captured the strains measured in the LST quite well for both the M/S and F/W penetrations.

POST-TEST ANALYSIS OF LINER TEARS WHICH OCCURRED AWAY FROM PENETRATIONS

Detailed analytical investigation was conducted of liner tears that occurred away from penetrations but where welding details may have caused local liner strain concentrations. The PCCV model exhibited 16 distinct locations at which liner tears occurred. All 16 locations were near vertical weld seams, but with some variation in the configuration of a horizontal stiffener or rat-hole. By comparing "before and after" photos taken by SNL (such as shown in Figure 23) and with reference

to a posttest metallurgical study [6], it was observed that liner welding irregularities were present at almost all of the tear locations. These irregularities included points of extensive repair, such as grinding, points of discontinuous or missing back-up bars, or points with weld and liner seam fit-up irregular geometry. Some locations, where a seam and rat-hole existed and high strains were measured, but a tear did not occur provide additional evidence of the importance of the welding details to liner tearing. Ultrasonic measurements showed substantial reductions in thickness near many tears. Measurements showed ~23% thickness reduction in many locations, and more (up to 40% in a few locations).

A posttest liner seam analysis study (using the model shown in Figure 24) was aimed at quantifying effects of welding irregularities and distinguishing these from strain concentrations solely related to geometry. A mesh-size sensitivity study was conducted. Analyses were then conducted to assess material and geometry variations. The first variation implemented varying material properties near the weld areas. This included assignment of different material properties to the base metal, heat affected zone (HAZ), and weld fusion zone (WFZ) regions of the model. The second variation only modified the material in the WFZ. The final phase incorporated geometry modifications to the model near the weld lines. This included thinning of elements and varying the extent of thinning in the vicinity of the welds due to grinding. The geometry modifications were coupled with modified material properties ranging from uniform to including variations of base metal, HAZ, and WFZ regions. A typical strain contour result for one of the detailed liner analyses is shown in Figure 25.

The conclusions of the liner seam/rat-hole modeling study are summarized below:

- By comparison with strain gages and posttest liner tear observations, some of the finite element weld seam analyses are able to generate strain fields in and around the rat-holes and liner welds which agree reasonably well with strain gage measurements and which exceed the liner tearing strain criteria at locations where tears were observed.
- Competing mechanisms between the weld zone and ends of stiffeners make yield and ultimate strength adjustments to the HAZ material properties necessary to correctly predict strain concentration location and intensity.
- The models with back-up bars, nominal geometric properties, and best-estimate material properties yielded the best simulations of defect-free construction of rat-hole/weld-seam details. However, even models without back-up bars also provided reasonable correlation with gages at these locations.
- A case with severe (~40%) amounts of thinning appears to provide the best simulation of the behavior of tear occurrences in which severe liner thinning (due to weld repair grinding) was reported.
- If a rat-hole/liner-seam detail is subjected to additionally elevated strain (i.e. strain across the liner model that is larger than free-field global strain) a tear even earlier than 3.0 P_d can be justified. In practice, such a prediction could approximately be made using a strain concentration factor approach. The strain concentration factors (K = peak ε_{eff} divided by global ε_{hoop}) implied by this liner seam study are as follows: K = 48 (tear at stiffener end, no back-up bar); K = 45 (tear at stiffener end, with back-up bar); K = 59 (tear at HAZ, no back-up bar, and 40% thickness reduction due to grinding); K = 91 if a short segment of horizontal weld seam back-up bar is missing.
- Using a model of the rat-hole/seam locations without defects showed that liner tears still would have developed by pressure of 3.4 P_d, so liner tearing and leakage would still have been the failure mode (for quasi-static pressurization) even in the absence of liner welding irregularities.

ANALYSIS OF THE STRUCTURAL FAILURE MODE TEST

The LST resulted in liner tearing and leakage, but not a structural failure. Structural damage was limited to concrete cracking, and the overall structural response (displacements, rebar and tendon strains, etc.) was only slightly beyond yield. (Global hoop strains at the midheight of the cylinder only reached 0.4%, approximately twice the yield strain in steel.) In order to provide additional structural response data to compare with in-elastic response conditions, the PCCV model was resealed, filled nearly full with water, as shown in Figure 26, and repressurized during the SFMT to a maximum pressure of 3.6 P_d. The test ended when a catastrophic rupture occurred as was shown in Figure 3. The SFMT posttest analysis showed that good simulation of the PCCV global behavior through and including tendon rupture is possible with a 3D shell model as shown in Figure 27. The main limitations of the shell model were a lack of local liner strain concentration prediction and a lack of accuracy in the predictions of local wall-base-juncture behavior. However, accuracy in global behavior prediction did not seem to be lost when a bonded tendon assumption was used.

The SFMT model provided additional insight as to how the structural failure likely developed. Near the 0 - 6 degree azimuth of the cylinder, there is a reduction in inner and outer hoop rebar area of 38% (from alternating D19, D16 bars to a pattern of 1D16/3D13 bars). At 3.49 P_d, the wall and tendon strain at the 0 - 6 degree location is higher than all other azimuths as shown in Figure 28, and a tendon rupture occurs. The analysis then shows neighboring tendons rupturing and deformations spreading quickly along this azimuth. The secondary tendon ruptures spread upward. From review of test video, this appears to agree with observations. By 3.65 P_d, the analysis shows rupture to have spread over a vertical line spanning about 6 m. This also agrees with observations. A comparison of cylinder midheight radial displacement, test versus SFMT post-test analysis is shown in Figure 29. Deformed shape "slice" views of the cylinder midheight radial displacements can be seen in Figure 30, showing the development of the failure near the 0 degree azimuth.

After wall rupture, a secondary event occurred in the SFMT: through-wall failure around the circumference of the wall at about 1.5 m elevation. While it is difficult to say at what azimuth this failure initiated, it seems clear that this was a shear or combined shear/flexural failure of the wall. The plotting of analysis shear results in the SFMT analysis model showed that such failure may have initiated at the buttresses (evidenced by the high shear stresses predicted there) and then "unzipped." With the triggering event of a massive wall rupture, one of two mechanisms may have caused shear demand to exceed capacity: 1) a large deformation of the wall opening, creating large rotations near the base of the wall, would crush the outer concrete of the flexural section and thereby reduce the capacity, or 2) the water jet-induced momentum imbalance would cause added shear demand; this would create tangential shear at some azimuths and would be the maximum at the buttresses; such shear acting in combination with the already high radial shear stresses could have increased shear stress demand enough to induce the shear failure.

SPECIAL STUDIES ON TENDON FRICTION MODELING

In 2003, a new approach to modeling the tendon friction was investigated. To begin the study the final post-test 3DCM model ("Run 9") was reduced to a ring model representing an infinitely long cylinder as shown in Figure 31. Similar to the semi-global 3DCM model the concrete was modeled with brick elements, the liner with shell elements and the rebar was included as rebar sub-elements. Tendons were modeled with a truss element and, initially, friction truss-ties to adjacent concrete nodes. The initial run with the truss-ties was used to compare with the original 3DCM model and establish a baseline ring model to evaluate the effects of varying tendon modeling parameters.

Once the baseline ring model had been developed and tested, the friction truss-ties were removed and replaced with a sliding contact surface, coefficient of friction equal to 0.21. In the original 3DCM analysis the stress in the tendon was applied through an initial stress in elastic elements, external to the concrete mesh, at the end of each tendon. Anchor set losses in the tendons were simulated by adjusting the orientation of the friction truss-ties near the end of each tendon. The

friction truss-ties required the use of "small displacement" theory so that the tendon friction would be oriented correctly regardless of the movement of tendon nodes relative to concrete nodes. However, because the orientation of the truss-ties does not change, the shape of the tendon stress profile is "locked in," and this was found to have potentially significant effects on the analysis at intermediate pressures (pressures in the range of 1.5 Pd to 3 Pd). Because the truss-ties were eliminated in the contact surface model, the tendons could be stressed in two steps, similar to the way stressing operations occur in the field. The tendons were stressed first to the full design stress and then the stressing is reduced to simulate the anchor set losses. This second step, reducing the stress, allows the ends of the tendon to slip relative to the concrete. Because there is fairly large displacement of the tendon relative to the concrete nodes, now large displacement theory (geometric nonlinearity) was needed (in ABAQUS, done by including the "NLGEOM" parameter). Without activating large displacement theory the loss in the tendon as a result of reducing the stress was effective over the entire length of the tendon rather than just the anchor loss zone. By switching to large displacement theory the tendon stress profile matched the design stress profile quite closely. The initial tendon stress profiles of the two methods are shown to be nearly identical in Figure 32. But Figure 33 and Figure 36 show how the two models begin differing substantially once significant pressure is applied. Figures 32-34 show tendon stress comparisons and Figures 35-37 show radial deformation. At pressures of about 2.0 P_d and larger, the results using the two methods differ significantly. Comparison to the measured radial displacements shown in Figure 38 show that the contact surface model provides the best prediction of 3D behavior of the cylinder, even at intermediate pressures.

Two models were run with the contact surface. In Model 1 the initial stress profile attempted to match the stress profile from the latest post-test analysis, namely a relatively small anchor set, corresponding to ~2 mm. In the post-test analysis this was accomplished by orienting the truss-ties perpendicular to the tendon over the anchor set zone of ~15 degrees of azimuth. For the ring model with the contact surface, the stress profile was obtained by reducing the initial stress from 100% to 97%. Model 2 included an anchor loss zone of approximately 45 degrees, which corresponds to the design anchor set of ~6 mm. For this analysis the anchor stress was reduced to 89%. Once the initial stress profile was determined for each of the analyses, pressure loads were applied the same as to the 3DCM model. Comparisons are presented for tendon force and displaced shapes for each of the models in Figures 39-42.

When comparing the displaced shapes, significant differences exist between the contact model with different anchor sets at P=2.0 P_d. In the large anchor set model the largest radial displacements are occurring near the buttress location similar to the 3DCM model. This creates an elliptical displaced shape. However, in the small anchor set model the displacement is more uniform over the entire circumference of the model with the smallest displacements occurring at the buttress. This has been judged to be closer to what was observed in the test.

The comparisons of tendon force show that, overall, the tendon behavior is quite similar between all three models. Because the tendon forces are similar and the displaced shapes are quite different, it indicates that there is significant sliding of the tendon relative to the concrete that the truss-tie approach may not be capturing correctly. Further evidenceof this is provided in Figure 43 which shows tangential motion of Tendon H68 relative to the concrete at the anchorage (azimuth 90 degrees) and at 180 degrees from the anchorage (Azimuth 270 degrees). All deviations from the "flat" line are sliding movements of the tendon after anchorage lock-off; these appear to be somewhat important to include in analytical simulations.

The overall conclusions of the study are that the contact surface approach provides improved simulation of cylinder response and tendon behavior at intermediate pressures of say 1.5 P_d to 3P_d, but that near the tendon limit state of ~3.5 P_d, all methods provide a reasonable prediction. Further, it is concluded that the PCCV test model probably experienced anchor set lower than the design value of 6 mm, and probably in the range of 3-4 mm.

DISCUSSION OF MODEL SCALING ISSUES

One of the goals of the final phase of SNL's containment research is to apply lessons learned from scale model testing and analysis to full scale containments. This is also a parallel goal of the ISP48 exercise. Before making direct comparisons of the 1:4 scale PCCV to full scale prototypes, however, examination and analyses of several model scaling issues was performed, and this is summarized below.

Three basic analytical models were developed at full scale: global axisymmetric, the "ring model" for examining tendon friction, and the local liner model of liner welded connections. Each finite element model was changed to full scale based on comparison of geometry of the existing 1:4 scale models to the OHI-3 containment geometry. In the global axisymmetric model, the density was reduced in the full scale model so that with the application of gravity, the vertical stress in the cylinder at the base of the wall was the same at full and quarter scale.

Some results of the full scale axisymmetric model compared to the quarter scale results are shown in Figures 44-46. Figure 44 shows comparisons of radial displacement at cylinder midheight, vertical displacement at springline, and strain in meridional rebar near the inner surface of the wall-base juncture. Here the displacements of the scale model were multiplied by 4 in order to make direct comparison. These plots show that while hoop response of the cylinders are "identical," vertical displacement and flexural strains at the wall-base juncture are somewhat reduced. The wall-base flexure response illustrates the difficulties encountered in concrete model scaling, because shear and flexure behavior tend to scale differently. These differences are also illustrated in the strain comparison plots of Figure 45 and Figure 46. The vertical and shear strains are somewhat lower in the full scale prototype model. The vertical strains show that the neutral axis has shifted somewhat. The shear strains are an indicator of damage to the concrete in the wall base juncture. The result implies increased separation of cylinder midheight versus wall-base juncture shear failure modes for a full scale versus 1:4 scale model. This is actually a favorable result because it means that the scaling of the 1:4 scale PCCV did not "mask" a failure mode that could be more likely to occur at full scale. Instead, the analysis results indicate that quarter-scaling could make a wall-base shear failure somewhat more likely than in the prototype.

Full scale axisymmetric analysis was also used to examine the effects of including the reactor pit in the center of the basemat (as shown for OHI-3 in Figure 47). These studies showed virtually no influence on the basemat or the cylinder response, except for some very localized strain differences in the immediate vicinity of the pit at the center of the basemat.

Full scale liner weld seam (rat-hole) model analysis showed similar strain concentrations as the 1:4 scale model. However, the 1:4 scale liner rat-hole models which were found to best simulate the observed behavior of the LST were those with 20% and 40% liner thickness reductions due to "over-grinding" near welds that were found present in the 1:4 scale model. Since grinding and other thickness irregularities are likely to scale closer to 1:1 than 1:4, such conditions, if they exist at all, would only scale to, at most, 5%-10% of total liner thicknes. When these thickness reductions were introduced, the intensity of strain concentrations near the weld seams was significantly reduced. Conclusion: premature tears of the type that occurred as early as 2.5 P_d in the 1:4 scale PCCV are much less likely to occur in full scale containment. On the other hand, the 1:4 scale liner rat-hole studies of models without thickness reductions predicted liner tear at ~3.4 P_d and these results are judged to be fully applicable at full scale. It should also be noted that most full scale containment liners use back-up bars at all liner seam weld locations, and this was found through earlier analytical studies to further reduce the possibility of premature liner tear near weld seams.

Finally, with regard to tendon scaling, the axisymmetric model offers some insights about vertical tendons and the ring model provided insights into hoop tendon scaling issues. Comparison of vertical tendon behavior at 1:4 scale to full scale showed the 1:4 scale structure had a larger level overall prestress in the cylinder than would be found in a full scale containment. This stems from the fact that angular friction losses in the dome at 1:4 scale were much larger than at full scale (again,

0.21 friction versus the normal 0.11 friction), so prestress had to be increased to compensate for this. The result of this scaling difference, however, was not found to have any significant influence on behavior.

The hoop tendon stress and displacement comparisons between 1:4 scale and "equivalent full scale" shown in Figures 48-51. The changes at "full scale" are two-fold: 1) Friction coefficient is reduced from 0.21 to 0.11 (0.11 is the traditional assumption in design, while for the smaller radius 1:4 scale model, tests conducted by NUPEC resulted in 0.21); 2) Extent of affected azimuth of anchor set is reduced, because anchor set is a length, on the order of 3 to 6 mm, regardless of scaling. For purposes of this study, 6 mm of anchor set was assumed, which produces an anchor set zone of influence of ~15 degrees for a full scale containment. The results show that with the results of earlier sensitivity studies, these scaling differences in hoop tendon friction affect cylinder radial deformed shape at intermediate pressures of ~2.0 P_d to 3.0 P_d (with the full scale shape being more "pinched" at the buttresses), but at pressures higher than 3.0 P_d when the tendons begin reaching yield, behaviors of all friction and anchor set assumptions approach the same deformed shape and tendon stress distribution.

CONCLUSIONS AND LESSONS LEARNED

The 1:4 scale PCCV test showed that the response quantity driving the limit state of the vessel is cylinder radial expansion. This aspect of response must be predicted correctly in order to reasonably predict vessel capacity and predict, at least approximately, the many other local aspects of response (local liner strains, etc.) that are driven by the cylinder expansion. With this test, as with other steel-lined concrete vessel tests, many competing strain concentrations occur around the mid-height of the cylinder. Although it is difficult to predict which local liner detail will tear first, and although some particular response quantities, like basemat uplift, were not predicted exactly by the ANATECH/SNL pretest analysis of the PCCV model, the radial expansion of the cylinder was predicted very accurately. A response mechanism that also appears to have been well predicted was cylinder wall-base flexure and shear, another mechanism that, if predicted incorrectly, could lead to erroneous pressure capacity/failure mode conclusions. The minimum requirement for a containment overpressure evaluation should certainly be a robust axisymmetric analysis.

Other steps, guidelines, and lessons learned are provided in [3]. The lessons learned which may be most novel that result from this work are those related to tendon friction behavior. It was found that the best calculation methods recommended for tendon friction modeling are, in descending order of preference, 1) an advanced contact friction surface between the tendons and the concrete, 2) pre-set friction ties applied in one direction during prestressing and then added in the other direction during pressurization (3DCM run 9) and 3) if neither of these methods are practical within the scope of the calculation, it is best to start with an "average" stress level (using a friction loss design formula), but assume uniform stress distribution in the tendons throughout pressurization, i.e., an unbonded tendon assumption, and finally 4) same as 3, but using a bonded tendon assumption.

By recently examining some possible scaling issues, it has also been concluded that this work, and the analysis methods demonstrated, are also highly relevant to full size prestressed concrete containments. Cylindrical hoop expansion behaviors were found to be the same, regardless of scaling, except for minor variations that occur at intermediate pressures (~2.0 P_d to ~3.0 P_d) due to tendon friction differences. Wall-base flexure/shear behavior and vertical response of the containment are slightly influenced by scaling, but the likelihood of a wall-base shear failure appears to be even lower at full scale than at 1:4 scale. And finally, liner tearing near liner stiffness discontinuities remains the most likely "first" failure mode from static pressurization, but very early tears due to flaws near liner weld seams appears to be much less likely at full scale than what was observed in the 1:4 scale PCCV.

Figure 1. NUPEC/NRC 1:4 Scale PCCV Model Built at Sandia National Laboratories

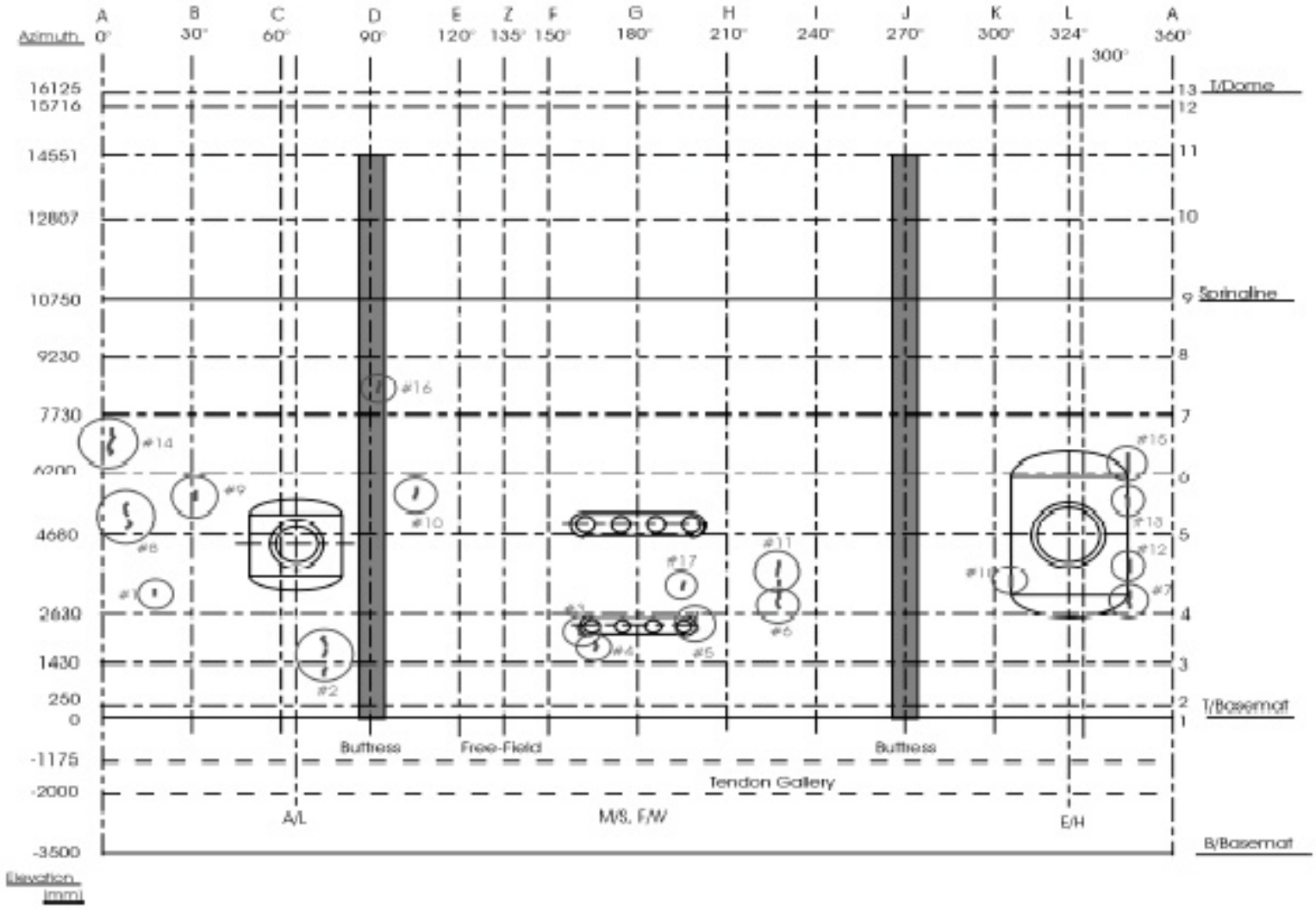

Figure 2. Liner Tears Observed After LST

Figure 3. PCCV Model after Structural Failure Mode Test

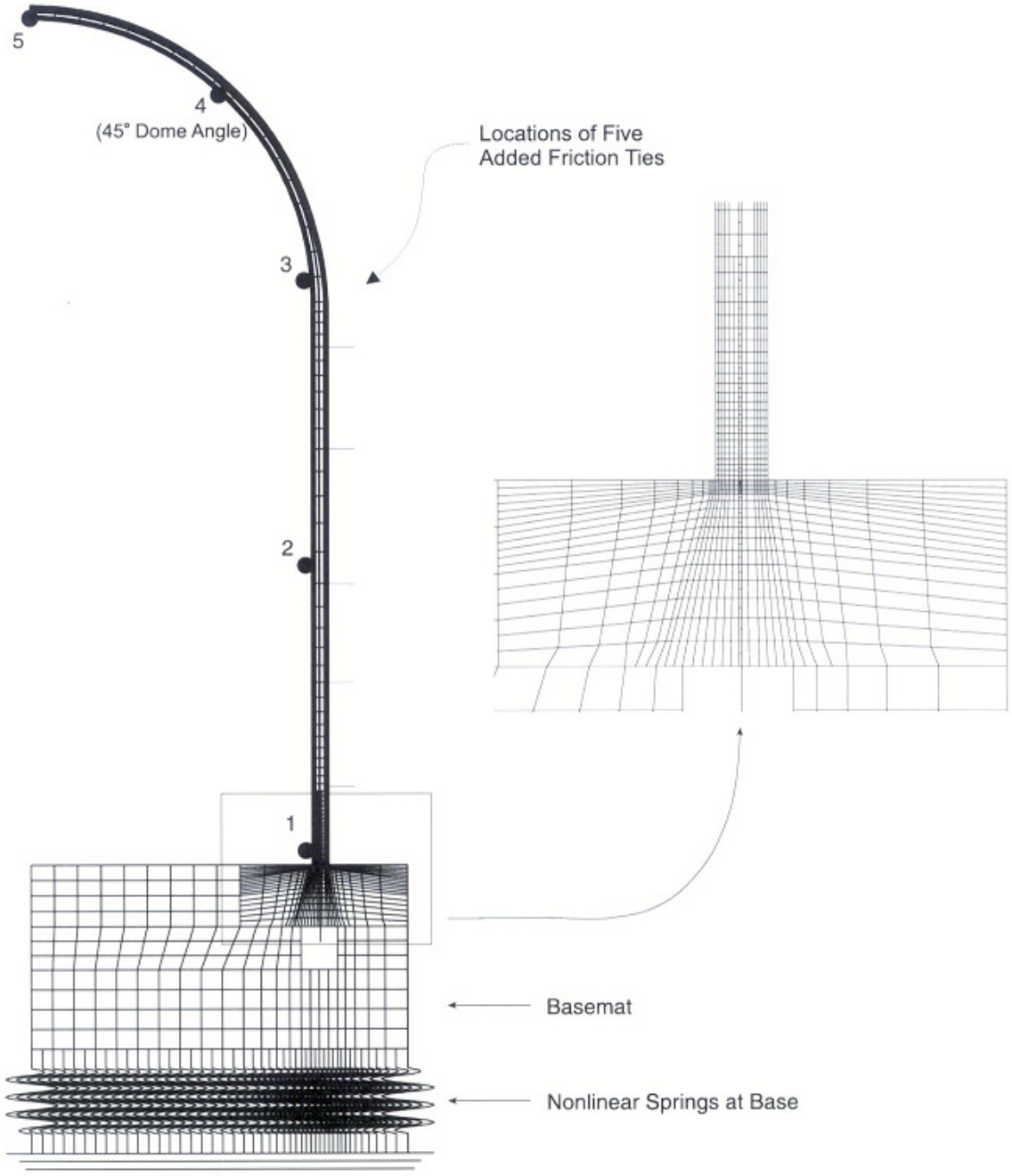

Figure 4. Axisymmetric Model of PCCV and Locations for Plotted Output

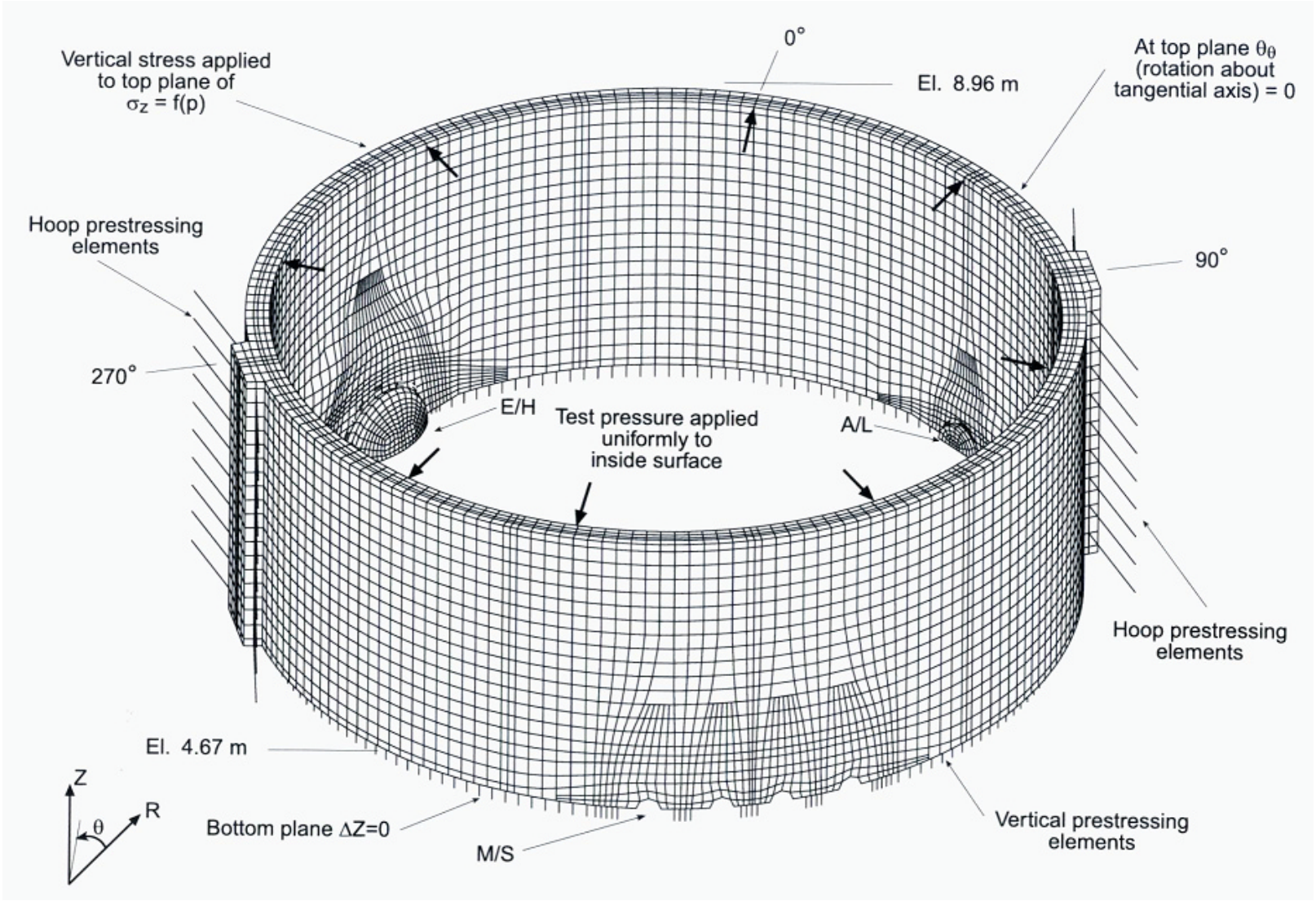

Figure 5. 3DCM Model and Vertical Boundary Conditions

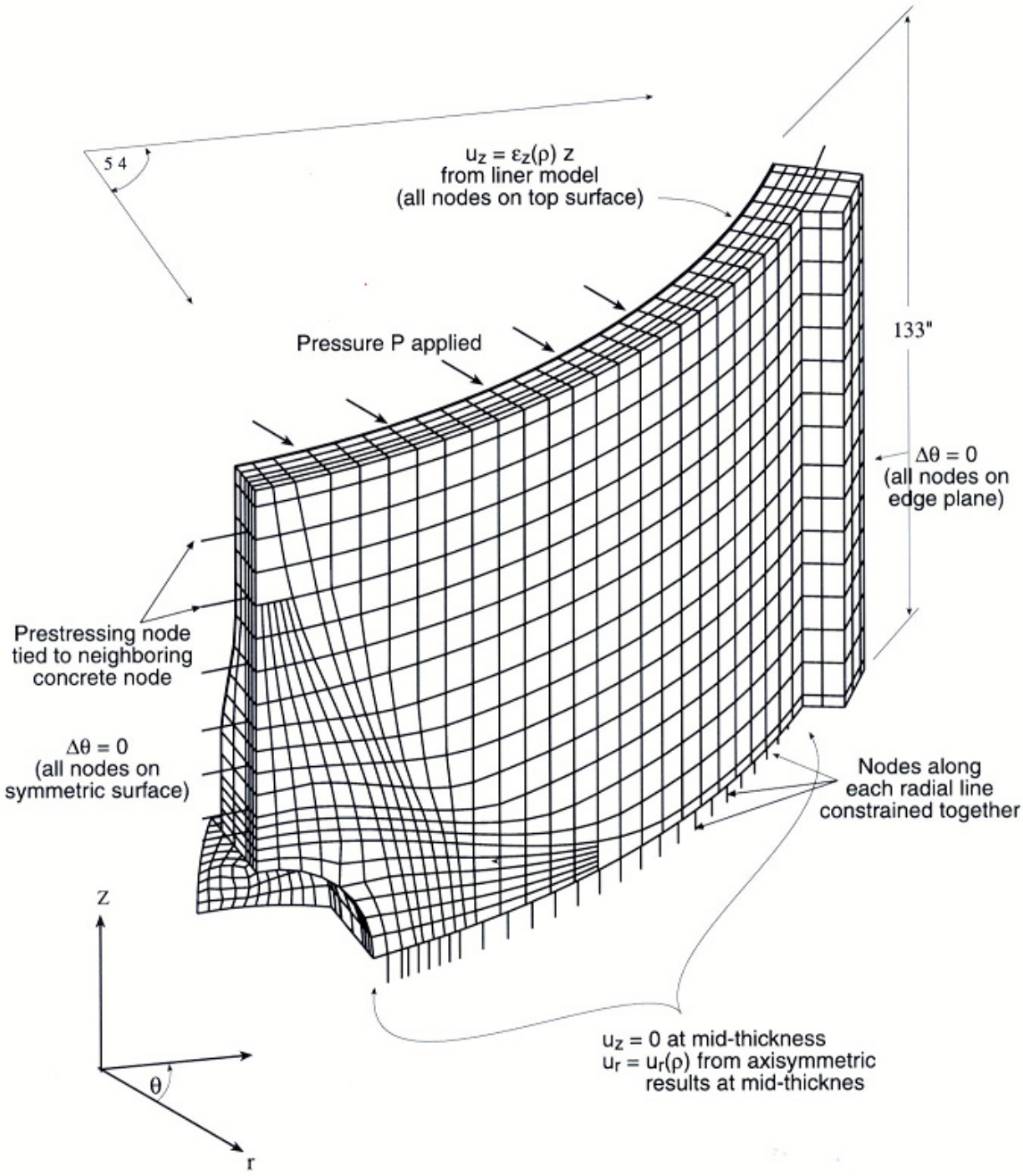

Figure 6. Boundary Conditions and Geometry for the 3D E/H Model Used in Pretest Analysis

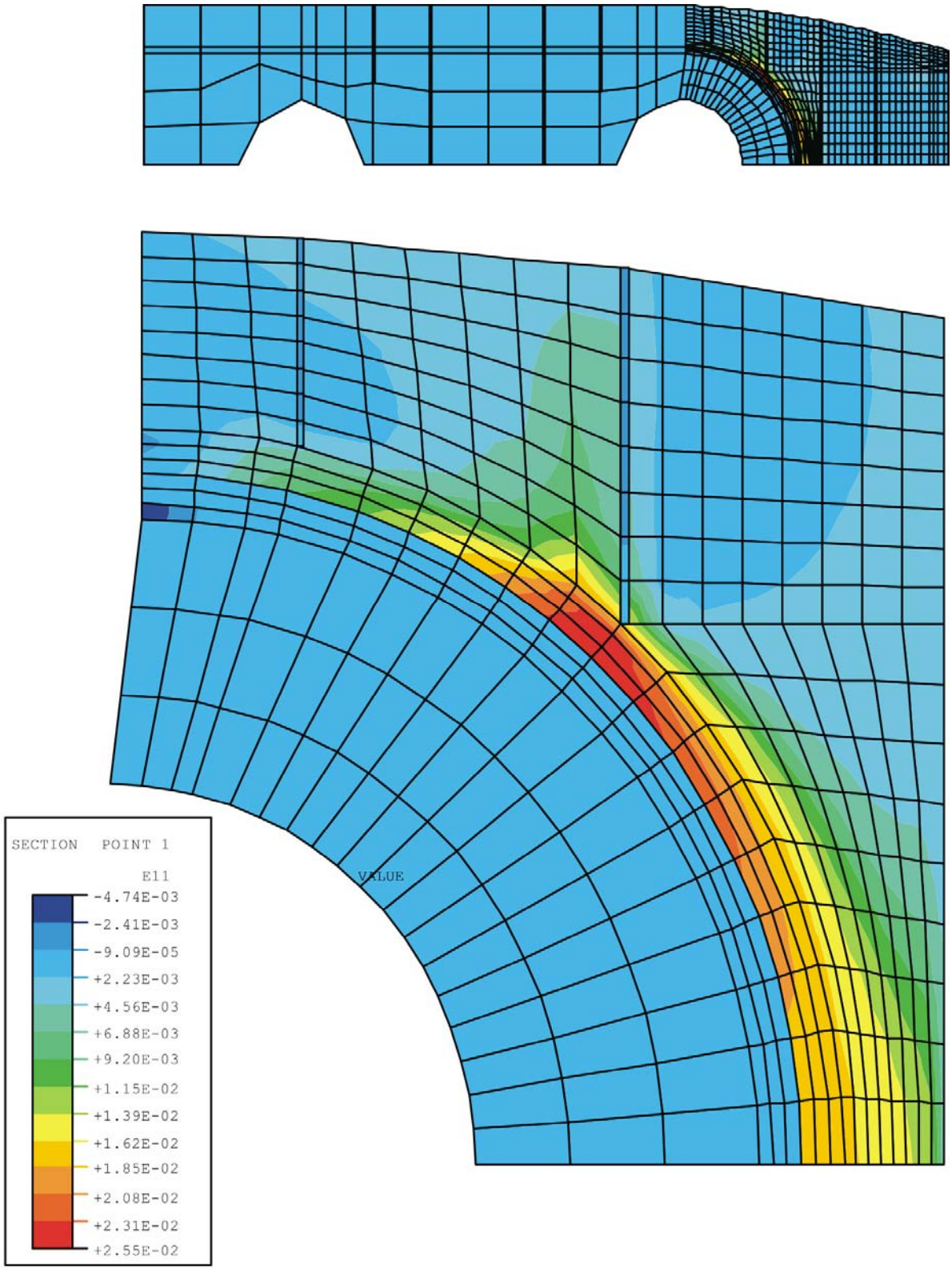

Figure 7. Hoop Strains for Posttest M/S Analysis at $P=3.3P_d$

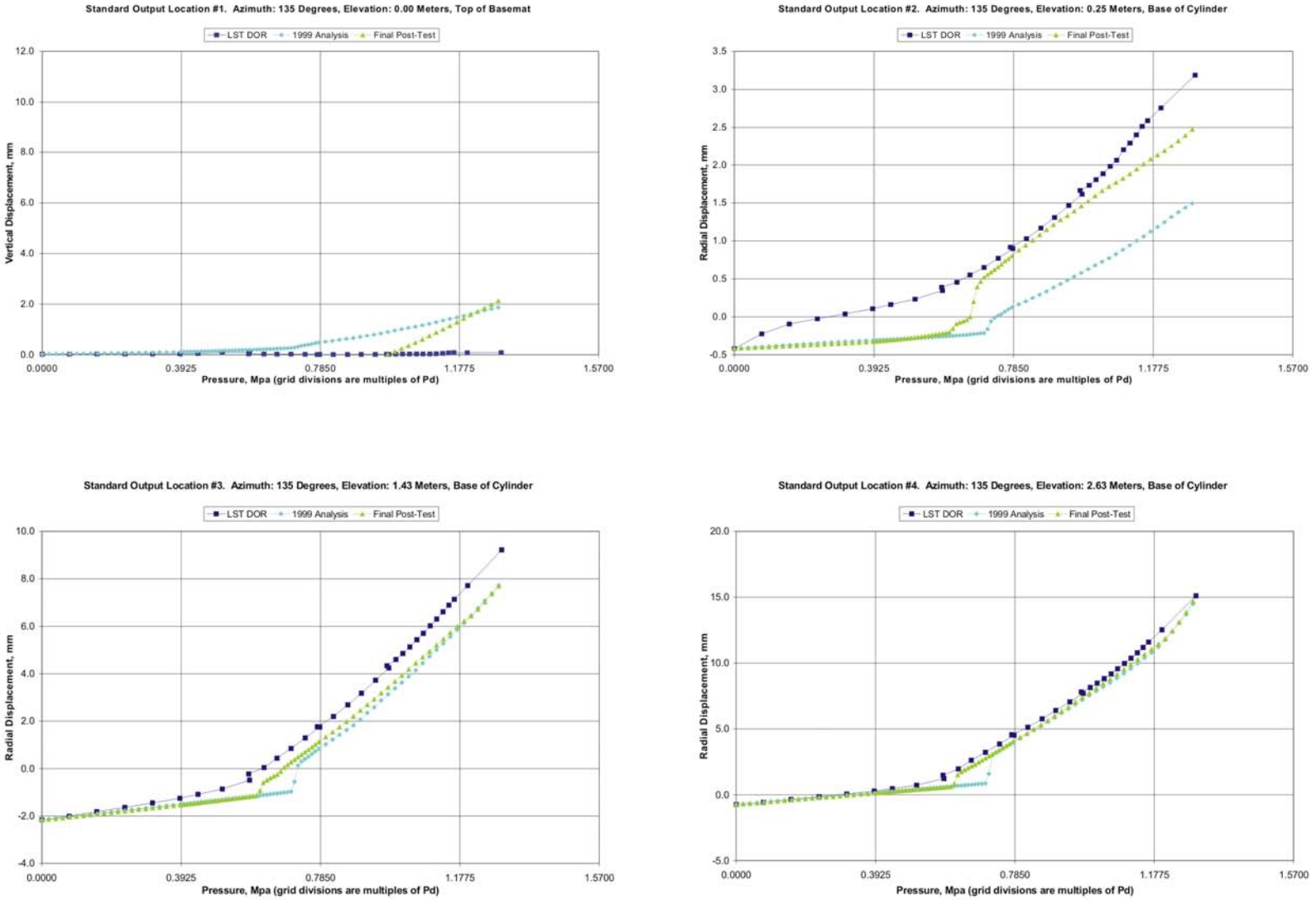

Figure 8. Comparison at Standard Output Locations 1, 2, 3 and 4

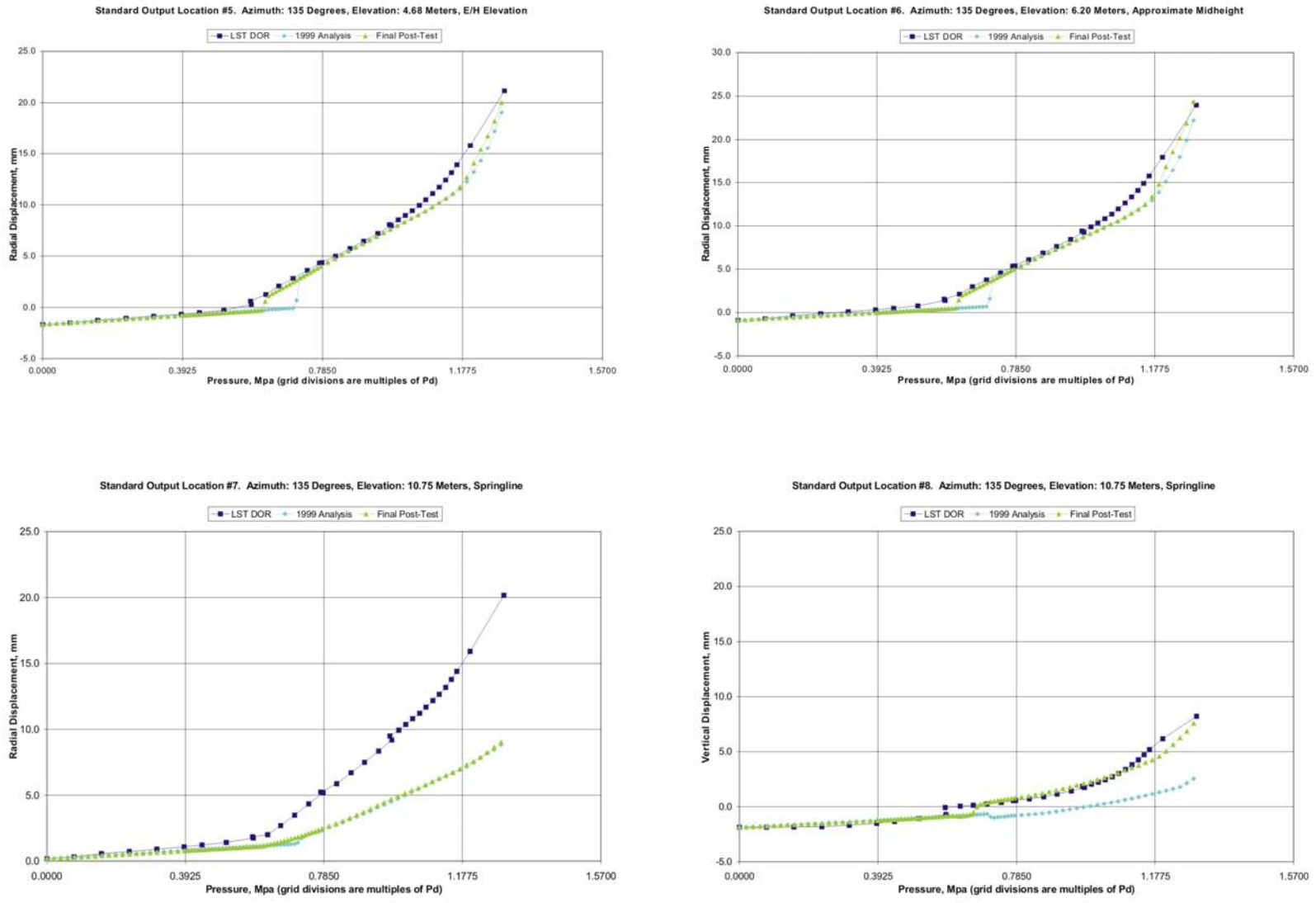

Figure 9. Comparison at Standard Output Locations 5, 6, 7 and 8

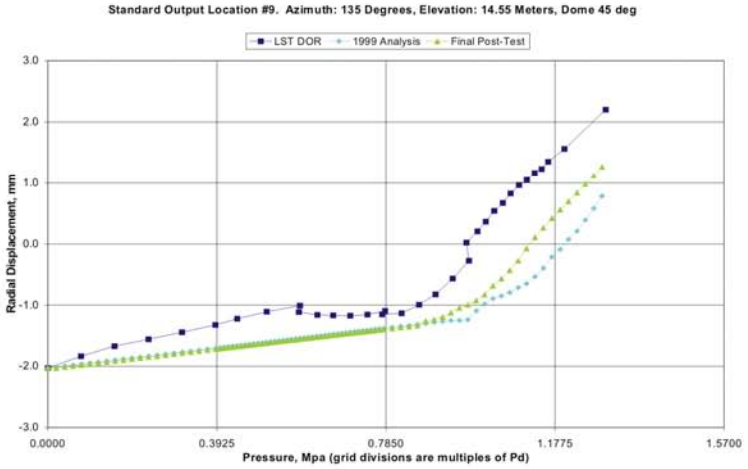

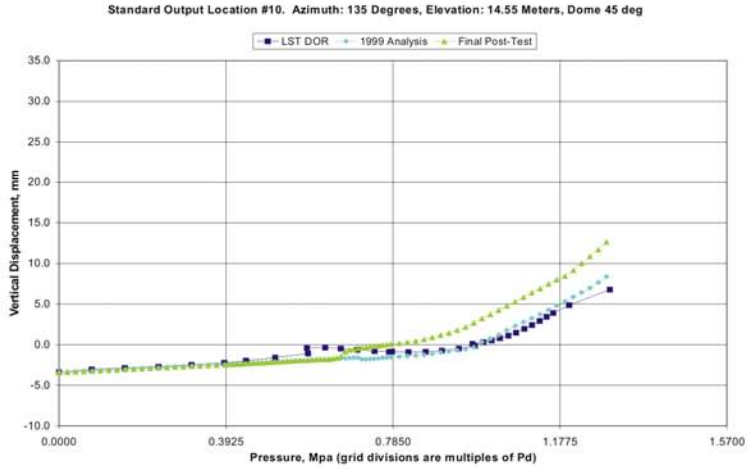

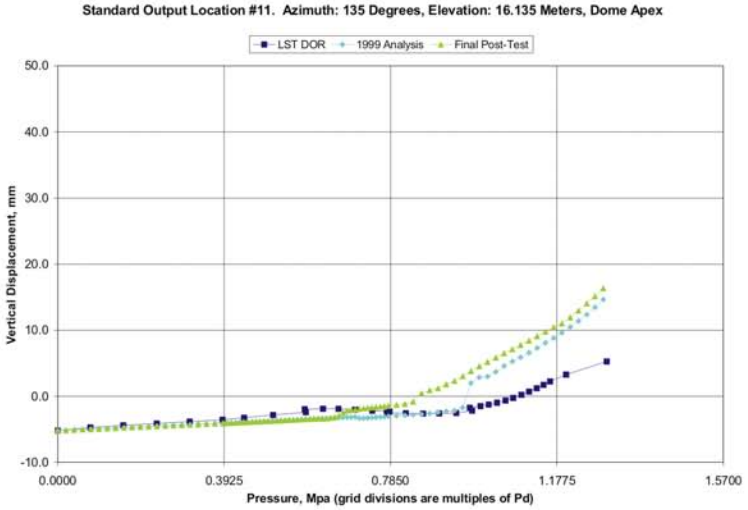

Figure 10. Comparison at Standard Output Locations 9, 10 and 11

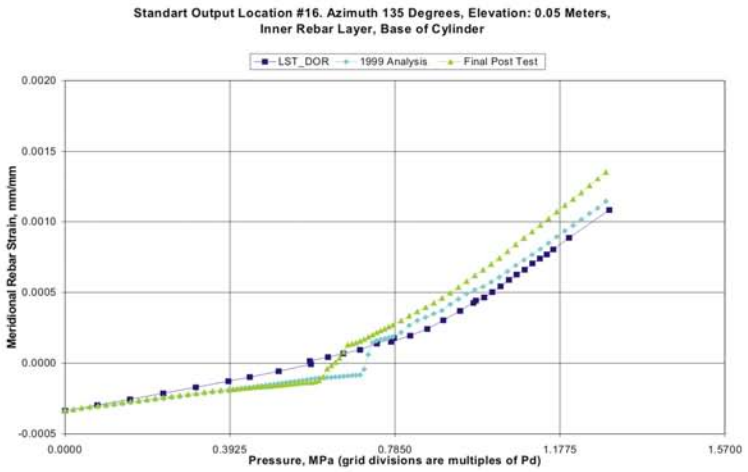

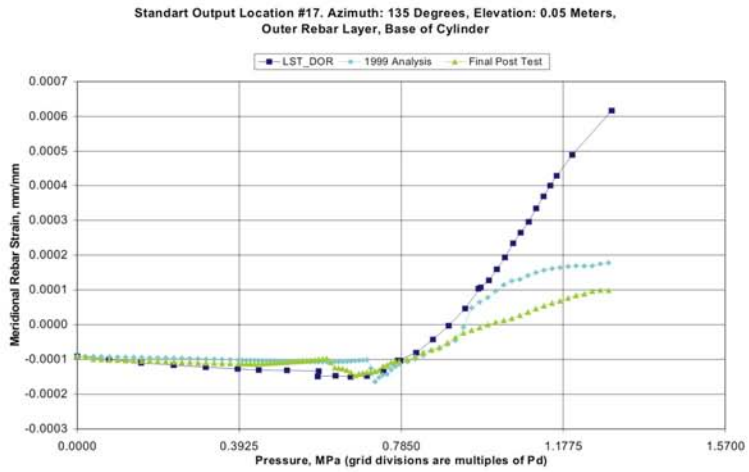

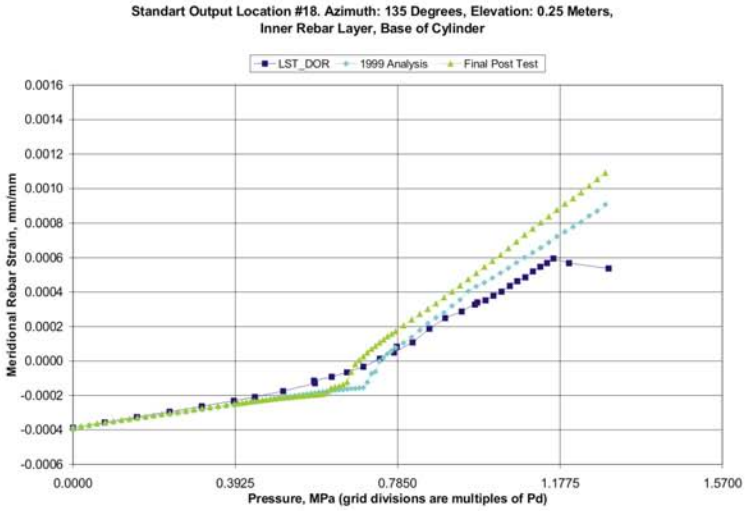

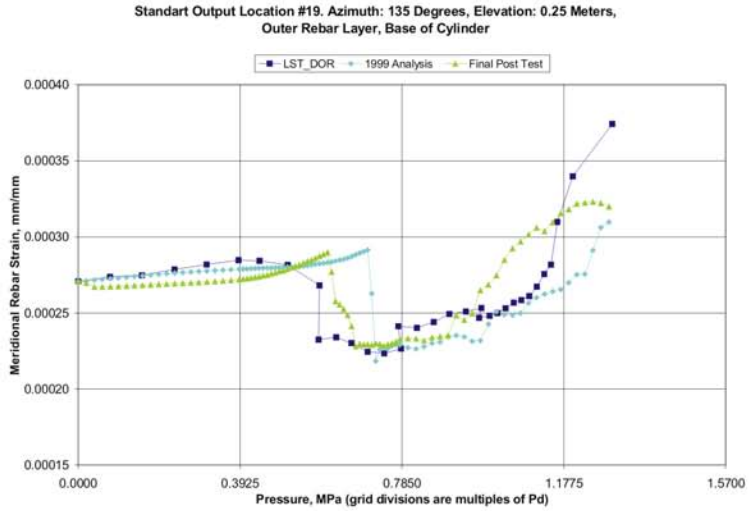

Figure 11. Comparison at Standard Output Locations 16, 17, 18 and 19

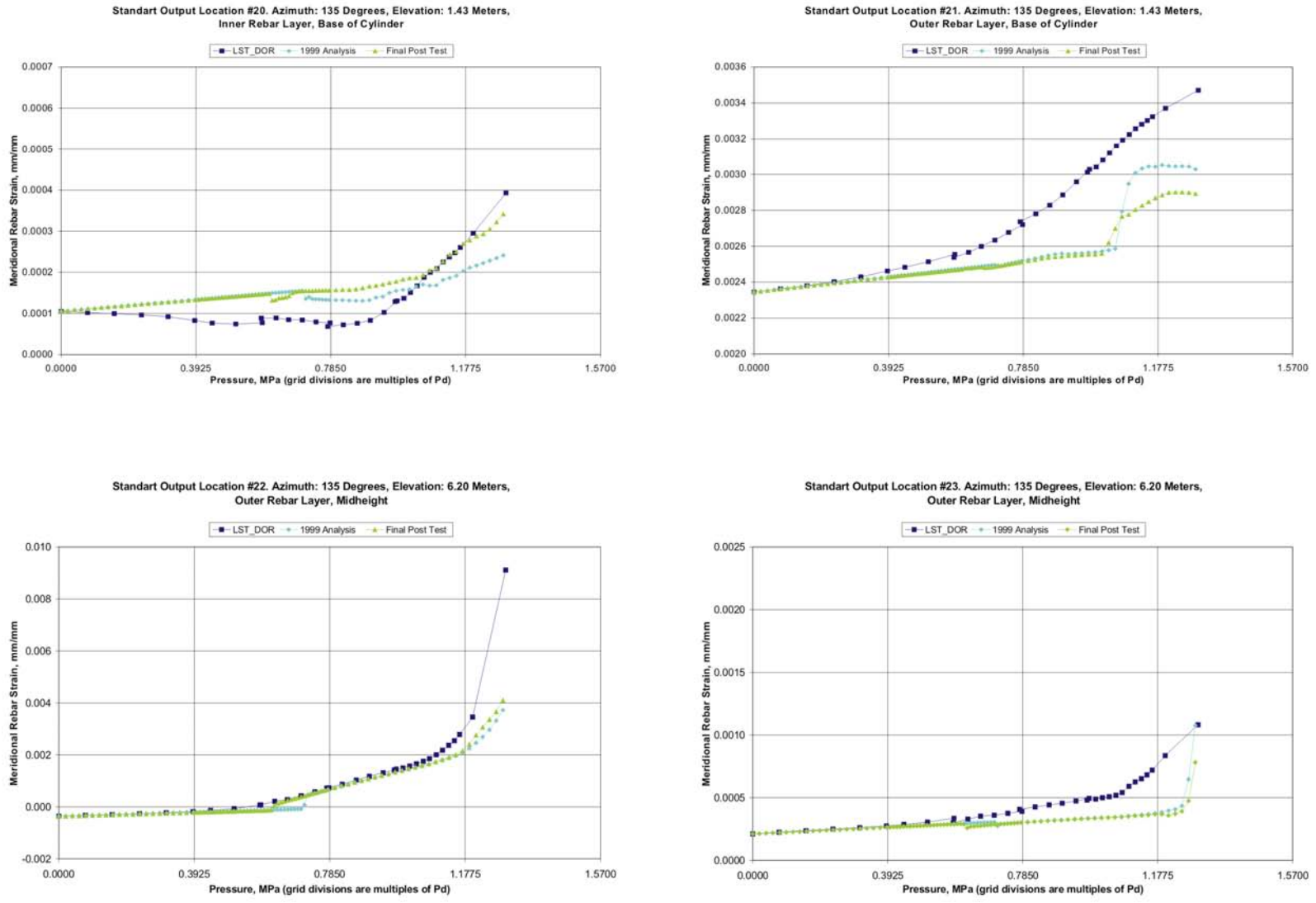

Figure 12. Comparison at Standard Output Locations 20, 21, 22 and 23

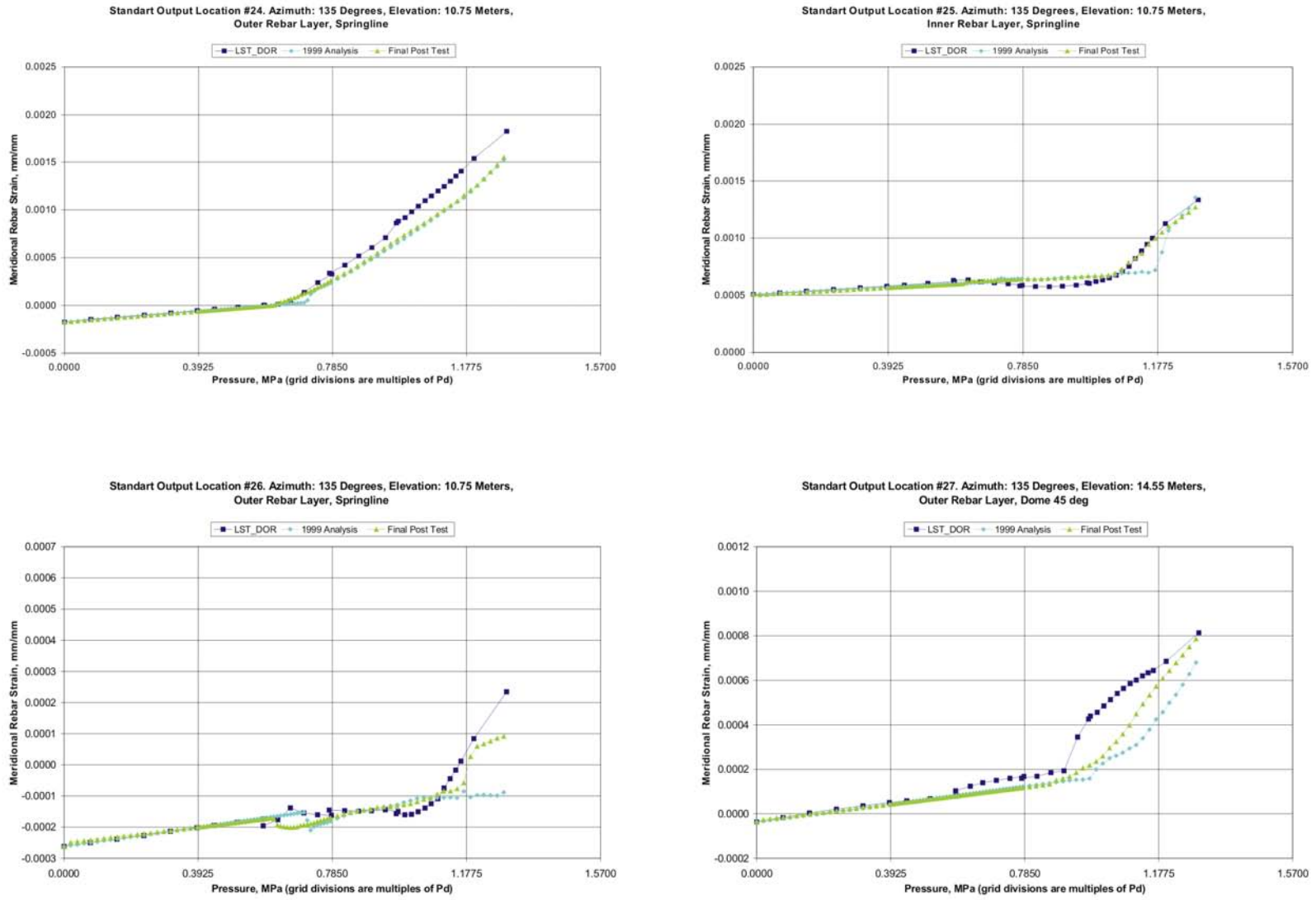

Figure 13. Comparison at Standard Output Locations 24, 25, 26 and 27

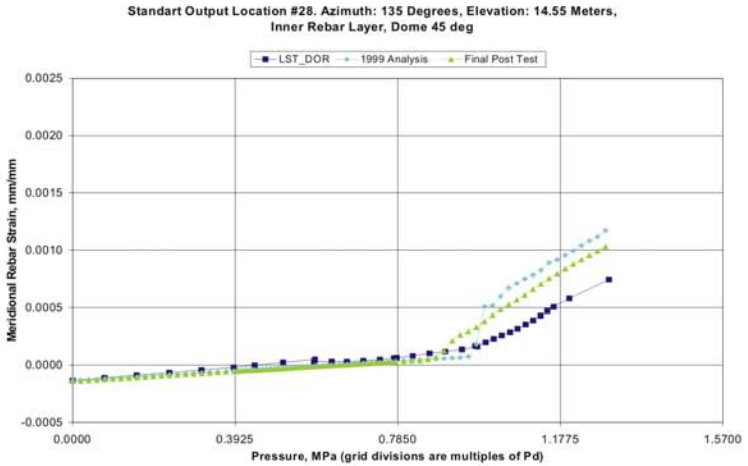

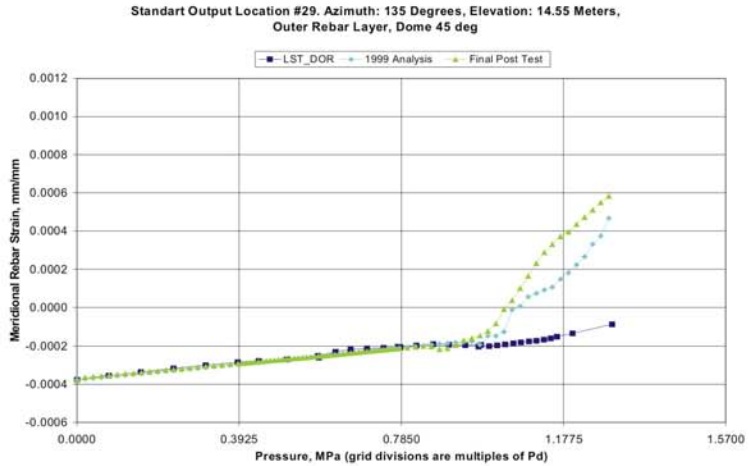

Figure 14. Comparison at Standard Output Locations 28 and 29

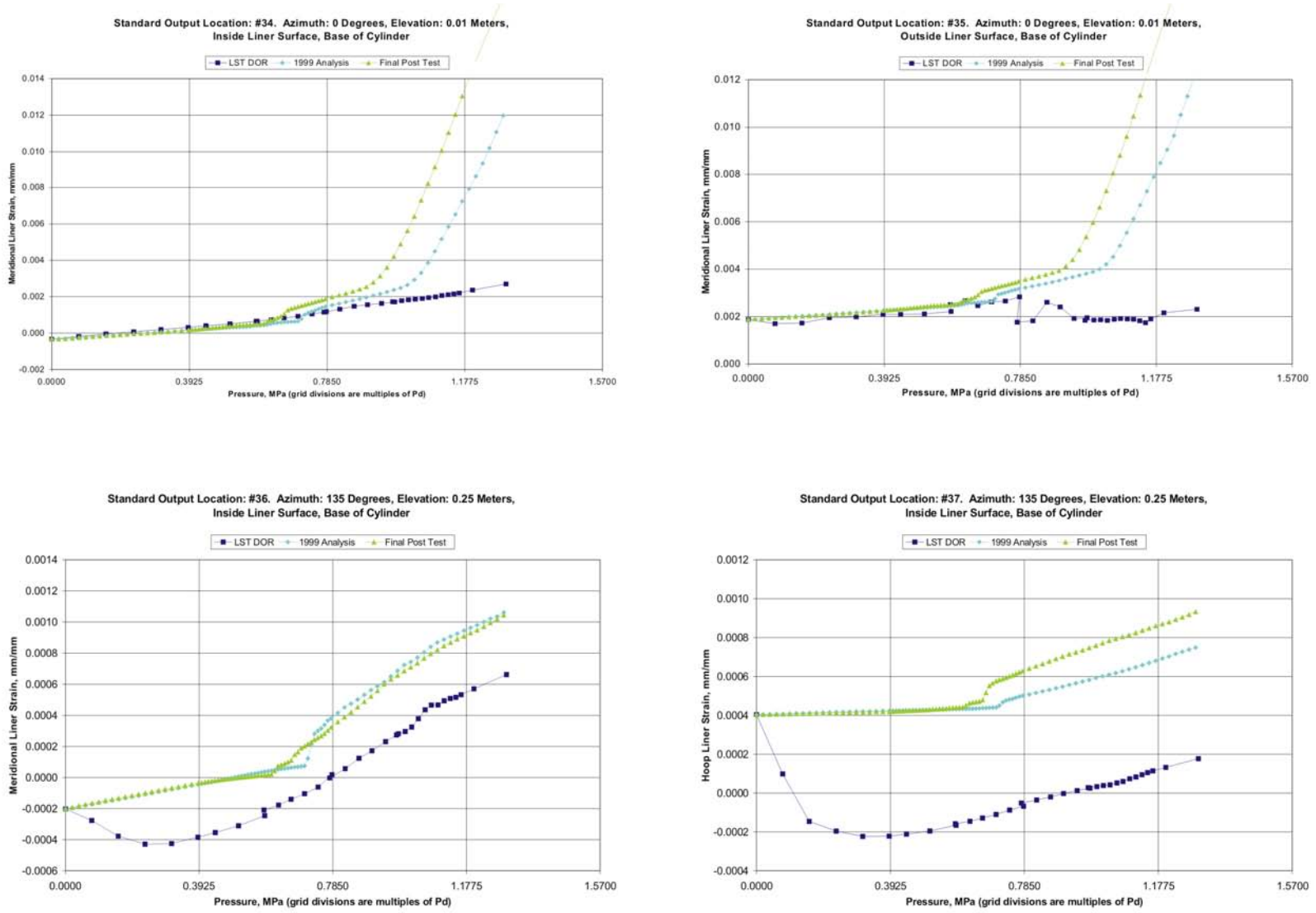

Figure 15. Comparison at Standard Output Locations 34, 35, 36 and 37

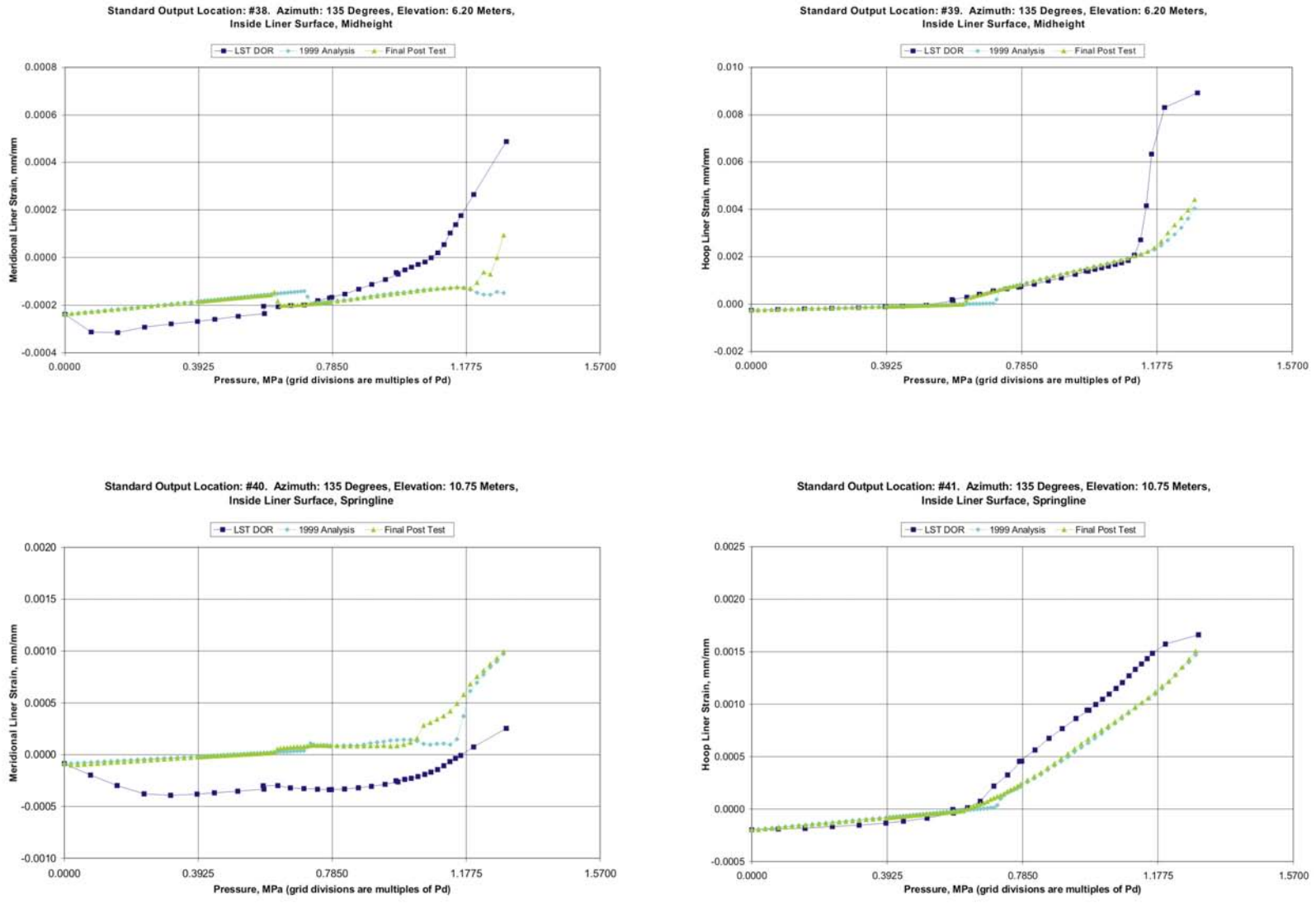

Figure 16. Comparison at Standard Output Locations 38, 39, 40 and 41

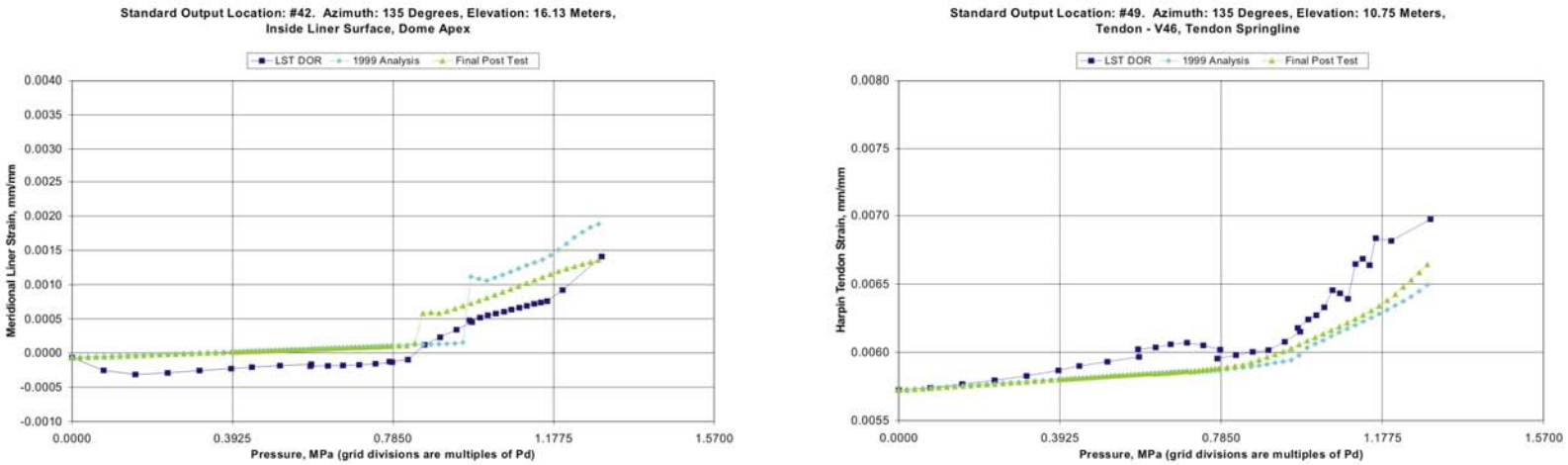

Figure 17. Comparison at Standard Output Locations 42 and 49

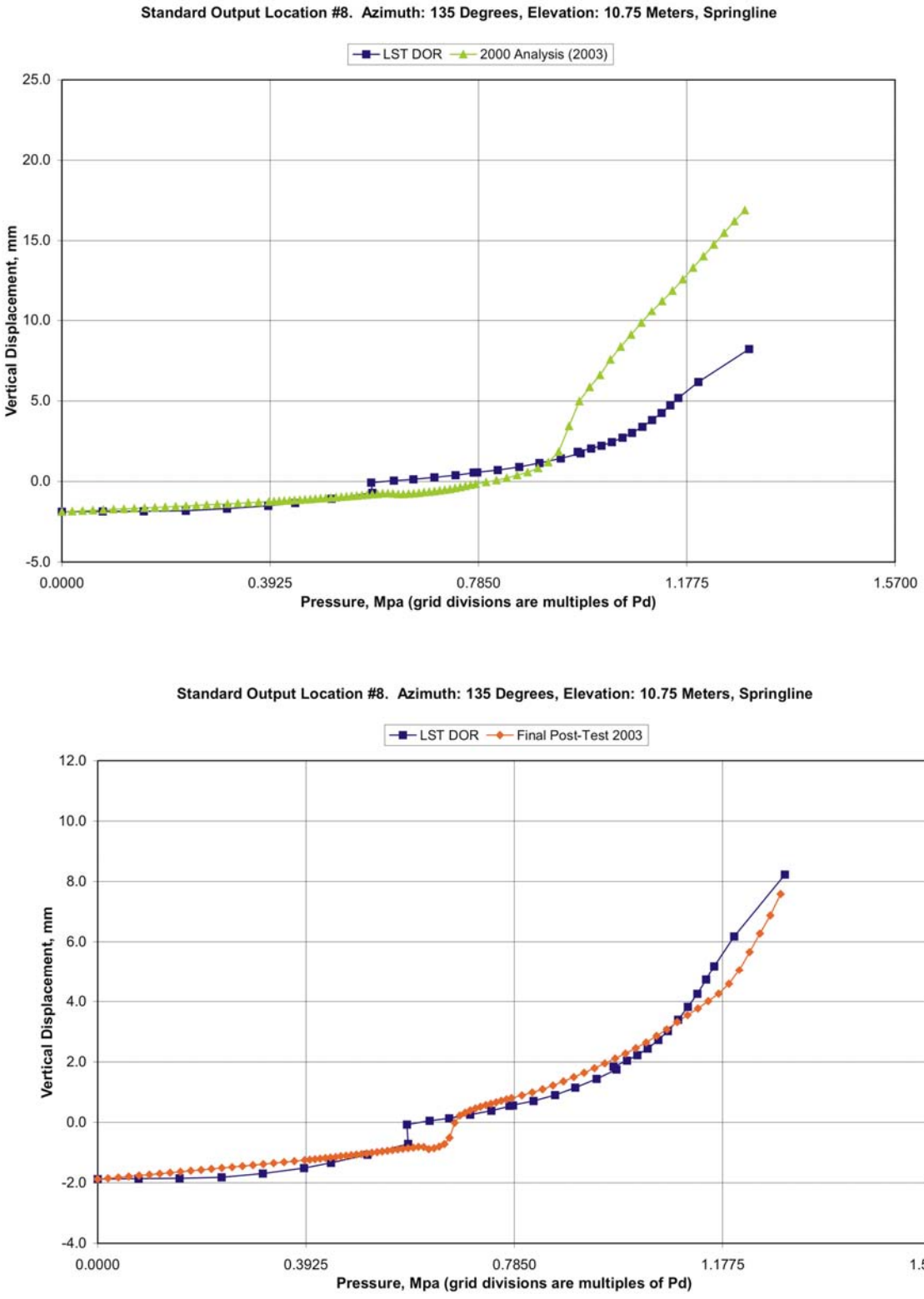

Figure 18. Comparison of Pretest (Upper) and Posttest (Lower) Analysis, Vertical Displacement of Springline to Test Data

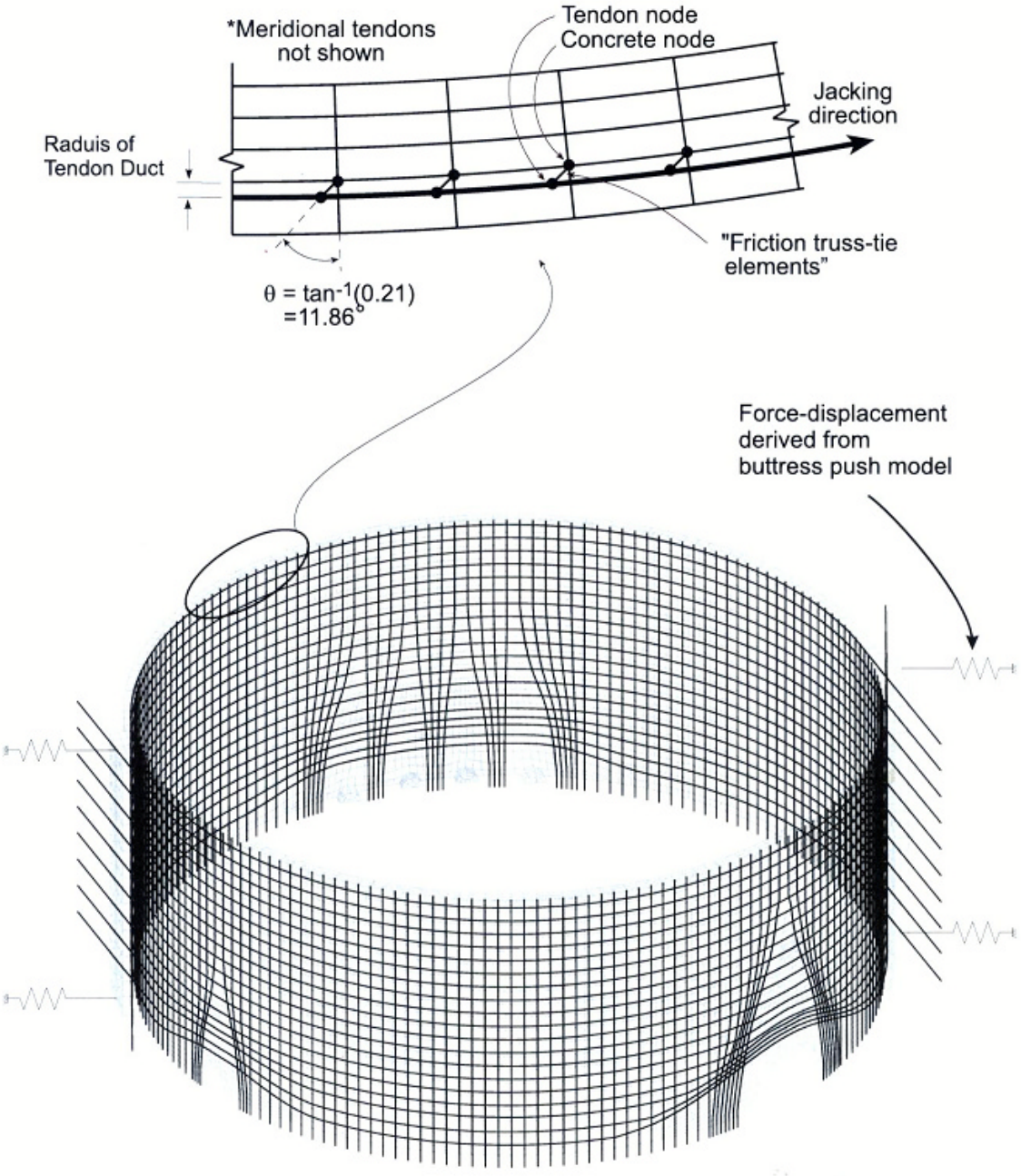

Figure 19. 3DCM Model; Added Buttress Springs; Tendon Friction Modeling

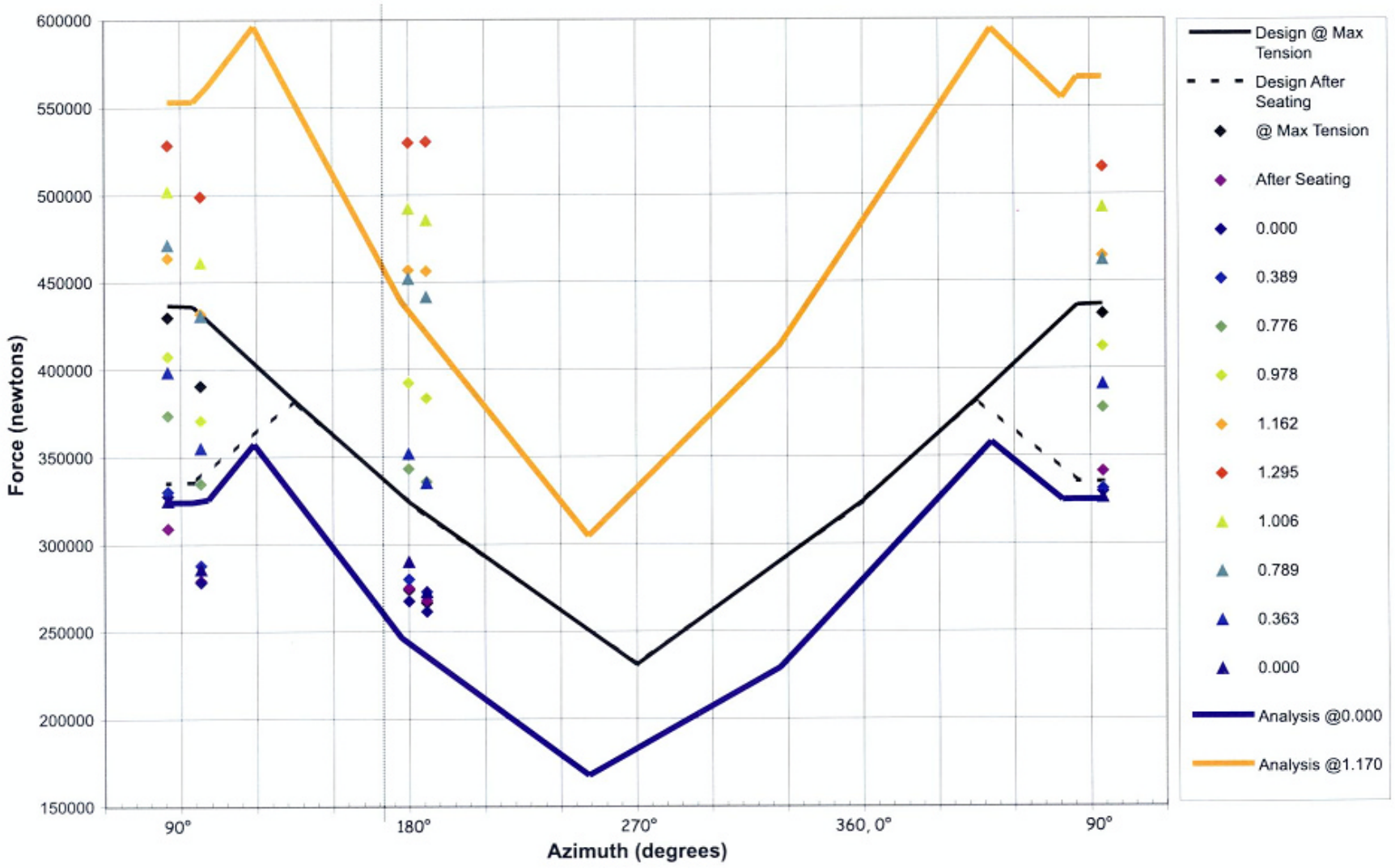

Figure 20. H35 Tendon Force Comparisons to Pretest

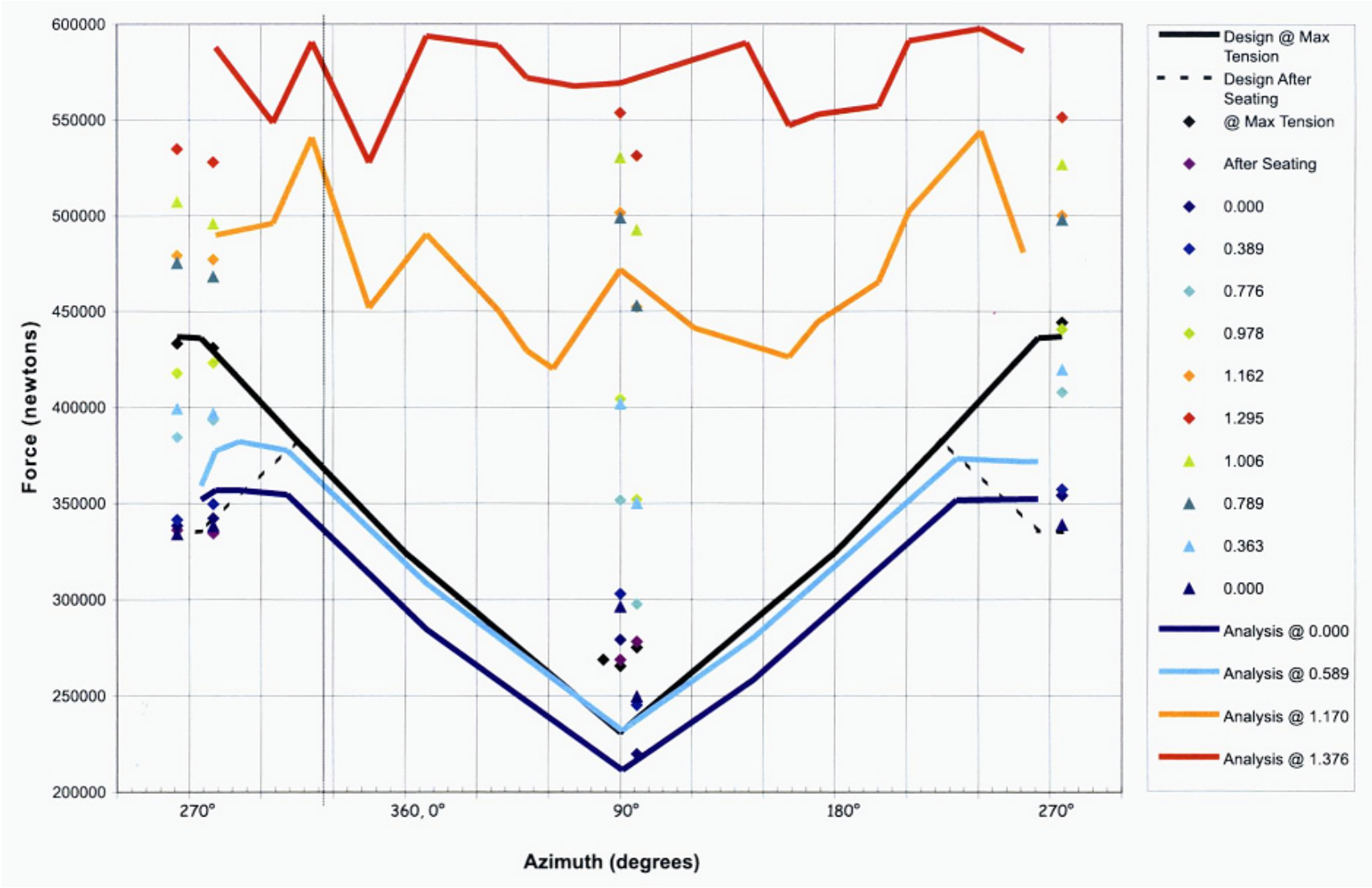

Figure 21. H53 Hoop Tendon Force Comparisons to Posttest Run #9 (with two-way friction)

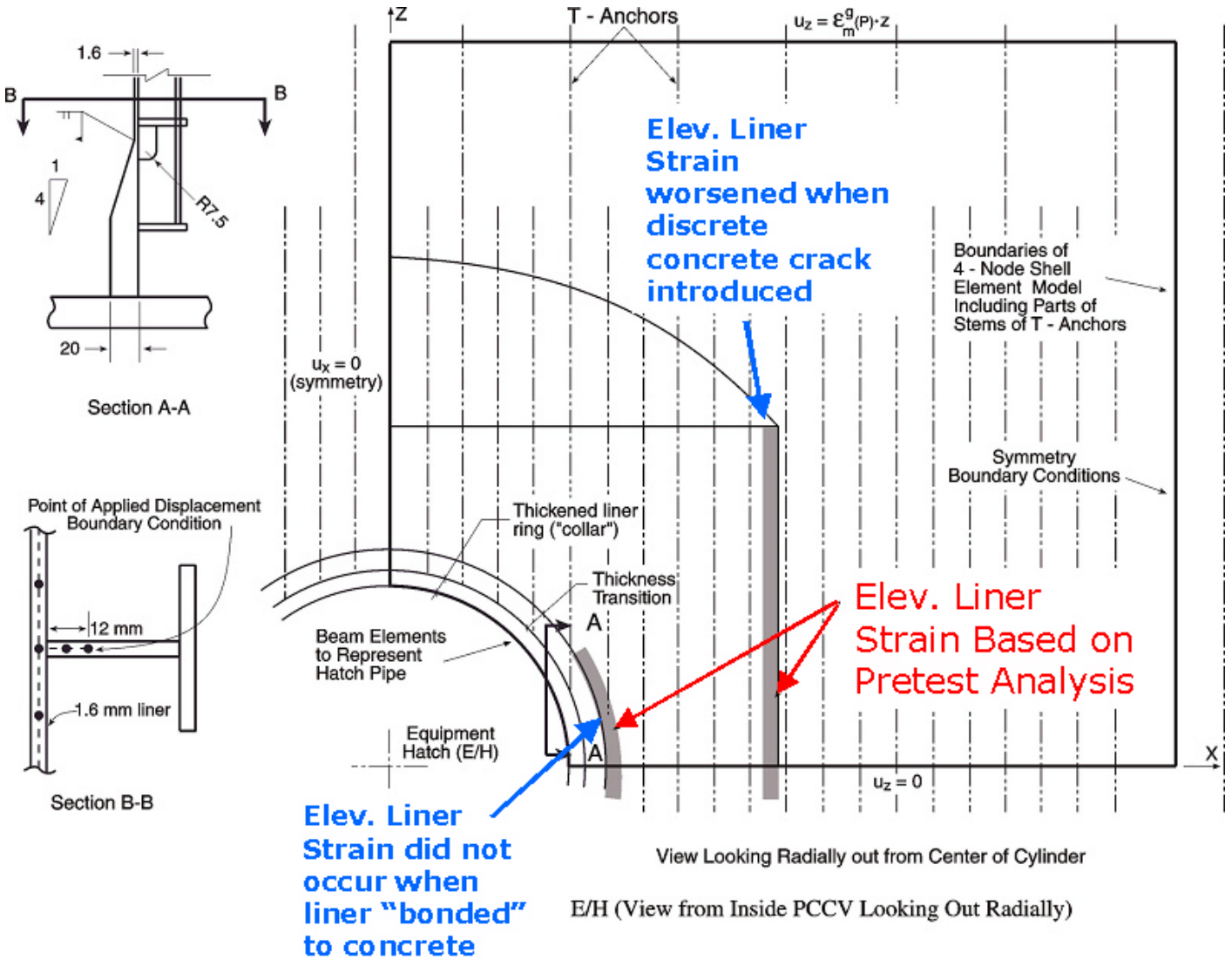

Figure 22. Details of Liner Modeling for Local E/H Model

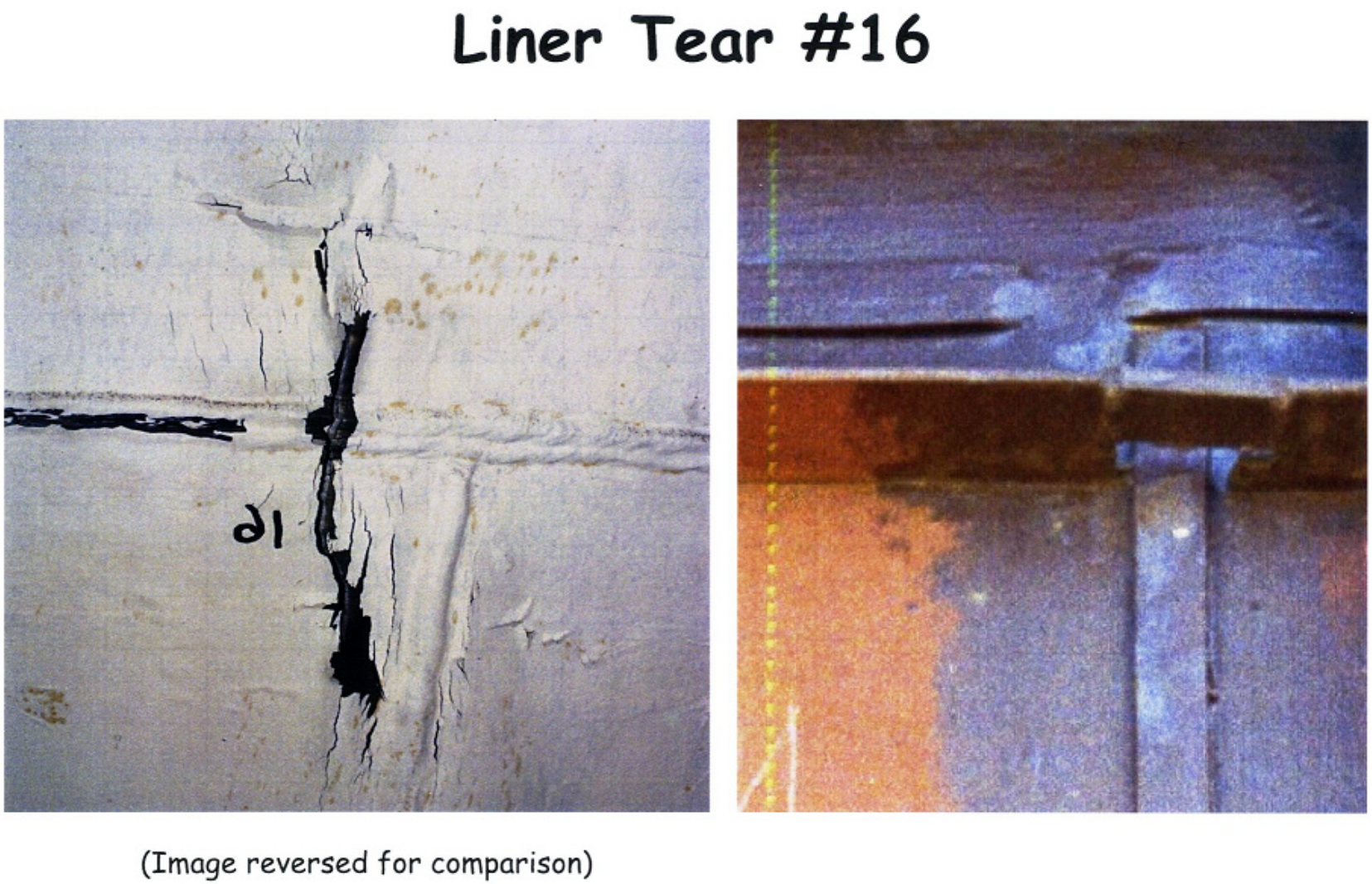

Figure 23. LST - Typical Tear Location

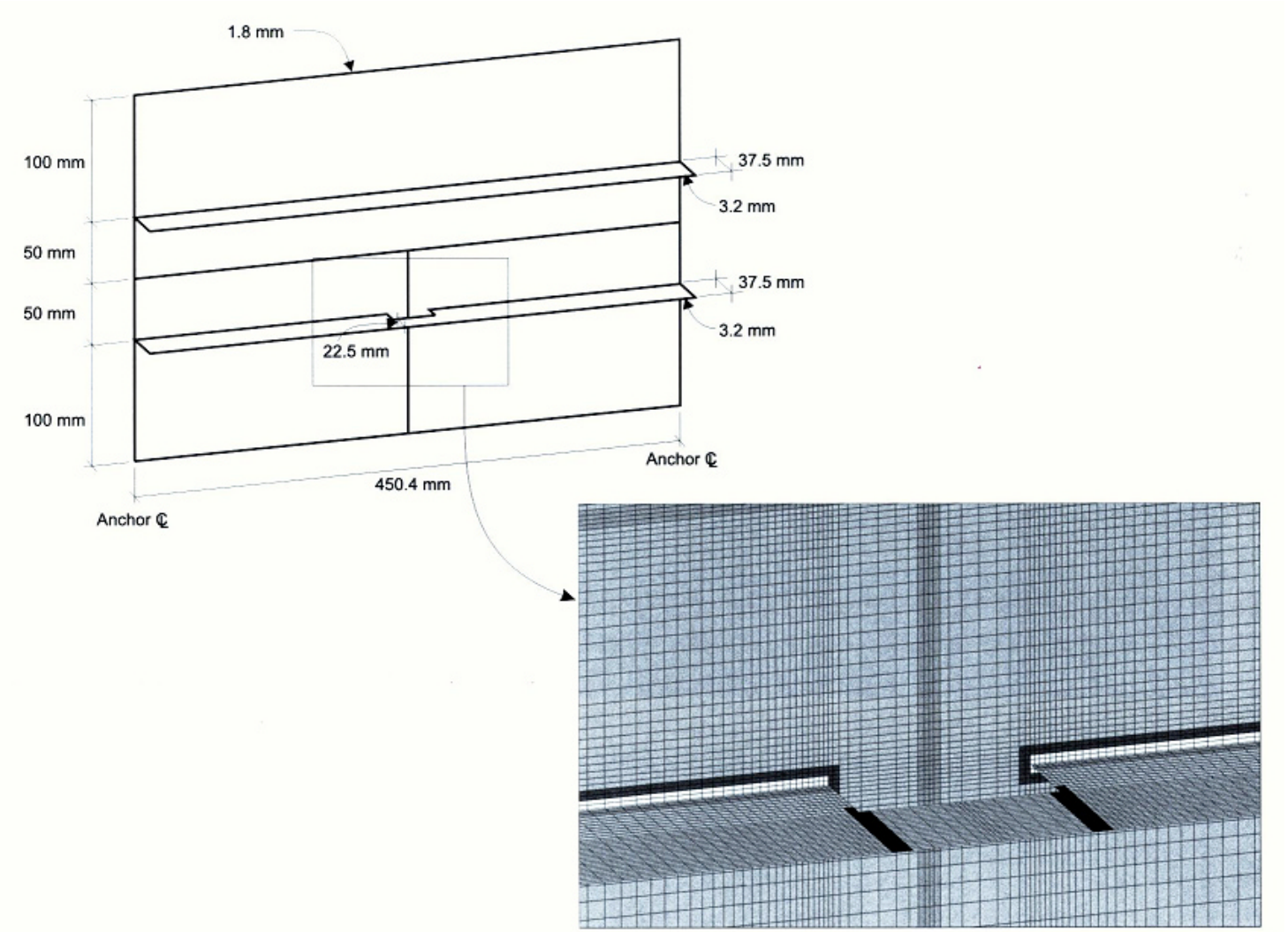

Figure 24. Liner Seam Model Geometric Details

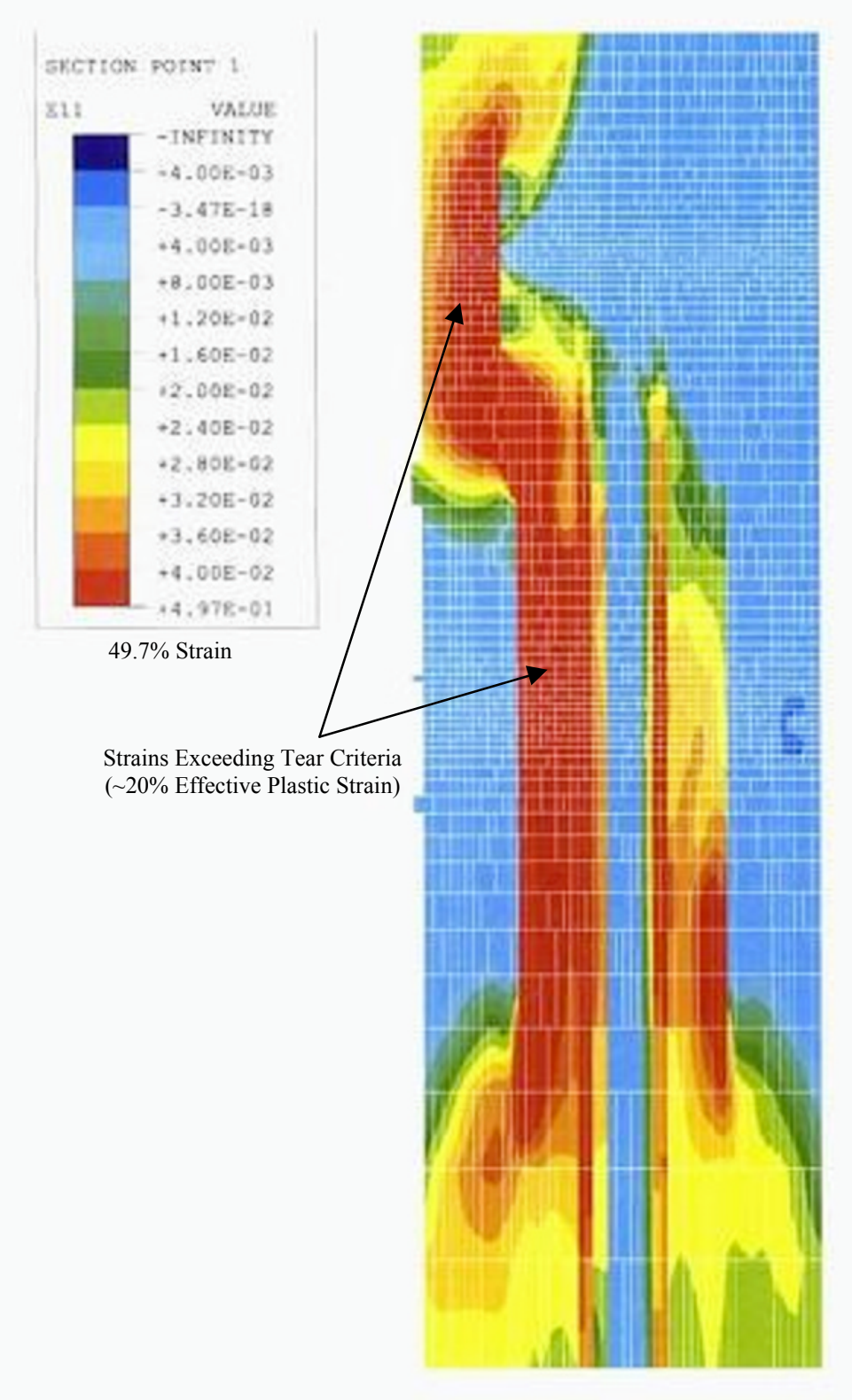

Figure 25. Local Liner Seam Analysis Model (Simulation of Tear 16)

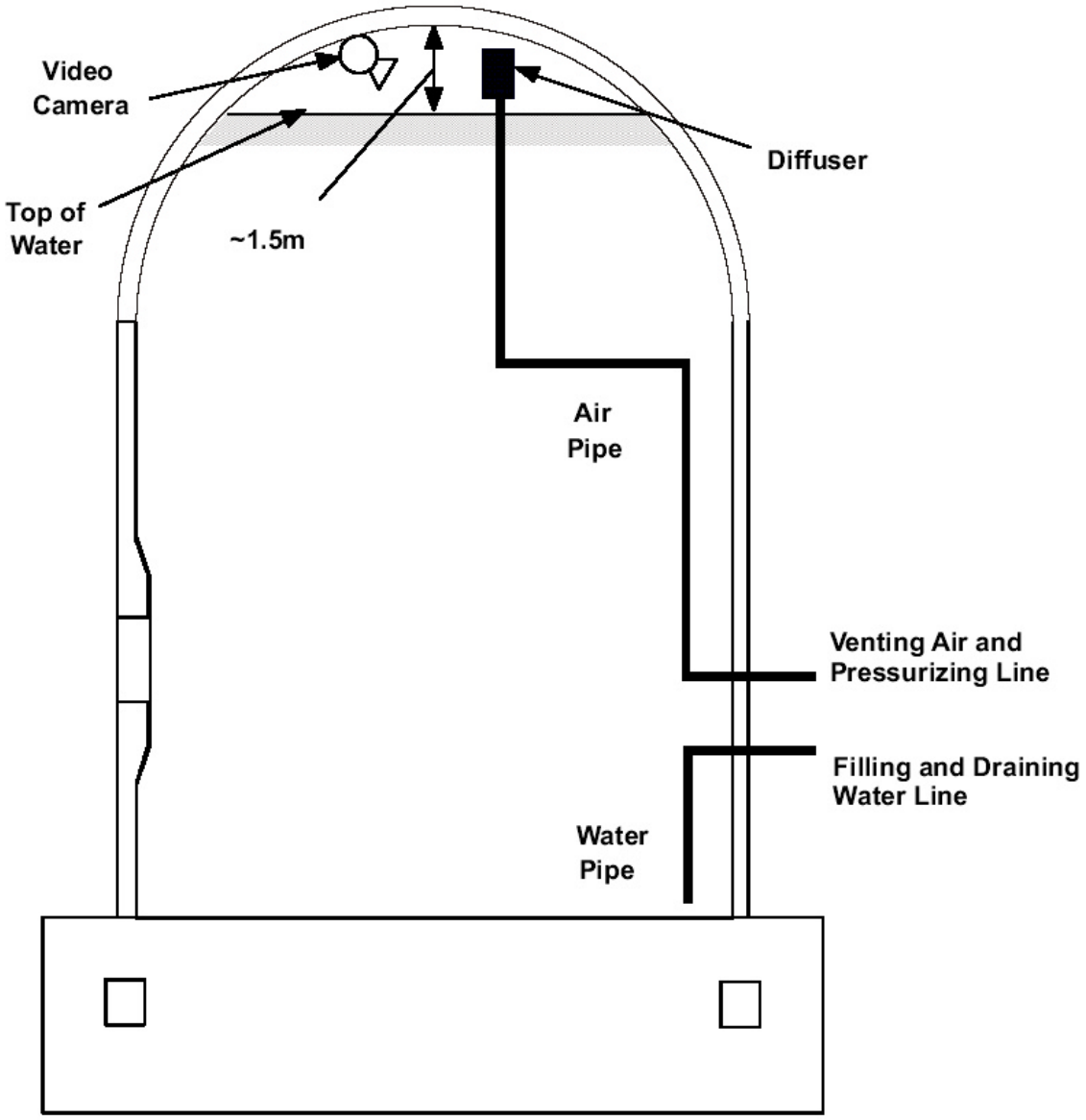

Figure 26. PCCV SFMT Pressurization Configuration

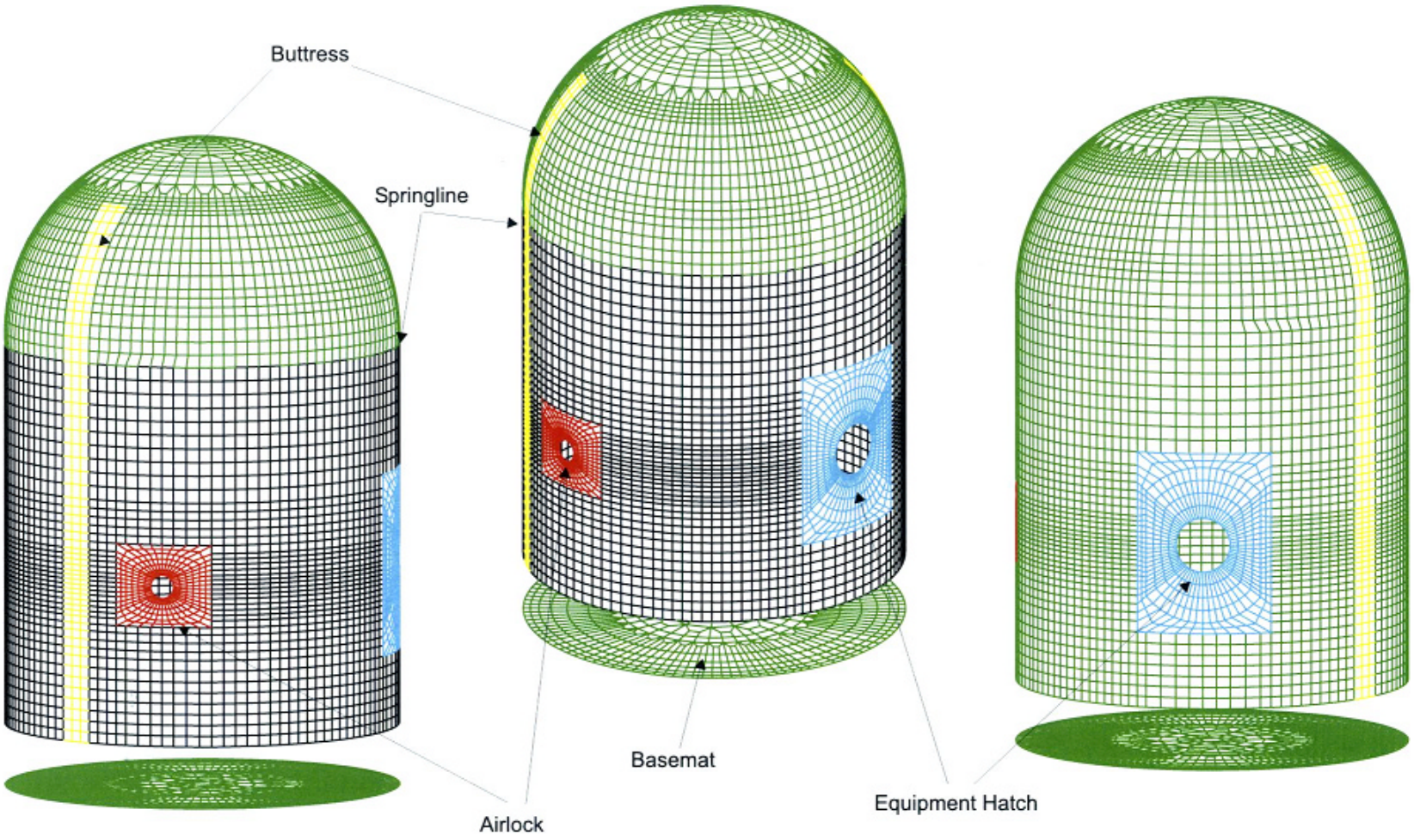

Figure 27. PCCV SFMT, 3D Global Shell Model

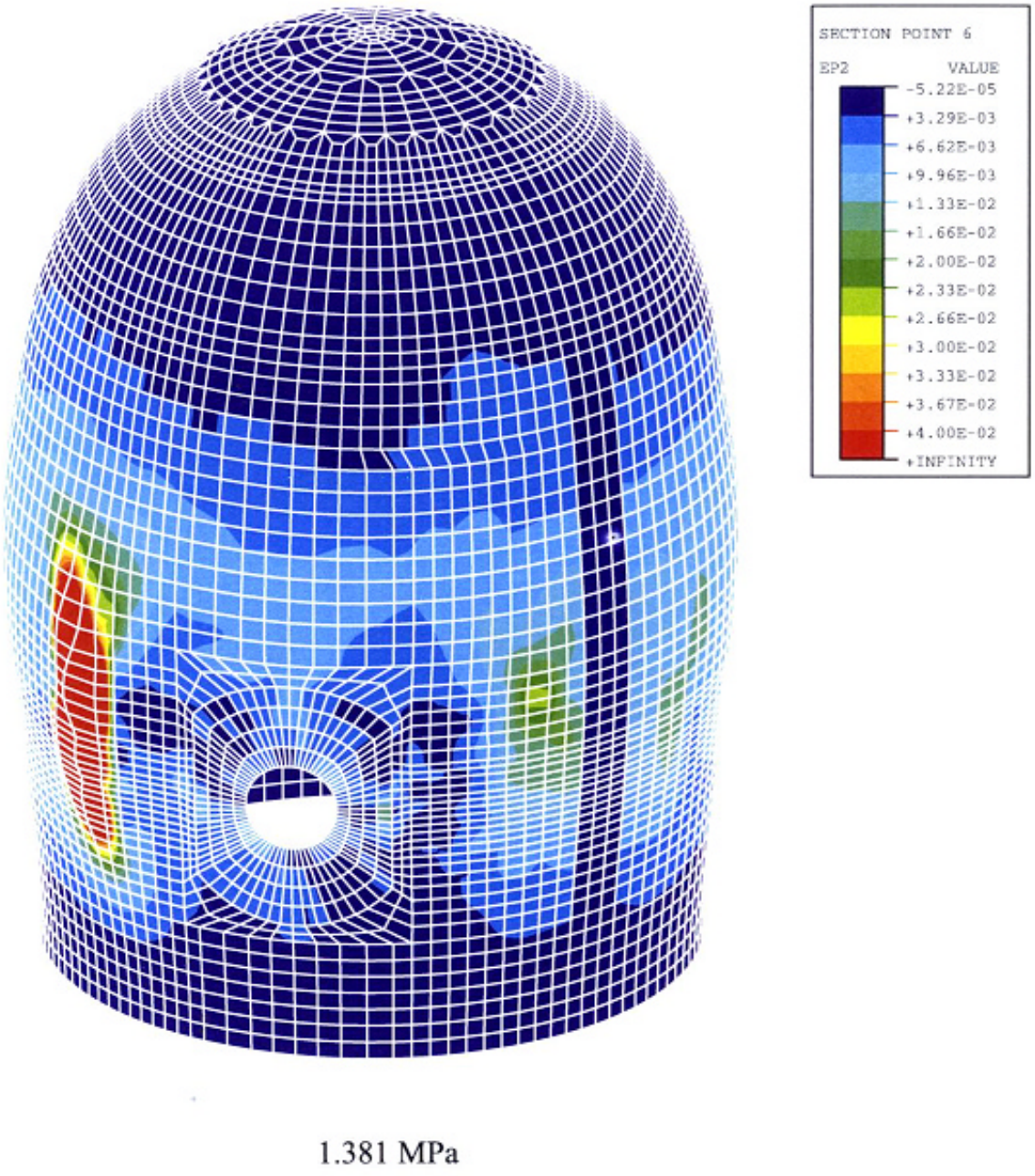

Figure 28. PCCV SFMT, 3D Global Shell Tendon Rupture Model. Concrete Maximum Principal Strain. For Pressure at 1.381 MPa ($3.51P_d$), Displacement x10.

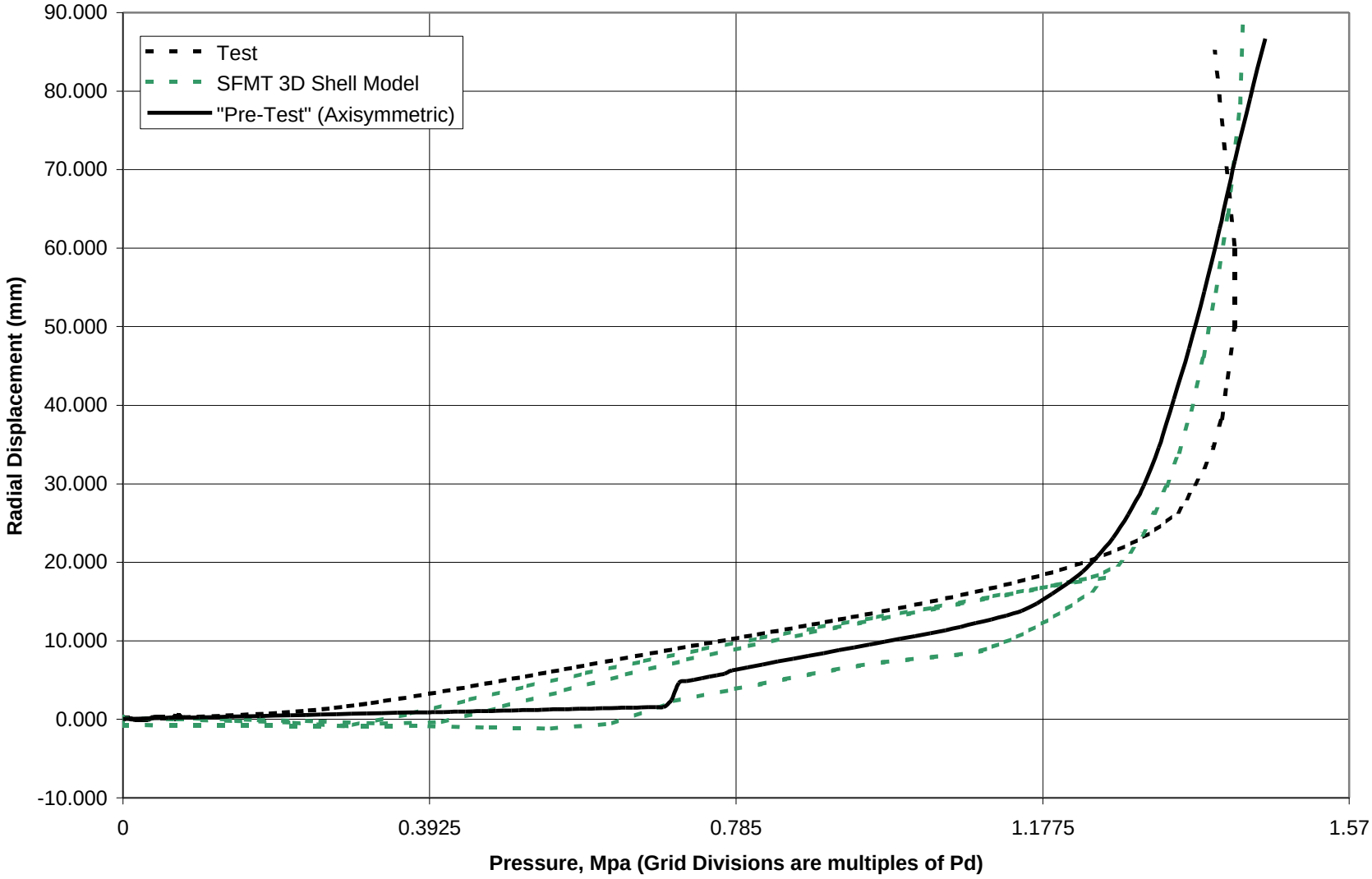

Figure 29. 3D Global Shell Model - Gage R-Z6-05 Comparison, Radial Displacement, 135 Degrees, Elevation 6.20m

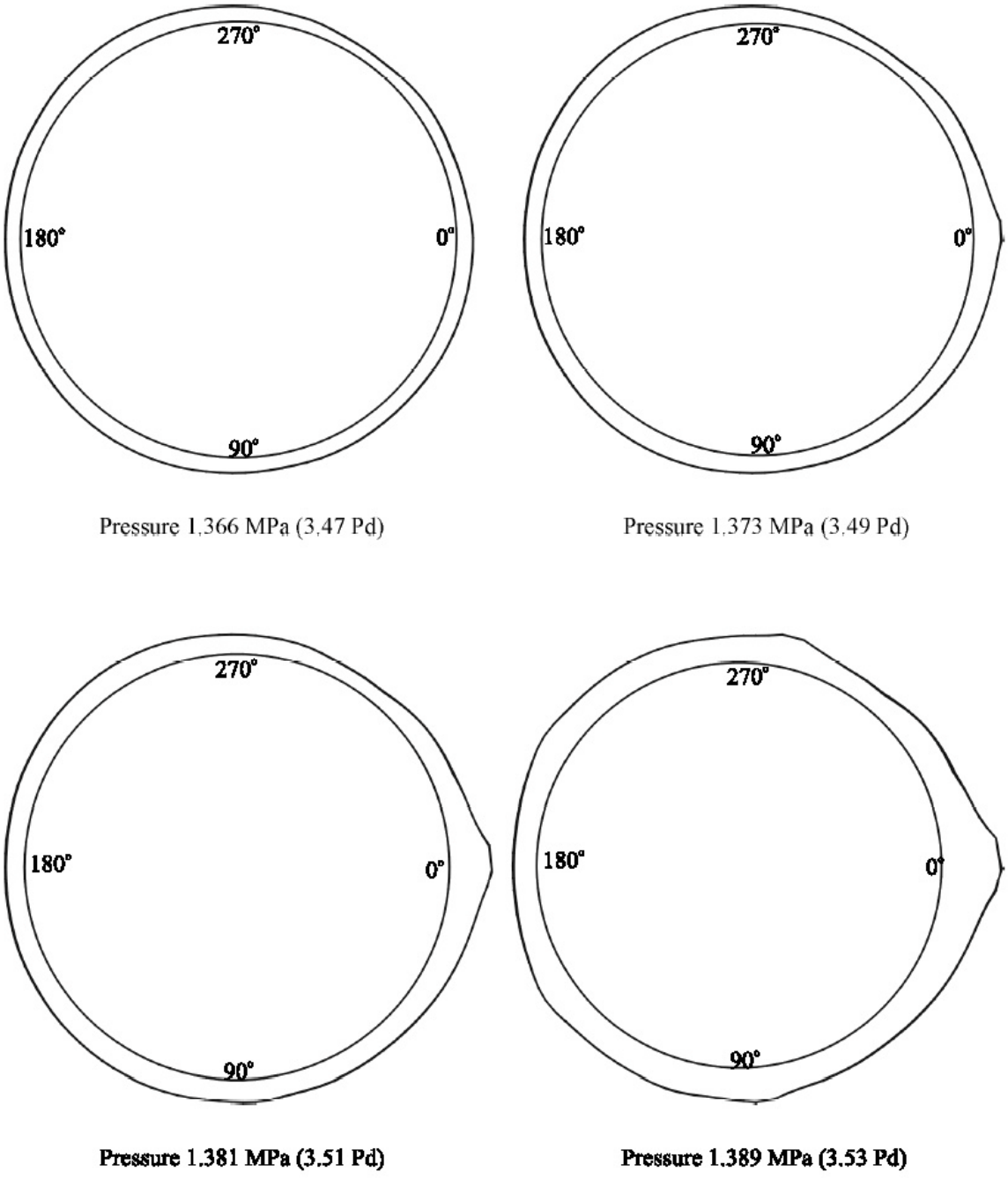

Figure 30. PCCV SFMT, 3D Global Shell Tendon Rupture Model. Deformed Shape. For Elevation of 6.5m. Displacement x10.

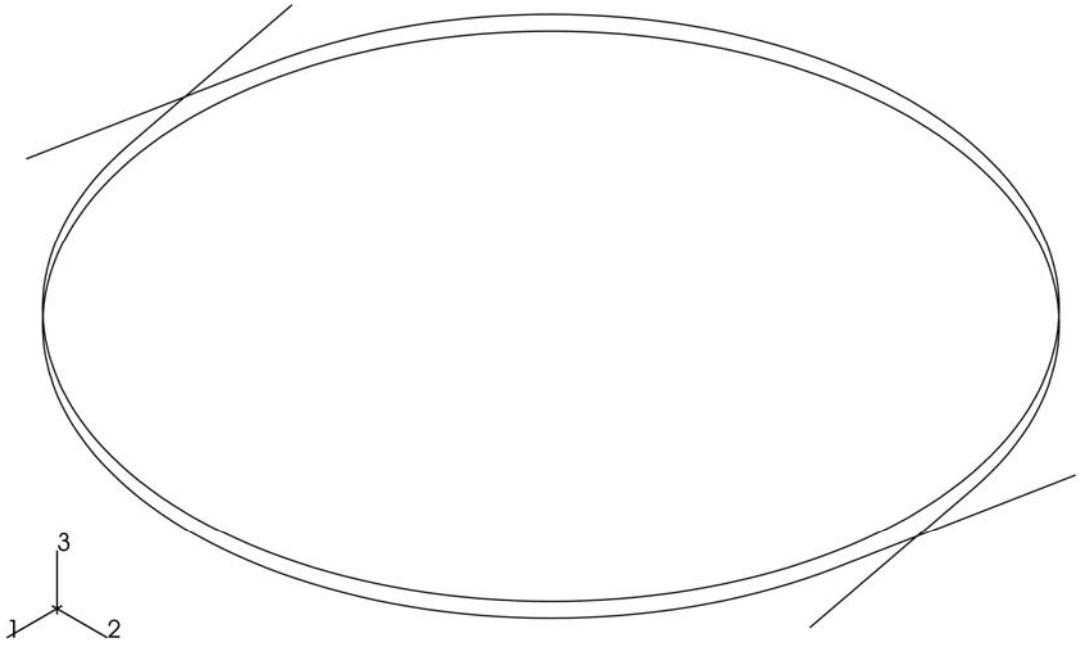

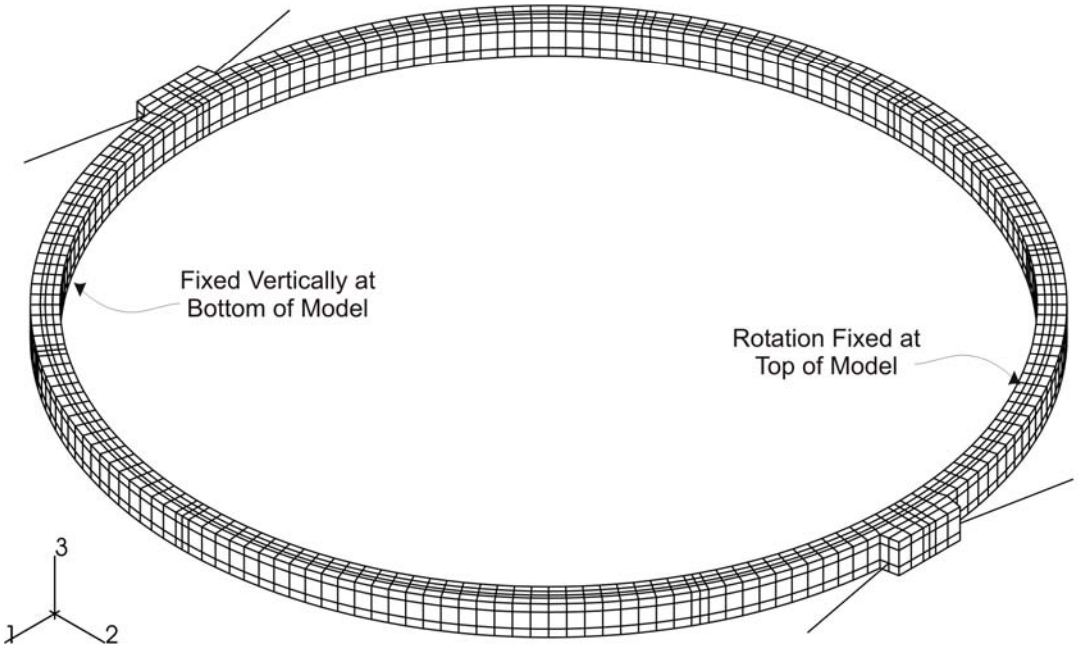

Figure 31. Ring Model Tendons and Boundary Conditions

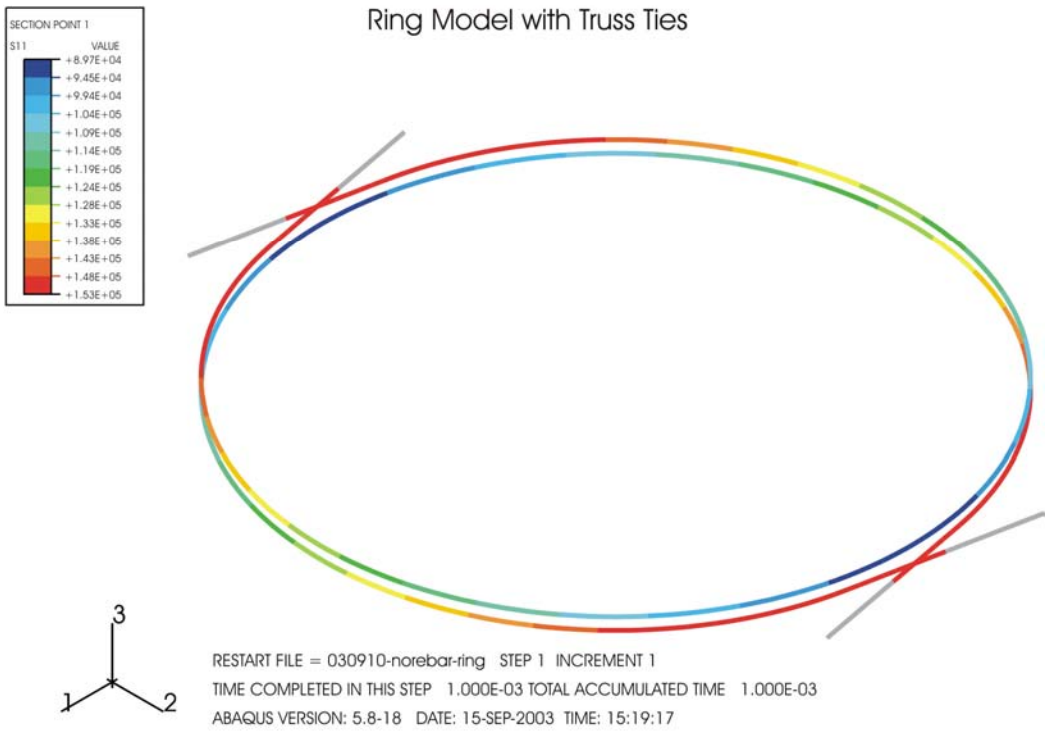

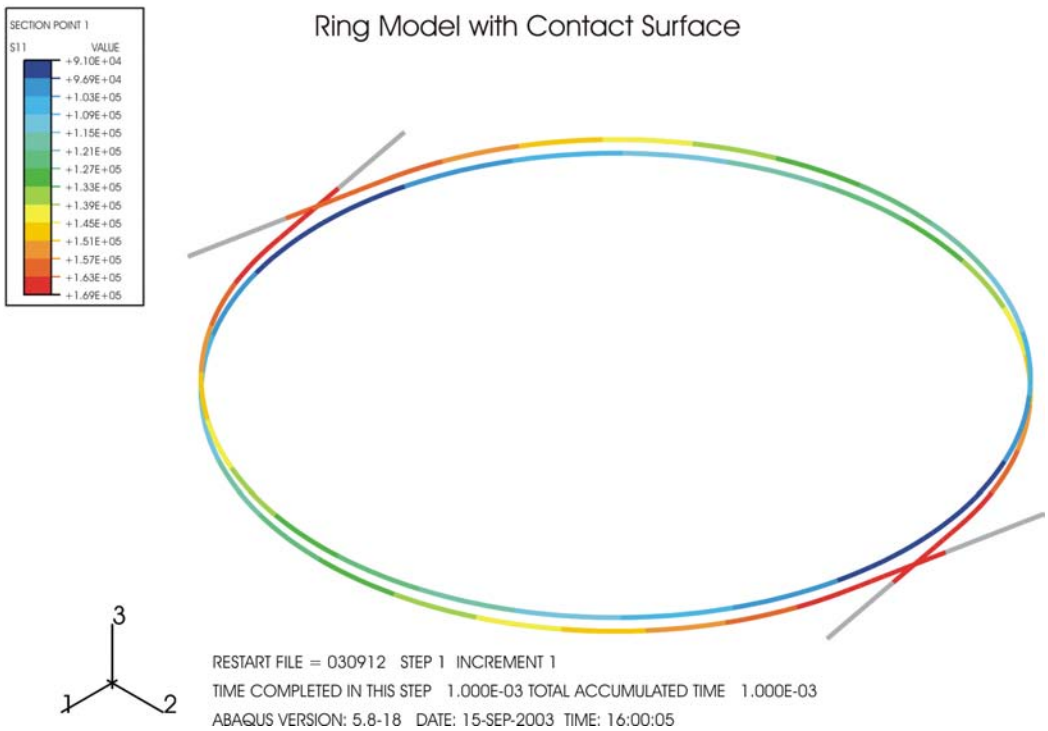

Figure 32. Tendon Stress Contour (Initial Prestress)

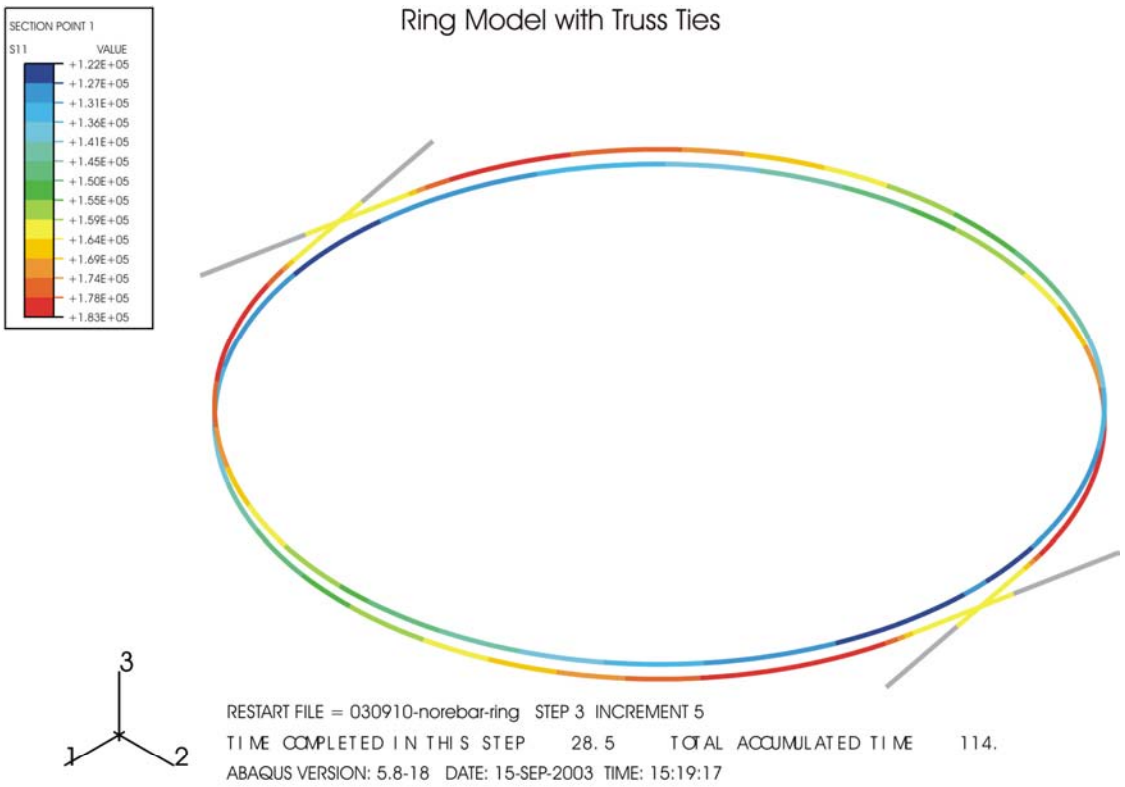

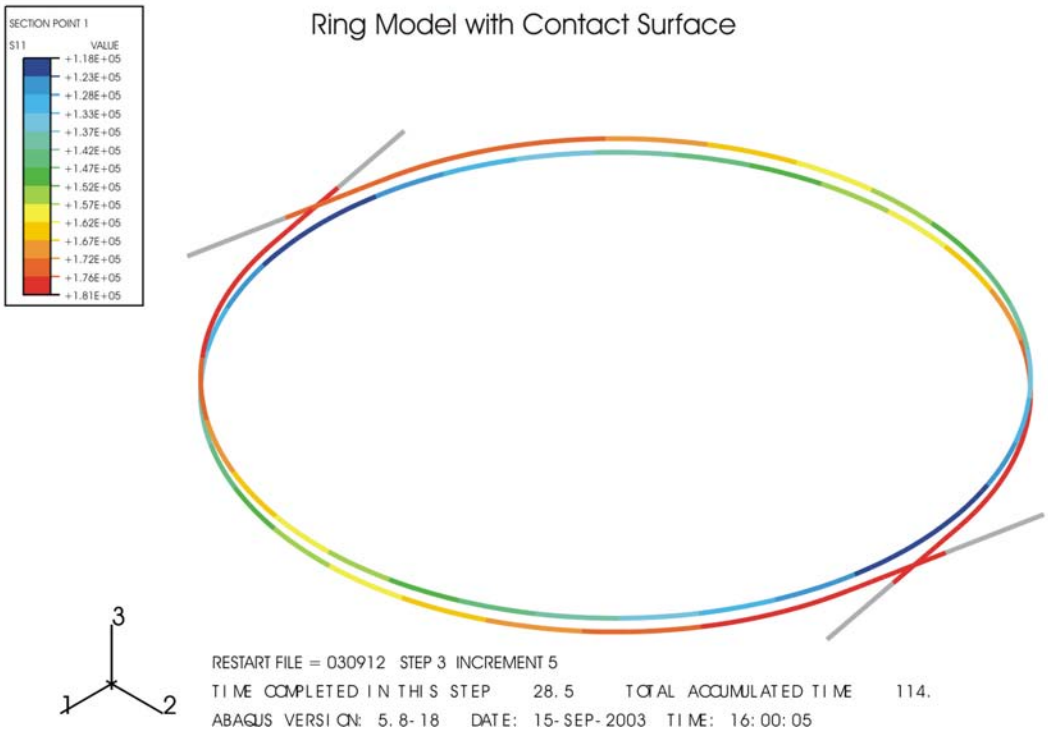

Figure 33. Tendon Stress Contour (Pressure=2.0P_d)

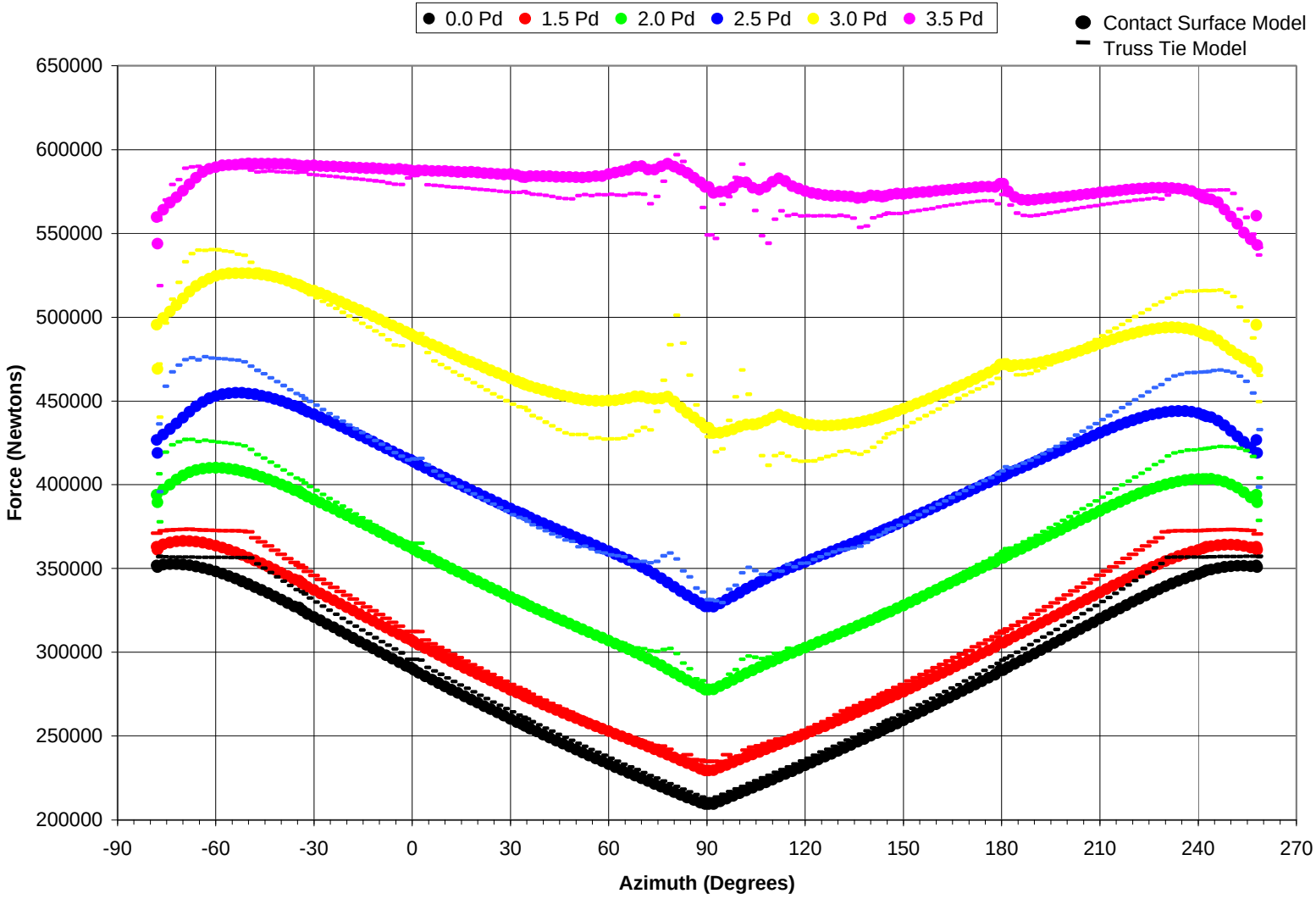

Figure 34. Comparison of Tendon Modeling in Ring Model for Tendon H68

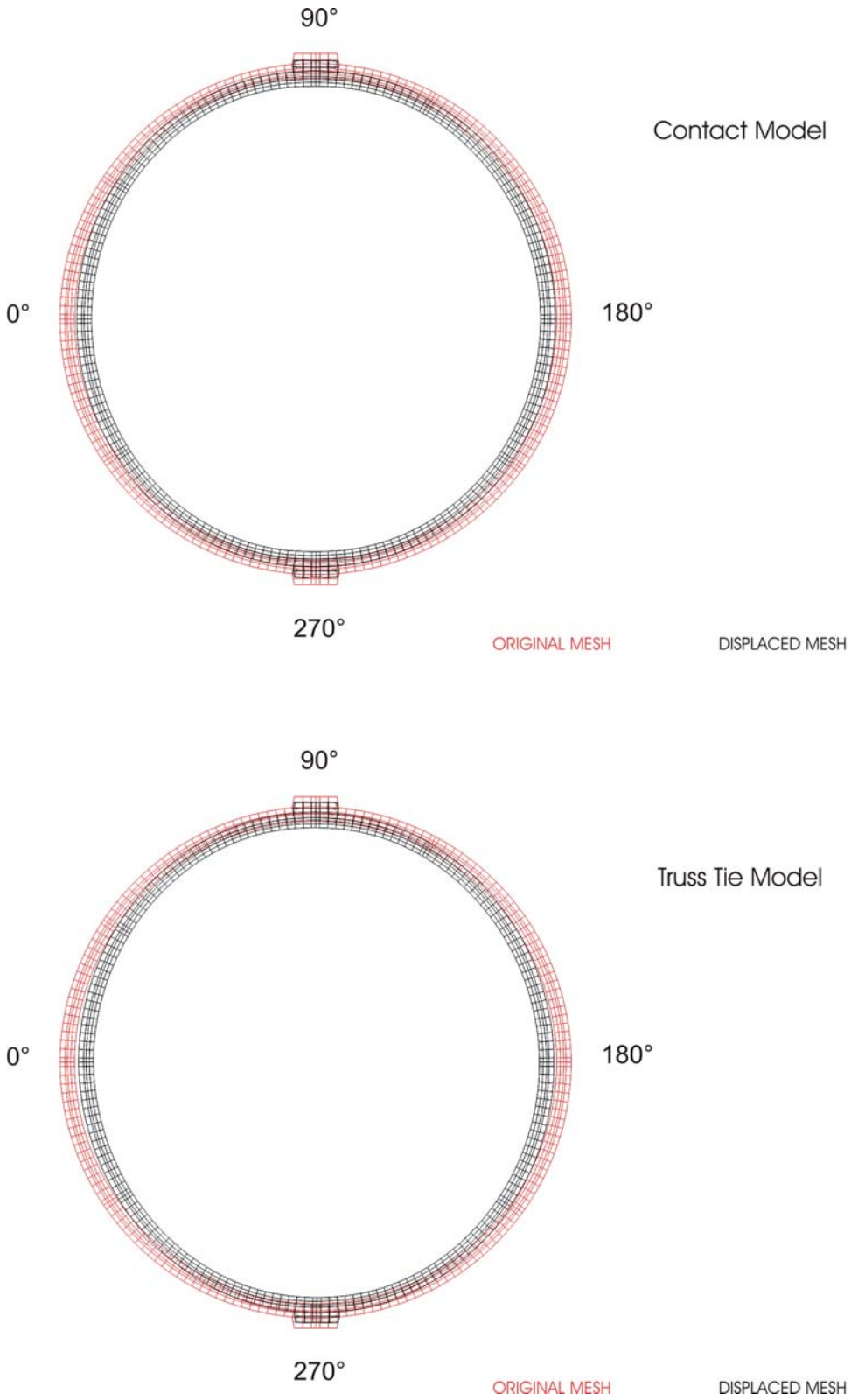

Figure 35. Comparison of Deformed Shapes (displ. x 200) Using Tendon Friction Truss Ties vs. the Contact Surface Model at P=0P_d; After Prestress

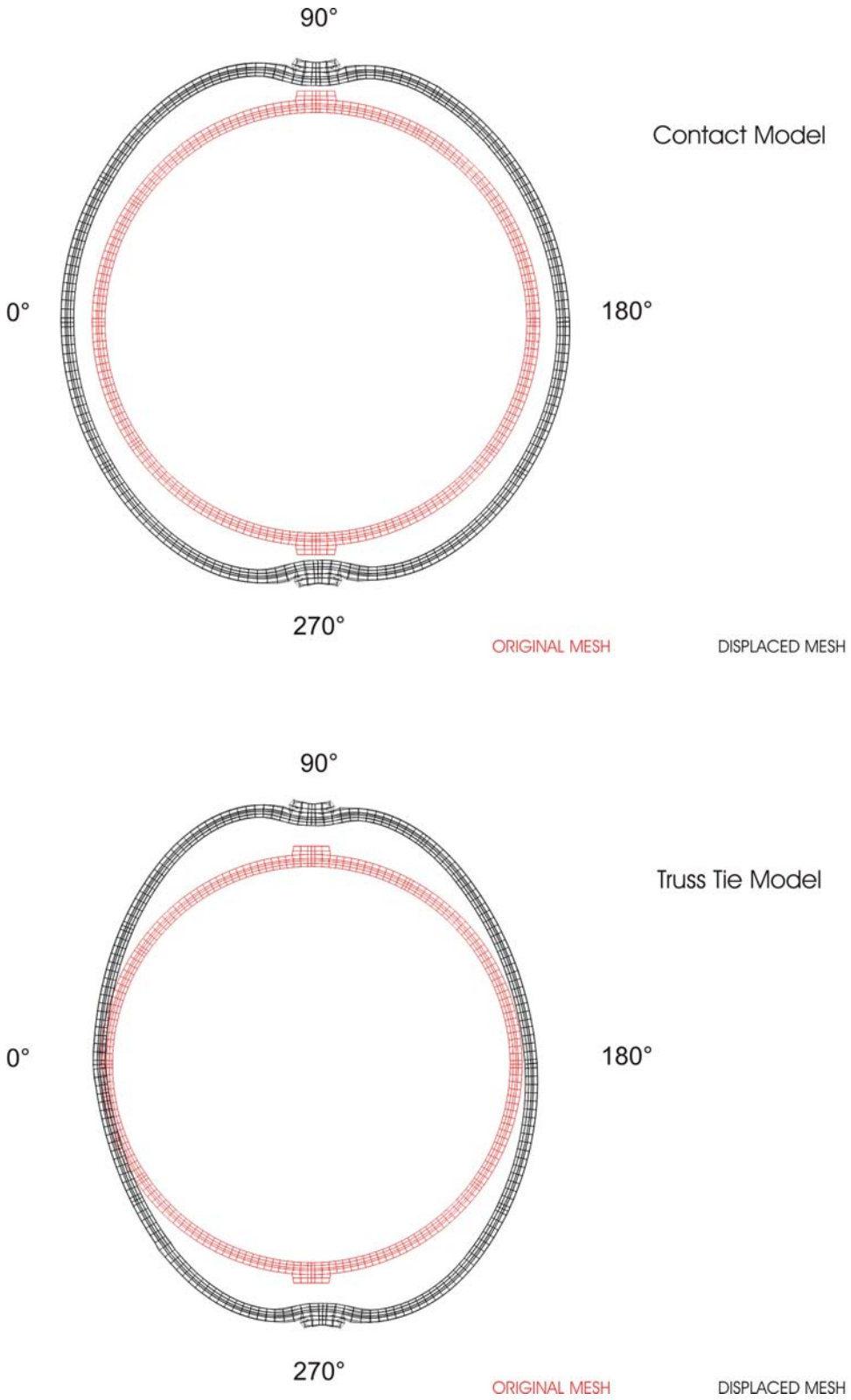

Figure 36. Comparison of Deformed Shapes (displ. x 200) Using Tendon Friction Truss Ties vs. the Contact Surface Model at P=2.0P_d

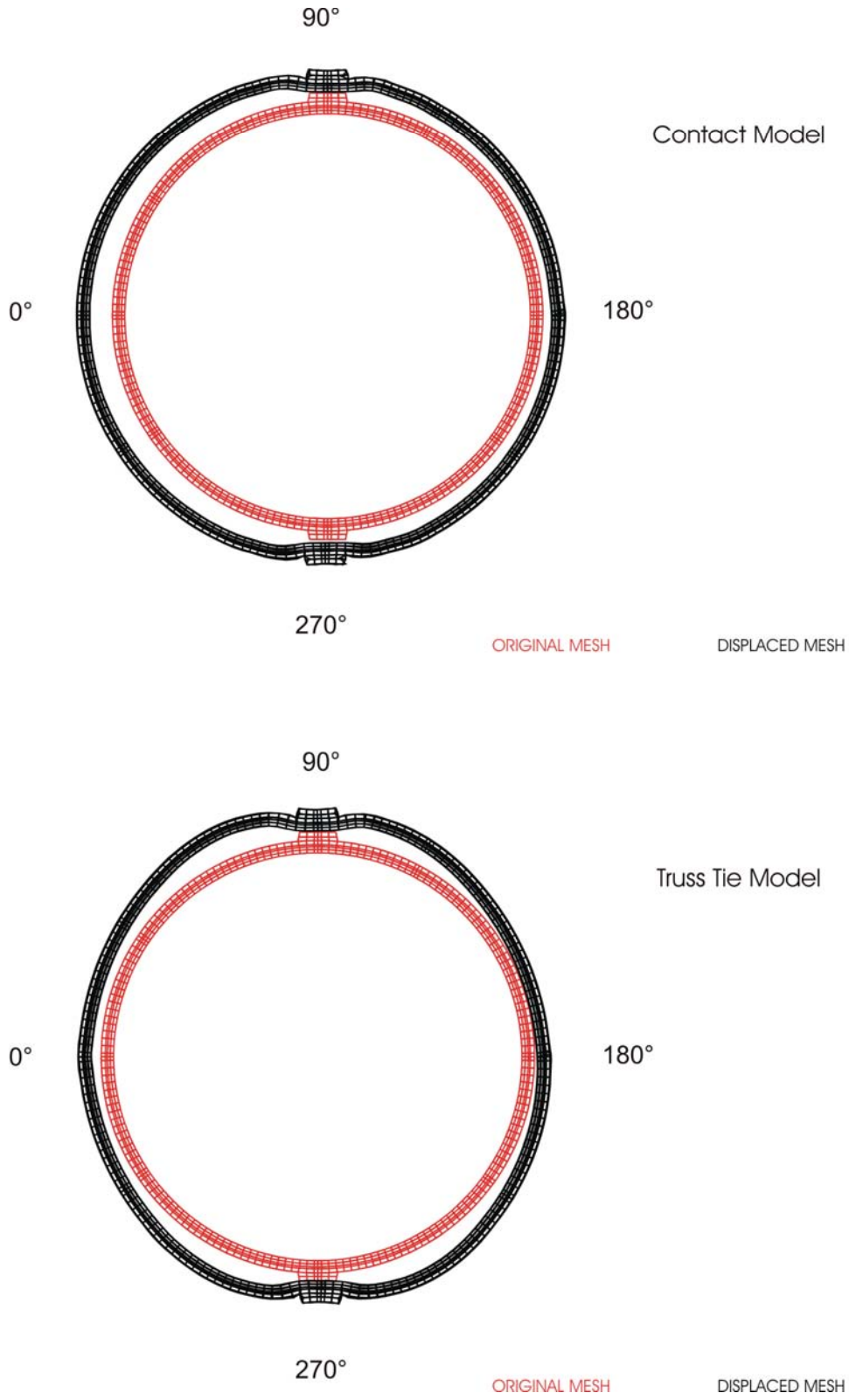

Figure 37. Comparison of Deformed Shapes (displ. x 20) Using Tendon Friction Truss Ties vs. the Contact Surface Model at $P=3.5P_d$

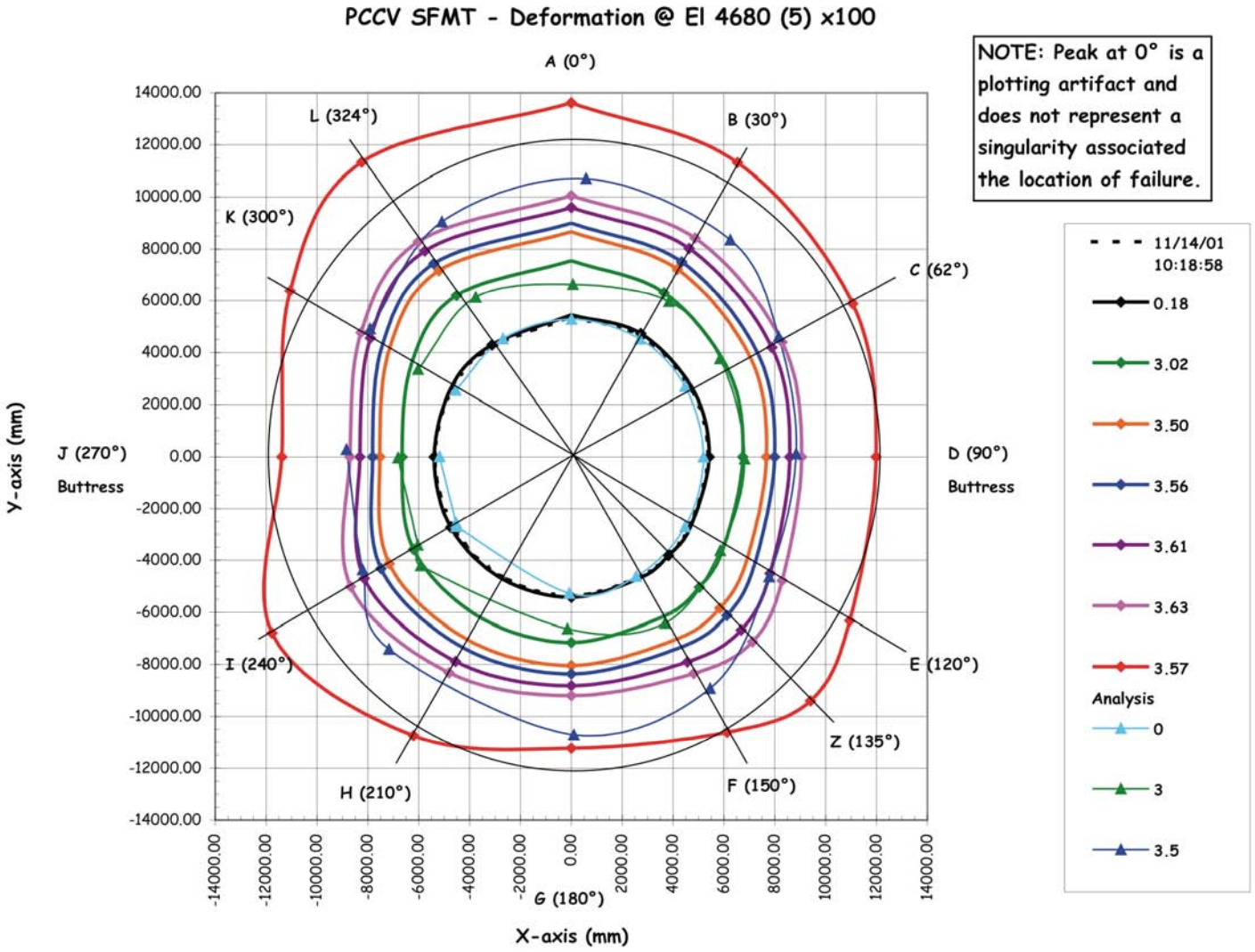

Figure 38. SFMT Deformation versus Ring Model Deformation

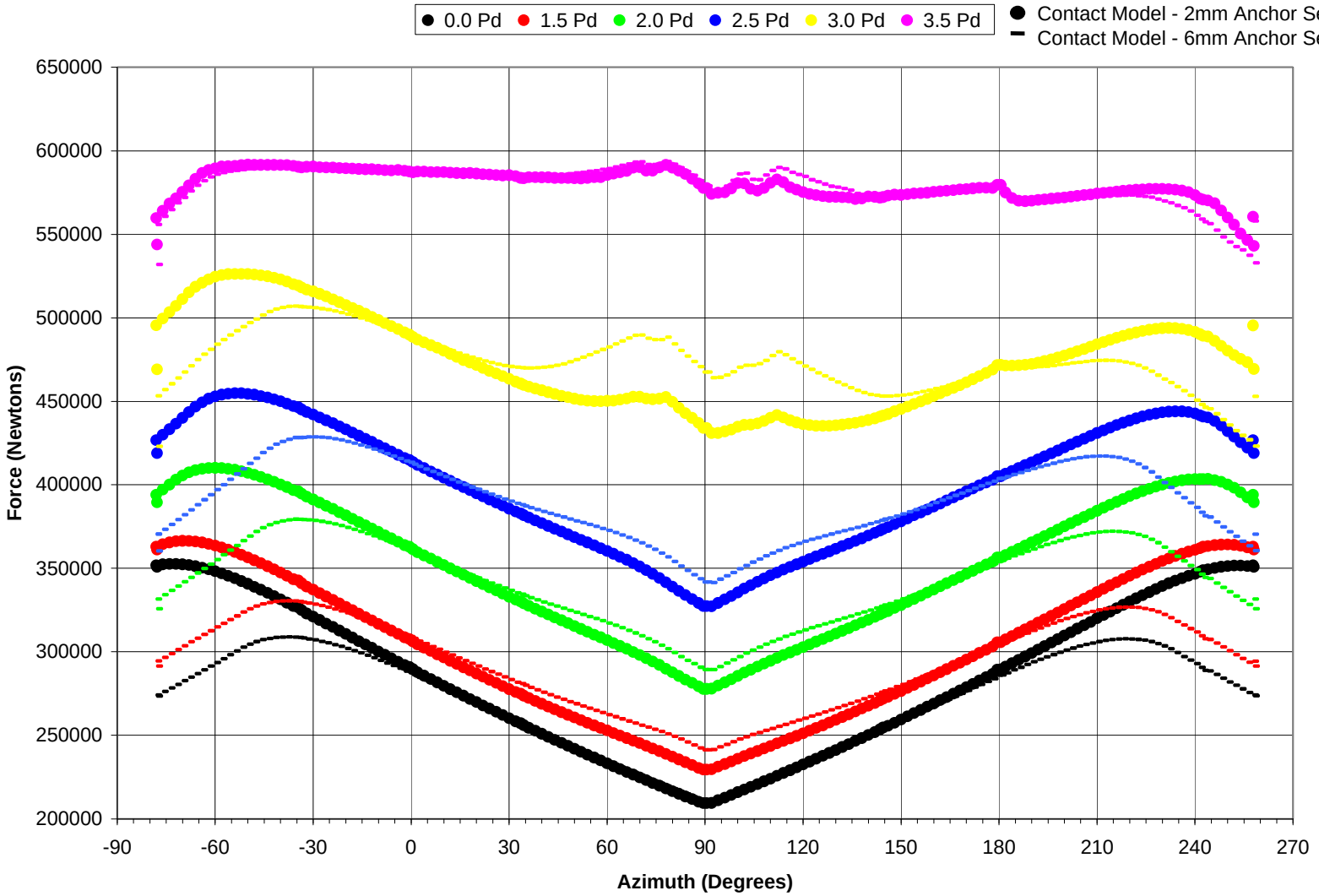

Figure 39. Comparison of Tendon Modeling in Ring Model for Tendon H68

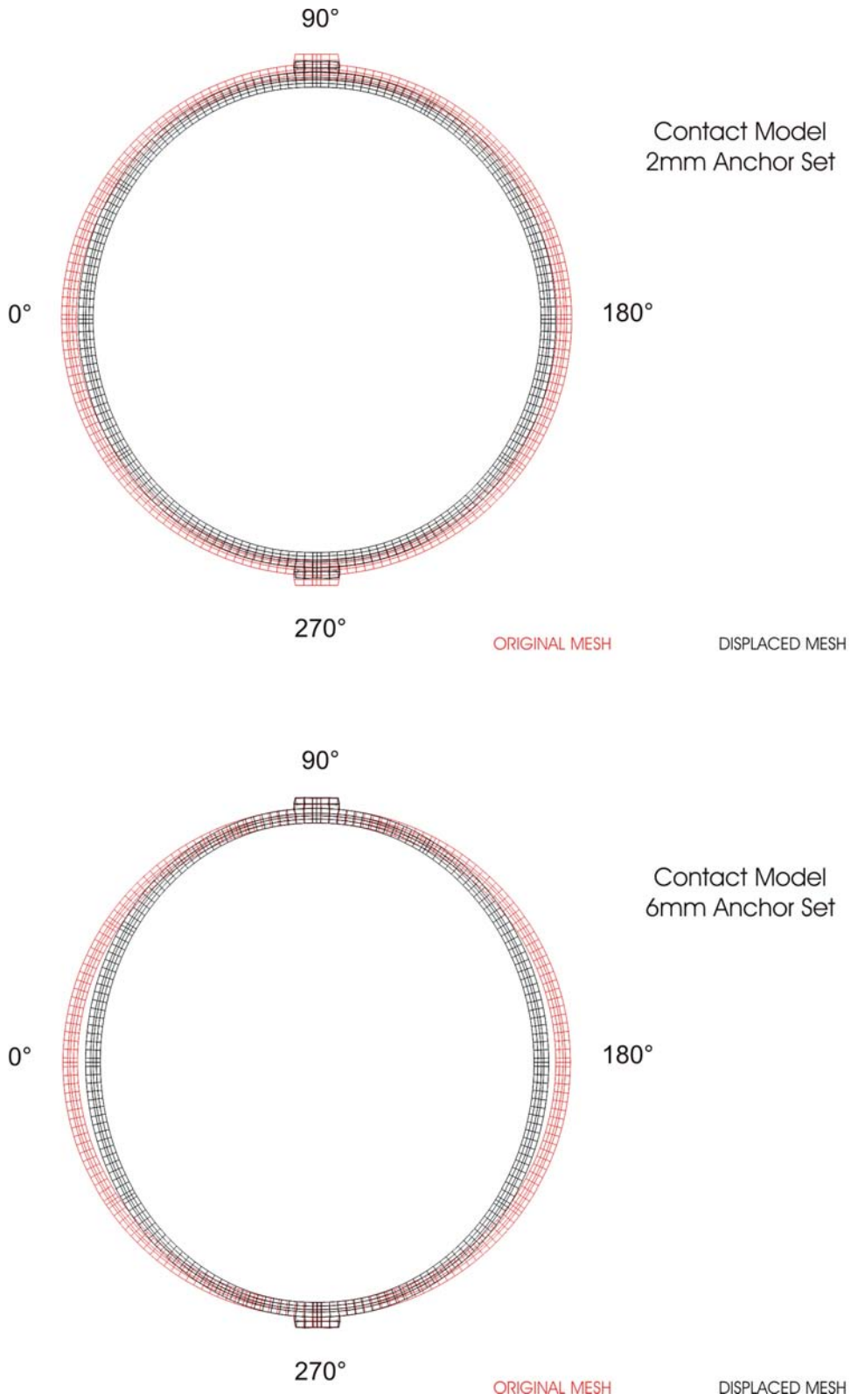

Figure 40. Comparison of Deformed Shapes (displ. x 200) Using Contact Surface Models with 2mm and 6mm of Anchor Set; After Prestress

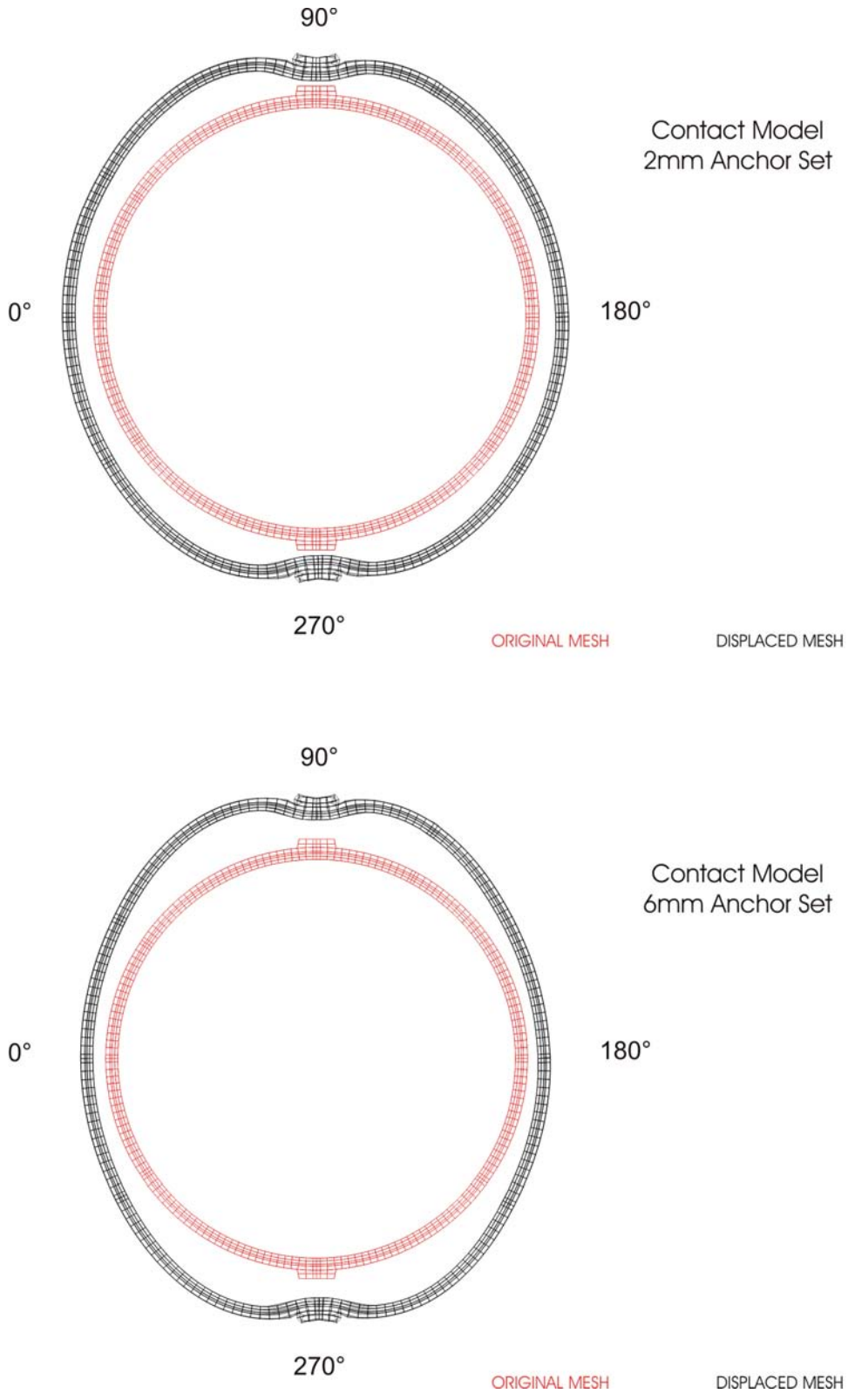

Figure 41. Comparison of Deformed Shapes (displ. x 200) Using Contact Surface Models with 2mm and 6mm of Anchor Set; P=2.0P_d

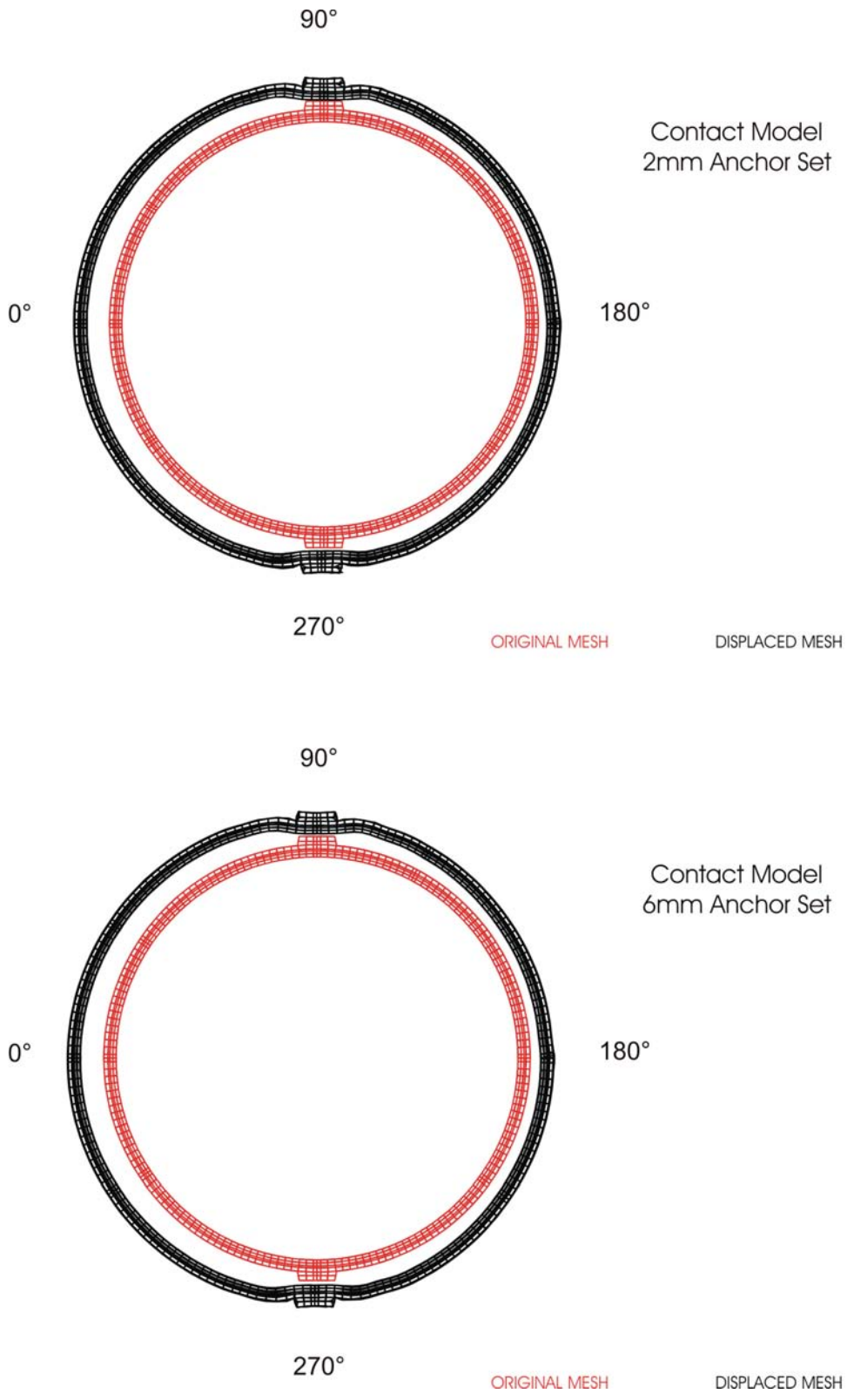

Figure 42. Comparison of Deformed Shapes (displ. x 20) Using Contact Surface Models with 2mm and 6mm of Anchor Set; P=3.5P_d

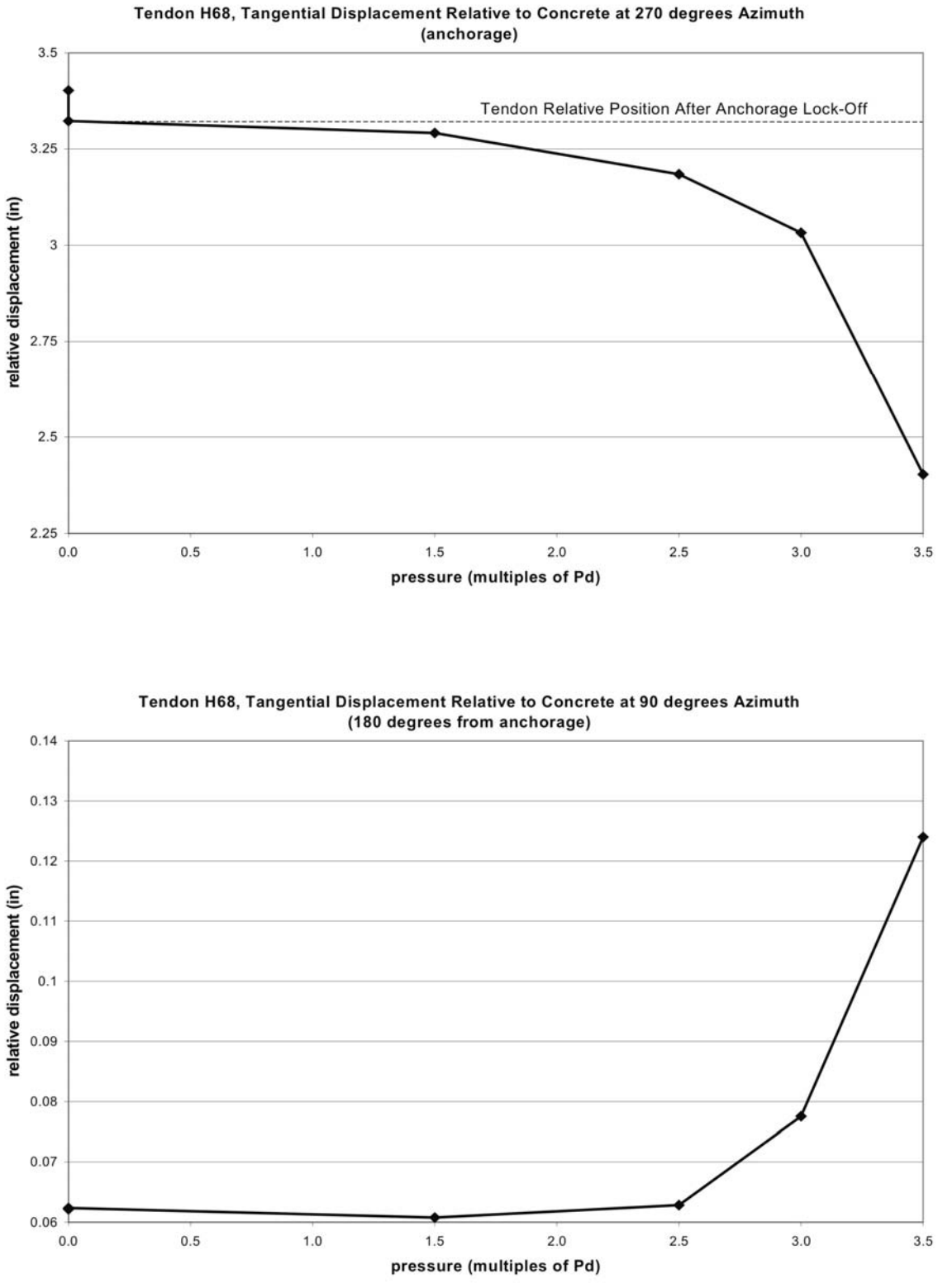

Figure 43. Tendon H68 Relative Displacement, Contact Model with 2mm Anchor Set

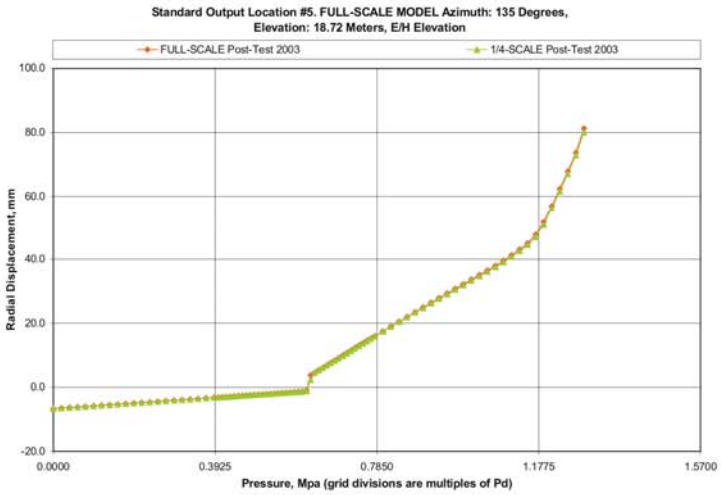

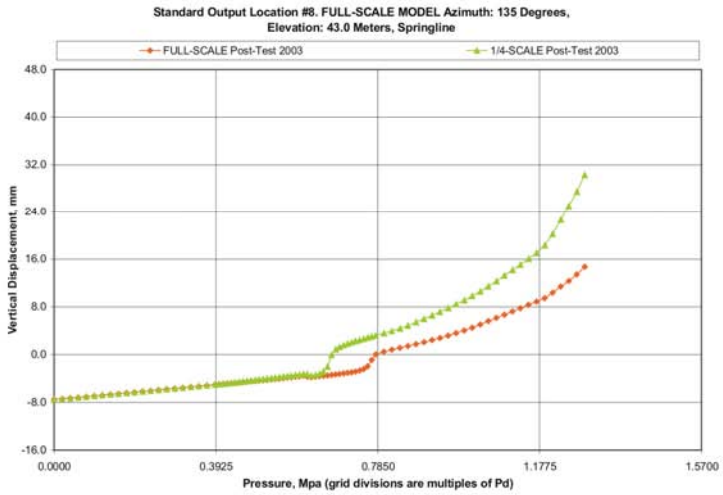

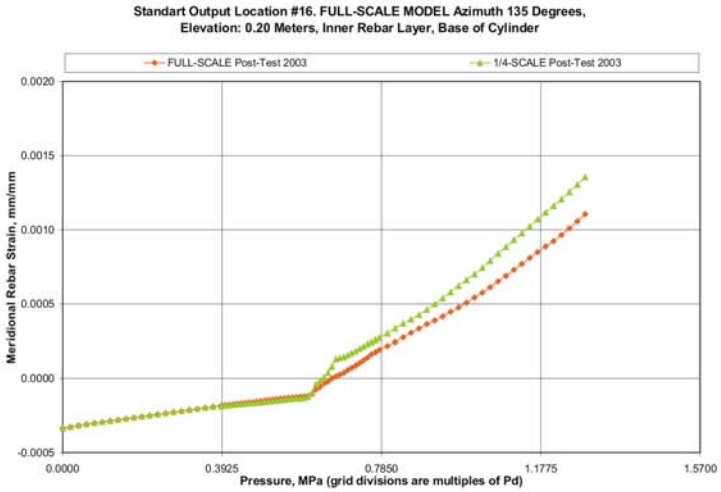

Figure 44. 1/4-Scale vs. Full-Scale Model Comparison at Standard Output Locations 5, 8 and 16

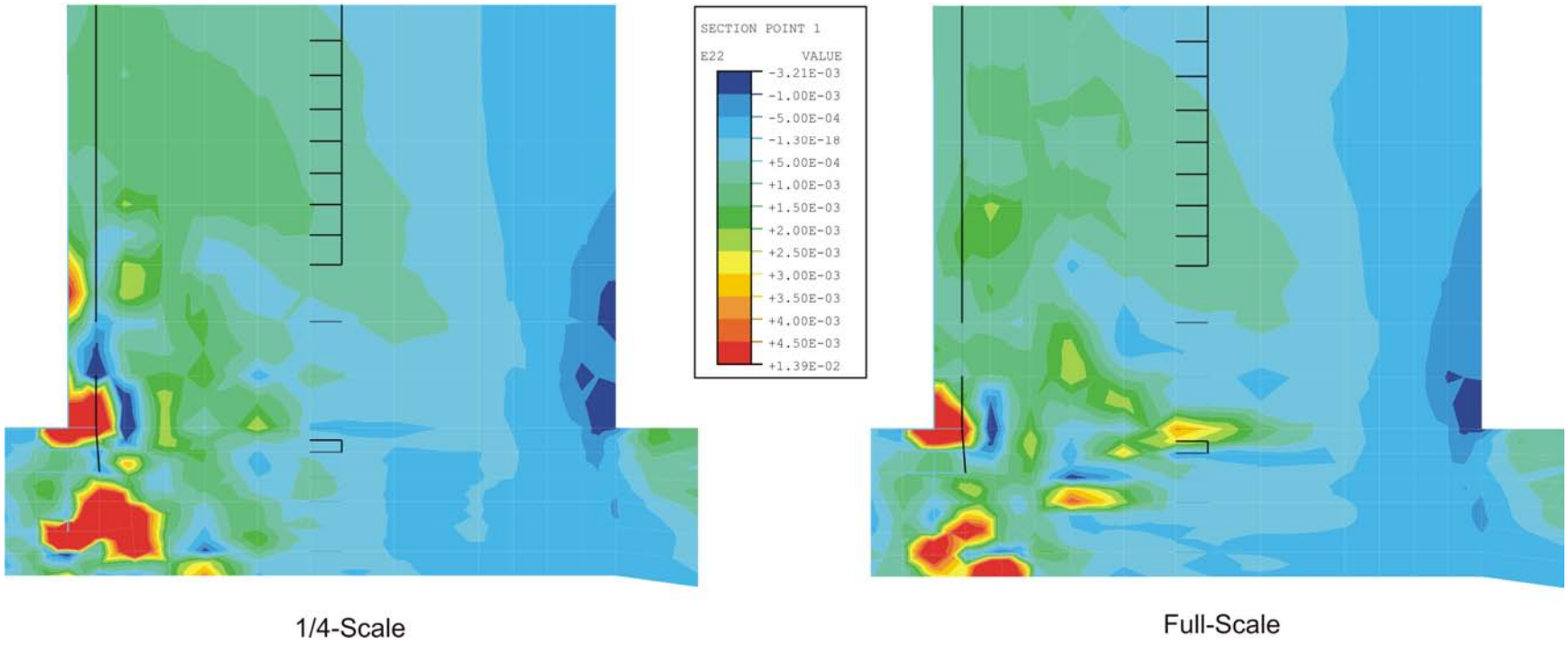

Figure 45. 1/4-Scale vs. Full-Scale Vertical Strain Comparison

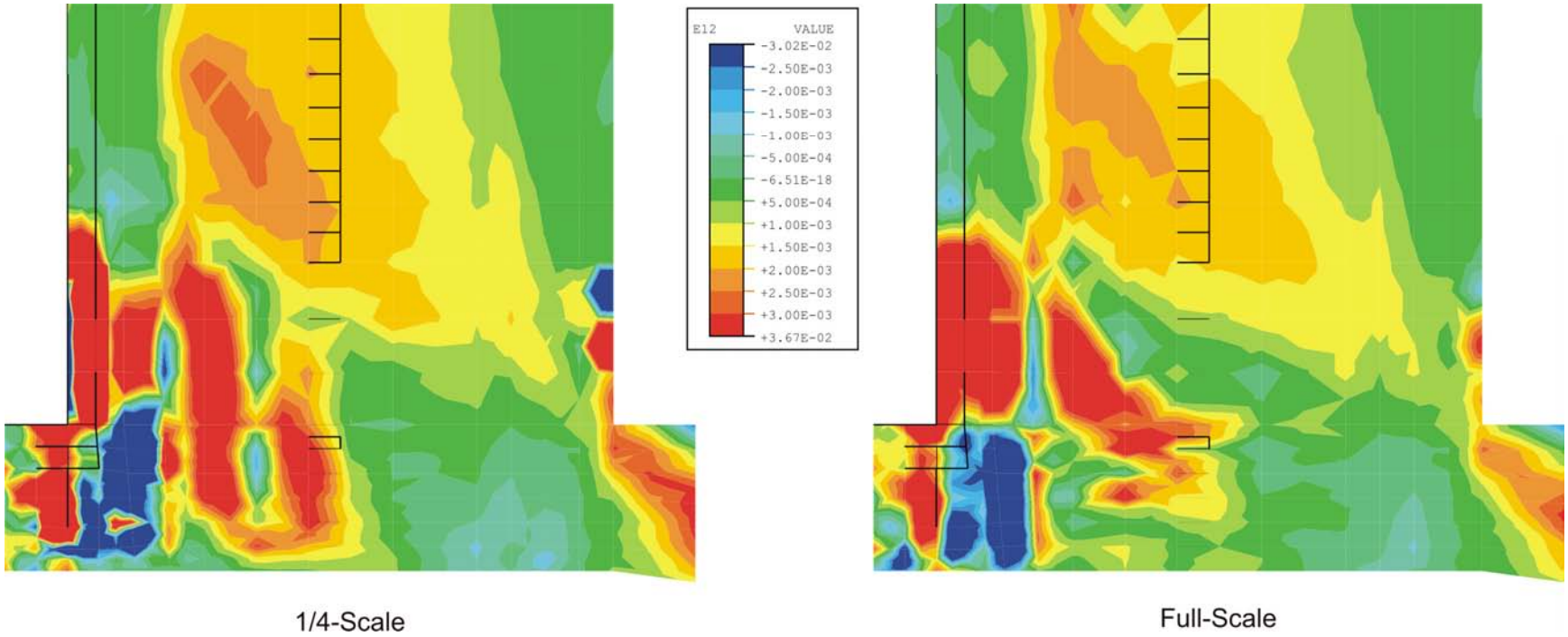

Figure 46. 1/4-Scale vs. Full-Scale Shear Strain Comparison

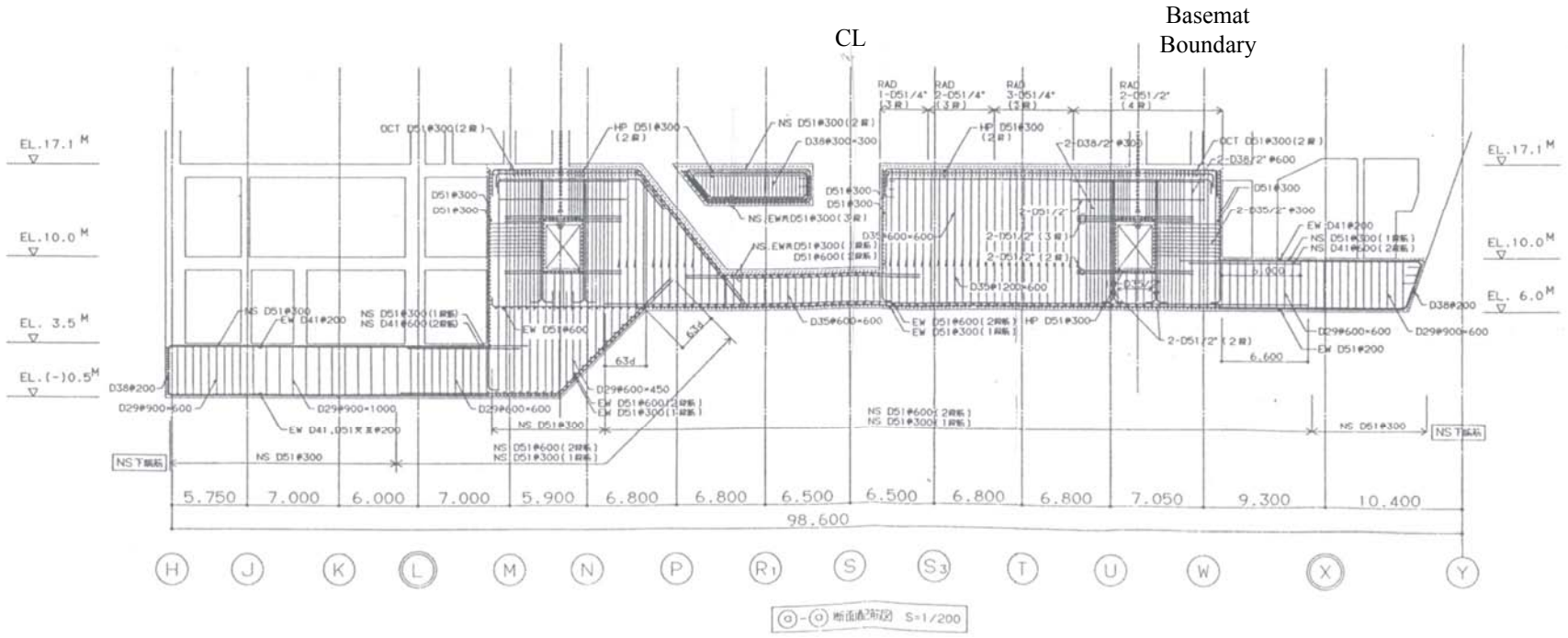

Figure 47. Reactor Pit Detail

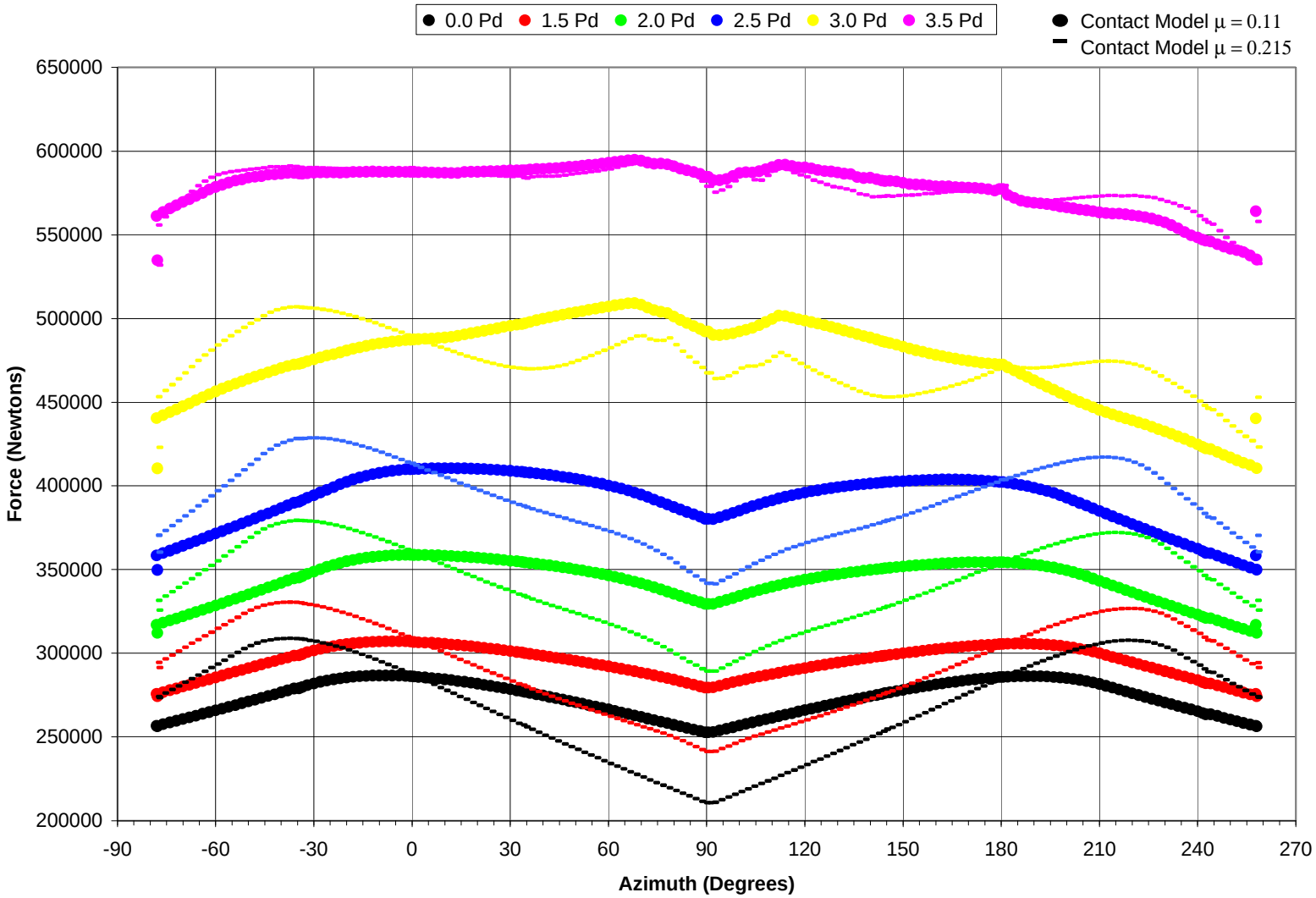

Figure 48. Comparison of Tendon Modeling in Ring Model for Tendon H68

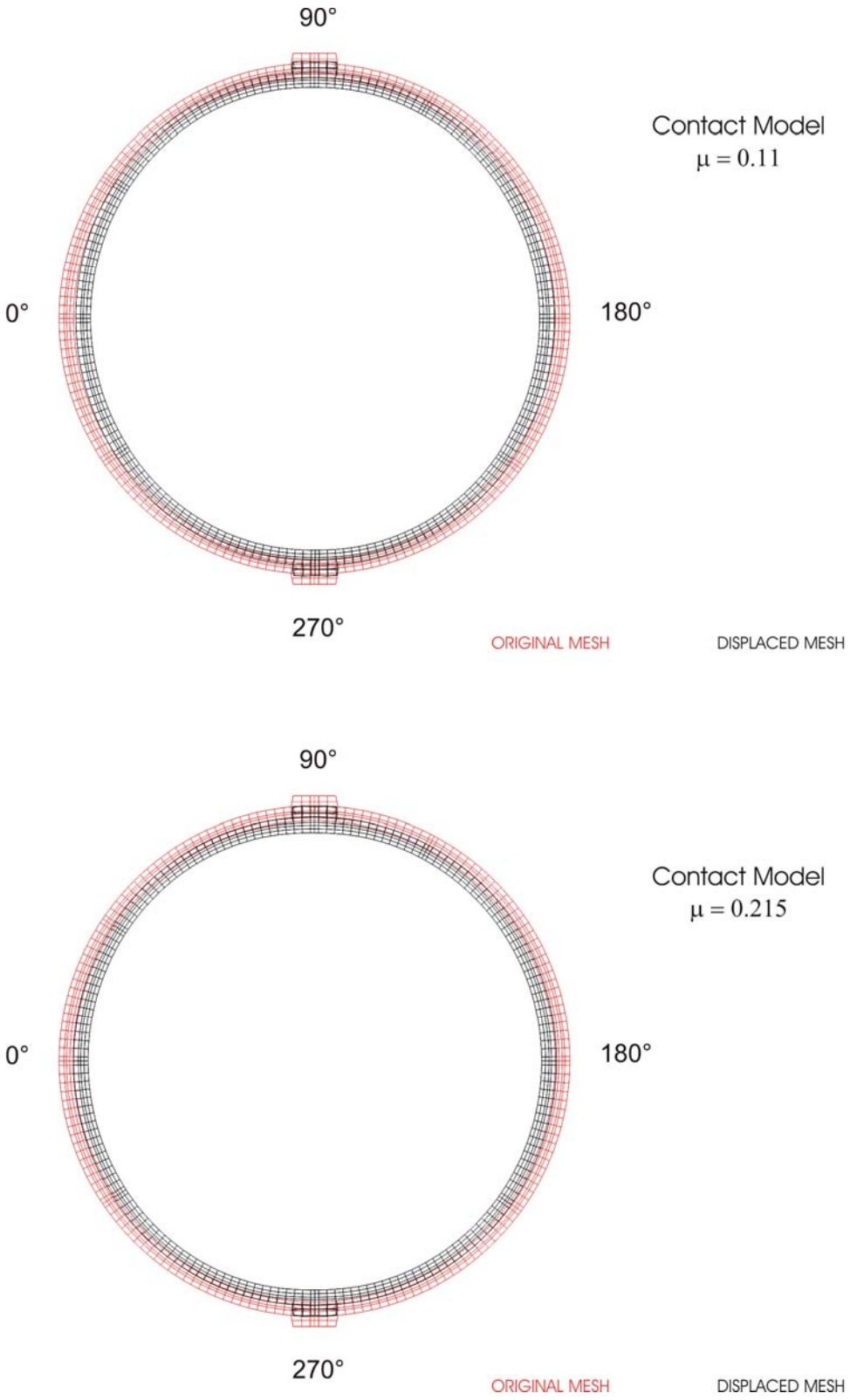

Figure 49. Comparison of Deformed Shapes (displ. x 200) Using Contact Surface Models with m=0.11 and m=0.215; After Prestress

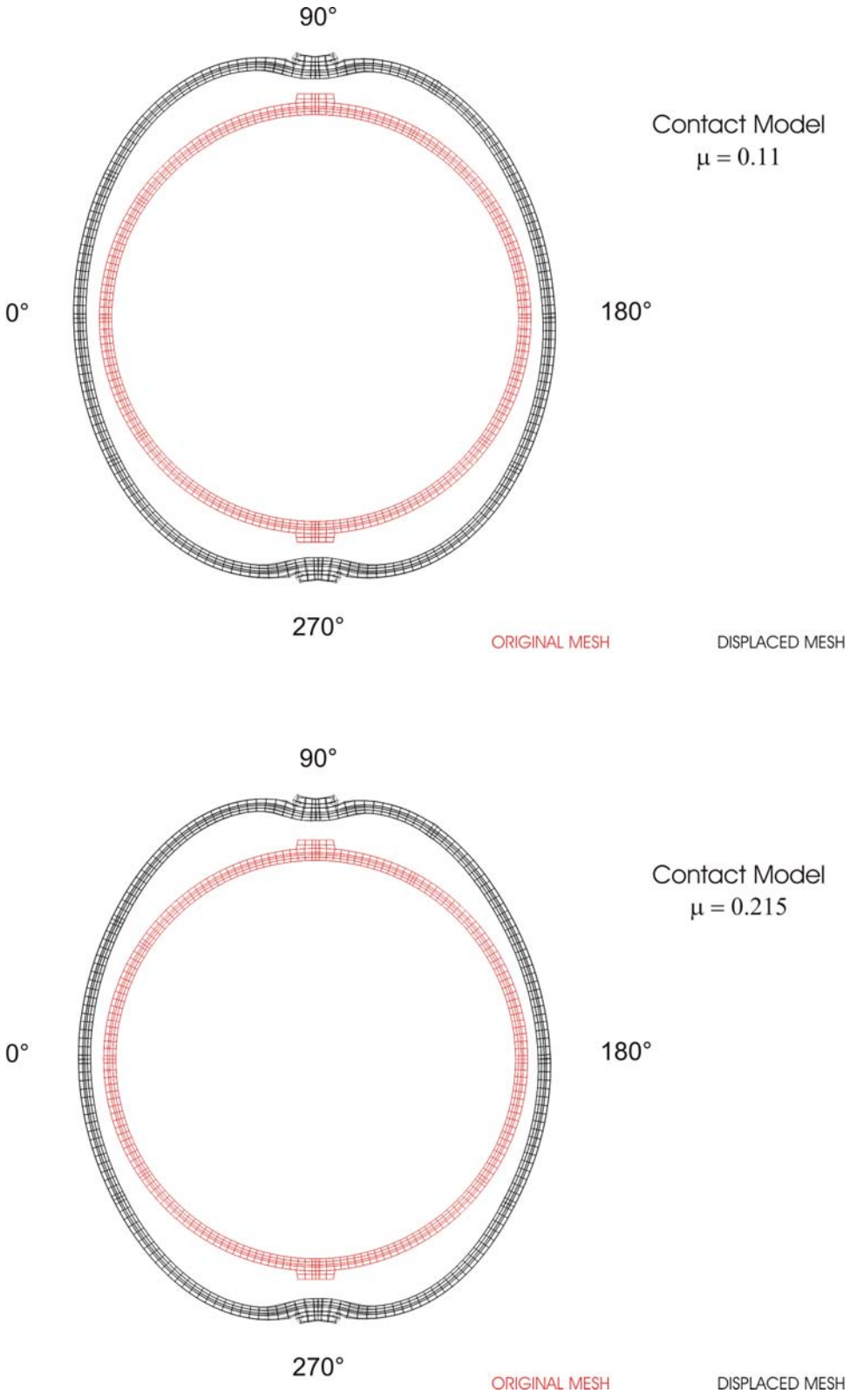

Figure 50. Comparison of Deformed Shapes (displ. x 200) Using Contact Surface Models with m=0.11 and m=0.215; P=2.0P_d

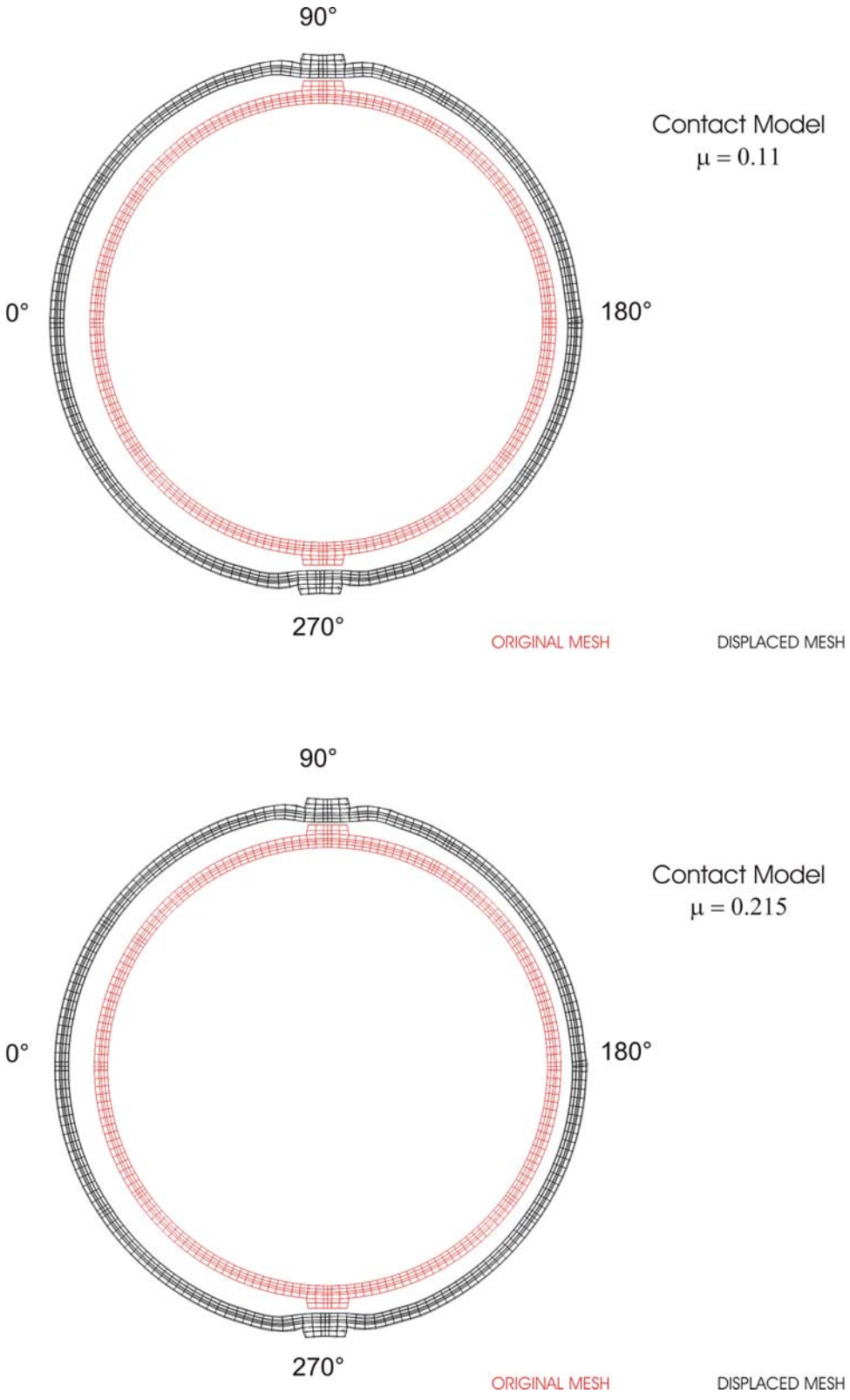

Figure 51. Comparison of Deformed Shapes (displ. x 20) Using Contact Surface Models with m=0.11 and m=0.215; P=3.5P_d

Table 1. Results Summary

Participant	Cracking		Liner Yield	Hoop Tendon Stress		Pressure	Free Field	Mode
	Hoop	Meridonal	(Rebar Yield)	Yield	2%	@ Failure	Hoop Strain	
SNL	0.62	1.14	0.85 (1.10)	1.15	-	1.26	0.35%	Liner Tear, leakage
LST	**0.59-0.78**	**?**	**1.10**	**1.17**	**-**	**0.98** **1.294**	**0.17%** **0.42%**	**Liner tear, 1% mass/day leak** **Max. pressure @ 1000% mass/day leak**

REFERENCES

1. Dameron, R. A., Rashid, Y. R., Luk, V. K. and Hessheimer, M. F. 1977. "Preliminary Analysis of a 1:4 Scale Prestressed Concrete Containment Vessel Model," in *Proceedings of the 14th International Conference on Structural Mechanics in Reactor Technology,* Vol. 5, pp 89-96, Lyon France.

2. Dameron, R. A., et al. 2000. *Pretest Analysis of a 1:4-Scale Prestressed Concrete Containment Vessel Model*, NUREG/CR-6685, SAND2000-2093. Albuquerque, NM: Sandia National Laboratories.

3. Dameron, R.A., et al. 2002. Posttest Analysis of the NUPEC/Sandia 1:4 Scale Prestressed Concrete Containment Vessell. NUREG/CR-6809, SAND2003-0839P, Albuquerque, NM: Sandia National Laboratories.

4. *ABAQUS Users Manual*, Version 5.8, 1998. Providence, RI: Hibbitt, Karlsson & Sorensen, Inc.

5. *ANACAP-U User's Manual*, Version 2.5, 1997. San Diego, CA: ANATECH Corp.

6. Luk, V. K. 2000. *Pretest Round Robin Analyses of a Prestressed Concrete Containment Vessel Model.* NUREG/CR-6678, SAND00-1535. Albuquerque, NM: Sandia National Laboratories.

7. Hessheimer, M. F., et al. 2002. *Overpressurization Test of a 1:4-Scale Prestressed Concrete Containment Vessel Model*, NUREG/CR-6810, SAND2003-0840P, Sandia National Laboratories, Albuquerque, NM.

Page intentionally left blank

US NRC/SNL/DEA Submittal
for
ISP48 Phase 3 Analysis

Analysis of Prestressed Concrete Containment Vessel (PCCV) Under Combined Pressure and Thermal Loading

May, 2005

R. Dameron and B. Hansen, ***David Evans and Associates, Inc.***

M. Hessheimer, ***Sandia National Laboratories***

1. BACKGROUND

The Nuclear Power Engineering Corporation (NUPEC) of Japan and the U.S. Nuclear Regulatory Commission (NRC), Office of Nuclear Regulatory Research, co-sponsored a Cooperative Containment Research Program at Sandia National Laboratories (SNL) in Albuquerque, New Mexico. As part of the program, a prestressed concrete containment vessel (PCCV) model was subjected to a series of overpressurization tests at SNL beginning in July 2000 and culminating in a functional failure mode or Limit State Test (LST) in September 2000 and a Structural Failure Mode Test (SFMT) in November 2001. The PCCV model, uniformly scaled at 1:4, is representative of the containment structure of an actual Pressurized Water Reactor (PWR) plant (OHI-3) in Japan. The objectives of the pressurization tests were to obtain measurement of the structural response to pressure loading beyond design basis accident in order to validate analytical modeling, to find pressure capacity of the model, and to observe its failure mechanisms. The model's limit state reached during the LST was liner tearing and leakage at various locations in the cylinder. The structural failure mode during the SFMT was a large rupture of the cylinder wall.

2. PRESSURE LOADING ANALYSIS

All of the pretest (pressure-loading) analyses of the PCCV and much of the post-test analyses were performed by ANATECH Corp. under contract with SNL. These analyses, conducted up to 2002, are documented in detail in References [1] and [2]. The analysis tools used for this work and the current work are the ABAQUS general purpose finite element program [3] and the ANACAP-U material modeling software developed by ANATECH Corp. [4].

Under the sponsorship of the US Nuclear Regulatory Commission, Sandia National Labs is also participating in the International Standard Problem (ISP 48) on containment integrity and providing assistance to NEA/CNSI in distributing data and interpretations from the PCCV model test to participants in the analysis exercise. David Evans & Associates (DEA), under a contract with SNL which began in 2003, is supporting SNL's involvement in the ISP 48 by conducting additional post-test analytical studies for the Phase 2 and Phase 3 ISP48 Workshops. The first phase of the DEA work focused on aspects of the PCCV behavior where analytical predictions were significantly different than the test measurements, and on possible scaling issues and "test model artifacts" that may have influenced interpretations and judgment obtained from the test. That work, all performed with pressure-only loading, culminated in the SNL submittal to the ISP 48 Phase 2 Analysis Workshop – Mechanical Loading [5]. It compared results of pretest analytical studies of the PCCV model to the PCCV high pressure test measurements and described results of post-test analytical studies. Reference [5] also summarized the finite element modeling and analysis tools, comparisons between measured behavior and predicted behavior of the liner, concrete, rebar, and tendons, and the various failure modes and locations that were investigated. So such background information is only briefly summarized here. Observations on the accuracy and adequacy of the prediction analyses, lessons learned from the 1:4 Scale PCCV, such as the modeling and behavior of prestressing and some unique liner seam details, are also discussed in [5], so are only briefly covered here.

2.1. Description of the Finite Element Models

2.1.1. FE Models

The models that constituted the final pretest predictions in [2] were the global axisymmetric, the semi-global three-dimensional cylinder mid-height (3DCM) model, local models of the E/H, Personnel Airlock (A/L), Main Steam (M/S) penetrations, a typical liner weld connection model ("liner rat-hole detail), and a hoop-tendon friction model. The global axisymmetric was the primary tool used for the ISP-48 Analysis work, but the Main Steam, liner rat-hole, and hoop-tendon friction models have also been examined in the temperature analysis work. These models are shown in Figures 1 through 4. (Figure 2 also shows strain contour result information plotted onto the finite element model.)

2.1.2. Material Modeling

The ABAQUS general purpose finite element program [3] and the ANACAP-U concrete and steel constitutive modeling modules [4] (developed by ANATECH) were used for the analysis. Tendons and their prestressing were modeled to replicate expected tendon stress-strain behavior and friction effects. Concrete cracking was simulated with the "smeared crack" approach, where cracking is introduced at the finite element integration points. Cracks can form at orthogonal directions, up to three cracks per integration point, and once a crack forms, it can never heal. Rebar was modeled with ABAQUS rebar sub-elements, which reside within the "parent" concrete element, and therefore are required to have strain compatibility with the concrete. However, the rebar stress-strain law is completely different than the concrete and is represented by a J2 plasticity model available within ANACAP-U. The tendons were modeled in various ways for the different models, depending on the

level of detail. In some cases, the tendons were modeled with rebar sub-elements, and in other cases, modeled individually with beam elements in which the tendon elements were allowed to slide relative to the concrete. In these cases, friction was represented in various ways. Tendon friction modeling was studied in detail in [5], and this is discussed again in this report in the context of adding thermal effects.

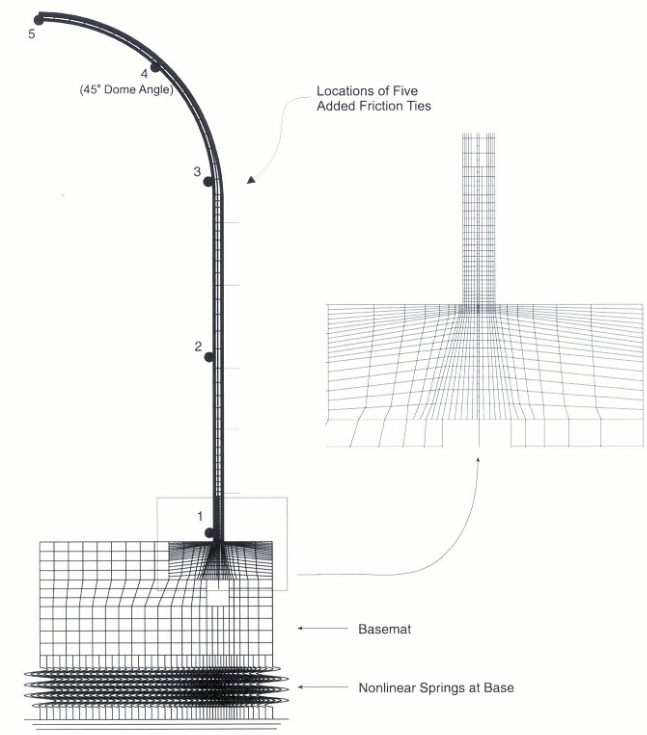

Figure 1. Axisymmetric Model of PCCV and Locations for Plotted Output

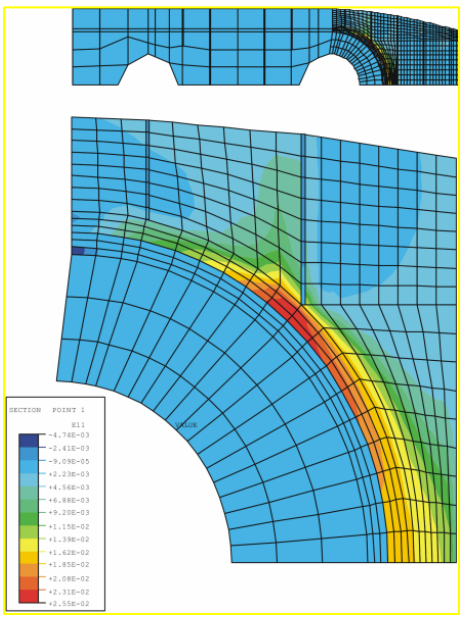

Figure 2. Hoop Strains for Posttest M/S Analysis at P = 3.3P_d

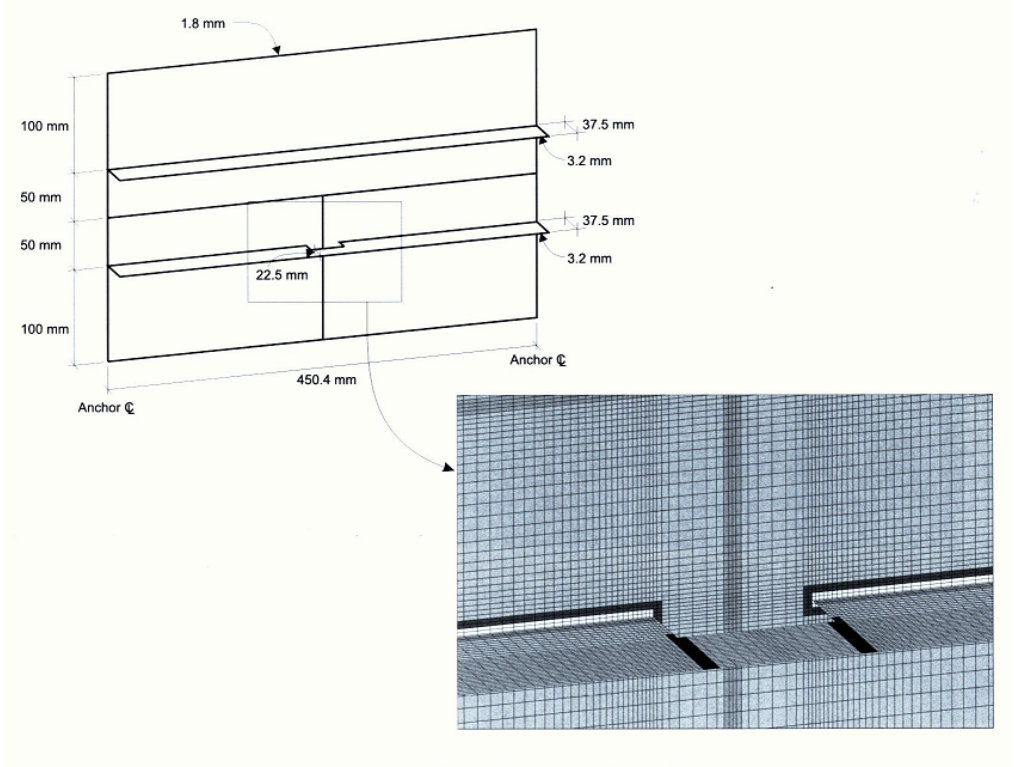

Figure 3. Liner Seam Model Geometric Details

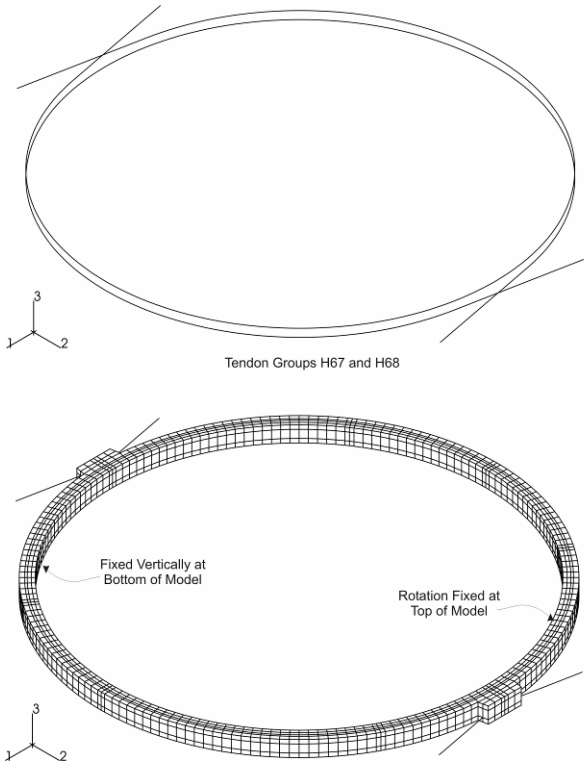

Figure 4. Ring Model, Tendons and Boundary Conditions

3. COMBINED THERMAL-PRESSURE ANALYSIS

The thermal-mechanical solution strategy adopted uses the ABAQUS finite element program [3], and a semi-coupled thermal mechanical analysis procedure using a combination of applied temperature (liner), convection (cylinder wall and dome), and conduction (basemat/soil) boundary conditions. The analysis advances through time (a pseudo-time step for Case 1 and about 60 hours for Case 2), at which point the combined pressure and temperature exceed the capacity of the containment model.

Description of the thermal analyses was sent to all participants in 2004 is described in the main body of this report (Section 5.2).

3.1. Assumptions for Thermal Property Degradation

The choice of generic properties to use for the Phase 3 Analysis was based on an approximate "median" of the data rather than a bounding or conservative selection. For concrete, the "unstressed-hot" versions of data were used because in the PCCV loading scenarios, the temperatures and pressures are increasing simultaneously. The "stressed-hot" would imply a large pressure challenge existing and held constant during the temperature rise. The "actual" challenge in the PCCV is likely to be somewhere between an "unstressed-hot" case and a "stressed-hot" case. Based on this and on the trends observed in other references, a smooth curve for strength degradation versus temperature was estimated below and plotted in Figure 5.

Concrete Strength Ratio, $S_{Rc} = \exp^{-}(T/632)^{1.8}$ where T is in degrees C.

The derivation of this curve was based on assumption of a basic shape as observed from the data, and then pegging the curve to the following points:

Temperature (°C)	Strength Reduction
0.0	1.0
200	0.88
600	0.40
1000	0.10

Further, based on the literature, it appears reasonable to continue to base the modulus on the standard ACI formula: $E = 57{,}000\sqrt{fc'}$ (English Units) such that a Modulus Reduction Ratio can be defined as:

$$M_R = (S_R)^{\frac{1}{2}}$$

It should be noted that the peak strain at which the concrete compressive strength limit is reached also shifts with increasing temperature. While at 25C, this strain is approximately 0.002, it can reach two to three times this value at high temperatures.

Temperature variation of steel is also important for the highest temperatures. This variation has been idealized based on curves provided in Reference 11 and trends observed in other texts and papers:

Steel Yield Strength Ratio, $S_{Rs} = \exp^{-}((T-340)/300)^{1.9}$ where T is in degrees C.

For steel, the Young's Modulus tends to follow the yield strength one-to-one, rather than the square-root relationship found in concrete. The steel yield strength reduction is shown in Figure 6.

$$S_{Rs} = 1.0, T \le 340C$$

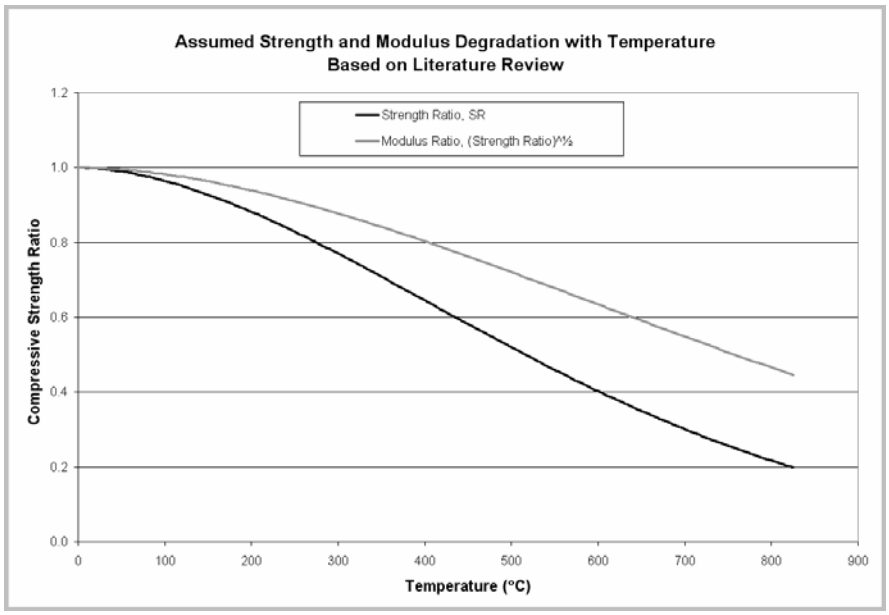

Figure 5. Concrete Compression Strength Ratio vs. Temperature

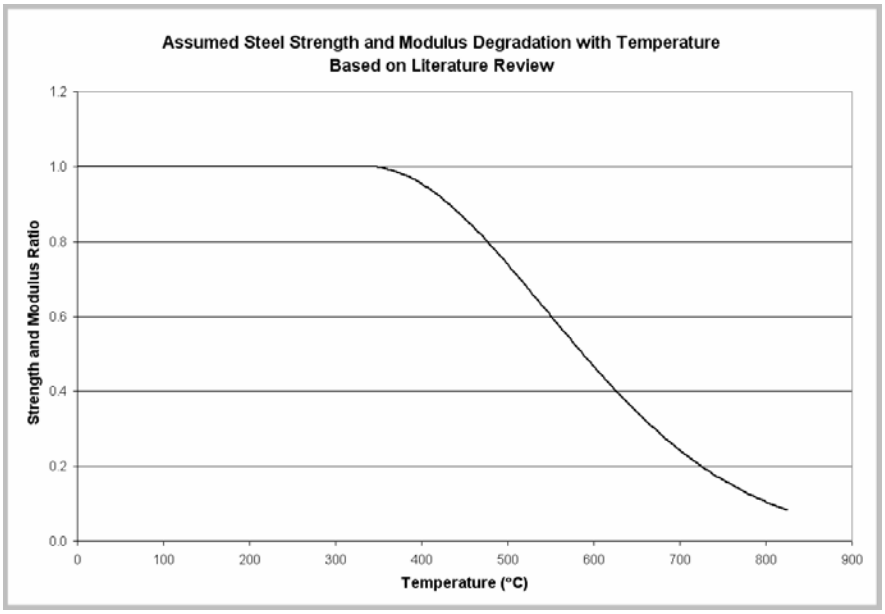

Figure 6. Steel Yield Strength and Modulus Ratio vs. Temperature Assumed for Analysis

3.2. Thermal-Mechanical Analysis With Thermal Property Degradation

As previously discussed, the first analysis step conducted was with combined thermal and mechanical solutions without temperature degradation of concrete and steel properties, and these are documented herein. The final step in the process, combined thermal and mechanical analysis with property degradation, was found to be more numerically difficult, and significant effort was conducted to arrive at a solution strategy for which the solution could be advanced to high pressure and temperature before numerical difficulties led to premature analysis terminations. The methodology eventually employed for the Phase 3 submittal was based on engineering approximations to property degradation versus temperature. The analyses were again performed using ABAQUS Version 5.8 and ANACAP-U (licensed from ANATECH Corp.), the same tools as used for pretest and post-test analyses of the PCCV.

Figure 7 shows the sections through the containment wall and basemat where the temperature gradients were calculated. Gradients for Section 2 for Temperature Cases 1 and 2 are shown in Figures 8 and 9. These and the gradients at other sections were studied and used to make engineering judgments as to introducing thermal material property degradation. Based on review of all the gradients, the following conclusions were reached as to reasonable assumptions and approach:

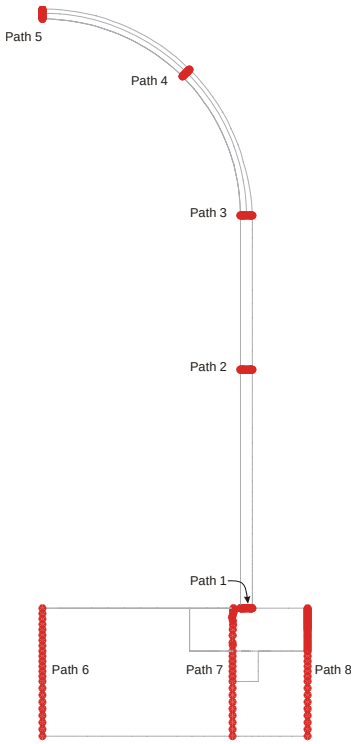

Figure 7. Calculated Thermal Gradient Locations

- The temperature gradients at Sections 1 through 5 (cylinder and dome sections) are all very similar, so it is reasonable to use Section 2 as a representative section for all;

- Similarly, Sections 6 and 7 through the basemat, can be represented by Section 7. Section 8 does not matter, because none of this section ever gets hot enough to degrade properties.

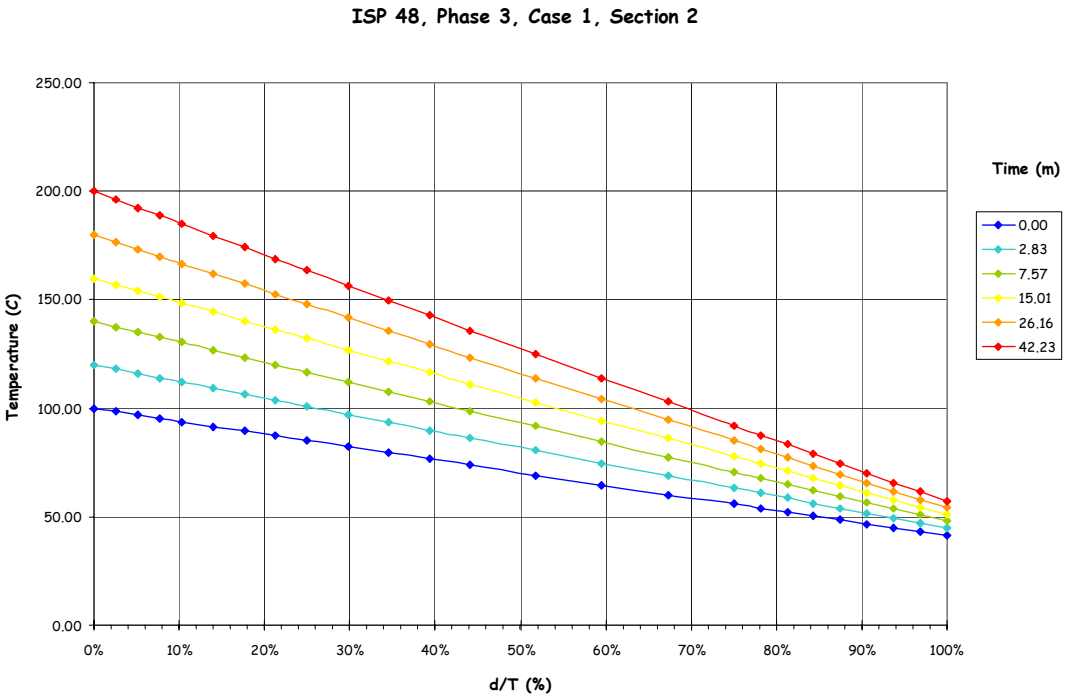

Figure 8. Thermal Gradients at Mid-height of Cylinder Wall for Saturated Steam Conditions (Case 1)

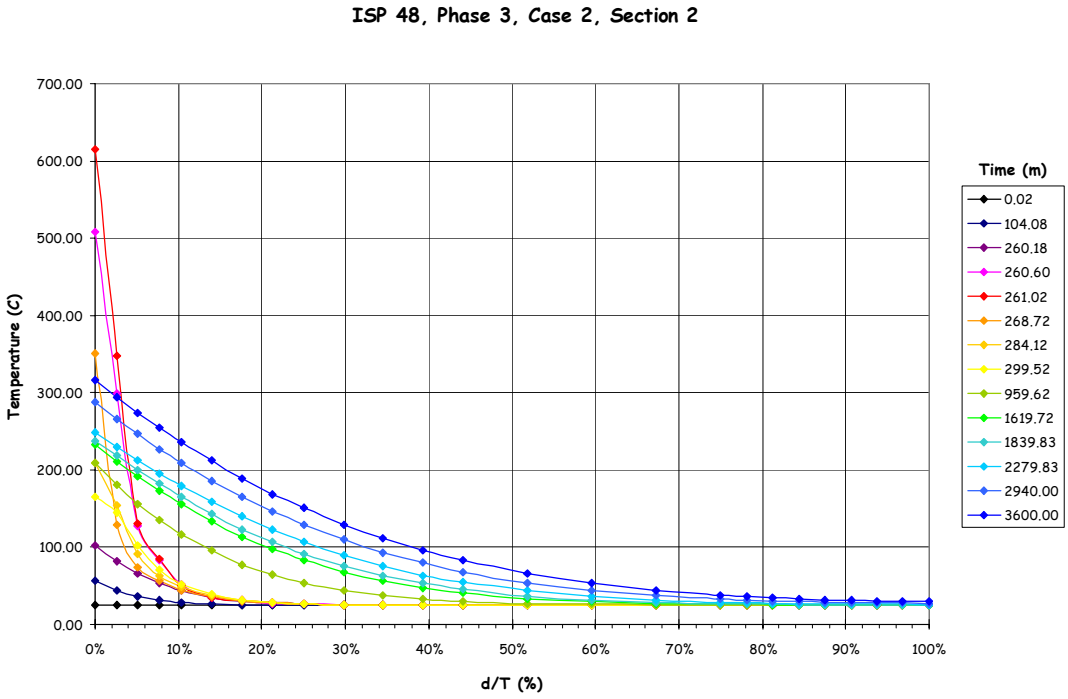

Figure 9. Thermal Gradients at Mid-height of Cylinder Wall for Station Blackout (Case 2)

To investigate the potential effects of property degradation, it was found reasonable to divide the concrete into four "zones" through the thickness. These zones are shown color-coded onto the FE mesh in Figure 10. The zone boundaries are at d/T (depth through the thickness) ratios of 17%, 33%, and 60%. The "average" temperature in the zone was assigned to the entire zone. The liner, being a discrete point in the model, can be assigned the exact applied temperature, not an averaged one.

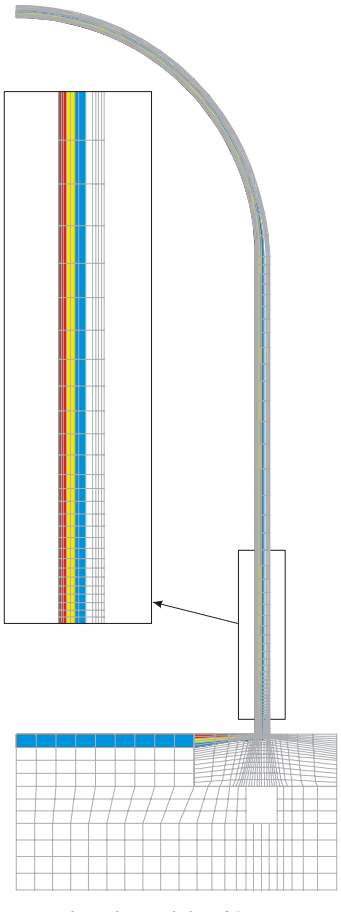

Figure 10. Location of Elements with Degraded Properties

To find the "upper bound" of the influence of property degradation it was found reasonable to degrade the properties based on the temperature reached at or near the conditions when the PCCV is near failure, i.e., the end of the analysis. Such temperature assumption can later be modified if "failure" is reached earlier than expected, or in order to conduct sensitivity studies of the effects of these assumptions.

Based on these assumptions, the property degradations introduced for the Case 1 and Case 2 analyses are as follows:

<u>Case 1. Reaches 200C at same time as P=1.42 Mpa (3.6 Pd), so try using this temp as the bounding case</u>

Concrete:

Zone 1 (red)	180C	fc'*=0.90fc'	E*=0.95E
Zone 2 (yellow)	160C	fc'*=0.92fc'	E*=0.96E

Zone 3 (blue)	130C	fc'*=0.94fc'	E*=0.97E
Zone 4 (white)		No Change	

Steel:

None of the zones have temperatures reaching 340C, so there are no effects on steel

Case 2. Reaches a very critical state at the early "spike", where temperature is 600C, and pressure is 0.8Mpa (2Pd), so this temperature is the bounding case

Concrete:

Zone 1 (red)	260C	fc'*=0.82fc'	E*=0.90E
		(temp drops off very rapidly for transient event)	
Zone 2 (yellow)	170C	fc'*=0.91fc'	E*=0.95E
Zone 3 (blue)	80C	No Change	
Zone 4 (white)		No Change	

Steel:

Due to the steep temperature gradient through the wall thickness, no rebar or tendon reaches 340C, so no changes were needed for rebar or tendons. But the liner is affected. It reaches 600C, such that fy*=0.47fy, and E*=0.47E. A uniform factor of 0.47 was applied to all points on the yield curve. Temperature effects on ductility are also considered in the evaluation of results and in the failure prediction.

3.3. Failure Criteria

For the pretest and post-test analysis of the PCCV, failure predictions have been made based on criteria developed during containment research of the 1980s, and refined by large scale tests and supporting analysis. While for years there has been extensive debate in the literature over what is meant by "failure" of containments, for the work performed here, the term "failure" is taken to mean the occurrence of such large deformations (strains) of the liner or of a containment structural element, that a breach of the containment pressure boundary is predicted.

The failure criteria are analytically based insofar as analytically predicted strains are compared to a material limit to predict failure of the component or structural element. It is important to note that containment breach is not explicitly simulated in the Lagrangian finite element mesh. So prediction of "failure" relies on surrogate criteria (e.g. displacement, strain) based on empirical data and engineering judgment. Failure of components can be categorized into functional failure, e.g. liner tearing resulting in leakage, or structural failure where the demand exceeds the resistance available in the structure, e.g. rupture of a number of tendons or reinforcing bars leading to collapse. Gross liner failure is assumed to coincide with structural collapse.

Local liner failure predictions for pressure-only analysis are based on either the explicit prediction of liner strains high enough to exceed the often used Davis Triaxiality Factor strain criteria [1], if the finite element mesh is fine enough, or the assumed existence of high strains occurring near a liner stiffness discontinuity, if the stiffness discontinuity is not explicitly modeled or not modeled with a highly refined mesh. Again, for pressure-only analysis, this latter "extrapolation" has become widely accepted based on large scale tests, and there is extensive evidence that supports the assumption that for steel lined concrete vessels with quasi-static pressurization, local liner tears will occur when the driving strain of the wall to which the liner is attached reaches between 1% and 2% "global" strain. What may be less widely agreed, is the relative likelihood or dominance of a leak-before-break failure

mode associated with liner tearing. The question is not whether the 1%-2% global strain will lead to liner tear, but rather, what will happen after liner tear? In the case of the SFMT of the Sandia 1:4 Scale PCCV, tendons began rupturing at these deformation levels, and the cylinder "unzipped" catastrophically. The current ISP work will probably not settle this debate, but instead turns attention onto the effects temperature may have on failure behavior.

The local failure predictions of the PCCV pretest [1] and posttest [2] analyses were all driven by response versus pressure histories calculated by the global axisymmetric and 3DCM models. The pretest failure predictions consisted of predictions of liner tearing locations, all occurring near the mid-height of the cylinder near penetrations and weld seams with "rat-hole" details. The most likely location for the liner tearing failure was predicted to be near the Equipment Hatch (E/H) at the ending point of a vertical T-anchor, near where the liner is attached to the thickened liner insert plate (also a weld seam). The failure pressure was predicted to be 3.2 times the design pressure (Pd) of 0.39 MPa or 1.27 MPa. During the LST, liner tearing and leakage failure were first detected at a pressure of 2.5Pd, and a subsequent increase in pressure to 3.3Pd resulted in very extensive tearing at many strain concentration locations, some of which were predicted and some (including the E/H vertical T-anchor location) were not. Ultimately, the leak rate through the tears exceeded the flow capacity of the pressurization system so the test was concluded at 3.3Pd. Structural damage at the end of the LST was limited to concrete cracking, and the overall structural response (displacements, rebar and tendon strains, etc.) was only slightly beyond yield. (Global hoop strains at the mid-height of the cylinder only reached 0.4%, approximately twice the yield strain in steel.) In order to provide additional structural response data to compare with in-elastic response conditions, the PCCV model was resealed, filled nearly full with water, and re-pressurized during the SFMT to a maximum pressure of 3.6 Pd.

The failure predictions for the pressure-plus-temperature analyses have been made by similar means as in earlier work, but also taking into account the effect temperature may have on ductility of the steel strength components. As part of this work, a literature review was also conducted to examine this effect. As previously described, there is extensive literature supporting the conclusions on "knockdown" factors related to stiffness and yield-strength, but information is much more sparse on temperature related reductions in ductility for carbon steels. (Some typical information is provided in References [6, 7, 8].) It is well known that as the yield strength decreases with temperature, the ductility increases, but quantifying this increase is very complex because it is highly dependent on load duration. Prediction of material fracture at 600C becomes a creep-rupture problem in which the creep strains can be as large as the plastic strains. Some very elaborate predictive models have been developed for predicting creep rupture in reactor pressure vessels (e.g., [6]), and these models make use of empirical parameters like the Larson-Miller parameter. There are also issues related to the steel's ability to recover strength after exposure to 600C temperature. But a prediction of this type was judged to be beyond the scope of the current work. Instead, and based on the literature review, at 600C (max temperature the liner reaches for Temperature Case 2), it has been assumed that ductility (strain at failure) could increase approximately by half. Thus where maximum elongations in the liner (including biaxiality effects) were assumed to be about 20% [1], under 600C temperature, it is assumed they are capable of withstanding 30%.

3.4. Analysis Results

3.4.1. Review of Pressure-Only Analysis

In reviewing the PCCV test data, the 55 Standard Output Locations (SOLs) used for the Round Robin prediction exercise held in 1999 [9] were very useful comparison points. Pretest analysis test data comparisons show comparisons of typical displacements, liner strains, and rebar strains. Analysis data curves were initialized or "re-zeroed" to the first point of the test data, i.e. the data reading occurring

at the start of the test. This slightly shifted the analysis data, but it simplified the comparison of the response to internal pressure and eliminated differences in response to dead load, prestressing and creep or other time-dependent effects. This same procedure was followed in the plots of analysis results for the pressure-only and pressure plus temperature analysis.

The conclusions from the comparisons of the pretest analysis with the LST were that:

- Radial displacements in the cylinder wall were well predicted by global axisymmetric analysis, but dome and overall vertical displacements were over-predicted.

- Wall-base juncture behavior, including many rebar and liner strain measurements, were well predicted by the detailed wall-base juncture (axisymmetric) modeling.

- Functional failure (i.e. leakage in excess of 1% mass/day) at a pressure of 2.5 Pd occurred at a liner tear in an area of high strain that was not examined in detail by analysis, but was probably amplified due to defects associated with weld seam repair.

- Maximum pressure, 187.9 psig (3.30 Pd), was closely predicted by analysis, but the predicted failure location did not manifest itself. (Maximum pressure was also limited by the capacity of the pressurization system.) Ultimately, liner tears at many locations occurred, and many of these were identified by analysis.

In the post-test analysis work, some aspects of the global axisymmetric analyses, i.e., the dome response and basemat uplift response were improved, and analyses were conducted that explained the lack of a liner tear at the E/H vertical T-anchor location, and the frequent occurrence of liner tears at weld seams. But the primary aspects of the global response prediction have been relatively unchanged, dating back to the pretest analysis. And these analysis results form the basis of the pressure-only analyses presented herein.

3.4.2. Pressure and Temperature Analysis

While some model conversions (conversions of element types and the elimination of reinforcement) were necessary to perform the heat transfer analysis to obtain the nodal point temperature histories, the same models as were used for the pressure-only analysis were used for the thermal-mechanical analyses.

The Standard Output locations (SOLs) that were selected for ISP48 are identified in the main body of this report. Appendix B compares the SOL results for the Temperature Case 1 (Saturated Steam) analyses and Temperature Case 2 (Station Black Out) analyses. For each plot the response quantity is plotted versus pressure, but note that temperature also varies. For Case 2 plots, a few responses are plotted versus time, since the pressure is not monotonically increasing. These results are contrasted with the Phase 2 results for pressure only, provided in Appendix A. (The revised pressure only analyses for Phase 3 are not included in the report.) The main addition to the results for Phase 3 is the inclusion of liner stresses. In preliminary strain plots, it was noted that the addition of stresses would add to the level of understanding of thermal behavior of the PCCV.

The pressure-only data, though reanalyzed since 2003 to verify model consistency, is essentially the same as was published in post-test analysis, as compared to the PCCV LST experimental data. But it should be noted that for purposes of the current comparisons, the analysis data has not been “re-zeroed” to agree with the test measurement data at the start of the test, so the response curves may

appear to be slightly shifted when compared to earlier reports. This is done to preserve the value of making pure comparisons to the thermal analyses.

Discussion of Case 1 (Saturated Steam) Results

The basic results for both of the temperature cases are those provided for the Standard Output Locations. And since the temperatures are higher for Case 2, discussion of Case 2 provides some detailed observations about effects due to temperature. But some general observations of the Case 1 results can still be made:

- All of the cases, including pressure only, begin at 25C (77F), but because Case 1 is for Saturated Steam, the temperature starts out at 100C (212 F), so the response plots show an immediate jump in deformation relative to the pressure-only case. This is to be expected, and has been approximately verified with a hand calculation check.

- The deformations associated with temperature are very significant, especially for vertical displacement. For radial displacement at cylinder mid-height (SOL 5), displacement with temperature at 3Pd and 185C, are ~20 mm versus ~12 mm for pressure alone. For vertical displacement at cylinder top (springline) (SOL 8) pressure only displacement is 2.4 mm versus temperature Case 1 displacement of 18.5 mm at 3Pd and 185C.

- The thermally induced displacements are significant, and when translated to a full-scale containment (multiplying by 4), the thermal displacements are very large and may even lead to piping and equipment interference problems. For example, vertical displacement at top of cylinder (springline) and 3Pd / 185C, reach 92mm!

- Lastly, in all results plotted for Temperature Case 1, the differences due to thermally induced material property degradation, are very minor. This tends to justify the use of an approximate material property degradation approach, at least for the Case 1 Temperature scenario.

Discussion of Case 2 (Station Black-Out) Results

Some of the general observations of the Case 2 results are similar to Case 1, but since the temperatures are substantially higher, there are important differences. And since with higher temperatures, temperature effects in general are more significant, Case 2 is used to point out general observations about these effects.

A subset of the SOL plots for Case 2 is included, for observation and discussion, in Figures 11-20. The plots included are SOLs 5, 8, 16, 17, 25, 26, 36, 38, 39, 41, and it includes a sampling of displacement, rebar strain, and liner strain and stress plots. The displacements are plotted at Location #2 and #3 as referenced in Figure 1.

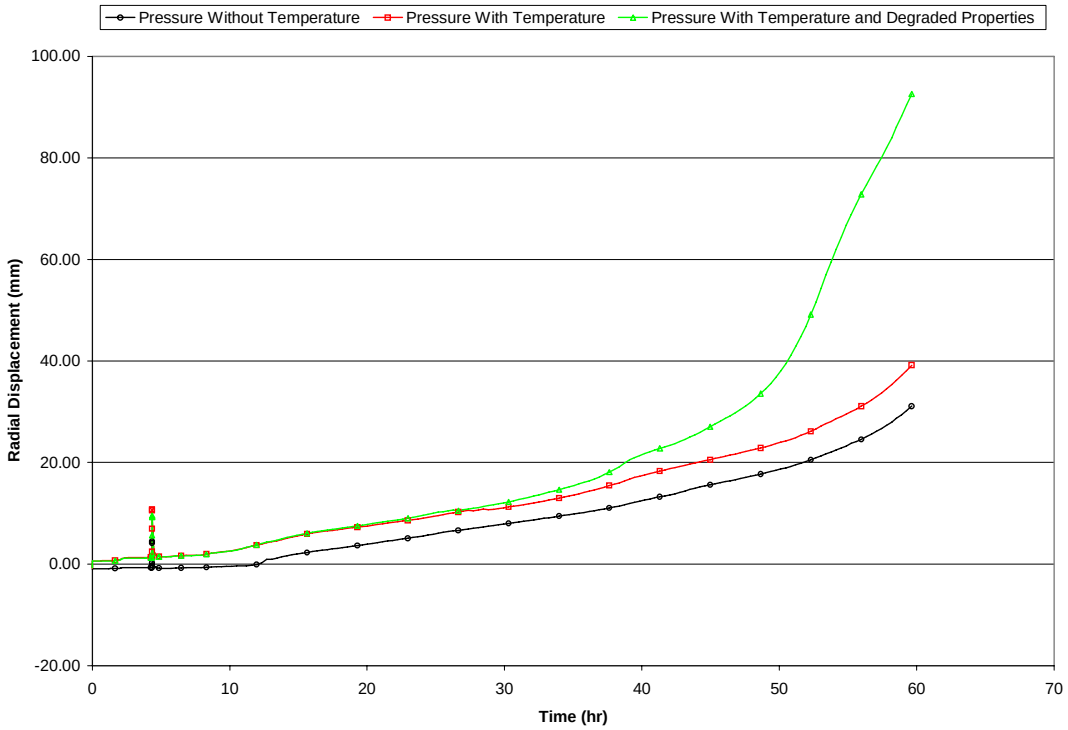

Figure 11. 1:4 Scale PCCV With Temperature Case 2 – Standard Output Location #5. Azimuth: 135 Degrees, Elevation: 4.68 Meters, E/H Elevation

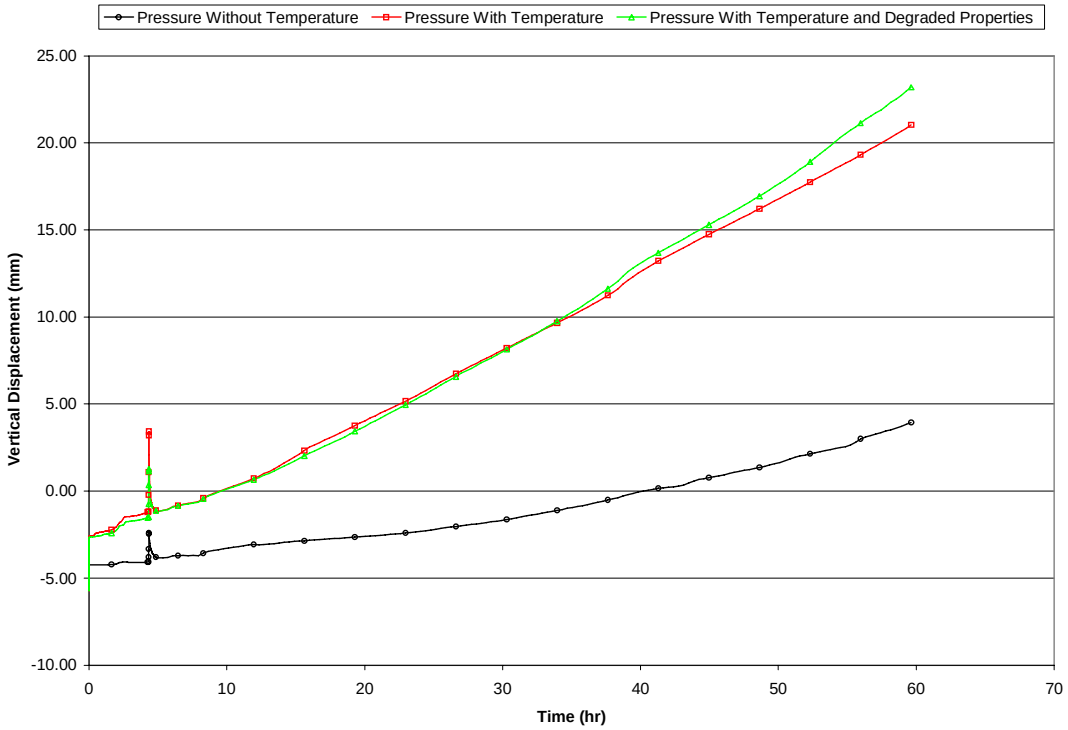

Figure 12. 1:4 Scale PCCV With Temperature Case 2 – Standard Output Location #8. Azimuth: 135 Degrees, Elevation: 10.75 Meters, Springline

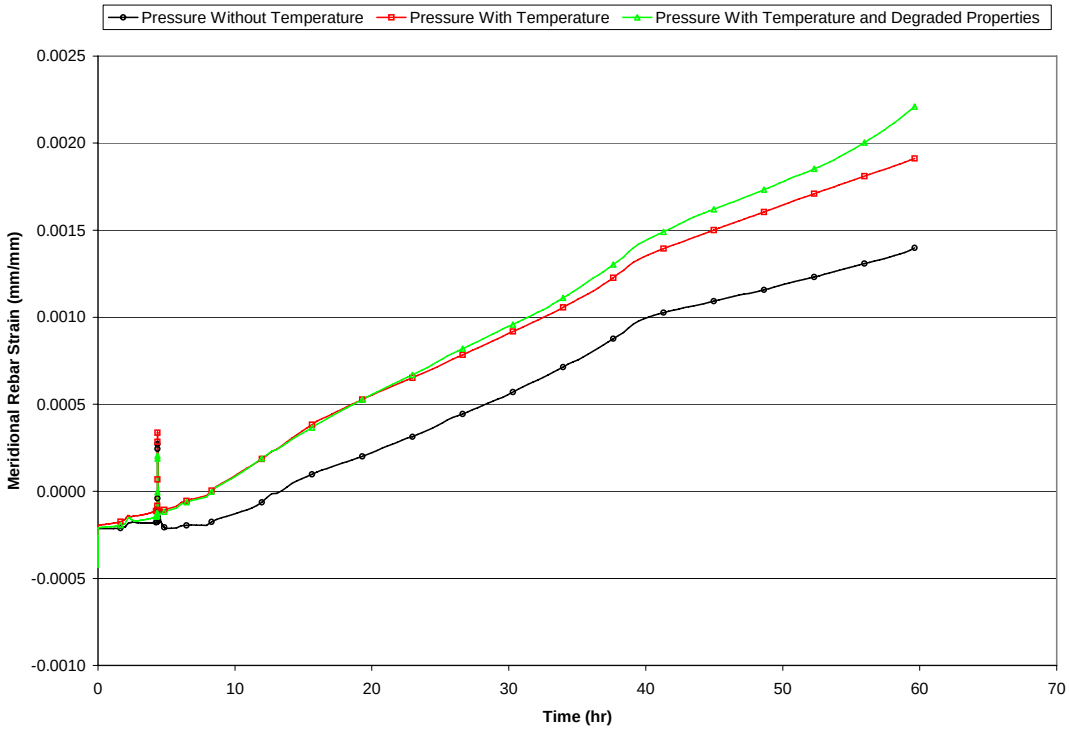

Figure 13. 1:4 Scale PCCV With Temperature Case 2 – Standard Output Location #16. Azimuth 135 Degrees, Elevation: 0.05 Meters, Inner Rebar Layer, Base of Cylinder

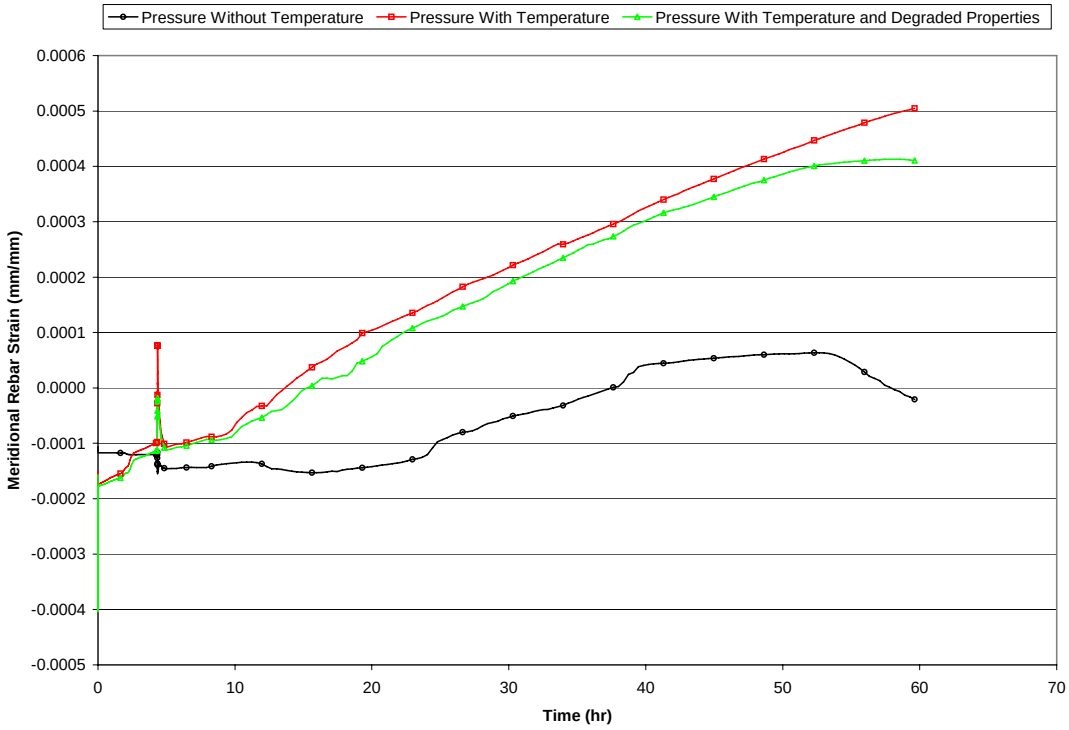

Figure 14. 1:4 Scale PCCV With Temperature Case 2 – Standard Output Location #17. Azimuth: 135 Degrees, Elevation: 0.05 Meters, Outer Rebar Layer, Base of Cylinder

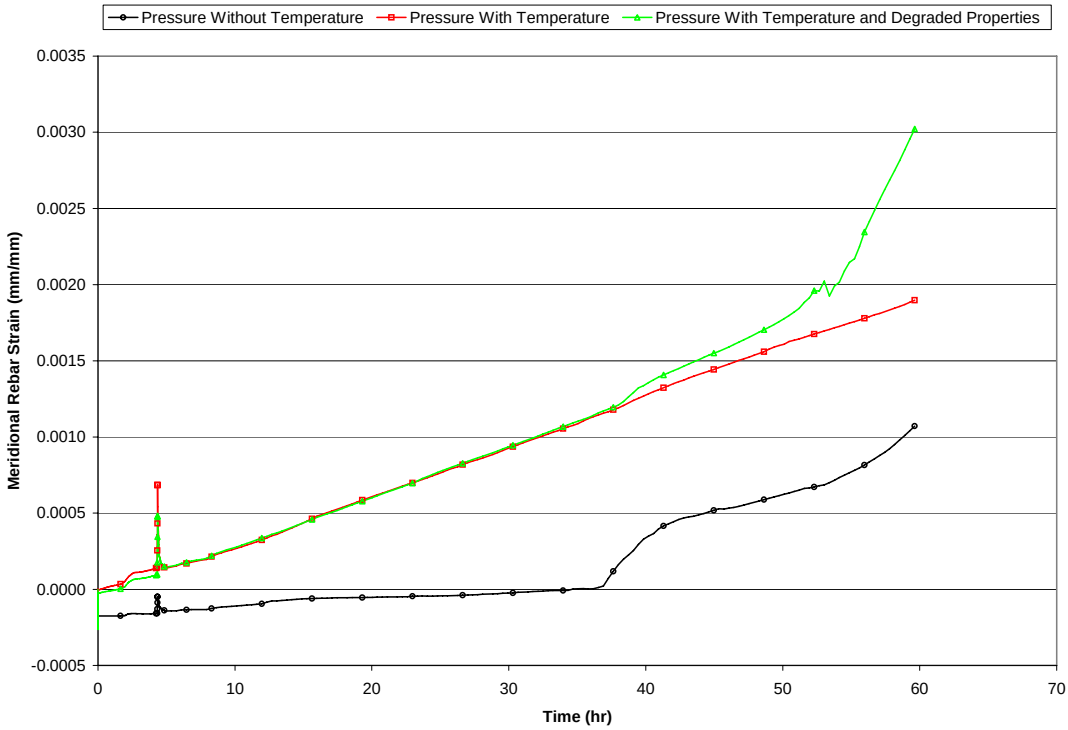

Figure 15. 1:4 Scale PCCV With Temperature Case 2 – Standard Output Location #25. Azimuth: 135 Degrees, Elevation: 10.75 Meters, Inner Rebar Layer, Springline

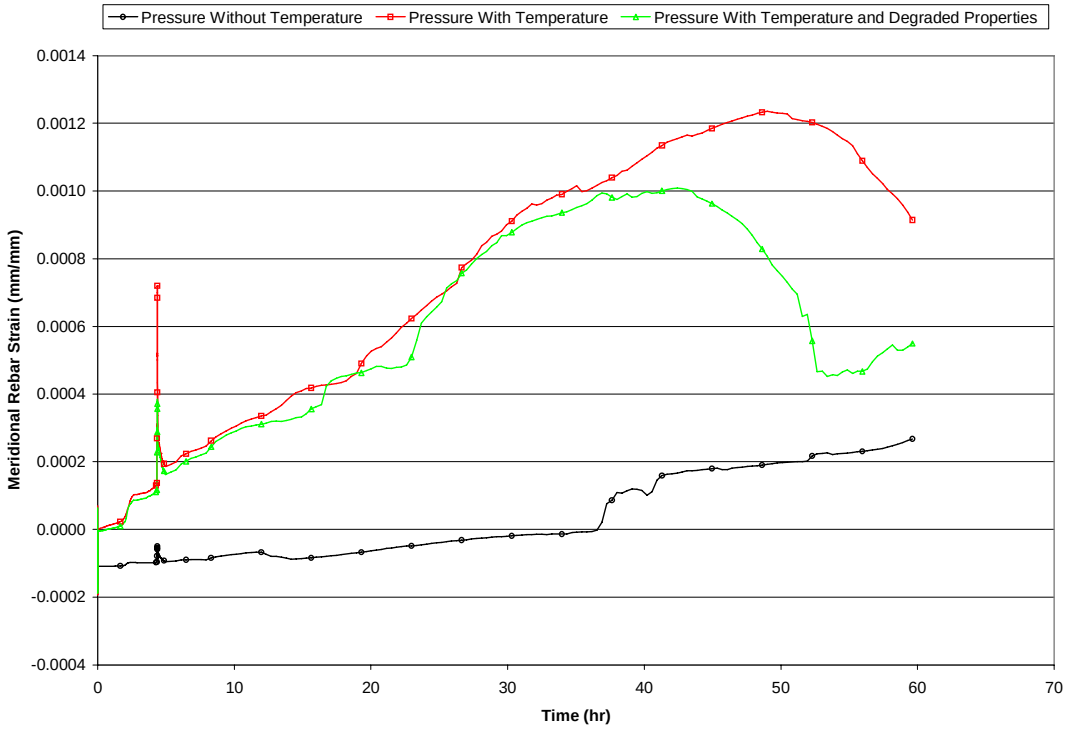

Figure 16. 1:4 Scale PCCV With Temperature Case 2 – Standard Output Location #26. Azimuth: 135 Degrees, Elevation: 10.75 Meters, Outer Rebar Layer, Springline

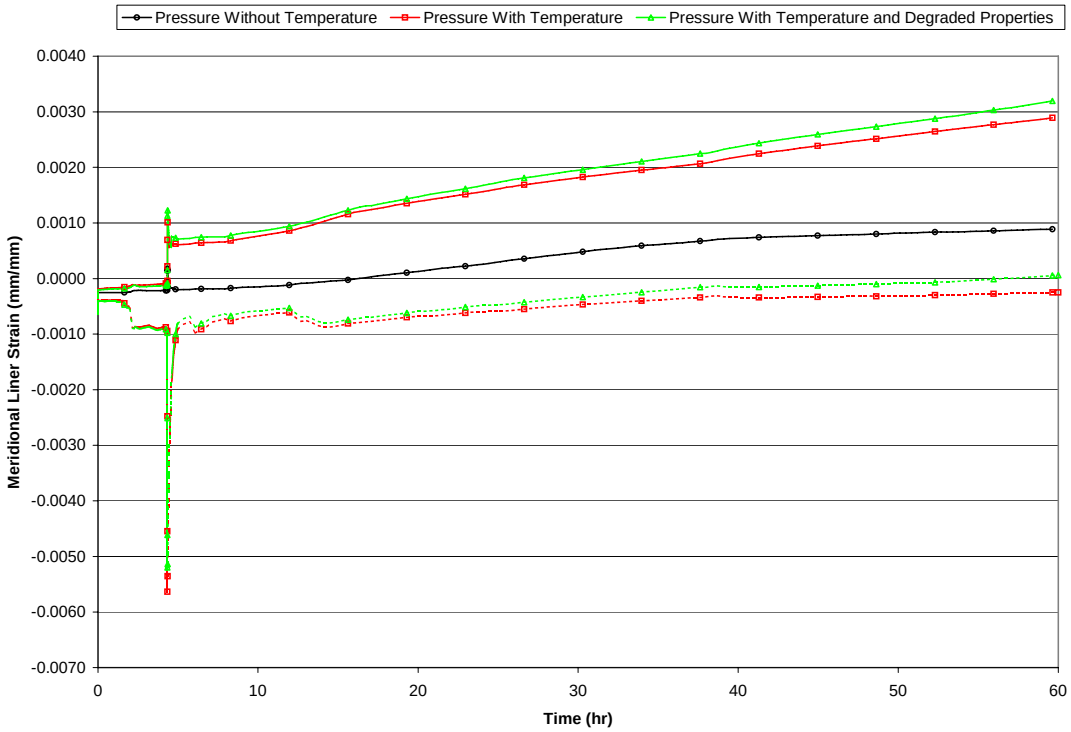

Figure 17a. 1:4 Scale PCCV With Temperature Case 2 – Standard Output Location #36. Azimuth: 135 Degrees, Elevation: 0.25 Meters, Inside Liner Surface, Base of Cylinder (Dashed Lines Show Total Strain - $\alpha\Delta T$)

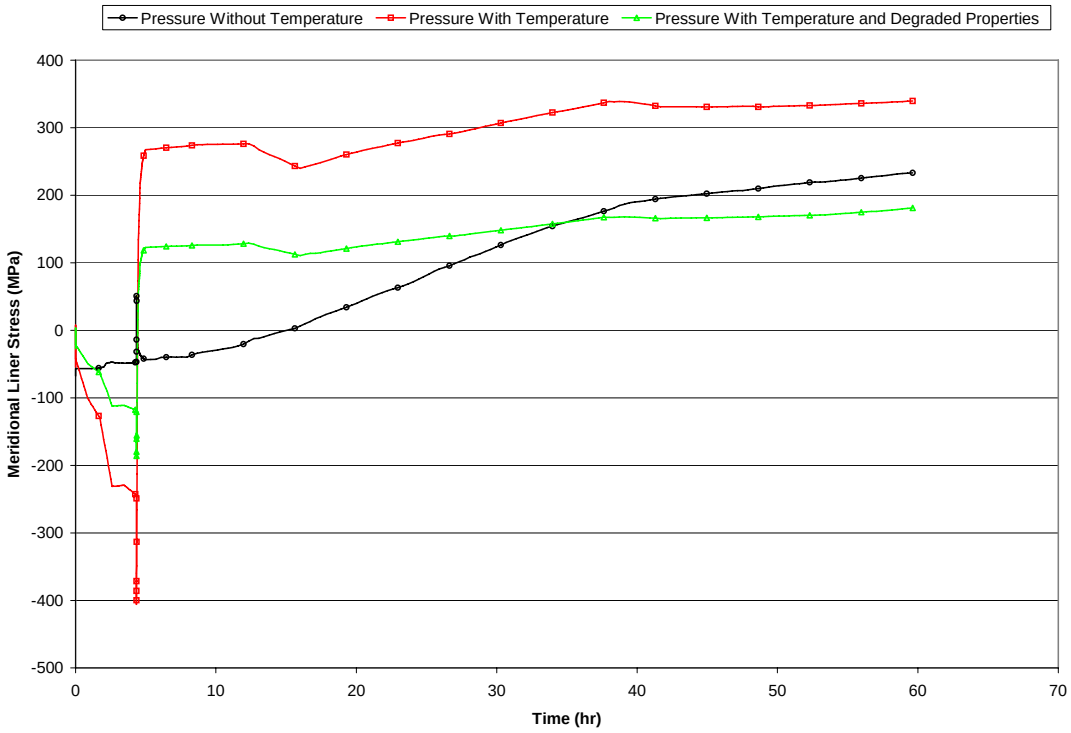

Figure 17b. 1:4 Scale PCCV With Temperature Case 2 – Standard Output Location #36. Azimuth: 135 Degrees, Elevation: 0.25 Meters, Inside Liner Surface, Base of Cylinder

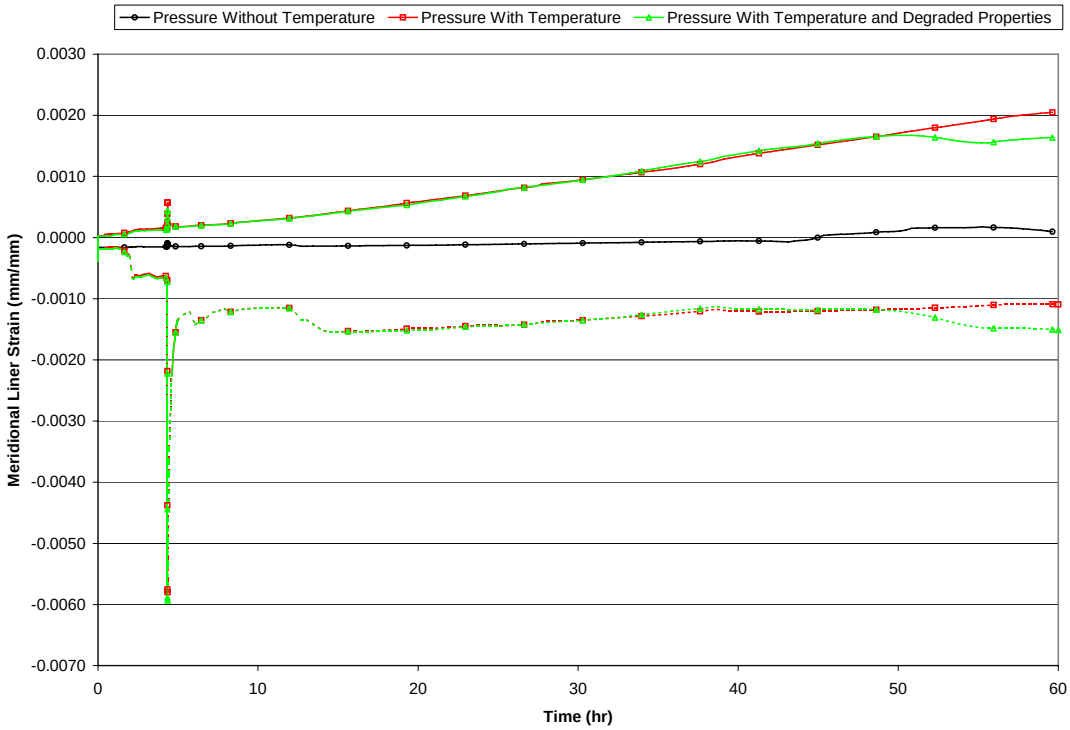

Figure 18a. 1:4 Scale PCCV With Temperature Case 2 – Standard Output Location #38 Azimuth: 135 Degrees, Elevation: 6.20 Meters, Inside Liner Surface, Mid-height (Dashed Lines Show Total Strain - $\alpha\Delta T$)

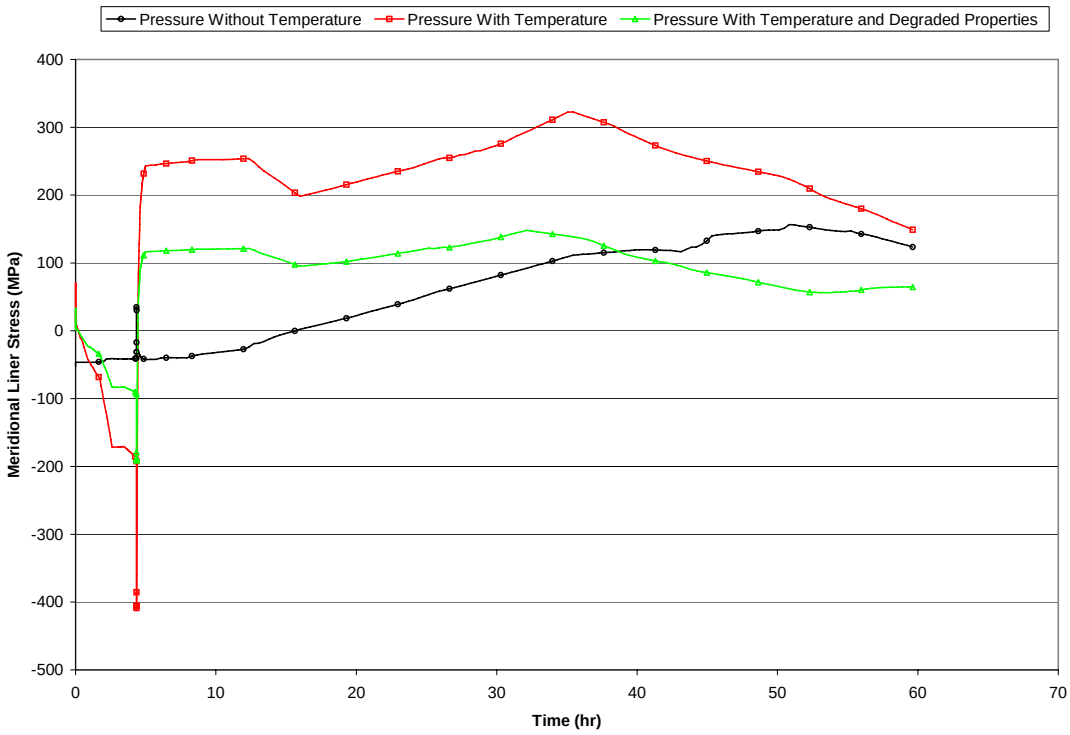

Figure 18b. 1:4 Scale PCCV With Temperature Case 2 – Standard Output Location #38 Azimuth: 135 Degrees, Elevation: 6.20 Meters, Inside Liner Surface, Mid-height

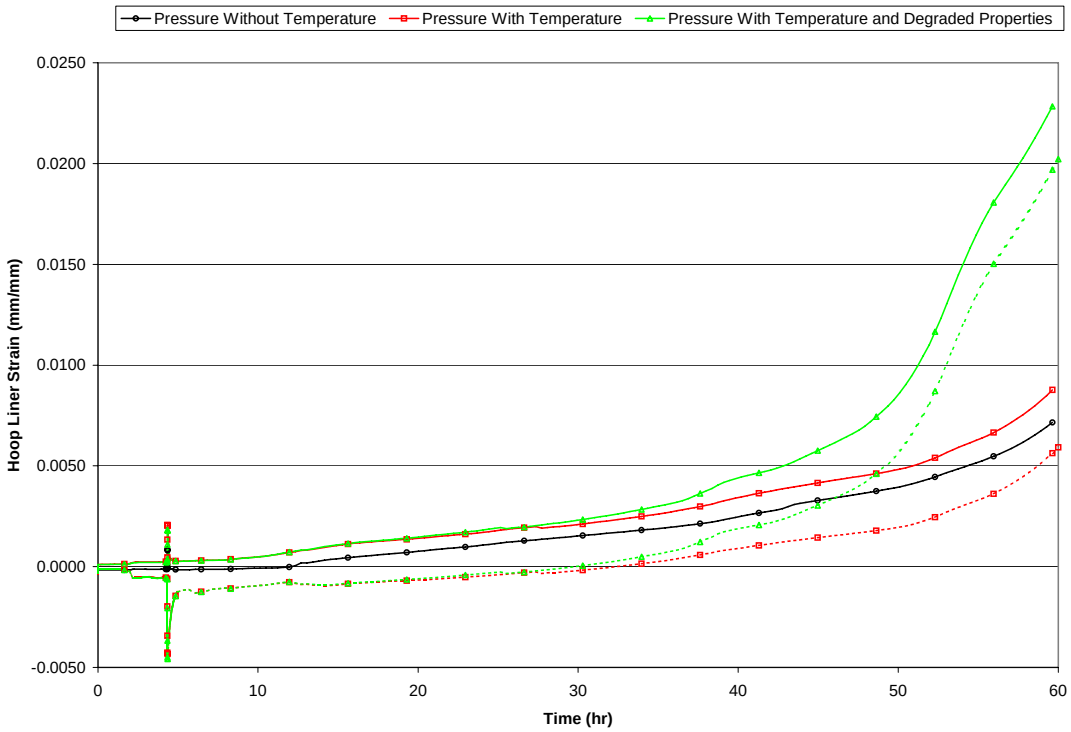

Figure 19a. 1:4 Scale PCCV With Temperature Case 2 – Standard Output Location #39 Azimuth: 135 Degrees, Elevation: 6.20 Meters, Inside Liner Surface, Mid-height (Dashed Lines Show Total Strain - $\alpha\Delta T$)

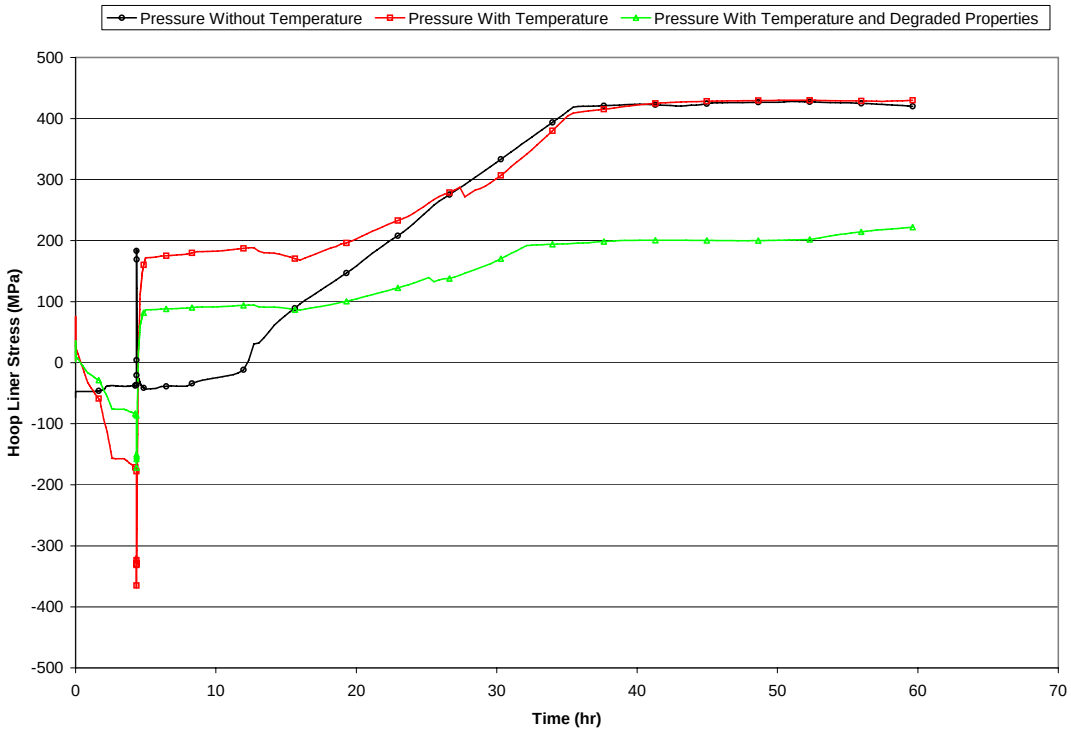

Figure 19b. 1:4 Scale PCCV With Temperature Case 2 – Standard Output Location #39 Azimuth: 135 Degrees, Elevation: 6.20 Meters, Inside Liner Surface, Mid-height

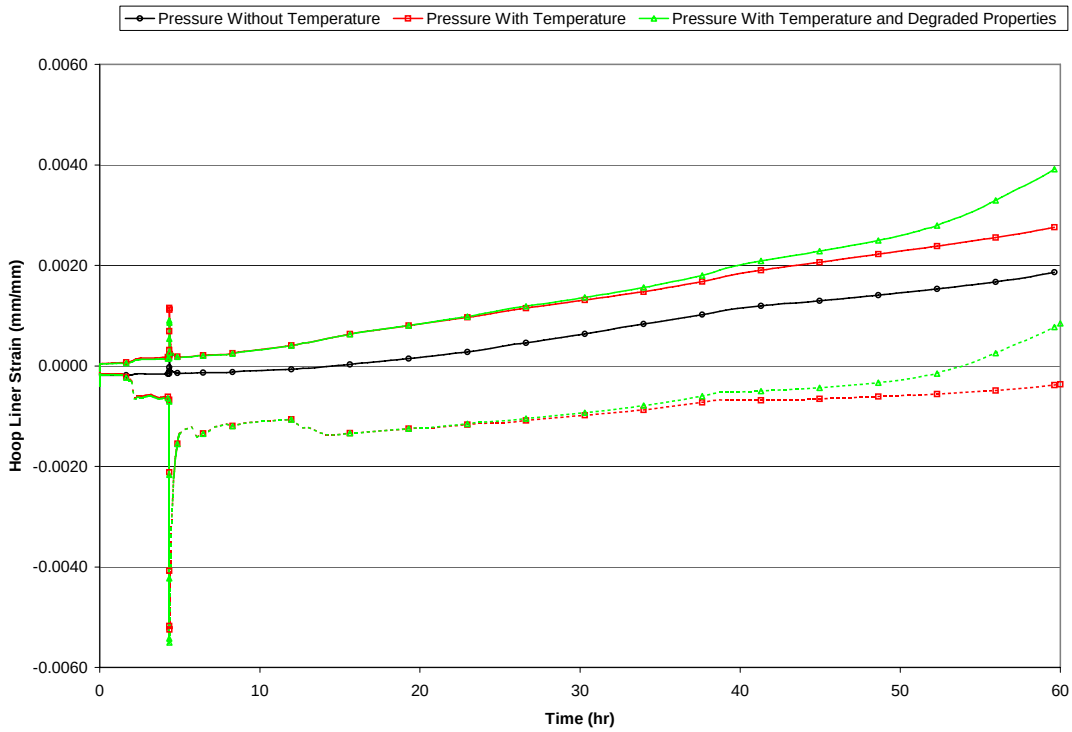

Figure 20a. 1:4 Scale PCCV With Temperature Case 2 – Standard Output Location #41 Azimuth: 135 Degrees, Elevation: 10.75 Meters, Inside Liner Surface, Springline (Dashed Lines Show Total Strain - $\alpha\Delta T$)

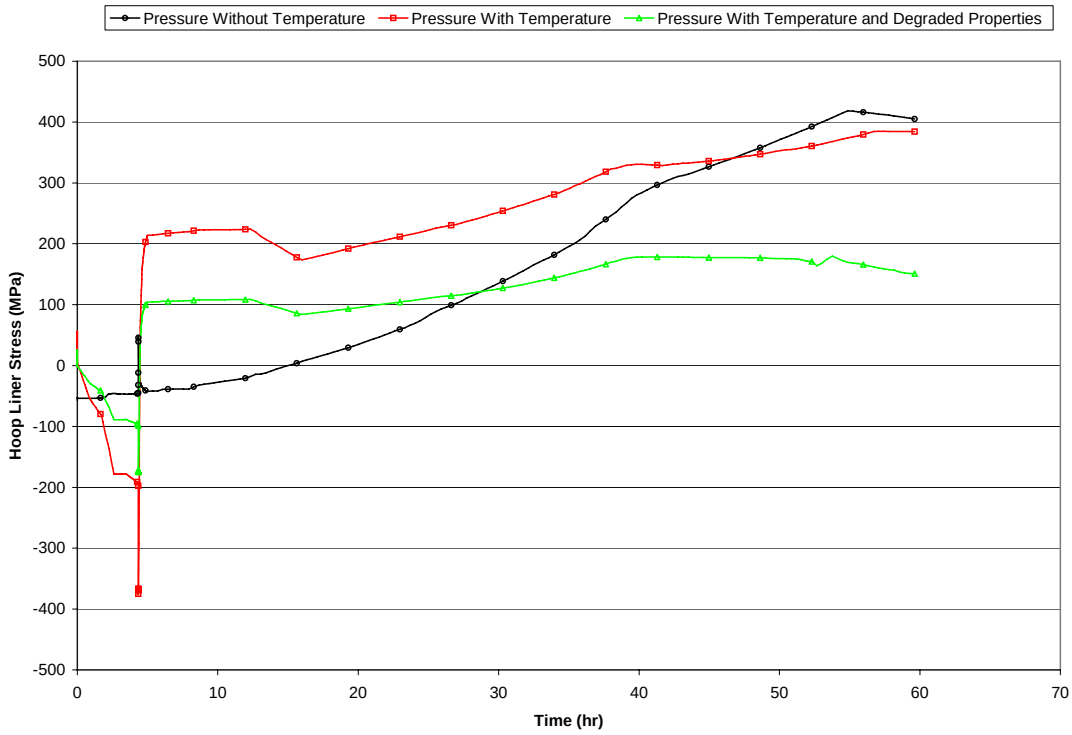

Figure 20b. 1:4 Scale PCCV With Temperature Case 2 – Standard Output Location #41 Azimuth: 135 Degrees, Elevation: 10.75 Meters, Inside Liner Surface, Springline

The observations of differences in the Case 2 results are as follows.

For Temperature Case 2, the temperature starts lower, i.e., at 24 degrees C, so the pressure-only and temperature results start out nearly together at low pressure and early time.

The Case 2 analyses were much more numerically sensitive and difficult to run, especially to get through the temperature/pressure spike that occurs at about time of 4 hours.

For Case 2, as shown in Figures 11 and 12, the temperature induces large displacements, and the vertical displacements are especially large. Also, the vertical displacements are not significantly influenced by the material property degradation, but the radial displacements are. At the cylinder wall mid-height, for example (Figure 11, or similarly at Elevation 6.2m, which shows similar or even larger displacements), the thermal solution with and without material property degradation track closely together out to ~35 hours, or P= 2.8 Pd / T=240C, but then begin to separate. By time=50 hours, P=3.2Pd / T=295C, the cylinder mid-height (Elev. 6.2 m) radial displacements are at 20 mm, 26 mm, and 40 mm for the pressure-only, pressure + temp, and pressure + temp + property degradation analyses, respectively. So while the temperature alone accounts for some differences, property degradation, especially the loss of most of the liner strength, creates a doubling of radial displacement.

Turning next to Figures 13 and 14, the meridional rebar strains near the base of the cylinder increase significantly due to the thermal deformations. The outer rebar strain changes dramatically, and this is notable because the concrete in this region is not significantly heated. All of this strain difference is a result of deformation of the cross-section caused by heat applied to the inner portion of the containment wall. It is particularly interesting to note that the temperature case removes the tendency toward concrete compressive crushing at the outer surface of the wall-base juncture.

Figures 15 and 16 show similar plots for meridional rebar at the springline (Elev. 10.75 m). The plots show a significant separation between the analysis with and without thermal property degradation, beginning at time equal 40 hours. Here the cylinder is expanding significantly in the radial direction, and this causes flexure at the springline. For the Case 2, this flexure grows quite large, and is much larger than for the pressure-only case. The flexure becomes large enough to induce meridional yielding of the liner and of the inner meridional rebar, whereas these components remained elastic in the pressure-only analysis.

The next series of plots, Figures 17-20 show liner strains and stresses at the base of the cylinder, mid-height, and springline. An interesting phenomenon that has emerged related to the pressure-plus-temperature results is liner stress behavior. In most of the containment research program, the analyses have not looked closely into study of liner stress because the focus of the Containment Capacity Research has been on beyond design basis loads, where liner strains are most important for predicting failure. But when temperature is added, examination of stresses becomes very important, since strains alone can be deceptive for predicting failure. Extracting further information from the analyses to fully understand the pressure-plus-temperature behavior is necessary.

The two additional pieces of information for the liner are stress, and also strain adjusted for thermal strain. In the elastic regime, temperature produces a strain in the absence of stress. In the plastic regime the relations become more complex, but it is still instructive to plot an estimate of the "strain producing stress," as

$$\varepsilon^{e} = \varepsilon_{total} - \alpha\,(T-T_0)$$

The strains pulled directly from the ABAQUS analysis are ε_{total}, and these are plotted in the usual way as the solid curves in Figures 17a, 18a, 19a, 20a. The estimates of "strain producing stress" or "ε_e" are shown as dashed lines on these figures. The most significant observation is that for Case 2, the liner reaches general compressive yield during the early temperature spike. In fact, the thermally induced stress is three-times large enough to cause yield, thus causing plastic strains such that the liner reaches tensile yield upon cooling of this pressure spike. This phenomenon is illustrated in stress-strain space in Figure 21. Then the liner remains in a state of general yield throughout the rest of the analysis, as more pressure is applied. This phenomenon leads to large differences in the liner stress-histories between pressure-alone versus pressure-plus-temperature, even though the strain histories are not that much different.

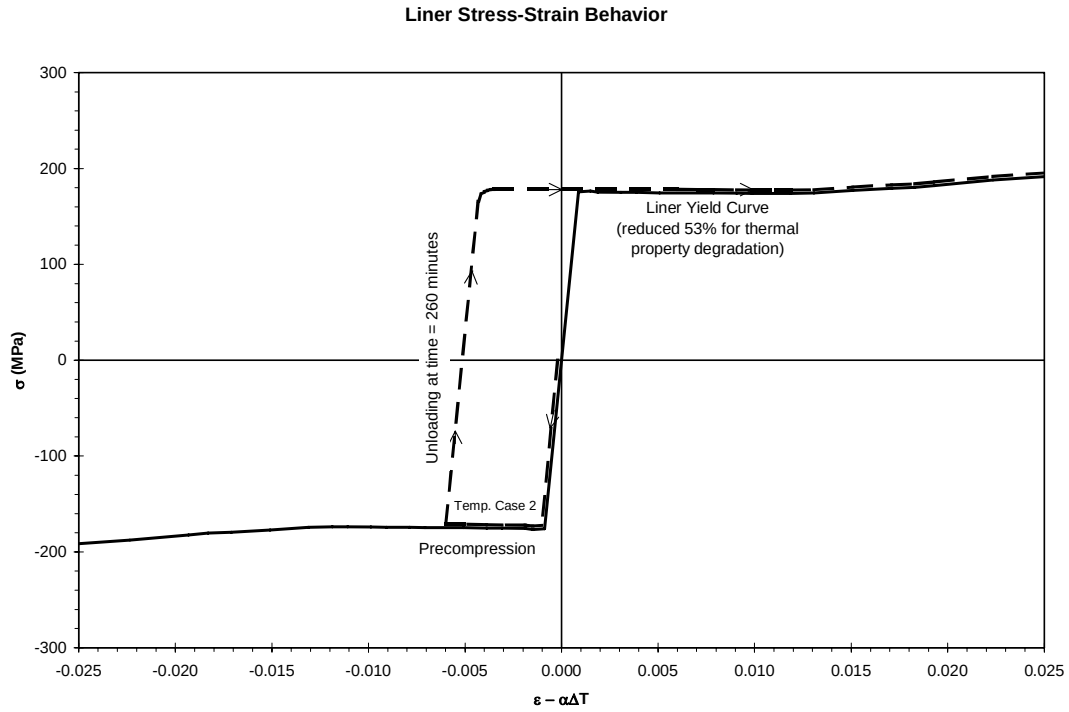

Figure 21. Liner Stress-Strain Behavior showing Schematic of Mid-height hoop Stress-Strain, Temp Case 2.

The corresponding stress histories are plotted in Figures 17b, 18b, 19b, 20b. In evaluating these plots, two observations can be made. First, there is a small mismatch between the pressure-only analysis and the pressure-plus-temperature analyses, at the start of the analyses. While for Case 1, this is directly due to the initial conditions of the analysis, i.e., 100C, for Case 2 the explanation is partly numerical. At the start of the analyses, the dead load, tendon prestress, and initial temperature (23 degrees C) are all applied as initial conditions in ABAQUS, but numerically, applied in a 10 increment step in order to allow the program to reach equilibrium before applying the pressure and temperature "time" history. But ABAQUS applies the prestress 100% in one increment, while the dead load and temperature are applied as "ramping" up proportionately to the number of increments in the step. 25 degrees C is input to the program as the "reference temperature" or the temperature at zero thermal strain. But in increment 1 of Step 1, ABAQUS internally applies a temperature of 2.5 degrees C, and in increment 2, 5.0 degrees C, and so forth until 25 degrees C is reached at the end of the Step. So during this step, the liner is first cooled, which adds some tensile stresses to the liner. Unfortunately, by the end of the first step, not all of this initial tension is recovered, and this leads to the mismatch in

initial stresses seen in the plots. This is not thought to be significant in evaluating the results, but it does point to a lesson learned: it would probably be preferable to modify the temperature history and the solution strategy such that the reference temperature be made zero. The temperature history would all be reduced by 25 degrees C, and then ABAQUS would not start the run by cycling temperature down to zero and back to 25 degrees in the first load step.

The second observation is that the stress curves for the analysis with degraded properties is significantly different than without degraded properties. This is attributable to the "knockdown" factor applied to the yield curve and to Young's modulus of 0.47, to account for the high temperature reached in the initial temperature spike.

One of the most important plots to draw conclusions from is Figure 19a, because this shows the largest "free-field" liner strains in the analysis. As previously mentioned, it is important to consider the dashed lines, since this is an approximation of the "strain causing stress." Based on a revised (at temperature) failure criteria assigning a 50% increase in ductility, and using the pressure-only studies as a baseline for prediction of liner tearing, then the liner tearing mode with temperature is predicted to occur at a maximum free-field hoop strain of approximately 1.11%. For the analysis with pressure-plus-temperature-and-degraded-properties, the hoop liner strain reaches 0.011 at Time of 3160 minutes. This corresponds to an event pressure 1.28 MPa and temperature of 299 C.

3.5. Ring Model Analysis Results

The ring model for studying hoop tendon behavior (Figure 4) was utilized for, and described in detail in, the ISP Phase 2 submittal. However, to address some of the limitations of the axisymmetric model analyzed with ABAQUS Version 5.8 (using uncoupled thermally degraded material properties), a new ring model was developed 'from scratch' using ABAQUS Version 6.4. Using this version enabled use of the ABAQUS 'concrete damaged plasticity model' and full coupling of material properties with temperature. The material property degradation was assigned versus temperature according to the formulae derived earlier in this report. The temperature distribution through the wall was applied to the nodes and updated at every step in the analysis. As described in the Phase 2 report, the ring model uses 'contact surfaces' between the concrete and tendons, and a tendon friction coefficient between the surfaces. In this way, the tendons are prestressed in a stepwise process, similar to how it occurs in the field, with jacking forces applied first, and then relaxed to simulate anchor slip. The tendon force distribution in a typical tendon is shown in Figure 22, the curve labeled 'Initial Post-tensioning.'

The first case that was run was Case 2, since this controlled most of the failure prediction results. The tendon force distribution at the top of the pressure/temperature spike (time~4.3 hours) and at time=35 hours are shown for analysis with no temperature effects, temperature effects, and temperature effects and degraded properties. It is interesting to note the shifting of tendon forces with azimuth due to the combination of temperature, friction and cylinder radial expansion.

The tendon strain history is shown in Figure 23. Tendon force history looks the same, but with a multiplier of approximately 66×10^6 on strain to get Force (in Newtons). Due to convergence difficulties, the analysis could not be advanced farther than 38 hours, which corresponds to a pressure and temperature of 250C and 1.15 MPa (2.9 x Pd). But the analysis still shows the hoop tendon response trend. Hoop tendon force and strain increase with temperature for Case 2, because the expansion of the liner and the concrete near the liner force the tendon to larger strain. Comparing the green with the black curve, at 36 hours, strain increases from .0055 to .0063, or 15%. Extrapolating from this, the trend indicated in the ring model for Case 2 appears to support the same conclusions that are drawn from the axisymmetric analysis.

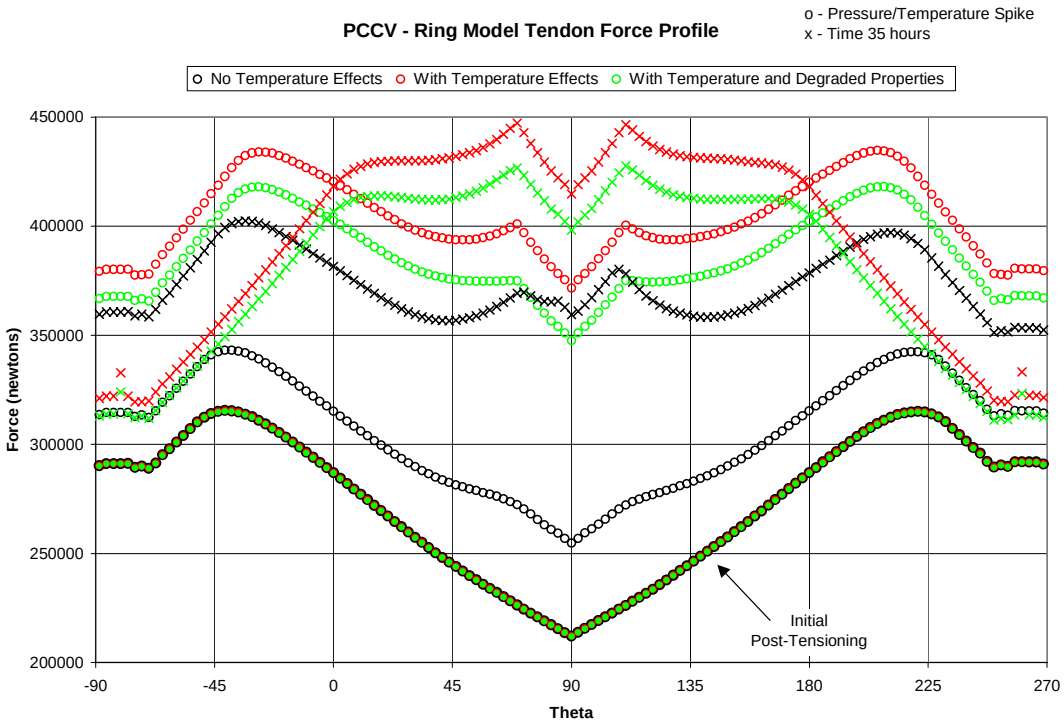

Figure 22. Hoop Tendon Force distribution for Ring Model, Temp Case 2 Analysis

The ring model hoop tendon results for Case 1 show a similar trend. The Case 1 analyses converged to time=38, which corresponds to pressure of 1.32 MPa (3.33 Pd), and temperature of 195ºC. (It should be reminded that Case 1 this is a 'steady state' solution so the units of time are essentially irrelevant.) This is approximately the same pressure as was reached in the LST for the 1:4 Scale PCCV. The force distributions at several pressures are shown in Figure 24, and the strain 'history' for 0-degree azimuth is shown in Figure 25, and for 135-degree azimuth is shown in Figure 26. The force distributions show similar trends as those of the pressure-only, ABAQUS-5.8 analyses reported in the ISP-Phase-2 work. As the cylinder expands at larger pressure, the 'V-shaped' tendon force pattern caused by friction eventually changes to a more uniform force along the tendon, and ultimately, to where the largest force occurs mid-way between buttresses.

The hoop tendon strain for the analysis with temperature and degraded properties has reached 0.008, which exceeds the global hoop strain at which many liner tears led to the end of the LST test. It is also interesting to note that the difference between the analysis with temperature and without temperature is decreasing at larger pressures. By 3.33 Pd for the Case 1 analysis, the tendon strain with temperature effects is only 5% larger than for analysis with pressure alone. This provides further support to the conclusions being drawn about temperature effects on global behavior.

A last point to make is comparing radial displacement at 135-degree azimuth between the ring and axisymmetric models. The PCCV LST test largest radial displacement was approximately 30 mm, reached at a pressure of 1.3 MPa. The ring model and axisymmetric models reach this 30 mm radial displacement at pressures of Ring Model Pressure Only – 1.27 MPa, Axisymmetric Pressure Only – 1.31 MPa, Ring Model Pressure + Temp – 1.26 MPa, Axisymmetric Pressure + Temp – 1.28 MPa. Such a comparison shows close enough agreement that conclusions made about global tendon behavior taken from the ring model can be applied also to the axisymmetric analysis with reasonable confidence.

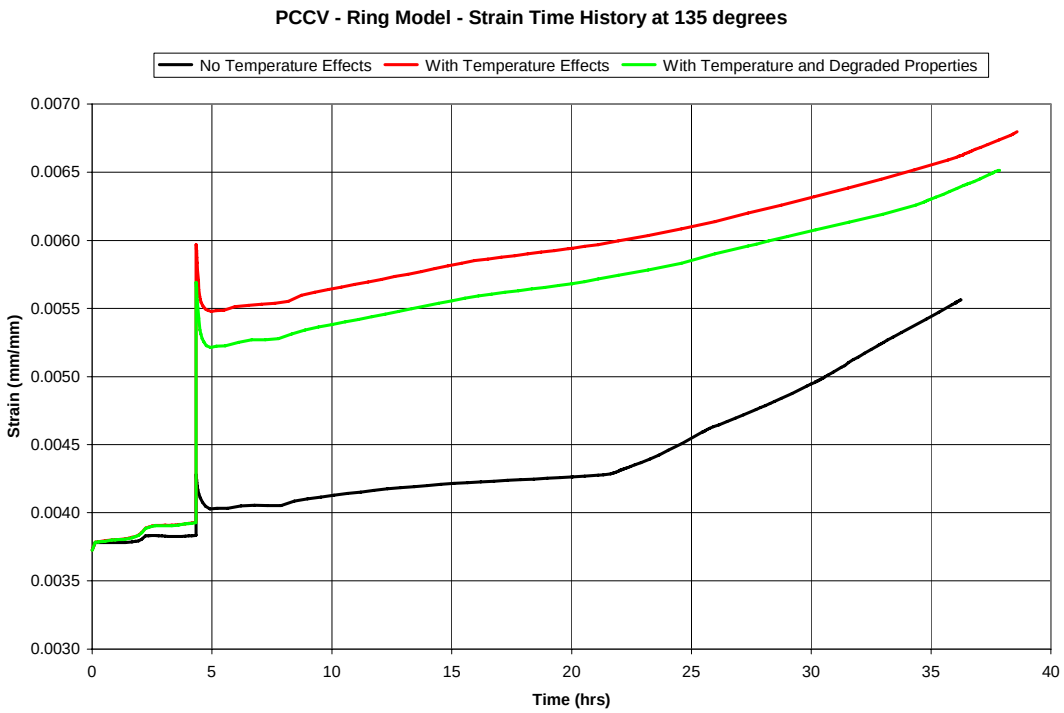

Figure 23. Hoop Tendon Strain History for Ring Model, Temp Case 2 Analysis, at 135-degree Azimuth

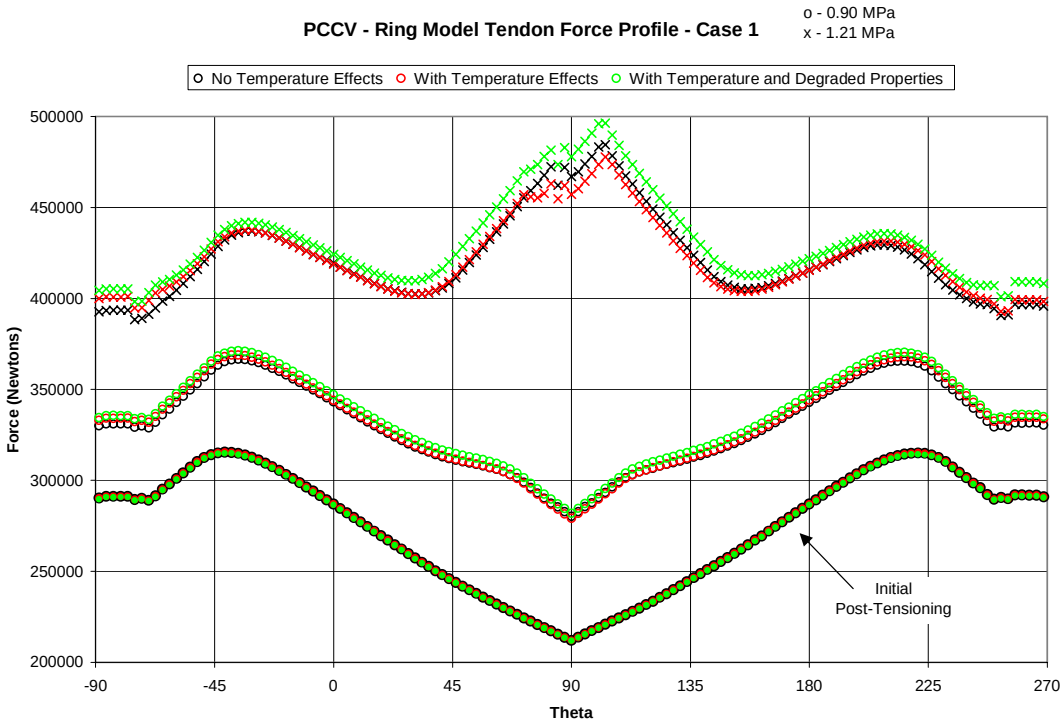

Figure 24. Hoop Tendon Force distribution for Ring Model, Temp Case 1 Analysis

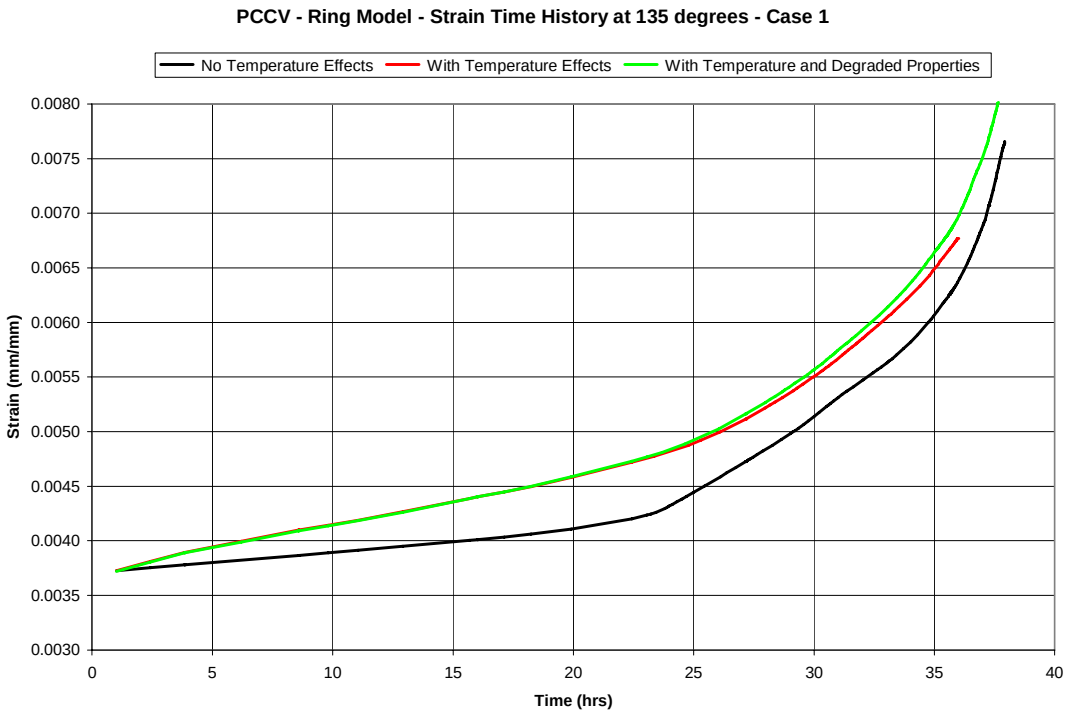

Figure 25. Hoop Tendon Strain History for Ring Model, Temp Case 1 Analysis, at 135-degree Azimuth

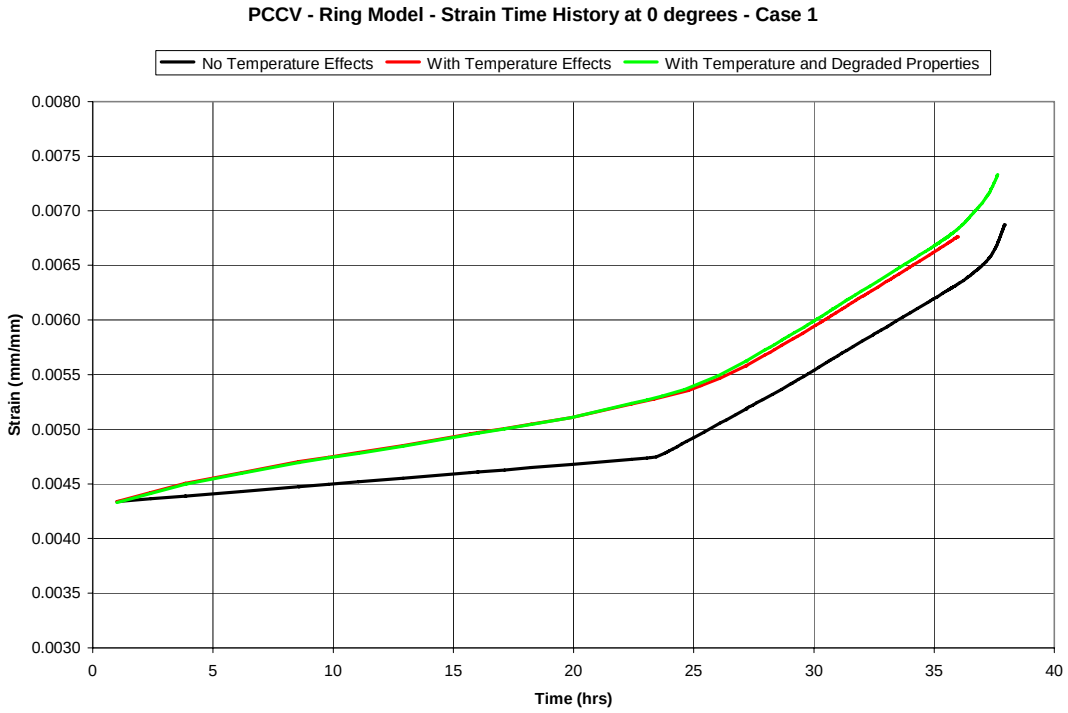

Figure 26. Hoop Tendon Strain History for Ring Model, Temp Case 1 Analysis, at 0-degree Azimuth

4. CONCLUSIONS

The axisymmetric analyses for 1:4 and full scale finite element models of the PCCV subjected to pressure and temperature, with and without material property degradation, have led to the following conclusions:

- All of the cases, including pressure only, begin at 25C (77F), but because Case 1 is for Saturated Steam, the temperature starts out at 100C (212 F), so the thermal response for Case 1 shows generally an immediate jump in deformation associated with temperature relative to the pressure-only case.

- The deformations associated with temperature are very significant, especially for vertical displacement. For radial displacement at cylinder mid-height, displacement with temperature at 3Pd and 185C, are nearly double those for pressure alone. For vertical displacement at cylinder top (springline) displacement with temperature and 3Pd is nearly 8-times the pressure only displacement. At full scale, the thermally induced displacements can be very large and may lead to piping and equipment interference problems.

- For Case 1, in all cases, the differences due to thermally induced material property degradation, are very minor, and this tends to justify the use of an approximate material property degradation approach, at least for Case 1.

- The Case 2 analyses were much more numerically sensitive and difficult to run, especially to get through the temperature/pressure spike at about time equal 4 hours.

- For Case 2, the temperature again induces large displacements, and the vertical displacements are quite large. Also, the vertical displacements are not significantly influenced by the material property degradation.

- For Case 2, the radial displacements are significantly influenced by the material property degradation. At the cylinder wall mid-height, the thermal solution with and without material property degradation track closely together out to ~35 hours, or P= 2.8 Pd / T=240C, but then begin to separate. By time=50 hours, P=3.2Pd / T=295C, the cylinder mid-height radial displacements are nearly double for the temperature/property degradation case over the pressure case, and are about 50% higher than the pressure + temperature case without property degradation.

- It appears that thermal and property degradation analysis in a Case 2 scenario would reduce the pressure causing failure of the vessel. It appears that “global” failure of the vessel would be reduced from the 3.6Pd that occurred in the SFMT to approximately 3.4Pd. And local liner failure pressure would be affected since these are “driven” by global displacements and liner strains.

The final prediction summaries are shown in the tables as requested for the ISP. The liner tearing “leakage” pressure reduces from pressure-only prediction of 1.33 MPa to 1.28 MPa.

Table 1. Results Summary With pressure-only

Event Pressure (MPa) Milestones For Pressure-only Analysis

Cracking		Liner Yield	Liner Rupture	Rebar Yield		Hoop Tendon Stress			Pressure @ Failure	Free Field Hoop Strain @ Failure
Hoop	Meridonal			Hoop	Meridonal	Yield	2%	Rupture		
0.60	0.60	1.02	1.33**	1.10	1.30	1.18	1.35	1.42	1.33*	0.74%*

**Assumes "perfect welds" and no grinding flaws

Table 2. Results Summary With pressure-plus-temperature (Case 2)

Event Milestones for Pressure-Plus-Temperature Analysis with Temperature Property Degradation

	Cracking		Liner Yield**	Liner Rupture	Rebar Yield		Hoop Tendon Stress			Pressure @ Failure	Free Field Hoop Strain @ Failure
	Hoop	Meridonal			Hoop	Meridonal	Yield	2%	Rupture		
Pressure	0.50	0.40	1.10	1.28	1.13	1.10	1.15	1.30	1.33	1.28*	1.11%*
Temperature	380	240	245	299	248	245	254	302	310	299	
Time	260	260	2200	3160	2280	2200	2360	3240	3600	3160	at free-field Elev. 6.2 m

*Assumes “perfect welds” and no grinding flaws, tendon rupture at 2% strain

**Liner yields in compression at 0.5MPa, 220C, on initial pressure spike

Pressure in Mpa, Temp in degrees C, time in minutes

All data in this table is for Temp Case 2, because it is the controlling case.

5. REFERENCES

1. Dameron, R. A., Hansen, B. E., Vargas, M. R., Rashid, Y. R., Pretest Analysis of a 1:4-Scale Prestressed Concrete Containment Vessel Model," NUREG/CR-6685, SAND2000-2093. Albuquerque, NM: Sandia National Laboratories, 2000.

2. Dameron, R.A., et al, "Posttest Analysis of the NUPEC/Sandia 1:4 Scale Prestressed Concrete Containment Vessel," NUREG/CR-6809, SAND2003-0839P, Albuquerque, NM: Sandia National Laboratories, 2003.

3. "ABAQUS Users Manual," Version 5.8, 1998. Providence, RI: Hibbitt, Karlsson & Sorensen, Inc.

4. "ANACAP-U User's Manual," Version 2.5, 1997. San Diego, CA: ANATECH Corp.

5. M. Hessheimer, *International Standard Problem No. 48, Containment Capacity*, NEA/CSNI/R(2004)11, OECD Nuclear Energy Agency, Paris, FR, July, 2004.

6. H.G. Willschuutz, et al, "Simulation of Creep Tests with French or German RPV-steel and investigation of a RPV-support against failure," Pergamon, "Annals of Nuclear Energy," December, 2002.

7. A. Wada, et al, "Study of Structural Redundancy of High-Rise Steel Building Due to the Effect of Heat and Loss of Vertical Structural Members.

8. FEMA, "Word Trade Center Building Performance Study, FEMA403, 2002.

9. Luk, V. K., *Pretest Round Robin Analysis of a Prestressed Concrete Containment Vessel Model*, NUREG/CR-6678, SAND00-1535, Sandia National Laboratories, Albuquerque, NM, August, 2000.

Appendix L: Scanscot Technology
Phase 2 and Phase 3: L-1 to L-223

Page intentionally left blank

SCANSCOT Technology

	Ref.	Edition
Technical Report	**03402/TR-01**	**2**

Title

ISP 48: Posttest analysis of the NUPEC/NRC 1:4-scale prestressed concrete containment vessel model

Abstract

The design events for a reactor containment usually refers to accidental loading conditions for which leak-tightness and load-bearing capacity should be verified. This involves the containment being loaded far into the non-linear range, putting high demands on the engineering simulations. It is therefore of vital importance to ensure that the methods applied for advanced structural analysis can be verified and validated.

This report presents a method of utilizing the finite element technique for determining the load effects due to internal overpressurization in combination with temperature loads for pre-stressed concrete reactor containments. The method is verified and validated by comparison with test data from a large-scale overpressurization test performed on the NUPEC/NRC 1:4-scale model of a prestressed concrete containment vessel model at Sandia National Laboratory, USA. The prototype for the model is the containment building of unit 3 at the Ohi Nuclear Power Station in Japan, an 1127 MW Pressurized Water Reactor (PWR) unit.

The structural response predicted by applying a three-dimensional model approach agrees very well with registred test data. Pressure levels related to cracking of concrete, yielding of the steel liner, and the collapse of the containment are captured in conformity with registred test data. To capture the pressure level at which rupture of the steel liner occurs, more detailed local models are needed, this is beyond the scope of this report. However, the analysis methods are capable of catching the zones where excessive yielding of the steel liner occurs, corresponding well with the first registred liner rupture position. The applied analysis method accuratly predicts the displacements of the containment, and strains in the steel liner, the rebars and the pre-stressing tendons.

Some different approaches on how to model unbonded pre-stressing tendons have been evaluated in the report. The chosen approach predicts pre-stressing forces very well in accordance with registred test data. This method makes it possible to take into consideration the transition from the initial uneven pre-stressing force distribution along the tendons, to a more or less even distribution along the tendons during pressurization.

The proposed method can be used for the design of new containments as well as for the structural verification of existing containments. The method can be applied in case of design or evaluation against specified pressure levels and acceptance criterias according to national standards, or to calculate the leak-tightness and load-bearing capacity in order to estimate the safety margins of the structure. Furthermore, the analysis results can be used as a point estimate of leakage or structural collapse to be used in a probability safety assessment (PSA) of the plant.

It is also possible to utilize the method when verifying safety-related structures for other types of accidental load effects.

Edition	Date	Author	Reviewed	Approved
1	2004-04-20	O. Jovall/M. Pålsson/B. Svärd	Jan-Anders Larsson	Jan-Anders Larsson
2	2005-02-23	O. Jovall/M. Pålsson/B. Svärd	Jan-Anders Larsson	Jan-Anders Larsson

Scanscot Technology AB
Ideon Research Park, S-223 70 Lund, Sweden
Telephone: +46 46 286 23 03 Telefax: +46 46 12 87 45

Technical Report 03402/TR-01

ISP 48: Posttest analysis of the NUPEC/NRC 1:4-scale prestressed concrete containment vessel model

TABLE OF CONTENTS

List of Revisions

Edition	Date	Revised pages	Revision refer to
1	2004-04-20	New report	
2	2005-02-23	Chapter 8. Part II and part III. Abstract.	New chapter added. New parts added to the report. Revised according to the new parts.

PREFACE

This report is structured in the following three parts, Part I: Structural analysis and comparison with test data, Part II: Pressure + temperature load analysis, and finally Part III: Conclusions.

In Part I, a finite element analysis of a pre-stressed concrete reactor containment exposed to overpressurization is carried out. The analysis results are compared with test data registred during a large-scale overpressurization test performed on a 1:4-scale model of a prestressed concrete containment vessel model at Sandia National Laboratory, USA.

The scope of Part II covers a FE analysis of the same reactor containment as in Part I, but exposed to overpressurization in combination with temperature loads.

In Part III, conclusions are drawn based on the work carried out in Part I and Part II of this report.

We would like to thank the organizers of the ISP 48 project, Eric Mathet at OECD/NEA, and Michael F. Hessheimer at Sandia National Laboratory.

We would also like to take the opportunity to thank our sponsors who have made our participation in the ISP 48 project possible;

- The Swedish Nuclear Power Inspectorate (SKI)
- The Swedish operators Forsmark Kraftgrupp AB, OKG Aktiebolag, and Ringhals AB
- The Finnish operator Teollisuuden Voima Oy (TVO)

Lund 2005 Ola Jovall

Please note that this report is intended to be printed in colour. To get a free digital colour copy of this report please send and e-mail to jovall@scanscot.com.

ABSTRACT

The design events for a reactor containment usually refers to accidental loading conditions for which leak-tightness and load-bearing capacity should be verified. This involves the containment being loaded far into the non-linear range, putting high demands on the engineering simulations. It is therefore of vital importance to ensure that the methods applied for advanced structural analysis can be verified and validated.

This report presents a method of utilizing the finite element technique for determining the load effects due to internal overpressurization in combination with temperature loads for pre-stressed concrete reactor containments. The method is verified and validated by comparison with test data from a large-scale overpressurization test performed on the NUPEC/NRC 1:4-scale model of a prestressed concrete containment vessel model at Sandia National Laboratory, USA. The prototype for the model is the containment building of unit 3 at the Ohi Nuclear Power Station in Japan, an 1127 MW Pressurized Water Reactor (PWR) unit.

The structural response predicted by applying a three-dimensional model approach agrees very well with registred test data. Pressure levels related to cracking of concrete, yielding of the steel liner, and the collapse of the containment are captured in conformity with registred test data. To capture the pressure level at which rupture of the steel liner occurs, more detailed local models are needed, this is beyond the scope of this report. However, the analysis methods are capable of catching the zones where excessive yielding of the steel liner occurs, corresponding well with the first registred liner rupture position. The applied analysis method accuratly predicts the displacements of the containment, and strains in the steel liner, the rebars and the pre-stressing tendons.

Some different approaches on how to model unbonded pre-stressing tendons have been evaluated in the report. The chosen approach predicts pre-stressing forces very well in accordance with registred test data. This method makes it possible to take into consideration the transition from the initial uneven pre-stressing force distribution along the tendons, to a more or less even distribution along the tendons during pressurization.

The proposed method can be used for the design of new containments as well as for the structural verification of existing containments. The method can be applied in case of design or evaluation against specified pressure levels and acceptance criterias according to national standards, or to calculate the leak-tightness and load-bearing capacity in order to estimate the safety margins of the structure. Furthermore, the analysis results can be used as a point estimate of leakage or structural collapse to be used in a probability safety assessment (PSA) of the plant.

It is also possible to utilize the method when verifying safety-related structures for other types of accidental load effects.

PART I

STRUCTURAL ANALYSIS AND COMPARISON WITH TEST DATA

1. INTRODUCTION

1.1 Background

The design event for a reactor containment refers usually to accidental loading conditions for which leak-tightness and load-bearing capacity should be verified. This involves the containment to be loaded far into the non-linear range, putting high demands on the engineering simulations.

It is therefore of vital importance to ensure that the methods applied for advanced structural analysis can be verified and validated. The verification of codes for structural analyses (FEA-software) is made by the supplier, usually at the local finite element level. The codes are also usually verified with the help of experimental tests on smaller test cubes, columns, beams and slabs loaded to failure, i.e. laboratory tests. To achieve an even higher accuracy in analysis results it is necessary to compare analysis results with the measured response from tests on large-scale structures, see Figure 1.1.

In the ISP 48 project, benchmark studies are performed in order to compare structural analysis results to test data from a large-scale test of a 1:4-scale prestressed concrete containment vessel.

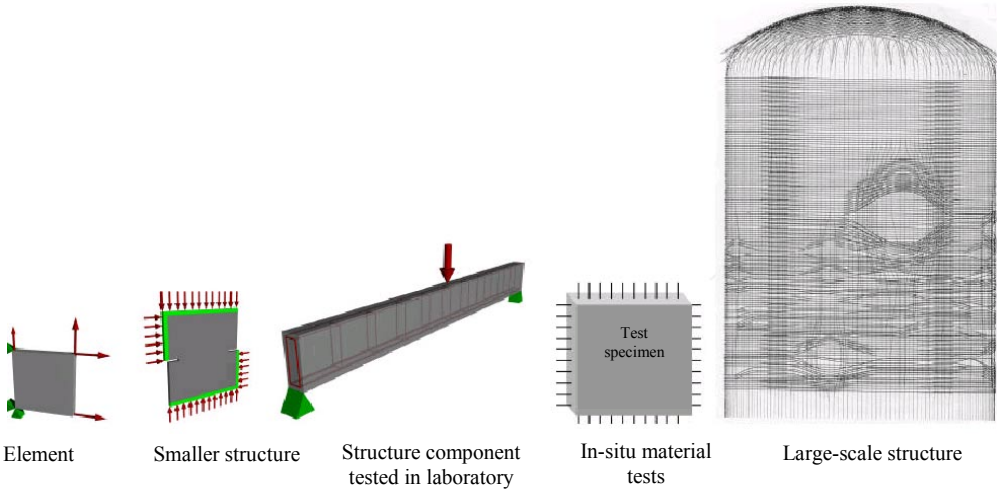

Figure 1.1 Examples of structural analysis verification.

Scanscot Technology has for more than ten years carried out reactor containment investigations for the nuclear power industry in Sweden, using advanced finite element analysis methods. The ISP 48 project gives us the possibility to validate our software by comparing analysis results with large-scale experimental test results. Another important benefit from the project is to share experience and knowledge with colleagues from other countries who are also working in this subject field

Participation in this project also provides valuable input to the ongoing EURATOM 5th framework programme project CONMOD [1], in which Scanscot Technology is one of the participants. The CONMOD project aims to

create a system which will ensure that safety requirements for concrete containment structures will be up-held during the entire planned lifetime of plants and possibly during an extended lifetime. An important part of the project is to develop the application and understanding of Non-Destructive Testing (NDT) techniques for the assessment of conformity and the condition of concrete reactor containments as well as to integrate this with state-of-the-art and developed Finite Element (FE) modelling techniques and analysis of structural behaviour. The objective being to create a diagnostic method for the evaluation of defects, ageing and degradation of concrete containments.

Our possibility to participate in ISP 48 has been made possible by financial support from the Swedish and Finnish nuclear power industry (Oskarshamn, Ringhals, Forsmark and TVO), and the Swedish Nuclear Power Inspectorate.

1.2 General

The Nuclear Power Engineering Corporation (NUPEC) of Japan and the U.S. Nuclear Regulatory Commission (NRC) cosponsored and jointly funded a Cooperative Containment Research Program at Sandia National Laboratories (SNL), USA, from July, 1991 through December, 2002.

As a part of this program, a 1:4-scale model of a pre-stressed concrete containment vessel (PCCV) was conducted and pressurized up to failure. The prototype for the model is the containment building of unit 3 at the Ohi Nuclear Power Station in Japan, an 1127 MW Pressurized Water Reactor (PWR) unit. The design accident overpressure, P_d, of both the prototype and the model containment is 0.39 MPa.

The objectives of the model containment test were to;

- simulate some aspects of the severe accident loads on containment vessels
- observe the model failure mechanisms
- obtain structural response data up to failure for comparison with analytical models

Construction of the model containment commenced January, 1997, and ended June, 2000. During September, 2000, the limit state pressurization test (LST) was carried out. At the end of 2002, the limit state test was complemented with a pressurization up to total collapse of the structure, the structural failure mode test (SFMT). During pressurization the structural response was monitored, giving information on displacements, liner, rebar, concrete and tendon strains and tendon anchor forces. In addition, acoustic monitoring, video and still photography were used to monitor the structural behaviour.

During 2002, the Nuclear Energy Agency (NEA) at OECD, decided to include the NUPEC/NRC model containment test as an International Standard Problem (ISP) on containment capacity, ISP 48. At a first meeting in Stockholm, Sweden, the objectives and schedule was set up. The ISP 48 project started up January, 2003 and will be ended June, 2005.

The objective of the ISP 48 is to extend the understanding of capacities of actual containment structures based on results of the NUPEC/NRC model containment test and other previous research. Two questions regarding full size structures arise; How to transpose to real size containment (would the onset of leakage be later and much closer to the burst pressure)? How would including the effect(s) of accident temperature change the outcome?

The ISP 48 posttest analysis of the NUPEC/NRC model containment was decided to consist of four phases;

1. Data collection and identification
2. Calculation of the limit state test (LST) – mechanical loading
3. Calculation of the response under both mechanical and thermal loadings
4. Reporting, Workshop

A detailed description of these four phases with a corresponding time-schedule is given in Appendix 1. Appendix 1 also includes a table of the names of the ISP 48 participants.

The scope of part I of this report covers the phase 2 calculations performed by Scanscot Technology.

1.3 Over-pressurization test

The model containment was a 1:4-scale model of the prestressed concrete containment vessel (PCCV) of an actual nuclear power plant in Japan, Ohi-3 (Figure 1.2). Ohi-3 is an 1127 MW Pressurized Water Reactor (PWR) unit, one of four units comprising the Ohi Nuclear Power station located in Fukui Prefecture, owned and operated by Kansai Electric Power Company.

The prototype containment, Ohi-3, consists of a thin prestressed concrete cylindrical shell with a hemispherical dome and a continuous steel liner anchored to a reinforced concrete basemat which extends beyond the containment to support other plant structures.

The features and scale of the model containment were chosen so that the response of the model would mimic the global behavior of the prototype but also to represent local details, particularly those around penetrations. One of the primary considerations was the desire to utilize construction materials that were identical, or nearly so, to the material used in the construction of the prototype.

It was decided that the scale of the model would be a uniform 1:4, with minor exceptions to accommodate fabrication and construction concerns. This was judged to be the minimum scale that would allow the steel liner to be constructed from prototypical materials and fabricated with details and procedures that were representative of the prototype. The model containment and its overall geometry and dimensions are shown in Figure 1.3 and Figure 1.4.

It was also decided that the model containment would include representation of the major penetrations, namely the equipment hatch (E/H), the personnel air lock (A/L), the main steam (M/S) and the feed water (F/W) penetrations.

Key elements of the design philosophy of the model containment included;

- The model containment would be a uniform 1:4-scale model of the prototype or actual prestressed concrete containment vessel of Ohi Unit 3.
- Elements of the model which would affect the ultimate strength would be equivalent to the prototype. The model liner would be one-fourth the thickness of the prototype liner. Reinforcing ratios would be maintained and the number and arrangement of the prestressing tendons would, to the extent possible, be identical to the prototype.
- The model should be capable of reproducing the failure modes postulated for the prototype, including;
  a) Hoop tensile failure of the cylinder wall
  b) Bending-shear failure at the junction of the cylinder wall with the basemat
  c) Shear failure in the basemat above the tendon gallery
  d) Bearing failure at the tendon anchors
  e) Bending-shear failure at the large penetrations
  f) Bending-shear at the small penetrations
  g) Liner tearing due to strain concentrations at local discontinuities (stiffeners/anchors, thickened reinforcing plates at penetrations and embedments)
  h) Leakage at penetration seals due to ovalization or distortion of the sealing surfaces
- Avoid introduction of non-representative failure modes, as a result of scaling or other modeling artifacts

The general arrangement of the prototype and representative failure mode locations are shown in Figure 1.2.

The decision was to perform a static, pneumatic over-pressurization test at ambient temperature. The test was terminated following a functional failure, i.e. a leak in the model containment, with only limited structural damage occurring. Subsequently, it was decided to re-pressurize the model containment prior to demolition, in an attempt to observe larger inelastic response and, if possible, a global structural failure. This test was performed as a combined pneumatic-hydrostatic test.

Milestones in the construction and testing of the model containment include the following;

12 February 1997	First Basemat Pour (F1)
19 June 1997	First Liner Panel Installed
15 April 1999	Final Dome Pour (D3)
12-14 October 1999	Pretest Round Robin Meeting

8 March-3 May 2000	Prestressing
25 June 2000	Construction Completed
12-14 September 2000	Structural Integrity and Integrated Leak Rate Test
27-28 September 2000	Limit State Test
22 August 2001	Posttest Round Robin Meeting
14 November 2002	Structural Failure Mode Test
3 May 2002	Demolition and Site Restoration Completed

The model containment was not 'designed' in a conventional sense, instead its features were scaled directly from the prototype containment Ohi-3 design with some simplification to facilitate construction, but without compromising the objectives of the test. The basic design philosophies were to ensure that all elements of the containment structure respond essentially elastically (with some minor exceptions for secondary stresses) to the specified design loading conditions.

A detailed presentation of the overpressurization test is given in [2].

a) Plant

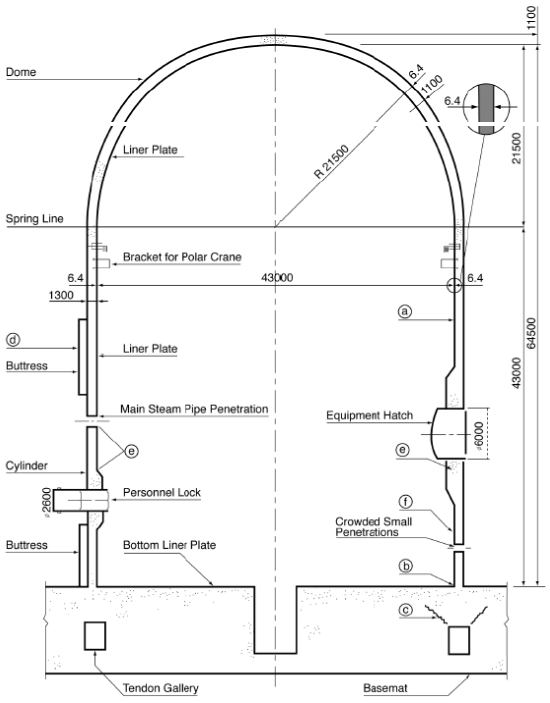

No.	Potential failure description
a	Hoop tensile failure of the cylinder wall
b	Bending-shear failure at the junction of the cylinder wall with the basemat
c	Shear failure in the basemat above the tendon gallery
d	Bearing failure at the tendon anchors
e	Bending-shear failure at the large penetrations
f	Bending-shear at the small penetrations
g	Liner tearing due to strain concentrations at local discontinuities (stiffeners/anchors, thickened reinforcing plates at penetrations and embedments)
h	Leakage at penetration seals due to ovalization or distortion of the sealing surfaces.

b) Geometry and potential failure locations

Figure 1.2 Prototype containment:
Ohi Nuclear Power Station, Ohi-cho, Fukui, Japan (from [2]).

Figure 1.3 The model containment (from [2]).

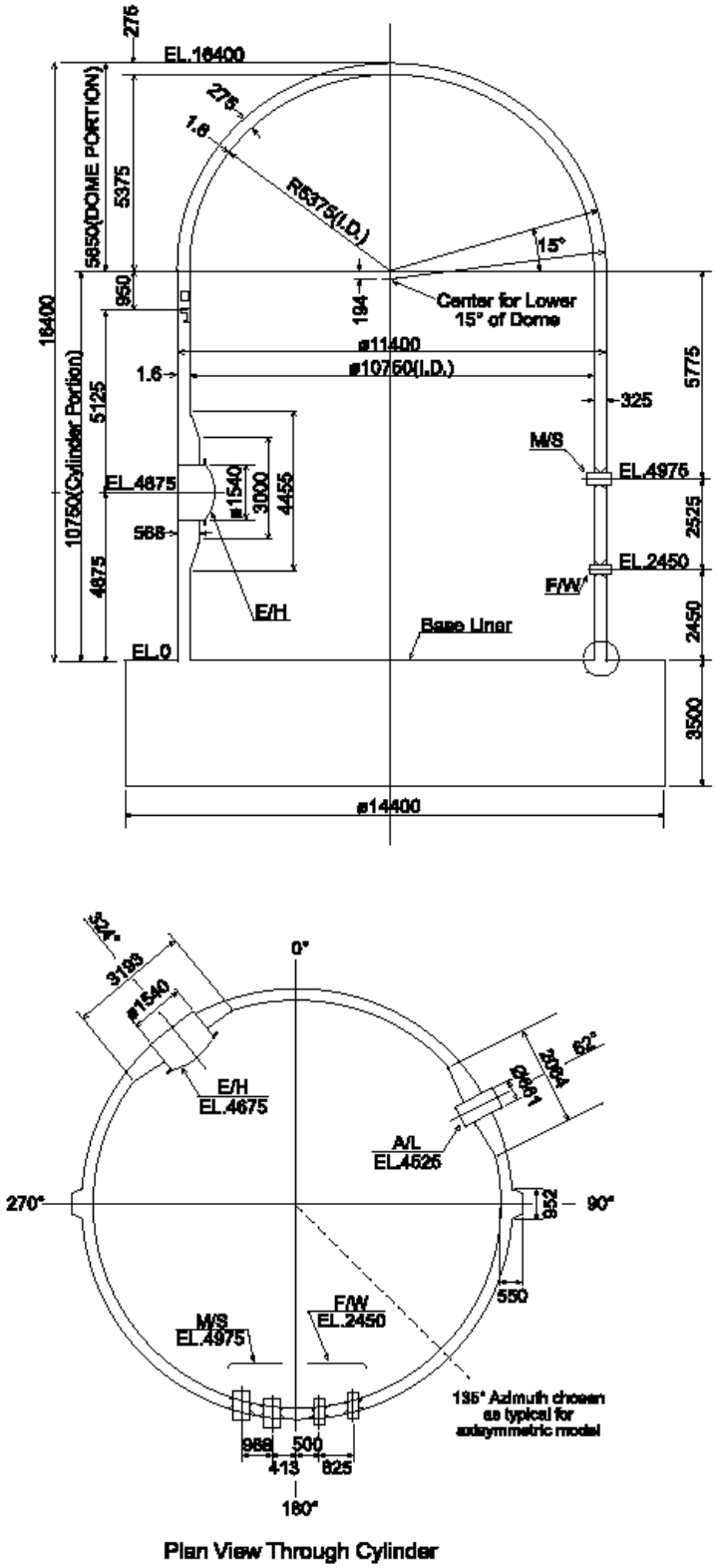

Figure 1.4 Model containment geometry (dimensions in mm), from [2].

2. METHODS OF ANALYSIS

2.1 General

In principle, four major levels of analysis approaches are applicable when utilizing the finite element technique for studying the structural behaviour of a prestressed concrete reactor containment;

1. Axi-symmetrical analysis
2. Three-dimensional global analysis
3. Local analysis at critical areas
4. Detailed studies of the leak-tightness integrity

These levels are examplified in Figure 2.1, and discussed here below.

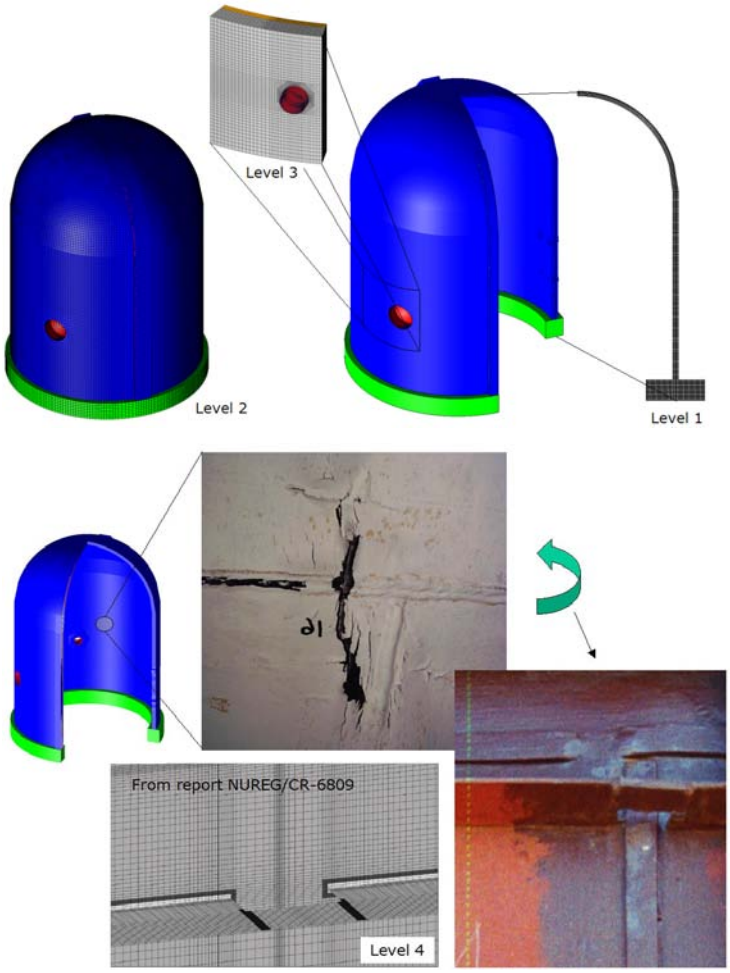

Figure 2.1 FE modeling, levels of detailing.

A reactor containment constitutes in principle a cylindrical construction and is therefore suitable to be analysed with the help of an axi-symmetrical model

when affected by globally distributed loads of the type overpressures. An axi-symmetric analysis can thus be used to understand the global behaviour of the model containment in an un-disturbed region, as a first approximation of the leak-tightness and structural capacity. The local behaviour of the wall-basemat connection can also be studied, if the model is detailed enough. Otherwise, a separate local model has to be used.

Another advantage with an axi-symmetric model is to execute parametrical studies and sensitivity analysis in an efficient way, in order to provide a good basis for defining high-quality model assumptions for the three-dimensional analysis.

The axi-symmetrical model is not capable of catching the structural effects due to major penetrations, pre-stressing buttresses, non-uniform layout of the pre-stressing tendons and reinforcement, and non-uniform and pressure-dependent pre-stressing effects. These effects will to a major extent influence the structural behaviour of the containment, including overpressure levels at leakage and collapse, as well as rupture positions. To take these matters into consideration, a fully three-dimensional model has to be used.

This is evident not only from the outcome of this report, but also from other studies, see for example Figure 2.2 from [1], illustrating the influence on the response from a containment buttress.

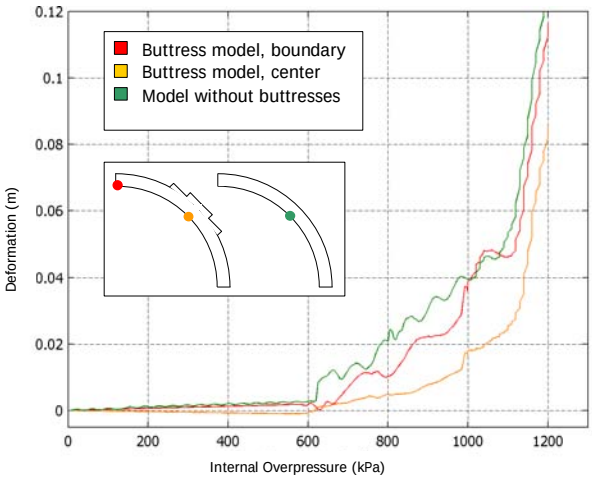

Figure 2.2 Study of influence of buttress on radial deformation (from [1]).

The need for advanced models is even more pronounced for the more complicated geometries of type BWR containments, see Figure 2.3. At the Swedish and Finnish BWR containments, there is another complication in the sense that the steel liner is embedded approximatly 20-30 cm from the inside of the containment wall. The liner is not anchored to the concrete wall with any mechanical anchors, except at a few locations. Thus, the friction between the embedded liner and the surrounding concrete is an important paramater to take into consideration.

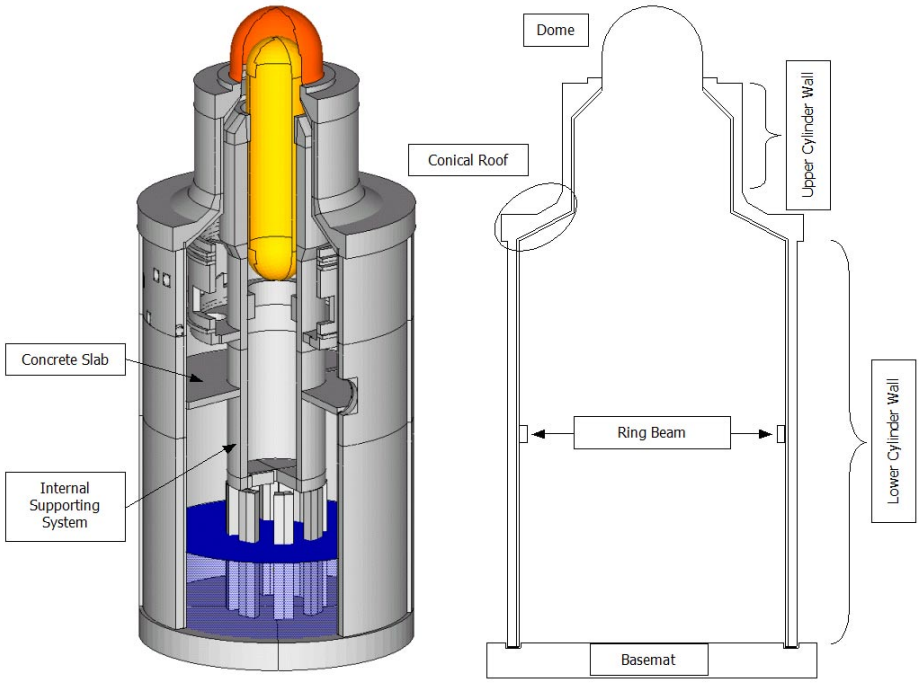

Figure 2.3 Typical Swedish BWR containment.

For some important and more complicated parts of the containment, such as the major penetrations, local detailed models can be used instead of increasing the discretization level in the global 3D-model. When using local models, submodeling can be a useful technique, where the boundary conditions of the local model is driven by the deformation calculated in the global analysis.

To fully reach the objective of this project, i.e. to determine good estimates of the pressure level and rupture position at leakage, even more detailed local models of the steel liner including welds and stiffeners etc are needed. This due to the fact that the rupture is dependent on local strain as well as workmanship of the welds.

In general, the degree of detailing to be used is dependent on the objectives of the analysis, and the different requirements to be regarded:

- Design or evaluation against specified pressure levels and acceptance criterias according to national standards.
- Analysis results to be used as input to a probabilistic safety assessment (PSA) of the plant, where input may be a point estimate of leakage, or structural collapse.
- Best estimate of leak-tightness and load-bearing capacity and safety margins of the structure based on nominal or measured parameters (as in the CONMOD project, see section 1.1 and [1]).

The interpretation of the acceptance criterias, or failure criterias, to be assest in the finite element analysis will of course differ depending on the objective of the analysis, but also on the modeling and analysis approaches to be applied.

2.2 Model containment

The objective of this project is to simulate the behaviour of the model containment pressurized to rupture. With the aim of describing the pressurization event as realistic as possible the analysis have been carried out using a fully three-dimensional (3D) global model applying non-linear material models.

An axi-symmetrical model has been applied for parametrical studies, in order to minimize executional runtimes. The parametrical studies have provided the basis for model assumptions for the 3D-model analysis.

2.3 Software

In the main analysis, the finite element program ABAQUS/Explicit version 6.4 has been used. Comparative calculations have been performed with ABAQUS/Standard version 6.4 For pre- and postprocessing both ABAQUS/CAE and Altair/HyperMesh have been used.

3. STRUCTURAL SYSTEM

3.1 General

This chapter will cover a description of the structural system of the model containment.

3.2 Description of the structural system

3.2.1 General

The model containment can be devided into three main structural parts, the basemat, the cylindrical wall and the dome, see Figure 3.1. These are briefly presented below, followed by a description of the structural elements in each part. A detailed description of the model containment is given in [2].

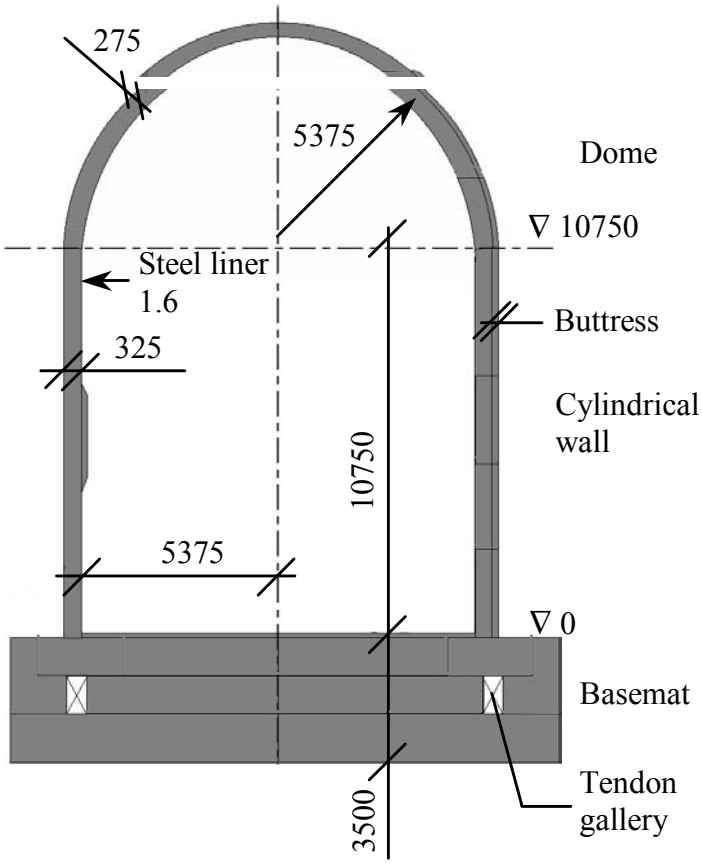

Figure 3.1 Model containment, main structural parts and dimensions [mm].

3.2.2 Basemat

The basemat consists of a 3.5 m thick reinforced concrete slab on a 0.3 m thick mudmat of concrete, cast on an approximately 8 m thick engineered backfill.

The basemat includes the tendon gallery, situated underneath the cylindrical wall, where the vertical wall tendons are tensioned and anchored.

A steel liner is placed on top of the basemat.

3.2.3 Cylindrical wall

The wall has a thickness of 0.325 m, locally thickened at the major penetrations. The wall is pre-stressed in both the vertical and horizontal directions. Two vertical pre-stressing buttresses are erected at 90 and 270 degrees, where the hoop tendons are tensioned and anchored. The buttresses start at the top of the basemat and extend halfway into the dome. The wall includes conventionally arranged reinforcement bars.

The steel liner is placed on the inside of the wall and anchored to the concrete by means of mechanical anchors, see section 3.2.5.

All penetrations through the containment are situated in the cylindrical wall, see section 3.2.6.

3.2.4 Dome

The dome thickness is 0.275 m. At the connection to the wall the thickness is gradually increased to 0.325 m, in order to match the thickness of the wall. The vertical tendons in the wall are continued throughout the dome, constituting an orthogonal pattern of tendons, see Figure 3.2 and Figure 3.6. Hoop tendons are placed in the dome except for the uppermost part. The dome also includes conventionally arranged reinforcement bars.

Figure 3.2 Arrangement of tendons in the dome.

The steel liner is placed on the inside of the dome and anchored to the concrete by means of mechanical anchors, see section 3.2.5.

3.2.5 Steel liner

3.2.5.1 Steel liner

The steel liner is fabricated from carbon steel and has a thickness of 1.6 mm. The as-built liner is 1.8 mm, the extra 0.2 mm providing a fabrication allowance. The liner was shop welded to liner plates approximately 3 meters square. During this construction phase the vertical anchors were also welded to the plates. Plates for the dome and around penetrations where generally smaller. To prevent buckling during erection horizontal stiffeners where welded to the plates. These stiffeners had no structural function after the model containment construction was completed. The plates were welded together at site. At penetrations, locally thickened plates were used, connected to the penetration assemblies.

3.2.5.2 Welds

The liner was shop welded into plates using computer controlled automatic welders. Also anchors and stiffeners were continuously welded to the liner during this phase. All shop welding was done without the use of back-up bars. When connecting the liner plates at site, back-up bars were used during welding.

3.2.5.3 Anchors

The steel liner was anchored to the concrete with vertical T-anchors continuously welded to the liner. They are spaced 0.45 m, except in the regions of the penetrations where they are more closely spaced, 0.15 m apart. The liner anchor layout is presented in Figure 3.3.

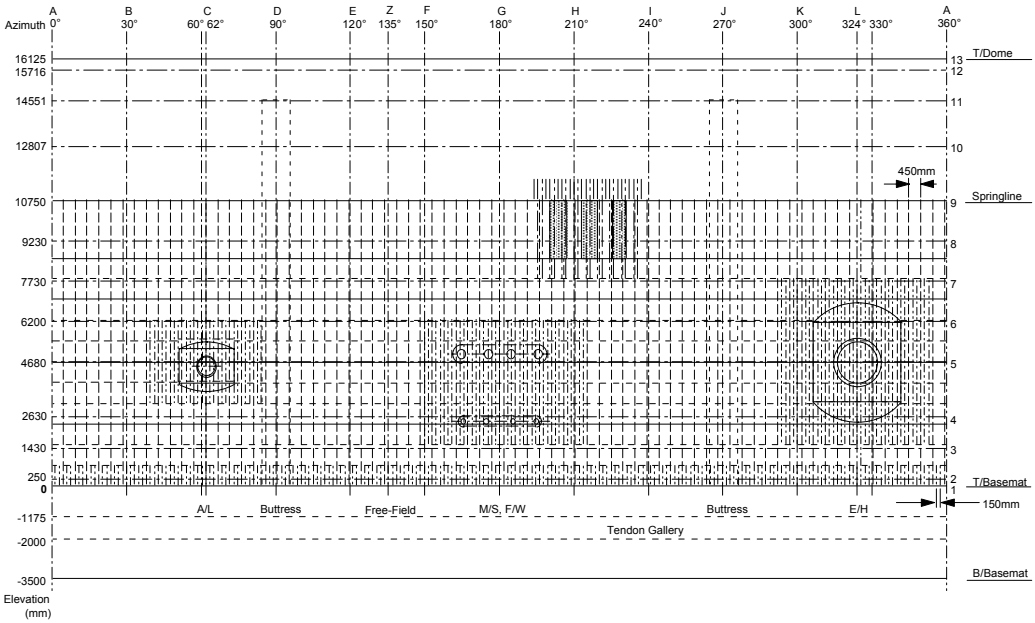

Figure 3.3 Liner anchor layout.

The vertical T-anchors are not extended into the dome. Here the liner is instead anchored to the dome with small stud-type anchors.

3.2.6 Penetrations

There are several penetrations through the model containment; the equipment hatch (E/H), the personnel airlock (A/L), the main steam (M/S) and the feedwater (F/W) penetrations. All penetrations are placed in the cylindrical wall, the layout of the penetrations is shown in Figure 3.4. The E/H and A/L penetration assemblies are 1:4-scale functional representations, while the M/S and F/W penetrations only includes the penetration sleeve and reinforcing plates.

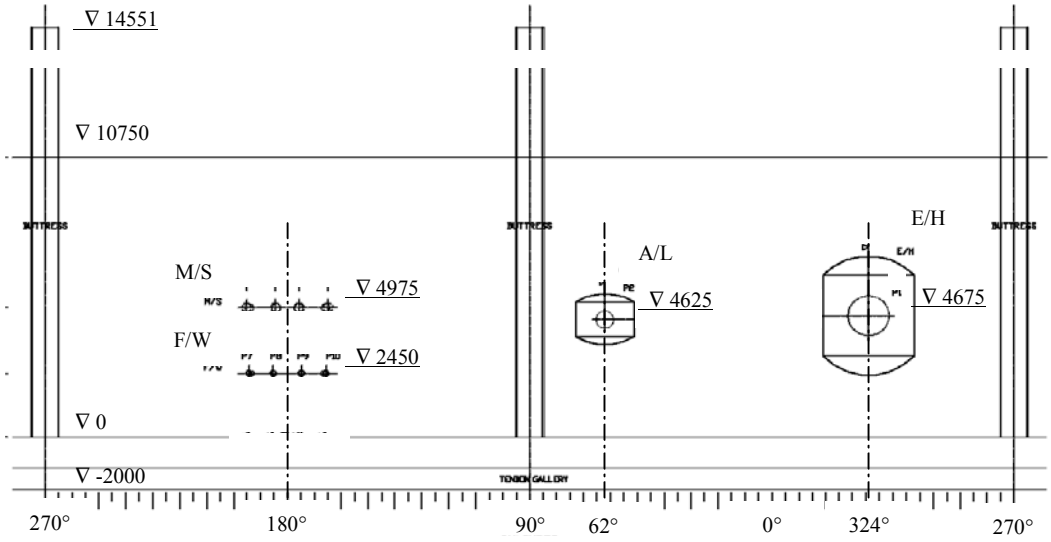

Figure 3.4 Layout of the penetrations (elevation, outside containment).

3.2.7 Pre-stressing tendons

The cylindrical wall and the dome are pre-stressed using unbonded tendons. The tendons consists of 3 pieces of 13.7 mm seven wire strands placed in metal ducts, normally 35 mm in diameter. The tendons were erected in the ducts after the concrete was cast and cured, and then tensioned.

The hoop tendons consist of 360° tendons with both ends anchored at the same vertical buttress. These tendons are tensioned from both ends. Every other tendon is anchored at the 90° buttress and 270° buttress respectively. The vertical tendons in the wall and dome are tensioned and anchored in the basemat tendon gallery. The tendon layout is shown in Figure 3.5, Figure 3.6 and Figure 3.7.

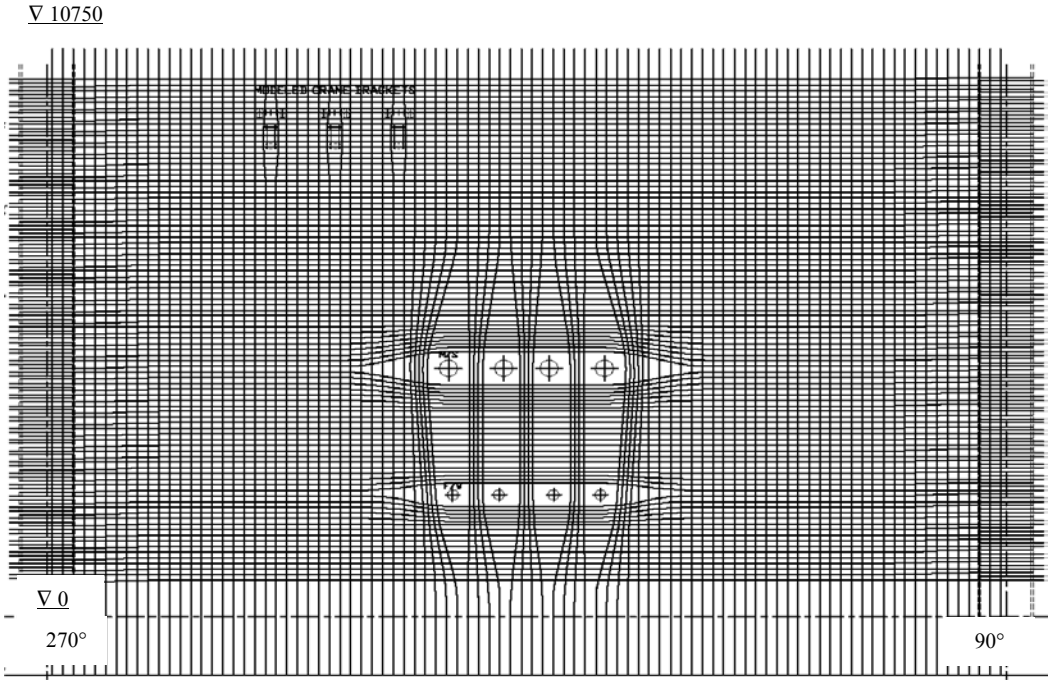

a) Pre-stressing tendon arrangement in cylindrical wall, elevation, outside containment, 270° - 90°

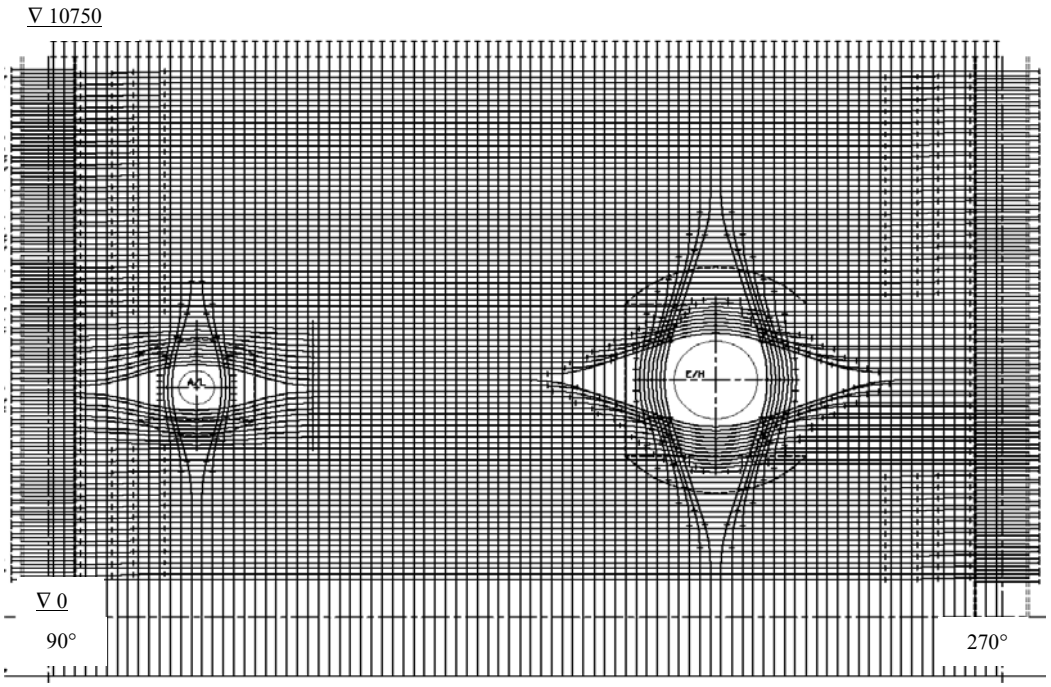

b) Pre-stressing tendon arrangement in cylindrical wall, elevation, outside containment, 90° - 270°

Figure 3. Pre-stressing tendon arrangement, cylindrical part (elevation).

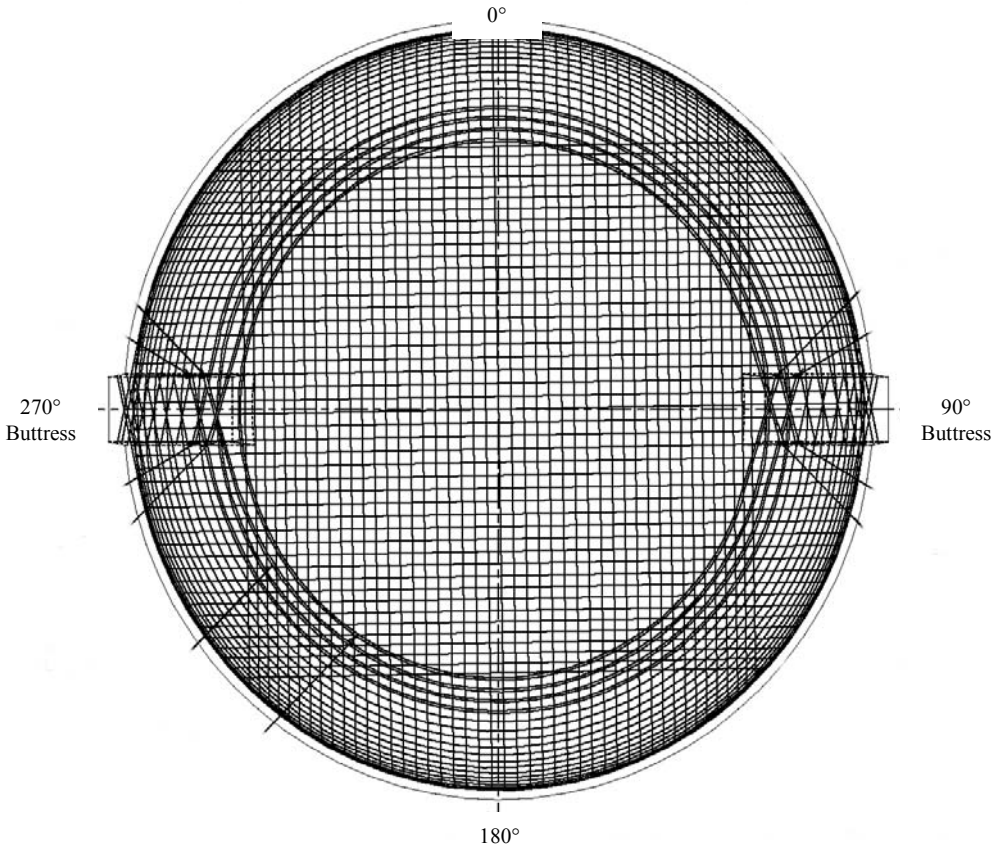

Figure 3.6 Pre-stressing tendon arrangement, dome (plan view from above).

3.2.8 Reinforcing steel

All outside and inside surfaces of the containment are conventionally reinforced with carbon steel deformed rebars. Also, all structural parts have shear reinforcement. Additional reinforcing is placed around penetrations, near the wall-basemat junction and at tendon anchoring zones, i.e. tendon gallery and buttresses. The general rebar layout is shown in Figure 3.7. The bars in the vertical direction are of diameter 10-19 mm, and the bars in the horizontal direction of diameter 10-22 mm.

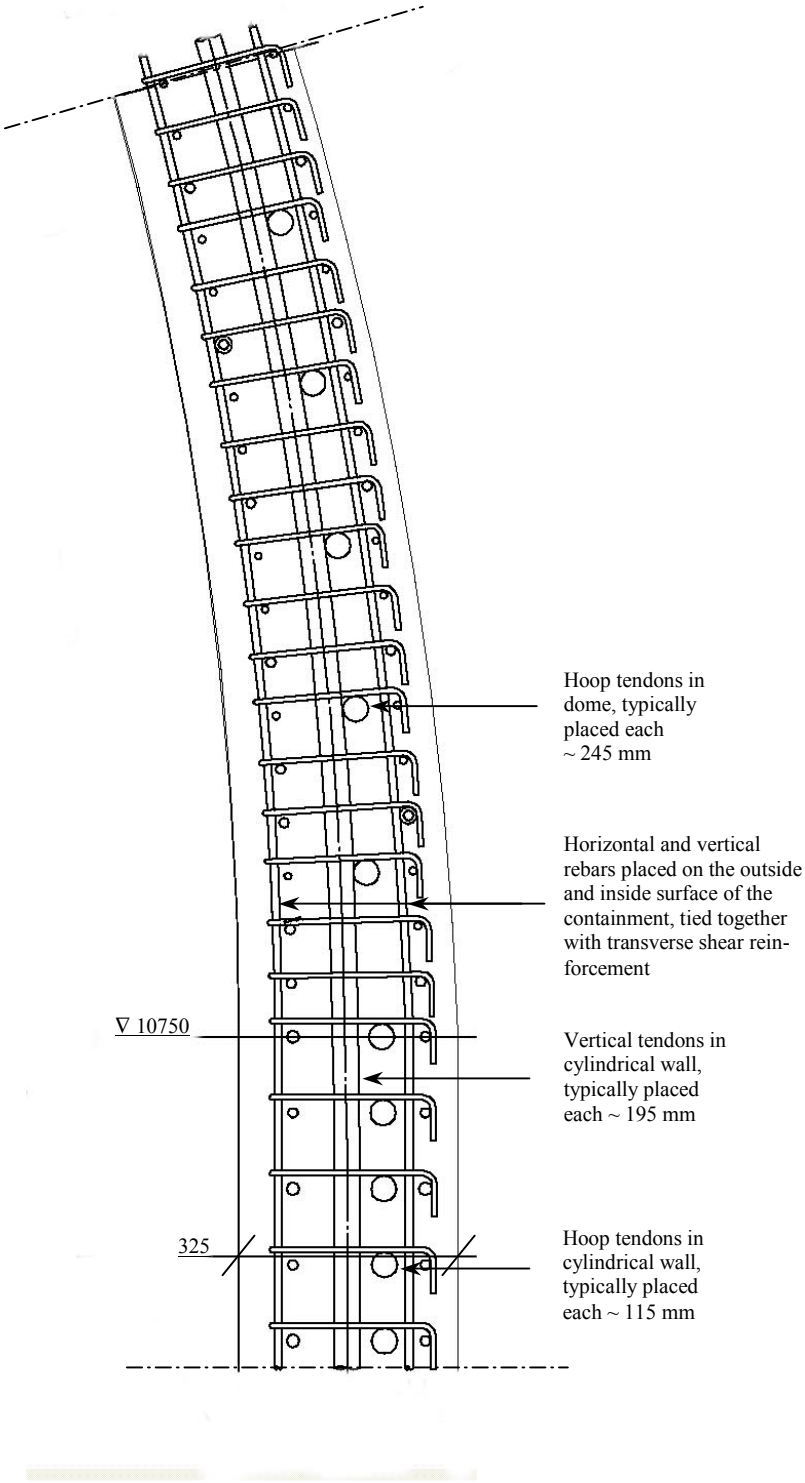

Figure 3.7 Pre-stressing tendons and rebar arrangement, section through wall/dome.

3.2.9 Concrete

A concrete mix with the same properties as for the prototype structure where used for the model containment. Two different concrete strengths where used, 30 MPa for the majority of the basemat and 45 MPa for the wall and dome as well as above the basemat tendon gallery. Concrete lifts and strengths are shown in Figure 3.8.

The concrete mix used is air-entrained and contains flyash and superplasticizer. Maximum aggregate size is 10 mm.

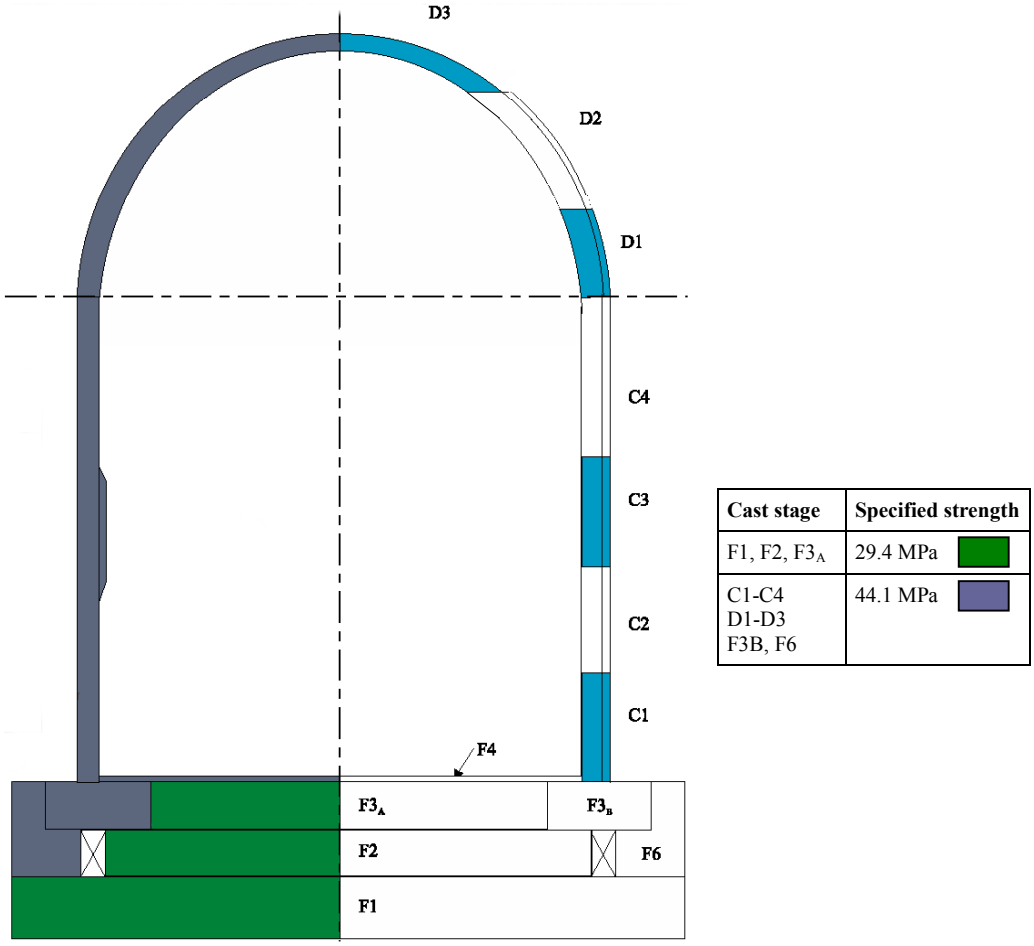

Figure 3.8 Concrete quality and cast stages.

3.3 Material

3.3.1 General

The aim of this project is to simulate the actual structural response of the model containment. The values of material parameters are therefore based on tests performed on material specimens from the model containment, and mean values are

chosen. The tension-stiffening curves are chosen as piece-wise linear curves fitting test data.

3.3.2 Stress and strain measures

In order to describe the behavior of the material on a local element level, *ABAQUS* uses true stresses and strains, even referred to as logarithmic strains. The following convention is used to translate the nominal stresses and strains to true stresses and strains for isotropic materials:

$$\sigma_{true} = \sigma_{nom} \cdot (1 + \varepsilon_{nom})$$

$$\varepsilon_{\ln}^{pl} = \ln(1 + \varepsilon_{nom}) - \frac{\sigma_{true}}{E}$$

where E is the Young's modulus.

3.3.3 Failure criteria

In *ABAQUS* it is possible to define material failure criteria. When the strains in an element reach the prescribed failure criterion that element is no longer active in the model. A failure criterion is introduced for every steel structural part when ε_{max} is reached. The concrete material failure criteria is explained in section 3.3.4 below.

3.3.4 Concrete

The following mean values for the concrete material properties at the time for the limit state test (LST) have been identified from the given test data presented in [2]:

Dome and cylinder, specified strength 44.1 MPa

f_c^{LST} = 58.5 MPa

E_c^{LST} = 26.8 GPa

Basemat, regions with specified strength 29.4 MPa

f_c^{LST} = 49.2 MPa

E_c^{LST} = 26.0 Gpa

Basemat, regions with specified strength 44.1 MPa

f_c^{LST} = 59.4 MPa

E_c^{LST} = 28.0 GPa

The strain at peak stress is chosen to 0.0026.

Tensile strength values are also provided. Since visual inspection of the model containment before the start of the LST test revealed the existence of micro-cracking throughout the cylinder, the tensile concrete strength was reduced to correspond to a cracking strain of $\varepsilon_{cr} = 40 \cdot 10^{-6}$. A typical value for Mode I fracture energy G_f^I is chosen to 120 N/m according to CEB-FIP Model Code 1990

[11]. This value is reduced as shown in Figure 3.9. The general tension-stiffening curve for concrete exposed to tension is also presented in Figure 3.9.

The Poisson´s ratio is set to 0.2, also based on test results.

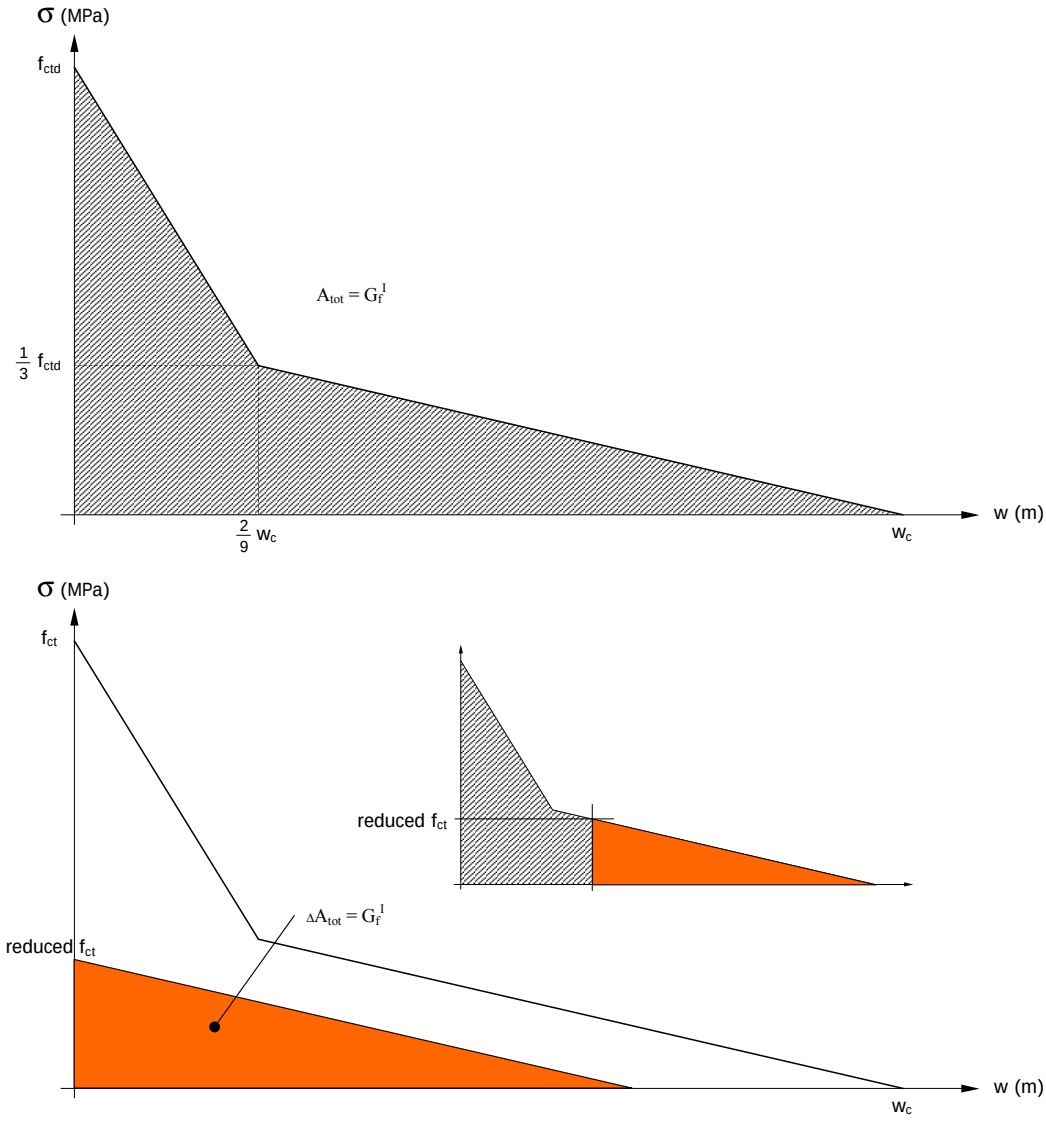

Figure 3.9 General tension-stiffening curve for concrete.
Upper diagram: Crack-free concrete.
Lower diagram: Idealization for concrete with micro-cracks, modeled with reduced strength f_{ct}.

3.3.5 Pre-stressing tendons

The following mean values for the pre-stressing tendon material parameters have been identified from the test data provided in [2]:

f_y = 1713 MPa

f_u = 1882 MPa

E_s = 191 GPa

ε_{max} = 3.83 %

These values are calculated using given test data of force-elongation and cross sectional area for the tendon system. Each tendon has an ultimate capacity of 638 kN.

The general tension-stiffening curve for pre-stressing tendons is presented in Figure 3.10.

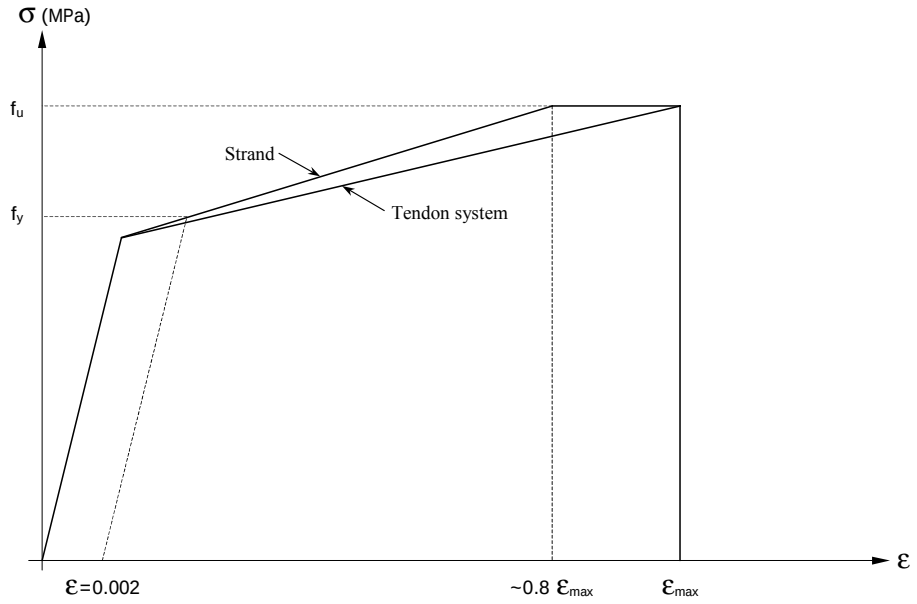

Figure 3.10 General tension-stiffening curve for pre-stressing tendons.

3.3.6 Reinforcement

The following mean values for the rebar material parameters have been identified from the test data provided in [2]:

Reinforcing steel, specified yield strength 392 MPa

f_y = 440 MPa

f_u = 610 MPa

E_s = 183 GPa

ε_2 = 0.85 %

ε_3 = 8.64 %

ε_{max} = 13 % (estimated value of strain at maximum engineering stress)

The general tension-stiffening curve for reinforcement, shell main bars, is presented in Figure 3.11.

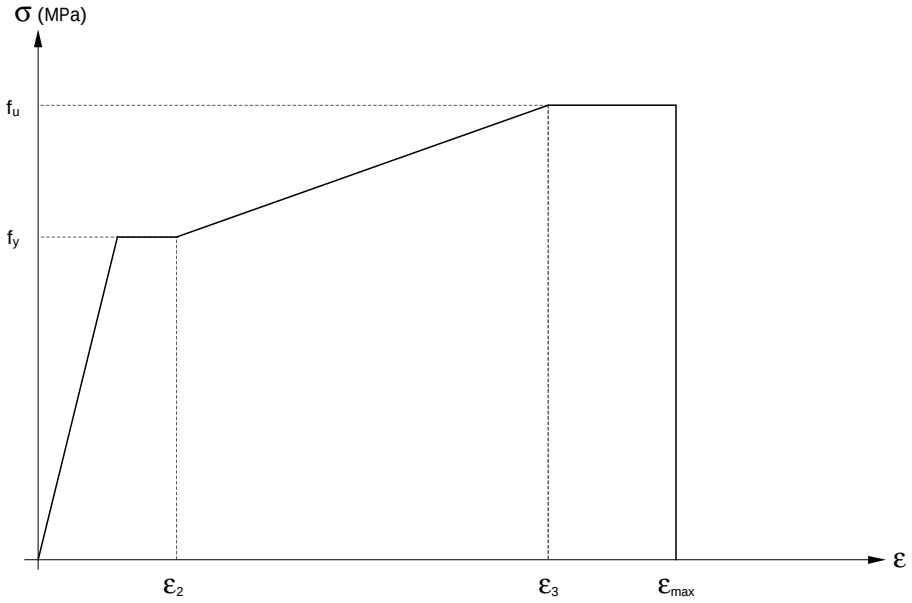

Figure 3.11 General tension-stiffening curve for reinforcement steel.

3.3.7 Steel liner

The following mean values for the steel liner material parameters, not affected by welding, have been identified from the test data provided in [2]:

f_y = 383 MPa

f_u = 498 MPa

E_s = 219 GPa

ε_{max} = 20 % (estimated value of strain at maximum engineering stress)

ε_2 = 1.37 %

ε_3 = 6.77 %

The general tension-stiffening curve for steel liner is presented in Figure 3.12.

Corresponding values for steel liner in zones affected by welding are:

ε_{max} = 18 % (estimated value of strain at maximum engineering stress)

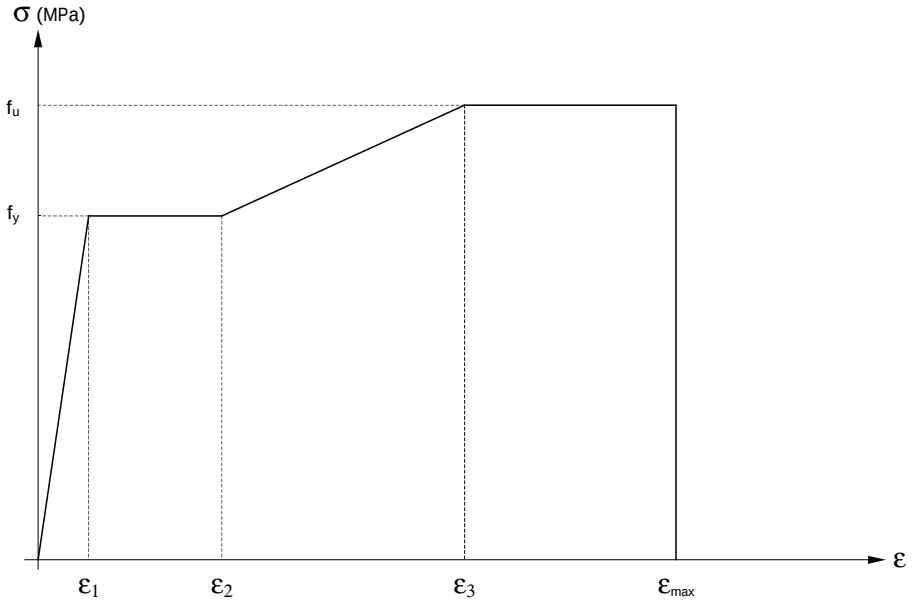

Figure 3.12 General tension-stiffening curve for steel liner.

3.4 Loads

3.4.1 General

Here below follows a presentation of the loads applied in the analyses.

3.4.2 Dead load

The dead load of the structural parts is based on the material densities specified in Table 3.1 below.

Material	**Density [kN/m^3]**
Concrete	21.9
Reinforcement	78
Steel liner	78
Pre-stressing tendons	78

Table 3.1 Densities for structural parts.

3.4.3 Pre-stressing load

The forces in the pre-stressing tendons prior to pressurization are chosen as the values measured at site two months after completion of the pre-stressing operation. These measurements were performed approximately two months before the start of the limit state test. No adjustments have, however, been done due to time

dependent losses for the period of time between measurement and start of the LST test. This because the tendon forces appear to be very stable, when compared to measurements performed earlier. In Table 3.2 pre-stressing data are given, as average values in the vertical and the horizontal directions respectively.

Average values	**Hoop tendons**	**Vertical tendons**
Load cell force	331 kN	435 kN
Friction coefficient	0.18	0.21
Seating loss	3.95 mm	4.95 mm
Seating loss force	95.6 kN	47.9 kN

Table 3.2 Pre-stressing data summary.

The variation of the pre-stressing force along the tendon due to friction and seating loss can be calculated using measured values of the friction coefficient and seating loss, as well as test data giving strains in discrete positions along the tendons. In Figure 3.13 and Figure 3.14 variation of pre-stressing force along the tendons valid for horizontal and vertical directions respectively are presented. These are average values supposed to be valid for all tendons not affected by penetrations. Near penetrations, tendons have increased curvature giving rise to additional losses due to friction. How the tendon force distribution during pressurization is handled is presented in section 5.

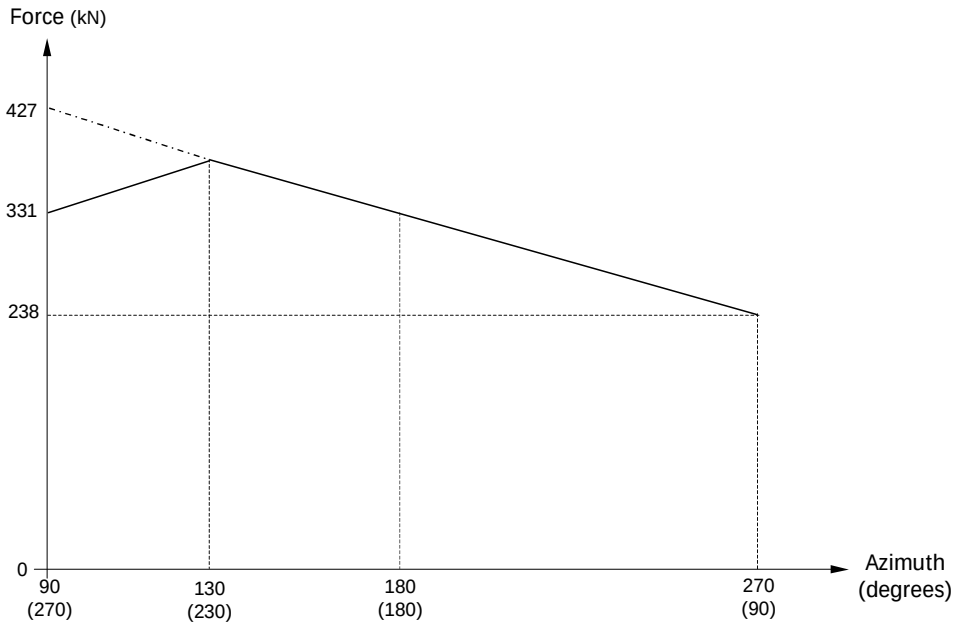

Figure 3.13 Horizontal tendon force variation.

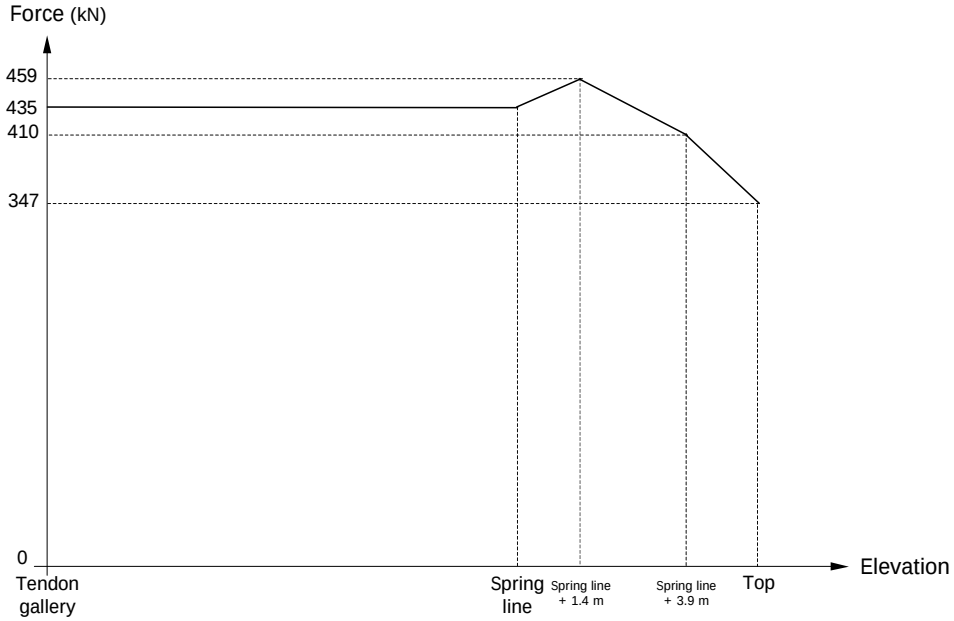

Figure 3.14 Vertical tendon force variation.

The Young´s modulus of the concrete at pre-stressing and at the start of the LST test show only a minor difference (~1-2%). The same modulus can thus be used both when simulating the tensioning of the tendons and the pressurization of the model containment during the LST test.

3.4.4 Over-pressurization

The over-pressurization studied in this report correspond to the limit state test (LST). The pressure history for all tests performed is given in Figure 3.15 below. A linear monotonic increasing internal pressure load is applied as an over-pressure in relation to normal atmosphere pressure.

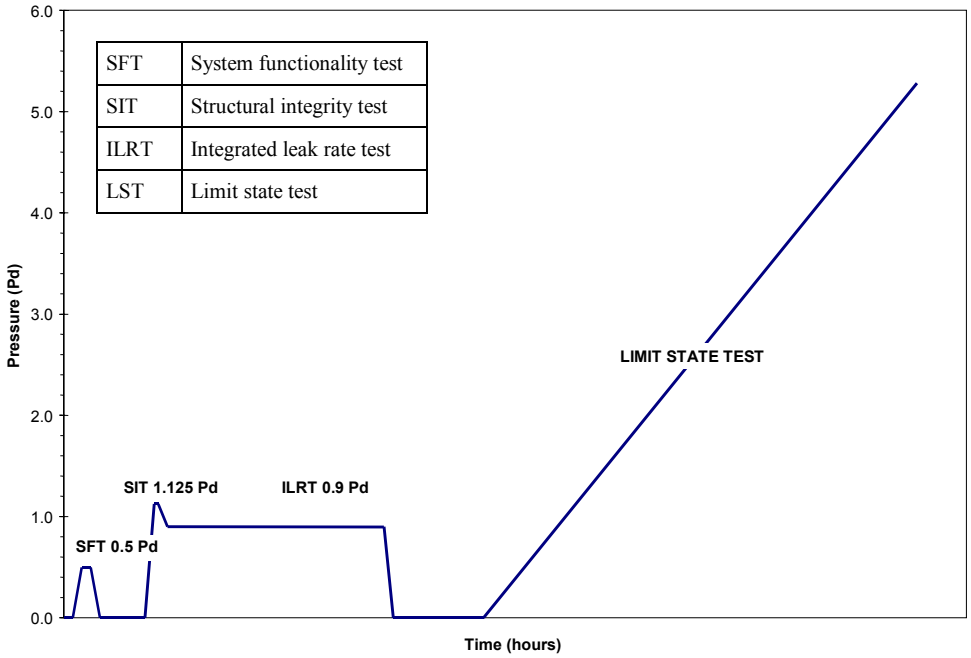

Figure 3.1 Pressurization of the model containment.

4. PARAMETRICAL STUDIES: AXI-SYMMETRICAL MODEL

4.1 General

The model containment can be reasonably well analysed with an axi-symmetrical model when studying global behaviour in the event of over-pressurization. An axi-symmetric analysis can be used to understand the global behaviour of the model containment in an un-disturbed region, i.e. as a first approximation of the leak-tightness and structural capacity.

However, the main purpose of an axi-symmetric model is to provide efficient executional runtimes in order to facilitate parametrical studies and sensitivity analysis. This to be able to define high-quality model assumptions for the three-dimensional model to be used in the main structural analysis (section 6).

Only a small part of the basemat is included in the axi-symmetric model since the local non-linear behaviour close to the wall-basemet connection is dominating over the global effects of the basemat to the containment wall, as is shown in the parametrical study presented in section 4.6. The basemat behaviour, and specially the tendon gallery zone, has then to be studied in a separate analysis.

4.2 Structural model

4.2.1 Geometry

The axi-symmetrical model has been established out of drawings provided in [2]. General dimensions are presented in section 3 above. The axi-symmetrical model is shown in Figure 4.1.

The finite element model represents the geometry of the model containment at approximately azimuth 135°, see Figure 4.1. This section is relatively free from geometrical disturbances like e.g. buttresses and penetrations. Furthermore, the force in the pre-stressing tendons is here representative.

For comparative studies, an axi-symmetric model including both the base-slab and the underground, mudmat and engineering backfill, has been built as shown in Figure 4.2. The mudmat of concrete and the engineering backfill are modeled using linear elastic material properties. Between the bottom of the base-slab and the mudmat, a contact formulation is specified, allowing uplift of the baseslab. The material properties of the underground are adjusted to correspond to a settlement of 25 mm for the dead weight of the containment, as registred on site during construction.

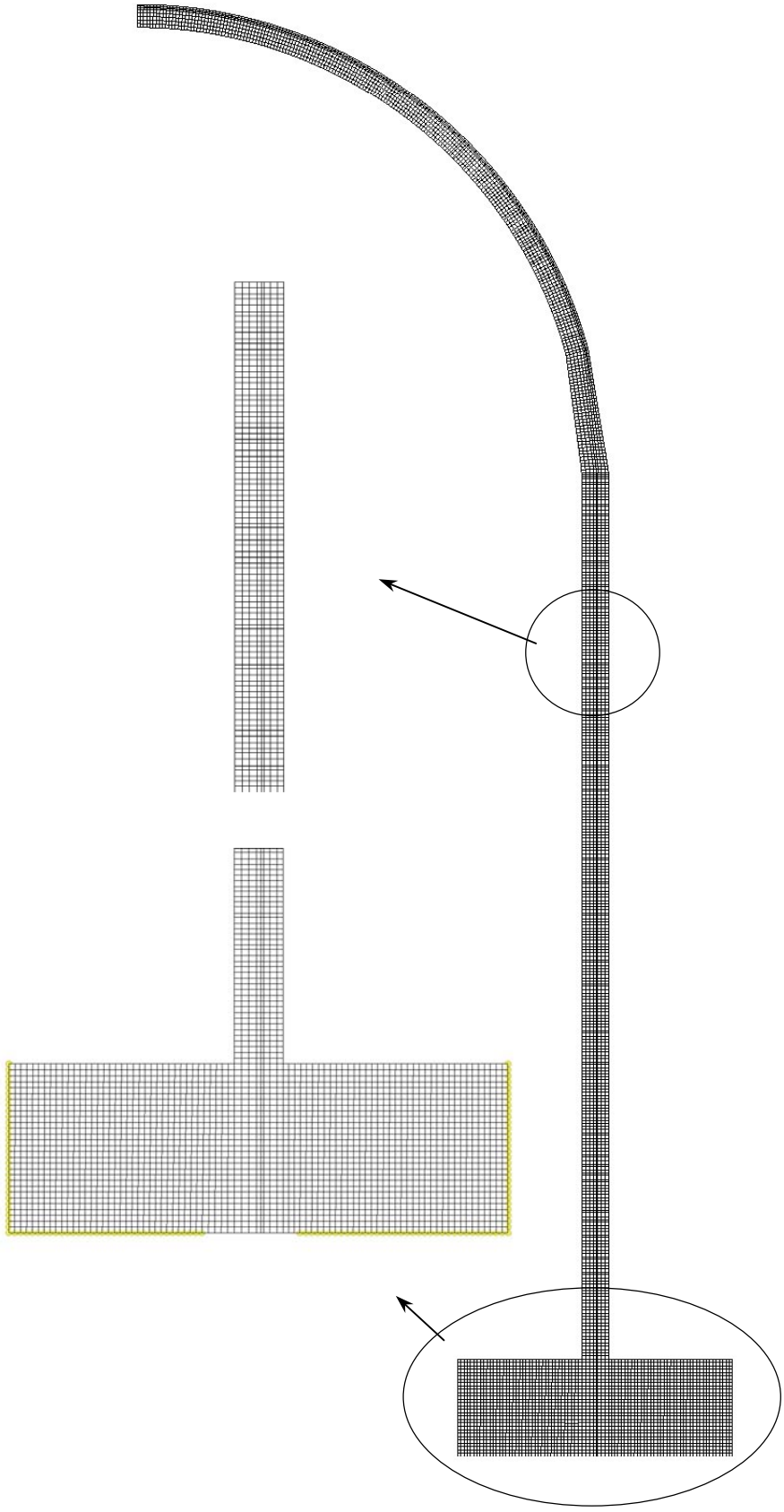

Figure 4.1 Axi-symmetric model.

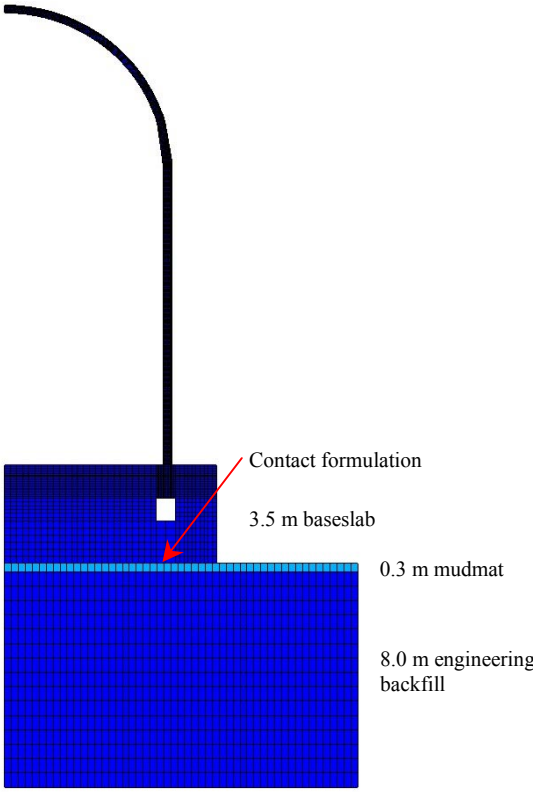

Figure 4.2 Axi-symmetric model including underground.

4.2.2 Types of finite element

The concrete parts in the FE-model are represented by axi-symmetrical continuum elements with a reduced number of integration points denominated CAX4R. The steel liner is represented by axi-symmetrical shell elements denominated SAX1. Both the pre-stressing tendons and the reinforcement are desribed by using the rebar modeling feature in ABAQUS. The reinforcement is modeled by rebars in the form of a layer inside the underlying continuum elements (concrete). The tendons are defined as single rebars in the underlying element.

4.2.3 Boundary conditions

Only a minor part of the basemat is included in the FE-model, the part between the cylindrical wall connection and the tendon gallery, i.e. approximately corresponding to the cast stage $F3_B$, see Figure 3.8 in section 3.2.9. The bottom and the vertical faces of the basemat part are constrained in both vertical and horizontal direction. No constrains are applied on the nodes situated directly above the tendon gallery. Constrained nodes are shown in Figure 4.3.

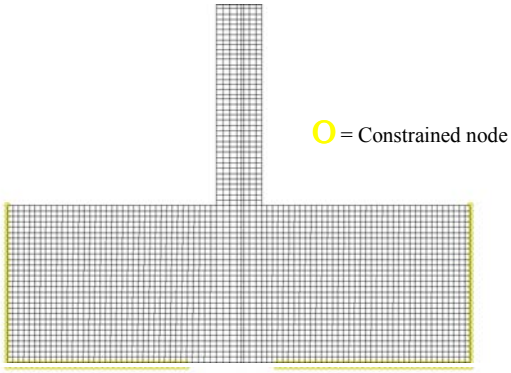

Figure 4.3 Boundary conditions applied to the basemat part.

In order to describe the symmetry conditions at the top of the dome the horizontal degree of freedom are constrained, see Figure 4.4.

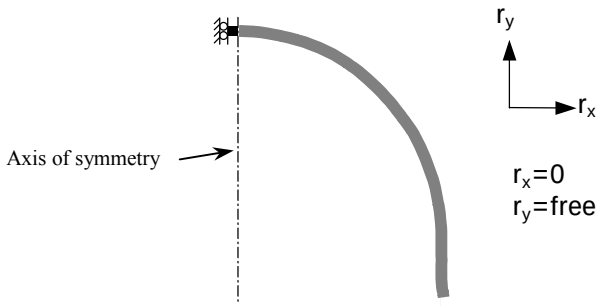

Figure 4.4 Axi-symmetric boundary conditions at the top of the dome.

4.2.4 Reinforcement

The reinforcement layout in the cylindrical wall, i.e. elements including rebar specification, is shown in Figure 4.5. The rebars are rigidly connected to the concrete.

4.2.5 Pre-stressing tendons

The tendon layout is shown in Figure 4.5. The tendons are simplified and modeled as rigidly connected to the concrete, i.e. modeled as grouted, since it is not possible to do otherwise for the hoop tendons in an axi-symmetric model. For the vertical tendon, the effect of longitudinal variation has lesser influence than for the horizontal tendons, as can be noticed when comparing the tendon force variation presented in Figure 3.13 and Figure 3.14.

The tensioning of the tendons is modeled by applying a temperature load to the tendons, giving a uniformly pre-stressing force along the length of the tendon.

The tendons in the horizontal direction are tensioned to 928 MPa, corresponding to a pre-stressing force of 320 kN, and the tendons in the vertical direction to 1300 MPa, corresponding to a force of 447 kN.

4.2.6 Steel liner

The steel liner is positioned on the inside of the containment as shown in Figure 4.5. The steel liner is rigidly connected to the concrete elements.

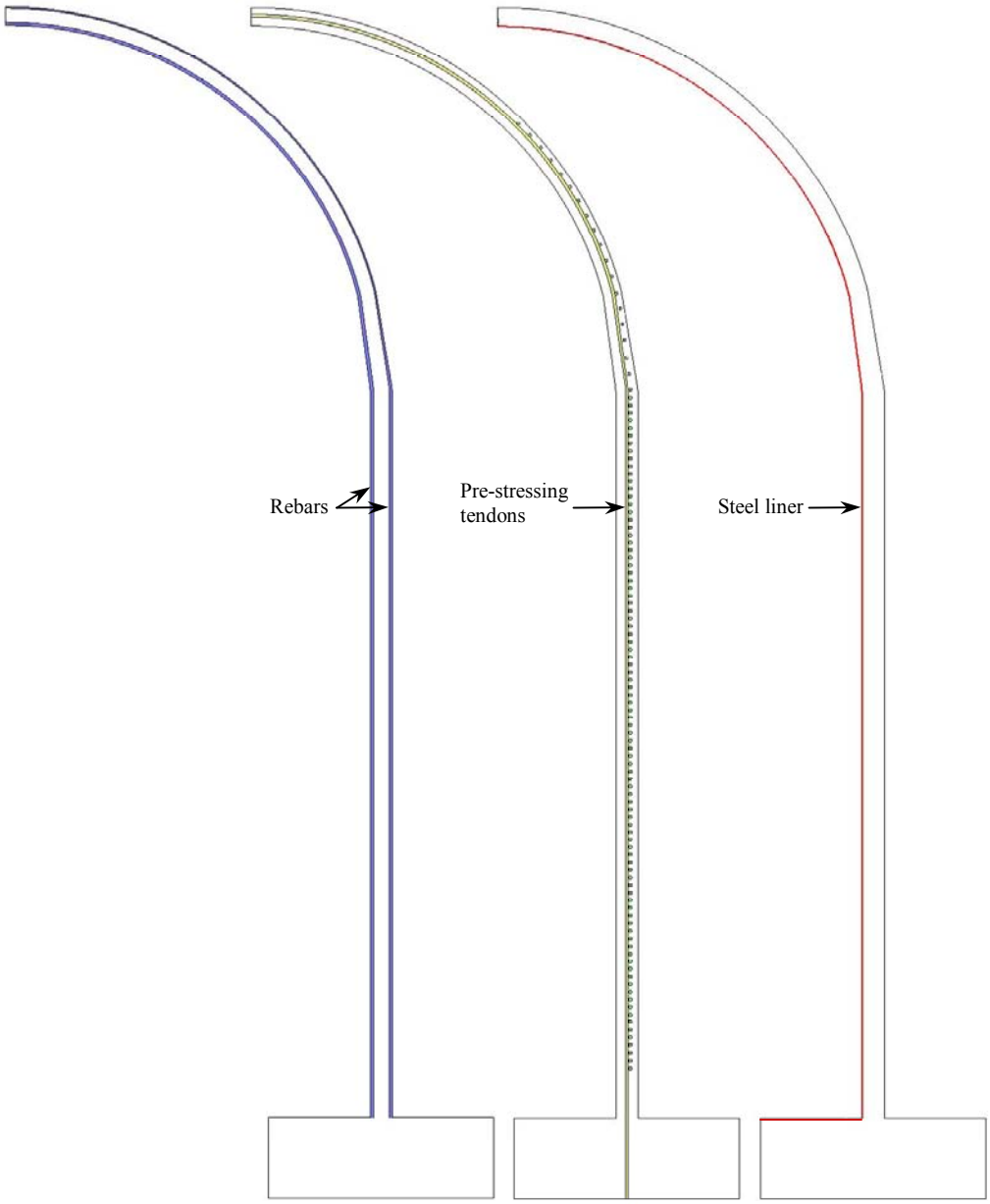

Figure 4. Positions of rebar, pre-stressing tendons and steel liner.

4.2.7 Application of loads

Dead weight is modeled applying a field of gravity acting downwards, using the gravitational constant 9.81 m/s^2.

The internal overpressure is applied as a linear monotonic increasing internal pressure load to the inside of the containment, i.e. to the shell element representing the steel liner.

4.3 Structural analysis

4.3.1 General

Five comparative studies regarding FE-analysis techniques have been carried out;

1. Comparison between implicit and explicit solving techniques, i.e. the analysis are executed using ABAQUS/Standard and ABAQUS/Explicit respectively.
2. Comparison between two different material models for concrete. The material models compared are the Brittle Cracking (BC) model and the Concrete Damage Plasticity (CDP) model, both included in ABAQUS to be used when modeling concrete structures. For further information see [3].
3. Comparison of the influence on results when modeling the baseslab and underground in detail. An analysis modeling only a small part of the baseslab is compared with an analysis including both the baseslab as well as the underground (mudmat and engineering backfill).
4. Loading rate and mass scaling are important issues to regard influencing the executional runtime in explicit analysis. These parameters are trimmed with the help of parametrical studies.
5. Modeling of horizontal pre-stressing tendons using membrane and truss elements respectively, are compared.

4.3.2 Result positions

Results are presented in the nodes of the model corresponding to test data positions. In Figure 4.6 result positions from the axi-symmetrical analysis are shown. All points correspond to azimuth 135°.

Due to the fact that the main purpose of the axi-symmetric analysis is to carry out parametrical studies, only displacement data are presented. However, the axi-symmetrical results for all output postions at azimuth 135 are presented in the result diagrams for the 3D-analysis as a comparison, see section 7.3.3.

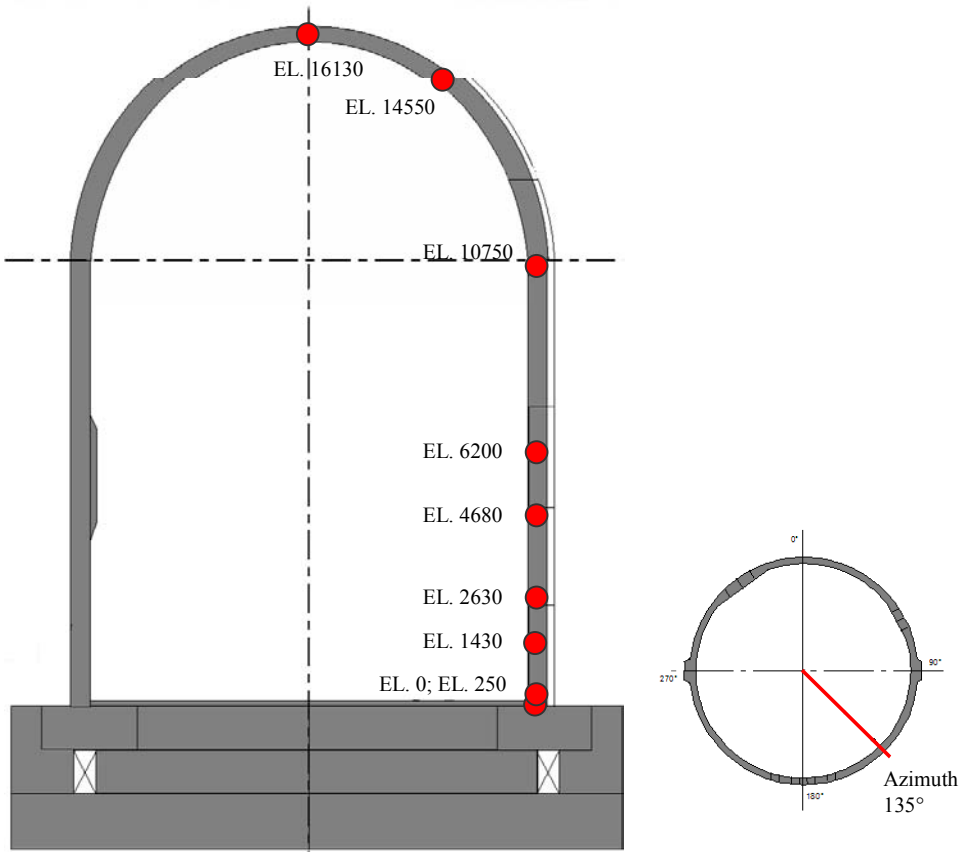

Figure 4.6 Result positions, axi-symmetric model azimuth 13 °[mm].

4.4 Parametrical study 1: Solver techniques

4.4.1 General

In this section, results from parametrical studies regarding comparison between implicit and explicit solving techniques are given, i.e. the analysis are executed using ABAQUS/Standard and ABAQUS/Explicit respectively.

4.4.2 Displacements

Displacements in the radial direction are presented with the initial position of the structure before pressurization as reference. Displacements in the vertical direction are presented with the upper part of the basemat as reference, i.e. excluding any basemat uplift.

In Figure 4.7 to Figure 4.17 in the next section analysis results regarding radial and vertical displacement are presented together with measured displacements during the limit state test (LST) of the model containment.

The analysis results agree very well with corresponding test data regarding displacements in the radial direction. In the vertical direction, the results for the

dome differ from test results when using the Concrete Damage Plasticity (CDP) model as described in section 4.5.2.

As can be seen in the diagrams, there is a good agreement between analysis using implicit and explicit time integration schemes, respectively.

4.4.3 Conclusions

Due to the fact that there is no difference in results between using implicit or explicit solver, the explicit solver will be used in the main three-dimensional analysis.

4.5 Parametrical study 2: Constitutive models for concrete

4.5.1 General

Results from a comparison between two different material models for concrete is presented in this section. The material models compared are the Brittle Cracking (BC) model and the Concrete Damage Plasticity (CDP) model, both included in ABAQUS to be used when modeling concrete structures. For further information see [3].

4.5.2 Displacements

Displacements in the radial direction are presented with the initial position of the structure before pressurization as reference. Displacements in the vertical direction are presented with the upper part of the basemat as reference, i.e. excluding any basemat uplift.

In Figure 4.7 to Figure 4.17 analysis results regarding radial and vertical displacement are presented together with measured displacements during the limit state test (LST) of the model containment.

The analysis results agree very well with corresponding test data regarding displacements in the radial direction. In the vertical direction, the results for the dome differ from test results when using the Concrete Damage Plasticity (CDP) model. When the concrete starts to crack, the analysis result using the CDP model shows a decrease in vertical displacement, not registered during the test. This can be explained by the fact that in the CDP model no consideration is taken to the direction of the concrete cracks. Instead, the stiffness in the concrete is decreased in all directions, not only in the principal tension direction. Therefore, even if the concrete is cracked only due to hoop stresses, the stiffness in the vertical direction drops as well. When the pressure level is reached cracking in the hoop direction occurs, there are compression stresses in the vertical direction due to the pre-stressing force. This will give rise to a displacement directed downwards due to the aritifical decrease in stiffness. In the Brittle Cracking model, crack direction is taken into consideration, thus giving a much better estimation of the displacement in the vertical direction.

There is a good agreement between the two different concrete material models used, except in the vertical direction as explained above.

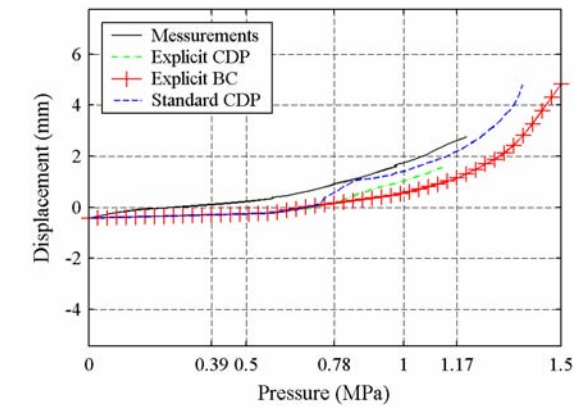

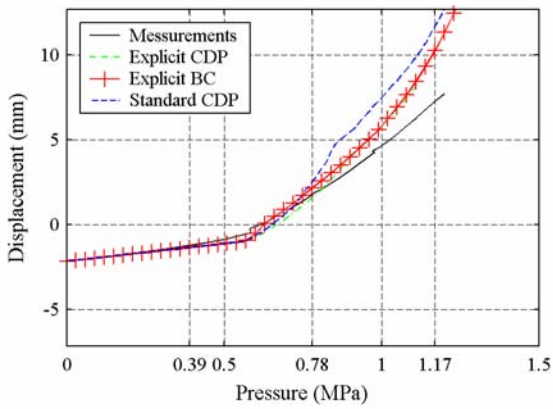

Figure 4.7 Displacement in the radial direction at elevation 2 0 (left)

Figure 4.8 Displacement in the radial direction at elevation 1430 (right)

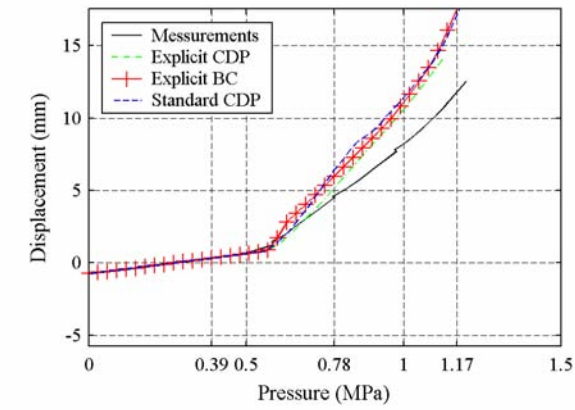

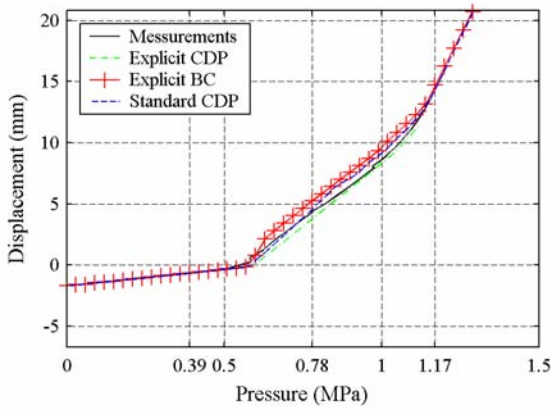

Figure 4.9 Displacement in the radial direction at elevation 2630 (left)

Figure 4.10 Displacement in the radial direction at elevation 4680 (right)

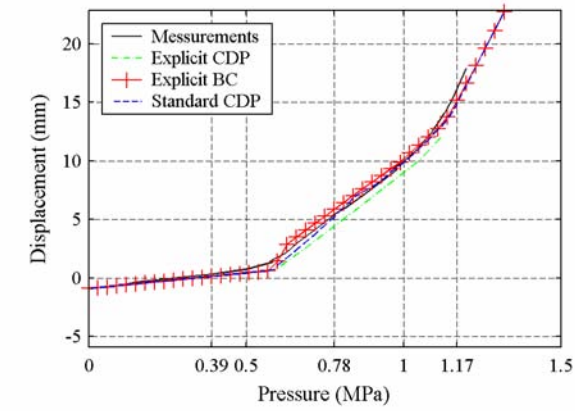

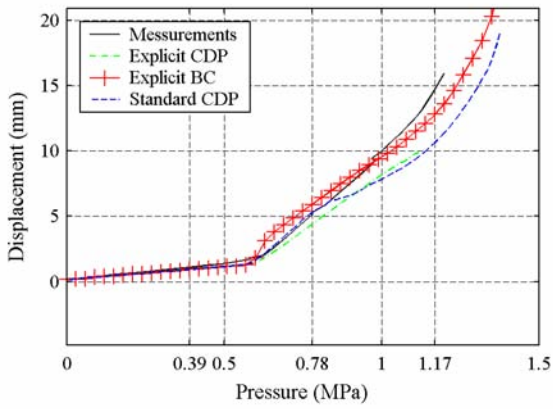

Figure 4.11 Displacement in the radial direction at elevation 6200 (left)

Figure 4.12 Displacement in the radial direction at elevation 107 0 (right)

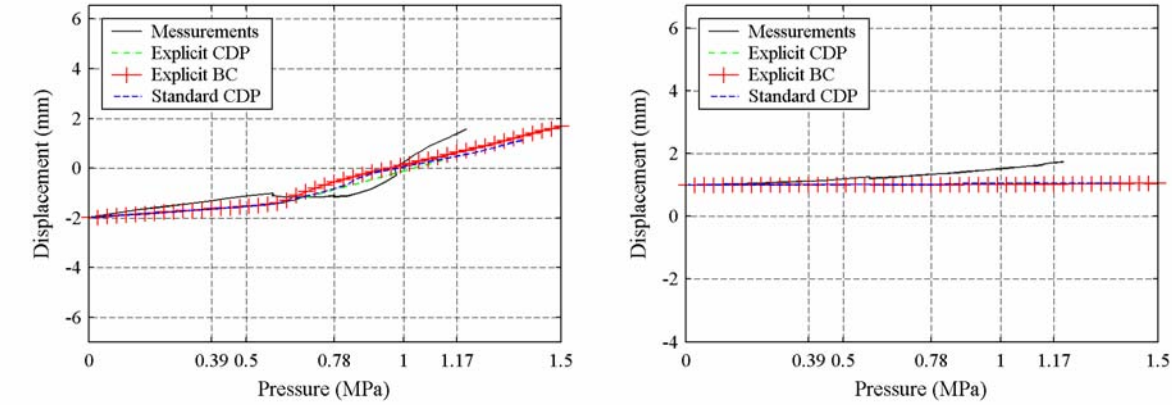

Figure 4.13 Displacement in the horizontal direction at elevation 14_ 0(left)

Figure 4.14 Displacement in the vertical direction at elevation 0 (right)

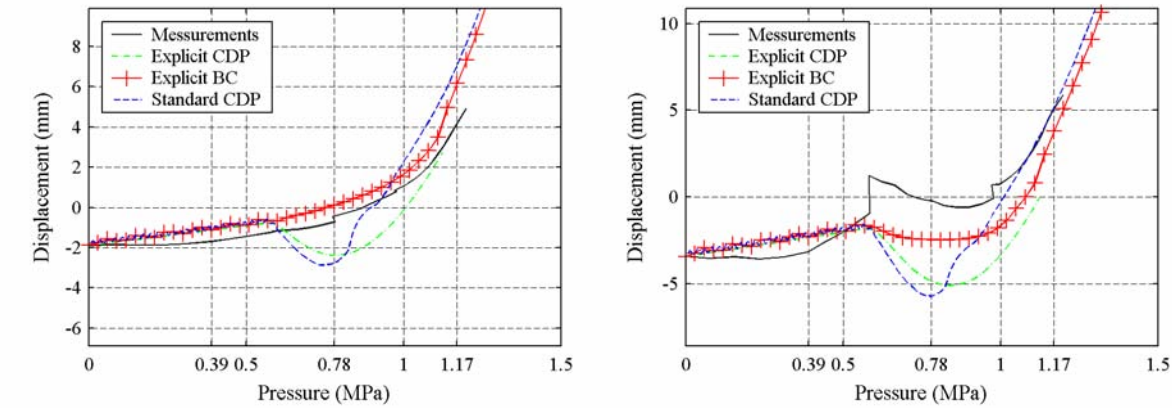

Figure 4.1 Displacement in the vertical direction at elevation 107 0 (left)

Figure 4.16 Displacement in the vertical direction at elevation 14_ 0 (right)

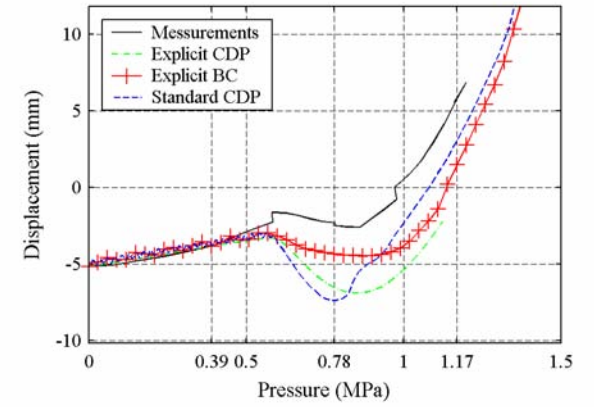

Figure 4.17 Displacement in the vertical direction at elevation 16130

4.5.3 Conclusions

Because the Concrete Damage Plasticity model gives some non-accurate results for the typical stress state prevalent in the containment, the Brittle Cracking model is chosen for the main analysis.

4.6 Parametrical study 3: Basemat and underground

4.6.1 General

To be able to minimize the model size for the three-dimensional model, it would be conveniant if most of the basemat and the underground could be neglected. Therefore, in the third parametrical study a comparison between modeling the baseslab and underground in detail (Figure 4.2) with modeling only a small part of the baseslab (Figure 4.1) is done.

4.6.2 Displacements

The radial displacement is in principal equal for both of the analysis. The vertical deformation also agrees well.

4.6.3 Conclusions

Due to the fact that the results from the the two comparative analysis do not differ, the central part of the basemat and the underground can be neglected when creating the three-dimensional model.

4.7 Parametrical study 4: Loading rate and mass scaling

In an explicit dynamic analysis the load has to be applied quasi-statically during a sufficiently long period of time, in order not to introduce any dynamical effects on the structure, i.e. inertia forces and kinetic energy can be regarded as negligible. A loading rate well below the critical value has to be chosen.

To minimize the executional runtime, mass-scaling can be used. Mass-scaling is only to be used during the linear elastic response phase of the analysis, that is up to an overpressure of 600 kPa. Mass-scaling increases the effect of inertia forces so care must be taken not to introduce any dynamical effects in the quasi-static analysis. The benefits of using mass-scaling is explained below.

An estimate of the stability limit in explicit dynamics procedure can be expressed as

$$\Delta t = \frac{L^e}{c_d}$$

where Δt is the stable time increment, L^e is the smallest characteristic element length and c_d is the dilatational wave speed of the material. The dilatational wave speed in a linear elastic material (with Poisson´s ratio equal to zero) is

$$c_d = \sqrt{\frac{E}{\rho}}$$

where E is the elastic modulus and ρ is the material density.

If we artificially increase the material density by a factor of f^2, the wave speed decreases by a factor of f, and therefore the stable time increment increases by a factor of f. This increase in stable time increment will give rise to a corresponding reduction in executional runtime.

The mass-scaling chosen in the presented analysis has reduced the executional runtime with approximately 40 percent. This reduction is of great importance when analyzing large FE-models, or in the case of performing comprehensive sensitivity studies.

4.8 Parametrical study 5: Modeling of horizontal tendons

4.8.1 General

In section 5.2.1 and 5.2.2, two methods of modeling unbonded tendons using contact formulation are presented. The first one models the horizontal tendons with membranes in zones with no curvature in the vertical direction, while the second one models the tendons as discrete truss elements everywhere. The method of using a membrane is a way to minimize the modeling work. This parametrical study has been carried out using a fully three-dimensional model, see Figure 4.18.

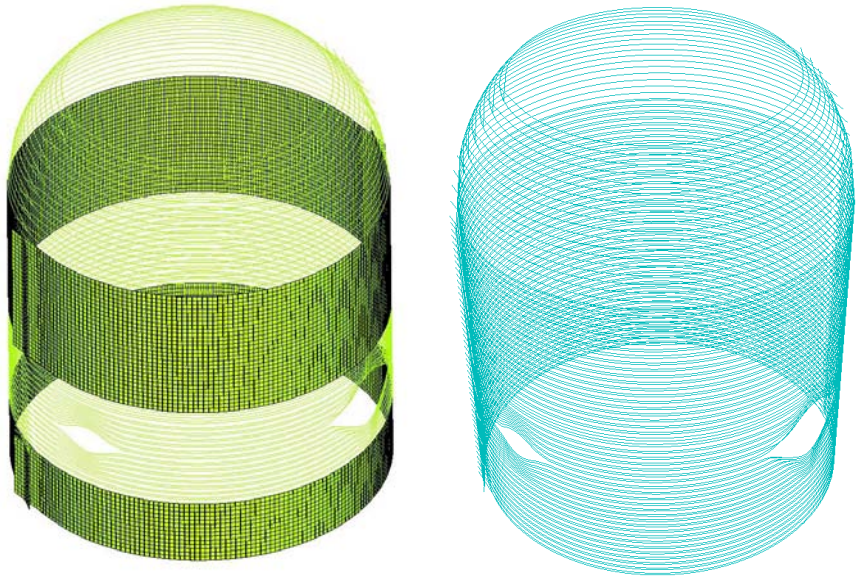

Figure 4.18 Modeling of horizontal tendons. a) Membrane. b) Truss elements.

4.8.2 Conclusions

The results achieved using the two different analysis techniques do not differ.

5. MODELING OF PRE-STRESSING TENDONS

5.1 Overview

One of the most important modeling issues is the modeling of the pre-stressing tendons. The tendons in the model containment are non-grouted, i.e. unbonded. These types of tendons can be modeled at different levels of sophistication;

Level 1 Taking into consideration the actual friction between the tendon and the concrete, not only during the tensioning and seating procedure, but also during the pressurization of the containment.

Level 2 The tendon force is specified by taking the variation of tendon force along the tendon into consideration during tensioning due to friction and seat losses etc. During the pressurization process the tendon is modeled as fully bonded to the concrete.

Level 3 The tendon force is specified as a constant force along the tendon, initially specified as a mean value taking friction and seat losses etc into consideration. During the pressurization process the tendon is modeled as fully bonded to the concrete.

The test results show, as expected, that the force distribution along the tendon is un-evenly distributed due to friction and seating losses during the tensioning procedure. This force distribution, however, will gradually change to a more or less evenly distributed force along the tendon when the internal pressure in the containment rises. The change of force distribution starts to appear when the hoop forces equilibrate the pre-stressing force and the distribution will then gradually approach an even distribution for further increase in pressure load. In this phase the tendon force increases as expected as a consequence of elongation due to the radial deformation of the containment.

Due to this tendon behaviour, it is an advantage if the modeling method is in accordance with the level 1 approach described above.

5.2 Test of level 1 modeling methods

We have used ABAQUS in order to test four different level 1 methods to enable to take into consideration the friction and slip between the unbonded tendon and the concrete during both construction, i.e tensioning and seating, and during pressurization. These methods are briefly presented in sections 5.2.1 – 5.2.4 below. A comparision of results is also made using the level 2 approach, i.e. to model the tendons fully bonded to the concrete during pressurization.

The test is carried out as a basis for choosing modeling methods to be used in the 3D FE-analysis of the model containment. Three main areas are evaluated in the test;

- Simulation capabilities, i.e. the possibility to simulate the true tendon forces along the tendon.

- Computational runtime.
- Modeling effort.

The evaluation of the modeling effort is a subjective matter and to some extent dependent on the pre-processor available, however a relative comparison will be presented. Computational runtimes will be presented as relative values because the absolute values are of course dependent on the computer capacity at hand.

The test calculations are carried out using a horizontal 180° segment of an 0.3 meter high un-disturbed part of the model containment wall including 3 pre-stressing tendons, see Figure 5.1. The loading sequence of the model is tensioning, seating and finaly pressurization. Geometry, loading conditions and material parameters are the same as for the analysis of the model containment.

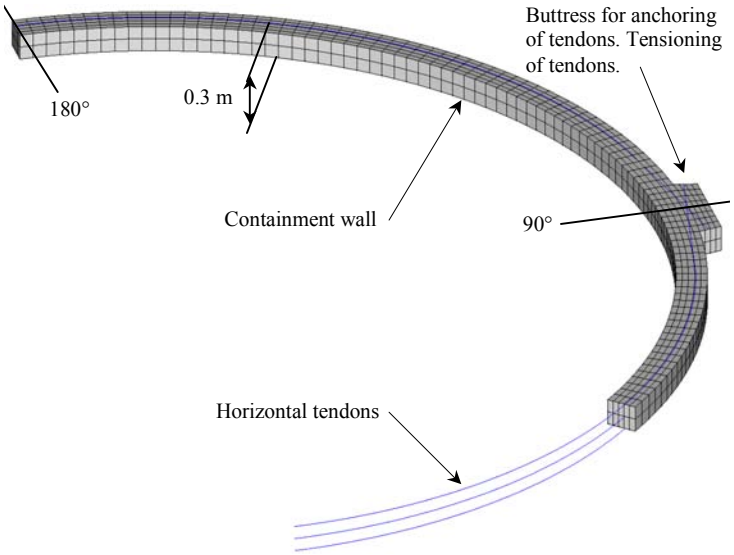

Figure 5.1 Horizontal 180° segment model including three pre-stressing tendons.

5.2.1 Contact formulation between tendon and concrete (truss elements)

The tendons are modeled with truss elements and the concrete with solid elements. The interaction between the truss elements and the solid elements is modeled with a contact formulation. A friction coefficient is specified between the tendon and the concrete.

Using this method the force distribution along the tendon during tensioning and seating is automatically calculated. Also, the re-distribution of tendon force and increase in friction force during pressurization is automatically taken into consideration in the analysis.

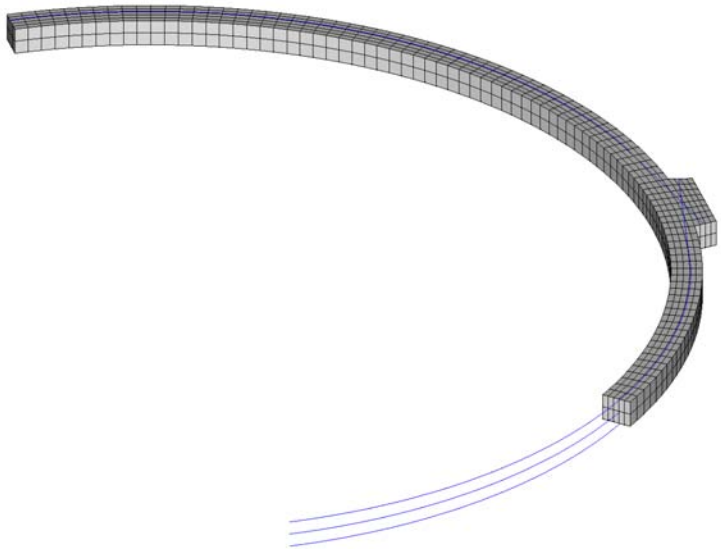

Figure 5.2 Horizontal tendons modeled with trusses, interaction between tendon and concrete modeled with a contact formulation.

The element and node positions for truss and solid elements respectively can be specified independently of each other making the modeling work straightforward.

The contact formulation increases the computational runtime in comparison to the other methods using coupling elements between the tendon and concrete nodes, i.e. friction connectors and friction trusses.

5.2.2 Contact formulation between tendon and concrete (membrane elements)

This method is identical to the one specified in section 5.2.1 above, except that the tendons are modeled using membrane elements instead of truss elements, see Figure 5.3. Using this method it is not necessary to explicitly model each tendon.

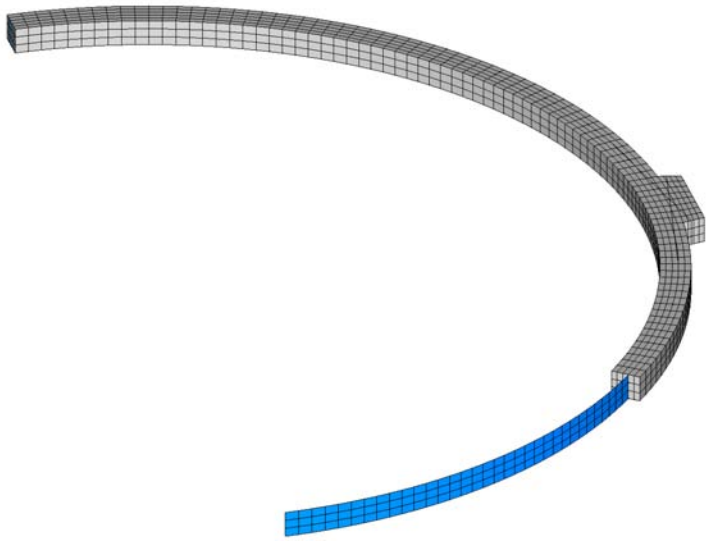

Figure .3 Horizontal tendons modeled with membrane, interaction between tendon and concrete modeled with a contact formulation.

This method is favourable when the tendon curvature is only in one plane, and the tendons are evenly distributed at rather small distances. It is possible to use the method also for curvature in more than one plane by using rotated material directions, see Figure 5.4. However, this increases the modeling effort, and therfore modeling tendons explicitly with truss elements would in this case be an equal or even better alternative.

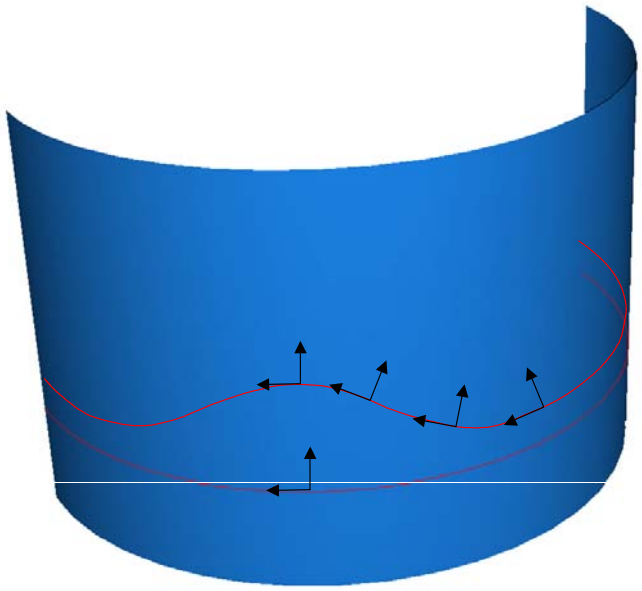

Figure .4 Rotating material directions (upper tendon) for tendon curvature in more than one direction, when using membrane elements modeling the tendons.

5.2.3 Friction connectors between tendon and concrete

The tendons are modeled with truss elements and the concrete with solid elements. The interaction between the truss elements and the solid elements is modeled with friction connectors. A friction force is specified and this force will be activated in the correct direction based on the relative motion between the coupled nodes.

Using this method the force distribution along the tendon during tensioning and seating is automatically calculated. Also, the re-distribution of tendon force during pressurization is automatically taken into consideration in the analysis. During pressurization, the friction force will increase. Therefore the friction force specified with the connector element has to be a function of the pressure load. This dependency has to be calculated before the finite element analysis starts and given as input data.

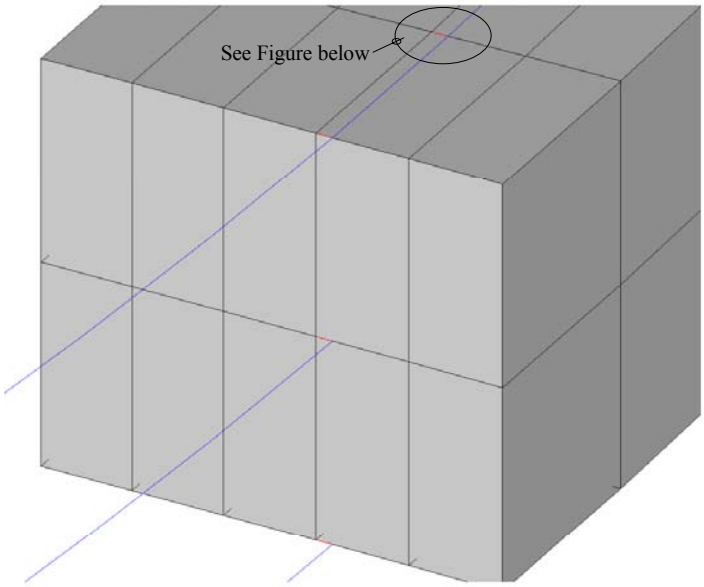

Figure L-54 Interaction between tendon and concrete modeled with friction connectors.

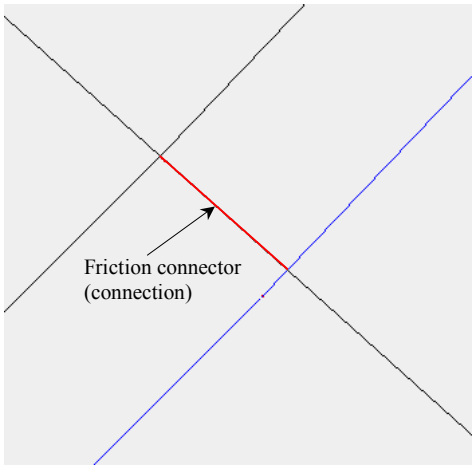

Figure 5.6 Interaction between tendon and concrete modeled with friction connectors.

In this method the truss nodes are connected to the nearest solid element node. Therefore the node positions for truss and solid elements respectively can not be specified to far away from each other, putting some constraints on the modeling work. However, this will often be easily handled by using approximatly the same element size for truss elements and solid elements and due to the fact that the element size has to be rather small in any case.

5.2.4 Friction trusses between tendon and concrete

The tendons are modeled with truss elements and the concrete with solid elements. The interaction between the truss elements and the solid elements is modeled with friction trusses. This method is presented in [4]. The direction of the friction trusses have to coincide with the angle of friction. Therefore the direction of the friction trusses have to be adjusted when the direction of slip is changed. This is the case when going from tensioning to seating, but also in some areas during pressurization, see Figure 5.14.

Using this method the force distribution along the tendon during tensioning and seating is calculated. Also, the re-distribution of tendon force and increase in friction force during pressurization is taken into consideration in the analysis. However, this is only true as long as the friction force doesn´t change direction. When a direction change is at hand the model has to be changed by adjusting the direction of the friction trusses, see Figure 5.8.

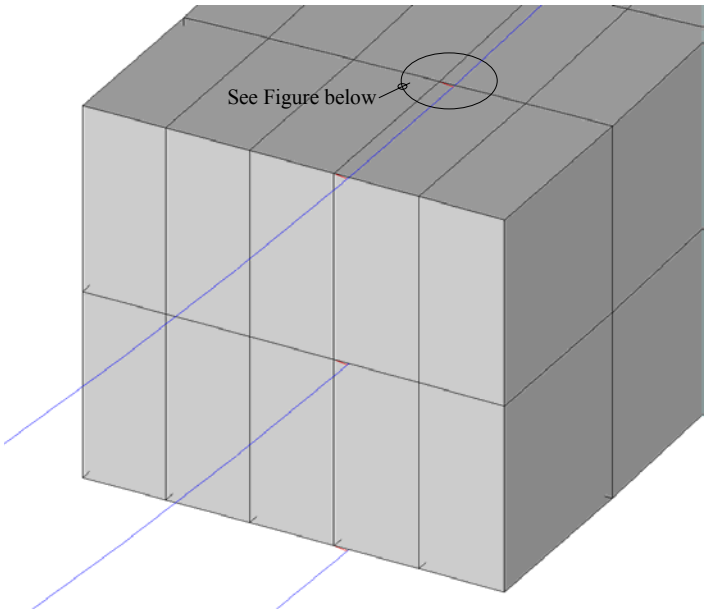

Figure .7 Interaction between tendon and concrete modeled with friction trusses.

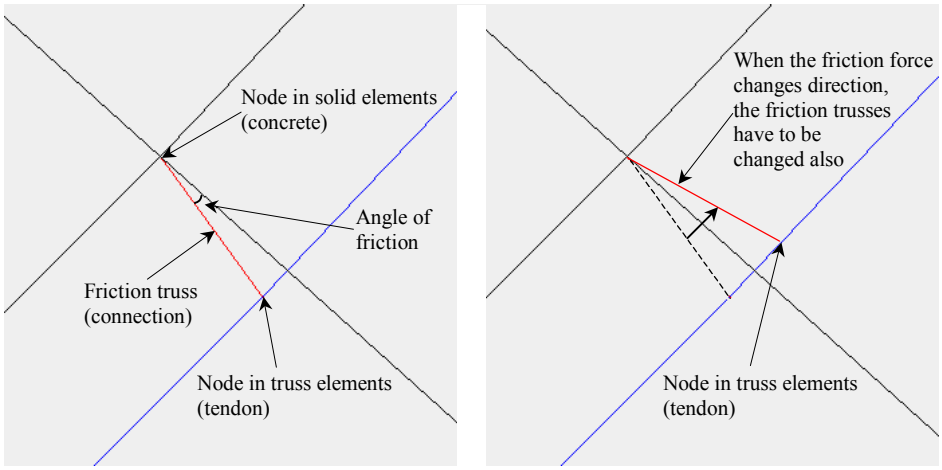

Figure .8 Interaction between tendon and concrete modeled with friction trusses, plan view.

To receive the correct direction of the friction trusses when connecting the truss elements with the solid elements, the spatial positioning of the nodes have to be very exact. Also, in zones were the friction force changes direction two nodes have to be specified for the truss element for each solid element connecting node. The demands on spatial positioning of nodes will increase the time to build the model to a great extent, if an automated process is not available, i.e through a specially tailored pre-processor or script.

5.2.5 Results

All methods provide accurate results when modeling tensioning and seating, as can be seen in Figure 5.9. In this figure the curve named Contact represents both the method using trusses and membranes for modeling the tendons.

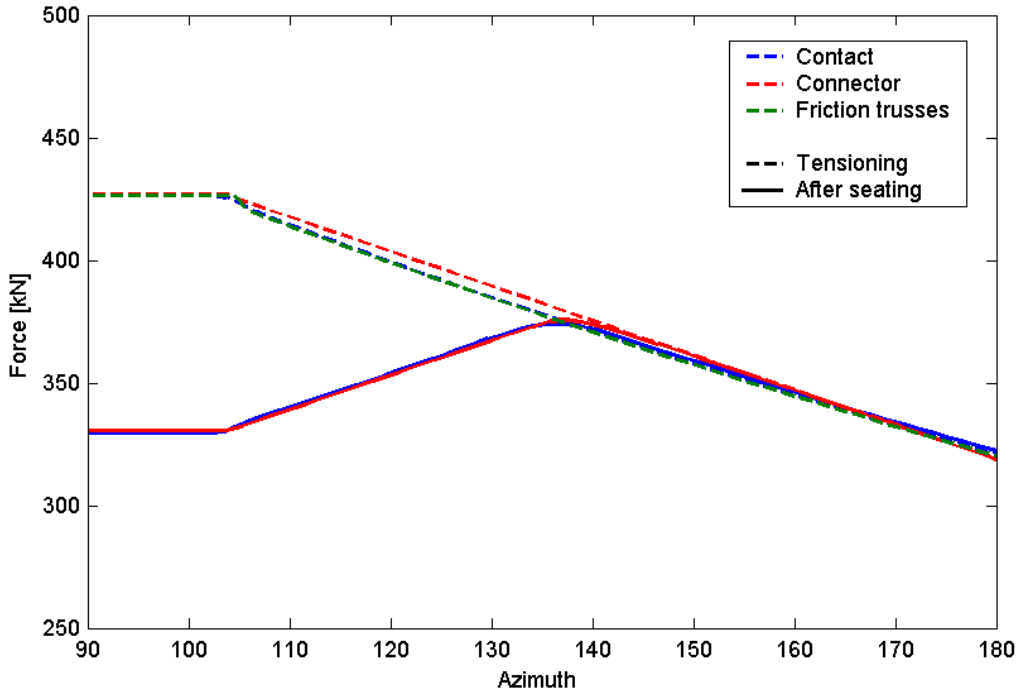

Figure 5.9 Distribution of pre-stressing force for unbonded tendons at tensioning using different modeling techniques.

During pressurization the method using friction trusses has been excluded due to the fact that the direction of the friction trusses has to be modified when the friction force changes direction. The direction of the friction force changes several times, see Figure 5.14. The three remaining methods can in an accurate way capture the changes in tendon force distribution along the tendon during pressurization.

Figure 5.10 and Figure 5.11 present the tendon stresses after tensioning and after seating respectively. In Figure 5.12 tendon forces along the tendon at different loading levels are shown.

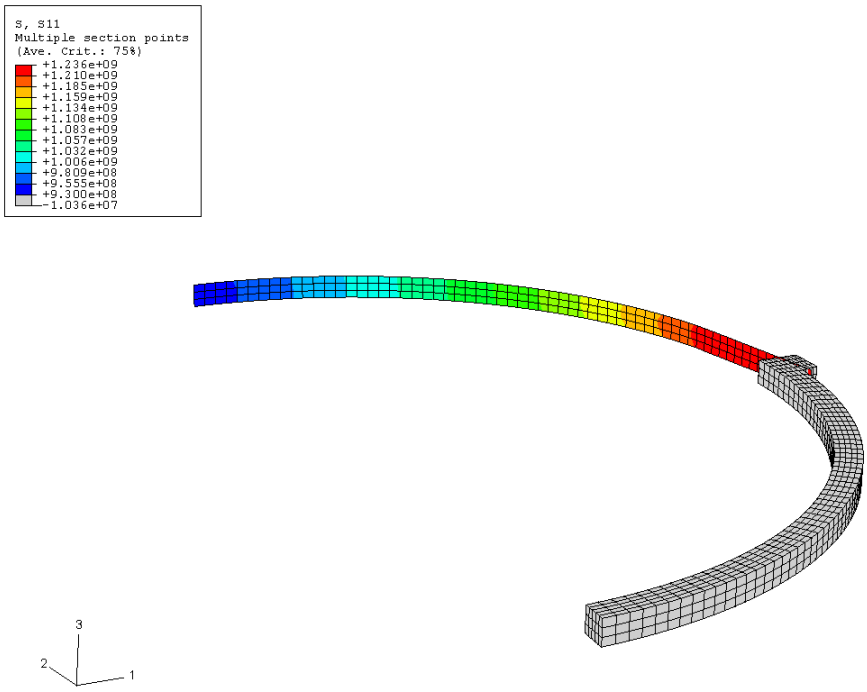

Figure .10 Pre-stressing tendons modeled with membrane elements/contact formulation, tensioned using translatory connectors: tensioning phase.

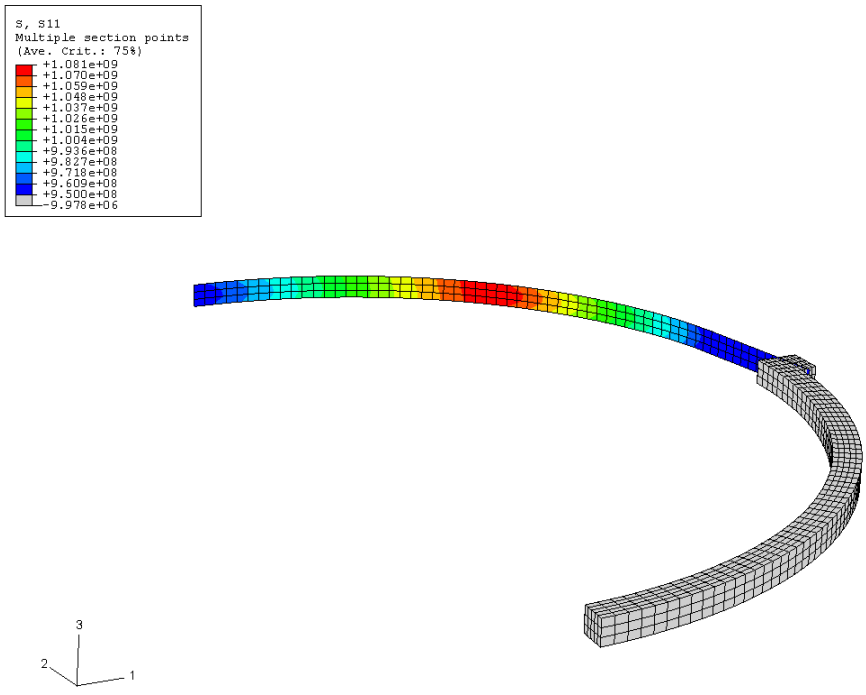

Figure .11 Pre-stressing tendons modeled with membrane elements/contact formulation, tensioned using translatory connectors: after seating.

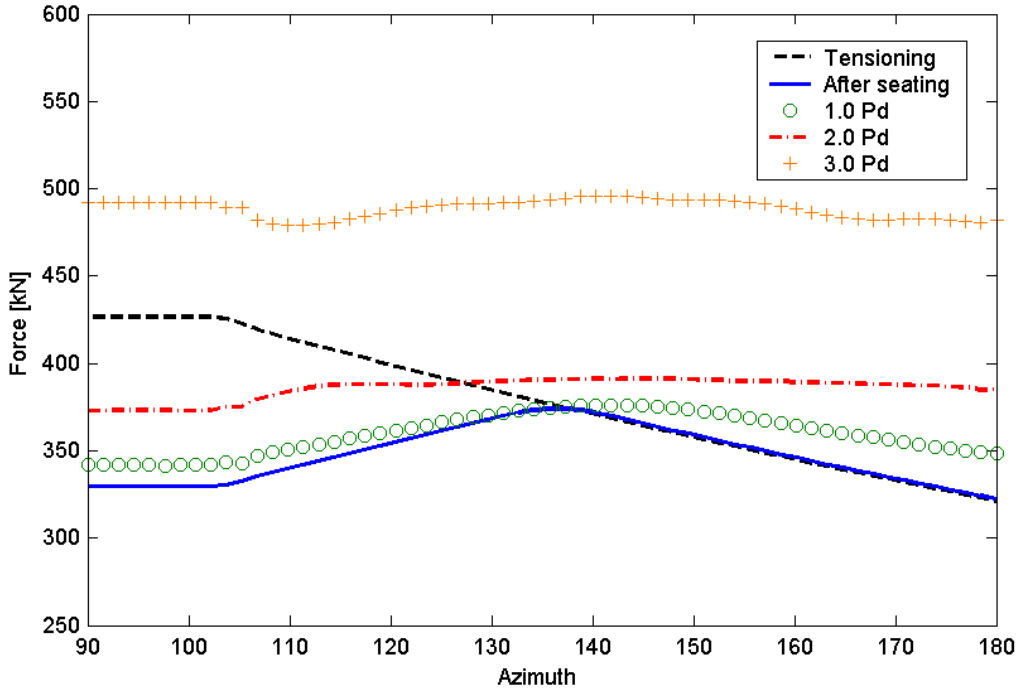

Figure .12 Pre-stressing tendons modeled with truss or membrane elements/contact formulation: distribution of pre-stressing force for unbonded tendon at different loading stages.

A comparison with level 2 methods, i.e. modeling the tendons as fully bonded to the concrete during pressurization, is made in Figure 5.13. Here we see that the force in the tendons differ to a great extent in some regions. If these regions coincide with critical areas regarding leak-tightness, the difference has a non-negligible effect.

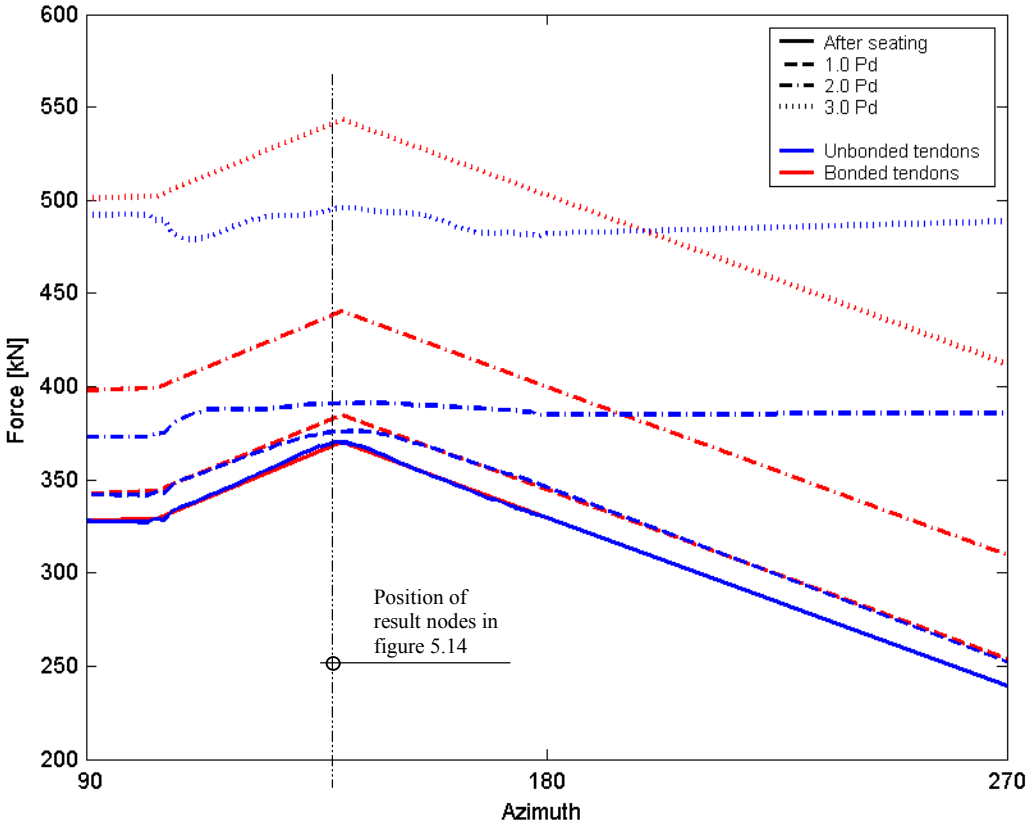

Figure .13 Pre-stressing tendons modeled with truss or membrane elements/contact formulation: distribution of pre-stressing force for unbonded tendon at different loading stages. As comparison, theoretically determined force distribution for fully bonded tendon, and uniform strain along the tendon, are shown.

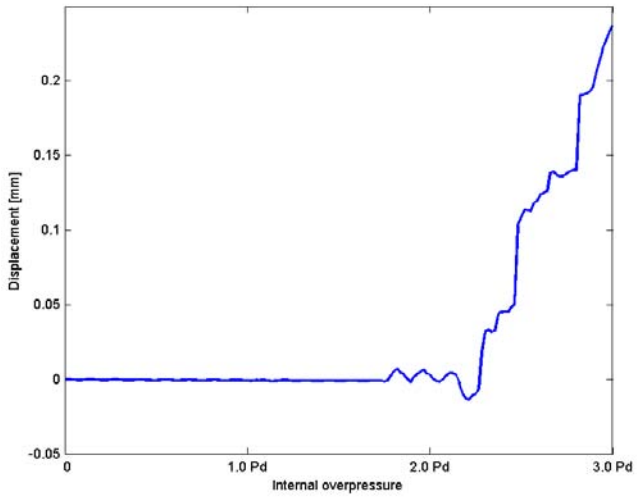

Figure .14 Differential displacement between a concretre node and a tendon node due to slippage during pressurization. The node is positioned at approximatly azimuth 120, see figure .13.

5.2.6 Conclusions

In Table 5.1 a short summary of the different modeling techniques is given.

As can be seen in Figure 5.13, the re-distribution of the tendon force along the tendon occurs between the overpressurization levels $1*P_d$ and $2*P_d$. Due to the fact that the yielding and rupture of the liner occurs at pressure levels well above this, we have decided to take this phenomena into consideraiton in the 3D-model analysis.

In the 3D-model of the model containment trusses have been chosen for the modeling of the tendons together with the contact formulation/friction coefficient to simulate the interaction between tendons and concrete, see section 5.2.1.

Method **Area**	**Contact** (sections 5.2.1, 5.2.2)	**Friction connector** (section 5.2.3)	**Friction trusses** (section 5.2.4)
Simulation capabilities	Tendon force distribution along the tendon during tensioning and seating automatically calculated. Friction coefficient has to be specified as input data. Re-distribution of tendon force during pressurization automatically calculated. Increase in friction force during pressurization automatically calculated. Can be used both for implicit and explicit codes, but convergence problems can occur when using implicit codes.	Tendon force distribution along the tendon during tensioning and seating automatically calculated. Friction forces has to specified as input data. Re-distribution of tendon force during pressurization automatically calculated. Increase in friction force during pressurization has to be specificed as a function of the pressure load and given as input data. Can be used both for implicit and explicit codes.	Tendon force distribution along the tendon during tensioning and seating calculated. Change of model necessary when friction force changes direction, i.e between the tensioning and the seating phase. Angle of friction implicitly specified when defining geometry. Re-distribution of tendon force during pressurization automatically calculated only as long as the direction of the friction forces not change, otherwise the model has to be changed as stated above. Increase in friction force during pressurization automatically calculated. Cannot be used with explicit codes or using large deformation theory with implicit codes.
Computational runtime	1	~ 0.5	~ 0.5
Modeling effort	1 (tendons modeled with trusses) ~ 0.75 (tendons modeled with membranes)	~ 2	~ 4
Comments	Modeling technique selected to be used in the 3D-model (section 6).		

Table L.1 Comparison between friction modeling methods when modeling unbonded pre-stressing tendons.

6. MAIN ANALYSIS: GLOBAL THREE-DIMENSIONAL MODEL

6.1 General

The axi-symmetrical approach applied in the parametrical studies (section 4) provides a first estimate regarding the global response of the structure. However, the axi-symmetrical model is not capable of catching effects due to for example major penetrations, pre-stressing buttresses, non-uniform layout of the pre-stressing tendons and reinforcement, and the non-uniform and pressure-dependent pre-stressing effects. These effects will to a major extent influence the structural behaviour of the containment, including overpressure levels at leakage and collapse, as well as rupture positions. To take into consideration all these matters, a fully three-dimensional model has to be used.

Modeling assumptions are based on the parametrical studies carried out in section 4, and the investigation regarding modeling techniques for unbonded tendons presented in section 5.

6.2 Structural model

6.2.1 Geometry

The global three-dimensional model has been established out of drawings provided in [2]. General dimensions are presented in section 3 above. The model is shown in Figure 6.1, Figure 6.2 and Figure 6.3.

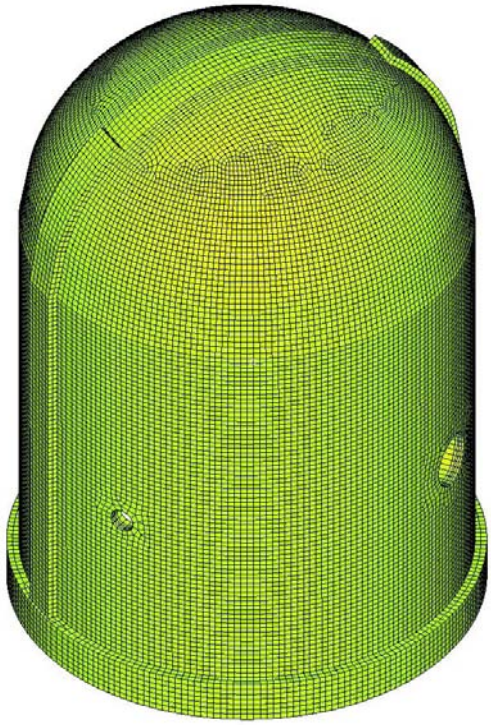

Figure 6.1 Global three-dimensional model.

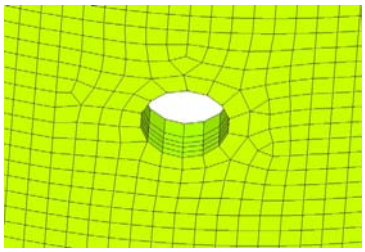

Figure 6.2 Global three-dimensional model, modeling of A/L.

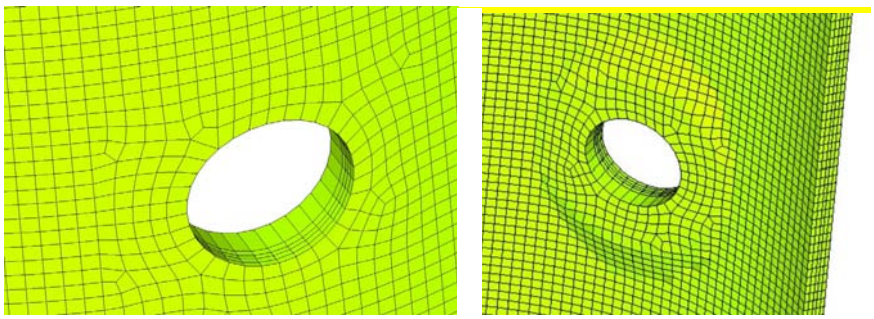

Figure 6.3 Global three-dimensional model, modeling of E/H, outside (left) and inside (right).

6.2.2 Types of element

The concrete parts are in the FE-model represented by rectangular solid continuum elements with a reduced number of integration points denominated C3D8R. The steel liner is represented by rectangular shell elements denominated S4R. A very limited number of the elements are triangle elements denominated C3D6R and S3R respectively. The pre-stressing tendons are modeled by using truss elements. The reinforcement are described by using the rebar modeling feature in ABAQUS. The reinforcement are then modeled by rebars in form of a layer inside the underlying continuum elements (concrete).

6.2.3 Boundary conditions

Only a minor part of the basemat is included in the FE-model, the part between the cylindrical wall connection and the tendon gallery, i.e. approximately corresponding to the cast stage $F3_B$, see Figure 3.8 in section 3. The bottom and the vertical faces of the basemet part are constrained in both the vertical and the horizontal direction. No constrains are applied on the nodes situated directly above the tendon gallery. Constrained nodes are shown in 6.4.

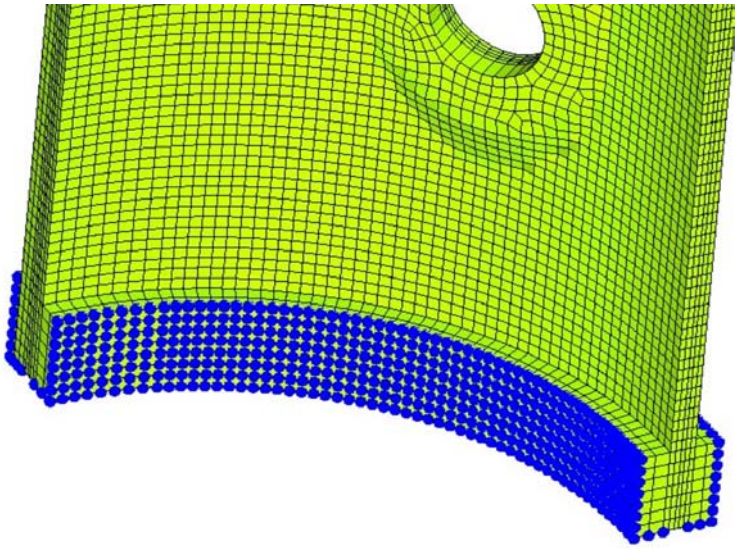

Figure 6.4 Boundary conditions applied to the basemat part.

6.2.4 Contact

In order to get a realistic interaction between the pre-stressing tendons and the concrete, contact definitions have been introduced in the model. In the contact definition the coefficient of friction between the structural parts has to be defined. The coefficients of friction controls the amount of transferable shear force between the tendon and the concrete due to compressive stress over the contact surface. When tensile stresses occur over the contact surface, neither normal stresses or shear stresses can be transferred.

In Figure 6.5 the principles of contact definition between the pre-stressing tendons and the concrete are presented.

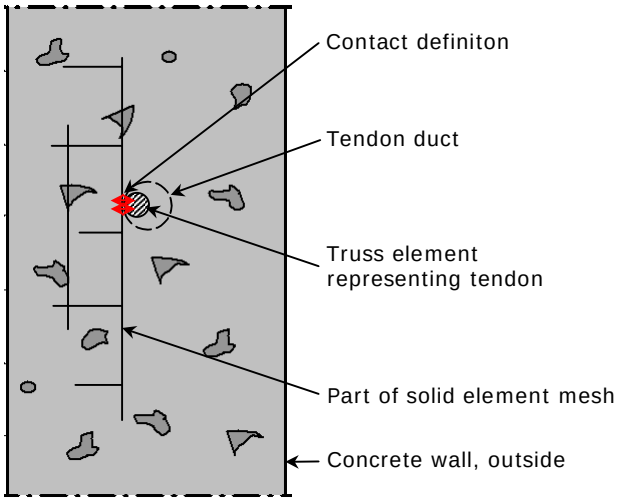

Figure 6. Contact definition between pre-stressing tendon and concrete.

6.2.5 Pre-stressing tendons

The tendons are connected to the concrete by applying a contact definition, see section 6.2.4 above, i.e. they are modeled as un-grouted (unbonded). The tensioning of the tendons is modeled by using translator connector elements, connecting the end of the tendons to a steel anchorplate. The anchorplate is connected to the buttress concrete. The tensioning and seating process are then simulated in the analysis, stretching the tendons with the help of the connector element to the same amount as done with the jack during construction, see Figure 6.6.

This procedure gives rise to an un-evenly distributed tendon force along the length of the tendon, due to the friction specified in the contact definition, thus matching the actual tendon force variation.

With the method chosen for the modeling of the tendons, during pressurization, the pre-stressing force along the tendon is automatically changed from an un-even distribution to a more or less evenly distributed force, see section 5.2.1 and Table 5.1.

The tendons in the horizontal direction are tensioned to a maximum stress after seating of 1120 MPa, corresponding to a pre-stressing force of 380 kN, and the tendons in the vertical direction to 1280 MPa, corresponding to a force of 435 kN. The modeling of the tendons is shown in Figure 6.7 and Figure 6.8.

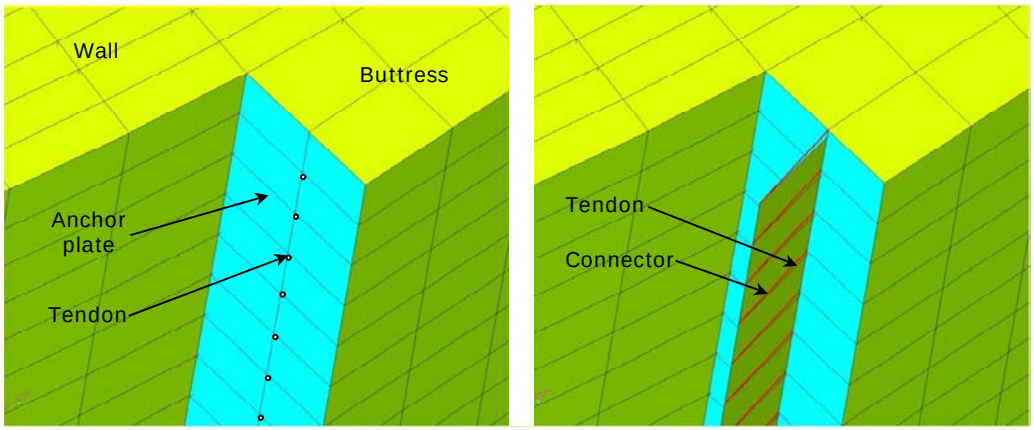

Figure 6.6 Tensioning of cables using Connector elements: before tensioning (left) and after tensioning (right) respectively.

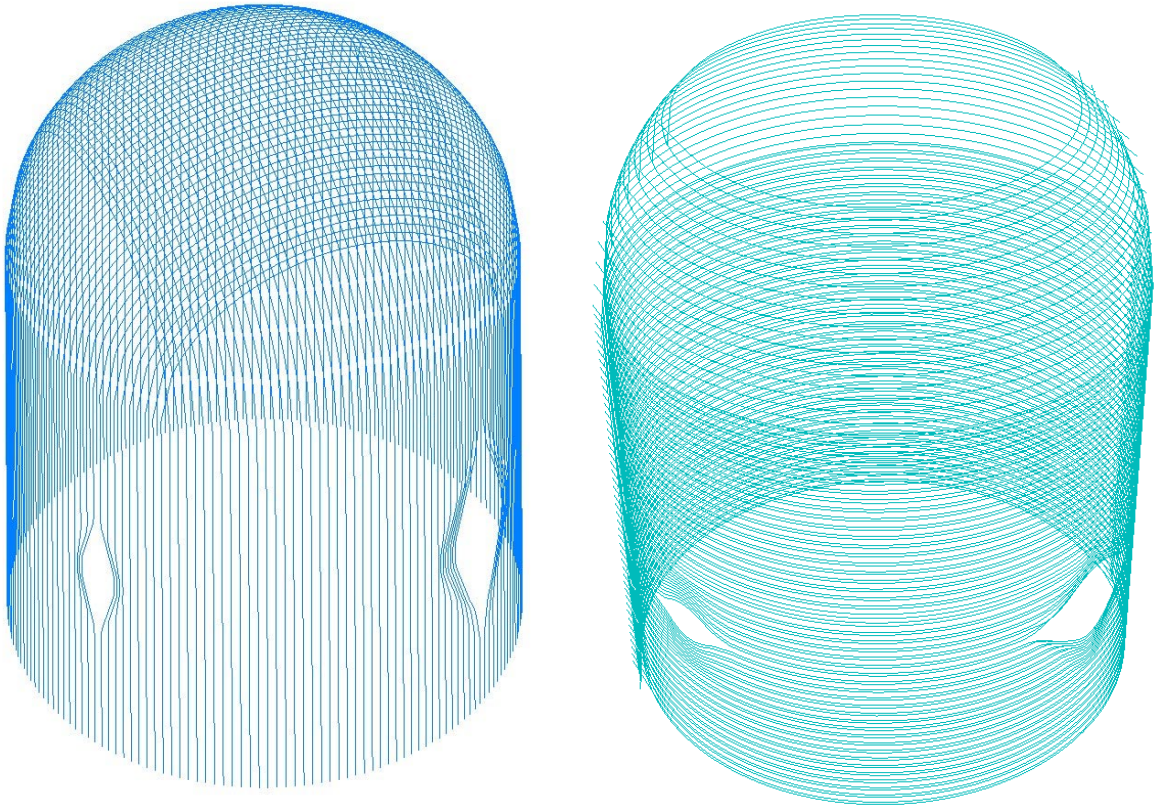

Figure 6.7 Vertical pre-stressing tendons (left). Horizontal pre-stressing tendons (right).

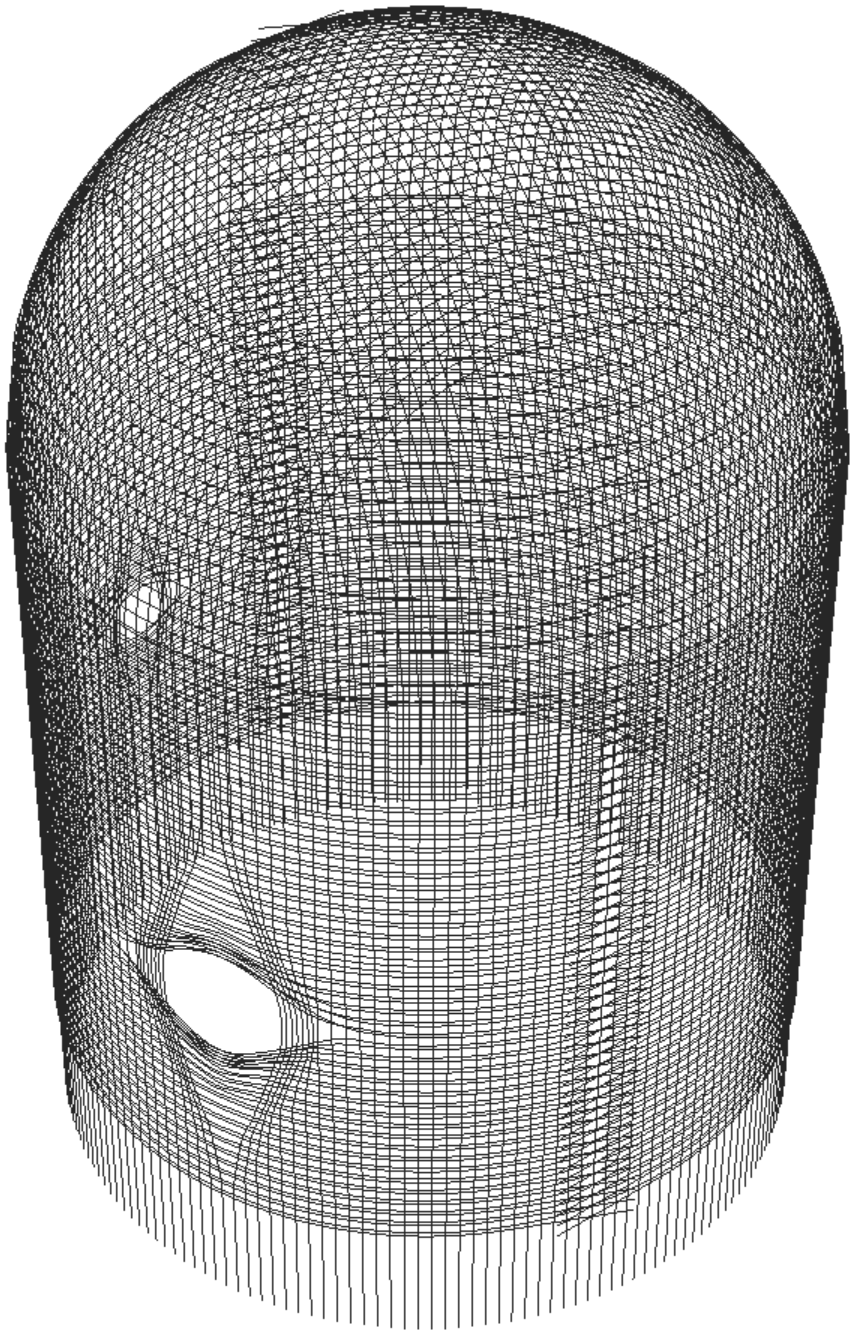

Figure 6.8 All pre-stressing tendons.

6.2.6 Reinforcement

The reinforcement bars at the inner and outer surface of the model containment are in principle modeled as shown in Figure 6.9 and Figure 6.10. The different colours represent regions with different reinforcement content. The rebars are rigidly connected to the concrete as described in section 6.2.2 above.

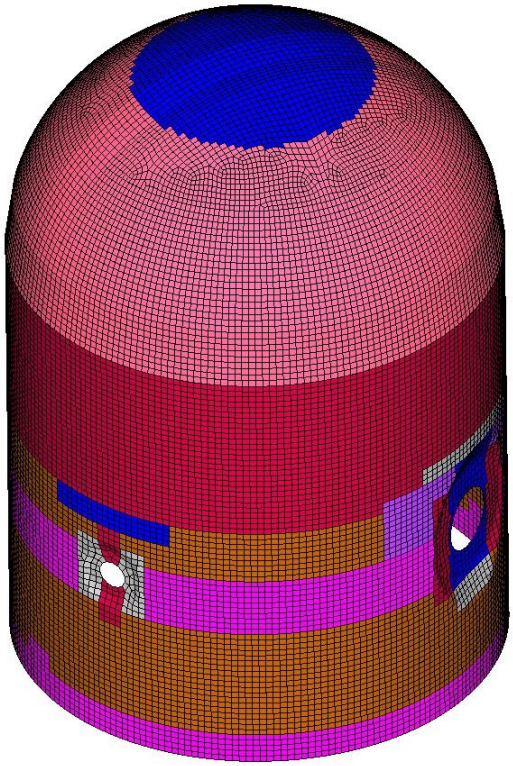

Figure 6.9 Reinforcement regions, inner surface.

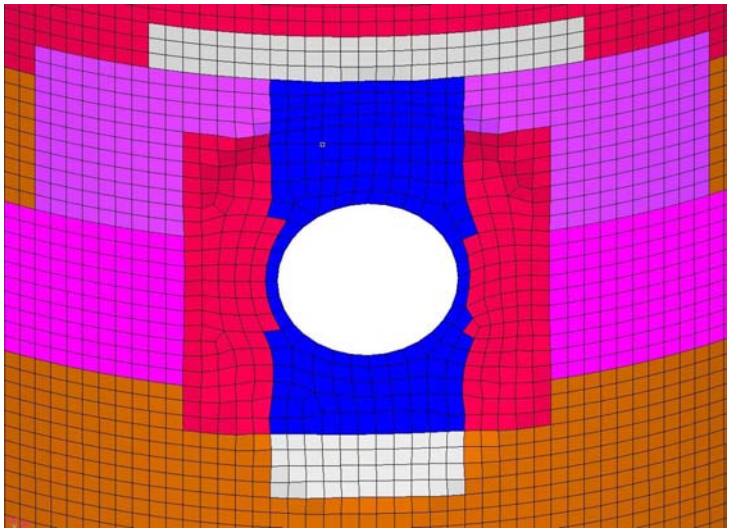

Figure 6.10 Reinforcement regions, inner surface, around E/H.

6.2.7 Steel liner

The steel liner is positioned on the inside of the containment and is rigidly connected to the concrete elements.

6.2.8 Application of loads

Dead weight is modeled applying a field of gravity acting downwards, using the gravitational constant 9.81 m/s^2.

The internal overpressure is applied as a linear monotonic increasing pressure load at the inner face of the containment, i.e. to the shell element representing the steel liner.

Since an explicit dynamic analysis has been executed the load has been applied quasi-statically during a sufficient long period of time, in order not to introduce any dynamical effects on the structure, i.e. inertia forces and kinetic energy can be regarded as negligible. This means for the 3D-model a loading-rate of 1000 kPa/s according to Figure 6.11. The internal overpressure in the containment has been limited to 2000 kPa, which is well above the ultimate load bearing capacity of the containment model.

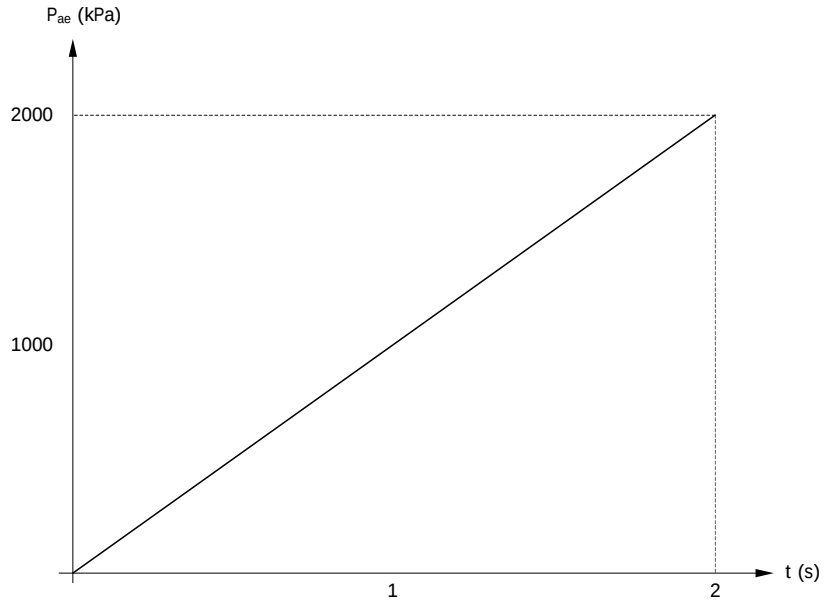

Figure 6.11 Load-time history of the internal overpressure in the explicit dynamic analysis.

7. STRUCTURAL ANALYSIS AND RESULTS

7.1 General

In this chapter the results from the structural analysis are compared to test data at pre-defined positions. In addition, pressure-levels corresponding to important characteristic events, i.e. cracking of concrete, yielding of the steel liner, and tendon rupture leading to burst of the structure, are estimated. An estimation of pressure-level at first leakage, i.e. liner rupture, is somewhat cumbersome to carry out because of the large rupture strain of the liner given by material tests, even for the welded zones. The load level at leakage has in principle to be estimated using more detailed models (modeling approach level 3 and 4 according to Figure 2.1) taking into consideration major penetrations, localized strains, construction details and workmanship etc. Therefore, no prediction of these pressure levels has been made within the scope of this report. Instead, the maximum steel liner strain in the analysis is provided at the test pressure levels corresponding to first leakage and excessive leakage respectively.

In addition to the pressure levels, factors of the design pressure P_d (0.39 MPa internal overpressure) are shown in tables and in result diagrams to facilitate the result interpretation.

All results presented, if not otherwise stated, are taken from the main analysis using the global three-dimensional model.

7.2 Result summary of important events and output parameters

7.2.1 General

Major characteristic events of interest are;

- Start of non-linear structural response, i.e. cracking of concrete.
- Risk of leakage, i.e. yielding of steel liner.
- Excessive leakage, i.e failure of steel liner.
- Collapse of the structure, i.e. failure of tendons.

In Table 7.1 overpressure levels, when these events occur during the experimental tests, are presented and compared with estimated values from the three-dimensional model and the axi-symmetrical model analysis. The events are then discussed in more detail in section 7.2.2 – 7.2.5.

In section 7.2.6, a summary of the outcome of overpressure histories at pre-defined positions for several output parameters is presented. Detailed output parameter results are presented in section 7.3.

Model	**Concrete**	**Steel liner**			**Hoop tendons**			**Unit**
	Cracking	Yield	First failure	Excessive leakage	Yield	2%	Failure	
Test	**0.59-0.78** 1.5-2.0	- [1]	**0.98** 2.5 0.17 %[2]	**1.29** 3.31 0.42 %[2]	**1.17** 3.0	-	**1.4** 3.59	MPa *P_d
3D	**0.55-0.7** 1.41-1.79	**0.8** 2.05	- - 0.9 %[3]	- - 2.4 %[3]	**1.12** 2.87	**1.35** 3.46	**1.38** 3.54	MPa *P_d
Axi	0.52-0.62 1.33-1.59	1.02 2.62	- - 0.17 %[3]	- - 0.42 %[3]	1.29 3.31	1.47 3.78	~1.75 4.49	MPa *P_d

1) A test value of 1.1 MPa is specified. However, the strain gauges were not placed in the position of first yielding.
2) Free field hoop strain given as test result.
3) Maximum strain in the steel liner obtained in the structural analysis at overpressure levels corresponding to first leakage (0.98 MPa) and to excessive leakage (1.29 MPa), respectively. Failure strain of the liner is of the order of 10-20 %. See section 7.1 for disussion.

Table 7.1 Result summary of important events.

7.2.2 Cracking of concrete

In Figure 7.1 predicted initial cracking of the concrete is shown. As can be seen the first cracking occurs at the major penetrations and near the buttresses.

The major cracking of concrete occurs at overpressure levels of 0.59-0.78 MPa. By analysis predicted overpressure at cracking of concrete is 0.55-0.7 MPa, i.e. that is in good agreement with test results.

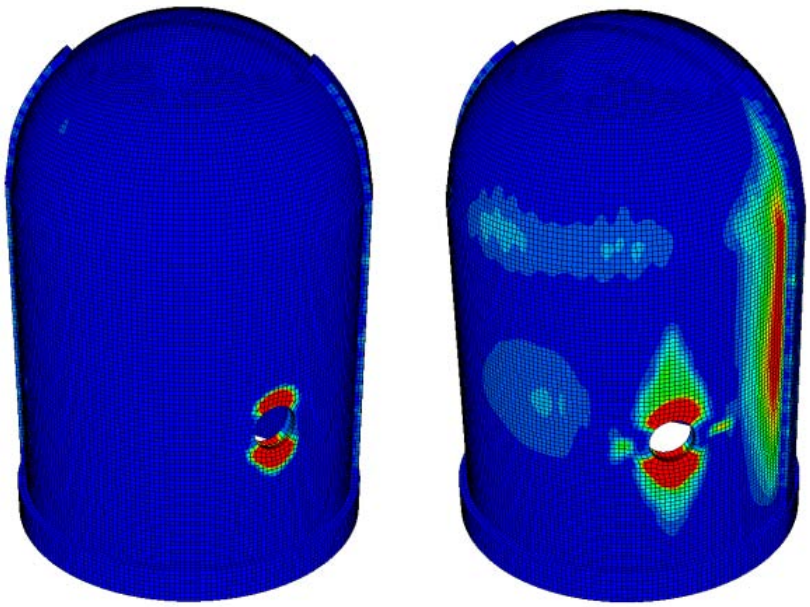

Figure 7.1 Cracking of concrete (red colour indicates the largest cracking).

7.2.3 Steel liner

In Figure 7.2 predicted yielding of the steel liner is shown, and in Figure 7.3 the position of predicted yielding is compared with steel liner rupture positions mapped after completion of the overpresurization test. The analysis results and test results agree well.

As can bee seen in Figure 7.3, the position of first yielding near the equipment hatch (E/H) predicted by the analysis (position I) differ to a small extent from the actual rupture position during test. This is due to the fact that the rupture of the liner during the test occurs at a position where the thickness of the steel liner changes. This sectional change is not included in the model used, giving a rupture position placed underneath the E/H instead of at the side of the hatch.

The first yielding of the steel liner during test is registred for an overpressure of 1.1 MPa. However, the strain gauges measuring the strains in the steel liner are not placed at the position for first yielding, i.e first yielding has to occur at an lower overpressure level. By analysis, predicted first yielding of the steel liner occurs at an overpressure of 0.8 MPa, which is in agreement with the conclusions stated above.

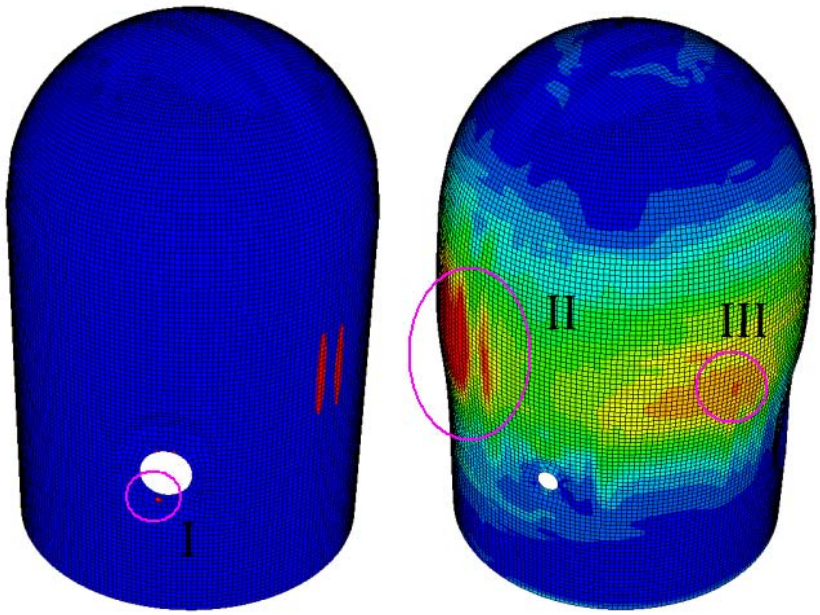

Figure 7.2 Yielding of steel liner (red colour indicates maximum yielding).

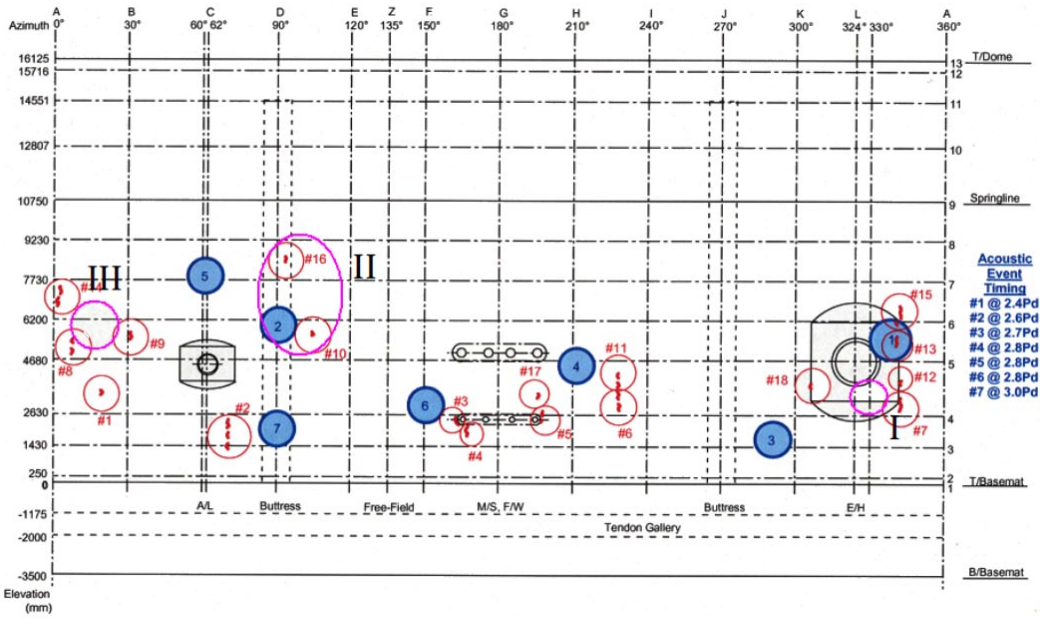

Figure 7.3 Liner rupture positions from test compared with analysis results.

7.2.4 Collapse of structure

In Figure 7.4 (left) the predicted position of rupture of the containment during structural collapse is shown. The predicted position agrees very well with the actual rupture (burst) position during test, as can be seen in Figure 7.4 (right).

Collapse of the model containment during the test occurred at an overpressure level of 1.4 MPa. By analysis, using the 3D-model, collapse was predicted to occurre at an overpressure of 1.38 MPa, in good agreement with test data. The axi-symmetrical model, however, overestimate the load-bearing capacity of the containment, predicting a collapse pressure of more than 1.75 MPa.

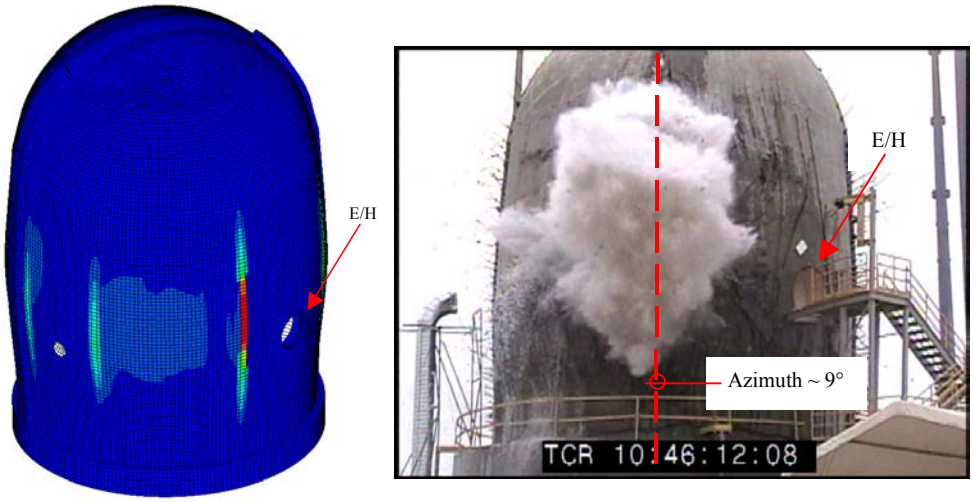

Figure 7.4 Rupture position (red colour).

7.2.5 Results at pre-defined positions

Results for several output parameters as a function of overpressure are presented in section 7.3 for different standard output locations (SOL) in the structure, in total 55 diagrams. These result outputs correspond to experimental test data positions. In Table 7.2 below, a summary and evaluation of the analysis results is presented.

The most important result parameters are the radial deformation, strains in the steel liner and strains in the tendons. This is due to the fact that the radial stresses and strains governs the capacity of the model containment, not the stresses/strains in the vertical direction. Further more, the strain in the liner is the most important parameter to determine the leak-tightness capacity, and the strains in the tendons, the corresponding parameter to govern the load-bearing capacity. For these parameters there is good agreement between measured test data and calculated analysis results. The same applies for vertical deformation and rebar strain.

Result component	**Result evaluation**
Displacements	
Radial:	Good – very good
Vertical:	Accurate - good
Rebar strain	
Hoop:	Accurate - good
Meridional:	Accurate - good
Liner strain	
Hoop:	Accurate – very good
Meridional:	Accurate – very good
Tendon strain	
Hoop:	Very good
Vertical:	Very good

Table 7.2 Evaluation summary of results for the output locations.

For azimuth 135, the axi-symmetrical model also gives good results regarding displacements. However, due to the fact that the radial displacement varies a lot depending on the circumferential position (azimuth), as can be seen in Table 7.3, it is evident that the axi-symmetrical model is not quite capable of capturing the true behaviour of the contaiment. For rebar strain the axi-symmetrical model gives poor results, while the three-dimensional models gives good results. Correspondingly for liner strains the 3D-model gives more accurate results than the axi-symmetrical model.

Level	Azimuth	Displacement	
		Measured test data	Results from axi-symmetrical model (azimuth 135)
4.6	66	9 mm	-
	135	8 mm	10 mm
	334	13 mm	-
6.2	90	6 mm	-
	135	10 mm	10 mm

Table 7.3 Comparison between during the test measured radial displacement, at overpressure 1 MPa, in different circumferential positions with displacement calculated using the axi-symmetrical model.

7.3 3D-model analysis

7.3.1 General

The main analysis of the model containment is carried out using a three-dimensional model as discussed in section 2.

In this section analysis results from the 3D-model analysis are compared to test data. For results at azimuth 135 degrees, corresponding results from the axi-symmetrical analysis are also shown for comparison.

7.3.2 Result positions

Results are presented in 55 standard output locations (SOL) corresponding to test data positions. In Figure 7.5 and Figure 7.6 result positions used for presentation are shown. Most of the positions correspond to azimuth 135°, but results are also presented at azimuth 0, 58, 66, 90, 180, 241, 275, 280 and 334 respectively, as indicated in the figures.

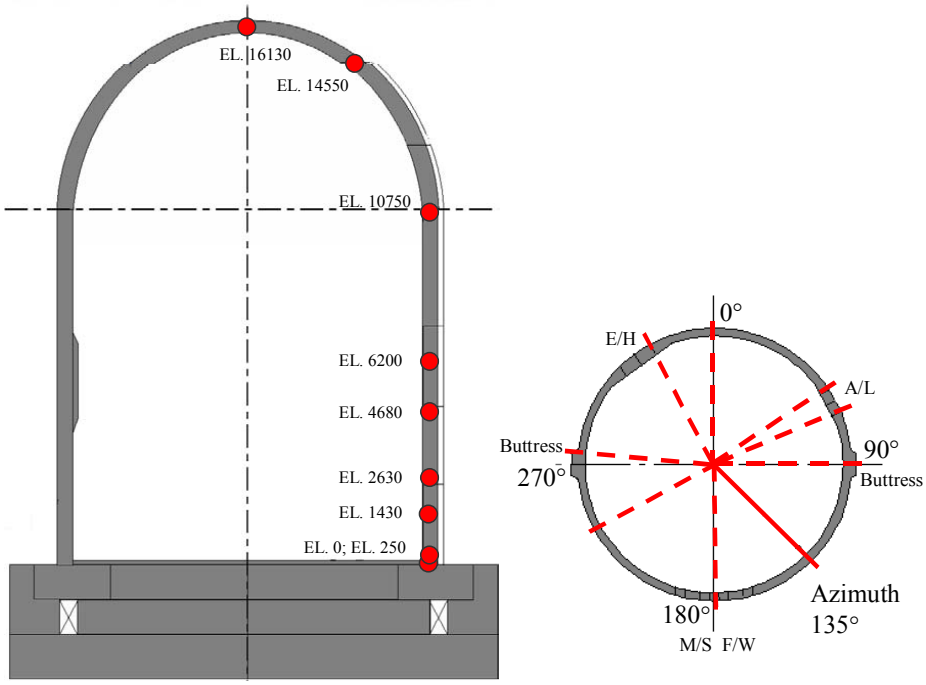

Figure 7. Result positions for 3D-model.

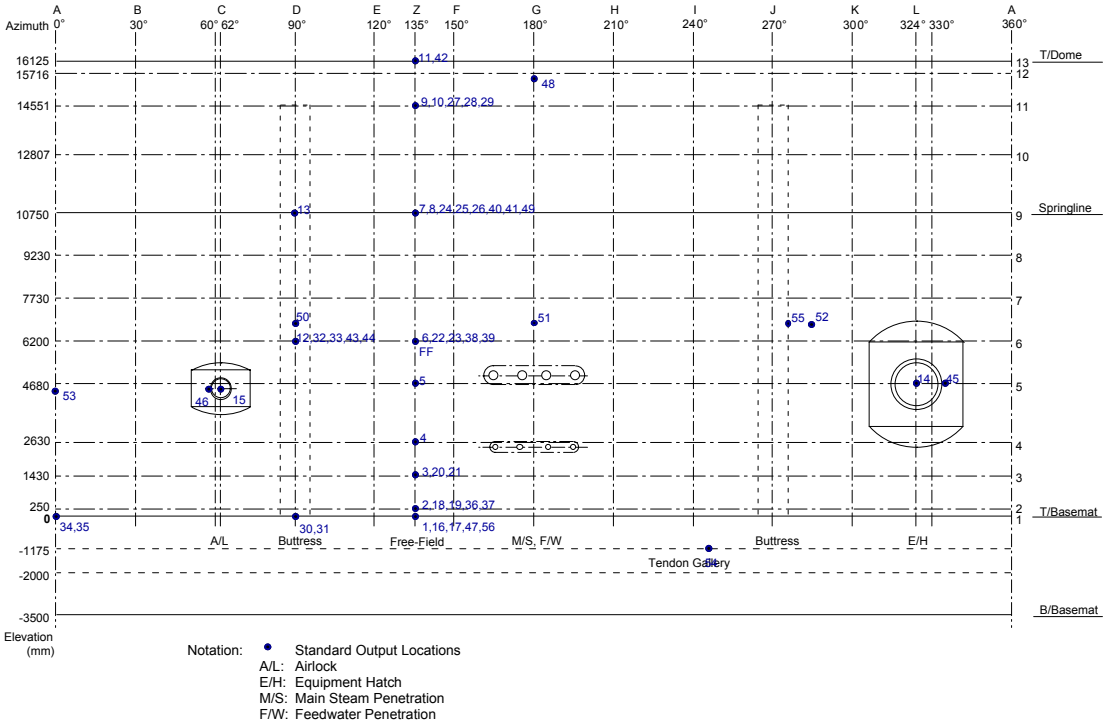

Figure 7.6 Result positions for 3D-model (elevation of inside surface).

7.3.3 Result presentation

7.3.3.1 Displacements

Displacements in the radial direction are presented, using the initial position of the structure before pressurization as reference position. Displacement in the vertical direction are presented with the upper part of the basemat as reference, i.e. excluding any basemat uplift.

In Figure 7.7 to Figure 7.21 analysis results regarding radial and vertical displacement are presented together with measured displacements during the limit state test (LST) of the model containment.

The analysis results agree very well to corresponding test data regarding displacements in the radial direction. The results in the vertical direction also agree well to corresponding test data.

7.3.3.2 Rebar strain

In Figure 7.22 to Figure 7.39 analysis results regarding rebar strain are shown. For the main analysis using the 3D-model the results agree well with test data. However for the axi-symmetrical analysis, a large deviation from test data occurs.

7.3.3.3 Liner strain

In Figure 7.40 to Figure 7.51 analysis results regarding liner strain are shown. The results agree well to corresponding test data.

7.3.3.4 Tendon strain

In Figure 7.52 to Figure 7.58 analysis results regarding tendon strain are shown. The results agree very well to corresponding test data.

7.3.3.5 Result diagrams

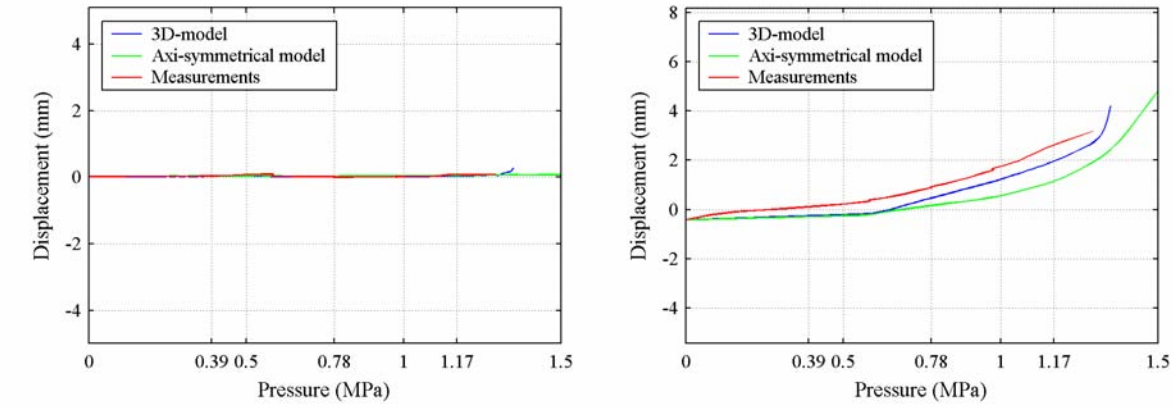

Figure 7.7 Pos. 1-Displacement in vertical direction for el 0.0 and az 13 (left).

Figure 7.8 Pos. 2-Displacement in radial direction for el 0.2 and az 13 (right).

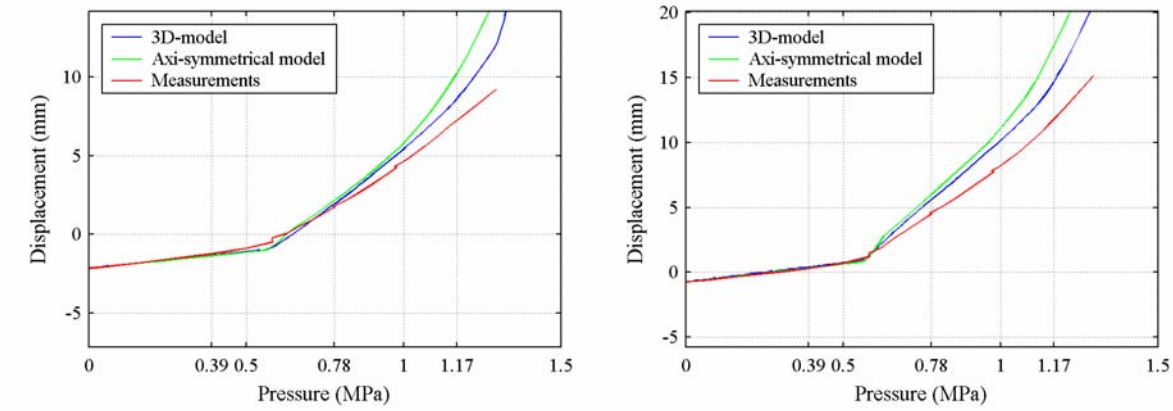

Figure 7.9 Pos. 3-Displacement in radial direction for el 1.43 and az 13 (left).

Figure 7.10 Pos. 4-Displacement in radial direction for el 2.63 and az 13 (right).

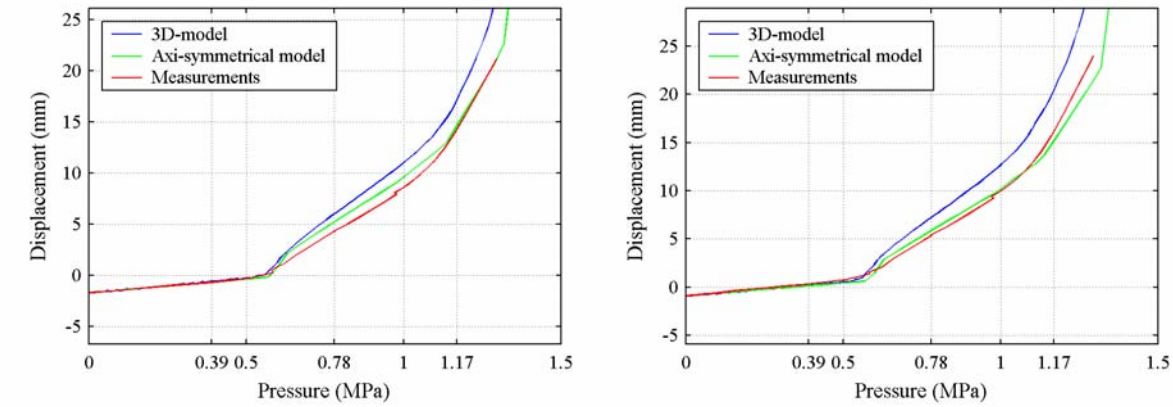

Figure 7.11 Pos. -Displacement in radial direction for el 4.68 and az 13 (left).

Figure 7.12 Pos. 6-Displacement in radial direction for el 6.2 and az 13 (right).

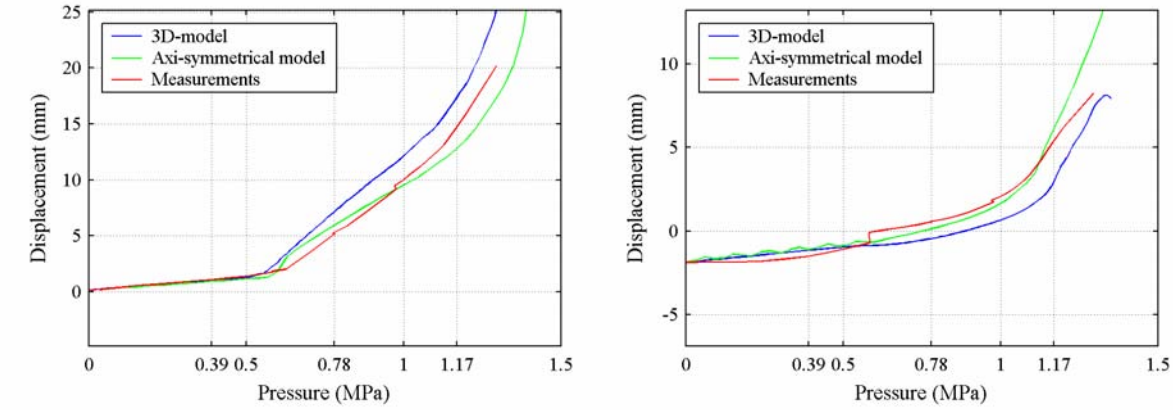

Figure 7.13 Pos. 7-Displacement in radial direction for el 10.7 and az 13 (left).

Figure 7.14 Pos. 8-Displacement in vertical direction for el 10.7 and az 13 (right).

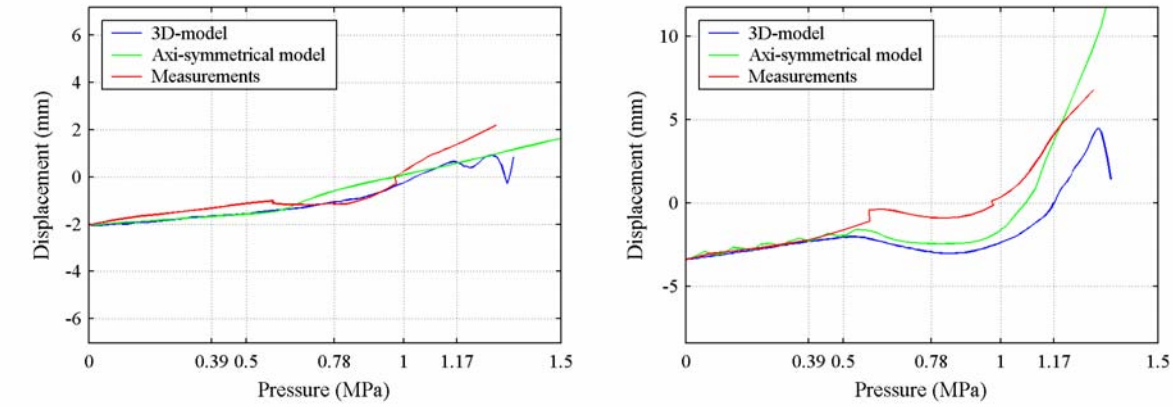

Figure 7.15 Pos. 9-Displacement in radial direction for el 14.5 and az 135 (left).

Figure 7.16 Pos. 10-Displacement in vertical direction for el 14.5 and az 135 (right).

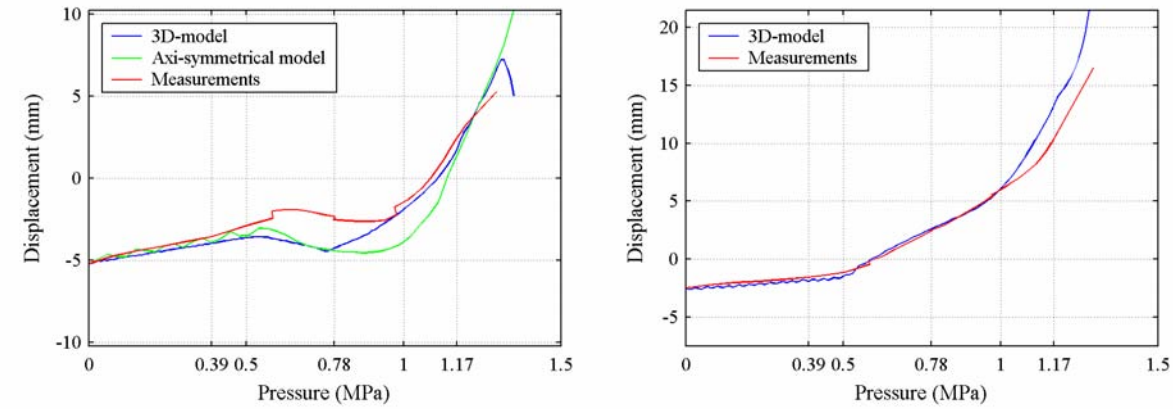

Figure 7.17 Pos. 11-Displacement in vertical direction for el 16.13 and az 135 (left).

Figure 7.18 Pos. 12-Displacement in radial direction for el 6.2 and az 90 (right).

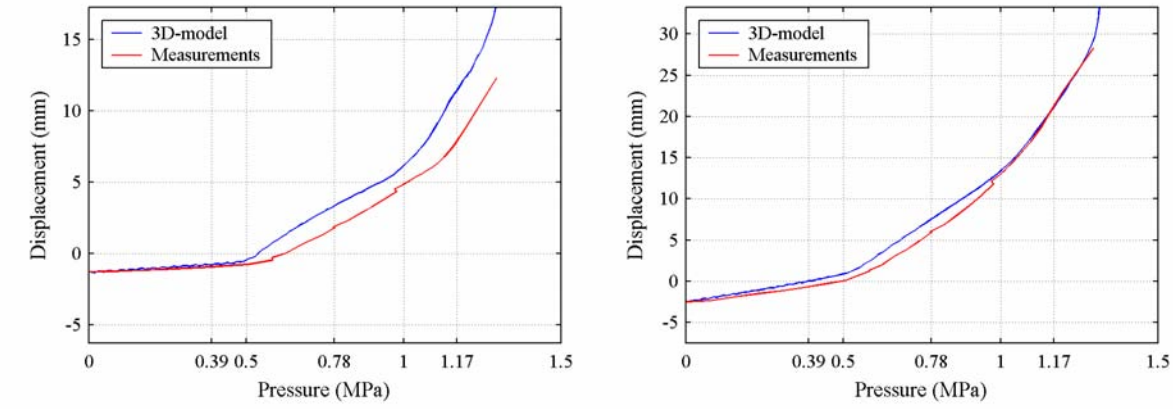

Figure 7.19 Pos. 13-Displacement in radial direction for el 10.7 and az 90 (left).

Figure 7.20 Pos. 14-Displacement in radial direction for el 4.67 and az 334 (right).

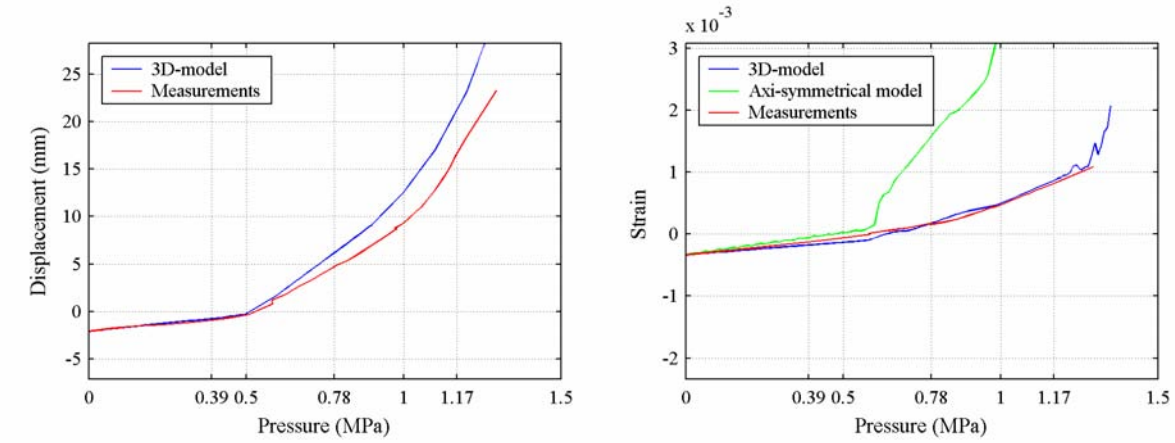

Figure 7.21 Pos. 1 -Displacement in radial direction for el 4. 2 and az 66 (left).

Figure 7.22 Pos. 16-Rebar strain inside layer, meridional direction, el 0.0 , az 13 (right).

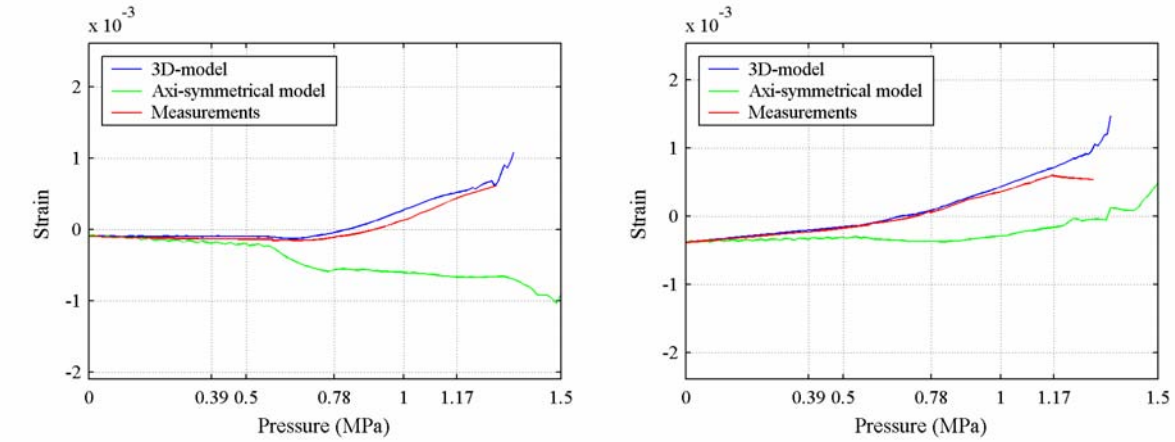

Figure 7.23 Pos. 17-Rebar strain outside layer, meridional direction, el 0.0 , az 13 (left).

Figure 7.24 Pos. 18-Rebar strain inside layer, meridional direction, el 0.2 , az 13 (right).

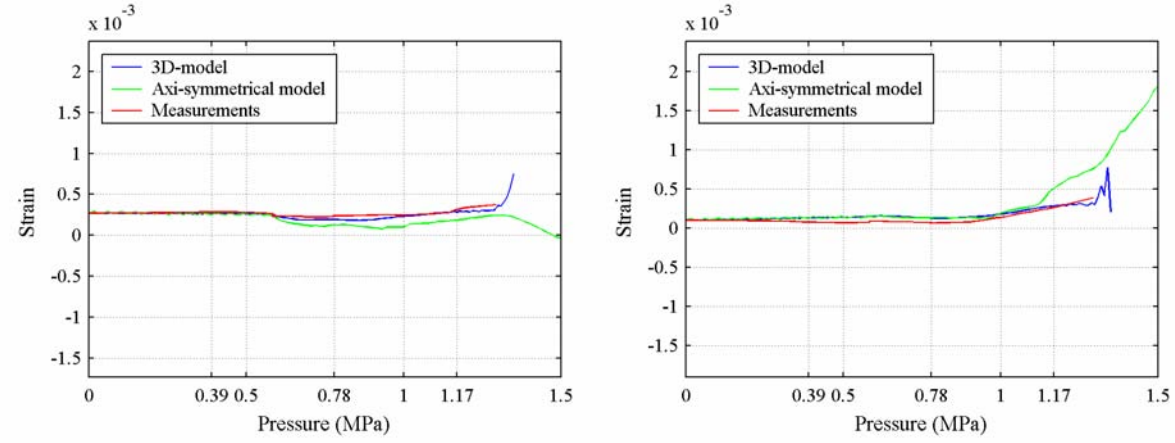

Figure 7.2 Pos. 19-Rebar strain outside layer, meridional direction, el 0.2 , az 13 (left).

Figure 7.26 Pos. 20-Rebar strain inside layer, meridional direction, el 1.43, az 13 (right).

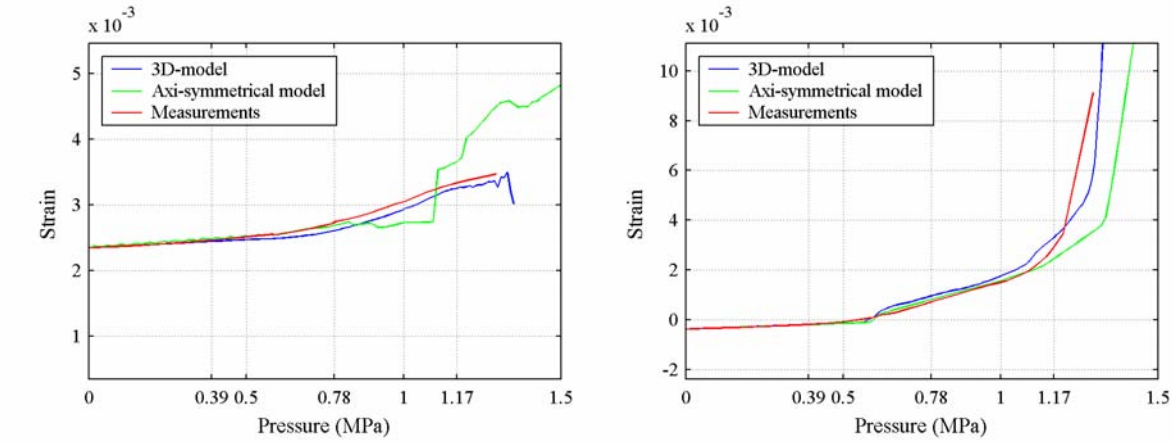

Figure 7.27 Pos. 21-Rebar strain outside layer, meridional direction, el 1.43, az 13 (left).

Figure 7.28 Pos. 22-Rebar strain outside layer, hoop direction for el 6.2 and az 13 (right).

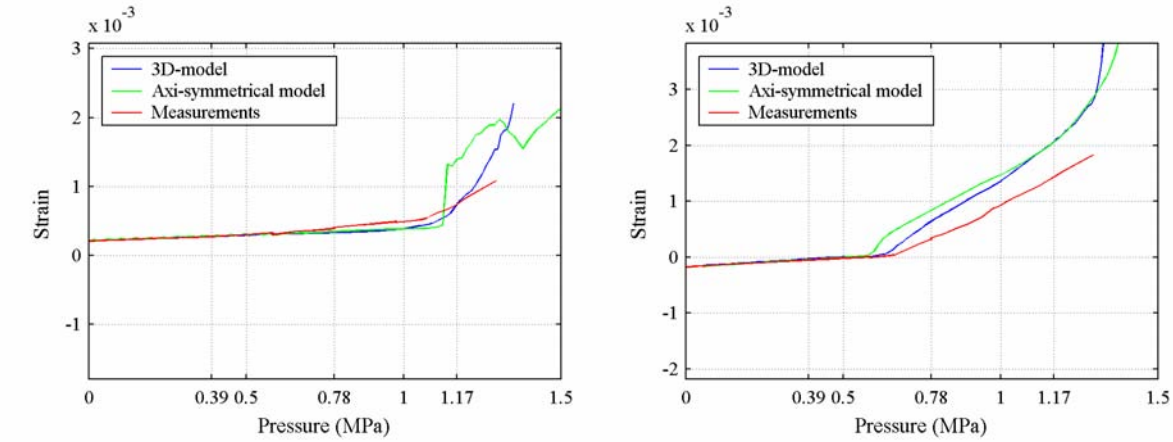

Figure 7.29 Pos. 23-Rebar strain outside layer, meridional direction, el 6.2 and az 13 (left).

Figure 7.30 Pos. 24-Rebar strain outside layer, hoop direction, el 10.7 and az 13 (right).

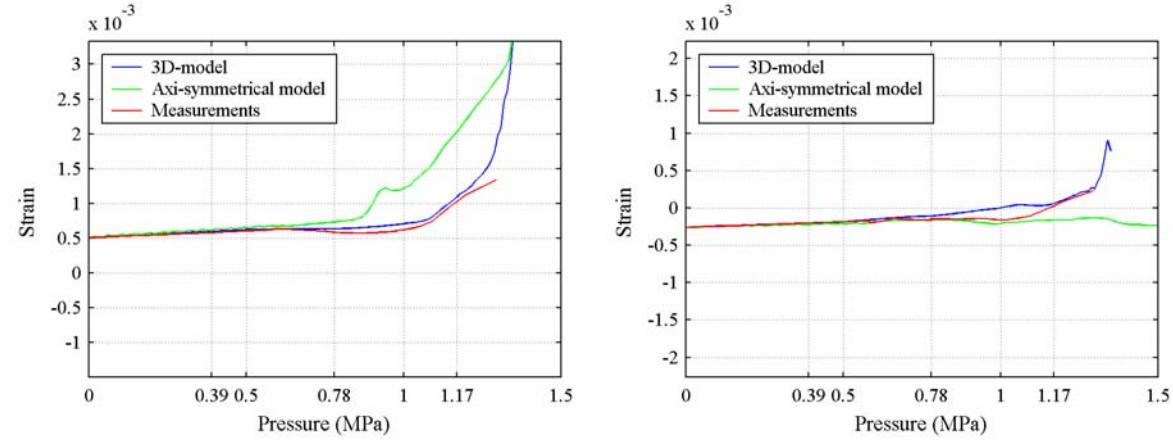

Figure 7.31 Pos. 2 -Rebar strain inside layer, meridional direction, el 10.7 , az 13 (left).

Figure 7.32 Pos. 26-Rebar strain outside layer, meridional direction, el 10.7 , az 13 (right).

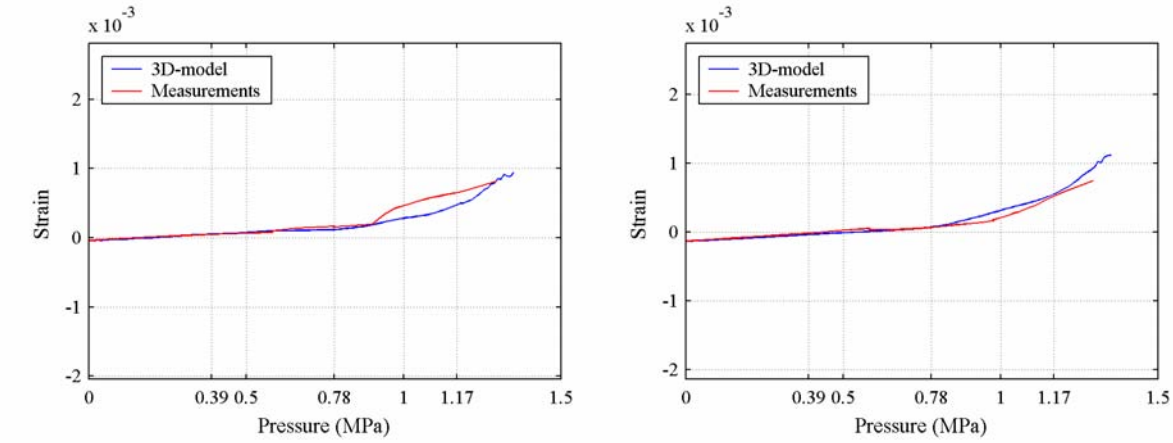

Figure 7.33 Pos. 27-Rebar strain outside layer, hoop direction for el 14.5 and az 135 (left).

Figure 7.34 Pos. 28-Rebar strain inside layer, meridional direction, el 10.7 , az 135 (right).

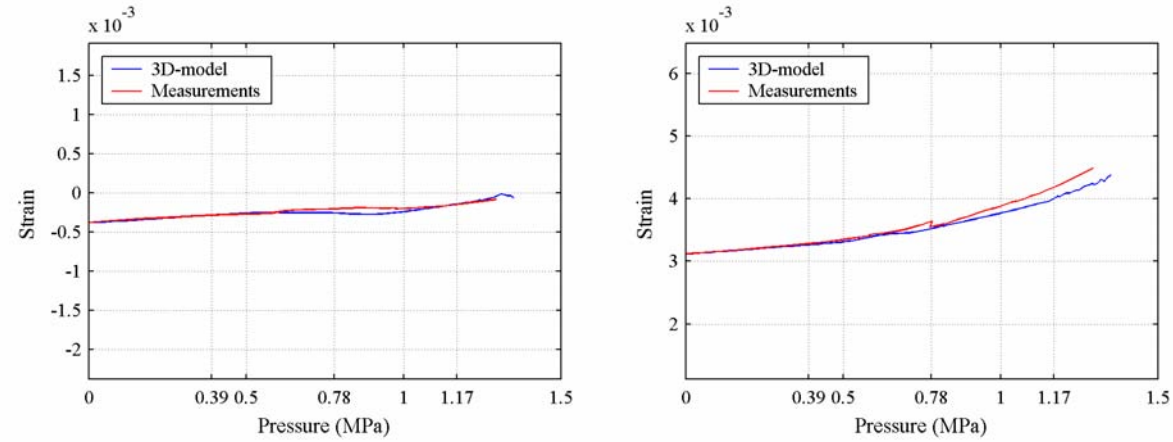

Figure 7.35 Pos. 29-Rebar strain outside layer, meridional direction, el 10.7 , az 135 (left).

Figure 7.36 Pos. 30-Rebar strain inside layer, meridional direction, el 0.0 , az 90 (right).

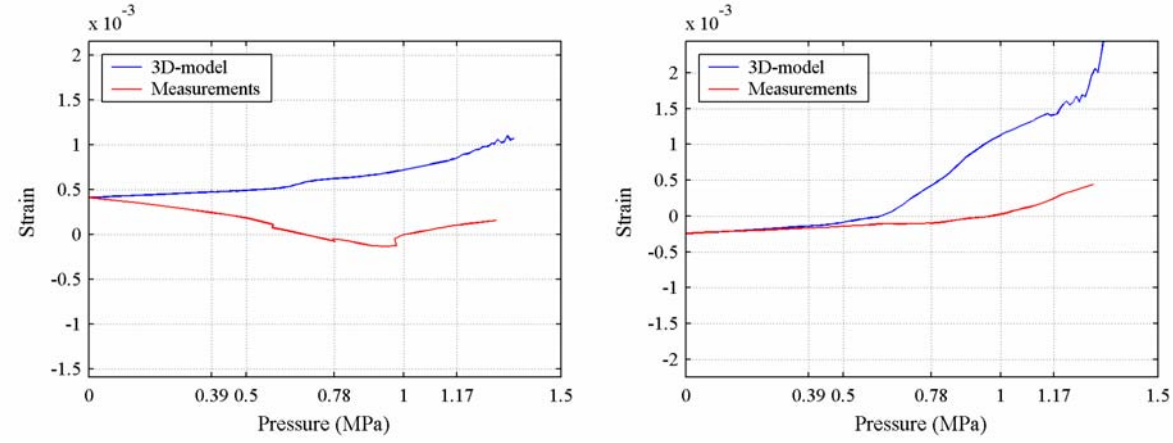

Figure 7.37 Pos. 31-Rebar strain outside layer, meridional direction, el 0.0 and az 90 (left).

Figure 7.38 Pos. 32-Rebar strain outside layer in hoop direction for el 6.2 and az 90 (right).

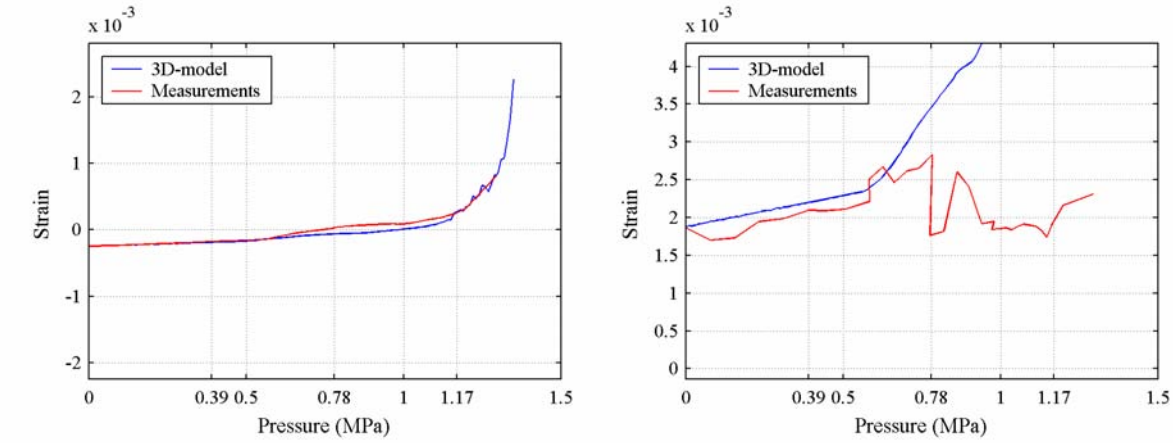

Figure 7.39 Pos. 33-Rebar strain outside layer, meridional direction, el 6.2 and az 90 (left).

Figure 7.40 Pos. 3 -Liner strain in meridional direction for el 0.01 and az 0 (right).

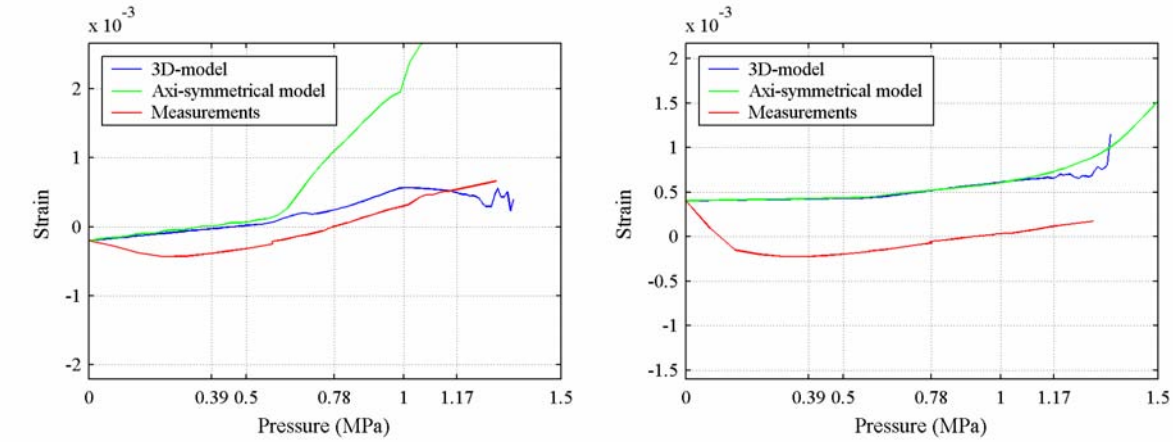

Figure 7.41 Pos. 36-Liner strain in meridional direction for el 0.2 and az 13 (left).

Figure 7.42 Pos. 37-Liner strain in hoop direction for el 0.2 and az 13 (right).

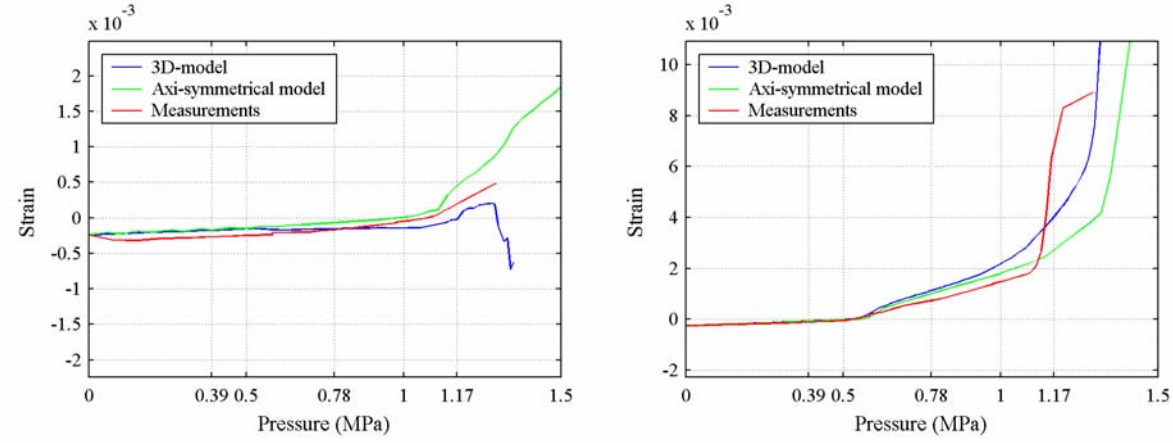

Figure 7.43 Pos. 38-Liner strain in meridional direction for el 6.2 and az 13 (left).

Figure 7.44 Pos. 39-Liner strain in hoop direction for el 6.2 and az 13 (right).

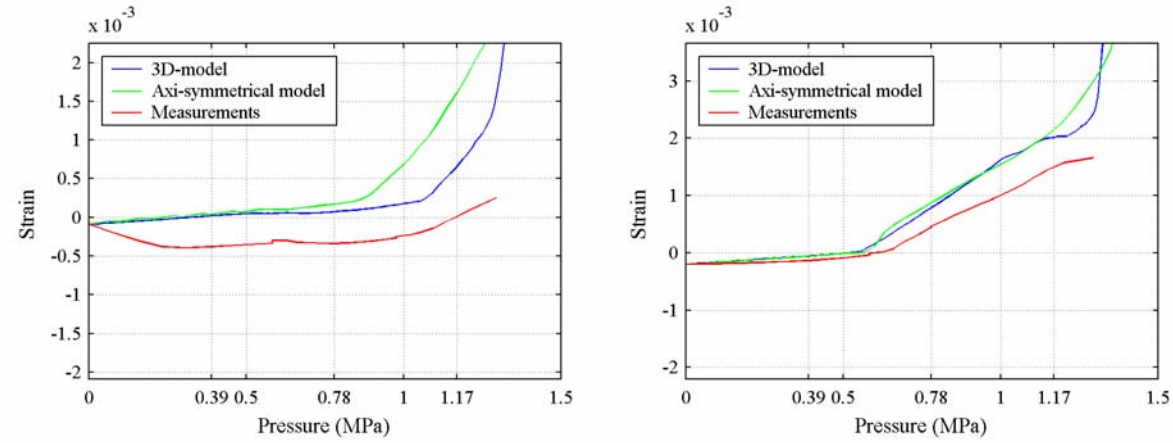

Figure 7.4 Pos. 40-Liner strain in meridional direction for el 10.7 and az 13 (left).

Figure 7.46 Pos. 41-Liner strain in hoop direction for el 10.7 and az 13 (right).

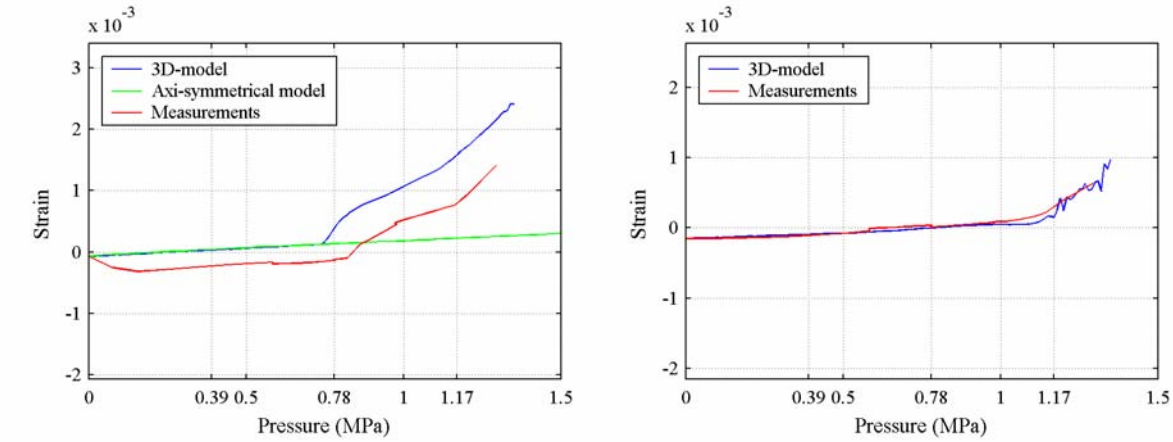

Figure 7.47 Pos. 42-Liner strain in meridional direction for el 16.13 and az 13 (left).

Figure 7.48 Pos. 43-Liner strain in meridional direction for el 6.2 and az 90 (right).

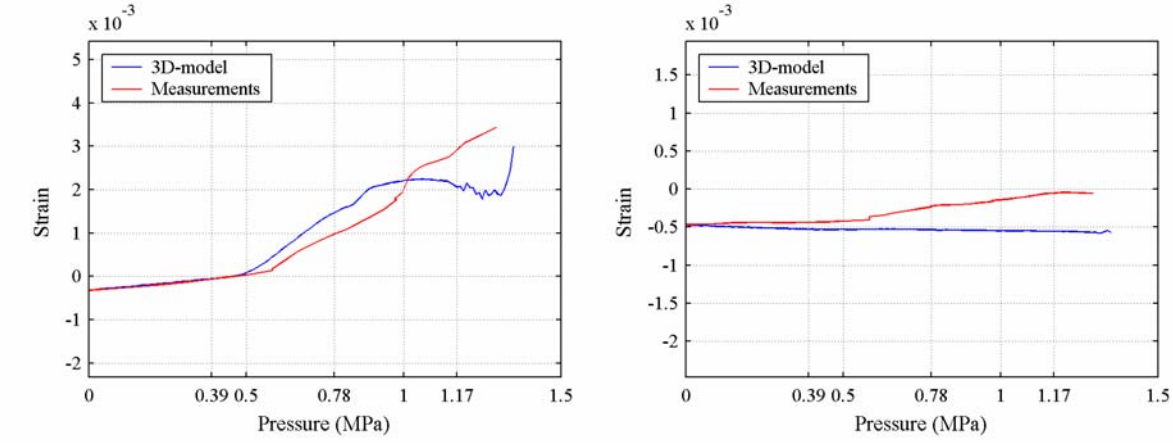

Figure 7.49 Pos. 44-Liner strain in hoop direction for el 6.2 and az 90 (left).

Figure 7. 0 Pos. 4 -Liner strain in hoop direction for el 4.67 and az 334 (right).

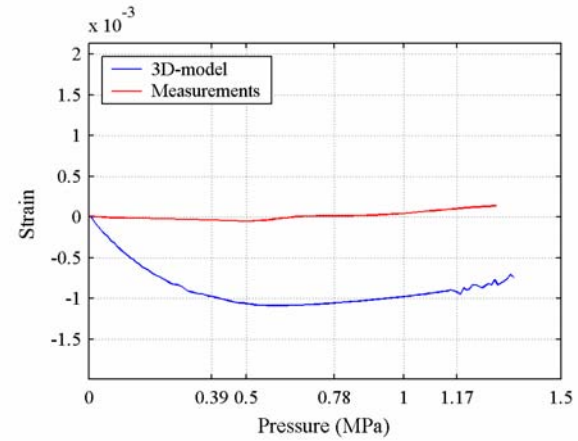

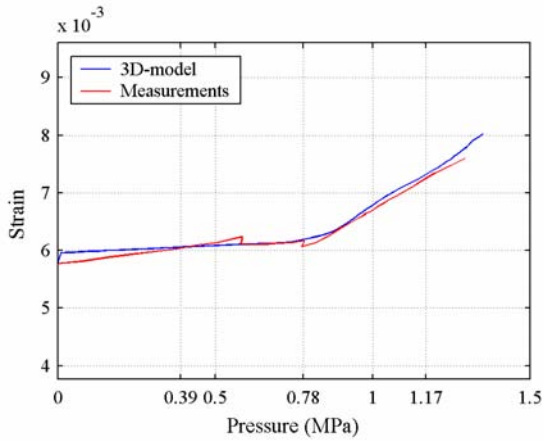

Figure 7. 1 Pos. 46-Liner strain in hoop direction for el 4. 2 and az 8 (left).

Figure 7. 2 Pos. 48-Tendon strain in vertical direction for el 1 .6 and az 180 (right).

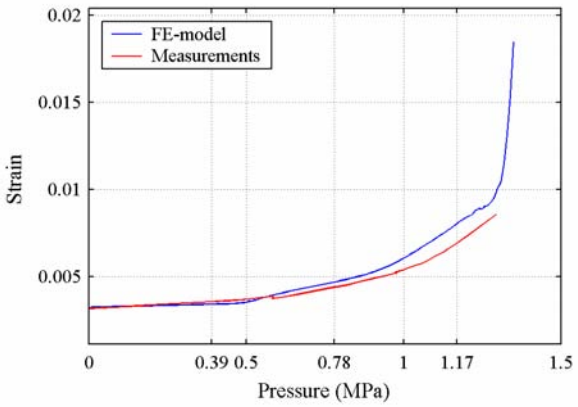

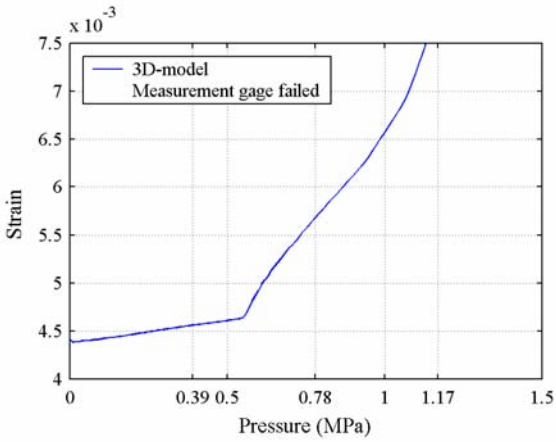

Figure 7. 3 Pos. 0-Tendon strain in hoop direction for el 6. 8.6 and az 90 (left).

Figure 7. 4 Pos. 1-Tendon strain in hoop direction for el 6. 8 and az 180 (right).

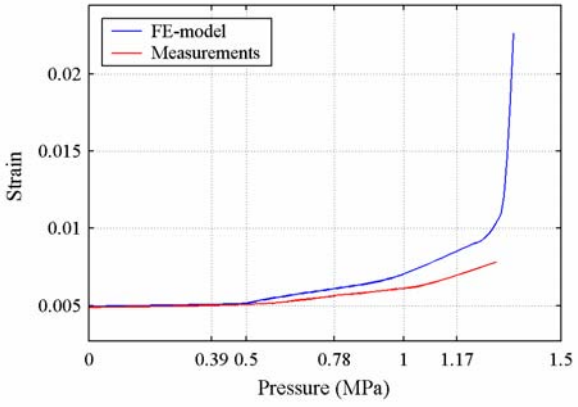

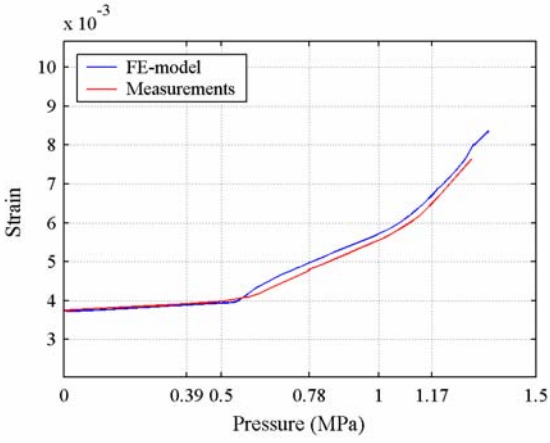

Figure 7. Pos. 2-Tendon strain in hoop direction for el 6. 8 and az 280 (left).

Figure 7. 6 Pos. 3-Tendon strain in hoop direction for el 4. 7 and az 0 (right).

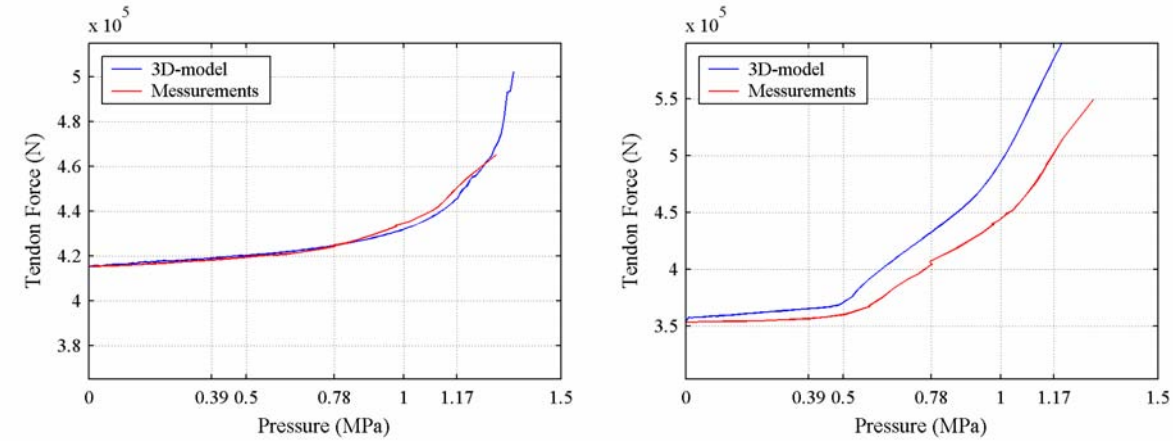

Figure 7.7 Pos. 4-Tendon force in hairpin direction for el-1.16 and az 241 (left).

Figure 7.8 Pos. -Tendon force in hoop direction for el 6.8 and az 27 (right).

8. TENSION STIFFENING

8.1 Introduction

A reinforced concrete member subjected to axial tension will achieve its first crack at the position where the tensile strength (f_{ct}) of the concrete is first exceeded. At the crack, the tensile stress in the concrete rather suddenly decreases to zero and the total tension is then resisted by the rebars only. The sudden increase in stress in the rebars produces strain in the steel that is incompatible with the strain in the adjacent concrete. This results in a widening of the crack.

Away from the crack, concrete bonded to the reinforcement, tends to restrain its elongation and the bond stress transmits a part of the tensile force from the bar to the surrounding concrete. At a certain distance *s* from the first crack, strain compatibility is recovered and the tensile strength in the concrete is again reached, causing a second crack to develop.

Figure 8.1 shows the principal variation of steel stress, bond stress and concrete stress over the length of a cracked member subjected to an axial force (adopted from [6]).

The contribution to the stiffness of a cracked member from the tensioned concrete between cracks is here called “tension stiffening”.

When modeling reinforced concrete using the finite element method, the load-deflection can to some extent be mesh sensitive. This is due to the fact that if all, or almost all, finite elements that are in tension have been cracked, the stiffness of uncracked concrete between discrete cracks (the tension stiffening effect) are not present in the analysis model, giving a to weak response. The onset of cracking can also be influenced.

The stiffness of uncracked concrete can be taken into account by introducing the tension stiffening effect into the model by artificially adjusting some model parameter(s). This will be discussed in section 8.3. Another possibility is to decrease the element size sufficiently, as presented in section 8.2. However, this can in some cases lead to too large FE models.

Often, neglecting the effect of tension stiffening will led to conservatism in the results. Therefore it is not always necessary to take it into consideration in structural design or in structural verification of safety-related structures. For example, it will not influence the pressure level at cracking of the concrete, or the ultimate capacity of the structure. However, if deatiled knowledge of the structural response during the whole overpressurization course of a reactor containment is of importance, the extent of the tension stiffening effect has to be evaluated.

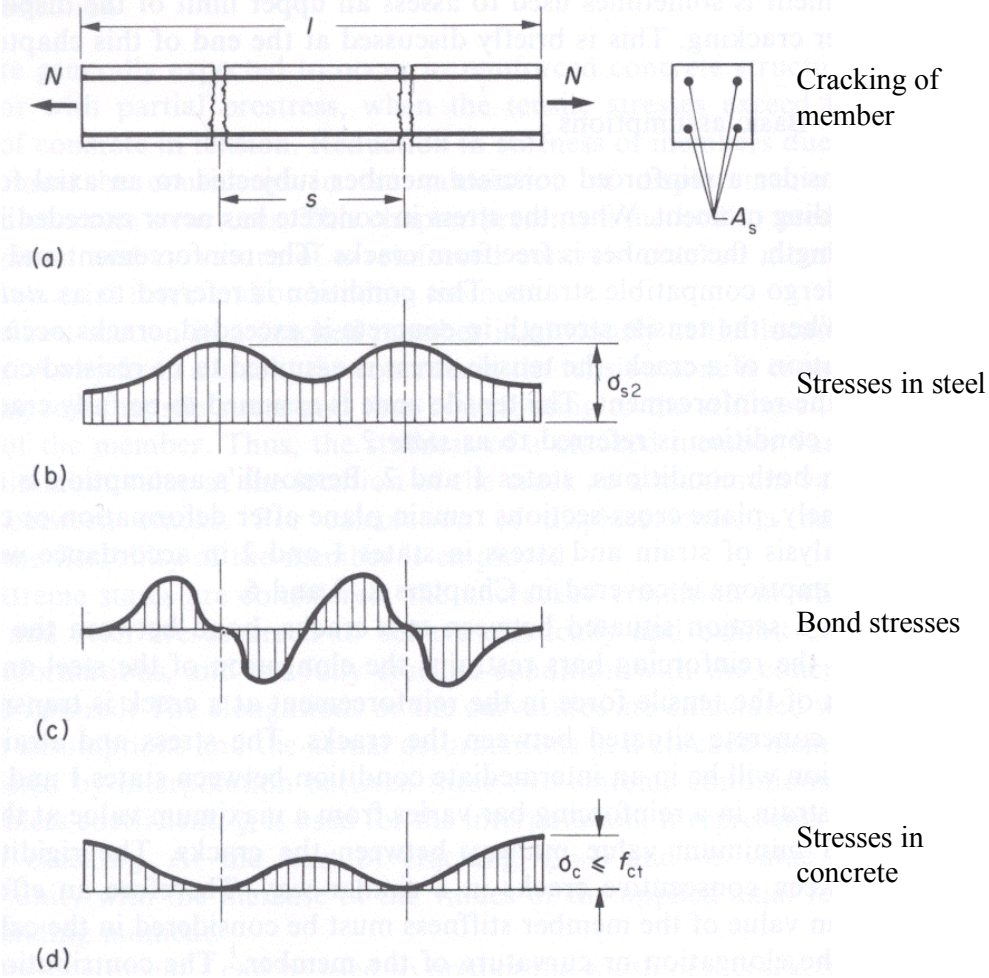

Figure 8.1 Stresses in reinforced concrete member cracked due to axial force (from [6]).

8.2 Parametrical study of decreased mesh size

In Figure 8.2 –8.5 a mesh study regarding the tension stiffening effect is presented for a part of the ISP 48 containment wall. A solid element sub-model of a typical slice part of the containment wall in an undisturbed area is used in the study (Figure 8.2). The wall is loaded with an increasing internal overpressure up until collapse of the structure.

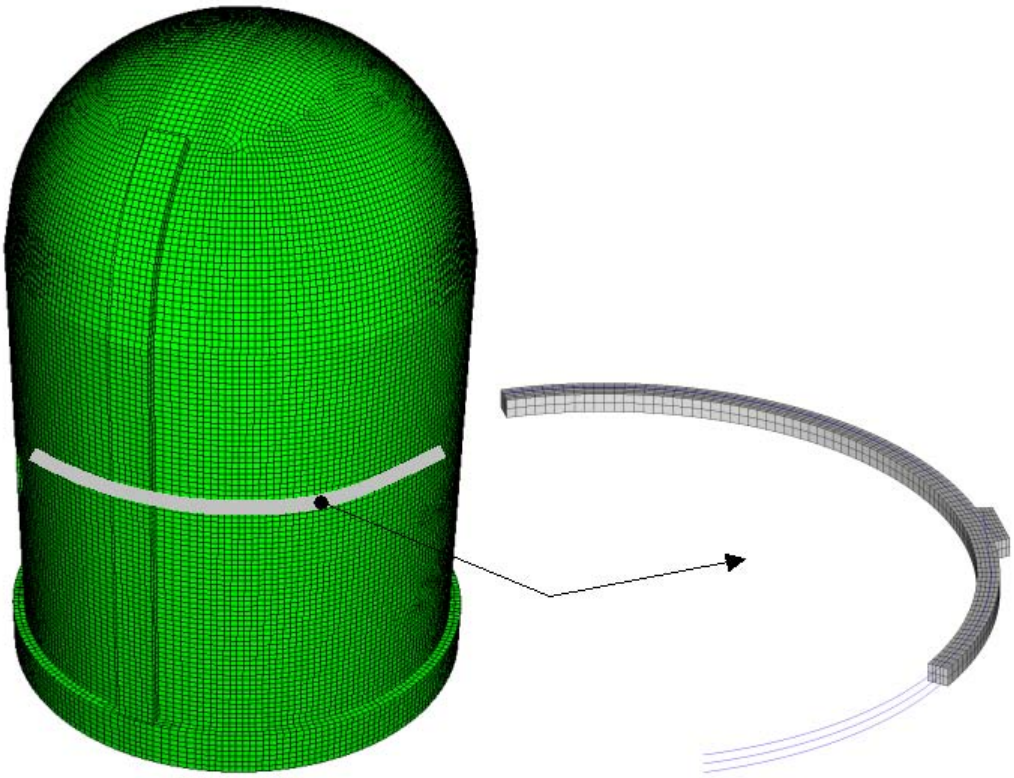

Global model

Sub-model, horizontal slice (for details, see Figure 5.1)

Figure 8.2 Horizontal slice model of part of the containment wall including pre-stressing tendons, rebars and buttresses.

In Figure 8.3, the radial deformation as a function of internal overpressure is presented for four different finite element mesh densities, with a side length ranging from 37.5 to 300 mm. As can be seen in the figure, the stiffness of the structure increases as the element size decreases. For the smallest element sizes it seems that the result has converged. The correct response regarding tension stiffening effect is given when the element length approximatly equals the length of the zone affected by cracks in the real concrete structure (see Figure 8.1).

In Figure 8.4 the crack pattern in the model at an overpressure of 800, 880 and 950 kPa is presented, for models with three different mesh sizes; 150, 75 and 37.5 mm respectively. The warmer the color, the more severe cracking has occurred, i.e. black/blue color represents the smallest cracking, while red color represents the most severe cracked areas of the members. In Figure 8.5 a typical crack pattern through the thickness of the containment wall model is shown.

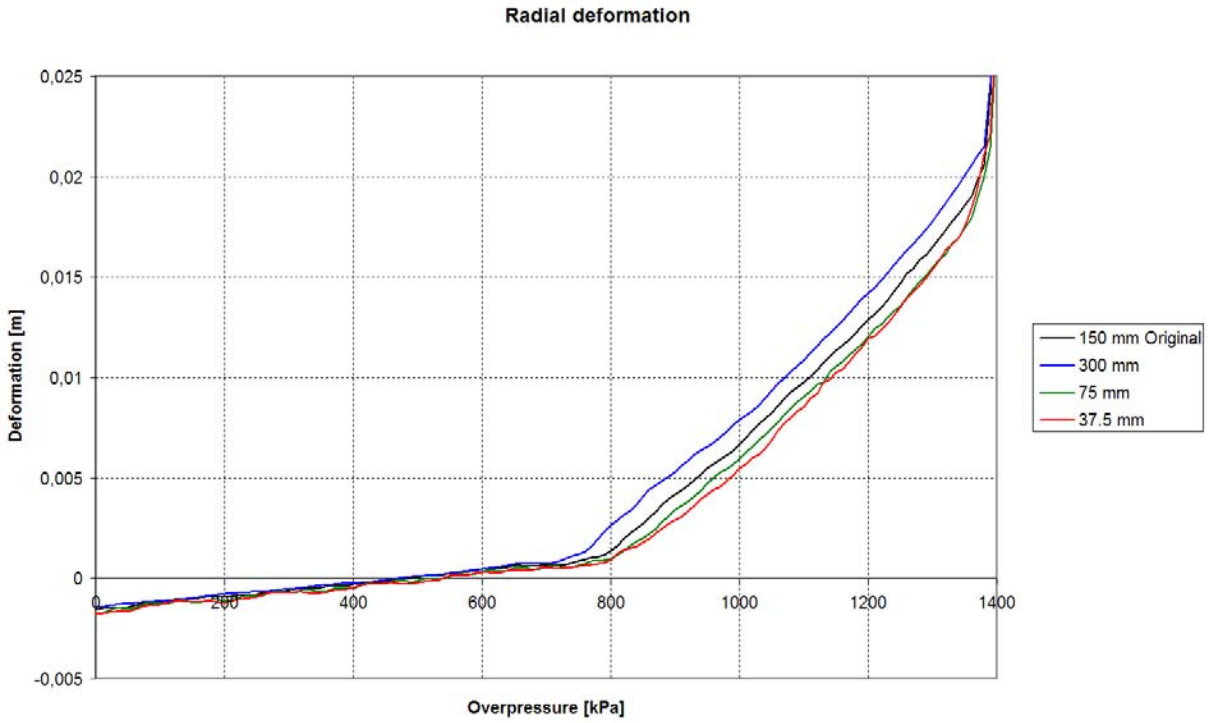

Figure 8.3 Radial deformation of the containment wall as a function of internal overpressure. Results are given for different finite element mesh sizes. The result converges upon mesh refinement. The element size called "150 mm Original" is the same as the element size used in the 3D analyis presented in part I.

At an internal overpressure of 800 kPa, the cracking in the models with the three different mesh sizes are approximatly the same, also giving almost the same radial deformation (Figure 8.3). However, for increased overpressure (Figure 8.4 b) and c)) the amount of cracking differ to a great extent between the models with different mesh sizes, the largest mesh size having the most severe cracking. As expected, this gives rise to different radial deformations, as can be seen in Figure 8.3 above. The model with the smallest mesh size gives the smallest radial deformation, and the model with the largest elements the largest deformation.

In the global analysis carried out in chapter 7 using a three-dimensional model with an element size of approximatly 150 mm side length, the predicted response seems a little bit to weak. This can to a great extent be attributed to the tension stiffening effect as can be seen in Figure 8.3 comparing the different radial response for the mesh sizes "150 mm Original" and "37.5 mm" respectively. However, in the global axi-symemtric model, presented in chapter 4, with an element size of approximatly 45 mm, no weak response is present.

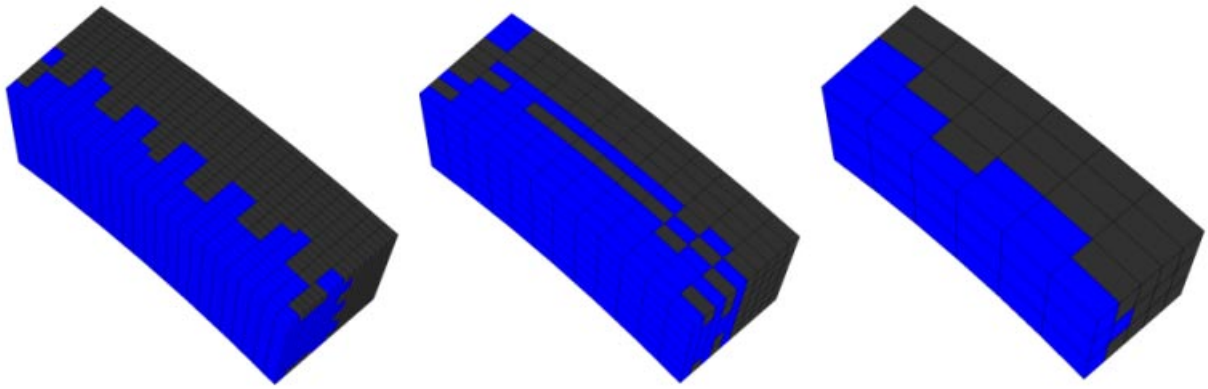

37.5 mm 75 mm 150 mm

a) Crack pattern at overpressure 800 kPa.

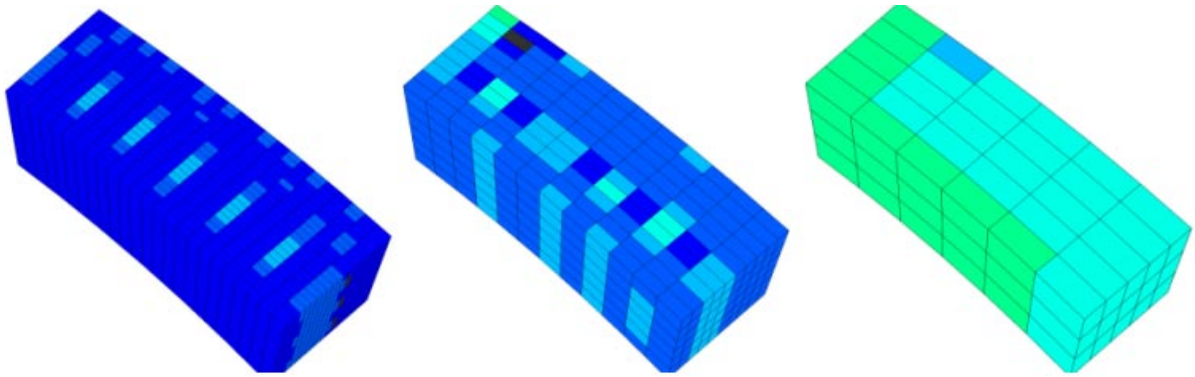

37.5 mm 75 mm 150 mm

b) Crack pattern at overpressure 880 kPa.

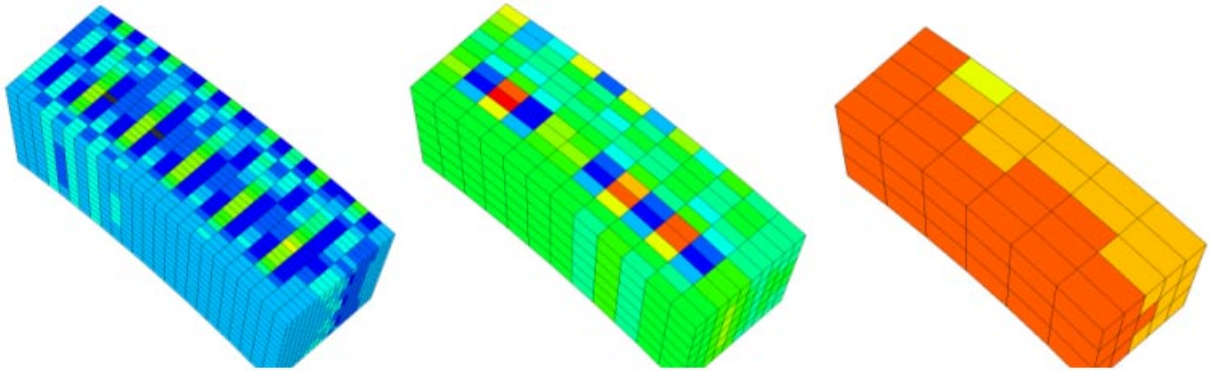

37.5 mm 75 mm 150 mm

c) Crack pattern at overpressure 950 kPa.

Figure 8.4 Crack pattern shown for part of the containment wall model at different values of overpressure and mesh sizes respectively. Black/blue color represents the smallest cracking, while red color represents the most severe cracking of the members.

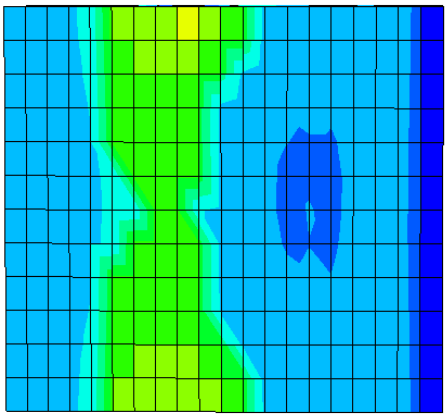

Mesh size 37.5 mm

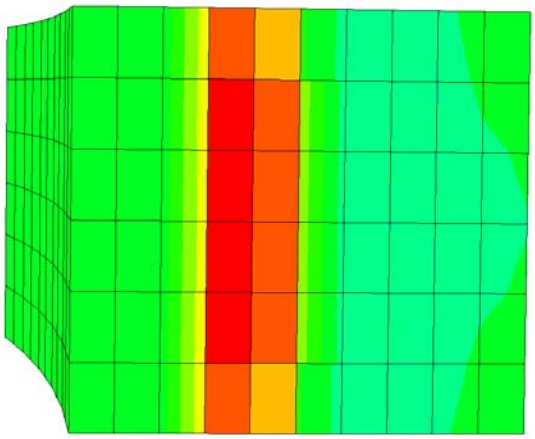

Mesh size 75 mm

Figure 8.5 Typical crack pattern through the thickness of the containment wall model.

8.3 How to model the tension stiffening effect

8.3.1 General

The first step when taking the tension stiffening into consideration is to in some way determine the influence from tension stiffening on the load-deflection response of the FE model. This can be done by carrying out experiments, by parametrical studies, handbook equations (such as in [6]), or by engineering judgement. When utilizing parametrical studies, a finite element sub-model may well be used. This was done in section 8.2 where a horizontal slice of the containment wall was used instead of the whole three-dimensional FE model of the containment structure, see Figure 8.2.

One of the most common ways to take into consideration the tension stiffening effect is to artificially adjusting material properties, increasing the stiffness of the structure after cracking of concrete. This method will be further discussed in the next section.

8.3.2 Adjustment of material properties

The stiffness of uncracked concrete between cracks (tension stiffening) can be taken into account by introducing a fictitious descending branch in the tensile stress-strain curve after crack formation, i.e increasing the fracture energy. This approach is recommended in the ABAQUS manual [3], and a recommended value is given (corresponding to 10 times the failure strain of the concrete). Another possibility is to artificially increase the stiffness of the rebars, see for example [7].

In Figure 8.7, a parametrical study of the influence of fracture energy is presented, both for realistic values (40 and 120 Nm/m^2), and for fictive values (400, 800 and 1200 Nm/m^2 respectively) as a method to take into consideration the tension stiffening effect in the model. The different values of fracture energy used are presented in Figure 8.6. The model used in this parametrical study has an element side length of 150 mm. An increase of the fracture energy will of course give a more stiff response of the structure, as can be seen in Figure 8.7. When the tension resistance of the concrete element is totally lost, the curves will converge to each other (black, green and blue curve) due to the fact that then only the steel parts add to the stiffness of the structure. Note that the collapse of the structure is delayed when using very high, fictive, values of fracture energy (purple and red curve), the nearly vertical part of the curves to the right in Figure 8.7 do not coincide.

As can be seen by comparing the results in Figure 8.3 and 8.7, increasing the fracture energy gives results converging to the same results arrived at using smaller and smaller finite elements, except for the to high ultimate capacity predicted by high fracture energy values.

When introducing artifical fracture energy in the material model of concrete as a method to take tension stiffening effect into consideration, care has to be taken not to alter the structural behaviour of the structure, unintentionally influencing other failure modes of the structure. For example, when estimating the ultimate capacity of the containment, the real value of fracture energy should be used.

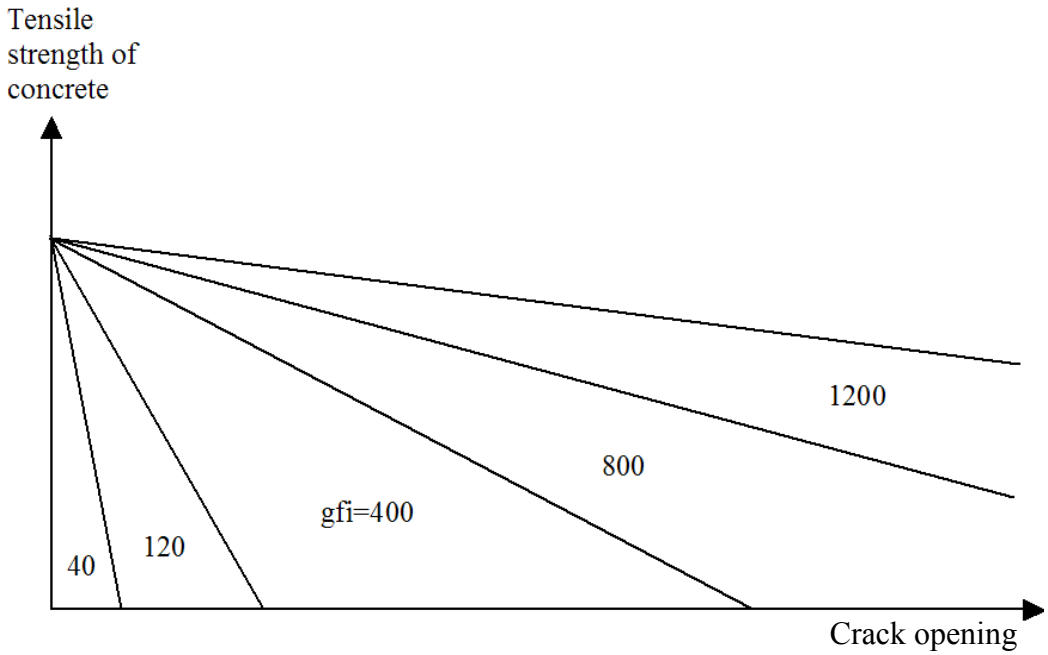

Figure 8.6 Fracture energy levels (Nm/m^2) used in parametrical study.

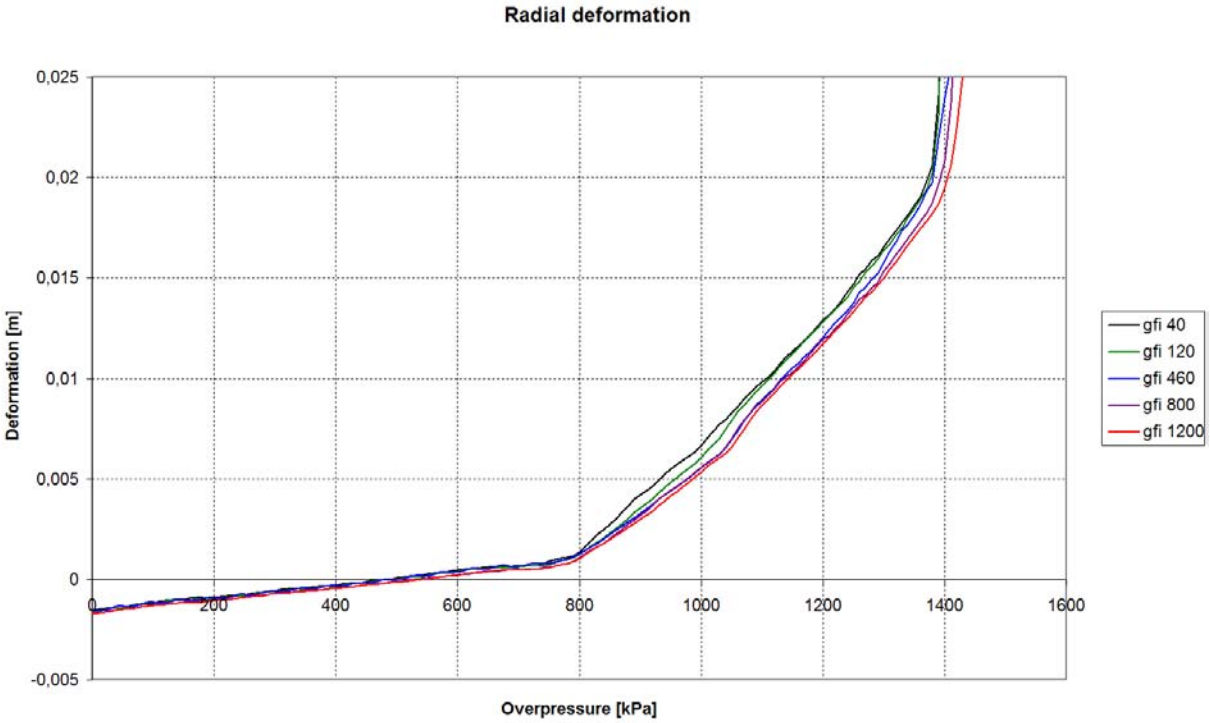

Figure 8.7 Radial deformation for different values of fracture energy, gfi.

To sum up, a method of adjusting material properties can be as follows:

1. First, the influence of tension stiffening effect on the FE model response is studied using a sub-model (section 8.2) where the element size is decreased until convergence in (radial) deformation is reached.
2. If the element sizes corresponding to the converged element mesh will result in a too large global model, an artificial adjustment of the material properties is introduced into the sub-model. In this sub-model the mesh element size is chosen equivalent to the element sizes to be used in the global model.
3. The adjustment required is determined by calibrating the results from the sub-model analysis with changed material properties applying element size equal to the global model (point 2), to the sub-model analysis with small enough elements to directly include the effect of tensioning stiffening, as described in point 1 above.
4. This artificial adjustment is then introduced into the global model of the structure, and the global analysis is carried out.

PART II

PRESSURE + TEMPERATURE LOAD ANALYSIS

9. GENERAL

In the first part of this report internal overpressurization of the containment has been simulated by using finite element analysis. The results have been compared with test data as a way of validating the analysis methods used.

In this second part, analysis are presented for the case of combining overpressure and temperature loads. These analysis are carried out with the aim to identify the difference in behaviour of a containment loaded by overpressure only, and a containment loaded with a combination of overpressure and temperature loads. It should be stressed that for this combined loading no test data is available for comparison.

Two different scenarios are studied, as specified in [5];

- Case 1, saturated steam. An increasing internal overpressure is applied, together with the belonging saturated steam temperature.
- Case 2, large dry PWR SBO, no containment leakage. Time histories for pressure and temperature are applied to the containment.

Case 1 is to be used in a direct comparison with the results achieved for pressure load only. Case 2 represents a more realistic scenario, taking time-dependent effects of temperature into consideration.

These loading scenarioas are presented in detail in section 10.3.

10. STRUCTURAL SYSTEM

10.1 Description of structural system

The structural system is identical to the system presented in section 3.2 for the no temperature (i.e. pressure load only) analysis.

10.2 Material

10.2.1 General

The material description follows the presentation given in section 3.3, except that material parameters are described as dependent on the temperature for each structural part. Also, specific input parameters for the temperature analyses need to be defined.

10.2.2 Concrete

The following concrete material properties, not specified in section 3.3.4, has been used in the analysis, as proposed in [5]:

Density = 2290 kg/cm^3 (including reinforcing steel and other embedments)

Specific heat = 0.879 kJkg^{-1}K^{-1}

Thermal conductivity = 1.4 Wm^{-1}C^{-1}

Thermal expansion coefficient = 1.1 e^{-5}

The material parameters presented in section 3.3.4 are valid at ambient temperature. In Figure 10.1 the temperature dependency of strength and stiffness parameters are presented (from [5]).

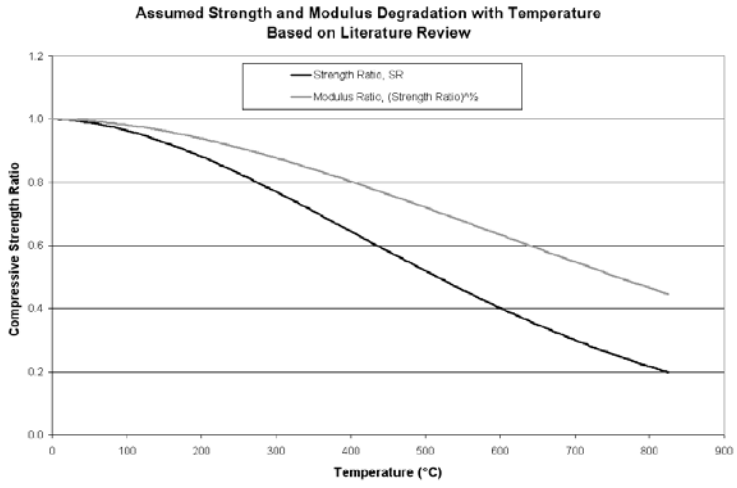

Figure 10.1 Concrete compression strength and modulus ratio vs. temperature.

10.2.3 Steel parts

The material parameters presented in section 3.3.5-7 are valid at ambient temperature. In Figure 10.2 the temperature dependency of strength and stiffness parameters are presented (from [5]).

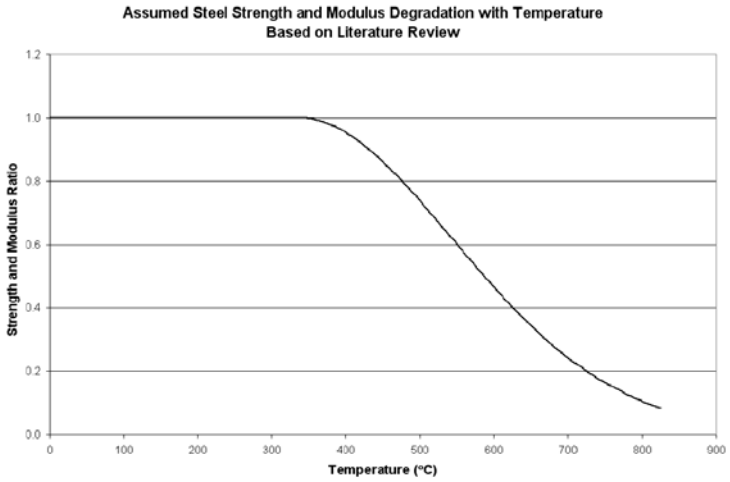

Figure 10.2 Steel yield strength and modulus ratio vs. temperature.

10.3 Loads

Two different scenarios are studied,

- Case 1, saturated steam. An increasing internal overpressure is applied, together with the belonging saturated steam temperature.
- Case 2, large dry PWR SBO, no containment leakage. Time histories for pressure and temperature are applied to the containment.

These loading scenarioas are presented below.

10.3.1 Case 1

Case 1 represents a monotonically increasing internal overpressure, applied untill collapse of the structure (Figure 10.3). At the same time, the temperature inside the containment is as specified in Figure 10.3. The temperatures in the structure are taken as the steady state temperature values at each time step. The ambient temperature is constant at 25 °C.

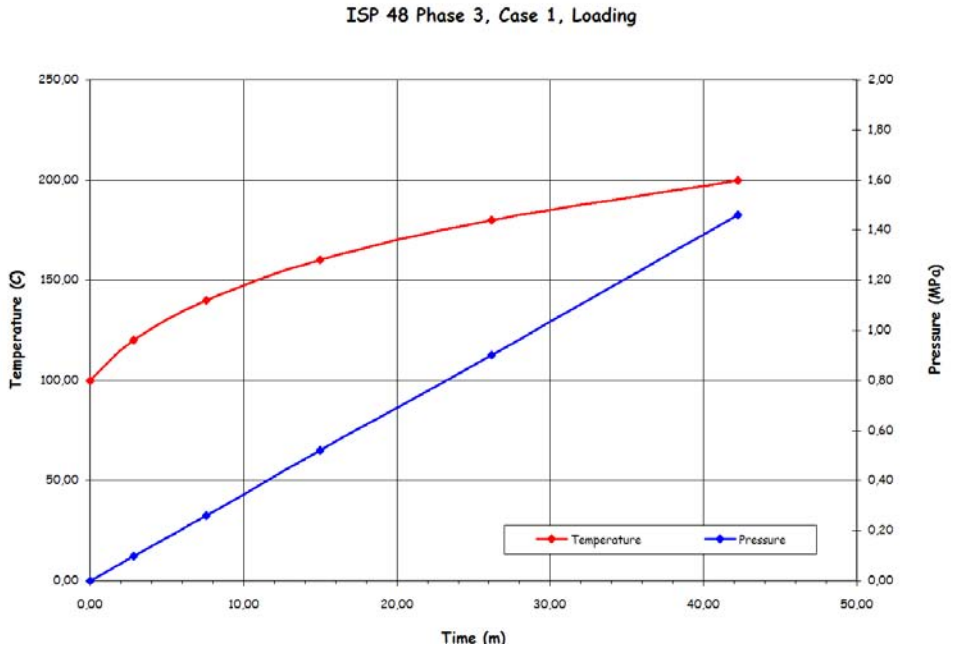

Figure 10.3 Monotonically increasing pressure, and belonging temperature for steady state analysis.

10.3.2 Case 2

In this case, the pressure and temperature load histories presented in Figure 10.4 are used in the analysis. The temperature field in the structure is calculated based on the temperature time history specified, and an ambient temperature of 25 °C (constant throughout the analysis).

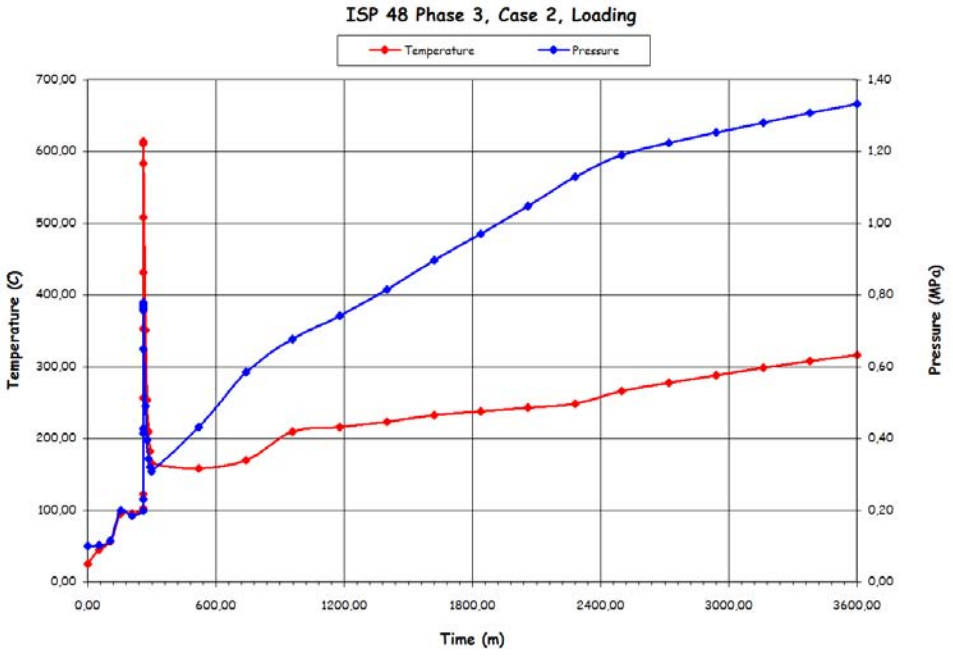

Figure 10.4 Temperature and pressure load time histories.

11. STRUCTURAL MODEL

11.1 General

Analyses are carried out using an axi-symmetrical model, as well as a fully three-dimensional (3D) model. The same models are used as for the overpressurization analysis presented in section 4.2 and 6.2 respectively, with necessary adjustments to take into account the temperature load effects. The main analysis is carried out using the 3D-model.

11.2 Temperature model

Regarding the thermal analysis, to determine the temperature gradient, a free convection with air has been specified for the dome and the cylindrical wall. The heat transfer coefficent is then specified as a function of temperature as follows,

$h = 1.2(\Delta T)^{1/3}$ $Wm^{-2}K$

The boundary condition of the basemat has been specified as heat conduction with soil with the following heat transfer coefficent,

$h = 0.0181$ $Wm^{-2}K$

The temperature inside the containment is applied as a prescribed temperature boundary condition.

In Figure 11.1, calculated temperature gradients through the wall thickness are given. The thermal analysis has been carried out as for a 1:1-scale model, i.e. with a wall thickness of 1.3 m.

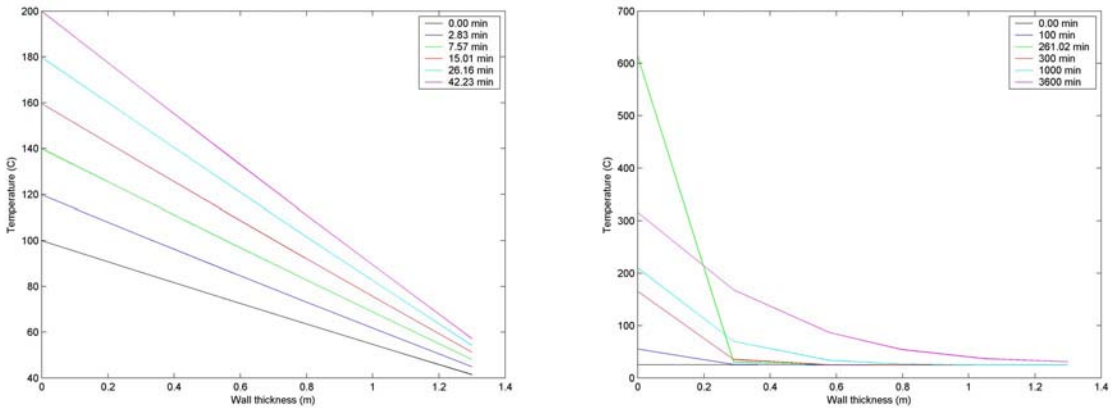

Figure 11.1 Temperature gradient through the wall thickness of the containment, elevation 6.82, azimuth 135. Case 1 (left), and case 2 (right).

12. STRUCTURAL ANALYSIS AND RESULTS

12.1 General

In this section the pressure + temperature load analysis are described and analysis results are provided. The results from the two different load cases (case 1 and case 2) are compared and evaluated against the no temperature analysis carried out in the previous part of this report (part I). These three load cases will in the following be denoted as follows;

No temp. Monotonically increased pressure load. No temperature load.
Load curve is provided in section 6.2.8, Figure 6.11.

Case 1 Monotonically increased pressure and temperature load.
Load curves are provided in section 10.3.1, Figure 10.3.

Case 2 Pressure and temperature load time history analysis.
Load curves are provided in section 10.3.2, Figure 10.4.

In section 12.2 the analysis method used for the combined pressure and temperature loading is briefly described. In the following section, a summary of important events and output parameters are given, together with a comparison of analysis results from the three load cases. Finally, in section 11.4, results in diagram form are shown for the standard output locations (SOL) specified in the ISP 48 project.

12.2 Analysis method

Two consecutive analysis steps have been carried out; first a temperature analysis calculating the temperature field, followed by a mechanical analysis taking advantage of the results from the temperature analysis as input data. Here the analysis method is described for case 2. The case 1 analysis has been carried out in a similar way.

In the first step the temperature field in the structure is calculated using ABAQUS/Standard (implicit solver) as a function of “real time” temperature loading (3600 minutes temperature time history), based on the temperature load scenarios presented in section 10.3.2.

In the second step, ABAQUS/Explicit (explicit solver) is used to carry out a quasi-static mechanical analysis for the combined load situation of pressure and temperature. The temperature in all the nodes calculated in the first analysis are then imported to the second step. The material properties (strength and stiffness) in the second analysis step are dependent on the temperature of the different structural parts, as specified in section 10.2.

The time scale in this second analysis step is compressed from 3600 minutes to approximatly 9 seconds. This to minimize the analysis runtime. The adjustment of the timescale is not constant over the time period, instead it is suited to give approximatly the same loading/deloading rate during the whole analysis (slope

of the curve given in Figure 12.1). Care has to be taken not to introduce any dynamical effects of importance in the analysis. At each analysis time step increment, the internal pressure is described by the adjusted load curve, and the corresponding temperature field is imported from the previous temperature analysis.

In Figure 12.1 the compressed pressure load time history used in the second analysis step is presented. In Figure 12.2 the kinetic energy introduced in the model is shown together with the total strain energy in the model. As can be seen, the kinetic energy is very low compared to the total strain energy, ensuring that no unwanted dynamical effects are introduced into the analysis.

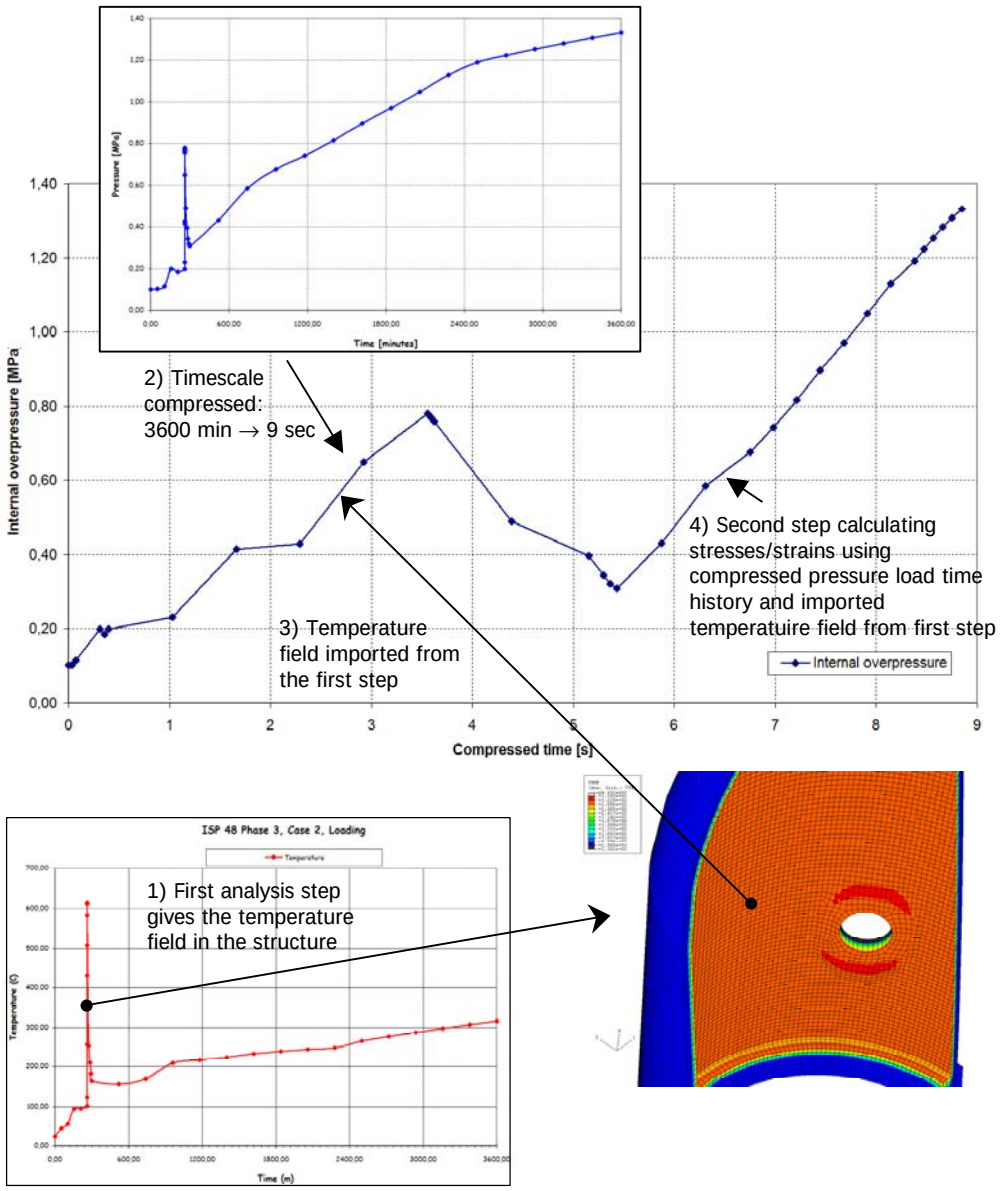

Figure 12.1 First and second analysis steps using different time scales.

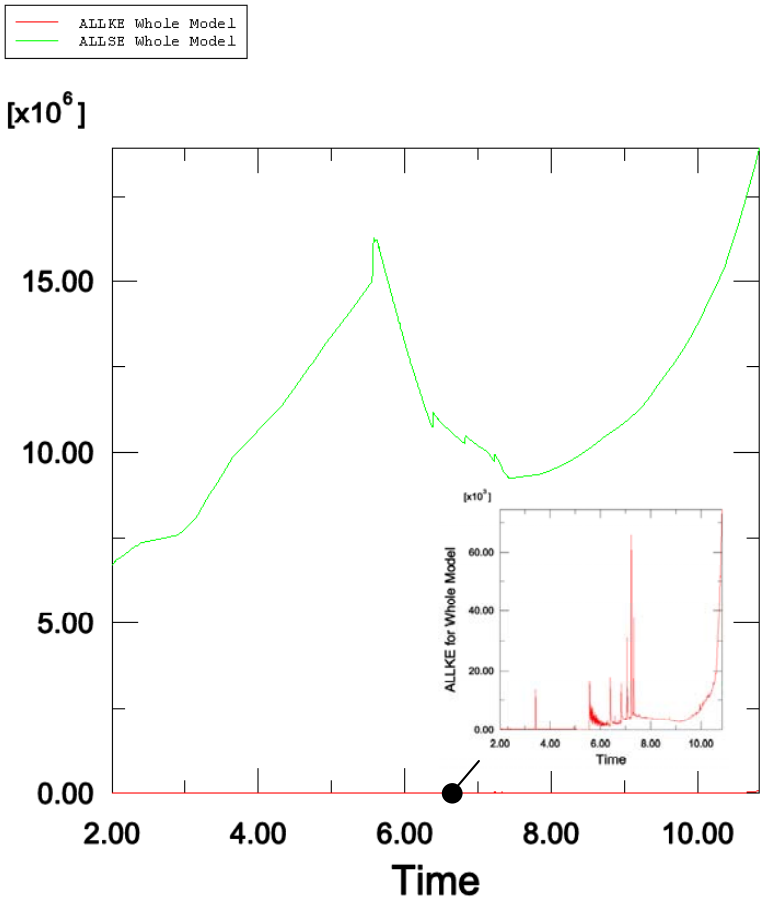

Figure 12.2 Comparison between total strain energy (ALLSE) and kinetic energy (ALLKE), second analysis.

12.3 Result summary of important events and output parameters

12.3.1 2D plots of displacement

The radial displacement gives a good indication of the behaviour of the containment structure during accidental loading. In this section 2D plots of radial displacement in horizontal as well as vertical cross sections are presented, in order to compare the results from the three different load cases.

In Figure 12.3, a contour plot of the magnitude of displacement is shown. The containment is then "cut" at elevation 6.82 m, and seen from above. The scale factor for the displacements in the figure is set to 50.

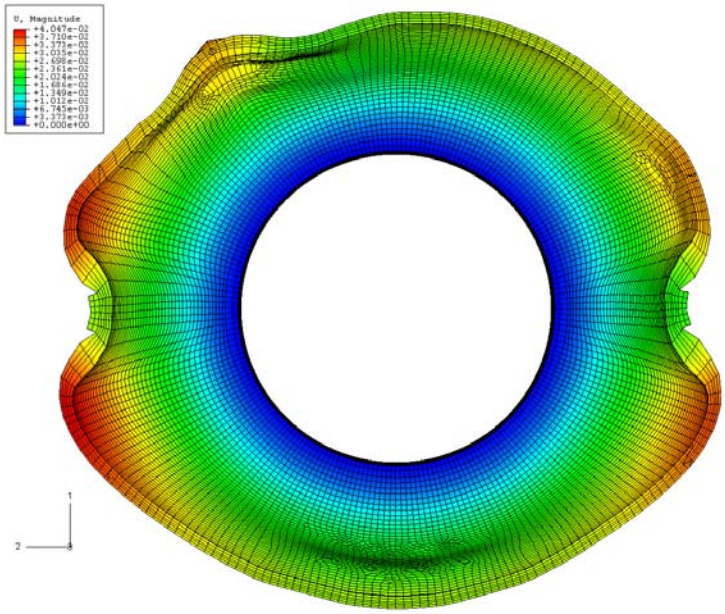

*Figure 12.3 Magnitude of deformation [mm] of containment at elevation 6.82, pressure 1.17 MPa (3*P_d), no temperature load. Scale factor 50.*

In Figure 12.4, the radial displacement is shown at elevation 6.82 m for zero pressure, for multiples of the design pressure, and for a pressure level near rupture of the structure. In Figure 12.4 a), displacements for case 1 are presented. As can be expected, there are displacements at zero pressure due to the increase of temperature inside the containment, from 25 up to 100 °C. In Figure 12.4 b), the corresponding displacements are shown for the no temperature load case. Of course, there is no displacement at zero pressure. As expected, the displacement is larger when the temperature load is present, compared to the case with pressure load only (no temperature).

It can also be recognised from the figures that the radial displacement clearly varies around the circumference of the containment. This is mainly due to the influence on the structural behaviour from the two pre-stressing buttresses, and from the major penetration, i.e. the equipment hatch (E/H). This difference in radial displacement, and curvature, will to a great extent influence the stresses in important structural parts of the containment, as will be explained later on.

In Figure 12.5 to 12.7, 2D plots of radial displacement along a vertical cross section at azimuth 135 (“undisturbed region”), at the equipment hatch, and at the buttresses respectively are presented for the following three load cases; No temperature, Case 1, and Case 2. The displacements are provided for several pressure levels, presented as multiples of the design pressure P_d = 390 kPa.

The radial deformation at 3 times the design pressure (1.17 MPa) is presented as vertical 2D plots in Figure 12.8 for azimuth 135 degrees, the buttress and the equipment hatch, for the same three load cases as above.

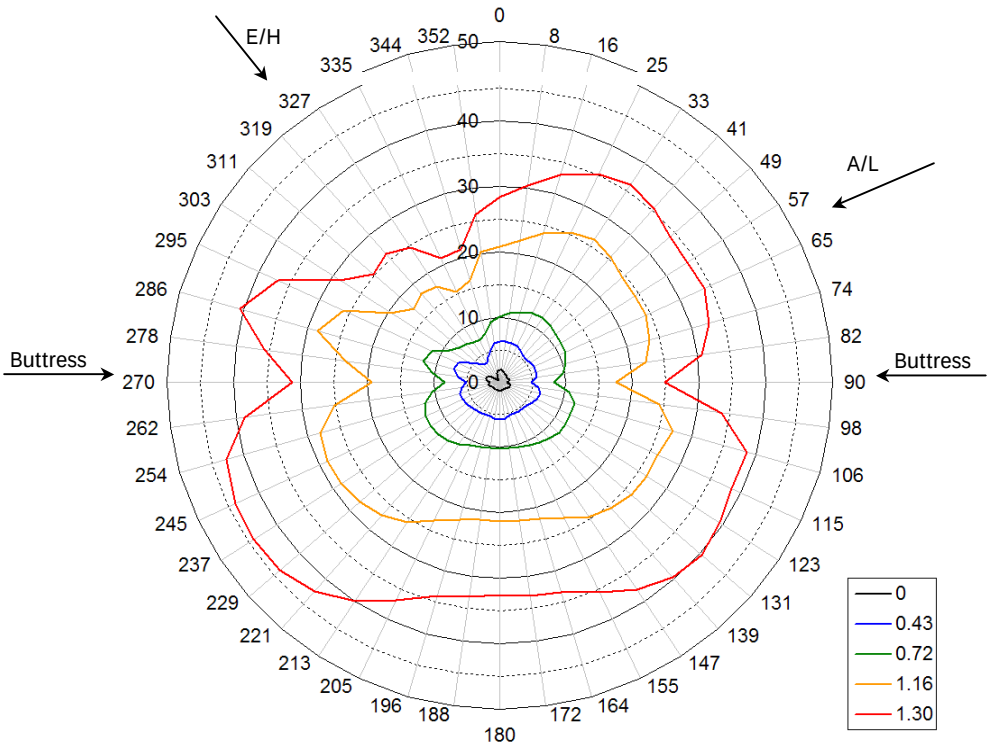

a) Pressure and temperature load, case 1.

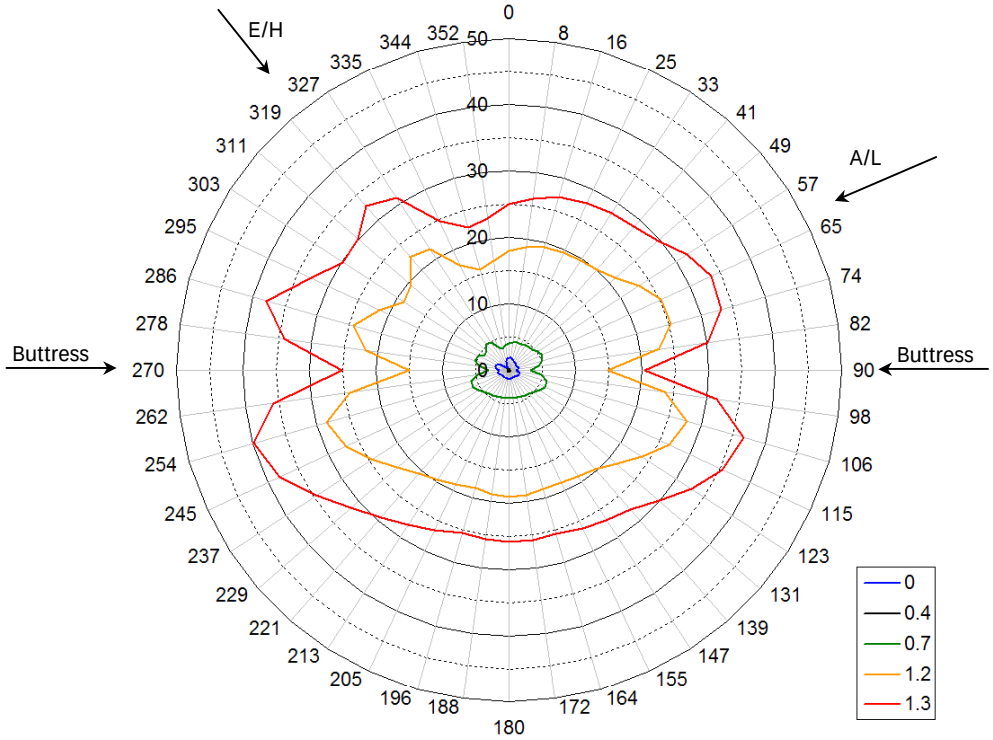

b) Pressure load (no temperature).

Figure 12.4 Radial deformation [mm] of containment at different pressure levels [MPa], horizontal 2D plot at level 6.82.

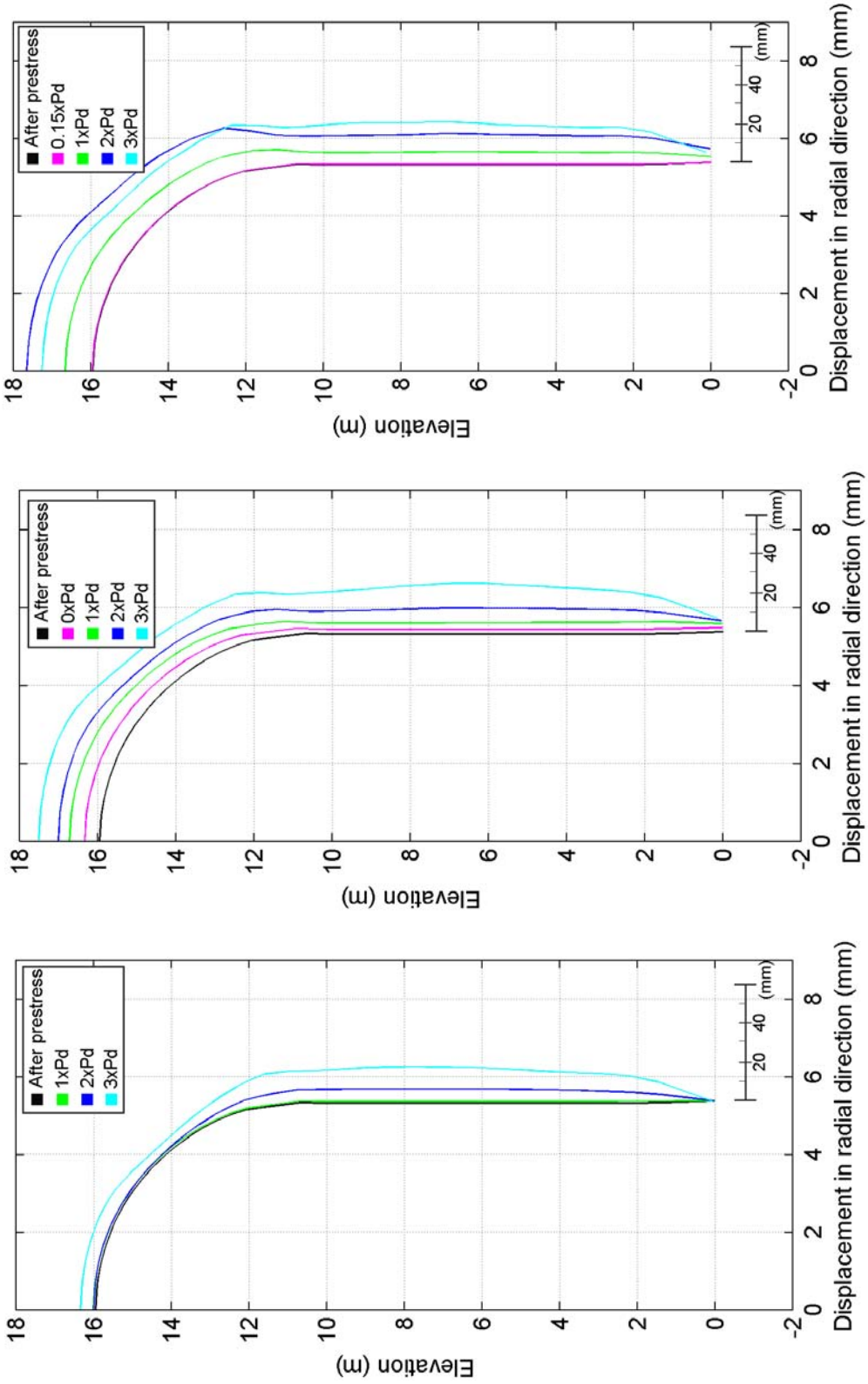

Figure 12.5 Radial deformation at azimuth 135 for different pressure levels. a) No temperature, b) Case 1, c) Case 2.

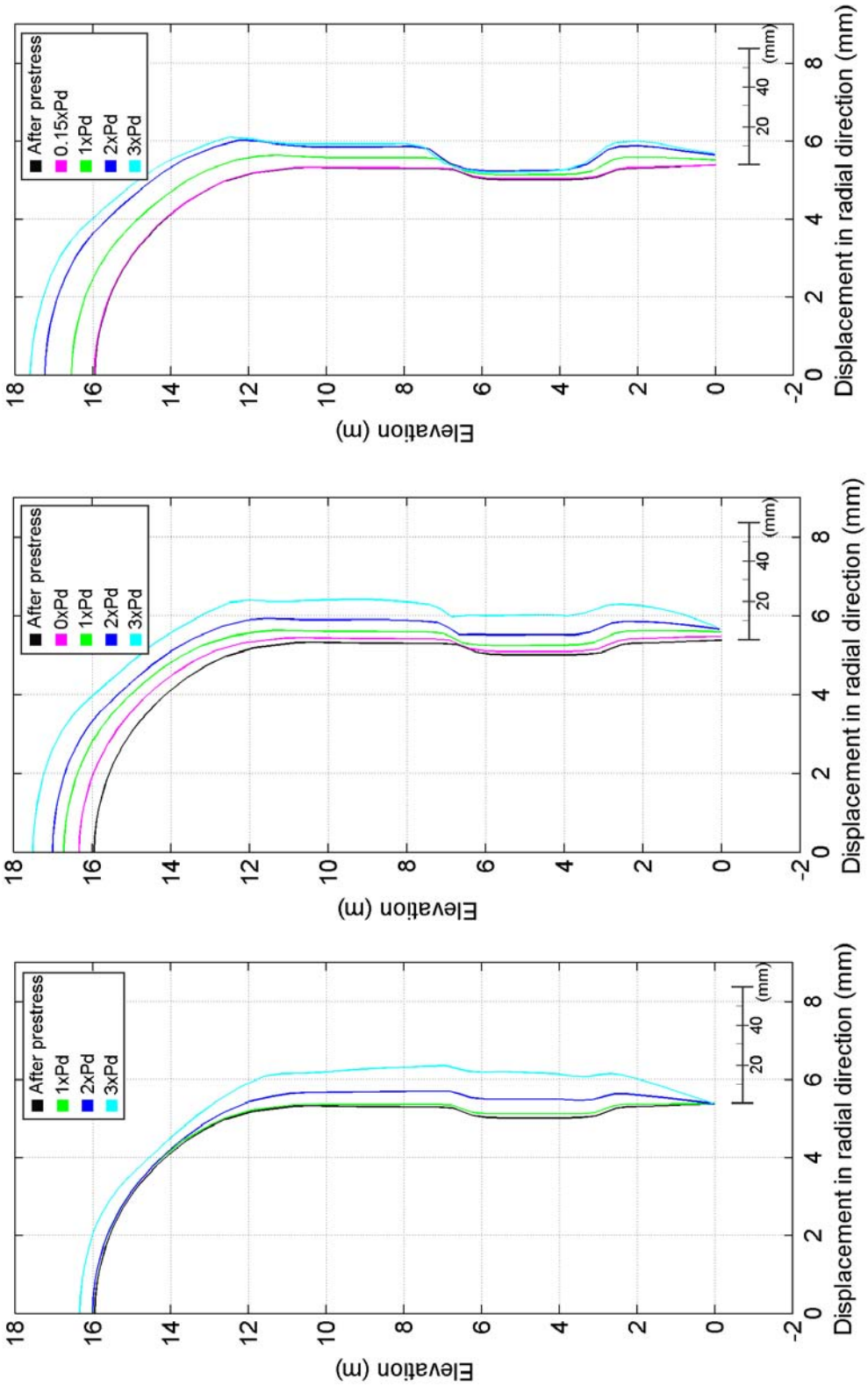

Figure 12.6 Radial deformation at E/H for different pressure levels. a) No temperature, b) Case 1, c) Case 2.

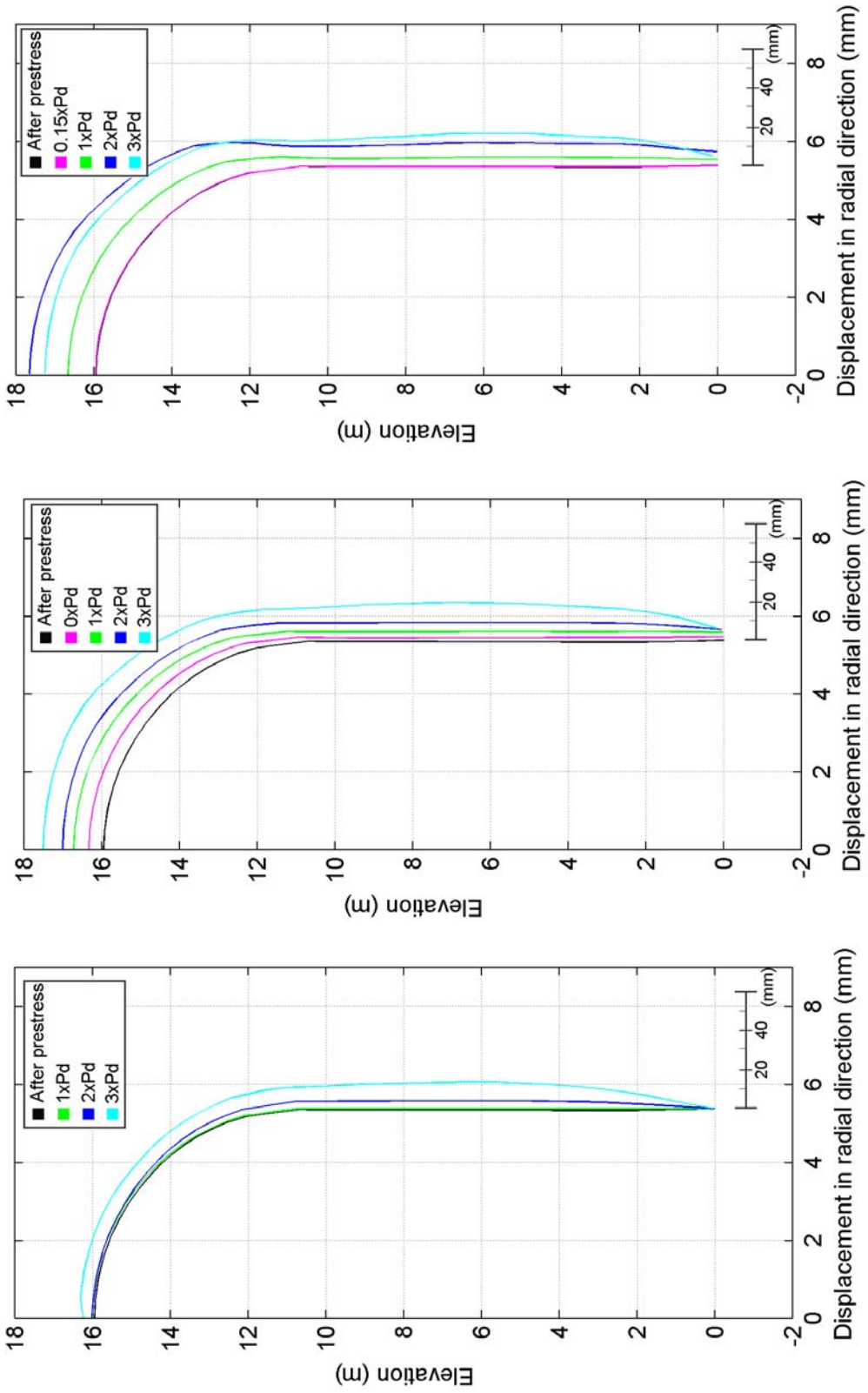

Figure 12.7 Radial deformation at buttress for different pressure levels. a) No temperature, b) Case 1, c) Case 2.

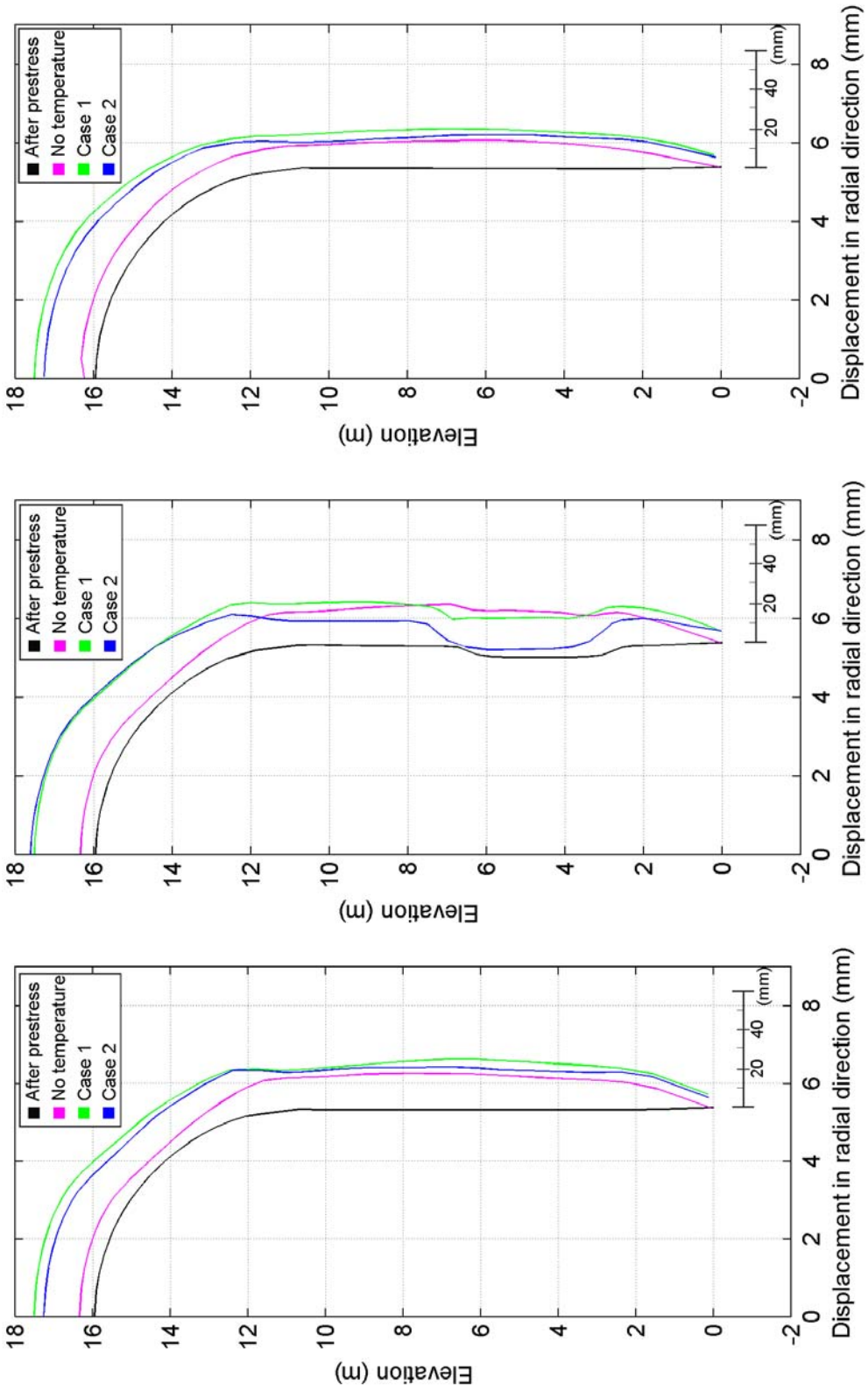

*Figure 12.8 Radial deformation at pressure level 3*P_d. for the load cases no temperature, case 1 and case 2 respectively. a) Azimuth 135, b) equipment hatch, c) buttress.*

12.3.2 Analysis history, important events and comparison between load cases

12.3.2.1 General

In section 12.3.2.2-4 follows a description of the structural response when the pressure and temperature load are increased following the time histories for case 1 and 2 respectively, as well as for the no temperature load case. Stated pressure values refer to overpressure in relation to normal atmospheric pressure. For the case no temp. (pressure load only) and for case 1, the description is given as a function of pressure. For case 2, it is given as a function of time. The internal overpressure is denominated P, and the temperature on the inside of the containment T. Separate descriptions are then, for each load case, given for the concrete, the pre-stressing tenodns, the rebars, and the steel liner respectively.

12.3.2.2 Load case no temperature

Concrete

P = 0 kPa (no temperature load)

Reference state. Only pre-stressing forces and dead weight act on the structure. Concrete in compression due to pre-stressing.

P = 200 kPa (no temperature load)

Local cracking near the equipment hatch, horizontal cracks.

P = 400 kPa (no temperature load)

Local cracking near the equipment hatch, vertical cracks.

P = 600 kPa (no temperature load)

Global cracking, vertical cracks.

P = 1000 kPa (no temperature load)

Global cracking, horizontal cracks.

Pre-stressing tendons

P = 0 kPa (no temperature load)

Reference state. Only pre-stressing forces and dead weight act on the structure.

P = 1200 kPa (no temperature load)

Yield starts in the tendons.

P = 1380 kPa (no temperature load)

First tendon rupture (horizontal tendon no 38, elevation ~5.0). See also section 12.3.5.2.

P = 1410 kPa (no temperature load)

Rupture of containment (tendon ruptures in large areas). See also section 12.3.5.2.

Rebars (see Figure 12.9)

P = 0 kPa (no temperature load)

Reference state. Only pre-stressing forces and dead weight act on the structure. Rebars in compression due to pre-stressing.

P = 1000 kPa (no temperature load)

Yield starts at the buttresses.

P = 1100 kPa (no temperature load)

Yielding more generally, especially at transition zones with different reinforcement areas (yielding in zones with less area).

P = 1200 kPa (no temperature load)

Global yielding.

P = 1400 kPa (no temperature load)

Rupture stresses reached at transition zones with different reinforcement areas, and near buttress.

Steel liner (see Figure 12.10)

P = 0 kPa (no temperature load)

Reference state. Only pre-stressing forces and dead weight act on the structure. Steel liner in compression due to pre-stressing.

P = 800 kPa (no temperature load)

Yield starts locally at the buttresses.

P = 900 kPa (no temperature load)

Yielding more generally at the buttresses

P = 1000 kPa (no temperature load)

Global yielding.

See also section 12.3.4.3.

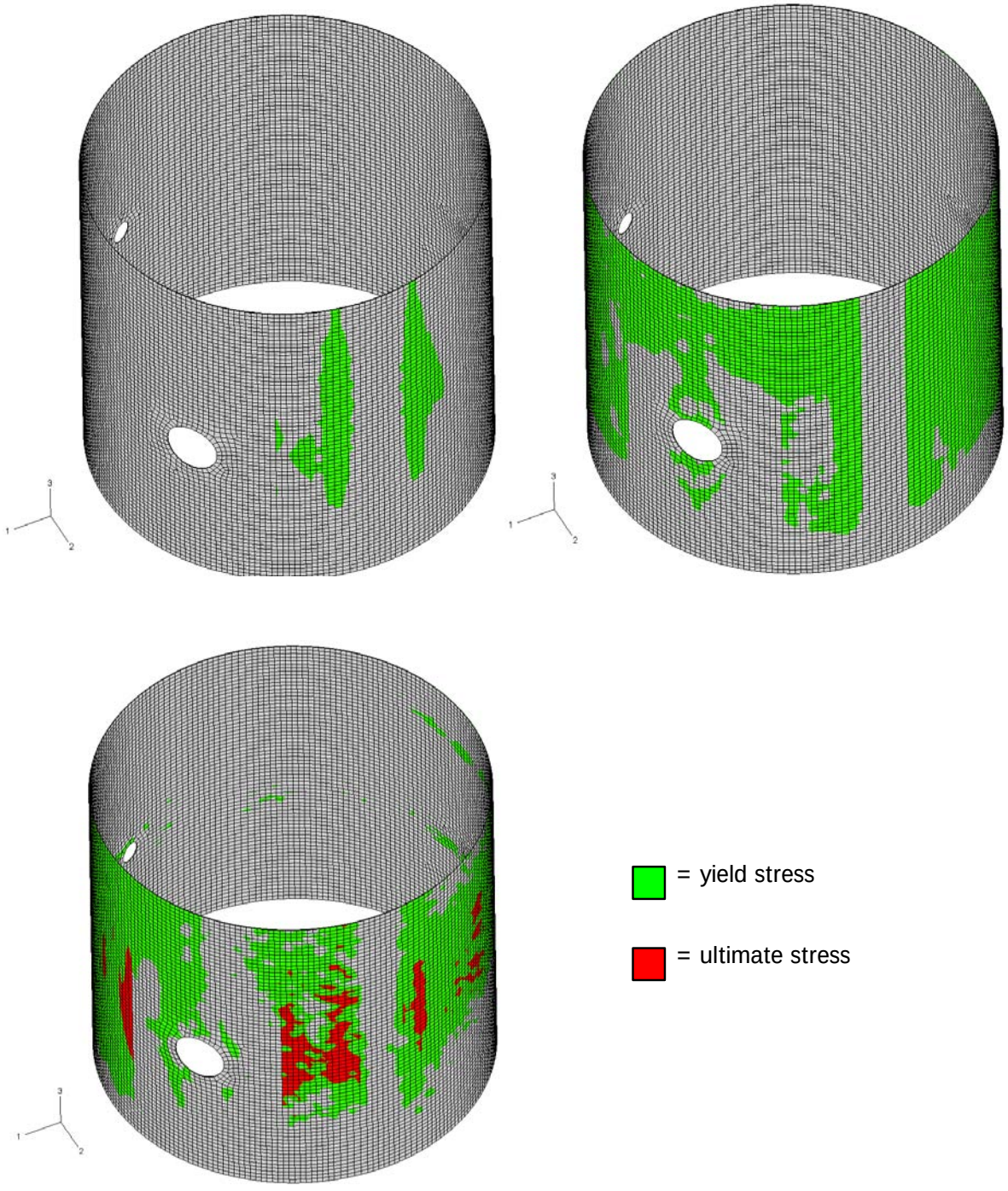

Figure 12.9 Development of yield in outer rebar layer: first at buttresses, then propagating to global yielding for increased load, and finally rupture (P=1000 MPa, 1200 MPa and 1400 MPa respectively).

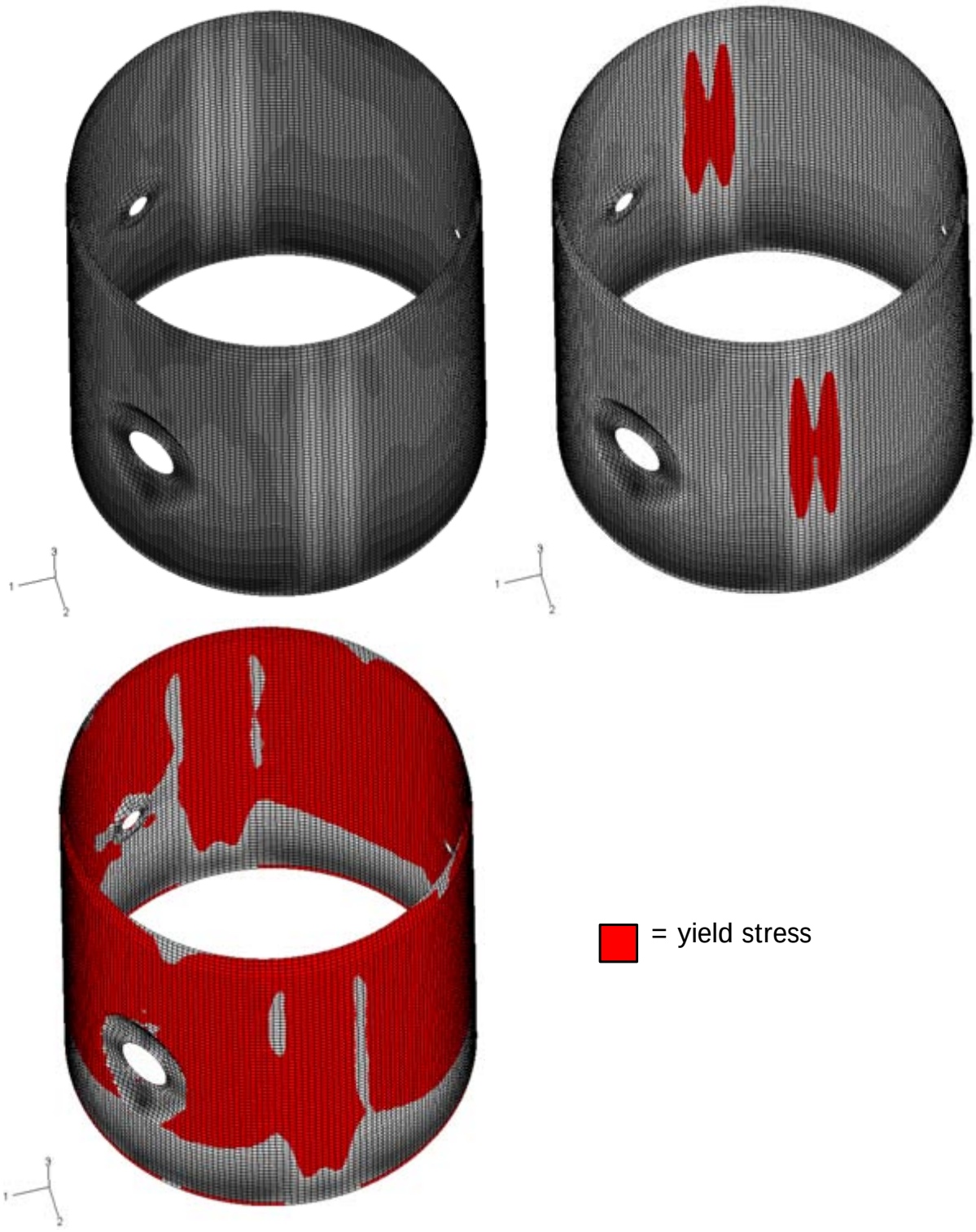

Figure 12.10 Development of yield in steel liner: First at buttresses, then propagating to global yielding for increased load (P=700 MPa, 800 MPa and 1000 MPa respectively).

12.3.2.3 Load case 1

Concrete (see Figure 12.11)

P = 0 kPa, T = 25 °C

Reference state. Only pre-stressing forces and dead weight act on the structure. Concrete in compression due to pre-stressing.

P = 0 kPa, T = 100 °C

At zero pressure, but after application of a temperature increase from 25 to 100 °C on the inside of the containment, horizontal cracks appear on the outside of the containment. The depth of the cracks are approximatly 20 % of the wall thickness. The inner part of the wall is in compression. Vertical cracks may also occur, but they are smaller than the horizontal ones. Cracks following the curved tendons around the large penetrations occur on the outside of the wall. The buttresses have now recieved horizontal cracks.

P = 150 kPa, T = 120 °C

The crack depth has now increased to approximatly 40 % of the wall thickness. The cracks around the penetrations have also increased, especially the ones above and below the penetration (oriented approximatly in the horizontal direction).

P = 285 kPa, T = 145 °C

Continued cracking, at this stage the containment is also fully cracked on the outside with both horizontal and vertical cracks. The crack depth is approximatly 60 % and 50 % respectively. Horizontal cracks in the buttresses, but no vertical cracks due to the horizontal pre-stressing tendons.

P = 430 kPa, T = 160 °C

Continued cracking.

P = 580 kPa, T = 165 °C

The horizontal cracks has now propagated all through the wall thickness, while the crack depth for vertical cracks are approximatly 55 % of the wall thickness.

P = 720 kPa, T = 170 °C

Now also the vertical cracks has propagated through the wall thickness, i.e. the containment is fully cracked.

Pre-stressing tendons

P = 0 kPa, T = 25 °C

Reference state. Only pre-stressing forces and dead weight act on the structure.

P = 0 kPa, T = 100 °C

The stresses in horizontal tendons will increase to a small extent due to the fact that they have a radius larger then the mean radius of the concrete structure.

P = 1165-1310 kPa, T = 185-190 °C

The tendons start to yield.

P = 1450 kPa, T = 200 °C

Tendon rupture has occurred. Rupture of the containment.

Rebars (see Figure 12.12 and 12.13)

P = 0 kPa, T = 25 °C

Reference state. Only pre-stressing forces and dead weight act on the structure. Rebars in compression due to pre-stressing.

P = 0 kPa, T = 100 °C

The temperature increase gives rise to some increase in compression stresses in the inner rebar layer, while the compression stresses in the outer layer has decreased to almost zero (Figure 12.12).

P = 870 kPa, T = 180 °C

The outer rebar layer at azimuth ~ 0° starts to yield, at the zone of decrease in rebar area, and at the buttreses, see Figure 12.13. The rebar on the inside has stresses approximatly half of the yield stress, with some peak stresses at the buttresses (~90 % of the yield stress).

P = 1015 kPa, T = 185 °C

First signs of yielding of the vertical reinforcement present, especially near the equipment hatch.

P = 1300 kPa, T = 195 °C

Global yielding of also the inner rebar layer, especially due to horizontal strains.

Steel liner (see Figure 12.14)

P = 0 kPa, T = 25 °C

Reference state. Only pre-stressing forces and dead weight acts on the structure. Steel liner in compression due to pre-stressing.

P = 0 kPa, T = 100 °C

Compression of the liner both in horizontal as well as vertical direction due to a combination of pre-stressing forces and temperature increase of the liner (temperature in the liner higher than in the concrete).

P = 1015 kPa, T = 185 °C

The liner yields at the buttresses.

P = 1160 kPa, T = 185 °C

The liner yields in large areas.

See also section 12.3.4.3.

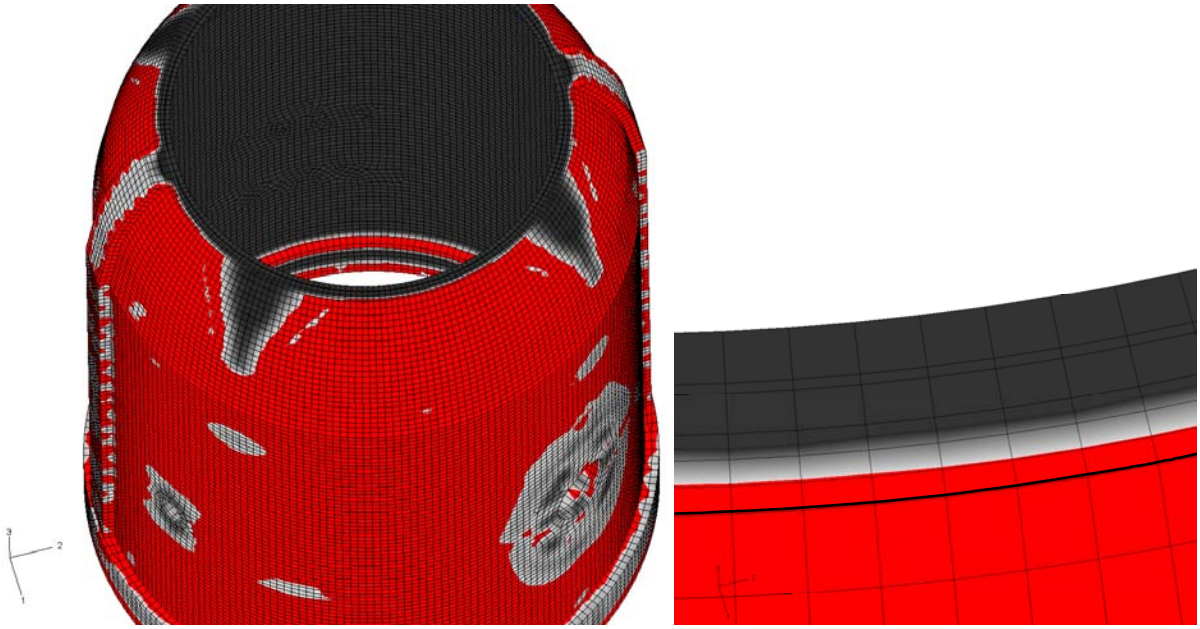

a) Cracking of concrete on the outside of the containment due to the temperature increase inside the containment. No pressure load.

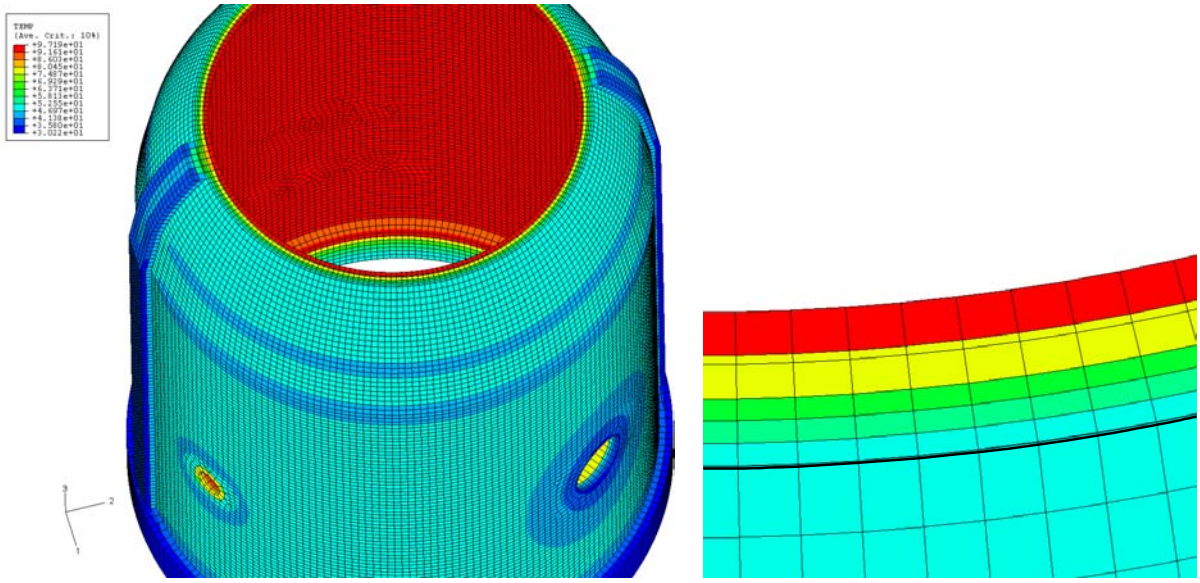

b) Initial temperature in the structure.

Figure 12.11 Cracking due to temperature increase.

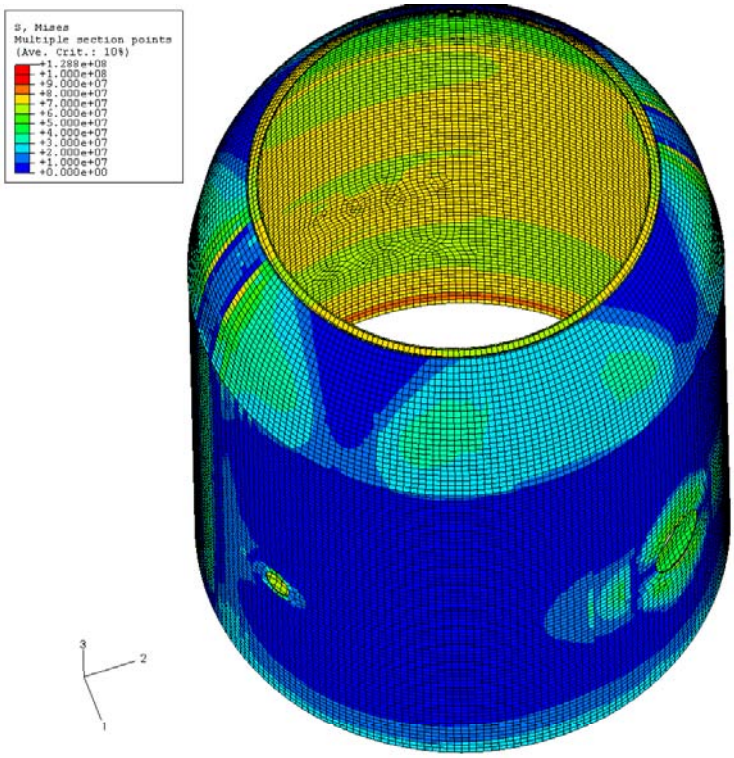

Figure 12.12 Stresses in rebars due to temperature increase inside the containment. Compression stresses occur in the inner layer, while the stresses in the outer layer is almost zero. No pressure load applied, temperature inside containment 100 ℃.

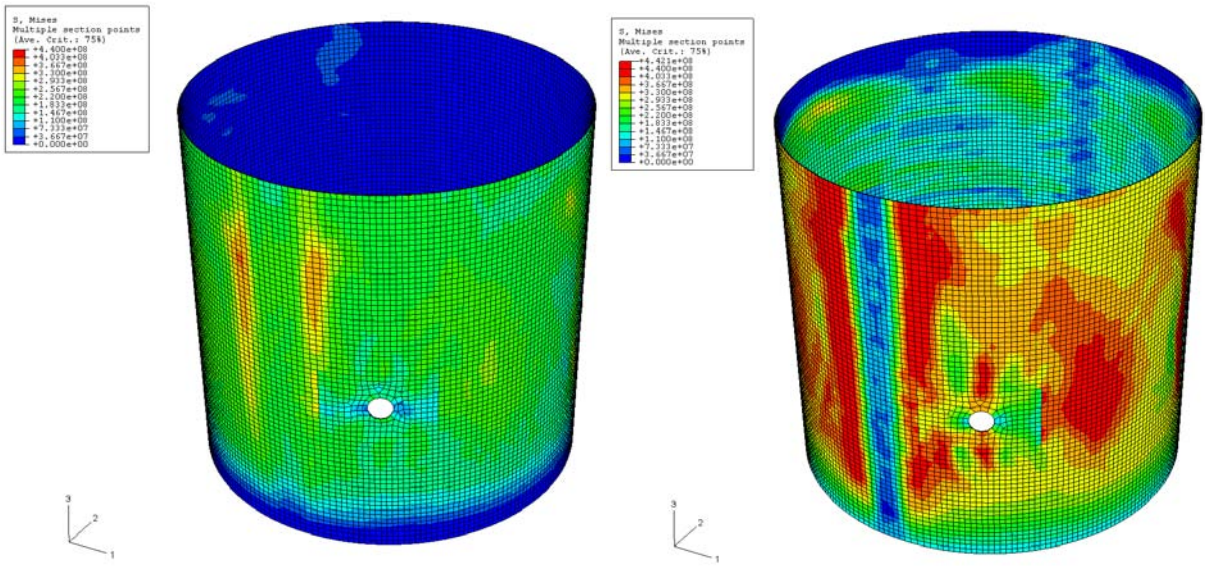

Figure 12.13 Stresses in rebars at azimuth 0 and buttress, P=870 kPa, T=180 ℃. Inside layer (left), outside layer (right).

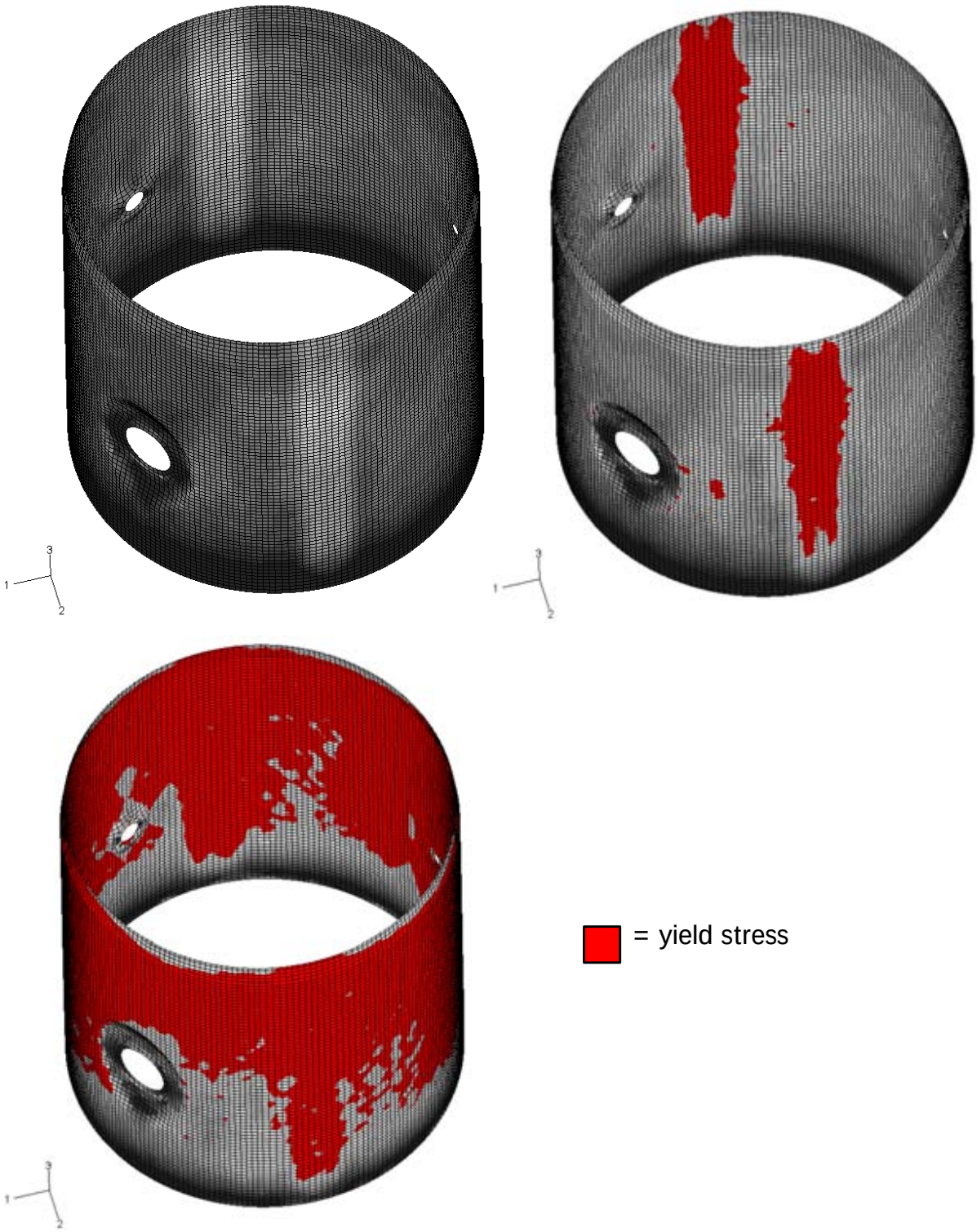

Figure 12.14 Development of yield in steel liner: first at buttresses, then propagating to global yielding for increased load (P=872 MPa, 1015 MPa and 1160 MPa respectively).

12.3.2.4 Load case 2

Concrete

Time = 0 minutes*:* P = 0 kPa, T = 25 °C

Reference state. Only pre-stressing forces and dead weight act on the structure. Concrete in compression due to pre-stressing.

Time = 260.2 – 260.6 minutes*:* P = 200-780 kPa, T = 106-508 °C

Peak loading, increase in load. Global cracking.

Time = 260.6 – 284.1 minutes*:* P = 780-345 kPa, T = 508-210 °C

Peak loading, decrease in load. No major changes of cracking.

Time = 284.1 minutes*:* P = 345 kPa, T = 210 °C

The cracks are now closed due to compression stresses in major parts of the concrete structure.

Time = 959.6 minutes*:* P = 676 kPa, T = 209 °C

Global cracks are now again open. The crack pressure load level for the case no temp. is passed.

Pre-stressing tendons (see Figure 12.15)

Time = 0 minutes*:* P = 0 kPa, T = 25 °C

Reference state. Only pre-stressing forces and dead weight acts on the structure.

Time = 260.6 minutes*:* P = 780 kPa, T = 508 °C

Peak load. No yielding of tendons. Maximum stress 1620 MPa (yield stress = 1700 MPa).

Time = 2719.8 minutes*:* P = 1223 kPa, T = 178 °C

Tendons start to yield.

Time = 3600 minutes*:* P = 1332 kPa, T = 316 °C

Global yielding of tendons (max. stress = 1850 MPa). Near rupture of tendons (failure stress = 1950 MPa) and of the containment.

Rebars (see Figure 12.16)

Time = 0 minutes*:* P = 0 kPa, T = 25 °C

Reference state. Only pre-stressing forces and dead weight act on the structure. Rebars in compression almost everywhere. Some very low tension stresses (< 10 MPa) near penetrations.

Time = 260.2 – 260.6 minutes*:* P = 200-780 kPa, T = 106-508 °C

Peak loading, increase in load. Global yielding of outer rebar layer, both horizontally and vertically. This to a large extent due to the temperature load. Considerable lower stresses in the inner layer, the vertical rebars are in compression, the horizontal in tension.

Time = 2500 minutes: P = 1190 kPa, T = 266 °C

Global yielding of rebars starts, both in the inner and outer layer.

Steel liner (see Figure 12.17)

Time = 0 minutes: P = 0 kPa, T = 25 °C

Reference state. Only pre-stressing forces and dead weight act on the structure. Steel liner in compression, both horizontally and vertically (appr. 50 MPa).

Time = 260.2 – 260.6 minutes: P = 200-780 kPa, T = 106-508 °C

Peak loading, increase in load. Steel liner starts to yield in compression at an overpressure of approximatly 320 MPa.

Time = 276.4 minutes: P = 400 kPa, T = 253 °C

The liner starts to yield in tension due to the decrease in temperature after peak value (suddenly decrease from 615 to 150°C). At full restraint this equals a stress 3 times the yield stress of the liner.

See also section 12.3.4.3 and 12.3.4.4.

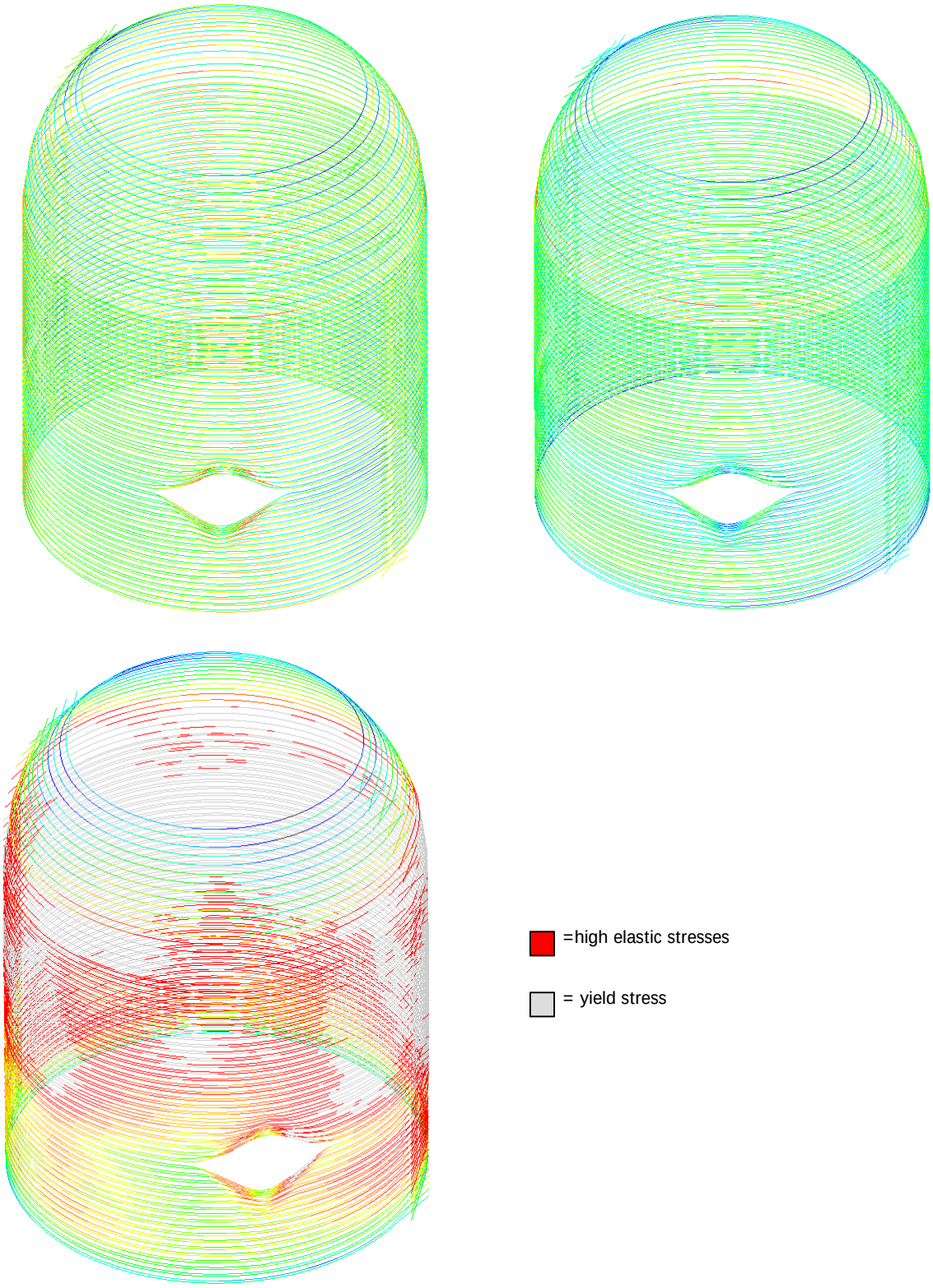

Figure 12.15 Stresses in tendons, case 2. Time = 0, 260.6 and 3600 minutes respectively.

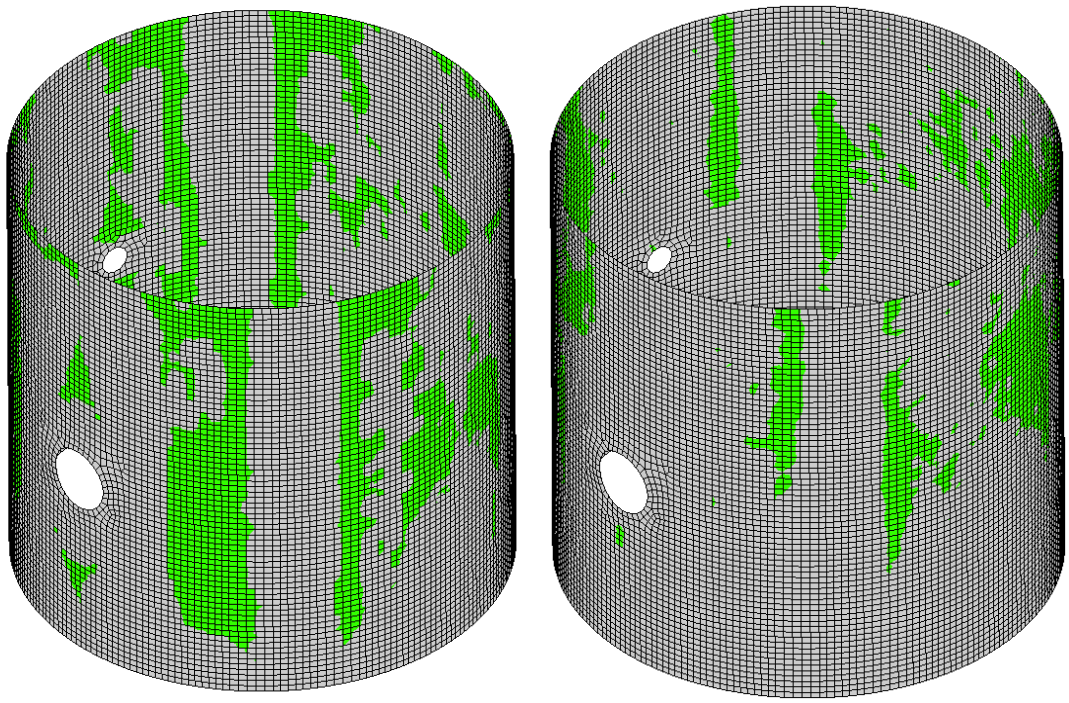

Figure 12.16 Yield stresses in rebars, case 2. Time = 260.6 and 2500 minutes respectively.

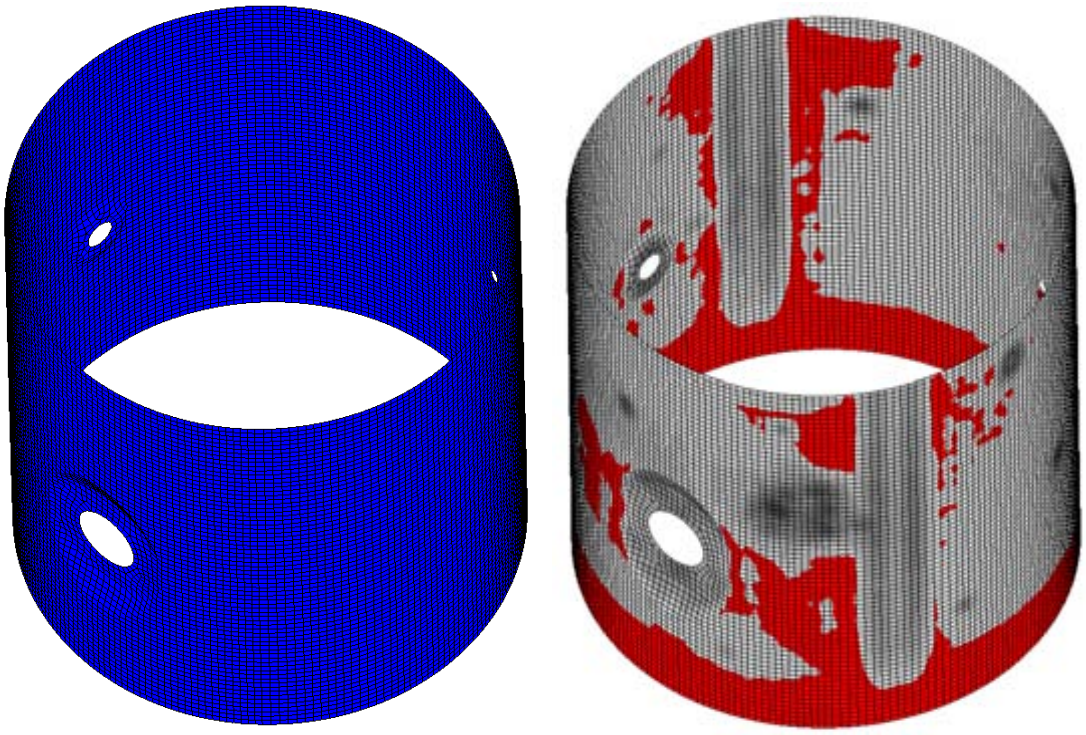

Figure 12.17 Yield stresses in steel liner, case 2 (blue = compression, red = tension). Time = 260.6 and 299.5 minutes respectively.

12.3.3 Detailed study of important result curves

12.3.3.1 General

In this section, a principal evaluation of important result curves is carried out. All results in this section are taken at elevation 6.82 for azimuth 135. First, all three load cases (no temp., case 1 and case 2) are compared, see section 12.3.3.2 and 12.3.3.3. Then some special features of the case 2 analysis are discussed (section 12.3.3.4).

12.3.3.2 Radial displacement as a function of pressure, comparison of all load cases

In Figure 12.18, the radial deformation as a function of internal overpressure is presented for the following three load cases:

- No temperature, pressure load only (green curve)
- Case 1, monotonically increased pressure and temperature (blue curve)
- Case 2, varying pressure and temperature load (red curve)

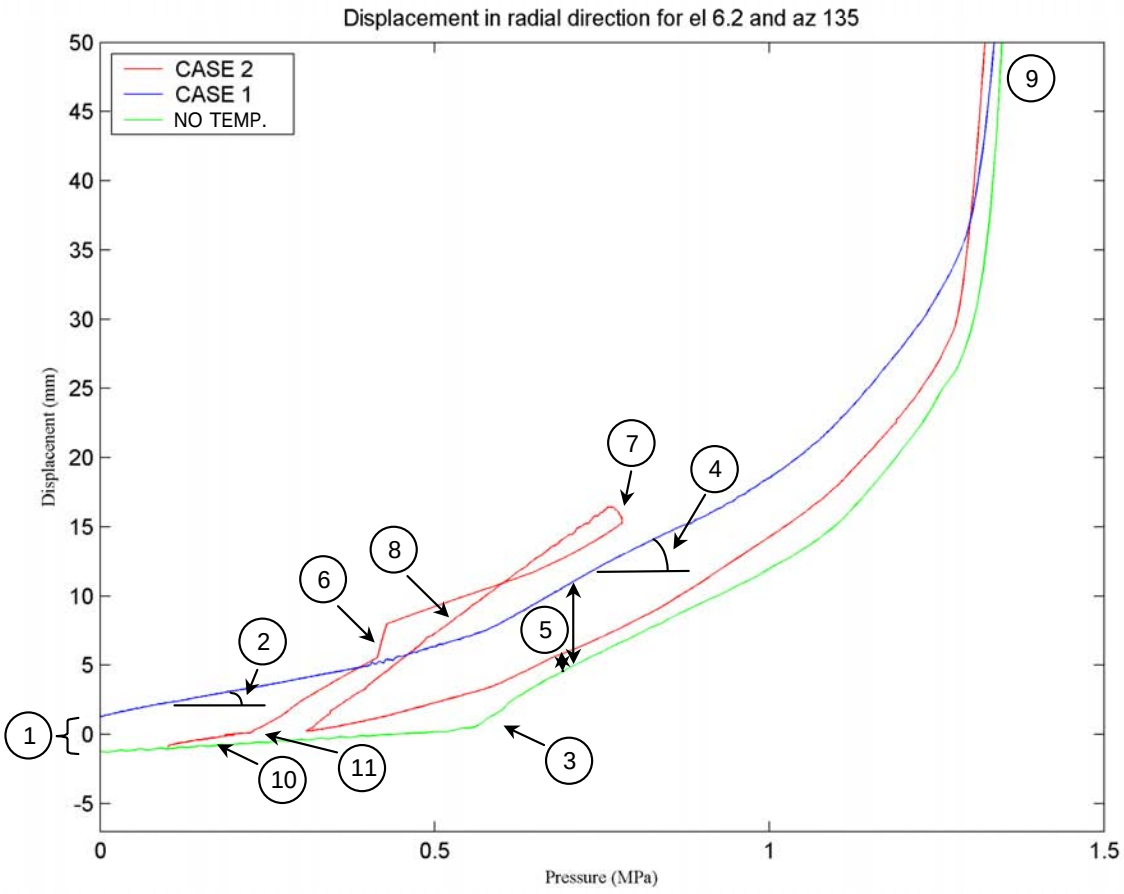

Figure 12.18 Radial deformation as a function of internal overpressure, comparison between load case no temperature, case 1 and case 2.

Some characteristics of the result can be observed from these curves (the numbers in the list below can also be found at relevant positions in Figure 12.18):

1. At $P = 0$, the radial deformation in case 1 is larger than for the other two load cases due to a steady state increase in temperature from 25 to 100 °C on the inside of the containment (thermal expansion) before pressure increase.
2. The slope of the case 1 and case 2 curves are higher compared to the no temp. analyses in the zone between 0 to ~600 kPa due to the early cracking of the outside part of the containment wall owing to the temperature increase inside the containment, and also due to the mean temperature increase giving rise to a volume increase of the concrete.
3. For the no temp. analysis (pressure load only), there is a rather distinct concrete cracking pressure, while for case 1 and case 2 analysis the cracking develops more smoothly.
4. After full cracking of the concrete the slope of the curves are approximatly the same.
5. The difference in radial deformation between the no temp. analysis and the case 1 analysis is due to the increase in mean temperature. The same is true for case 2 analysis. However, owing to that the temperature field corresponds to steady state condition in case 1 analysis, the mean temperature is higher than for case 2 analysis, in spite of the fact that the temperature increase on the inside of the containment is much larger for the case 2 simulation.
6. For case 2 analysis, the radial deformation increase due to a sudden increase in the pressure load, and to a smaller extent due to a simultaniously increase in the inside temperature. The sudden change in radial deformation at appr. 400 kPa is due to a sudden change in temperature, see Figure 12.22.
7. The radial deformation continues to increase even when the pressure decreases, this is due to an increase in mean temperature of the containment wall.
8. Decresase in pressure and temperature gives rise to a decrease in radial deformation.
9. The three analysis predicts, as expected, almost the same rupture capacity of the containment.
10. Increase in radial deformation for case 2 compared to case no temp. due to increase in mean temperature of the structure, and due to cracking on the outside part of the wall.
11. Cracking through the containment wall occurs approximatly at the same radial deformation for case no temp. and case 2.

12.3.3.3 Stresses as a function of pressure, comparison of all load cases

In Figure 12.19, the stresses in the steel liner as a function of internal overpressure is presented for the three load cases.

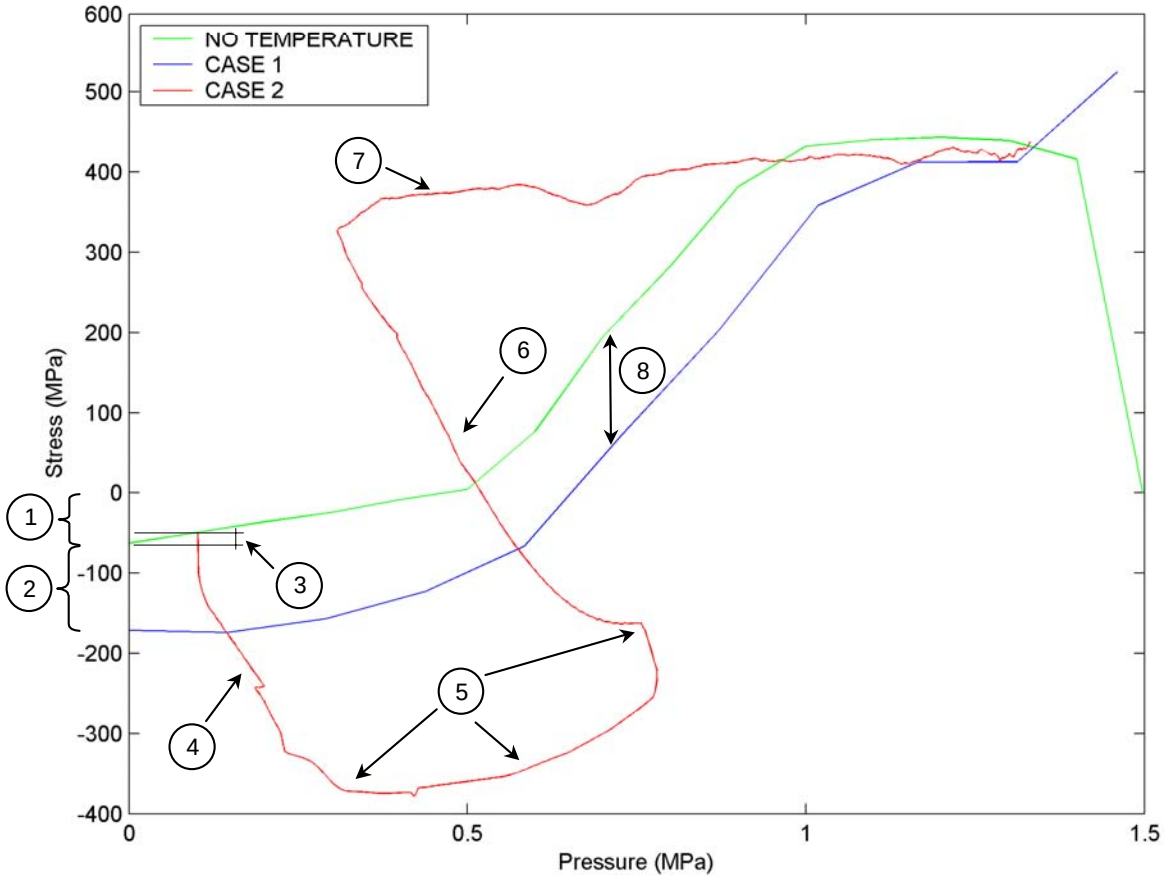

Figure 12.19 Stresses in steel liner as a function of internal overpressure, comparison between load case no temeprature, case 1 and case 2.

Some characteristics of the result can be evaluted from these curves (the numbers in the list below can also be found at relevant positions in Figure 12.19):

1. At $P = 0$, a compression stress is present in the liner due to the pre-streesing force and dead weight.
2. For case 1, the compression stress is further increased at $P = 0$ due to an increase of the temperature from 25 to 100 °C at the inside of the containment. The stress develops due to restrained temperature expansion.
3. For case 2, the compression stresses are decreased due to a suddenly applied internal overpressure of 100 kPa.
4. For case 2, during the increase in temperature of the liner, restrained temperature expansion gives rise to increased compression stresses in the liner. The increase in compression stress is somewhat counteracted by radial expansion of the containment due to an increase in internal overpressure and a mean temperature increase of the containment wall.
5. Case 2: During the peak loading the compression stress will reach the yield stress, and then decrease primarily due to decrease in yield stress as a result of the temperature increase of the steel material, but also due to increase in

radial deformation owing to pressure increase, cracking of concrete and increase in mean temperature of the containment wall.

6. Case 2: Then both the pressure and the temperature will decrease. A decrease in pressure (i.e. decrease in radial deformation) would normally give rise to an increase in compression. However, this is counteracted, and overtaken, by tension stresses due to restrained temperature contraction when the temperature in the steel liner decreases.
7. Case 2: When the pressure and temperature loads have went back to "normal" values, the tension stresses in the liner have reached appr. 320 MPa. The tension then increases due to increased pressure and temperature load and finally reach the yield stress in tension. Due to the fact that the increase in temperature of the liner gives rise to temperature expansion, the stress in the liner will not increase as fast as for pressure load only.
8. The differences in stresses between case 1 and the case no temp. depends on the stresses due to restrained temperature expansion.

12.3.3.4 Plastic strain as a function of pressure and temperature respectively, load case 2

In Figure 12.20, the stress as well the plastic strain in the steel liner as a function of internal overpressure is presented for load case 2. Some characteristics of the result can be evaluted from these curves (the numbers in the list below can also be found at relevant positions in Figure 12.20):

1. The stress curve is explained in Figure 12.19 above.
2. The liner yields in compression due to restrained thermal expansion (increase in liner temperature).
3. The sudden changes in radial deformations at appr. 400 kPa and 800 kPa pressure are due to sudden changes in temperature, see Figure 12.22.
4. Yield in tension due to restrained thermal contraction (decrease in liner temperature).
5. Increase in plastic strain primarily due to radial deformation of the containment wall.

In Figure 12.21, the plastic strain in the steel liner as a function of temperature on the inside of the containment (i.e. temperature load curve) is presented for load case 2. Some characteristics of the result can be evaluted from these curves(the numbers in the list below can also be found at relevant positions in Figure 12.21):

1. The liner yields in compression due to restrained thermal expansion (increase in liner temperature).
2. Yield in tension due to restrained thermal contraction (decrease in liner temperature).
3. Increase in plastic strain primarily due to radial deformation of the containment wall.

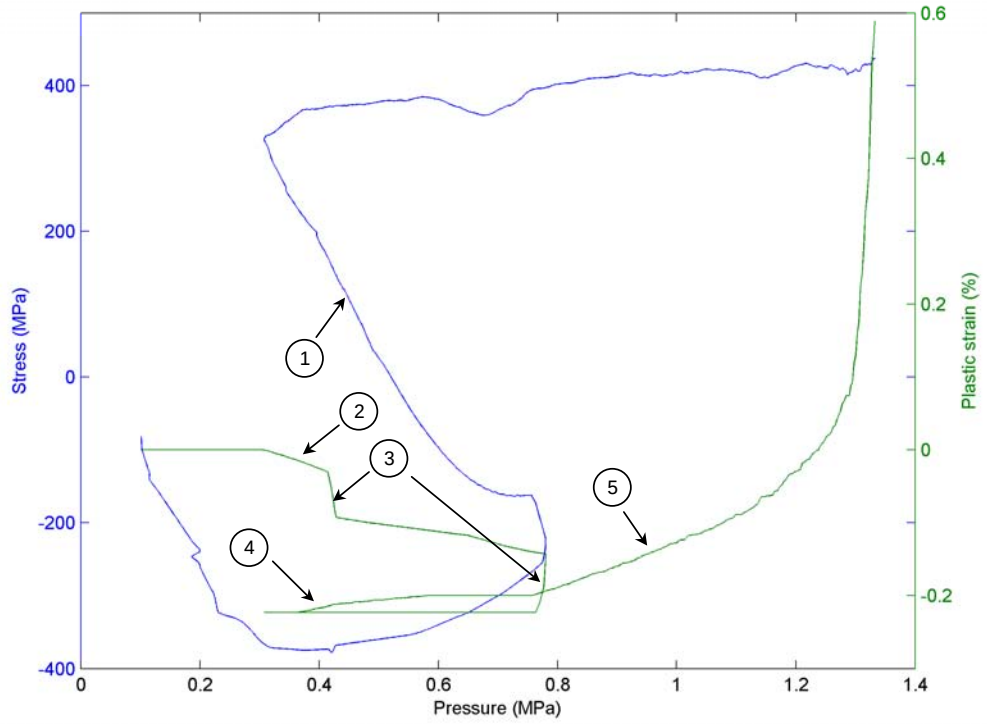

Figure 12.20 Stresses (blue curve) and plastic strains (green curve) in steel liner as a function of internal overpressure, load case 2.

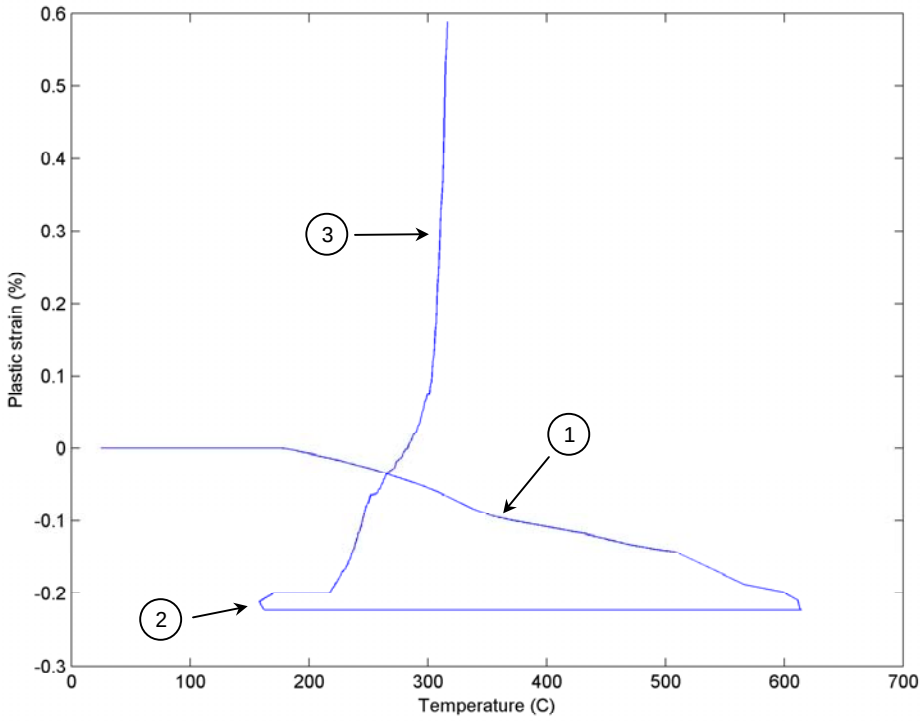

Figure 12.21 Plastic strain as a function of temperature, case 2.

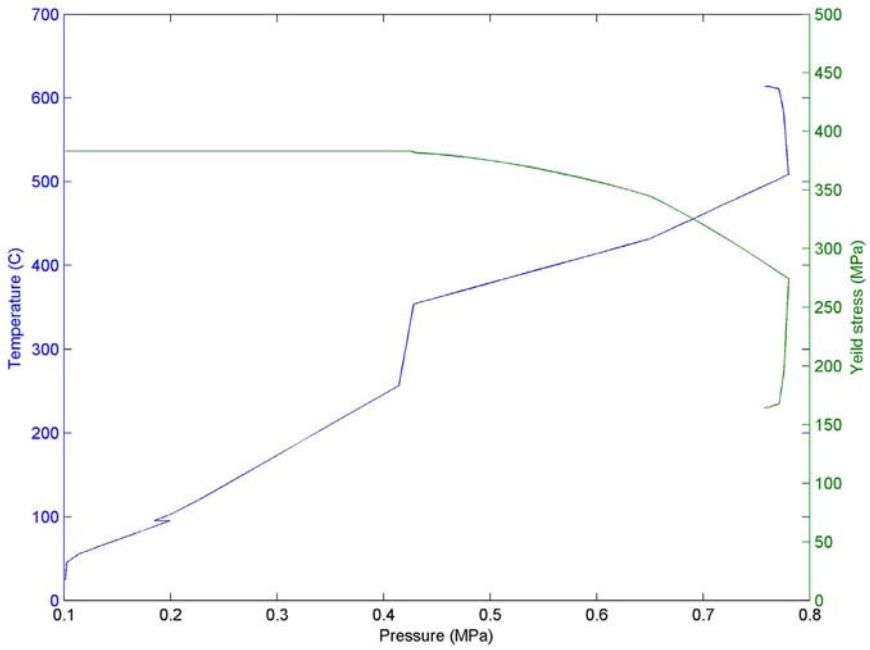

Figure 12.22 Temperature and yield stress as a function of pressure, case 2.

12.3.4 Rupture simulation

12.3.4.1 Leak-tightness

The onset of leakage due to a tear in the steel liner is here evaluated in the same way as for the no temp. analysis, i.e. based on test data. Therefore, when we arrive at an equivalent strain in the liner corresponding to the strain measured during pressure test at first leakage, a leakage is assumed to occur. This to make it possible to compare the outcome of the two analysis, hence determine the influence on the safety due to the adding of the temperature load. Due to the fact that the first leakage during the test occurred at a global hoop strain level as low as 0.17 % (see table 7.1 in part I), we use here yielding in the steel liner as a measure of leak-tightness. Then the pressure values stated below, should not be taken as the exact values coupled to leak-tightness, but only to be used for relative comparison between the three load cases.

In Figure 12.23, a comparison between the three load cases is presented. The figure shows the extent of yielding; first yielding and global yielding respectively. For load case no temperature and load case 1, the first yielding occurs in the areas near the buttresses, primarily due to a combination of hoop stresses and local bending stresses. The pressure level at first yielding for these load cases are approximatly 800 kPa, and 1000 kPa respectively. For load case 2, the first yielding in tension occurs much earlier, due to the restraint of thermal contraction of the liner performed by the concrete. This occurs when the temperature decreases much faster in the liner than in the concrete to which it is attached. This yiedling, as can be seen in Figure 12.23, starts in the lower part of the wall, at the basemat, because the high restraint of the liner in this region.

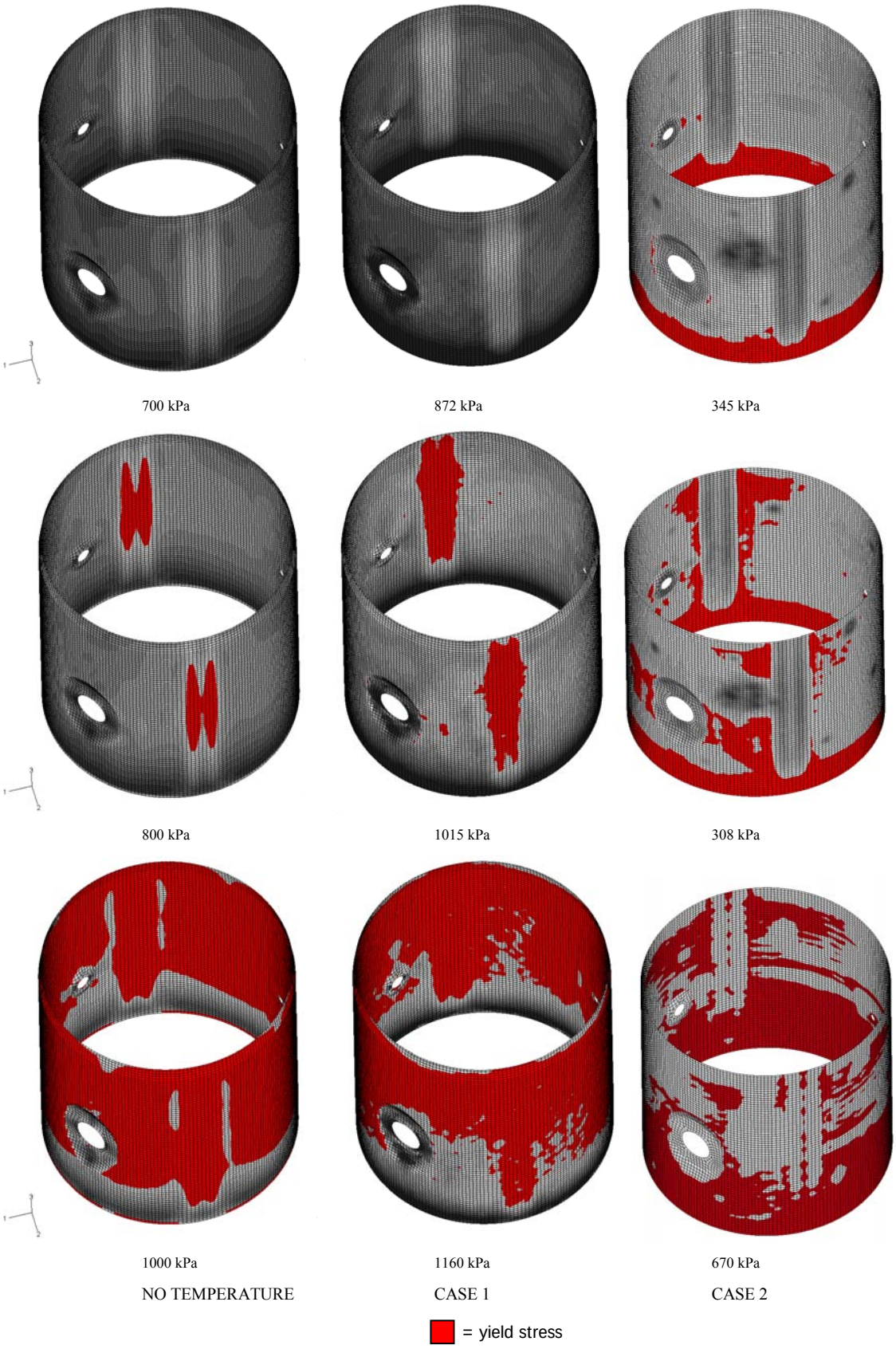

Figure 12.23 Development of yield in steel liner: first at buttresses, then propagating to global yielding for increased load.

Global yielding occurs at a pressure level of approximatly 1000 kPa for load case no temp., while it is reached at a pressure level maybe 150 kPa higher for case 1, but at an lower pressure for case 2, see Figure 12.23 above. This indicates that the onset of leakage can be delayed in the case of temperatrue load acting simultaneously as the pressure load, compared to no temp. load case. This effect, however, is dependent on the maximum value of the temperature, and of the rate of temperature changes.

12.3.4.2 Collapse of the structure

Rupture of pre-stressing tendons just before and at rupture of the containment is evaluated from the video taken during the SFMT test. As can be seen in Figure 12.25, the first tendon to rupture is at an elevation of approximatly 5.0 m, the second at approximatly 7.5 m, and the major tendon ruptures occurs in the zone between elevation 5-10 m.

The onset of rupture is at the same pressure levels in all three load cases (no temp., case 1 and case 2 respectively).

In the analysis, we observe the first tendon rupture in a horizontal tendon at level 5.2 m, see Figure 12.24 b). At the same output frame we have the highest stresses in tendons in the zone between elevation 5 and 9 m (Figure 12.24 a)). Just before rupture there are large areas with highly stressed tendons, as also can be seen in Figure 12.24 a).

Due to the fact that the tendons are modelled with contact formulation (see section 6.2.4 and 6.2.5) it is possible to capture different positions regarding first tendon rupture, and the final rupture of the containment. The rupture of the tendon is determined by in what position the ultimate capacity of the tendon is first reached, while the rupture position of the containment can be elsewhere, for example at a transition zone with smaller reinforcement area. Due to this modelling approach it is also easily recognized when, and where, the first rupture of the tendons occur, see Figure 12.24.

The total kinetic and strain energy of the whole model can also be used to evaluate the scenario near, and at rupture of the containment, see Figure 12.26 (the numbers in the list below can also be found at relevant positions in Figure 12.26):

1. The first substantial increase in kinetic energy indicates excessive yielding of tendons and rebars.
2. The major increase in kinetic energy indicates rupture of the first tendon.
3. Finally, the abrupt decrease in strain energy indicates rupture of the containment.

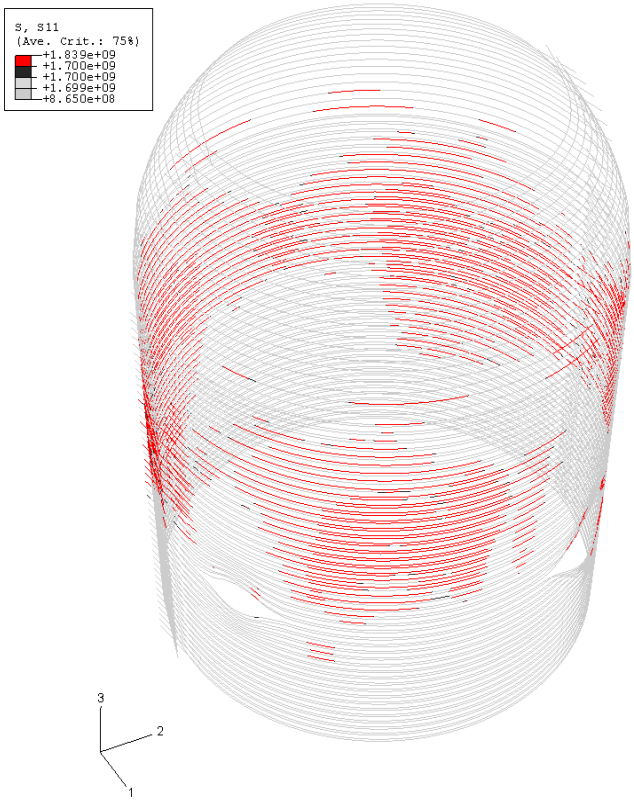

a) Areas with highest stresses (red color) in horizontal tendons at an internal pressure of 1.3 MPa, i.e. just before rupture of the containment.

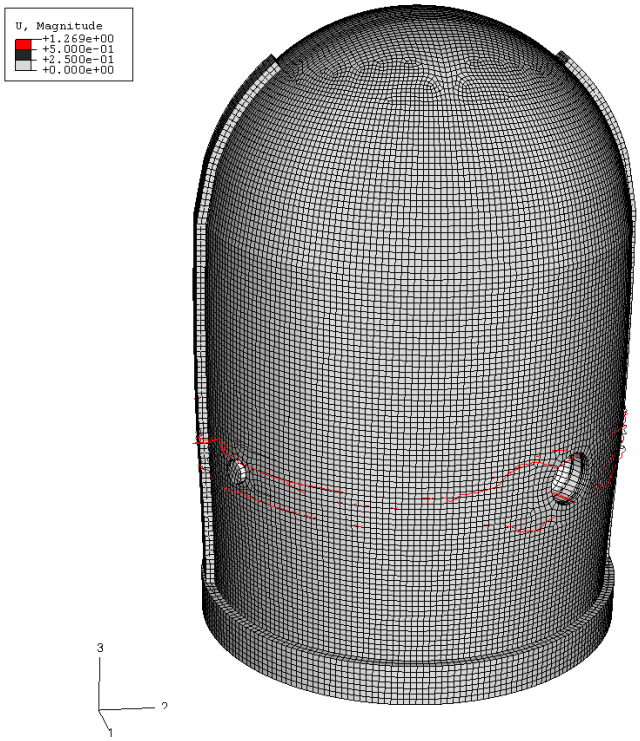

b) First tendon rupture just before rupture of the containment. Ruptured tendon shown in red. Due to the fact that the tendons are modelled using contact formulation, the tendon will spring loose after tendon rupture.

Figure 12.24 Tendon rupture.

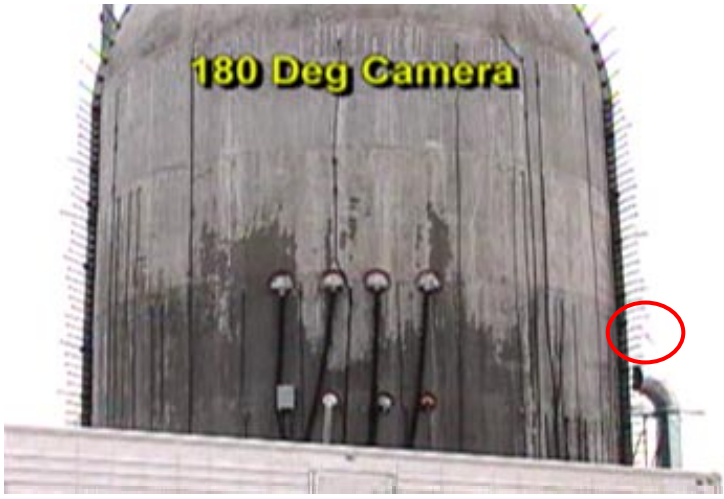

a) First tendon to rupture, elevation ~ 5.0 m. Approximatly 15 seconds before rupture of the containment.

b) Second tendon to rupture, elevation ~ 7.5 m. Approximatly 3 seconds before rupture of the containment.

b) Rupture of the containment, major tendon rupture at elevation ~ 5 -10 m.

Figure 12.25 Rupture of tendons as identfied from the video of the SFMT test.

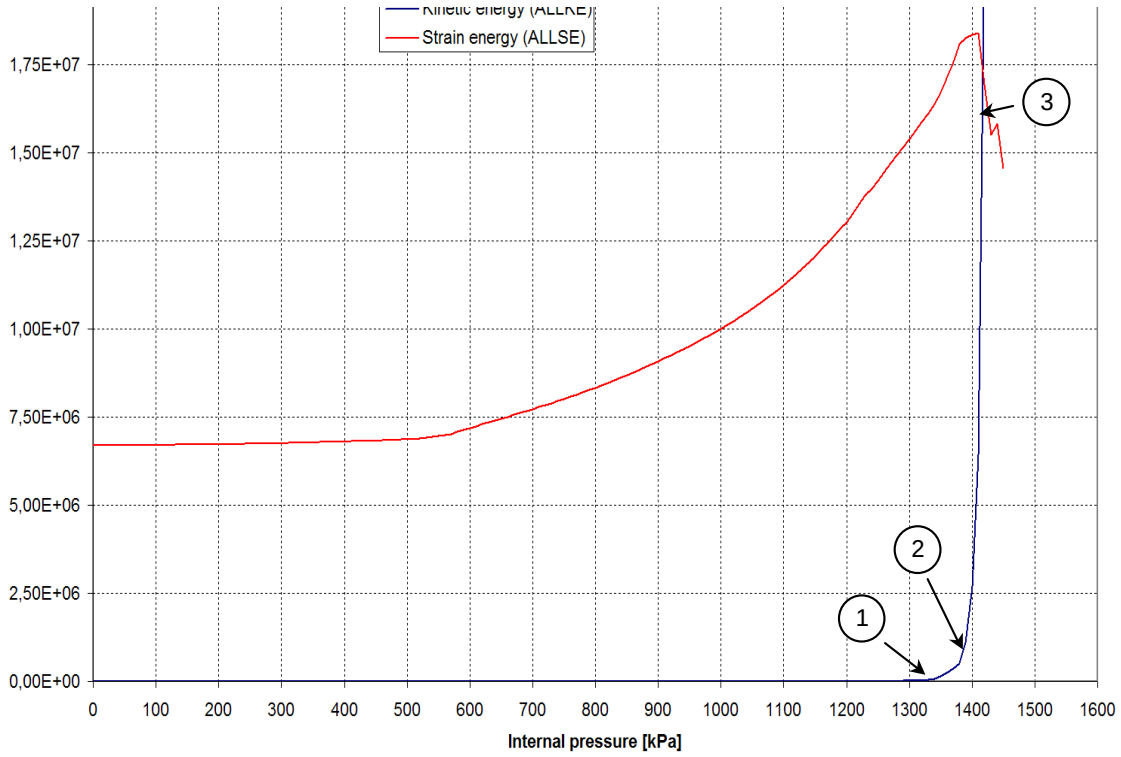

Figure 12.26 Kinetic and strain energy, no temp. analysis.

12.4 3D model analysis

In this section results from the main analysis using the fully three-dimensional FE model are presented. Results in the prescribed standard output locations, SOLs, are given both as a function of time, and as function of pressure load respectively. This to increase the possibility to evaluate the influence of the added temperatue load in comparison with analysis with pressure load only, as presented in the first part of this report.

During the pressure test, 55 SOL positions where specified, and results from the belonging finite element analysis for the pressure load only analysis are presented in section 7.3.3.5, together with registred test data. For the case 1 and 2 analysis (including temperature load) however, only a limited number of the SOLs are mandatory. In section 12.4.1 and 12.4.2, results at these selected SOLs are given at azimuth 135. In section 12.4.3, where results from all three load cases are compared to each other, results for all SOLs are given.

12.4.1 Case 1, results as a function of time

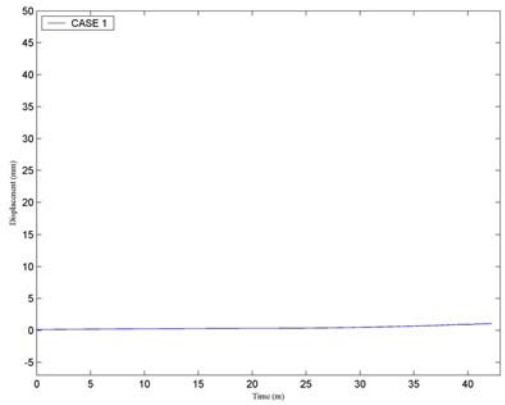

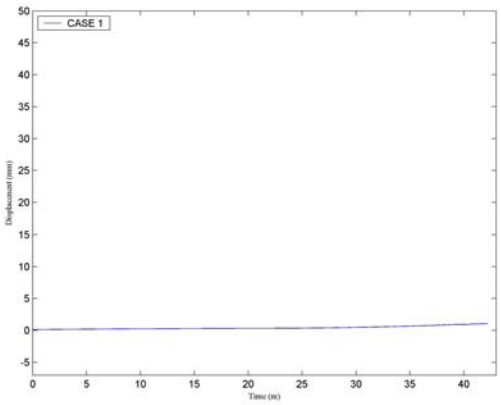

Figure 12.27 Pos. 1-Displacement in vertical direction for el 0.0 and az 135 (left).

Figure 12.28 Pos. 6-Displacement in radial direction for el 6.2 and az 135 (right).

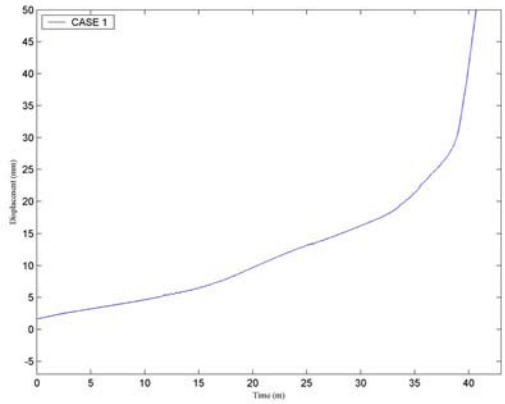

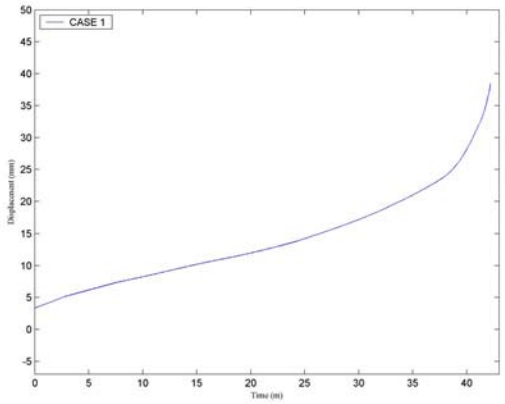

Figure 12.29 Pos. 7-Displacement in radial direction for el 10.75 and az 135 (left).

Figure 12.30 Pos. 8-Displacement in vertical direction for el 10.75 and az 135 (right).

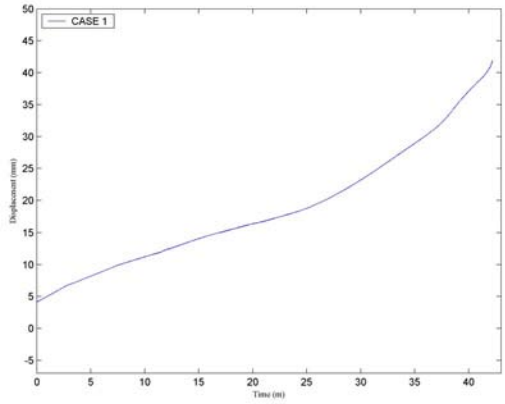

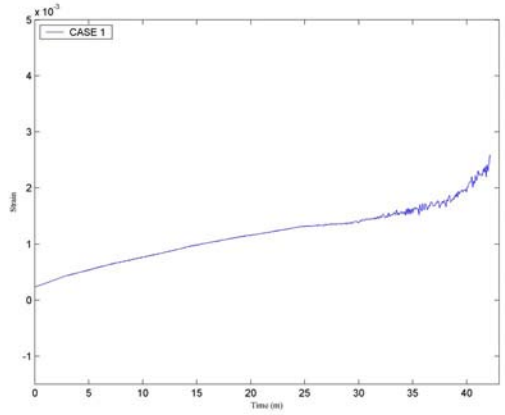

Figure 12.31 Pos. 11-Displacement in vertical direction for el 16.13 and az 135 (left).

Figure 12.32 Pos. 18-Rebar strain inside layer, meridional direction, el 0.25, az 135 (right).

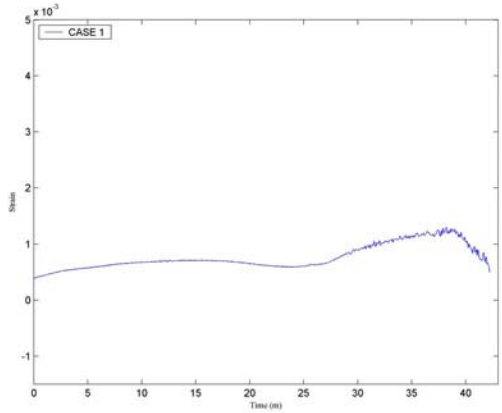

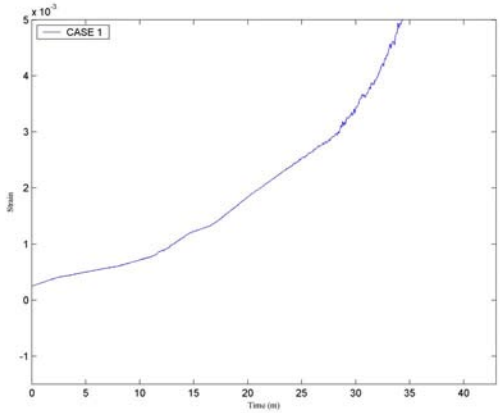

Figure 12.33 Pos. 19-Rebar strain outside layer, meridional direction, el 0.25, az 135 (left).
Figure 12.34 Pos. 22-Rebar strain outside layer, hoop direction for el 6.2 and az 135 (right).

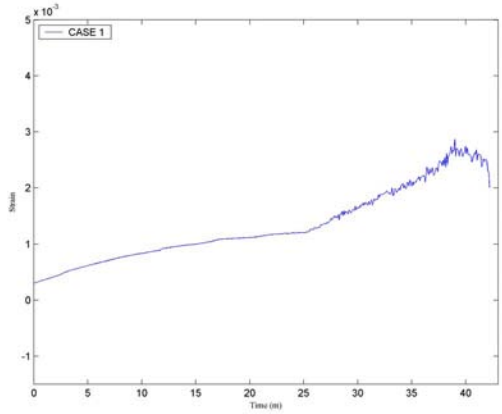

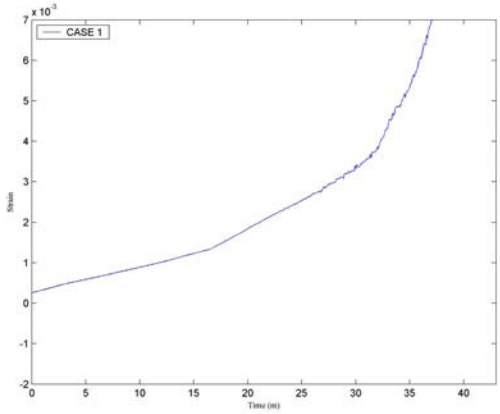

Figure 12.35 Pos. 23-Rebar strain outside layer, meridional direction, el 6.2 and az 135 (left).
Figure 12.36 Pos. 39-Liner strain in hoop direction for el 6.2 and az 135 (right).

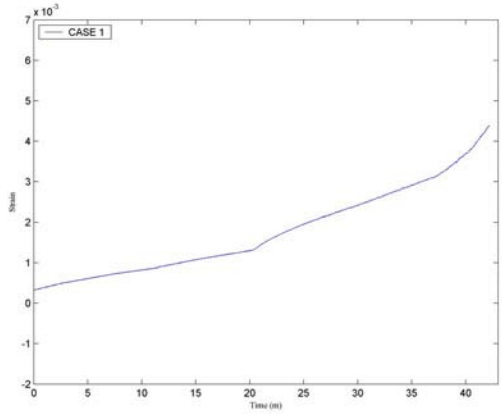

Figure 12.37 Pos. 42-Liner strain in meridional direction for el 16.13 and az 135.

12.4.2 Case 2, results as a function of time

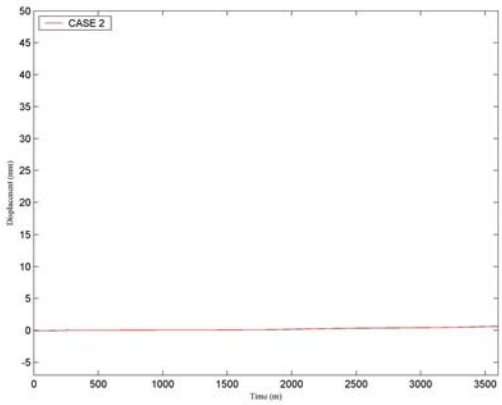

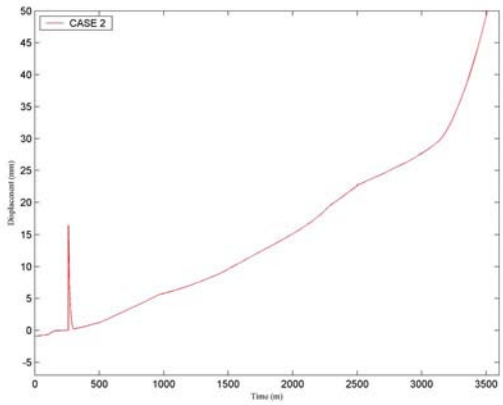

Figure 12.38 Pos. 1-Displacement in vertical direction for el 0.0 and az 135 (left).

Figure 12.39 Pos. 6-Displacement in radial direction for el 6.2 and az 135 (right).

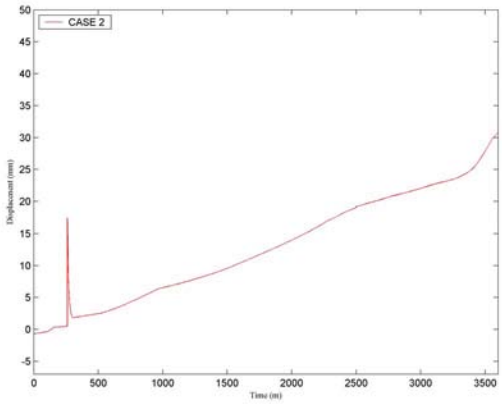

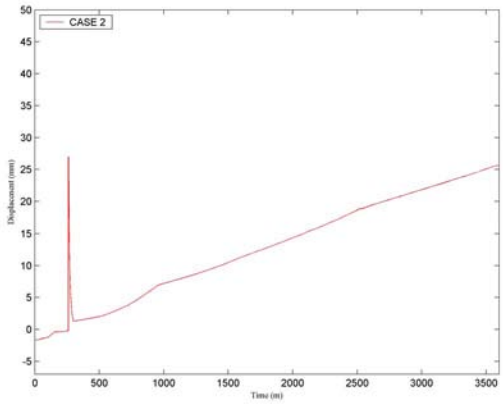

Figure 12.40 Pos. 7-Displacement in radial direction for el 10.75 and az 135 (left).

Figure 12.41 Pos. 8-Displacement in vertical direction for el 10.75 and az 135 (right).

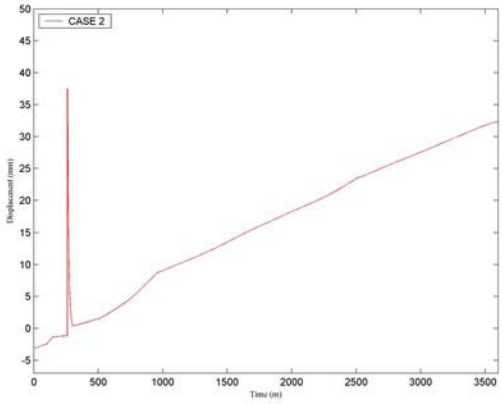

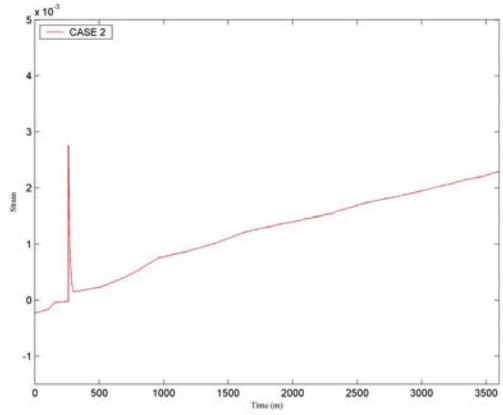

Figure 12.42 Pos. 11-Displacement in vertical direction for el 16.13 and az 135 (left).

Figure 12.43 Pos. 18-Rebar strain inside layer, meridional direction, el 0.25, az 135 (right).

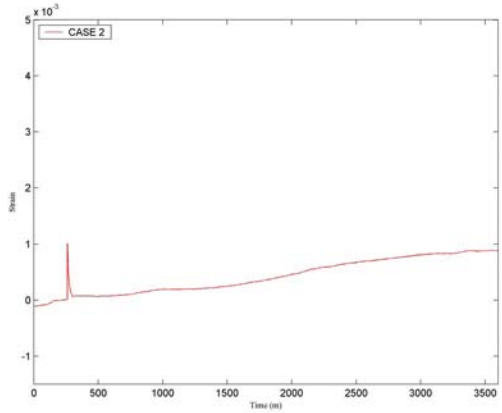

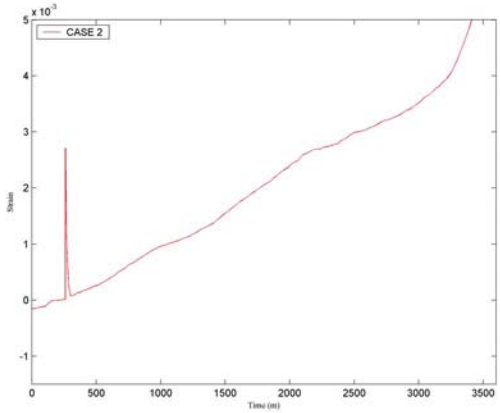

Figure 12.44 Pos. 19-Rebar strain outside layer, meridional direction, el 0.25, az 135 (left).
Figure 12.45 Pos. 22-Rebar strain outside layer, hoop direction for el 6.2 and az 135 (right).

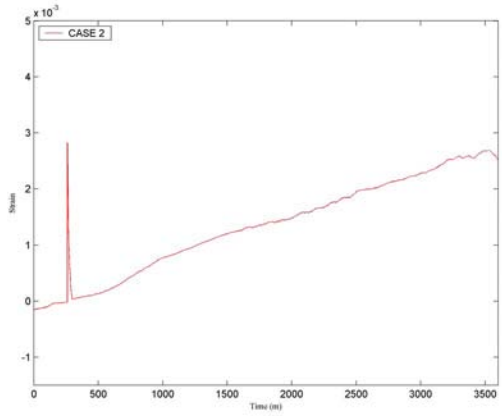

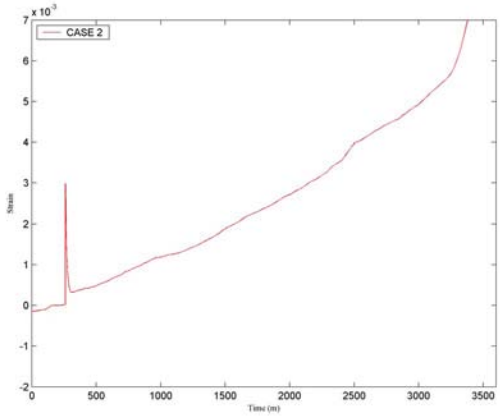

Figure 12.46 Pos. 23-Rebar strain outside layer, meridional direction, el 6.2 and az 135 (left).
Figure 12.47 Pos. 39-Liner strain in hoop direction for el 6.2 and az 135 (right).

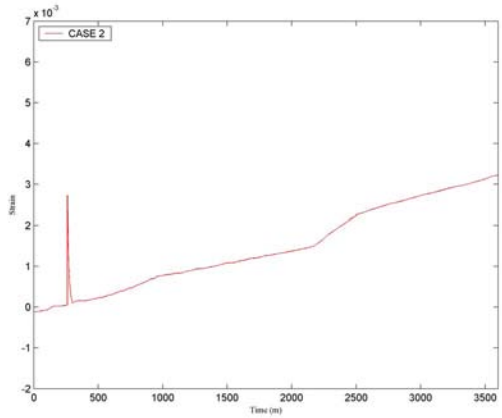

Figure 12.48 Pos. 42-Liner strain in meridional direction for el 16.13 and az 135.

12.4.3 Case no temp., case 1, and case 2, results as a function of pressure

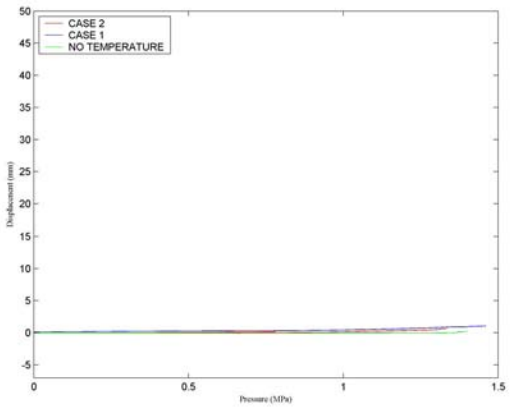

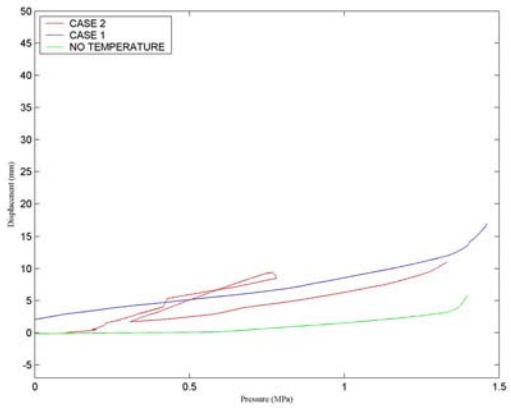

Figure 12.49 Pos. 1-Displacement in vertical direction for el 0.0 and az 135 (left).

Figure 12.50 Pos. 2-Displacement in radial direction for el 0.25 and az 135 (right).

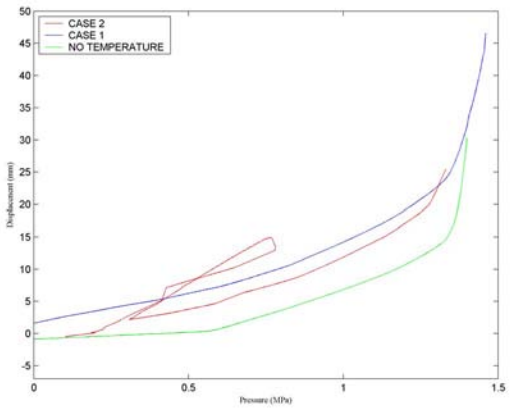

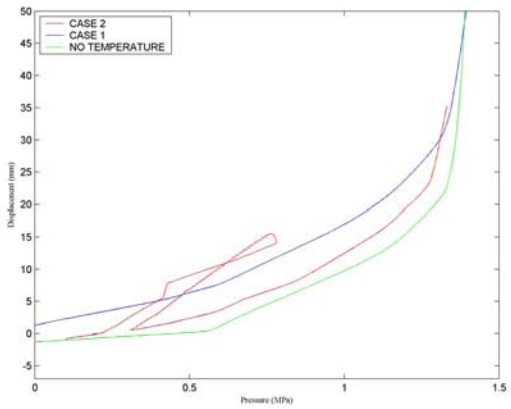

Figure 12.51 Pos. 3-Displacement in radial direction for el 1.43 and az 135 (left).

Figure 12.52 Pos. 4-Displacement in radial direction for el 2.63 and az 135 (right).

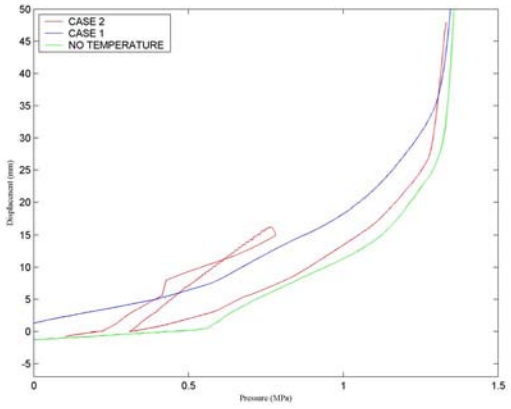

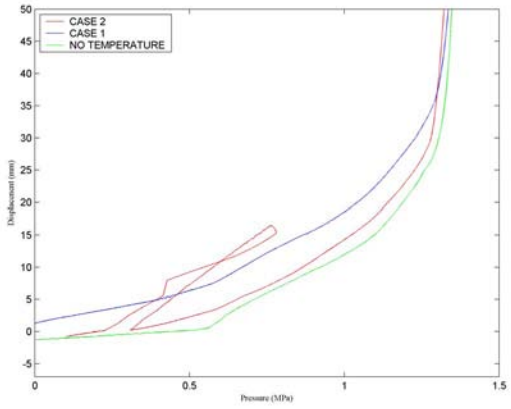

Figure 12.53 Pos. 5-Displacement in radial direction for el 4.68 and az 135 (left).

Figure 12.54 Pos. 6-Displacement in radial direction for el 6.2 and az 135 (right).

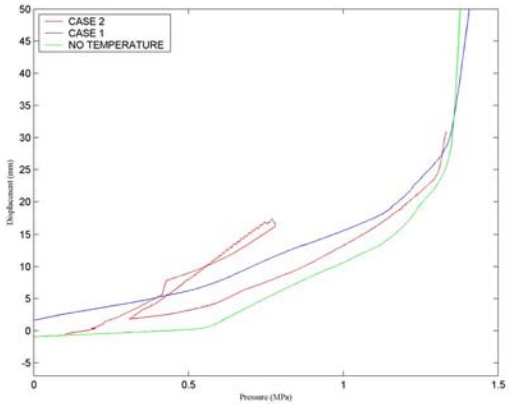

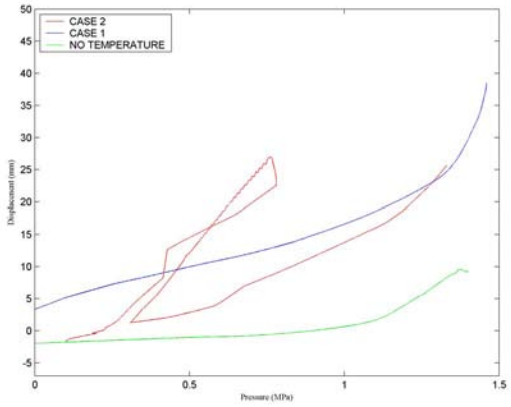

Figure 12.55 Pos. 7-Displacement in radial direction for el 10.75 and az 135 (left).

Figure 12.56 Pos. 8-Displacement in vertical direction for el 10.75 and az 135 (right).

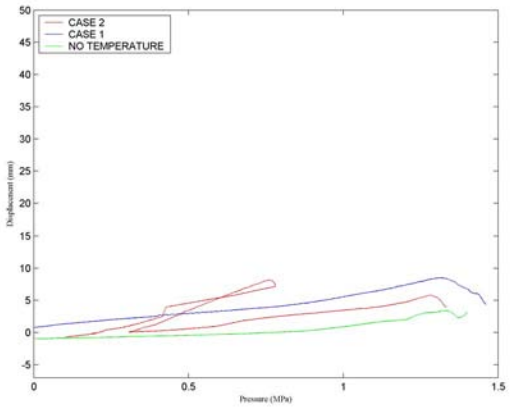

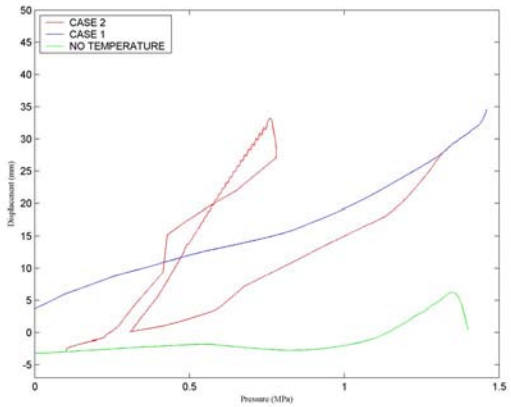

Figure 12.57 Pos. 9-Displacement in radial direction for el 14.55 and az 135 (left).

Figure 12.58 Pos. 10-Displacement in vertical direction for el 14.55 and az 135 (right).

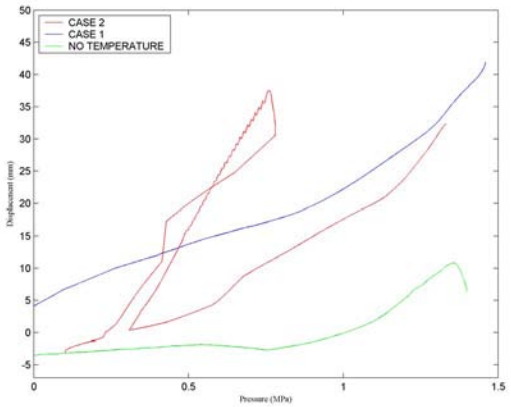

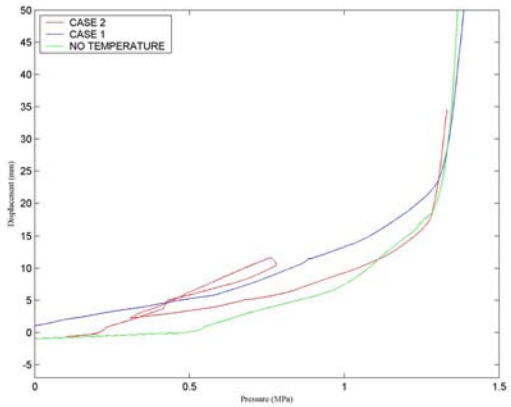

Figure 12.59 Pos. 11-Displacement in vertical direction for el 16.13 and az 135 (left).

Figure 12.60 Pos. 12-Displacement in radial direction for el 6.2 and az 90 (right).

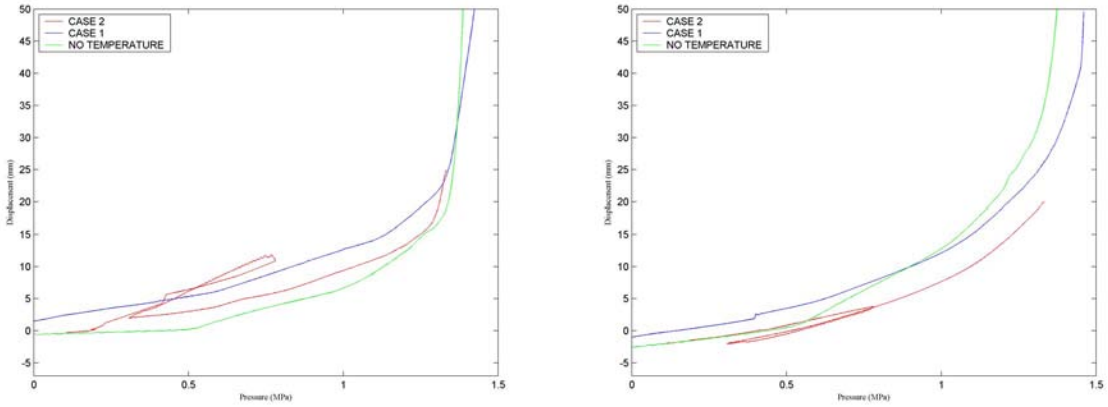

Figure 12.61 Pos. 13-Displacement in radial direction for el 10.7 and az 90 (left).

Figure 12.62 Pos. 14-Displacement in radial direction for el 4.675 and az 334 (right).

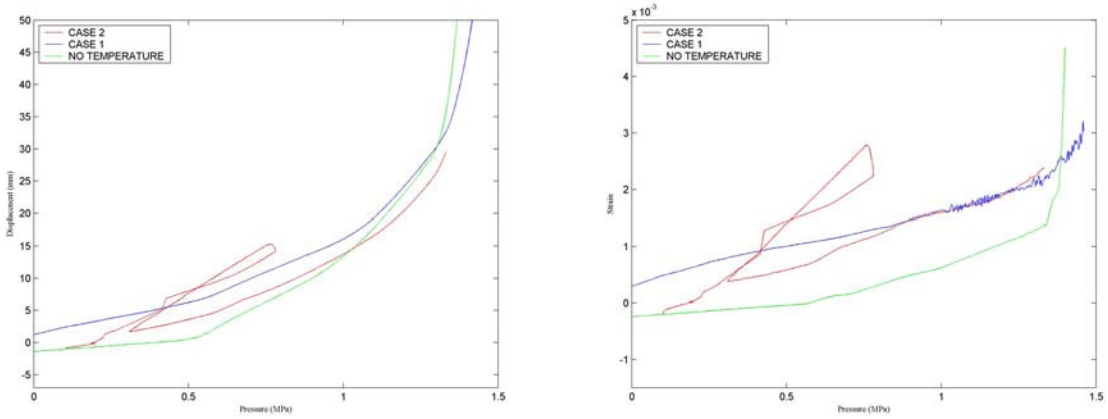

Figure 12.63 Pos. 15-Displacement in radial direction for el 4.525 and az 66 (left).

Figure 12.64 Pos. 16-Rebar strain inside layer, meridional direction, el 0.05, az 135 (right).

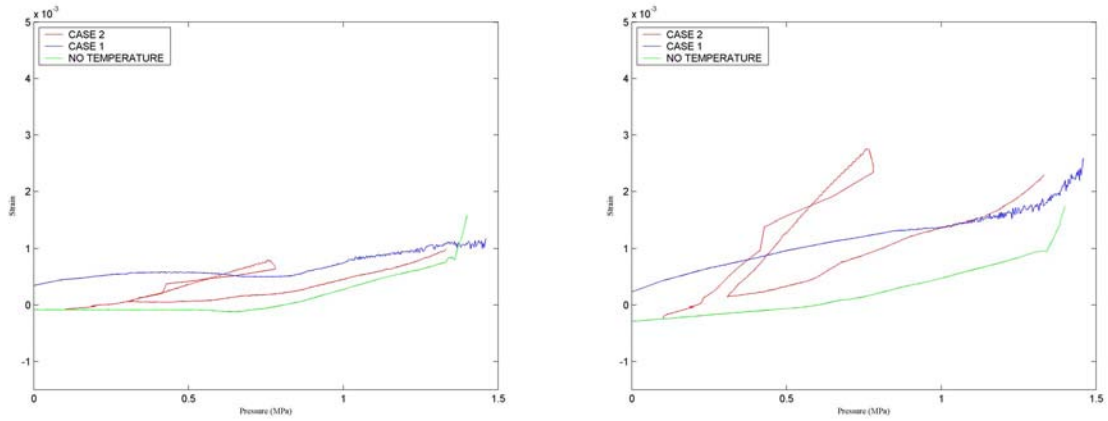

Figure 12.65 Pos. 17-Rebar strain outside layer, meridional direction, el 0.05, az 135 (left).

Figure 12.66 Pos. 18-Rebar strain inside layer, meridional direction, el 0.25, az 135 (right).

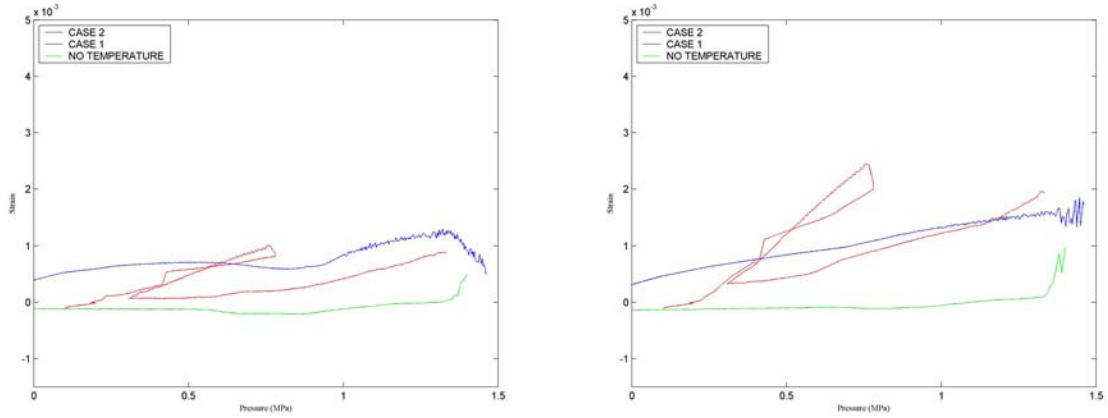

Figure 12.67 Pos. 19-Rebar strain outside layer, meridional direction, el 0.25, az 135 (left).

Figure 12.68 Pos. 20-Rebar strain inside layer, meridional direction, el 1.43, az 135 (right).

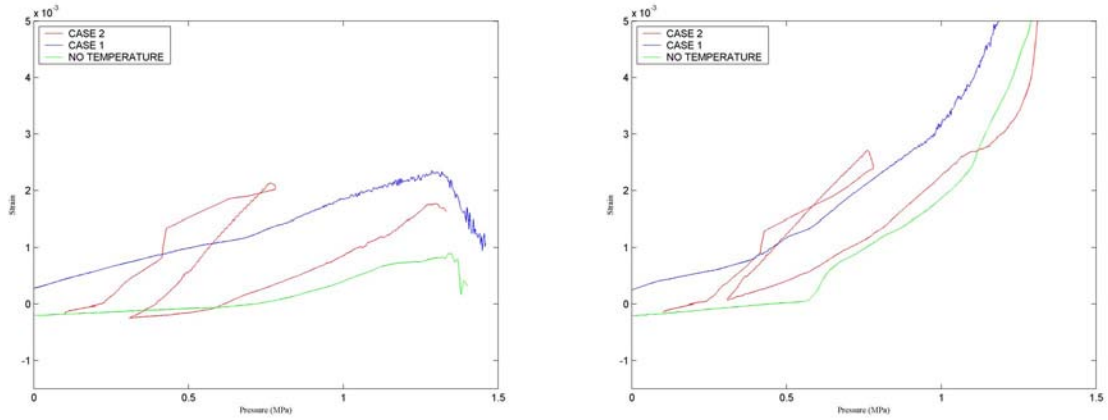

Figure 12.69 Pos. 21-Rebar strain outside layer, meridional direction, el 1.43, az 135 (left).

Figure 12.70 Pos. 22-Rebar strain outside layer, hoop direction for el 6.2 and az 135 (right).

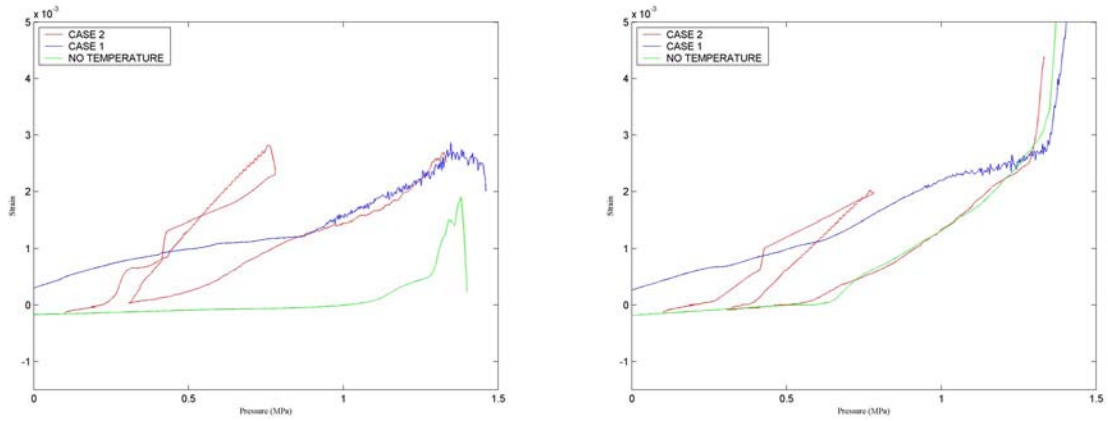

Figure 12.71 Pos. 23-Rebar strain outside layer, meridional direction, el 6.2 and az 135 (left).

Figure 12.72 Pos. 24-Rebar strain outside layer, hoop direction, el 10.75 and az 135 (right).

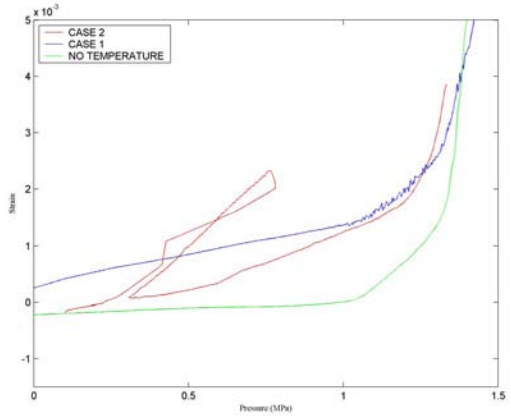

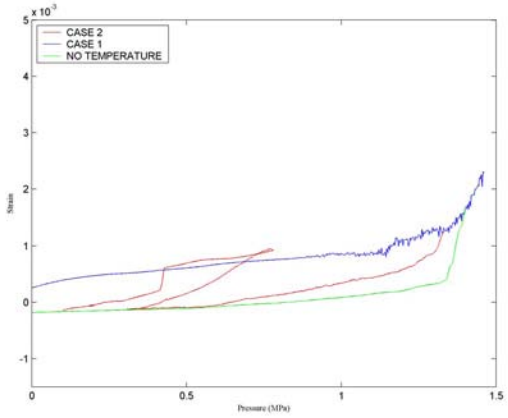

Figure 12.73 Pos. 25-Rebar strain inside layer, meridional direction, el 10.75, az 135 (left).

Figure 12.74 Pos. 26-Rebar strain outside layer, meridional direction, el 10.75, az 135 (right).

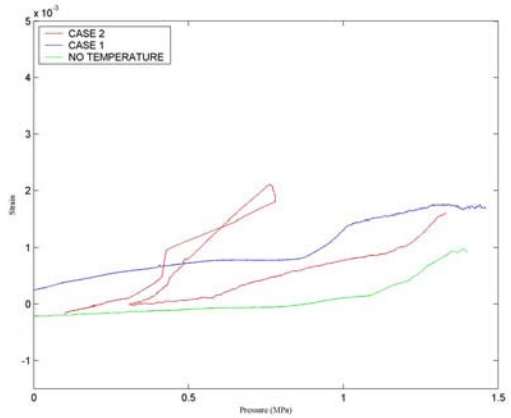

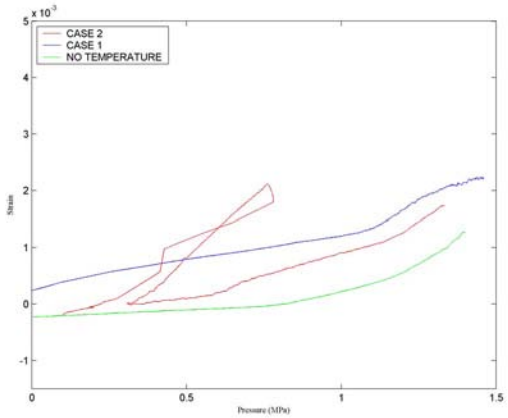

Figure 12.75 Pos. 27-Rebar strain outside layer, hoop direction for el 14.55 and az 135 (left).

Figure 12.76 Pos. 28-Rebar strain inside layer, meridional direction, el 10.75, az 135 (right).

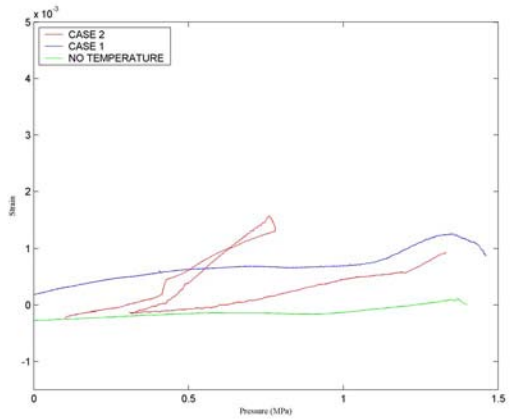

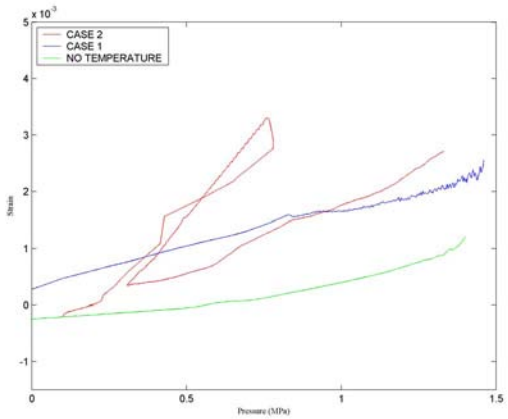

Figure 12.77 Pos. 29-Rebar strain outside layer, meridional direction, el 10.75, az 135 (left).

Figure 12.78 Pos. 30-Rebar strain inside layer, meridional direction, el 0.05, az 90 (right).

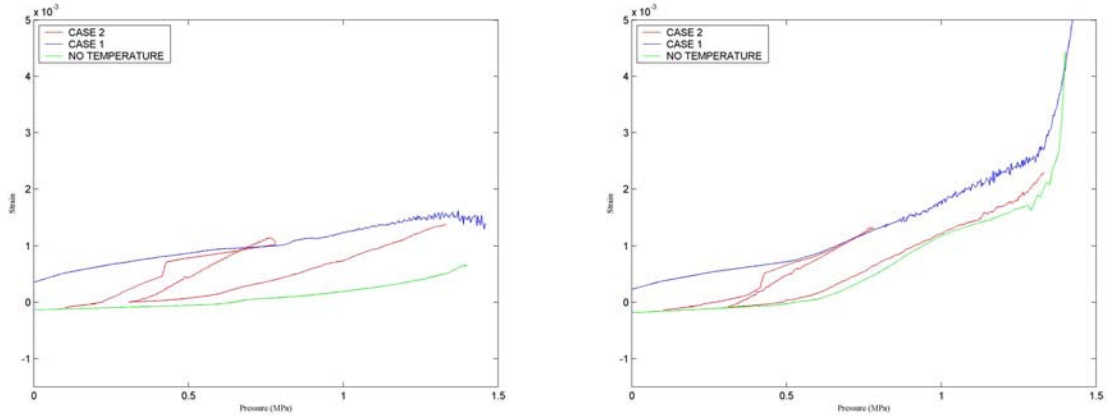

Figure 12.79 Pos. 31-Rebar strain outside layer, meridional direction, el 0.05 and az 90 (left).
Figure 12.80 Pos. 32-Rebar strain outside layer in hoop direction for el 6.2 and az 90 (right).

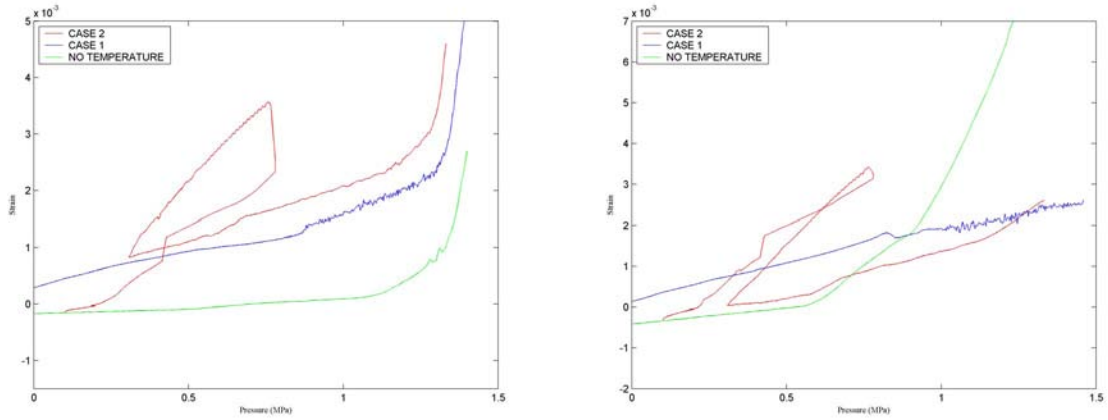

Figure 12.81 Pos. 33-Rebar strain outside layer, meridional direction, el 6.2 and az 90 (left).
Figure 12.82 34.

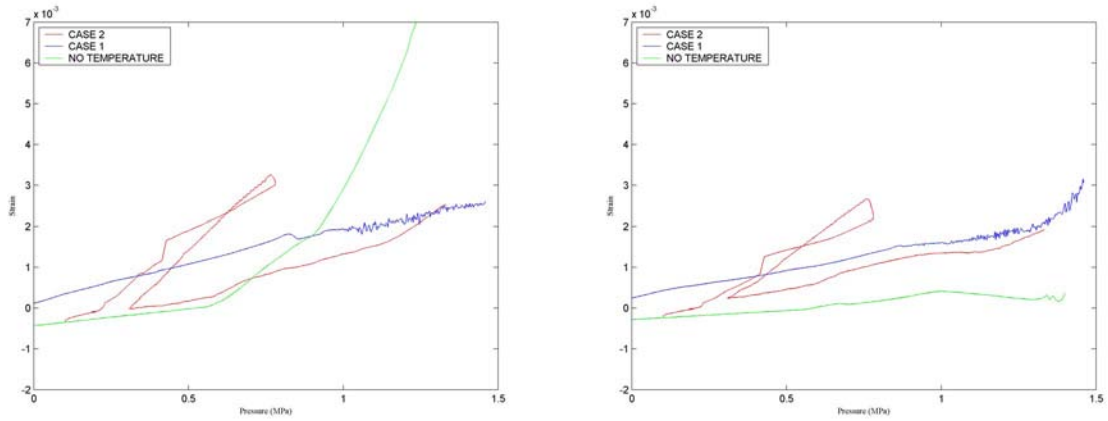

Figure 12.83 Pos. 35-Liner strain in meridional direction for el 0.01 and az 0 (left).
Figure 12.84 Pos. 36-Liner strain in meridional direction for el 0.25 and az 135 (right).

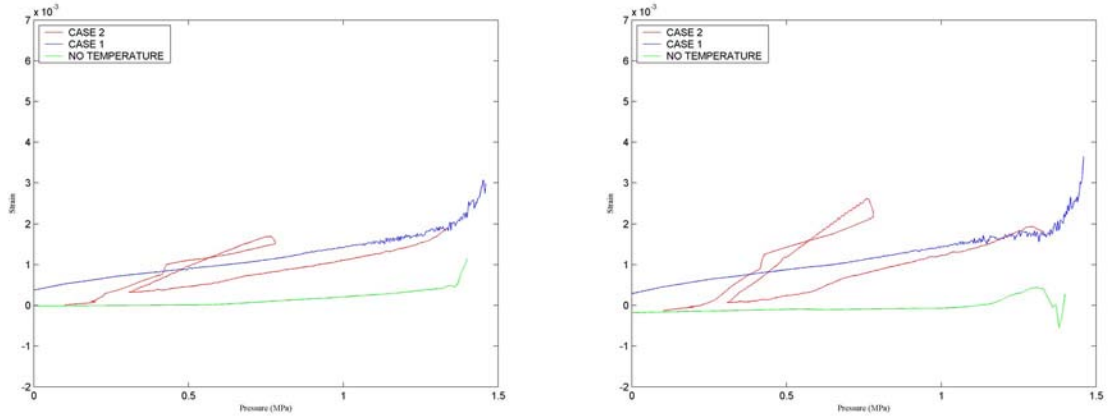

Figure 12.85 Pos. 37-Liner strain in hoop direction for el 0.25 and az 135 (left).

Figure 12.86 Pos. 38-Liner strain in meridional direction for el 6.2 and az 135 (right).

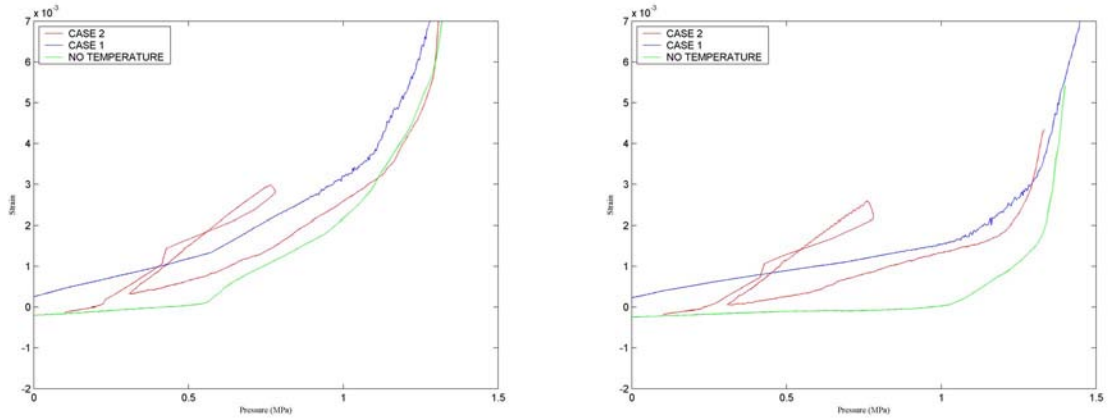

Figure 12.87 Pos. 39-Liner strain in hoop direction for el 6.2 and az 135 (left).

Figure 12.88 Pos. 40-Liner strain in meridional direction for el 10.75 and az 135 (right).

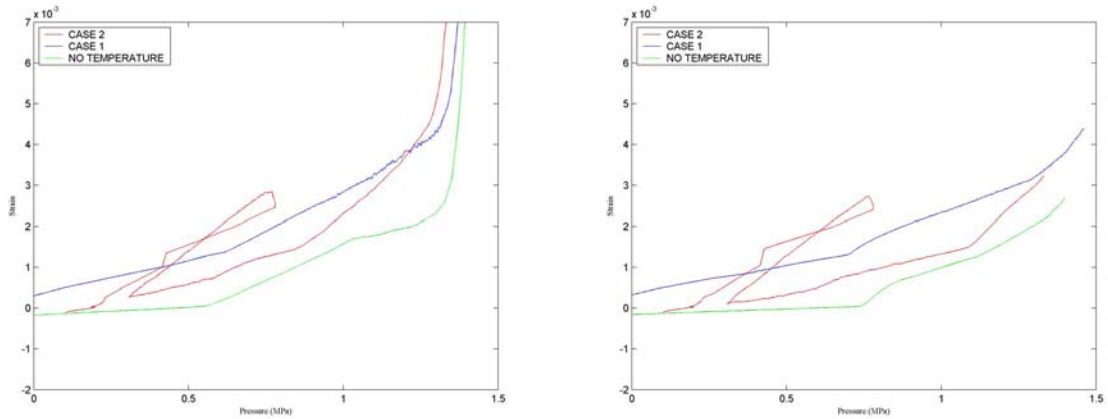

Figure 12.89 Pos. 41-Liner strain in hoop direction for el 10.75 and az 135 (left).

Figure 12.90 Pos. 42-Liner strain in meridional direction for el 16.13 and az 135 (right).

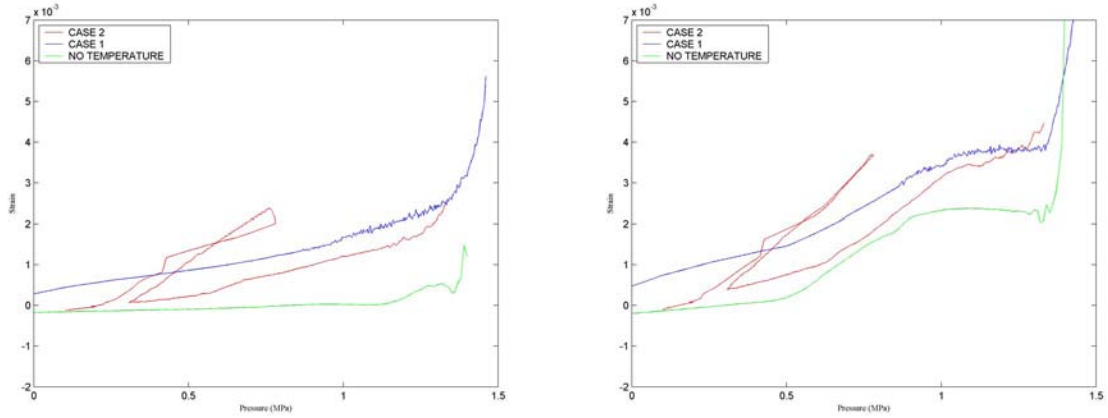

Figure 12.91 Pos. 43-Liner strain in meridional direction for el 6.2 and az 90 (left).

Figure 12.92 Pos. 44-Liner strain in hoop direction for el 6.2 and az 90 (right).

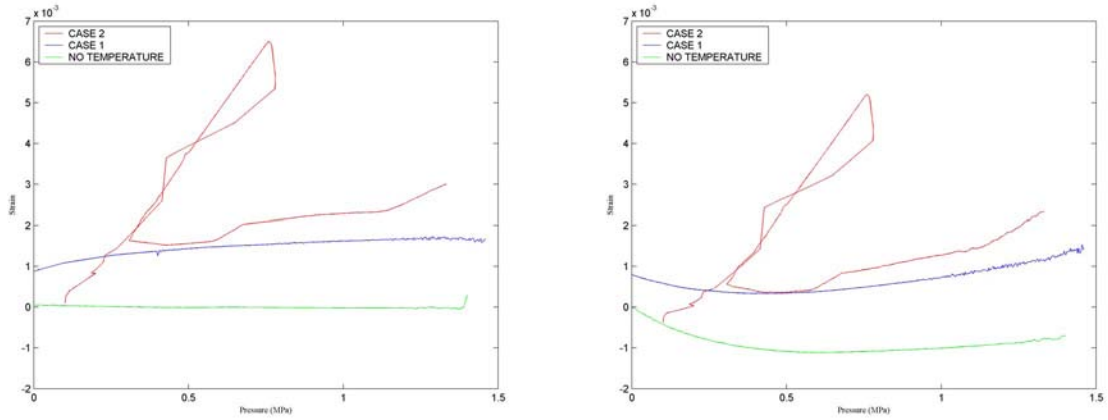

Figure 12.93 Pos. 45-Liner strain in hoop direction for el 4.675 and az 334 (left).

Figure 12.94 Pos. 46-Liner strain in hoop direction for el 4.525 and az 58 (right).

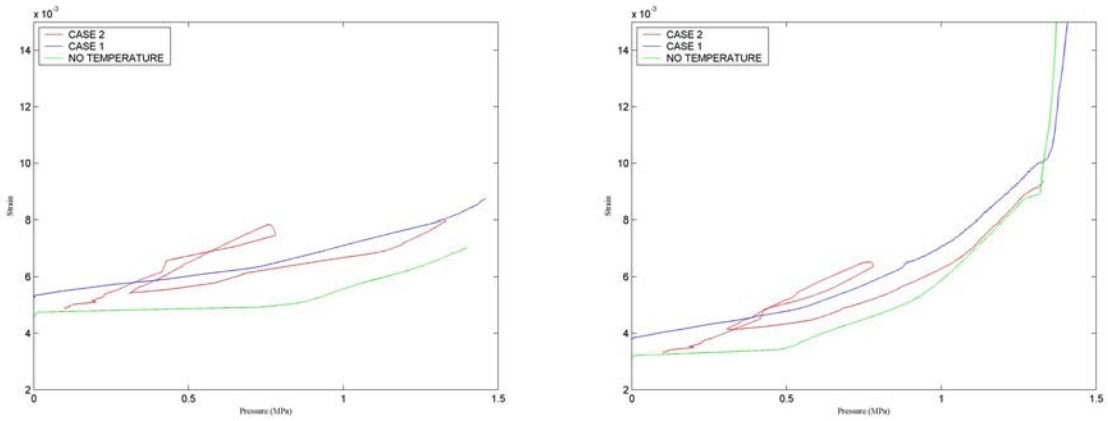

Figure 12.95 Pos. 48-Tendon strain in vertical direction for el 15.6 and az 180 (left).

Figure 12.96 Pos. 50-Tendon strain in hoop direction for el 6.58.6 and az 90 (right).

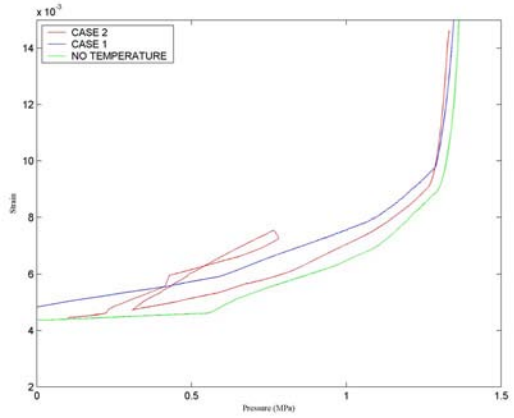

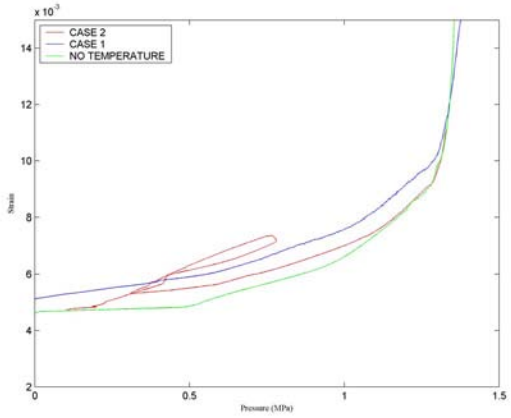

Figure 12.97 Pos. 51-Tendon strain in hoop direction for el 6.58 and az 180 (left).

Figure 12.98 Pos. 52-Tendon strain in hoop direction for el 6.58 and az 280 (right).

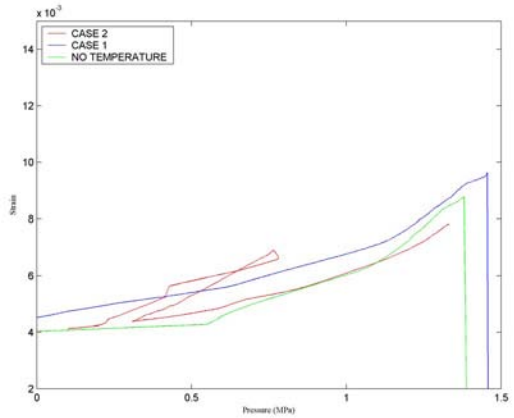

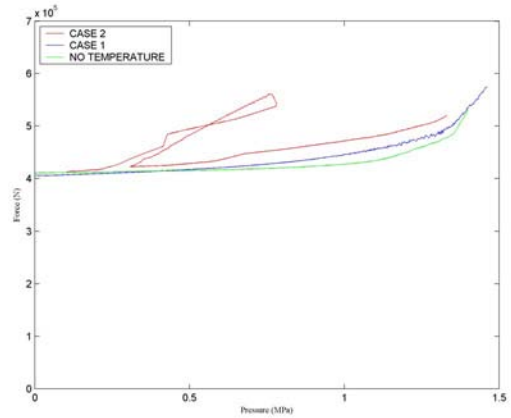

Figure 12.99 Pos. 53-Tendon strain in hoop direction for el 4.57 and az 0 (left).

Figure 12.100 Pos. 54-Tendon force in hairpin direction for el-1.16 and az 241 (right).

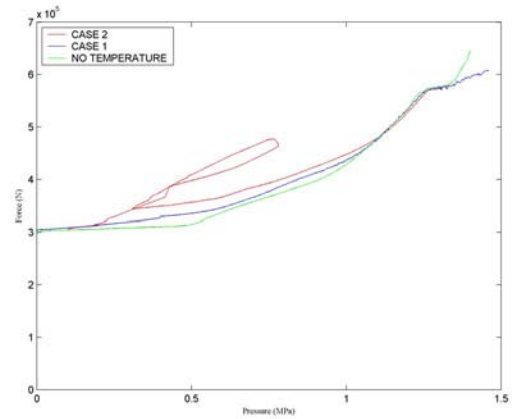

Figure 12.101 Pos. 55-Tendon force in hoop direction for el 6,58 and az 275.

PART III

CONCLUSIONS

13. CONCLUSIONS

13.1 Summary

The design events for a reactor containment usually refers to accidental loading conditions for which leak-tightness and load-bearing capacity should be verified. This involves the containment being loaded far into the non-linear range, putting high demands on the engineering simulations. It is therefore of vital importance to ensure that the methods applied for advanced structural analysis can be verified and validated.

This report presents a method of utilizing the finite element technique for determining the load effects due to internal overpressurization in combination with temperature loads for pre-stressed concrete reactor containments. The method is verified and validated by comparison with test data from a large-scale overpressurization test performed on the NUPEC/NRC 1:4-scale model of a prestressed concrete containment vessel model at Sandia National Laboratory, USA. The prototype for the model is the containment building of unit 3 at the Ohi Nuclear Power Station in Japan, an 1127 MW Pressurized Water Reactor (PWR) unit.

The structural response predicted by applying a three-dimensional model approach agrees very well with registred test data. Pressure levels related to cracking of concrete, yielding of the steel liner, and the collapse of the containment are captured in conformity with registred test data. To capture the pressure level at which rupture of the steel liner occurs, more detailed local models are needed, this is beyond the scope of this report. However, the analysis methods are capable of catching the zones where excessive yielding of the steel liner occurs, corresponding well with the first registred liner rupture position. The applied analysis method accuratly predicts the displacements of the containment, and strains in the steel liner, the rebars and the pre-stressing tendons.

Some different approaches on how to model unbonded pre-stressing tendons have been evaluated in the report. The chosen approach predicts pre-stressing forces very well in accordance with registred test data. This method makes it possible to take into consideration the transition from the initial uneven pre-stressing force distribution along the tendons, to a more or less even distribution along the tendons during pressurization.

The proposed method can be used for the design of new containments as well as for the structural verification of existing containments. The method can be applied in case of design or evaluation against specified pressure levels and acceptance criterias according to national standards, or to calculate the leak-tightness and load-bearing capacity in order to estimate the safety margins of the structure. Furthermore, the analysis results can be used as a point estimate of leakage or structural collapse to be used in a probability safety assessment (PSA) of the plant.

It is also possible to utilize the method when verifying safety-related structures for other types of accidental load effects.

13.2 Pressure load analysis

The structural response predicted by applying a three-dimensional model approach agrees very well with registred test data. Pressure levels related to cracking of concrete, yielding of the steel liner, and the collapse of the containment are captured in conformity with registred test data. To capture the pressure level at which rupture of the steel liner occurs, more detailed local models are needed, this is beyond the scope of this report. However, the analysis methods are capable of catching the zones where excessive yielding of the steel liner occurs, corresponding well with the first registred liner rupture position. The applied analysis methods also accuratly predict the displacements of the containment, and strains in the steel liner, the rebars and the pre-stressing tendons.

13.3 Pressure + temperature load analysis

For cases when a temperature load is applied simultanuosly with the pressure load the response will be quite different compared to pressure load only. The load effect is dependent on the temperature scenario, i.e. the maximum value of the temperature, and the rate of the temperature changes. For the case 1 temperature load scenario, onset of global yielding in the liner is delayed, while the ultimate capacity is unchanged. For the case 2 scenario however, yielding first in compression, and then in tension, occurs at rather low pressure levels due to a combination of the rapid changes in temperature and high temperature values inside the containment, this giving rise to restrained temperature expansion/contraction of the steel liner.

The temperature load increases the deformation of the containment due to an increase in mean temperature, while the temperature gradient gives rise to early cracking of the outside part of the concrete wall.

The maximum load-bearing capacity of the containment can be decreased by the increase in temperature. This due to the fact that the strength of the steel material is decreasing at elevated temperatures. However, for the cases studied in this report, the stipulated strength-temperature dependency does not result in such a decrease in strength.

13.4 Modeling technique

The radial deformation response of the containment structure due to overpressurization load is to a large extent influenced by “disturbed regions” such as the pre-stressing buttresses and the major penetrations. Therefore an axi-symmetrical model most often is not sufficient enough to capture the true response of a prestressed concrete reactor containment, preferably a fully three-dimensional model should be used instead. For example, bending effects near the buttresses are not captured in axi-symmetrical models. These load effects generally gives rise to a much earlier start of liner yielding.

A two step analysis method is utilized in this report to analyze the combined effect of pressure and temperature loading. In the first step, the temperature field is calculated using the actual temperature load history. In the second step a quasi-static mechanical analysis is carried out with the temperature result from

step one as input data. In this second analysis, a compressed time scale is used in order to minimize the analysis runtime.

Special focus has been put on how to model unbonded pre-stressing tendons. Each tendon is modeled separately, then contact formulation is applied to correctly simulate the friction interaction and slippage between concrete and tendons during increased pressure loads. The same technique can also be applied if the interaction between liner and concrete needs to be modeled, as for the Scandinavian design with an embedded steel liner, or in detailed studies of the liner to evaluate the leak-tightness capacity of the containment.

The rupture of an unbonded pre-stressing tendon occurs at the location where the ultimate capacity of the tendon is first reached, while the rupture position of the containment wall can arise elsewhere, for example at a transition zone with smaller reinforcement area. This effect is also possible to capture using the tendon modeling technique proposed in this report.

Furthermore, the effect of strained concrete between cracks (tension stiffening) has been discussed, and how to take this into consideration in the FE analysis. Two methods have been tested; applying a sufficiently small element size, or to artificially increase the fracture energy of the concrete.

13.5 Solver technique

13.5.1 General

Implicit or explicit solver techniques are available when carrying out finite element analysis. They are briefly presented below.

13.5.2 Implicit method

The implicit method is based on static equilibrium and is characterized by the simultaneous (implicit) solution of a set of linear equations. For a model to be in static equilibrium, the net force acting on each node must be zero. After a full set of linear equations has been assembled, this set of equilibrium equations is then solved simultaneously and the unknown nodal displacements are obtained. In non-linear analysis, within each increment an iteration is carried out until equilibrium convergence is reached. If contact formulation is used, an additional iteration procedure is necessary to satisfy also the contact constraints. In case of severe discontinuity, it may happen that neither the equilibrium nor contact criterias are met and, as a result, no solution can be obtained at all. This problem is further emphazised using highly non-linear material models such as for concrete.

To be able to achieve convergence in the analysis, the analyst sometimes applies increased tolerances regarding the nodal force equilibrium, or applies some form of artificial damping into the model. When doing so, care has to be taken in order not to alter the analysis results.

13.5.3 Explicit method

In the explicit procedure, the displacements, velocities and accelerations of each node are advanced explicitly through time. This means that the state of the model at the end of an increment is solely based on the displacements, velocities and accelerations at the beginning of the increment. The nodal velocities at the end of the increment are obtained assuming that the acceleration is constant during a small time increment. Similarly, the nodal displacements at the end of the increment can be computed by adding the displacements during the time increment to the displacements at the beginning of the increment. If contact formulation is included, it is first assumed that no contact occurs. If, at the end of the increment, overclosure is found, corrections for the kinematics of the contacting bodies are carried out to prevent penetration from taking place. Unlike the implicit approach, no convergence criteria are considered and, as a result, contact simulations proceed smoothly.

The analyst must assure that the timestep is small enough due to the fact that this method is conditionally stable. Stability is maintained using a sufficiently short timestep, based on the so called Courant-Friedrichs-Lewy stability condition, stating that no disturbance should be able to pass across more than one element width during a computational cycle (timestep).

13.5.4 Discussion

In section 4.4 of this report a parametrical study was carried out comparing implicit and explicit solver techniques. No major differences in results occurred. For the main analysis in this report, the explicit method has been used, and the results have proved to be in good agreement with registred test data from the pressurization test.

When utilizing non-linear constitutive models of concrete, convergence of analysis can be rather cumbersome using implicit solvers as discussed in section 13.5.2. It is often necessary to include contact formulations in the analysis to be able to correctly model unbonded pre-stressing tendons, or to simulate the interaction between concrete and steel liner. This is emphasized for the Scandinavian containments which include an embedded steel liner.

The explicit method provides a powerful technique to perform non-linear quasi-static analysis of containment structures. When dealing with material non-linearities and problems involving contact, the explicit solver provides a more straightforward approach compared to the implicit solver. The results in this report also verify that the explicit solver, provides accurate results compared to test data.

13.6 Acceptance criterias for leak-tightness

One major issue to be dealt with is how to state acceptance criteria for best estimate of leakage in containments with a steel liner as the primary leak-tightness barrier. At which strain level will the liner tear? In Scandinavian design practise a conservative approach has been taken, not allowing the stress in the liner to reach the yield stress [10]. In ASME [8], a minor yielding is acceptable. These

assumptions are valid for design, or for structural verification, and are therefore of course choosen with a great amount of conservatism due to the high safety demands.

A summary of different approaches on how to evaluate a best estimate of the real tear capacity of the steel liner has been presented in [9]. Here it concludes that a strain based capacity criterion comparing the plastic strain with some maximum allowable strain value is sufficient for containment analysis, in case the loading is dominantly monotonical. A method is presented on how to use uni-axial test values regarding the limit strain capacity of the steel, and to adjust this value using knock-down factors to arrive at a maximum allowable value to be used in best estimate analysis of containment leak-tightness. For design purposes however, values given in standards should be used. The knock-down factors given in [9] take into consideration multi-axial stress state, sophistication level in the FE analysis model, and variation in material properties. Especially the knock-down factor for FE model sophistication is due to a subjective choice of the analyst.

In the test setup of the model containment, the tear in the liner at leakage was heavily influenced by workmanship [2], giving rupture of the steel liner at an average hoop strain of the liner of only 0.17%, to be compared with an uni-axial strain capacity of the order of 10-20% [2]. However, due to the scaling effects the influence of workmanship when compared to “real” structures is probably overestimated. This illustrates the difficulty in stating allowable values of maximum strain.

Therefore, further investigations are probably needed regarding how to approach strain capacity issues to be used in evaluation of the best estimate of the leak-tightness capacity of containment structures, including taking into account the sophistication level of the FE model.

13.7 “Leak before break”?

There is a risk for rupture of the containment before leakage occurs, due to tears in the steel liner,. This due to the higher strain limit in the steel liner compared to the pre-stressing tendons. In Sweden, there are requirements on the containment design to include a pressure relief system, venting out the gas if a certain stipulated internal overpressure is exceeded. The gas is then vented via a scrubber building before being released to the outside air.

During the pressurization test of the model containment, the onset of leakage was influenced by workmanship, giving rise to leakage at a rather low strain level of the liner. This is probably not the case for real 1:1-scale structures.

The influence of temperature loading on the first leakage depends on the temperature time history as discussed in section 13.3 above. It can both delay, or advance, the start of yielding of the steel liner depending on the maximum value of the temperature, and the rate of temperature changes. Also, the maximum burst capacity of the containment can to some extent be decreased by increased temperature (see section 13.3).

14. REFERENCES

[1] Jovall O. et al, *Concrete containment management and modeling, CONMOD*, in Proceedings of the 17th International Conference on Structural Mechanics in Reactor Technology, SMiRT, Prague, 2003.

[2] Hessheimer M.F. et al, *Overpressurization test of a 1:4-scale prestressed concrete containment vessel model*, NUREG/CR-6810, SAND2003-0840P, Sandia National Laboratories, Albuquerque, 2003.

[3] *ABAQUS Analysis Users Manual*, version 6.4, ABAQUS Inc., Providence 2002.

[4] Dameron R.A. et al, *Posttest analysis of the 1:4-scale prestressed concrete containment vessel model*, NUREG/CR-6809, SAND2003-0839P, Sandia National Laboratories, Albuquerque, 2003.

[5] Dameron R. et al, *Analysis of axisymmetric concrete containment vessel (PCCV) including thermal effects. A summary of temperature section results, analytical assumptions and technical approach for use by the ISP48 analysis exercise participants*, Sandia National Laboratories, 2004.

[6] Ghali A, Favre R, *Concrete structures, stresses and deformations, second edition*, E & F Spon, 1994.

[7] Isenberg J., Editor, *Finite element analysis of reinforced concrete structures II*, ASCE 1993.

[8] *ASME boiler & pressure vessel code, section III, division 2 – Code for concrete containments*, ASME 2004.

[8] Cherry J.L., Smith J.A, *Capacity of steel and concrete containment vessels with corrosion damage*, Sandia National Laboratories, Albuquerque, 2001.

[10] Jovall O., Larsson J.A, Östlund L., *Design rules for buildings at nuclear facilities, DRB:2001* (in Swedish), Scanscot Technology AB/Barsebäck Kraft AB/OKG Aktiebolag 2002.

[11] *CEB-FIP Model Code 1990*, Thomas Telford Services Limited 1993.

APPENDIX 1: ISP 48

Phase 1: Data collection and identification

The group of members in ISP 48 agreed on the following basic principles: all participants should use the same data, calculate the same structure, and report on the same positions for comparison. It was also agreed that the most representative data should be used.

It was decided that

- The chairman would send the list of requests for completion to all participants within a week for all of them to comment within one week. The list will then be sent to SNL.
- SNL would provide the list of available data taking into account the list mentioned above to the extent possible. Deadline is Jan 15.
- Considering that participants may use different models, data needed may be different. Consequently, participants would review SNL's list and see if data fitted. Comments would have to be sent to SNL by end of February.
- SNL would deliver the data in a format appropriate with the use of computer codes and standard softwares.

With regard to the location of measurements, the group agreed that it would be easier to use the locations as for the round robin (displacement, strain, rebars strain, etc). The group would check if it was complete enough and make suggestion with regard to possible addition by Jan 15.

Phase 2: Calculation of the LST test (Limit State Test) performed at Sandia - Mechanical loading

Phase 2 will start on April 1, 2003 and delivery of individual reports is expected by the end of Dec 2003.

The following items were agreed upon:

- Computation up to leakage. It was nevertheless recognized that assessment of the time and the value of the leakage was very complicated.
- Displacements and stresses would be compared with test results.
- Concrete cracking, liner tearing and cable rupture would be compared with test results
- Individual reports would be issued by Dec 31, 2003 to SNL and circulated through participants in January 2004.

With regard to Phase 2 synthesis report by SNL, it was agreed that it would include:

- Comparison of all results including sensitivity of the results to models

- Proposals for transposition to real size containments.

With regard to the completion of Phase 2, it was agreed that a meeting would be held in Feb 2004 with the following preliminary agenda:

- Presentation of Phase 2 synthesis report
- Individual presentations on phase 2 calculations
- Conclusions by the group including thoughts on transposition to real size containments
- Definition of Phase 3 exercise including the data and thermal hypothesis to be used for the exercise

Phase 3: Calculation of the response under both mechanical and thermal loadings.

Considering that models would have been checked out against the test under mechanical loading after Phase 2, the objective of Phase 3 is to study the effect of temperature on the global behavior of the structure.

Although there was no test supporting this calculation, the group agreed that an increase in temperature was better and more realistic than a constant temperature. They thus approved the proposal made by IRSN to use the pressure and thermal loadings as defined in WASH1400. IRSN will provide the group with the evolution of temperature and pressure versus time by the end of March 2003.

As said before, the group decided to discuss thoroughly thermal hypothesis and data to be used during the phase 2 meeting. Nevertheless, the following were agreed upon:

- Temperature will be applied on the surface of the liner;
- Contact (i.e. no air gap) will be assumed between the liner and the concrete. The transfer coefficient will be specified;
- Boundary conditions will be the same for all participants and will be specified;
- Calculation should be performed up to 24 hours or up to rupture whichever comes first;
- As to results, it was decided to compare, at several times to be defined:
    - the temperature profile through the thickness;
    - tendon, liner stresses (to be determined);
    - displacements (less points that in phase 2 will be selected based on phase 2 results);
    - crack patterns;
    - etc

Individual reports will be delivered at the end of phase 3.

The duration of Phase 3 is still under discussion. This item is discussed under Phase 4 below.

Phase 4: Reporting, Workshop

The group decided that the ISP should be completed and presented at the June 2005 CSNI meeting.

Based on that, it was agreed that:

- a Workshop would be held in April 2005 to allow time for conclusions and recommendations to be written;
- the individual phase 3 reports should be delivered to SNL, copy to all, about 6 months before (i.e Nov 2004);
- between those dates, SNL would draft the phase 3 synthesis report and the outline of the draft final synthesis report with inputs from all participants.

ISP 48 time-schedule

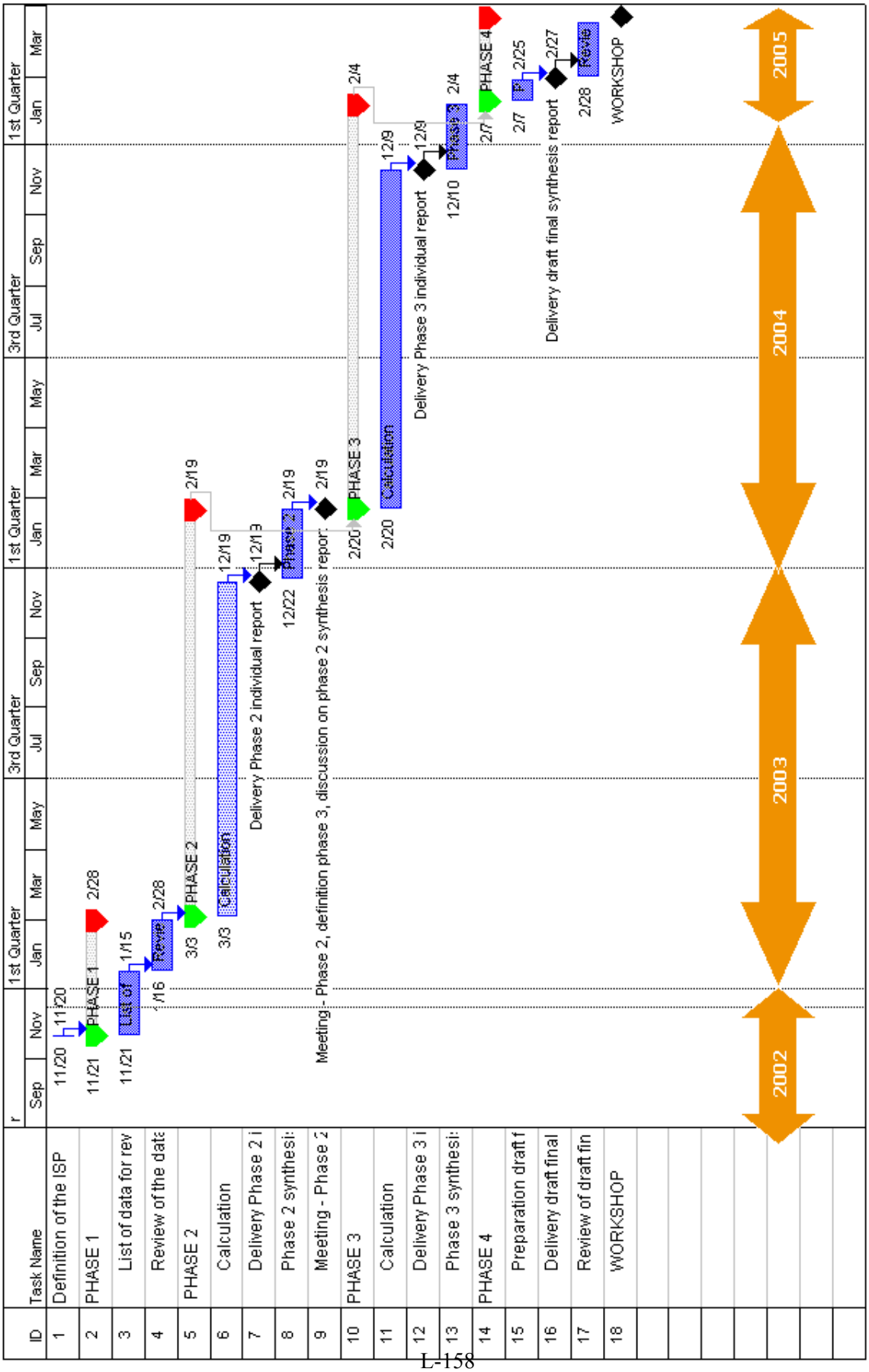

ISP 48 participants

Country	Organization	Name
CZECH REPUBLIC	EGP	Jan Maly
FINLAND	Fortum	Pentii Varpasuo
FRANCE	EDF	Jean-Pierre Touret
		Jean-Luc Valfort
	IRSN/CEA	Thierry Charras
		Georges Nahas
GERMANY	GRS	Hans Grebner
		Jurgen Sivers
	IFMB/UK	Christoph Niklasch
INTERNATIONAL	OECD/NEA/CSNI	Eric Mathet
JAPAN	JNES	Satoru Shibata
	JPRG	Takeshi Kawasato
KOREA (REPUBLIC OF)	KAERI	Hong-Pyo Lee
		Jeong-Moon Seo
	KOPEC	Nam-Hoo Lee
SLOVAK REPUBLIC	VUEZ	Milan Prandorfy
SWEDEN	Scanscot	Ola Jovall
		Mikael Pålsson
UNITED KINGDOM	BE/HSE/NNC	James Curley
		Graham E. Doughty
		Michael W. Johnston
		Nawal Prinja
		David Shepard
UNITED STATES OF AMERICA	NRC/SNL/DEA	Syed A. Ali
		Robert A. Dameron
		Michael F. Hessheimer
		Abdul Sheikh